

Studying Cosmic Evolution with the XMM-Newton Distant Cluster Project:

X-ray Luminous Galaxy Clusters at $z \gtrsim 1$
and their Galaxy Populations



Dissertation der Fakultät für Physik
der Ludwig-Maximilians-Universität München

vorgelegt von

Rene Fassbender

aus Diez/Lahn

München, Oktober 2007

1. Gutachter: Prof. Dr. Hans Böhringer
2. Gutachter: Prof. Dr. Andreas Burkert

Tag der mündlichen Prüfung: 29. November 2007

Dedicated to the memory of
Peter Schuecker
(1959–2006)

Beobachtung Kosmischer Entwicklung mit dem XMM-Newton Distant Cluster Project: Röntgenhelle Galaxienhaufen bei $z \gtrsim 1$ und ihre Galaxienpopulationen

Zusammenfassung

Röntgenhelle Galaxienhaufen bei hoher Rotverschiebung ($z \gtrsim 1$) ermöglichen einzigartige, aber herausfordernde, Untersuchungen der kosmischen Entwicklung dieser größten Objekte im Universum, der baryonischen Materie in Form des heißen Haufengases (Intracluster Medium, ICM), ihrer Galaxienpopulationen und des Einflusses der mysteriösen Dunklen Energie. Das Hauptziel der vorliegenden Doktorarbeit ist das Erstellen der Datengrundlage für das XMM-Newton Distant Cluster Project (XDCP). Diese neue Himmelsdurchmusterung im Röntgenlicht konzentriert sich auf die systematische Suche und Identifizierung von Galaxienhaufen bei den höchsten Rotverschiebungen von $z \gtrsim 1$ mittels einer gezielten Vorauswahl von ausgedehnten Röntgenquellen, Nachbeobachtungen in zwei photometrischen Bändern zum Nachweis und zur Entfernungsschätzung der Objekte sowie der abschließenden spektroskopischen Bestätigung. Als ersten Schritt habe ich insgesamt 80 Quadratgrad (469 Felder) langbelichteter Röntgenbeobachtungen aus dem XMM-Newton Datenarchiv mit einem neu entwickelten automatisierten Datenreduktionssystem analysiert. Damit konnte ich annähernd 1000 ausgedehnte Quellen als Galaxienhaufen-Kandidaten nachweisen, von denen sich 75% durch vorhandene optische Daten als Haufen und Gruppen bei $z \lesssim 0.6$ identifizieren ließen. Die verbleibenden ca. 250 Kandidaten mit typischen Röntgenflüssen von $\simeq 10^{-14} \text{ erg s}^{-1} \text{ cm}^{-2}$ (0.5–2.0 keV) erfordern weitere Schritte, um als entfernte Galaxienhaufen bestätigt werden zu können.

Dafür entwickelte ich eine neue Nahinfrarot-Beobachtungsstrategie, mit der sich die Identifizierung der ausgedehnten Röntgenquellen mittels Z- und H-Band Aufnahmen effizient durchführen lässt und die zur Rotverschiebungsabschätzung anhand der Z–H Farbe der ‘Red-Sequence’ der Frühtypgalaxien dient. Um das Potential dieser Methode voll auszuschöpfen, konzipierte ich ein neues Nahinfrarot-Datenverarbeitungsprogramm, mit dem die Nachbeobachtungen zweier Kampagnen mit dem 3.5 m Teleskop des Calar Alto Observatoriums für 25% der 250 entfernten Galaxienhaufen-Kandidaten ausgewertet wurden. Anhand dieser Daten konnte ich als erstes Hauptergebnis insgesamt mehr als 20 photometrisch bestätigte Neuendeckungen von entfernten röntgenhellen Galaxienhaufen bei $z \gtrsim 0.9$ nachweisen.

Desweiteren hat es die neue Z–H Beobachtungsmethode ermöglicht, erstmalig eine Galaxienhaufen-Stichprobe über die gesamte Rotverschiebungsspanne von $0.2 \lesssim z \lesssim 1.5$ zu untersuchen. Durch den Vergleich der beobachteten Farbentwicklung der ‘Red-Sequence’ mit Entwicklungsmodellen konnte ich die Entstehungsepoche der Sternpopulationen der Frühtypgalaxien auf $z_f = 4.2 \pm 1.1$ einschränken und damit ihr hohes Alter bestätigen. Eine weitere Vorstudie über die H-Band Leuchtkraftentwicklung von 63 hellsten Haufengalaxien (Brightest Cluster Galaxies, BCGs) über das gleiche Rotverschiebungsintervall ermöglichte es, erstmals direkte Beobachtungshinweise dafür zu liefern, dass sich die Masse der größten Galaxien im lokalen Universum seit $z \simeq 1.5$ mindestens verdoppelt hat. Mein vorläufiges Ergebnis, dass nahe BCGs alte Sternpopulationen besitzen, ihre Masse aber erst zum Großteil über die letzten 9 Milliarden Jahre angesammelt wurde, stimmt qualitativ mit den Vorhersagen der modernsten Simulationen zur hierarchischen Galaxienentstehung und -entwicklung innerhalb des theoretischen Standardmodells überein. Die Bestätigung und Verfeinerung dieser vorläufigen Ergebnisse werden zur Entwicklung einer widerspruchsfreien Beschreibung kosmischer Entwicklung von Galaxienpopulationen und der großräumigen Struktur beitragen.

Studying Cosmic Evolution with the XMM-Newton Distant Cluster Project: X-ray Luminous Galaxy Clusters at $z \gtrsim 1$ and their Galaxy Populations

Abstract

Investigating X-ray luminous galaxy clusters at high redshift ($z \gtrsim 1$) provides a challenging but fundamental constraint on evolutionary studies of the largest virialized structures in the Universe, the baryonic matter component in form of the hot intracluster medium (ICM), their galaxy populations, and the effects of the mysterious Dark Energy. The main aim of this thesis work is to establish the observational foundation for the XMM-Newton Distant Cluster Project (XDCCP). This new generation serendipitous X-ray survey is focused on the most distant galaxy clusters at $z \gtrsim 1$, based on the selection of extended X-ray sources, their identification as clusters and redshift estimation via two-band imaging, and their final spectroscopic confirmation.

As a first step, I have analyzed 80 deg^2 (469 fields) of deep XMM-Newton archival X-ray data with a new pipeline processing system and selected almost 1000 extended sources as galaxy cluster candidates, 75% of which could be identified as clusters or groups at $z \lesssim 0.6$ using available optical data. This left about 250 candidates with typical 0.5–2.0 keV X-ray fluxes of $\sim 10^{-14} \text{ erg s}^{-1} \text{ cm}^{-2}$ in need of confirmation as distant cluster sources.

Therefore, I have adopted a new strategy to efficiently establish the nature of these extended X-ray sources and estimate their redshifts, based on medium deep Z- and H-band photometry and the observed Z–H ‘red-sequence’ color of early-type cluster galaxies. To fully exploit this technique, I have designed a new near-infrared data reduction code, which was applied to the data collected for 25% of the 250 distant cluster candidates in two imaging campaigns at the 3.5m telescope at the Calar Alto Observatory. As a first main result, more than 20 X-ray luminous clusters were discovered to lie at a photometric redshift of $z \gtrsim 0.9$.

Furthermore, the new Z–H red-sequence method has allowed a cluster sample study over an unprecedented redshift baseline of $0.2 \lesssim z \lesssim 1.5$. From a comparison of the observed color evolution of the cluster red-sequence galaxies with model predictions, I could constrain the formation epoch of the bulk of their stellar populations as $z_f = 4.2 \pm 1.1$. This confirms the well-established old age of the stellar populations of early-type galaxies in clusters. The preliminary investigation of the H-band luminosity evolution of 63 brightest cluster galaxies (BCGs) over the same redshift range provides for the first time direct observational indications that the most massive cluster galaxies in the local Universe have doubled their stellar mass since $z \simeq 1.5$. My tentative finding that nearby BCGs have old, passively evolving stellar populations and were assembled in the last 9 Gyr is in qualitative agreement with predictions from the latest numerical simulations based on the standard cold dark matter scenario of galaxy formation and evolution via hierarchical merging. The confirmation and refinement of these preliminary results will contribute to the development of a consistent picture of the cosmic evolution of galaxy populations and the large-scale structure.

Contents

1	Introduction	1
2	Galaxy Clusters as Astrophysical Laboratories	3
2.1	General Properties	3
2.2	Clusters as Dark Matter Halos	4
2.3	X-ray Properties of the Intracuster Medium	6
2.3.1	Emission mechanisms	6
2.3.2	ICM structure	8
2.3.3	ICM formation	9
2.3.4	Scaling relations	11
2.3.5	Cool core clusters	15
2.3.6	Sunyaev-Zeldovich effect	16
2.4	The Cluster Galaxy Population	17
2.4.1	Cluster versus field galaxies	18
2.4.2	Formation of ellipticals and the cluster red-sequence	20
2.4.3	Evolution and environmental effects	23
2.4.4	Brightest cluster galaxies	26
3	Galaxy Clusters as Cosmological Probes	29
3.1	Cosmological Framework	29
3.1.1	Dynamics of the expanding Universe	29
3.1.2	Distance measures	33
3.2	Cosmic Structure Formation	38
3.2.1	Growth and collapse of density perturbations	38
3.2.2	Galaxy cluster statistics	41
3.3	Cosmological Tests with Galaxy Clusters	51
4	X-ray Cluster Surveys	57
4.1	X-ray Selection	57
4.2	Local Cluster Surveys	58
4.3	Deep Surveys	62
4.4	Distant Galaxy Clusters in 2004	64

5	The XMM-Newton Distant Cluster Project	67
5.1	Motivation	67
5.2	XDCP Survey Strategy	68
5.3	Pilot Study Results	70
5.4	XMMU J2235.3-2557	71
5.5	Thesis Data Overview	75
6	X-ray Analysis of XMM-Newton Archival Data	77
6.1	XMM-Newton in a Nutshell	77
6.2	X-ray Data Archive and Survey Definition	83
6.3	Development of an X-ray Reduction and Analysis Pipeline	85
6.3.1	Search strategy	85
6.3.2	X-ray data reduction	87
6.3.3	Detection of extended X-ray sources	94
6.3.4	X-ray-optical overlays	101
6.3.5	Distant cluster optimizations	103
6.4	Source Screening and Candidate Selection	104
6.4.1	Screening steps	106
6.4.2	Classification scheme	108
6.4.3	DSS identification limit	110
6.5	Performance Tests in the COSMOS Field	112
6.6	Field and Source Diagnostics	114
6.6.1	XMM data yield and field statistics	114
6.6.2	Extended source diagnostics	117
6.7	Summary	120
7	Near-Infrared Follow-up Imaging	121
7.1	A New NIR Imaging Strategy	121
7.1.1	Motivation	121
7.1.2	Imaging strategy	123
7.1.3	Performance expectations	126
7.2	Practical Implementation	130
7.2.1	OMEGA2000 in a nutshell	130
7.2.2	Observational strategy	132
7.2.3	Imaging data overview	133
7.3	Development of a NIR Science Reduction Pipeline	134
7.3.1	Requirements and specifications	134
7.3.2	NIR reduction steps	135
7.3.3	Faint object optimization	143
7.3.4	Pipeline and instrument performance	148
7.4	Photometric Analysis	153
7.4.1	General procedure	153
7.4.2	Photometric calibration	157

7.5	Summary	161
8	Spectroscopic Follow-up	163
8.1	Basics of Spectroscopy	163
8.2	Challenges of Distant Galaxy Spectroscopy	165
8.3	Spectroscopic Data Reduction	168
8.4	Redshift Determination	170
8.5	Summary	172
9	XDCP Survey Status and Outlook	173
9.1	X-ray Analysis Status	173
9.1.1	Sky coverage	173
9.1.2	Cluster number counts	175
9.1.3	Selection function	177
9.2	Imaging Status	180
9.3	Spectroscopy Status	183
9.4	XDCP Outlook	183
9.5	Spectroscopically Confirmed $z > 1$ Clusters in 2007	185
10	High-Redshift Cluster Studies: First Results	187
10.1	The Formation Epoch of Red-Sequence Galaxies	187
10.1.1	Calibration of the Z–H method	187
10.1.2	Discussion	190
10.2	Indications for Large-Scale Structure at $z \sim 1$	191
10.2.1	Observations	191
10.2.2	Discussion	195
10.3	Summary and Conclusions	200
11	Preliminary Studies and Science Outlook	201
11.1	The Assembly History of Brightest Cluster Galaxies	201
11.1.1	BCG sample and selection	201
11.1.2	The BCG H-band Hubble diagram	203
11.1.3	Observing the BCG assembly epoch	213
11.2	Cluster Red-Sequences Studies	218
11.3	Gallery of High-Redshift Clusters	219
11.4	Summary and Conclusions	219
12	The Future of Galaxy Cluster Surveys	223
12.1	SZE Surveys	223
12.2	eROSITA	225
12.3	VADER – A Concept Study	226
12.3.1	Science case	226
12.3.2	Satellite design concept	227

12.3.3 Survey and results	228
12.4 Concluding Remarks	230
A XDCP Survey Field List	231
B List of Technical Terms and Acronyms	245

Chapter 1

Introduction

X-ray studies of clusters of galaxies have come a long way over the past four decades since the first (spurious) detection of X-ray emission from Coma and the speculations of its thermal origin (Felten *et al.*, 1966). After the first pioneering imaging X-ray telescope EINSTEIN in the late seventies and the ground-breaking success of the ROSAT mission in the nineties, we are currently in the era of the third generation of X-ray observatories led by XMM-Newton and Chandra.

Early survey results (Gioia *et al.*, 1990; Henry *et al.*, 1992) were suggestive that the population of X-ray luminous galaxy clusters exhibits a rather rapid evolution, which gave rise to the widespread belief that these objects were absent by redshifts of $z \sim 1$. This was also predicted by theory for a $\Omega_m = 1$ Universe, the standard cosmological model at the time. Only one decade later, the situation had been completely reversed based on the results of the second generation cluster surveys. After discovering the first very distant systems, Rosati (2001) summarized the status for X-ray clusters in the following statement that has remained valid until the present: “*ROSAT deep surveys have failed to show any dramatic change in the space density of clusters out to $z \sim 1$, with the exception of the most luminous, massive systems.*”

Fundamental questions within the cosmic evolution scenario have so far lacked definite observational answers: (i) What is the formation epoch of the first X-ray clusters? (ii) How does the intracluster medium (ICM) form and when does it thermalize? (iii) When and how is the ICM polluted with metals and is it pre-heated? (iv) At what epoch do cluster galaxies form? (v) What drives their evolution in clusters? (vi) How and when do the most massive galaxies in cluster centers form?

Great advances in observational cosmology over the last years have profoundly impacted the standard world model and have led to the establishment of a new ‘*concordance*’ cosmology. Galaxy clusters in this respect have provided early evidence of a low matter density Universe and have proven to be sensitive cosmological probes. Meanwhile, the properties and physical foundations of the *Dark Energy* component have emerged as the most fundamental open questions of the concordance model. One of the most promising approaches for constraining *Dark Energy* is provided by *distant* galaxy clusters.

These open and central questions of cosmic evolution gave rise to the motivation to

initiate the **XMM-Newton Distant Cluster Project (XDCP)** as a *third generation* X-ray cluster survey with special focus on $z > 1$ systems. Starting about four years ago, the XDCP is a long-term, medium-size project with the following main goals:

1. Providing $z \gtrsim 1$ galaxy clusters at various masses as **individual astrophysical laboratories** for detailed cluster and galaxy evolution studies (Chaps. 2 & 10);
2. Compiling **pathfinder samples** to characterize high-redshift clusters as cosmological probes for major upcoming SZE and X-ray surveys (Chaps. 2, 3, 9 & 12);
3. Establishing a statistically complete **cosmological distant cluster sample** selected from a sufficiently large search volume for cosmological studies (Chaps. 3 & 9).

These different survey scopes are associated with increasing time lines. Whereas the current XDCP results mainly contribute to the first category, the project focus will shift towards the pathfinder role over the next 2–3 years and cosmological studies within about 4–5 years. The main scope for this work is to *establish the observational foundation* of the XMM-Newton Distant Cluster Project. The main agenda for the thesis can be subdivided into four parts:

Part I: The *theoretical background and state-of-the-art* in distant cluster studies is discussed in Chaps. 2–4. Chapter 2 introduces the basic properties of clusters, Chap. 3 establishes the cosmological framework and discusses clusters as cosmological probes, and Chap. 4 provides an overview of X-ray surveys. Owing to the rapid developments in the field over the last decade, the introductory concept aims at a broad overview of the current status in galaxy cluster research.

Part II: The *observational strategies and methods* are introduced in Chaps. 5–8. Chapter 5 discusses the general XDCP survey strategy, Chap. 6 summarizes the X-ray analysis techniques, Chap. 7 reviews follow-up imaging methods, and Chap. 8 provides a brief overview of optical spectroscopy. The treatise of these technical chapters is aimed at providing a profound insight to the different observational methods to those without deep prior knowledge of the applied techniques.

Part III: The *survey status and first results* are summarized in Chaps. 9–11. Chapter 9 evaluates the current status of the different survey stages and discusses open survey tasks. Chapter 10 presents first science applications based on spectroscopically confirmed clusters. Preliminary results of an extended photometrically characterized cluster sample are shown in Chap. 11.

Part IV: The thesis closes with an *outlook on future developments* in Chap. 12.

Chapter 2

Galaxy Clusters as Astrophysical Laboratories

This chapter will review selected aspects of the physical foundation of galaxy clusters. The main focus will be placed on the X-ray properties of the intracluster medium (ICM) and optical characteristics of the (distant) cluster galaxy population. The discussions on X-ray emission mechanisms, ICM structure and formation, and cool cores provide the background for understanding the high-redshift cluster detection procedure. X-ray scaling relations are critical for the mass calibration, whereas the red-sequence of cluster galaxies is used for the initial redshift estimation. The sections on galaxy formation, evolution, and environmental effects set the stage for the high-redshift cluster studies in Chaps. 10 & 11. More details can be found in the classic work of Sarazin (1986), the review of Voit (2005), or Biviano (2000) for a historical treatise of clusters.

2.1 General Properties

From a modern point of view, galaxy clusters can be considered as *dark matter halos*, whose gravitational potential wells are filled with a dilute hot gas, the *intracluster medium*, and which confine the bound *cluster galaxy populations*. The mass fractions of these three dominant cluster components are approximately 80–85% for the dark matter (DM), 12–15% for the intracluster medium, and only 2–5% for the total mass of the galaxies.

Galaxy clusters occupy the *top level of the cosmic object hierarchy* and are extraordinary objects in many respects. With typical masses of 10^{14} – $10^{15} M_{\odot}$ and sizes of a few Mega parsecs (Mpc), they are by far the largest and most massive virialized objects in the Universe. Galaxy clusters also lead the object classes in terms of their *dark matter domination*, which is manifested in a mass-to-light ratio of $M/L \simeq 200 (M_{\odot}/L_{\odot})$. On the other hand, clusters are unique for studying the *baryonic matter component*, since they define the only large volumes in the Universe from which the majority of baryons emit detectable radiation.

Clusters constitute important *astrophysical laboratories* for various fields in physics

and are observed and studied over the full electromagnetic spectrum. The *dark matter component* of the matter density is the main ingredient for cosmological structure formation theories in which the largest collapsed dark matter halos are identified with galaxy clusters (see Sect. 3.2). The theoretical dark matter distribution of clusters (Sect. 2.2) has been studied in detail with elaborate numerical simulation experiments for about three decades. New observational techniques using the *weak gravitational lensing* effect caused by the *total* mass concentration of a cluster have recently enabled direct observations of the DM structure of clusters.

The *hot intracluster medium* (Sect. 2.3) can be considered as a giant plasma physics laboratory filling several Mpc^3 of volume at very low electron densities of $n_e \simeq 10^2\text{--}10^5 \text{ m}^{-3}$, an environment which is not accessible for table top experiments. Owing to the plasma temperatures of $k_B T \simeq 2\text{--}10 \text{ keV}$, corresponding to $T \simeq (20\text{--}100) \times 10^6 \text{ K}$, the thermal ICM emission gives rise to X-ray luminosities of $L_X \simeq 10^{43}\text{--}3 \times 10^{45} \text{ erg s}^{-1}$, manifesting clusters as the most X-ray luminous objects in the Universe next to Active Galactic Nuclei (AGN). X-ray observations of the intracluster medium of nearby clusters nowadays allow precision measurements of the ICM structure, its thermodynamic state, and elemental abundances. Furthermore, the ICM enables studies of hydrodynamical and plasma physical processes on the largest scales such as shock fronts, contact discontinuities, propagation of sound waves, turbulence, heat conduction, and diffusion processes.

Last but not least, the *galaxy populations* of clusters (Sect. 2.4), accessible through optical and infrared observations, can be investigated in well defined environments for detailed studies on galaxy formation, evolution, and transformation processes. We will now have a closer look at the three major individual matter components of galaxy clusters, with a focus on important properties for high-redshift cluster studies.

2.2 Clusters as Dark Matter Halos

The *missing mass problem* was established 70 years ago in a seminal paper by Zwicky (1937), who noted that the visible mass in the Coma cluster was not consistent with total mass estimates based on the *Virial theorem*. Besides these very early indications for the need of a dark matter component, the best ‘direct’ empirical evidence for the existence of dark matter to date is also provided by galaxy clusters. Recent detailed studies of the ‘Bullet Cluster’ have shown that the center of mass of the luminous matter and the total mass distribution have been spatially separated as the consequence of a major merger event (Clowe *et al.*, 2006). Figure 2.1 shows the observed X-ray emission of the cluster in pink and the weak lensing reconstructed total mass distribution in blue. The bullet-shaped ICM emission in the right part is trailing the total mass of the infalling subcluster after the initial collision. Being the dominant *baryonic* mass component, the ICM center of mass can only deviate from the total mass center if *non-baryonic dark matter* is the main cluster constituent.

¹The image can be found at http://chandra.harvard.edu/photo/2006/1e0657/1e0657_scale.jpg.

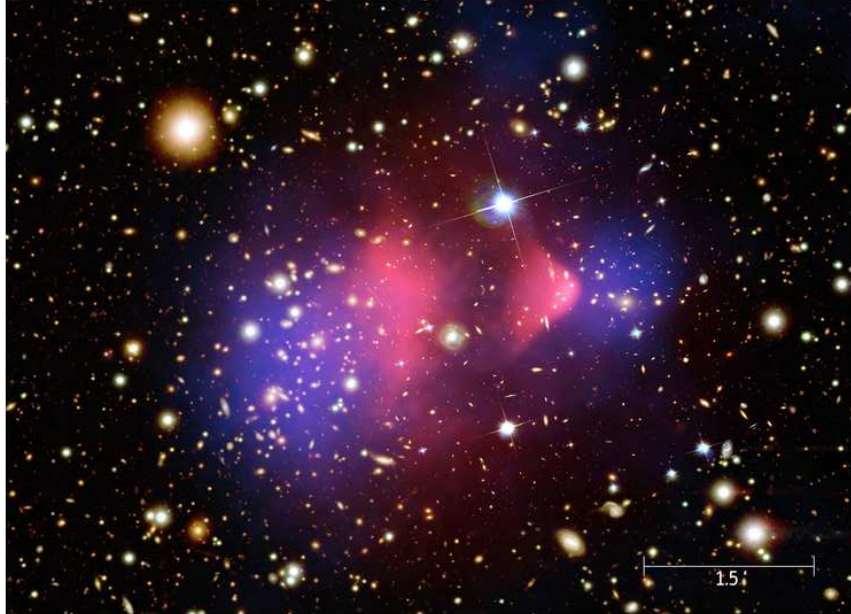


Figure 2.1: The ‘*Bullet Cluster*’ 1E 0657-56 at $z=0.296$ provides the best empirical evidence for the existence of dark matter (Clowe *et al.*, 2006). The cluster was formed through a major merger event which spatially separated the cluster constituents. The X-ray emission of the ICM, as the dominant baryonic component, is shown in pink; the blue shade indicates the weak lensing reconstructed mass concentrations, which are coincident with the galaxy overdensities. The fluid-like hot ICM gas trails the collisionless dark matter and galaxy components resulting in spatially distinct centers of the dominant visible matter (ICM) and the major mass constituent (dark matter). Image from press release¹.

The properties of dark matter halos, *i.e.* DM aggregates that form a quasi equilibrium configuration, have been investigated in detail by means of high-resolution numerical simulations. Navarro, Frenk, and White (NFW) (1997) found a universal DM halo density profile for virialized objects for the now standard *cold dark matter*² (CDM) paradigm. The widely used NFW fitting formula for the density profile $\rho_{\text{DM}}(r)$ has the form

$$\rho_{\text{DM}}(r) = \frac{\rho_s}{\left(\frac{r}{r_s}\right) \left(1 + \frac{r}{r_s}\right)^2}, \quad (2.1)$$

where r_s is a characteristic scale length and $\rho_s = \delta_c \rho_{\text{cr}}(z)$ the central density (see Equ. 3.10), which is linked to the cosmological model (see Sect. 3.2). At small radii $r \ll r_s$, the NFW profile exhibits a ‘cusp’ associated with the inner slope $\rho_{\text{DM}}(r) \propto r^{-1}$, whereas at cluster-centric distances of $r \gg r_s$ the density follows $\rho_{\text{DM}}(r) \propto r^{-3}$.

The characteristic central ‘cuspy’ shape of the NFW profile is a fundamental prediction of the CDM paradigm, quasi independent of halo mass and cosmological parameters. X-ray observations of galaxy clusters have meanwhile confirmed the predicted universal CDM profile (*e.g.* Pratt & Arnaud, 2002; Pointecouteau *et al.*, 2005), as shown in Fig. 2.3.

²*Cold* means that the kinetic energy of the particles is much smaller than their rest mass energy.

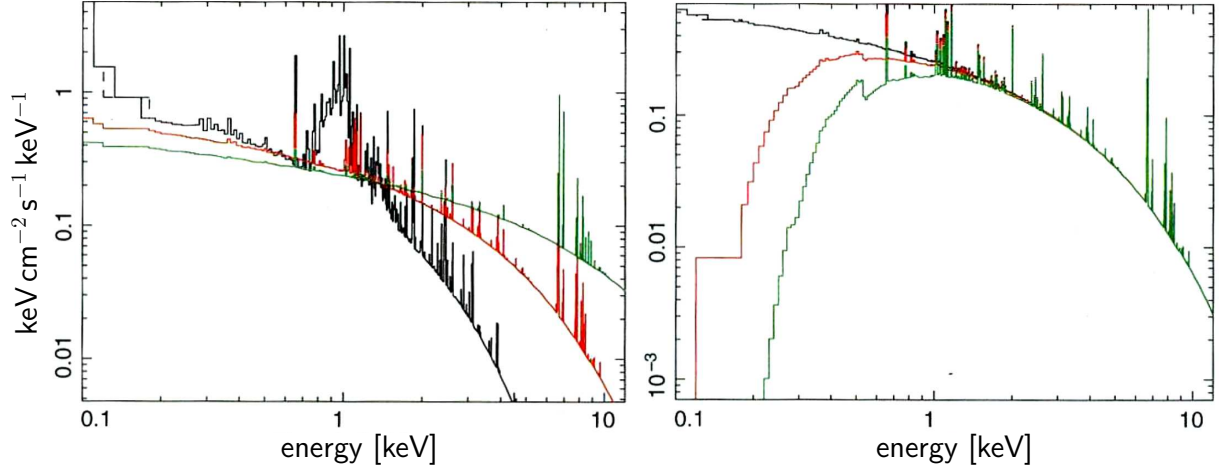


Figure 2.2: X-ray emission of the ICM. *Left:* Unabsorbed ICM model spectra of the bremsstrahlung continuum and line emission for plasmas with 0.4 solar metallicity and temperatures of 1 keV (black), 3 keV (red), and 9 keV (green). *Right:* Absorbed model spectra of $T=3$ keV observed through galactic hydrogen columns of 10^{21} cm^{-2} (green), $3 \times 10^{20} \text{ cm}^{-2}$ (red), and for the unabsorbed case (black). Plots from Schneider (2006a).

Concerning clusters at high redshift, the NFW profile predicts denser cores compared to recently formed objects as a consequence of the increased critical density $\rho_{\text{cr}}(z)$ at collapse time (see Sect. 3.2).

2.3 X-ray Properties of the Intracluster Medium

“Clusters of galaxies are X-ray sources because galaxy formation is inefficient” (Voit, 2005). About 90% of all baryons in the Universe reside in intergalactic space, but X-ray emitting gas temperatures are only reached in the deep potential wells of galaxy clusters. The main X-ray properties of the hot intracluster medium will be summarized in this section.

2.3.1 Emission mechanisms

The dominant X-ray emission mechanism for X-ray clusters at temperatures of $T \gtrsim 10^7 \text{ K}$ ($k_{\text{B}}T \gtrsim 1 \text{ keV}$) is *thermal bremsstrahlung* (free-free radiation). The intracluster medium is a collisionally ionized, optically thin plasma, which implies that essentially every emitted photon will escape from the cluster volume. The bremsstrahlung emissivity $\epsilon_{\nu}^{\text{ff}}$ for a plasma at temperature T , *i.e.* the luminosity per unit volume and frequency interval, is given by

$$\epsilon_{\nu}^{\text{ff}} \approx 6.8 \times 10^{-38} Z_i^2 n_e n_i g^{\text{ff}}(\nu, T) \frac{e^{-\frac{h_{\text{P}} \nu}{k_{\text{B}} T}}}{\sqrt{T}} \text{ erg s}^{-1} \text{ cm}^{-3} \text{ Hz}^{-1}, \quad (2.2)$$

where n_e and n_i denote³ the number densities of electrons and ions, Z_i the ion charge, and $g^{\text{ff}}(\nu, T) \propto \ln(9k_B T / (4h_P \nu))$ is the Gaunt factor, which is of order unity and corrects for quantum mechanical effects and distant collisions. Equation 2.2 implies that thermal bremsstrahlung spectra are essentially constant (in frequency space) for $h_P \nu \ll k_B T$ and exhibit a temperature dependent steep exponential cut-off at high frequencies of $h_P \nu \gtrsim k_B T$. One of the key features of X-ray observations is the proportionality of the bremsstrahlung emissivity (and all other radiation processes induced by particle collisions) to the *square* of the gas density $\epsilon_\nu^{\text{ff}} \propto n_e n_i \approx n_e^2$, which results in a peaked, high contrast signature of the central cluster regions. The total integrated (bolometric) volume emissivity of a thermal plasma with solar metal abundances is then

$$\epsilon_{\text{bol}}^{\text{ff}} = \int_0^\infty d\nu \epsilon_\nu^{\text{ff}} \approx 9.5 \times 10^{-32} \sqrt{\frac{T}{1 \text{ keV}}} \left(\frac{n_e}{10^{-3} \text{ cm}^{-3}} \right)^2 \text{ erg s}^{-1} \text{ cm}^{-3} \propto \sqrt{T}. \quad (2.3)$$

At temperatures of $T \lesssim 2 \text{ keV}$, recombination radiation (free-bound) and line emission radiation (bound-bound) become important⁴ as the ionization levels of the ICM metals decrease. For ions with an ionization potential χ_i of state i , the free-bound emissivity has the form

$$\epsilon_\nu^{\text{fb}} \propto g^{\text{fb}}(\nu, T) \frac{e^{-\frac{h_P \nu - \chi_i}{k_B T}}}{T^{\frac{3}{2}}}. \quad (2.4)$$

The most important X-ray line feature for massive clusters is the K-shell line complex of hydrogen-like iron Fe XXVI around 6.7 keV, with slightly shifted energies for other ionization states. At lower temperatures, additional important line features originate from the Fe L line complex at $\sim 1 \text{ keV}$ and ions of O, Mg, Si, S, Ar, Ca, and Ne.

Figure 2.2 illustrates in the left panel three thermal ICM model spectra for plasma temperatures of 9 keV (green), 3 keV (red), and 1 keV (black) including the bremsstrahlung continuum, recombination radiation, and line emission. The right panel shows the effects of the interstellar medium (ISM) absorption on an observed 3 keV cluster spectrum for hydrogen column densities of 10^{21} cm^{-2} (green), $3 \times 10^{20} \text{ cm}^{-2}$ (red), and in the unabsorbed case (black). The photoionization cross-section of neutral hydrogen, and similarly for the heavier elements of the ISM, exhibits approximately the photon energy dependence $a_E \propto E^{-3}$ (Cox, 2000), *i.e.* the extinction increases rapidly with decreasing energy (above the absorption edge). As can be seen from Fig. 2.2, the galactic ISM extinction introduces an effective cut-off in the observed spectrum at energies of about $\lesssim 0.3 \text{ keV}$ for the typical hydrogen columns of $2\text{--}5 \times 10^{20} \text{ cm}^{-2}$ in extragalactic survey fields.

The total luminosity of a cluster is obtained from the emissivity by integrating over the plasma volume and frequency $L_X = \int_V \int_V \epsilon_\nu dV d\nu \propto \text{EM}$, where $\text{EM} = \int_V n_e^2 dV$ is the emission measure. Observed along the line-of sight at projected radius $r = d_{\text{ang}}(z) \Theta$

³To avoid confusion with the Hubble constant parameter h and wavenumbers k , the Boltzmann constant is denoted as k_B and the Planck constant as h_P throughout this thesis.

⁴Modern ICM radiation codes account for *all* emission mechanisms at *all* temperatures.

(see Equ. 3.21), the emission measure $EM = \int n_e^2 dl = 4\pi (1+z)^4 S(\Theta)/\Lambda(T, z)$ gives direct observational access to the local electron density n_e , deduced from the measured surface brightness profile $S(\Theta)$ as a function of cluster-centric angle Θ in the soft X-ray band (see Equ. 2.6), and the redshifted and absorption corrected emissivity $\Lambda(T, z)$. The gas temperature T_X , as the second local X-ray observable, is obtained from a model fit to the redshifted X-ray spectrum, which achieves the highest temperature sensitivity in the hard band region.

2.3.2 ICM structure

The angle-averaged global spatial structure of the intracluster medium is commonly described by the *King model* for a self-gravitating, isothermal sphere (King, 1966). If one allows for an additional scaling of the ICM density profile with respect to the underlying dark matter profile of the form $\rho_{\text{gas}} \propto \rho_{\text{DM}}^\beta$, the three dimensional β -model for the radial ICM profile $\rho_{\text{gas}}(r)$ is obtained (Cavaliere and Fusco-Femiano, 1976)

$$\rho_{\text{gas}}(r) = \frac{\rho_{\text{gas},0}}{\left[1 + \left(\frac{r}{r_c}\right)^2\right]^{\frac{3\beta}{2}}} . \quad (2.5)$$

The core radius r_c determines the characteristic extent scale of the source, whereas the β parameter modulates the overall steepness of the profile. The original *King model* for the underlying dark matter potential is recovered by setting $\beta = 1$. Note that the central gas density $\rho_{\text{gas},0}$ defines the peak of the *core* of the profile, in contrast to the rising *cusp* of the NFW profile of Equ. 2.1.

The β -model for the global ICM structure assumes a spherically symmetric, isothermal gas in hydrostatic equilibrium. For β parameters deviating from unity, the galaxies, as dynamic tracers of the dark matter potential, exhibit a different velocity dispersion than the ICM gas according to $\sigma_{\text{gal}}^2 = \beta \sigma_{\text{gas}}^2$. Typical values of $\beta \simeq 2/3 \pm 0.2$ (Jones and Forman, 1984) indicate that the galaxy velocity dispersion in clusters is lower than for the gas. In effect, β is the ratio between the kinetic energy of tracers of the gravitational potential (*e.g.* galaxies) and the thermal energy of the gas $\beta = \mu m_p \sigma_r^2 / (k_B T_{\text{gas}})$, where σ_r denotes the radial velocity dispersion, m_p the proton mass, and μ the mean molecular weight of the gas ($\mu \simeq 0.6$ for a primordial gas composition). The empirically determined β values imply that the mean energy per unit mass is higher for the intracluster medium component than for the galaxies.

The observed two dimensional X-ray surface brightness profile $S(\Theta)$ of the β -model is obtained by relating the gas density profile $\rho_{\text{gas}}(r)$ to the X-ray emissivity (Equ. 2.2) and projecting the distribution on the plane of the sky. The resulting radially symmetric profile

$$S(\Theta) = \frac{S_0}{\left[1 + \left(\frac{\Theta}{\Theta_c}\right)^2\right]^{3\beta - \frac{1}{2}}} = \frac{S_0}{\left[1 + \left(\frac{\Theta}{\Theta_c}\right)^2\right]^{\frac{3}{2}}} \quad \text{for } \beta = \frac{2}{3} \quad (2.6)$$

contains the fit parameters Θ_c for the angular core radius size, the central surface brightness S_0 , and the β value. In the last step, the slope parameter is fixed to $\beta = 2/3$ in order to reduce the number of degrees of freedom for model fits of weak sources. This constrained surface brightness profile serves as a reference model for the detection of serendipitous extended X-ray sources (*e.g.* clusters) in Sect. 6.3.3, which contain typically a few hundred X-ray photons. Detailed investigations of the morphological properties of nearby clusters (*e.g.* Böhringer *et al.*, 2007b) require more elaborated structural parameters that account for multiple components and deviations from spherical symmetry.

2.3.3 ICM formation

Studies of the ICM formation process will be one of the important future applications of the XDCP survey; some basic considerations and models are now discussed. Scenarios for the intracluster medium formation need to account for two essential observational constraints: (i) the *total ICM mass* of $M_{\text{ICM}} \sim 10^{14} M_\odot$ for massive clusters, and (ii) the *metallicity enrichment* of the intracluster gas with values of $Z_{\text{ICM}} \sim 0.4 Z_\odot$.

We will first take a look at *infall models* for the ICM, which were proposed shortly after the first X-ray observations of clusters became available (*e.g.* Gott & Gunn, 1971; Gunn & Gott, 1972). Let us consider a primordial, cool gas initially at rest at large distance that falls into the potential well of an existing massive dark matter halo. Applying the *Virial theorem* for the final equilibrium state of the gas settled to the bottom of the potential, we obtain

$$2 \bar{E}_{\text{kin}} + \bar{E}_{\text{pot}} = 0 \simeq \langle v^2 \rangle - \frac{G M}{R_g} \simeq \frac{3 k_B T_{\text{gas}}}{\mu m_p} - \frac{G M}{R_g}, \quad (2.7)$$

where $\langle v^2 \rangle \equiv \sigma_r^2 = 3 \sigma_r^2$ is the squared (radial) velocity dispersion of particles in the potential and $R_g \equiv G M^2 / |\bar{E}_{\text{pot}}|$ is the gravitational radius of the cluster. In the last step, the kinetic particle energy was equated with the thermal energy of a monoatomic gas (*i.e.* $\beta \simeq 1$). This first order approximation yields ICM gas temperature estimates expressed in terms of the velocity dispersion of the potential of

$$T_{\text{gas}} \simeq \frac{\mu m_p \sigma_r^2}{k_B} \simeq 7.3 \times 10^7 \text{ K} \cdot \left(\frac{\sigma_r}{10^3 \text{ km s}^{-1}} \right)^2 \simeq 6.3 \text{ keV} \cdot \left(\frac{\sigma_r}{10^3 \text{ km s}^{-1}} \right)^2 \quad (2.8)$$

in reasonably good agreement with observations. The *hot ICM* temperatures can hence be explained as a natural consequence of gas infall to the dark matter halo. The *total ICM mass* can be accounted for when considering that clusters form via collapse of cosmic regions of $R_{\text{col}} \sim \mathcal{O}(10 \text{ Mpc})$ with an associated approximate baryon reservoir of $M_{\text{bar}} \sim (4/3) \pi R_{\text{col}}^3 \cdot \rho_{\text{cr}} \Omega_b (1 + \delta) \sim 10^{14} M_\odot$ (see Sect. 3.2 for explanation).

Several assumptions for the derived temperature estimate might not be well justified and could modify the gas temperatures: (i) the ICM infall *after* the DM halo formed, (ii) initially only *marginally bound* gas coming from a large distance, (iii) a *cold* medium before infall, and (iv) no radiative energy losses during collapse.

The purely gravitationally driven thermalization process of the ICM can be qualitatively described with a spherically symmetric smooth accretion model: (i) incoming cold gas enters the cluster in concentric shells, (ii) the gas is adiabatically compressed as it reaches the denser central regions, (iii) accretion shocks form when the gas motions become supersonic and the shocks propagate outwards, (iv) subsequent infalling shells pass through the accretion shocks of the inner shells and are shock-heated to the virial temperature of the cluster within about one sound crossing time t_{sound} . For hierarchical merger scenarios, accretion shocks are not well defined but form a complex network of shocks as different infalling subclusters mix with the ICM of the main halo. After shocks have passed, the ICM gas is in a nearly hydrostatic state and further evolution proceeds quasi-static. Since the cluster and ICM formation physics contains no characteristic scale, a self-similarity of the dark matter and gas internal structure is expected, *i.e.* the main object properties should only be scaled versions of each other.

The characteristic cluster formation time scale is given by the sound crossing time t_{sound} which can be expressed as

$$t_{\text{sound}} \simeq \frac{R}{c_{\text{sound}}} \simeq 0.66 \text{ Gyr} \cdot \left(\frac{R}{1 \text{ Mpc}} \right) \left(\frac{T_{\text{gas}}}{10^8 \text{ K}} \right)^{-\frac{1}{2}} \quad (2.9)$$

derived from the intracluster medium sound speed of

$$c_{\text{sound}} \simeq 1480 \text{ km s}^{-1} \cdot \left(\frac{T_{\text{gas}}}{10^8 \text{ K}} \right)^{\frac{1}{2}}. \quad (2.10)$$

The sound crossing timescale is hence short compared to the ages of low-redshift clusters, implying that the central cluster gas will reach a quasi-hydrostatic equilibrium about 1 Gyr after formation or major merger events. The situation for clusters at redshift $z \sim 1.5$ with a cosmic age of ~ 4 Gyrs (see Fig. 3.3) is already quite different and one would expect to find a large fraction of systems that have not yet fully virialized. Equation 2.9 additionally implies that cosmic regions with dimensions of $\gtrsim 10$ Mpc will not be able to virialize within a Hubble time and hence no relaxed objects larger than the cluster scale exist at the current epoch.

The ICM sound speed (Equ. 2.10) is comparable to the velocities of the cluster galaxies. The galaxy crossing time scale for a passage through the cluster t_{cross}

$$t_{\text{cross}} \simeq \frac{R}{\sigma_v} \simeq 1 \text{ Gyr} \cdot \left(\frac{R}{1 \text{ Mpc}} \right) \left(\frac{\sigma_v}{10^3 \text{ km s}^{-1}} \right)^{-1} \quad (2.11)$$

is hence similar to t_{sound} implying that the same arguments apply for the relaxation time scale of the galaxy population.

ICM *infall models* can reproduce basic properties of the intracluster medium, but do not account for the observed heavy element abundances of the initially metal free primordial gas. The detection of the 6.7 keV iron line (Mitchell and Culhane, 1977) provided early evidence that at least some of the gas must have been processed by stars and later been ejected from the galaxies. Heavy element abundances and their distribution in low

redshift clusters can now be consistently attributed to supernova explosion yields, which also provide sufficient energy for ejecting the metals out of the galaxies into the ICM (*e.g.* Böhringer, 2003).

As a last point concerning the formation process, we can now address the question of what determines the density of the intracluster medium, which is closely linked to the entropy of the ICM. The cluster entropy⁵ $K \equiv k_B T / (\mu m_p \rho_{\text{gas}}^{2/3})$ and the shape of the dark matter potential well are the main determinants for the ICM X-ray structure (Voit, 2005). As a second fundamental key feature, the cluster entropy contains a record of the thermodynamic history of the ICM gas.

The ICM structure of clusters is influenced by K because, in a simple picture, *high entropy gas floats and low entropy gas sinks*. The ICM gas thus convects⁶ until the equilibrium condition $dK/dr \geq 0$ is fulfilled throughout the cluster, *i.e.* a quasi-static configuration is achieved when the isentropic surfaces coincide with the equipotential surfaces of the dark matter potential.

For a purely gravitationally driven ICM collapse with initially cold gas, the accretion shocks are the only source of entropy for the ICM gas, with the consequence that the self-similar entropy profile $K(r) \propto r^{1.1}$ depends entirely on the mass accretion history $M(t)$. In the case that the accreted gas was not cold, an isentropic central entropy core is expected with a level similar to the pre-shock entropy. This so called *pre-heating* of ICM gas before infall makes gas harder to compress and thus lowers the density in the cluster center, where entropy is smallest. This mechanism can give rise to a breaking of the cluster self-similarity and is hence of great interest. Observations seem to be consistent with a minimum entropy floor⁷ level of about 100–200 keV cm², but the simple pre-heating model is likely to be complemented by entropy changing radiative cooling and heating processes.

Many fundamental questions concerning the intracluster medium formation have remained unanswered and are awaiting investigations using appropriate high-redshift X-ray cluster samples. (i) At what epoch does the thermal ICM X-ray emission start? (ii) Are non-gravitational processes important during the formation process? (iii) Is the gas pre-heated before falling into the cluster potential well? (iv) What is the source of (extra) entropy? (v) What is the early metal enrichment history and thermal evolution of the ICM?

2.3.4 Scaling relations

The expected (nearly) self-similar cluster formation process gives rise to general scaling relations of physical cluster properties. The comparison of observed relations with the

⁵ K is the constant of proportionality in the equation-of-state for an adiabatic monoatomic gas $P = K \rho_{\text{gas}}^{5/3}$ and is related to the standard thermodynamic entropy per particle through $s = k_B \ln K^{3/2} + s_0$. An alternative, widely used definition for the cluster entropy is $S = K_e = k_B T / n_e^{2/3}$.

⁶Observations deviate from the expected polytropic index of $\gamma = 5/3$ for a convectively established equilibrium, suggesting that also other processes are significant.

⁷This picture has recently been adjusted in terms of a gradual change of the entropy level as a function of ICM temperature.

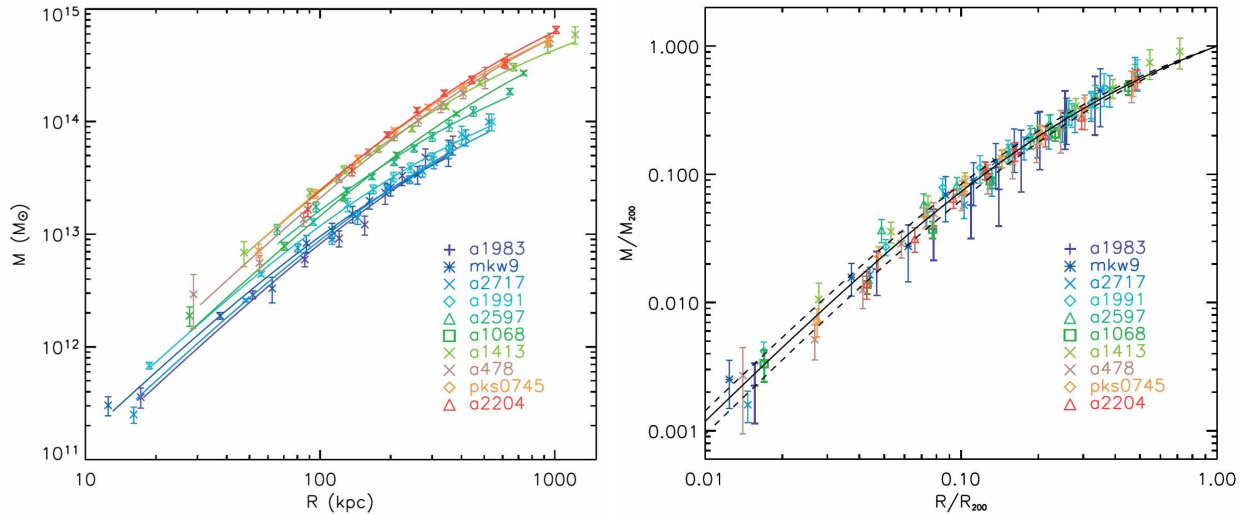


Figure 2.3: Galaxy cluster mass profiles for nearby clusters. *Left:* Integrated total mass profiles as a function of physical radius (kpc) for ten clusters with temperatures in the range 2–9 keV. Solid lines represent the best fitting NFW profiles. *Right:* Scaled mass profiles for the same clusters with masses scaled to M_{200} and radii to R_{200} . The black line gives the mean scaled NFW model. Plots from Pointecouteau *et al.* (2005).

scaling behavior of the self-similar predictions yield important clues on additional contributing physical processes. Scaling relations for distant cluster applications provide the crucial *mass proxy* in absence of high quality X-ray data for a detailed analysis, which requires $\gtrsim 1000$ X-ray photons. We will first introduce the standard method for deriving total cluster masses from X-ray data and will then discuss some important scaling relations.

With XMM-Newton and Chandra, the following physical cluster properties can be directly derived from sufficiently deep X-ray data: (i) the X-ray luminosity L_X from the source flux f_X (and redshift), (ii) the radial gas density profile $\rho_{\text{gas}}(r)$ from the local emission measure $\text{EM}(r)$ (iii) the total gas mass M_{gas} from the integrated density profile, (iv) the global mean temperature T_X from the observed spectrum, and (v) the temperature profile $T_X(r)$ from spatially resolved spectra. Using the spatially resolved density and temperature distributions, the (vi) entropy profile $K(r)$ and (vii) the total integrated mass profile $M_{\text{tot}}(< r)$ can be obtained.

Under the assumptions of spherical symmetry and hydrostatic equilibrium, the integrated total mass profile $M_{\text{tot}}(< r)$ can be derived from the ideal gas equation $p_{\text{gas}} = \rho_{\text{gas}} k_B T_X / (\mu m_p)$ and the hydrostatic equation for pressure equilibrium

$$\frac{dp_{\text{gas}}(r)}{dr} = -\rho_{\text{gas}}(r) \frac{G M_{\text{tot}}(< r)}{r^2} = \frac{k_B}{\mu m_p} \frac{d[\rho_{\text{gas}}(r) T_X(r)]}{dr}. \quad (2.12)$$

Solving for $M_{\text{tot}}(< r)$ yields the final important relationship for the total gravitating mass within radius r

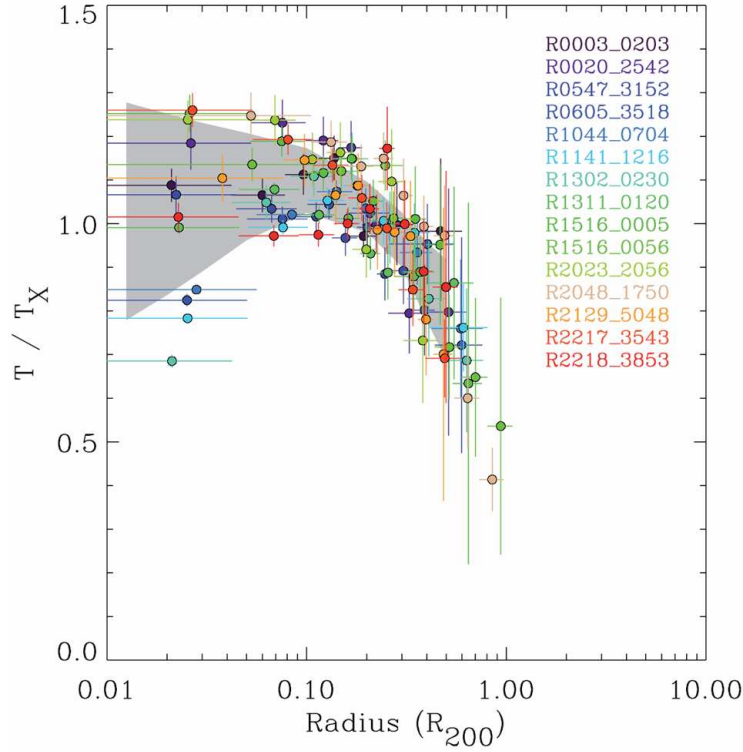


Figure 2.4: Scaled temperature profiles of 15 nearby clusters. The grey shaded area indicates the region enclosing the 1σ deviations around the mean profile. Temperatures are scaled to the averaged temperature in the outer cluster parts. Plot from Pratt *et al.* (2007).

$$M_{\text{tot}}(<r) = -\frac{k_B T(r) r}{G \mu m_p} \left(\frac{d \ln \rho_{\text{gas}}}{d \ln r} + \frac{d \ln T}{d \ln r} \right). \quad (2.13)$$

The integrated mass at radius r is hence determined by the local temperature $T(r)$ and the sum of the logarithmic slopes of the density and temperature profiles. Since galaxy clusters do not have a well-defined boundary, the total virialized mass $M_{\text{vir}} \equiv M_{200}$ is commonly defined within the radius $R_{\text{vir}} \equiv R_{200}$, where the average cluster density equals a specified density contrast $\delta \sim 200$ with respect to the critical density ρ_{cr} at the cluster redshift z (see Chap. 3)

$$\frac{M_{200}}{\frac{4\pi}{3} R_{200}^3} = \langle \rho \rangle_{\text{vir}} = \delta \rho_{\text{cr}}(z) \quad , \quad \delta \sim 200. \quad (2.14)$$

The left panel of Fig. 2.3 shows the determined integrated total mass profiles of ten nearby clusters within the temperature range of 2–9 keV (Pointecouteau *et al.*, 2005) with the best-fitting NFW dark matter profiles (Equ. 2.1) indicated by the solid lines. Once the mass profiles are scaled to units of R_{200} and M_{200} (right panel) the clusters reveal their self-similar property and are all consistent with a single universal NFW mass profile illustrated by the solid line. A similar universal scaling behavior can be observed for the outer regions of the temperature profiles as displayed in Fig. 2.4 (Pratt *et al.*, 2007). The inner cluster regions at $R \lesssim 0.1 R_{200}$ exhibit an increased temperature scatter due to additional non-gravitational physics in cluster centers (Sect. 2.3.5).

As for the scaled radial profiles, a self-similar behavior is expected for global properties (Kaiser, 1986). Under the assumptions that for systems in virial equilibrium (i) the bremsstrahlung emissivity scales with temperature as $\epsilon_{\text{bol}}^{\text{ff}} \propto \sqrt{T_X}$ (Equ. 2.3), (ii) the mass scales with a characteristic radius R_* as $M_{\text{tot}} \propto R_*^3$, (iii) a constant gas mass fraction $f_{\text{gas}} = M_{\text{gas}}/M_{\text{tot}} \approx \text{const}$, and (iv) self-similar dark matter halos (Equ. 2.1), global relations for purely gravitationally driven cluster physics can be derived. Since the NFW dark matter halos form a two parameter family, where the parameters are the total halo mass M_{tot} and the formation epoch z_{form} , the relations are expected to hold for all clusters that formed at the same redshift. The proper redshift dependence of the scaling relations can additionally be accounted for by considering the redshift evolution of the collapse threshold (Kitayama and Suto, 1996), which predominantly depends on the critical density at a given redshift $\rho_{\text{cr}}(z) = E^2(z) \rho_{\text{cr}}(0)$, parameterized by the evolution function $E(z)$ (see Eqs. 3.10 & 3.15), and to a lesser extent on the cosmological model parameters (see Sect. 3.2). As an example for the full redshift dependence, we consider the evolution of the cluster size scaling relation $R_{200}(z) \propto M_{200}^{1/3} E^{-2/3}(z)$, which indicates⁸ that objects at high redshift have smaller dimensions and are hence more compact.

We will now return to the discussion of four important global scaling relations for clusters of the same formation epoch. A summary of these relations is listed in Tab. 2.1. For a more detailed discussion of empirical parameters see Zhang (2005).

M– T_X : Equation 2.7 yields $T_X \propto \sigma_r^2 \propto M/R_* \propto M^{2/3}$ and consequently $M \propto T_X^{3/2}$. Slopes of empirical M – T_X relations are consistent with the self-similar expectation (*e.g.* Arnaud *et al.*, 2005). The M – T_X relation is one of the fundamental scaling laws because of the direct connection of mass and gas temperature through the *Virial theorem*. With the assumed constant gas mass fraction $M_{\text{gas}} = f_{\text{gas}} M$, the same self-similar scaling behavior is obtained for the M_{gas} – T_X relation.

L_X^{bol} – T_X : An averaged integration of the emissivity over the cluster volume yields $L_X^{\text{bol}} \propto \rho_{\text{gas}}^2 R_*^3 T_X^{1/2} \propto (f_{\text{gas}} M/R_*^3) R_*^3 T_X^{1/2} \propto M T_X^{1/2} \propto T_X^2$, where in the last step the result for the M – T_X relation was used. The measured scaling behavior of the L_X^{bol} – T_X relation reveals a systematically steeper logarithmic slope than expected.

L_X^{bol} – M : Combining the first two relations, we obtain $L_X^{\text{bol}} \propto T_X^2 \propto M^{4/3}$. The L_X^{bol} – M correlation is of fundamental importance for distant cluster cosmology since it provides the easiest means to determine masses for faint X-ray clusters. Reiprich & Böhringer (2002) empirically calibrated the relation and obtained a slightly steeper slope than the self-similar expectation (see Fig. 4.2). The approximate full empirical relationship between X-ray luminosity and total cluster mass is given by

$$L_X \simeq 10^{45.0 \pm 0.3} h_{70}^{-2} \text{ erg s}^{-1} \left(\frac{M_{200}}{10^{15} h_{70}^{-1} M_{\odot}} \right)^{1.8}. \quad (2.15)$$

⁸For $E(z) \geq 1$, *e.g.* for a concordance model.

Relation	Form	Self-Similar α	Observed α	Reference
$M_{500}-T_X$	$M_{500} \propto T_X^\alpha$	3/2	1.6 ± 0.1	Arnaud <i>et al.</i> (2005)
$L_X^{\text{bol}}-T_X$	$L_X^{\text{bol}} \propto T_X^\alpha$	2	2.9 ± 0.15	Arnaud & Evrard (1999)
$L_X^{\text{bol}}-M_{200}$	$L_X^{\text{bol}} \propto M_{200}^\alpha$	4/3	1.8 ± 0.1	Reiprich & Böhringer (2002)
$M_{500}-Y_X$	$M_{500} \propto Y_X^\alpha$	3/5	0.55 ± 0.05	Arnaud <i>et al.</i> (2007)

Table 2.1: Selected galaxy cluster scaling relations. The table lists the relation, the expected self-similar scaling behavior, and approximate observed values.

M- Y_X : The use of the combined parameter $Y_X = M_{\text{gas}} \cdot T_X$ as a robust, low-scatter mass proxy has been motivated by studies of the *Sunyaev-Zeldovich effect* (see Sect. 2.3.6) and has recently been calibrated with X-ray observations by Arnaud *et al.* (2007). The self-similar expectation is obtained from the first relation as $Y_X \propto M_{\text{gas}} T_X \propto f_{\text{gas}} M M^{2/3} \propto M^{5/3}$ and hence $M \propto Y_X^{3/5}$, consistent with the observed slopes.

The introduced scaling relations are of fundamental importance for the XDCP survey in two ways. First, a selected subset of newly discovered *individual* distant systems can be used to study and calibrate the evolution of the mass-observable relations at high redshift, possibly with deep X-ray follow-up observations in order to improve the achievable accuracies. Second, the calibrated scaling relations can then provide the mass proxy for future cosmological applications for the *full* survey sample.

Deviations from the expected gravitational self-similar scaling relations are commonly attributed to non-gravitational effects in the intracluster medium. ICM pre-heating and central cluster cooling and heating processes have been mentioned as possible mechanisms able to break self-similarity. The next section will briefly summarize some of the complex baryonic physics phenomena observed in cluster centers.

2.3.5 Cool core clusters

Cooling and heating in the centers of galaxy clusters is the subject of very active current research since the observed physical processes affect the evolution of both the cluster *and* the galaxy populations. A compilation of the latest results is available in the conference proceedings of Böhringer *et al.* (2007a). *Cool core clusters* (CCC) could also be important for high-redshift studies for two reasons. (i) The abundance and properties of high redshift cool core clusters are essentially unexplored (*e.g.* Vikhlinin *et al.*, 2007; Santos *et al.*, submitted), and (ii) CCC systems at $z > 1$, if they exist, could introduce survey selection biases owing to their highly peaked X-ray emission and the associated difficulty to discriminate them from point sources.

The radiative cooling time scale of the ICM can be approximated from the ratio of the specific enthalpy⁹ and the total volume emissivity and is inversely proportional to the gas density n

⁹The specific enthalpy h is to be used for an *isobaric* cooling of the gas.

$$t_{\text{cool}} \simeq \frac{\frac{5}{2} n k_B T}{\epsilon_{\text{bol}}^{\text{ff}}} \simeq 8.5 \times 10^{10} \text{ yr} \cdot \left(\frac{n}{10^{-3} \text{ cm}^{-3}} \right)^{-1} \left(\frac{T}{10^8 \text{ K}} \right)^{1/2} \propto \frac{1}{n}. \quad (2.16)$$

Throughout most regions of typical clusters, the cooling time scale is much longer than the Hubble time $t_H = H_0^{-1}$, justifying the assumption of hydrostatic equilibrium. However, in dense cluster cores, t_{cool} can become less than the age of the Universe and radiative cooling effects gain significance. The *cooling surface* is defined as the radius r_{cool} , where the cooling time equals the age of the cluster. Inside r_{cool} radiative cooling losses are significant and can cause a decline of the ICM temperature towards the center, as visible in some of the temperature profiles of Fig. 2.4. Such *cool core clusters* exhibit very peaked surface brightness profiles with central emission exceeding the β -model expectations of Equ. 2.6. Contributing about half to the *local* cluster population, current data is suggestive that the fraction of CCC is rapidly declining at $z \gtrsim 0.5$ (Vikhlinin *et al.*, 2007).

Early models of *cool core clusters* (*e.g.* Silk, 1976; Fabian & Nulsen, 1977) predicted that the central cooled ICM should gradually condense and be replaced by surrounding gas giving rise to a constant inward flow with mass deposition rates in the cluster centers of $\mathcal{O}(100 M_\odot)$ per year. However, observations with XMM-Newton showed that this *cooling flow* picture does not hold (Peterson *et al.*, 2001) and that the central gas temperatures do not decrease below a few keV. These results emphasized the need of a central heating source, which is sufficiently energetic and self-regulated to balance the radiative cooling losses and establish a stable ICM configuration. The current standard paradigm (*e.g.* Böhringer *et al.*, 2002b) attributes the heat source to a central AGN, which exhibits duty-cycles of increased activity and intermediate quiescent periods. This paradigm is consistent with observations of complex hydrodynamic phenomena in cluster centers such as X-ray cavities and shock fronts (*e.g.* McNamara *et al.*, 2005), buoyantly rising bubbles and propagating sound waves (*e.g.* Churazov *et al.*, 2001; Fabian *et al.*, 2003), or AGN jet interactions (*e.g.* McNamara *et al.*, 2007).

For cooling time scales of $\mathcal{O}(1 \text{ Gyr})$, characteristic features of CCC might already be observable at $z > 1$. The associated peaked X-ray surface brightness profile and possible additional central AGN activity have to be adequately considered for the cluster candidate selection process (Sect. 6.4) and the computation of the selection function (Sect. 9.1.3).

2.3.6 Sunyaev-Zeldovich effect

Measurements of the *Sunyaev-Zeldovich effect* (SZE) are expected to have a significant impact for future distant cluster studies and are therefore briefly summarized here. The hot electrons of the intracluster medium not only emit X-ray photons, they also lead to a characteristic distortion of the cosmic microwave background (CMB) radiation through *inverse Compton scattering*.

Low energy CMB photons propagating through the hot cluster ICM are on average ‘upscattered’ by the electrons, *i.e.* the collective effect of many scattering processes gives rise to a shift of the CMB spectrum towards higher temperatures. The SZE (Sunyaev and

Zeldovich, 1972) introduces spectral changes of the CMB intensity I of order $\Delta I/I_0 \sim 10^{-4}$ resulting in an increased CMB intensity in the higher energy *Wien* tail of the spectrum and a *CMB decrement* in the *Rayleigh-Jeans* tail. The transition from a CMB decrement to an increment occurs at a wavelength of $\lambda_{\text{null}} \simeq 0.14 \text{ cm}$ ($\sim 218 \text{ GHz}$). The SZE hence imprints a characteristic CMB spectral modulation of a decreased CMB intensity at $\lambda > \lambda_{\text{null}}$ ($\nu < 218 \text{ GHz}$), a null effect at λ_{null} , and an increment at $\lambda < \lambda_{\text{null}}$ ($\nu > 218 \text{ GHz}$).

The CMB decrement in the radio regime can be quantified as $\Delta I(\nu) = -2yI(\nu)$ by defining the *Compton- y parameter*

$$y \equiv \frac{\sigma_{\text{T}} k_{\text{B}}}{m_{\text{e}} c^2} \int T_{\text{e}} n_{\text{e}} dl, \quad (2.17)$$

where σ_{T} is the Thomson electron cross-section, m_{e} the electron mass, and the integration runs along the line-of-sight path element dl . To first order, the distorted CMB spectrum depends on the single y parameter, which is proportional to the probability that a photon will Compton scatter and the amount of energy the photon gains on average. A comparison to the ideal gas law $p = n k_{\text{B}} T$ reveals that the y parameter is proportional to the integrated pressure along the line-of-sight $y \propto \bar{p}$. The linear dependence on the gas density $y \propto n_{\text{e}}$ implies that cluster outskirts can be probed and that the SZE signal is less sensitive to ICM inhomogeneities compared to X-ray measurements.

In the case that the SZE signal of the cluster is not spatially resolved, an integrated version of the distortion parameter Y over the projected surface area is measured, $Y = \int y dA \propto n_{\text{e}} T dV \propto E_{\text{thermal}}$, which is proportional to the total thermal energy of the electrons. Since the Y parameter is directly linked to the cluster gas mass and the temperature, a scaling relation of the form $M_{\text{tot}} \propto Y^\alpha$ promises to yield a new robust mass proxy once calibrated.

The key feature of the SZE concerning distant cluster studies is its (almost) redshift independence (for resolved systems). The cosmological surface brightness dimming $S_{\text{bol}} \propto (1+z)^{-4}$ (see Equ. 3.22) of the SZE signal is exactly compensated by the increased CMB intensity at the given redshift $\Delta I \propto I \propto T_{\text{CMB}}^4 \propto (1+z)^4$. For this reason, future SZE cluster surveys (see Sect. 12.1) bear great hope for a profound impact on cosmological studies.

2.4 The Cluster Galaxy Population

Despite the small contribution of only a few percent to the total cluster mass, optical observations of the galaxies have long been the only means for cluster studies. Abell (1958) compiled the first large optically selected cluster catalog based on galaxy overdensities within a projected radius of $\Theta_{\text{A}} = 1.7/z$, corresponding to a physical scale of about 2 Mpc. Redshift estimates for the 1682 identified clusters containing more than 50 (projected) galaxies within two magnitudes of the third brightest member m_3 were obtained by using the tenth brightest cluster member m_{10} as a ‘standard candle’ (see Equ. 3.46).

Galaxy clusters play an important role for observational studies of galaxy evolution for several reasons: (i) they provide a large number of galaxies with the same general

environmental parameters and redshift, (ii) evolutionary processes are accelerated in high-density environments, and (iii) some classes of galaxies are only found in clusters. By going to high redshift, galaxy evolution effects are directly accessible to observations. Future studies of the evolutionary effects on the cluster galaxy populations will explore galaxy properties as a function of redshift *and* cluster mass over an increased redshift baseline. Whereas the cluster redshift fixes the cosmic age at the time of observation, the mass of the system determines the environmental properties. Disentangling the influence of different cluster specific effects on galaxies will thus require also a wide mass range at high redshift. The following sections illustrate selected aspects of the cluster galaxy populations that are of importance for distant cluster surveys.

2.4.1 Cluster versus field galaxies

The galaxy population is commonly divided into *cluster galaxies* and *field galaxies* depending on the environment they reside in. In the light of hierarchical structure formation scenarios, this distinction is not well defined over cosmic time as galaxies from the ‘field’ can enter cluster or group environments and groups subsequently merge with larger clusters. As a working definition, we can consider as *cluster galaxies* all objects which are located within the virial radius of a massive dark matter halo filled with an X-ray emitting ICM of minimum luminosity $L_X \gtrsim 10^{43} \text{ erg s}^{-1}$. Based on this ‘cluster definition’, three main differences distinguish the cluster environments from the ‘field’:

- the **confining dark matter potential well** associated with the DM density profile of Equ. 2.1;
- the **dilute hot intracluster medium** permeating the potential well with increasing densities towards the center;
- the **highly increased galaxy density** following a similar radial profile to the ICM.

All items of this special environment, as known from *existing* clusters, can introduce *nurture* effects on the galaxy population, *i.e.* object properties are transformed as a *reaction* to the environment. On the other hand, differences in the cluster versus field galaxy populations could originate from their different *nature*, *i.e.* they are inherited from the structure formation process covered in Sect. 3.2. In the following, some major consequences of the different physical cluster setting on the galaxy population are discussed.

Violent relaxation: A fluctuating gravitational potential Φ , as expected during the cluster collapse process, changes the energy of particles (galaxies or DM) according to $\dot{E} = m \dot{\Phi}$ and can produce a thermal equilibrium configuration on short timescales even for collisionless systems (Lynden-Bell, 1967). The initial cluster galaxy population is hence expected to be virialized shortly after cluster formation due to the collective gravitational effects of *violent relaxation*.

Dynamical friction and cannibalism: A massive galaxy moving at velocity v through a homogeneous background medium of lighter (dark matter) particles with mass density ρ suffers a drag force named *dynamical friction* (Chandrasekhar, 1943). Along the trajectory of the massive object, the background medium is ‘gravitationally polarized’ by the attractive force of the galaxy, leaving an overdense concentration of background particles in the wake of the galaxy. The collective effect of this friction force results in a slowing of the galaxy according to $\dot{v} \propto \rho M v^{-2}$. The drag force is independent of the mass of the individual background particles, but proportional to the galaxy mass M , which leads to a mass segregation of the largest galaxies in clusters on the *dynamical friction* time scale t_{DF}

$$t_{\text{DF}} \simeq 2 \text{ Gyr} \left(\frac{M}{10^{12} M_{\odot}} \right)^{-1} \left(\frac{v}{1000 \text{ km s}^{-1}} \right)^3 \left(\frac{R}{100 \text{ kpc}} \right)^2 \left(\frac{\sigma_r}{300 \text{ km s}^{-1}} \right)^{-2}, \quad (2.18)$$

where R is the distance from the cluster center, and σ_r the radial velocity dispersion of the dark matter halo potential well. Massive cluster galaxies can hence spiral towards the center on time scales of a few Giga years and form a giant object via a process named *galactic cannibalism*, the growing of a single galaxy by consuming its neighbors (Hausman and Ostriker, 1978).

Galaxy merging: The key parameter to determine the probability that two approaching galaxies will merge is their relative velocity V , which needs to be smaller than the relative escape velocity of the system of $\mathcal{O}(200 \text{ km s}^{-1})$ for a merging event to occur. If a significant fraction of the orbital energy is transferred to the stellar systems by tidal forces in a close encounter, a merger is likely. For two equal mass, spherically symmetric galaxies with a mass-weighted mean-square radius $\langle r^2 \rangle$ and relative velocity V , merging occurs if the bodies have an impact parameter b smaller than a critical value $b_{\text{crit}} = (32 G^2 M^2 \langle r^2 \rangle / 3)^{1/4} / V \propto \sqrt{M} / V$ (Peacock, 1999). The expected merger rate Γ can then be approximated as the product of the merging cross section $\sigma_{\text{merge}} = \pi b_{\text{crit}}^2$ and the particle flux $j_{\text{gal}} = n_{\text{gal}} V$

$$\Gamma = \sigma_{\text{merge}} j_{\text{gal}} \simeq \pi b_{\text{crit}}^2 n_{\text{gal}} V \propto \frac{1}{V}. \quad (2.19)$$

The inverse proportionality to the velocity generally favors merger events in lower mass groups rather than in clusters, where velocity dispersions are higher.

Galaxy harassment: Even if galaxies do not merge, the cumulative effects of the tidal forces of many weaker encounters can significantly influence cluster galaxies, in particular objects with lower masses. This *galaxy harassment* can lead to stripping of the outer galactic halos, disk deformations in spirals and S0 galaxies, or trigger star formation activity (Richstone, 1976).

Ram pressure stripping: Objects moving through a gaseous medium with density ρ_{gas} at velocity v are exerted to a *ram pressure* $p_{\text{ram}} = \rho_{\text{gas}} v_{\text{gal}}^2$. A galaxy passing through the dense central region of the ICM can this way be efficiently stripped from its internal gas on time scales of 10^7 – 10^8 years. A single passage of a galaxy through a cluster core can hence almost completely remove the interstellar medium from this galaxy and quench its star formation.

One could expect that these additional physical effects taking place in clusters modify or re-shape the galaxy luminosity functions (LF) of the cluster galaxy populations. However, the *individual* galaxy classes (*e.g.* E, S0, S) maintain a universal luminosity function with the same general *Schechter* function form as field galaxies (*e.g.* Andreon 1998; Popesso *et al.*, 2005)

$$\phi(L) dL = \phi_0 \left(\frac{L}{L^*} \right)^\alpha \exp \left(-\frac{L}{L^*} \right) \frac{dL}{L^*}, \quad (2.20)$$

where L^* is the characteristic luminosity, ϕ_0 the space density normalization, and α the faint-end slope. This universal form of the luminosity function has been confirmed out to redshifts of $z \simeq 1.3$ with typical slope parameters of $\alpha \simeq -1 \pm 0.3$ for the bright part of the composite LF and characteristic rest-frame absolute (AB) magnitudes of $Ks^* \simeq -23.5 \pm 0.5$ (Strazzullo *et al.*, 2006). Note that the frequently used notation m^*+1 refers to the apparent (observed) magnitude of a galaxy with a luminosity that is one magnitude, *i.e.* a factor of 2.51, *fainter* than the characteristic luminosity L^* at the given redshift. Similarly, M^*-2 denotes galaxies which are two magnitudes *brighter* in absolute luminosity, *i.e.* a factor of 6.3, compared to a characteristic L^* object of the given galaxy class.

2.4.2 Formation of ellipticals and the cluster red-sequence

Early-type galaxies, *i.e.* elliptical (E) and lenticular (S0) galaxies, play a distinct role in galaxy clusters. Not only they constitute the dominant galaxy class in the core regions of clusters, but their properties exhibit a high degree of homogeneity, which allows to place strong constraints on their formation history.

One of the key features of *cluster* galaxy populations is the existence of a tight sequence of red galaxies in the color-magnitude diagram (CMD), the so-called *cluster red-sequence*. This color-magnitude relation (CMR) in clusters has first been noticed by Baum (1959), but the full cosmological implications have only later been realized by Sandage & Visvanathan (1978). Bower, Lucey & Ellis (1992a; 1992b) confirmed the universality of the CMR in Virgo and Coma and established the red-sequence as distance indicator for clusters. The precision photometric study of these two clusters showed that the color-magnitude relations are intrinsically identical and that the observed color difference originates from the effects of the distance modulus (see Equ. 3.24). This study additionally established that the relation for the S0 population is less tight than for ellipticals, which exhibit a measured rms scatter along the red-sequence of 0.05 mag, mostly contributed by observational errors. The characteristic red-sequence with its minimal intrinsic scatter in low redshift clusters is

of key importance for the understanding of galaxy evolution and can furthermore be used for an optical search and identification of new clusters (*e.g.* Gladders & Yee, 2005).

The red-sequence in the CMD of the photometric bands X and Y can be characterized by (i) the color normalization $(X-Y)_{\text{CMR}}(Y^*)$ at the location of L^* galaxies, (ii) the slope of the sequence $d(X-Y)_{\text{CMR}}/dY$, and (iii) the (intrinsic) scatter σ_{CMR} . The color of the sequence is related to the luminosity-weighted age of the stellar populations in galaxies and can be compared to galaxy evolution models for the derivation of a formation redshift estimate. The intrinsic scatter σ_{CMR} provides information on the star formation histories of the red-sequence galaxies as a tight relation should be only observable if these objects formed their stars over a period which is short compared to the age of the galaxies.

The rising slope towards redder colors for more luminous objects can now be attributed to a *metallicity sequence* (Kodama and Arimoto, 1997). The required systematic increase towards higher metallicities and hence redder stellar populations¹⁰ can be quantitatively explained with supernova-driven wind models of ejected heated gas from the system. The deeper potential wells of massive galaxies, with increased gravitational binding energy per unit mass compared to smaller systems, can retain more metals and additionally trigger a more rapid metal production at early cosmic epochs.

The explanation of the observed local CMR with stellar population evolutionary synthesis models was not straightforward due to a general *age-metallicity degeneracy* (Worthey, 1994). Galaxy colors become redder as a consequence of increasing metallicity *or* increasing age of the stellar population (in absence of dust). This degeneracy could be broken by moving to higher redshifts, where the two scenarios predict different redshift evolutions of the CMR. Models for an evolving metallicity sequence predict the observed (almost) redshift independent slope. An age sequence, on the other hand, would feature a rapid steepening and a CMR truncation at higher redshifts, since the formation epoch is approached earlier for the faint younger blue galaxies than for the luminous older red ones (Kodama *et al.*, 1998).

The tightness of the red-sequence is expected to break down when the lookback time at the observed redshift z approaches the main epoch of star formation activity in (massive) early-type galaxies, *i.e.* when the stellar populations are ‘young’. However, all current known spectroscopically confirmed high-redshift galaxy clusters out to $z \sim 1.3$ show a pronounced red-sequence with a surprisingly small scatter. Figure 2.5 displays a recent Hubble Space Telescope (HST) color-magnitude diagram of the Lynx supercluster. Its two high-redshift clusters, the most distant ones discovered with ROSAT, exhibit intrinsic red-sequence scatters of merely 0.025 ± 0.015 mag for the elliptical population (Mei *et al.*, 2006b). From these observations, the formation redshift of the red-sequence galaxies can be estimated as $z_f > 2.5$, yielding strong constraints for evolution models.

Two competing formation paradigms for elliptical galaxies have been contrasted in the last few decades: the *monolithic collapse* model and the *hierarchical formation* scenario. The *monolithic collapse* model (Eggen *et al.*, 1962) assumes that ellipticals and bulges

¹⁰This reddening with increasing metallicity is primarily caused by a lower temperature of the metal rich stars at the main sequence turnoff (*e.g.* Renzini, 2006).

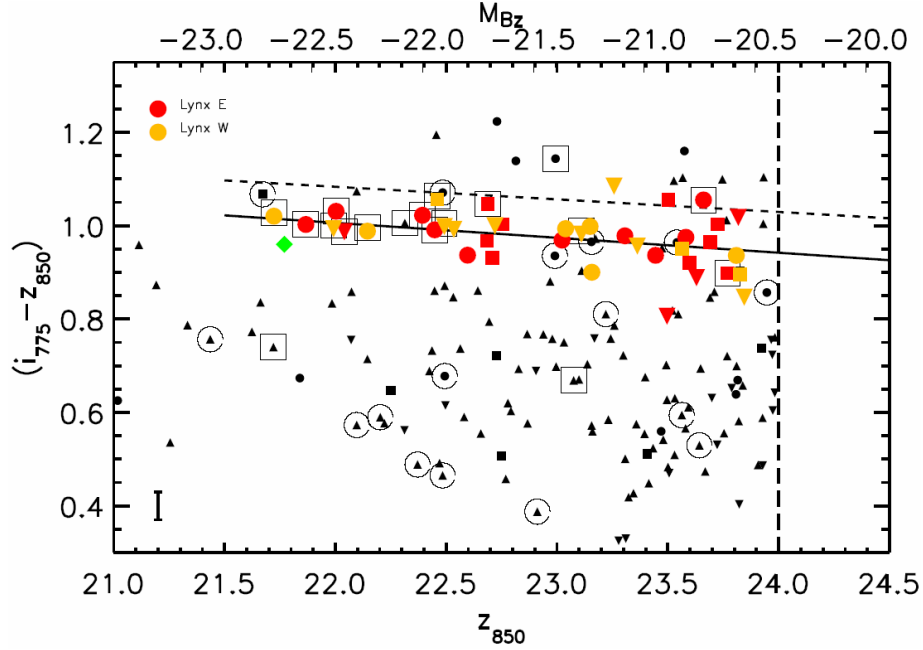


Figure 2.5: Color-magnitude diagram for the Lynx supercluster at $z = 1.26$, including the two most distant clusters known from the ROSAT era. Orange and red symbols indicate the individual clusters Lynx East and Lynx West. Elliptical galaxies are indicated by circles, S0s by squares, and spirals by triangles. Square boxes mark spectroscopically confirmed cluster members, open circles show interlopers, *i.e.* foreground objects. Plot from Mei *et al.* (2006b).

formed at high redshift, when gas clouds collapse rapidly and turn *instantaneously* into stars. After this violent star formation burst, no further generations of stars are formed, implying that the stellar population properties of a galaxy follow a passive evolution, *i.e.* the luminosity changes only due to the aging of stars. Within the *monolithic collapse* model, elliptical galaxies have not changed their overall appearance, mass, or identity since the formation redshift z_f , except for the ageing stellar population and the associated reddening of the spectral energy distribution (SED) with cosmic time. Note that essentially all observed cluster red-sequence colors are consistent with this simple galaxy formation model for bursts taking place at $z_f \gtrsim 3$ (see Sect. 7.1.2).

Conversely, the *hierarchical formation* scenario (*e.g.* White & Reese, 1978; Kauffmann, 1996; Kauffmann & Charlot, 1998) rests upon the physically motivated standard structure formation and evolution paradigm discussed in Sect. 3.2. *Hierarchical formation* in this respect means that small galaxy-size dark matter halos form first and massive galaxies originate from subsequent merging of smaller units. Major merging events can significantly alter the overall galaxy properties and lead to morphological transformations, trigger star burst events, or start nuclear activity in the galaxy centers. The main difference to the *monolithic collapse* model, however, is the expected late appearance of massive spheroids, as they are assembled over cosmic time. Consequently, a rapid decline of the space density of the most massive systems with redshift is expected. Luminous ellipticals are relatively

young objects in this scenario, mostly appearing at $z < 1$, which has long been at odds with discoveries of massive spheroids at $z > 1.5$ (e.g. Dunlop *et al.*, 1996; Cimatti *et al.*, 2004).

An important aspect of *hierarchical galaxy formation* is the fact that the appearance and identity of objects can change over cosmic time due to merging and evolutionary effects. This implies that the cluster elliptical population observed locally does not necessarily correspond to the ellipticals in high-redshift clusters, a consequence which has been named *progenitor-bias* (van Dokkum and Franx, 1996). A key for the consolidation of *hierarchical models* with observations is the strict distinction between the *formation epoch* of the stellar population in ellipticals and their *mass assembly history* (see Fig. 2.7). If star formation after merger events is absent (*dry merging*), massive ellipticals can exhibit old, passively evolving stellar populations, while their mass and luminosity growth might still continue to the present.

Recent progress in numerical simulations and semi-analytic modelling techniques have led to detailed predictions from the *hierarchical formation scenario* for the properties of the elliptical galaxy populations in clusters, now being largely consistent with observations (De Lucia *et al.*, 2006). The star formation activity for the largest local model spheroids peaks at $z \sim 5$, but only half of the systems possess progenitors with at least 50% of the final mass at $z \sim 1.5$, the lag between star formation epoch and assembly time increasing for more massive ellipticals. Hence the leverage for an observational distinction between *monolithic collapse* and *hierarchical formation* scenarios is highest for clusters at $z > 1$.

2.4.3 Evolution and environmental effects

Environmental effects and galaxy evolution are closely interlinked since the discussed external physical mechanisms at work in galaxy clusters can drastically change the galaxy properties over cosmic time. One of the key features of the cluster environment is the existence of a pronounced morphology-density relation (Dressler, 1980), *i.e.* the observed correlation between the frequency of various Hubble types and the local projected galaxy number density. In the local Universe, the fraction of spiral galaxies decreases from 60–70% in field environments to about 10% in dense cluster cores. The elliptical population, on the other hand, increases its relative contribution from approximately 10% in the field to roughly 50% in cluster centers. The fraction of lenticular (S0) galaxies rises more moderately from $\sim 30\%$ in low density environments to about 40% in high density ones.

Significant changes of the morphological galaxy mix can already be observed at redshifts of $z \sim 0.5$ (Dressler *et al.*, 1997). From $z = 0$ to $z = 0.5$, the S0 galaxy fraction in cluster centers has dropped by a factor of 2–3 to 15–20%, whereas the spiral fraction has proportionally increased to about 30–35%. Recent studies of the morphology-density relation at $z \sim 1$ confirm this trend and measure a combined early type fraction of $\langle f_{E+S0} \rangle \simeq 0.72 \pm 0.10$, which seems to be correlated with the bolometric X-ray luminosity of the cluster through the relation $f_{E+S0} \propto L_{X,bol}^{0.33 \pm 0.09}$ (Postman *et al.*, 2005). The rising fraction of ellipticals towards higher densities remains essentially unchanged, implying that the population of elliptical galaxies has been essentially in place since $z \sim 1$. Conversely, the decreasing S0 fraction with redshift suggests that an environment induced morphological

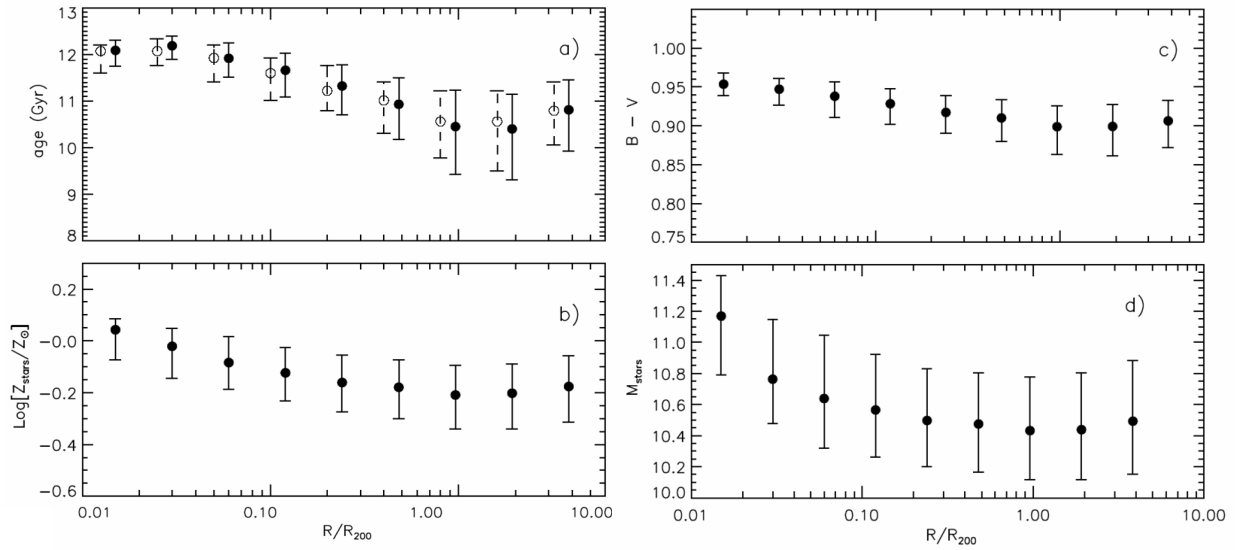


Figure 2.6: Variations of the properties of the elliptical galaxy population with cluster-centric distance as predicted at low redshift by the *Millennium Simulation*. Galaxy properties are extracted from massive dark matter halos with $M_{\text{tot}} \gtrsim 8 \times 10^{14} M_{\odot}$. Going from the cluster center towards the outskirts, the age (lookback time) of the stellar populations of ellipticals is predicted to decrease (*top left*), the metallicity to decrease (*bottom left*), and the typical galaxy colors to become bluer (*top right*). These trends are partly driven by mass segregation, *i.e.* the more massive galaxies are found close to the center (*bottom right*). From De Lucia *et al.* (2006).

transformation from spirals to S0s occurs at redshifts of $z \lesssim 1$ and continues until the present epoch.

This picture is qualitatively consistent with the *Butcher-Oemler effect*, which provided the first direct observational evidence for the evolution of the cluster galaxy population (Butcher and Oemler, 1978). The two-band photometry of clusters at $z \sim 0.4$ revealed an excess of blue galaxies compared to local rich clusters. A more recent study of 295 Abell clusters at $z < 0.38$ confirmed the original findings and quantified the evolution of the blue galaxy fraction as $f_B = (1.34 \pm 0.11) \cdot z - 0.03$, where objects more than 0.2 mag below the red-sequence were defined as *blue* (Margoniner *et al.*, 2001). Although the trend of such a relation is well established, the current form will obviously not hold at higher redshifts as it ‘predicts’ a vanishing of the red-sequence by $z \simeq 0.8$, at odds with observations (see Fig. 2.5).

The galaxy colors are closely linked to their star formation rates (SFR), which can be probed as a function of galaxy density with the Sloan Digital Sky Survey (SDSS) or the 2dF survey for low redshift cluster environments (Lewis *et al.*, 2002; Gómez *et al.*, 2003). These studies showed the existence of a sharp transition in the density–SFR relation starting from field-like star formation rates at local projected galaxy densities of $\Sigma \simeq 1 \text{ Mpc}^{-2}$ and converging to the suppressed star formation activity of cluster cores at $\Sigma \gtrsim 7 \text{ Mpc}^{-2}$. The transition from field to central cluster SFR properties is hence completed over a range of about seven in the local galaxy density and occurs roughly at the cluster virial radius. This large radius for the onset of star formation suppression, and the fact that a similar

density–SFR relation is found for group environments, give rise to a scenario where the transition from star forming to passive cluster objects already occurs during the infall along filaments towards the cluster (Bower and Balogh, 2004).

Using the high-resolution *Millennium Run* simulation (Springel *et al.*, 2005), detailed predictions for the changes of galaxy properties as a function of cluster-centric distance can be obtained. The results for the elliptical cluster galaxy population at low redshift are displayed in Fig. 2.6 (De Lucia *et al.*, 2006). Moving outwards from the high-density cluster centers, the simulations predict (i) decreasing ages, (ii) decreasing galaxy metallicities, (iii) bluer object colors, and (iv) decreasing stellar masses for the ellipticals. In other words, elliptical galaxies in cluster centers are expected to be older, more massive, redder, and more metal rich than their counterparts in lower density environments. These trends are partly driven by the dynamic friction induced mass segregation.

Moving towards higher redshifts, a study of A 851 at $z=0.41$ yielded the first indication for a sharp radial transition in the properties of faint ($<0.1 L^*$) galaxies (Kodama *et al.*, 2001). Using deep photometric data, an abrupt change from a predominantly red galaxy population towards bluer galaxies was observed at projected densities of $\Sigma \simeq 100 \text{ Mpc}^{-2}$, corresponding to the location of the cluster subclumps in the filaments of the surrounding large-scale structure (LSS). At medium distant redshifts, investigations of the LSS around a $z = 0.73$ cluster in the COSMOS field (see Sect. 4.4) show a weak trend towards redder colors with increasing local density for early-type galaxies (Cassata *et al.*, 2007). For RXJ J0910+5422 at $z = 1.11$, Mei *et al.* (2006a) observe an S0 population that is systematically bluer than the elliptical red-sequence by about 0.1 mag, suggesting that this population is still evolving towards the redder CMR colors of the ellipticals. However, in the Lynx clusters of Fig. 2.5, ellipticals and S0 galaxies lie on the same red-sequence, but the scatter increases with distance from the center (Mei *et al.*, 2006b).

Recently Cucciati *et al.* (2006) and Cooper *et al.* (2007) have investigated the general color–density relation out to $z \sim 1.5$ based on large spectroscopic galaxy surveys. These studies show that the fraction of red galaxies in dense environments gradually decreases with redshift, with a slower trend for the brightest objects. By redshifts of $z \sim 1.5$, the segregation of red and blue galaxies in dense regions has completely disappeared. These new results suggest that the maximal star formation activity shifts to galaxies with lower luminosities *and* in lower density environments with decreasing redshifts. This is possibly governed by a combination of biased galaxy formation in high density regions and environmentally induced star formation quenching.

The observation that the star formation activity in the most massive galaxies ceases at earlier epochs is a manifestation of the so-called ‘downsizing’ scenario (Faber *et al.*, 1995; Cowie *et al.*, 1996). A direct consequence of ‘downsizing’ in high-redshift clusters would be the ‘truncation’ of the red-sequence at a given redshift dependent magnitude, *i.e.* an increasing deficiency of faint red galaxies with increasing lookback time. Galaxies move towards the red-sequence in the color-magnitude diagram after star formation activity has ceased. If this occurs at earlier epochs for the more luminous galaxies, then the red-sequence will be progressively populated over cosmic time starting from the bright end. Observations of the resulting deficit of faint red galaxies on the red-sequence have been claimed by De Lucia *et al.* (2004) for clusters at $z \sim 0.8$ and by Tanaka *et al.* (2007) for a cluster at redshift $z = 1.24$.

2.4.4 Brightest cluster galaxies

For distant cluster searches, the brightest cluster galaxies (BCGs) are of particular importance in the cluster identification procedure. In fact, (i) BCGs often mark the center of the associated galaxy overdensity, (ii) they usually have the best photometry and color information available among all cluster galaxies, (iii) the BCG location in the color-magnitude diagram usually marks the bright end of the cluster red-sequence and is hence important for the redshift estimate, and (iv) BCGs are prime targets for spectroscopic follow-up.

The brightest cluster galaxies constitute a very special category of galaxies that still lacks a detailed understanding of the formation history. Compared to other galaxy classes, low redshift BCGs are more massive, have larger spatial extent, and are ultra-luminous with typical luminosities of $L_{\text{BCG}} \sim 10 L_*$ (Schombert, 1986) that correlate with cluster mass in the form $L_{\text{BCG}} \propto M_{200}^{0.26 \pm 0.04}$ (Lin and Mohr, 2004). In fact, the observed luminosity gap of the BCGs to the second ranked galaxies of massive clusters cannot be accounted for by a statistical sampling of the bright end of the Schechter LF (Equ. 2.20), indicating the need for a special formation process (Bhavsar and Barrow, 1985). In the local Universe, the first ranked cluster galaxies are predominantly located very close to the cluster's DM potential well minimum; 75% are found within the central 3% of the virial radius. They are often classified as radio-loud objects and are associated with the cooling core phenomenon (Sect. 2.3.5) in a complex way. BCGs are also found to have a higher fraction of dark matter compared to similar massive objects resulting in larger velocity dispersions for the stellar component (von der Linden *et al.*, 2007).

More than half of all BCGs in local X-ray clusters are classified as cD galaxies, a galaxy type exclusively found in the centers of clusters. cD galaxies were originally defined by Matthews, Morgan & Schmidt (1964) as supergiant galaxies with an additional extended low surface brightness envelope in excess of the radial light distribution of a normal elliptical galaxy at large radii. The outer cD halo has no clear edge and can extend far into the cluster (Schombert, 1988). The most prominent formation scenario for these centrally dominating supergiant galaxies is the *galactic cannibalism* model of Ostriker & Tremaine (1975). In this picture, cD galaxies grow through cannibalism of their neighbors as the most massive galaxies sink to the cluster center driven by dynamic friction. The formation scenario for giant ellipticals forming via merging in cluster centers has been confirmed by numerical simulations (*e.g.* White, 1976), but the reproduction of the characteristic extended halo has remained challenging until the present (*e.g.* Nipoti *et al.*, 2003). It seems likely, however, that the origin of the cD halo starlight is connected to tidally stripped material from the outer parts of galaxies or their tidal disruption (*e.g.* Zibetti *et al.*, 2005).

Despite their possibly ‘violent’ formation history, the brightest cluster galaxies constitute a surprisingly homogeneous class of objects with a low dispersion in their absolute magnitudes of $\langle M_V \rangle_{\text{BCG}} \simeq -24.5 \pm 0.3$. Local BCGs have been characterized as good ‘standard candles’ exhibiting a Gaussian scatter of the absolute magnitudes around the mean value (Postman and Lauer, 1995). Because of this characteristic, BCGs of massive clusters at redshifts $z \lesssim 1$ have been used for cosmological tests by applying the Hubble diagram of Sect. 3.3 (*e.g.* Aragon-Salamanca *et al.*, 1998; Collins & Mann, 1998). Over the redshift range covered, no signs of a significant BCG evolution have been found, other than the passive luminosity evolution (Burke *et al.*, 2000).

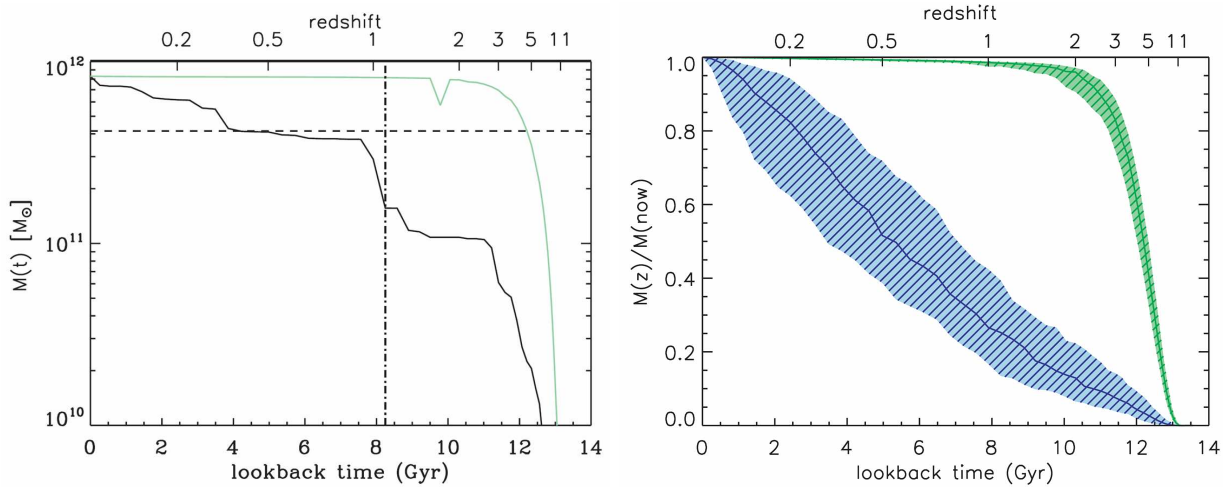


Figure 2.7: Mass assembly histories and formation times of BCGs as seen from the *Millennium Simulation*. *Left:* Stellar mass of the main BCG progenitor (lower black line) and the sum of all progenitors (top line) for a *single* case study BCG. The horizontal dashed line represents half of the final BCG mass. *Right:* Mass assembly history (blue) and stellar formation epoch (green) for the full BCG sample. Plots from De Lucia & Blaizot (2007).

To complete this introductory section on the cluster galaxy population, the predictions of the state-of-the-art *Millennium Run Simulation* concerning the cosmic evolution of BCGs are presented, which have been recently discussed by De Lucia & Blaizot (2007). Figures 2.7–2.9 establish the simulated reference model for comparison with observations. The 125 traced model BCGs were selected from local cluster halos more massive than $7 \times 10^{14} M_{\odot}$ and have absolute K-band magnitudes of $\langle M_K \rangle = -26.58$ mag with a dispersion of 0.2 mag. The galaxy *assembly time* is defined in the analysis as the epoch when the *single* main BCG progenitor contains half of the final ($z=0$) stellar mass. At the *formation time*, on the other hand, half of the final total stellar mass is present in the sum of *all* progenitor objects.

The predicted extreme hierarchical nature of the brightest cluster galaxies is illustrated in Fig. 2.7, which shows the mass evolution of a single case study BCG in the left panel and the averaged assembly history of the full sample in the right panel. The upper curves in both plots indicate that most of the BCG stars form at high redshift, 50% by $z \sim 5$ and 80% by $z \sim 3$, implying old, evolved, and red stellar populations as observed at the accessible redshifts. The mass assembly history of the main BCG progenitor is displayed by the lower lines showing the discrete merging events for the single galaxy on the left and the average sample evolution on the right, with a predicted mean mass growth by a factor of three from $z = 1$ to $z = 0$. Figure 2.8 provides testable predictions (see Sect. 11.1) for the evolution of the absolute rest-frame K-band luminosities (top panel) and after subtracting a passive luminosity evolution model with formation redshift $z_f = 5$ (lower panel). The distribution of BCG stellar masses at different cosmic epochs is illustrated by the red histograms in Fig. 2.9.

Observationally, the big questions *when* and *how* cD galaxies formed are yet to be explored. Between the *spiderweb galaxy* (Miley *et al.*, 2006), a possible cD precursor in a protocluster environment at redshift $z = 2.2$, and the well studied end products of the BCG evolution at $z \lesssim 0.8$, there is still a lot of redshift space to fill in.

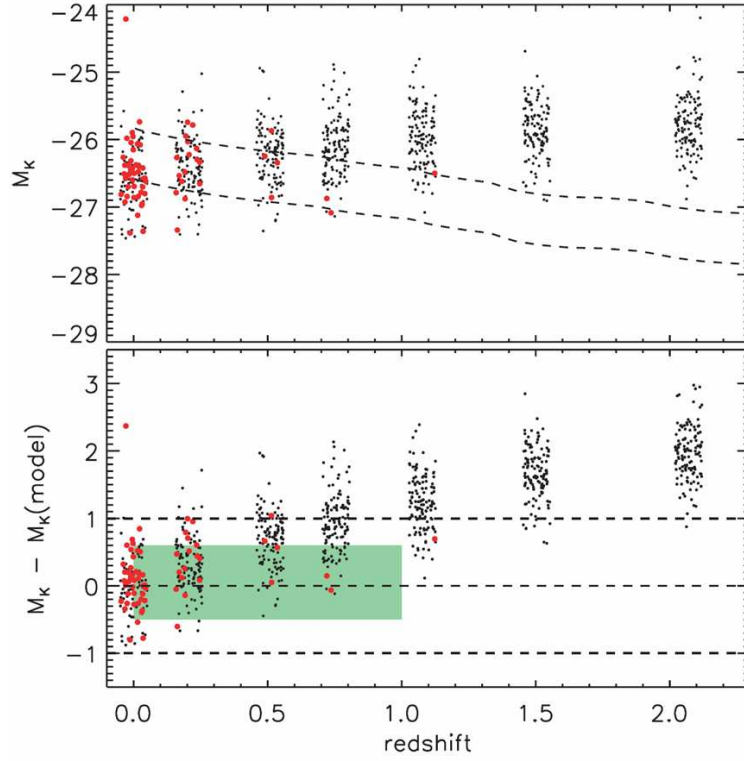


Figure 2.8: *Top:* Evolution of the absolute BCG K-band rest-frame magnitude as a function of redshift. Black dots represent model BCGs, red symbols indicate objects in halos more massive than $10^{15} M_{\odot}$. The dashed lines show burst model predictions for a formation redshift of $z_f = 5$ and fixed mass. *Bottom:* Residuals after subtracting the burst model. The green shaded area indicates the redshift range which has been probed observationally. Plot from De Lucia & Blaizot (2007).

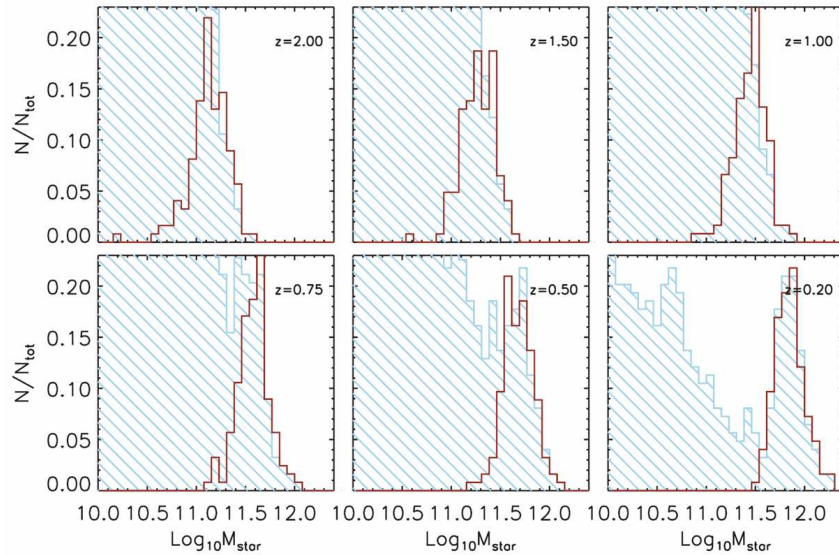


Figure 2.9: Evolution of the stellar mass distribution of high-redshift model BCGs (red histograms) and of progenitors of local BCGs (blue histograms). Plot from De Lucia & Blaizot (2007).

Chapter 3

Galaxy Clusters as Cosmological Probes

Besides their use as astrophysical laboratories, galaxy clusters are also sensitive cosmological probes of increasing importance. The NASA Dark Energy Task Force report¹, for example, recommends the study of cluster evolution as one of the four most promising pillars of future research in fundamental cosmology.

The distant galaxy clusters under focus for this thesis are observed at an epoch which corresponds to the second quarter of the lifetime of the Universe. Their general observational properties have thus to be interpreted within the standard (homogeneous) cosmological model and modern structure formation scenarios. More complete and detailed general introductions to cosmology can be found in the textbooks by *e.g.* Schneider (2006a) and Coles & Lucchin (2002). This chapter pursues the following main motivations and aims:

1. Provide the general cosmological framework and tools for the consistent description of $z > 1$ clusters within the concordance² Λ CDM cosmology (Sect. 3.1);
2. Introduce the main aspects of modern hierarchical structure formation scenarios with the focus on cluster formation and evolution (Sect. 3.2);
3. Compile a summary of cosmological tests using (distant) galaxy clusters which are feasible within the next decade(s) (Sect. 3.3).

3.1 Cosmological Framework

3.1.1 Dynamics of the expanding Universe

The dynamics of the scale factor $R(t)$ of standard relativistic world models is governed by the Friedman–Lemaître equations, which are derived from the field equations of general relativity (GR) for the case of a perfect homogeneous fluid

¹<http://www.science.doe.gov/hep/DETF-FinalRptJune30,2006.pdf>

² Λ CDM means that the dominant energy components are cold dark matter (CDM) and *Dark Energy*.

$$\ddot{R} = -\frac{4}{3}\pi GR \left(\rho + \frac{3p}{c^2} \right) + \frac{1}{3}\Lambda R \quad (3.1)$$

$$\dot{R}^2 = \frac{8}{3}\pi G\rho R^2 + \frac{1}{3}\Lambda R^2 - kc^2 . \quad (3.2)$$

Here dots represent time derivatives of the scale factor $R(t)$, ρ is the matter density, p the pressure, Λ Einstein's cosmological constant, and k the space time curvature constant. The scale factor $R(t)$ with the dimension of a length can be replaced by the dimensionless parameter $a(t) = R(t)/R_0$, which is normalized to the scale factor of the current epoch R_0 , *i.e.* $a(t_0) \equiv 1$.

The two equations for the expansion velocity \dot{R} (or \dot{a}) and acceleration rate \ddot{R} (or \ddot{a}) are not independent, but are linked³ through the adiabatic expansion equation (energy conservation in thermodynamics: $dU = -p dV$)

$$\frac{d}{dt}(a^3 \rho c^2) = -p \frac{d}{dt}(a^3) . \quad (3.3)$$

From Equ. 3.3 the density evolution during the expansion of the Universe can be derived for the different relevant energy components with their respective equations of state (EoS) $p = w\rho c^2$. In Λ CDM cosmologies, the major energy components with their density scaling relations are:

$$\text{matter (CDM and baryonic)} : \quad w = 0 \quad \rho_m \propto a^{-3} \quad (3.4)$$

$$\text{radiation} : \quad w = 1/3 \quad \rho_r \propto a^{-4} \quad (3.5)$$

$$\text{Dark Energy} : \quad w < -1/3 \quad \rho_{DE} \propto a^{-3(1+w)} \quad (3.6)$$

The pressureless matter density (Equ. 3.4) is just diluted as space expands, the radiation component (and relativistic matter) experiences an additional dilution factor of a^{-1} due to the cosmological redshift (see Equ. 3.8) and thus its energy density decreases faster than matter. In the last step, the *Dark Energy* component was generalized to account for its unknown nature. For the special case of the cosmological constant Λ ($w = -1$), Equ. 3.6 implies a constant energy density $\rho_\Lambda \propto a^0 = \text{const.}$

The ratio of the expansion velocity and the scale factor defines the Hubble parameter $H(a)$, *i.e.* the fractional increase of the Universe per unit time

$$H(a) \equiv \frac{\dot{a}}{a} . \quad (3.7)$$

Its present value $H_0 \equiv H(a_0)$ is the Hubble constant with $H_0 \approx 70 \text{ km s}^{-1} \text{ Mpc}^{-1} \approx 2.3 \times 10^{-18} \text{ s}^{-1}$ (*e.g.* Freedman *et al.*, 2001). The lowest order approximation of Equ. 3.7 yields the famous Hubble law, which relates the distance D to the cosmological recession velocity

³To see the general relationship, the time derivative of Equ. 3.2 is taken and solved for \ddot{a} . Reordering the right-hand side to match Equ. 3.1 leaves extra terms that can be identified with Equ. 3.3.

$v_{\text{recession}}$ (for small redshifts) via $D = v_{\text{recession}}/H_0$. Hence, at constant velocity (or redshift) all cosmological distances scale with the inverse of the value of the Hubble constant H_0^{-1} , *i.e.* a faster expansion rate results in a smaller (comoving) distance at a given redshift. This distance scaling property can be parameterized with the dimensionless constant $h = H_0/(100 \text{ km s}^{-1} \text{ Mpc}^{-1})$, or for a concordance cosmology as $h_{70} = H_0/(70 \text{ km s}^{-1} \text{ Mpc}^{-1})$. The dependency on the exact numerical value of the Hubble constant can then be accounted for by using the (parameterized) distance units $[D] = h^{-1} \text{ Mpc}$. Analogously all secondary derived quantities that are linked to cosmological distances scale with the appropriate powers of h : volumes as $[V] = h^{-3} \text{ Mpc}^3$, total cluster masses⁴ as $[M] = h^{-1} M_{\odot}$, densities as $[\rho] = h^2 \text{ g cm}^{-3}$, and luminosities as $[L] = h^{-2} \text{ erg s}^{-1}$.

Since all distance scales are stretched by the expansion of the Universe, this also applies to the wavelength λ of light propagating through space. This leads to the cosmological redshift z , which is given by the ratio of the scale factors, *i.e.* the stretching factor, at the time of observation a_0 and emission of the light $a(t)$

$$1 + z \equiv \frac{\lambda_{\text{obs}}}{\lambda_{\text{em}}} = \frac{a_0}{a} . \quad (3.8)$$

The redshift z is a direct observable and is hence of particular importance for observational cosmology. Through Equ. 3.8 redshifts are uniquely linked to the expansion state of the Universe and other quantities such as cosmic time and distances through the underlying cosmological model. Note that the cosmological redshift should not be interpreted as a recession velocity v_{rec} as in special relativity theory (SRT), although for small redshifts ($z \lesssim 0.3$) the results are consistent as is the case for the Hubble law. At high redshift ($z \gtrsim 1$), however, it can be shown empirically (Davis and Lineweaver, 2004) that the SRT interpretation fails and that super-luminal recession velocities are indeed allowed in the general relativistic treatment. In particular the *Hubble radius* d_{H} , defined as the sphere that presently recedes at the velocity of light

$$d_{\text{H}} = \frac{c}{H_0} = 2997.9 h^{-1} \text{ Mpc} \simeq 4280 h_{70}^{-1} \text{ Mpc} , \quad (3.9)$$

corresponds to a redshift of $z = 1.46$ in concordance cosmology. This implies that objects at higher redshift recede super-luminally at the current epoch, and the furthest spectroscopically confirmed galaxies at $z \sim 6$ have done so at all times⁵.

As the next step, all energy densities can be transformed into dimensionless parameters by stating them in units of the critical energy density ρ_{cr} . ρ_{cr} is defined as the total energy density that results in a flat global geometry of the Universe, *i.e.* $k \equiv 0$ in Equ. 3.2 (for $\Lambda = 0$), and is thus given by

$$\rho_{\text{cr}} \equiv \frac{3H_0^2}{8\pi G} = 1.879 \times 10^{-29} h^2 \text{ g cm}^{-3} = 2.775 \times 10^{11} h^2 M_{\odot} \text{ Mpc}^{-3} . \quad (3.10)$$

⁴The distance scaling depends on the mass determination method and is referring to Equ. 2.13. The X-ray determined cluster gas mass scales as $M_{\text{gas}} \propto h^{-5/2}$ (*e.g.* Sasaki, 1996).

⁵It is still possible to observe them, since the Hubble sphere is receding even more rapidly and can ‘overtake’ the emitted photons, see Davis and Lineweaver (2004) for more details.

The dimensionless energy components as measured today are then defined as

$$\Omega_{\text{m}} = \frac{\rho_{\text{m}}}{\rho_{\text{cr}}} ; \quad \Omega_{\text{DE}} = \frac{\rho_{\Lambda}}{\rho_{\text{cr}}} = \frac{\Lambda c^2}{3H_0^2} ; \quad \Omega_{\text{r}} = \frac{\rho_{\text{r}}}{\rho_{\text{cr}}} ; \quad \Omega_{\text{k}} = 1 - \Omega_{\text{m}} - \Omega_{\Lambda} - \Omega_{\text{r}} . \quad (3.11)$$

The total energy density is the sum of all contributing components

$$\Omega_{\text{tot}} = \Omega_{\text{m}} + \Omega_{\text{DE}} + \Omega_{\text{r}} . \quad (3.12)$$

The first two terms for the matter density Ω_{m} and the *Dark Energy* density Ω_{DE} are the dynamically dominant contributions today. In concordance cosmology, their sum (see Tab. 3.1) is very close to the critical density $\Omega_{\text{m}} + \Omega_{\text{DE}} \approx \Omega_{\text{tot}} \approx 1$, which implies a flat (or very close to flat) Universe with $\Omega_{\text{k}} \approx 0$ with percent level accuracy (Spergel *et al.*, 2007). The radiation term $\Omega_{\text{r}} \sim \mathcal{O}(10^{-4})$ is negligible today but has been of significant importance at early epochs of $z \gtrsim 1000$ (see Sect. 3.2), which can be seen from the density scaling relations in Equ. 3.5.

When combining equations 3.2, 3.7, and 3.11, the general Hubble expansion history is obtained as a function of the normalized scale factor

$$H^2(a) = H_0^2 \cdot \left[\Omega_{\text{m}} a^{-3} + \Omega_{\text{DE}} a^{-3(w+1)} + \Omega_{\text{r}} a^{-4} - (\Omega_{\text{tot}} - 1) a^{-2} \right] . \quad (3.13)$$

Here the *Dark Energy* equation-of-state parameter w is left as a free parameter as in Equ. 3.6. However, the most general form of *Dark Energy* also allows for a time evolution of the equation-of-state $w(z)$. In its simplest form the evolution can be parameterized as $w(z) = w_0 + w_1 \cdot z$ with a constant part w_0 and an evolving contribution w_1 . For an arbitrary time variation $w(z)$, the *Dark Energy* redshift scaling factor is integrated according to

$$\int_0^z d \left[(1+z')^{3[w(z')+1]} \right] = \exp \left(\int_0^z d \ln \left[(1+z')^{3[w(z')+1]} \right] \right) = \exp \left(3 \int_0^z \frac{1+w(z')}{1+z'} dz' \right) . \quad (3.14)$$

For expressing all relevant relations in terms of the observable redshift z , the scale factors are substituted according to $a \rightarrow (1+z)^{-1}$ and $da \rightarrow -dz(1+z)^{-2}$. As a final step, we can now define the cosmic evolution function $E(z)$, with which the final general form of the expansion history of the Universe $H(z)$ can be expressed in terms of H_0

$$E^2(z) = \Omega_{\text{m}}(1+z)^3 + \Omega_{\text{DE}} \cdot e^{3 \int_0^z \frac{1+w(z')}{1+z'} dz'} + \Omega_{\text{r}}(1+z)^4 + (1 - \Omega_{\text{tot}})(1+z)^2 \quad (3.15)$$

$$H^2(z) = H_0^2 \cdot E^2(z) . \quad (3.16)$$

Detailed measurements of the Hubble expansion history $H(z)$ are the core of many cosmological tests, in particular for future *Dark Energy* studies (see Sect. 3.3).

3.1.2 Distance measures

A meaningful general definition of distances in the Universe requires the knowledge of the metric for the global geometry. For the isotropic and homogeneous Universe (maximally symmetric space time) the general relativistic solution is the Robertson-Walker-Metric (RWM). The space time line element in spherical coordinates with curvature constant k and scale factor $R(t)$ can be written as

$$ds^2 = c^2 dt^2 - R^2(t) \left[\frac{dr^2}{1 - kr^2} + r^2 (\sin^2 \theta d\phi^2 + d\theta^2) \right] \quad (3.17)$$

with proper time t , radial comoving coordinate r , and angular coordinates ϕ and θ . As the global space time metric, the RWM is valid for all distances. For many applications the light propagation along radial coordinates is of prime interest. Since light travels on null geodesics, *i.e.* $ds^2 = 0$, Equ. 3.17 reduces to the simple form

$$c^2 dt^2 - R^2(t) \frac{dr^2}{1 - kr^2} = 0. \quad (3.18)$$

For the following discussion of distance measures, the specialization for a flat Universe ($k \equiv 0$) is assumed, which is valid for concordance cosmology. Small deviations from a flat geometry could still be possible, however, the additional correction functions $\sin(R_0 r)$ for $k = 1$ and $\sinh(R_0 r)$ for $k = -1$ for non-flat space times would inhibit the readability and clarity for this discussion and are therefore omitted.

Integrating Equ. 3.18 (for $k = 0$) yields the fundamental comoving distance D , *i.e.* the distance an object at redshift z has today,

$$D(z) = R_0 \cdot r(z) = R_0 \int_0^r dr' = c \int_t^{t_0} \frac{dt'}{a(t')} = c \int_0^z \frac{dz'}{H(z')} = \frac{c}{H_0} \int_0^z \frac{dz'}{E(z')}. \quad (3.19)$$

The second last step took advantage of Equ. 3.8 and its time derivative $dt = -dz(1+z)^{-1}H(z)^{-1}$ to relate time t and redshift z , and the final step made use of Equ. 3.16. From the observational point of view, two other alternative cosmological distance measures are of prime importance. Firstly, the luminosity distance d_{lum} relates the luminosity L of an object to its observed flux f in a way to reproduce the inverse square law of flat Euclidean space $f = L/(4\pi d_{\text{lum}}^2)$. Secondly, the angular diameter distance d_{ang} is defined to yield the Euclidean relation $dl = \theta \cdot d_{\text{ang}}$ for the apparent angular size θ of an object with physical size dl . Both observationally motivated distance measures can be expressed in terms of the comoving distance D as

$$d_{\text{lum}} = D \cdot (1 + z) \quad (3.20)$$

$$d_{\text{ang}} = \frac{D}{(1 + z)}. \quad (3.21)$$

The three main cosmological distance measures D , d_{lum} , and d_{ang} are illustrated in the left panel of Fig. 3.1⁶ for concordance model parameters. The fact that the angular size distance d_{ang} has a maximum at $z \approx 1.6$ has the important observational consequence that the apparent angular size of objects is practically constant at $z > 1$, as shown in the right panel of Fig. 3.1. This implies that high-redshift galaxies with typical physical sizes of 10 kpc are observed at angular scales of $1.2''$, 100 kpc cluster cores at $12''$, and 1 Mpc scale clusters of galaxies at $2'$.

Combining the relation $d_{\text{lum}} = d_{\text{ang}} \cdot (1+z)^2$ and the fact that the solid angle $d\Omega$ covered by an object follows $d\Omega \propto d_{\text{ang}}^2$ leads to the cosmological surface brightness dimming (*Tolman's Law*)

$$I_{\text{bol}}(\text{observed}) = \frac{I_{\text{bol}}(\text{emitted})}{(1+z)^4} . \quad (3.22)$$

For monochromatic flux measurements, the surface brightness dimming reduces to $I_{\text{mono}}(\text{observed}) \propto (1+z)^{-3}$, since the factor $(1+z)^{-1}$ for the effective narrowing of the observed rest-frame bandwidth is recovered.

If the rest-frame spectral energy distribution (SED) has a non-zero slope at the spectral interval of interest, then the observed flux will not only depend on the luminosity distance d_{lum} but also on the actually observed part of the rest-frame spectrum redshifted by the factor $(1+z)$. This is taken into account with the so-called K -correction, which can be defined as an additive term K_{QR} for the observed apparent magnitude m_{R} in band-pass R

$$m_{\text{R}} = M_{\text{Q}} + DM + K_{\text{QR}} , \quad (3.23)$$

where M_{Q} is the absolute magnitude of the source in the rest-frame band-pass Q and DM is the distance modulus

$$DM = m - M = 25 + 5 \log(d_{\text{lum}} [\text{Mpc}]) - 5 \log h_{70} . \quad (3.24)$$

This last relation follows directly from the definition of absolute magnitudes transformed to h_{70}^{-1} Mpc units⁷. For concordance cosmology, the last term is zero, and d_{lum} can be read off from Fig. 3.1. The K -correction term K_{QR} depends on the filter band, the redshift, and the spectral properties of the object under investigation (see Fig. 11.4). Positive correction terms imply a resulting K -dimming due to a decreasing SED with increasing frequency; negative terms result in K -brightening, *i.e.* objects actually appear brighter than expected at higher redshift. For efficient observations of the high-redshift Universe, the K -correction is an important consideration for the observing strategy as discussed in Sect. 7.1.

With the distance measures at hand, it is now possible to define comoving volume elements dV_{com} as

⁶The models for Figs. 3.1, 3.2, and 3.3 were computed with the cosmological calculators at <http://www.astro.ucla.edu/%7Ewright/CosmoCalc.html> and <http://faraday.uwyo.edu/%7Echip/misc/Cosmo2/cosmo.cgi>.

⁷The last term vanishes for concordance cosmology, but reflects the constant offset when changing the value of the Hubble constant H_0

$$dV_{\text{com}} = D^2 d\Omega dr = \frac{cD^2}{H(z)} d\Omega dz . \quad (3.25)$$

Here D is the comoving distance, $d\Omega$ the solid angle, and dr the radial thickness⁸ of the volume element. In the last step, the radial component was expressed in terms of a redshift interval dz as in Equ. 3.19. Figure 3.2 (right panel) displays the enclosed comoving volume out to redshift z per square degree for concordance cosmology parameters. The left panel depicts the observed (bolometric) flux for a selection of fiducial object luminosities as a function of redshift and illustrates the luminosity dependent search volumes for flux-limited observations.

When integrating a homogeneously distributed population of sources in Euclidean space over all luminosities (with arbitrary luminosity function), one obtains a universal relation for the cumulative number counts $N(> S)$ above flux S ⁹

$$N(> S) \propto S^{-\frac{3}{2}} . \quad (3.26)$$

The $\log N(> S)$ – $\log S$ plot thus shows a constant slope of $-3/2$ down to the flux limit of the observation, where the counting becomes incomplete (see also Equ. 3.45). The slope is due to the fact, that a lower flux reaches out further in distance (for any luminosity interval) $d_{\text{lum}} \propto S^{-\frac{1}{2}}$, and the enclosed volume grows proportional to the third power of the distance. Since this is only valid for static flat Euclidean space, the relation is expected to intrinsically flatten at a certain flux level when the effects of the expanding Universe and evolving populations become significant (see Sects 3.3 & 4.3).

For a population of objects with a constant comoving number density $n_0 = dN/dV_{\text{com}}$, the redshift distribution dN/dz is obtained by using Equ. 3.25

$$\frac{dN}{dz} = n_0 \frac{dV_{\text{com}}}{dz} = n_0 \frac{cD^2}{H(z)} d\Omega . \quad (3.27)$$

The unique link between redshift z and cosmic distance measures can also be generalized for cosmic time t . The time derivative of Equ. 3.8 yields $\dot{a} = -(1+z)^{-2} dz/dt$. Dividing by $a(t)$ and substituting with relation 3.7 results in $H(z) = -(1+z)^{-1} dz/dt$, which can be readily integrated by separation of variables to arrive at the lookback time t_{lookback}

$$t_{\text{lookback}}(z) = \int_{t_0}^t dt' = \frac{1}{H_0} \int_0^z \frac{dz'}{(1+z') \cdot E(z')} , \quad (3.28)$$

i.e. the time light from an object at redshift z has been travelling (light travelling time). Integrating to $z = \infty$ returns the age of the Universe t_0 , and the difference yields the age of the Universe at a given redshift $t_{\text{age}} = t_0 - t_{\text{lookback}}(z)$. Fig. 3.3 illustrates t_{age} and t_{lookback} for a concordance cosmology with $t_0 = 13.46$ Gyr.

Table 3.1 summarizes the main cosmological parameters of the concordance model following Spergel *et al.* (2007). These parameters will be used throughout this thesis for any background cosmological model unless otherwise stated.

⁸Strictly speaking $d(R_0 r)$, as the radial coordinate r is dimensionless.

⁹Same meaning as flux f , but S is typically used in the context of the $\log N$ – $\log S$ relation.

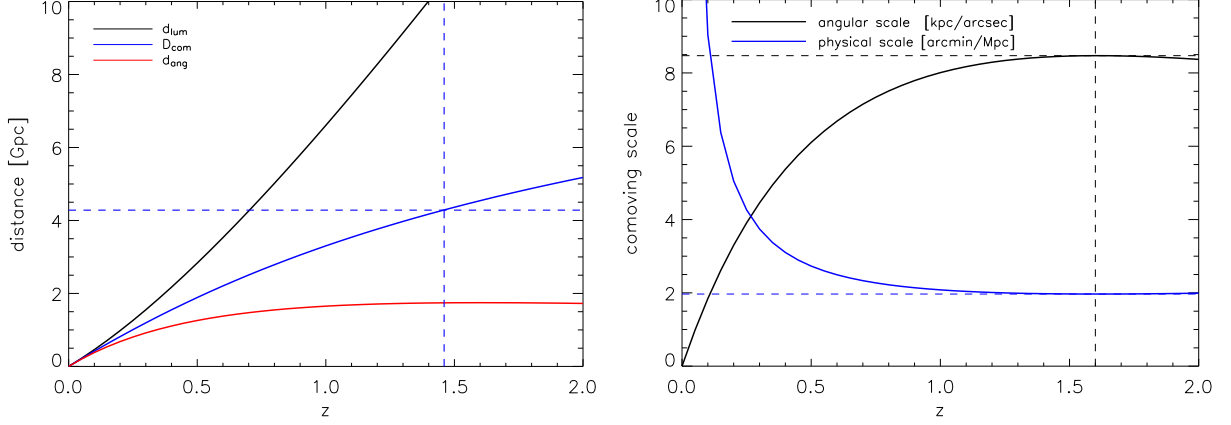


Figure 3.1: Cosmological distances and scales for objects at redshift z using concordance model parameters. *Left:* Comoving distance D (blue solid line), luminosity distance d_{lum} (black), and angular size distance d_{ang} (red) as a function of redshift. The Hubble radius d_H is indicated by the horizontal dashed line and corresponds to the comoving distance at redshift $z = 1.46$. *Right:* Physical and angular scale evolution with redshift. The black line depicts the physical comoving size of a fixed angular scale of $1''$ in units $[\text{kpc/arcsec}]$, the blue line traces the apparent angular size of a fixed physical scale of 1 Mpc in units $[\text{arcmin/Mpc}]$. Due to the global maximum of d_{ang} at $z \approx 1.6$, both functions assume their extrema at this redshift. However, at $z > 1$ the scales are almost redshift independent at approximately $8.4 \text{ kpc arcsec}^{-1}$ and correspondingly $2.0 \text{ arcmin Mpc}^{-1}$.

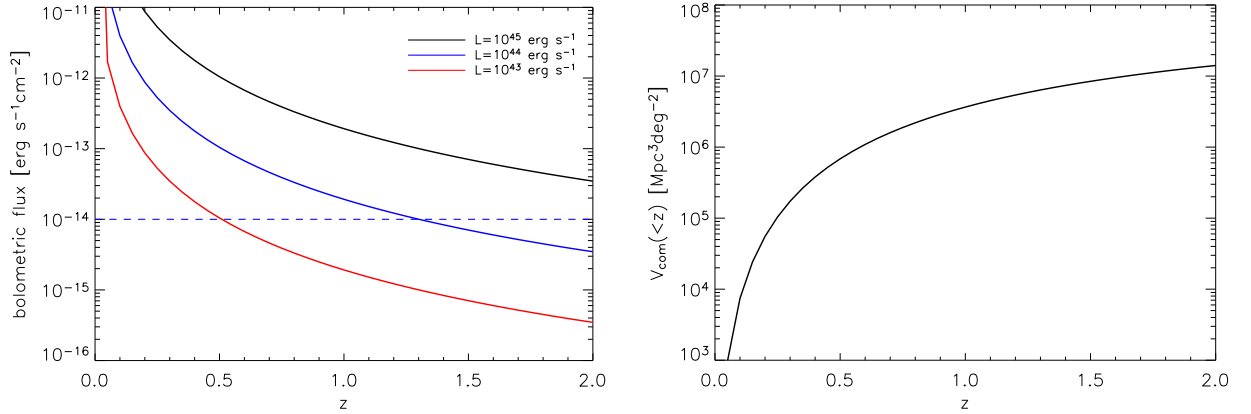


Figure 3.2: Bolometric flux evolution and comoving volumes as a function of redshift. *Left:* Received bolometric flux for three fiducial objects at redshift z with luminosities $10^{43} \text{ erg s}^{-1}$ (red line), $10^{44} \text{ erg s}^{-1}$ (blue line), and $10^{45} \text{ erg s}^{-1}$ (black line). A limited detection bandwidth will shift the curves down with an offset that depends on the flux fraction outside the filter band. At a given flux limit (e.g. $10^{-14} \text{ erg s}^{-1} \text{cm}^{-2}$ for the dashed horizontal line) objects are detectable out to a maximum redshift z_{max} , which is increasing with luminosity. *Right:* Comoving volume $V_{\text{com}}(<z)$ per square degree sky coverage from redshift 0 to z . The search volume increases roughly by a factor of 5 from redshift 0.5 to 1.0, and doubles again out to $z = 1.5$.

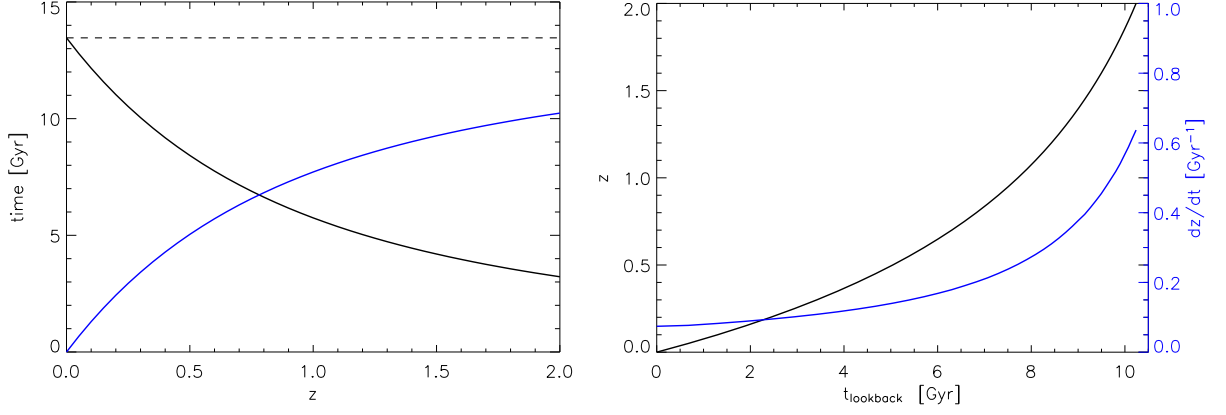


Figure 3.3: Cosmic time as a function of redshift for concordance model parameters. *Left:* The black solid line indicates the age of the Universe t_{age} at redshift z with the total age $t_0 = 13.46$ Gyr as represented by the horizontal dashed line. The blue line illustrates the lookback-time t_{lookback} from the current epoch to redshift z . The second quarter of the lifetime of the Universe ($6.8 \text{ Gyr} \lesssim t_{\text{lookback}} \lesssim 10.1 \text{ Gyr}$) is spanned by the redshift range $0.8 \lesssim z \lesssim 1.9$; from redshift $z = 1$ to $z = 1.5$ the lookback-time increases from 7.7 Gyr to 9.3 Gyr. *Right:* Redshift z versus lookback time t_{lookback} (black line with left scale). Many physical processes related to structure formation have characteristic timescales of ~ 1 Gyr, which translate into redshift in a non-linear way. The blue line (right scale) illustrates the changing redshift interval per Giga year lookback time dz/dt . Out to $z \lesssim 0.6$ the redshift intervals are almost constant at $\sim 0.1 \text{ Gyr}^{-1}$, *i.e.* redshift and time are linear to first order. By $z = 1$ the redshift interval per Giga year has increased to 0.25 Gyr^{-1} , at $z = 1.5$ to 0.4 Gyr^{-1} , and at $z = 2$ it is 0.6 Gyr^{-1} .

Parameters	Value	Parameters	Value
matter density	$\Omega_{\text{m}} = 0.3$	total energy density	$\Omega_0 = 1$
power spectrum normalization	$\sigma_8 = 0.8$	primordial PS slope	$n_{\text{S}} = 1$
Dark Energy density	$\Omega_{\Lambda} = 0.7$	age of Universe [Gyr]	$t_0 = 13.46$
Dark Energy EoS	$w = -1$	recombination redshift	$z_{\text{rec}} \sim 1100$
Hubble constant [$\text{km s}^{-1} \text{Mpc}^{-1}$]	$H_0 = 70$	matter-radiation equality	$z_{\text{equ}} \sim 3500$
baryon density	$\Omega_{\text{b}} = 0.045$		

Table 3.1: Cosmological concordance model parameters as used throughout this thesis. *Left:* Parameters for which galaxy cluster samples are particularly sensitive to. *Right:* Additional concordance model parameters that will be assumed for the background cosmology. The parameters σ_8 and n_{S} describe the properties of the initial power spectrum of density perturbations, all other parameters are linked to the global geometry of the Universe, which is assumed to be flat ($k=0$) in concordance cosmology. The chosen parameter values follow Spergel *et al.* (2007).

3.2 Cosmic Structure Formation

Whereas Sect. 3.1 set the framework for the *homogeneous Universe*, this part will introduce some relevant aspects of the *inhomogeneous Universe*, *i.e.* the formation and evolution of cosmic structure. In the hierarchical structure formation scenario, galaxy clusters play a distinct role as the largest and most recently virialized objects to form and mark the important transition regime between linear and non-linear gravitational dynamics.

The standard paradigm for the growth of density perturbations rests upon the following qualitative picture: (i) Quantum fluctuations in the very early Universe serve as initial density fluctuations. (ii) These fluctuations are stretched to macroscopic scales by an early inflationary phase which also imprints a characteristic primordial fluctuation power spectrum. (iii) After inflation, density perturbations grow only through gravitational instability within the expanding background cosmology. From this point on, the structure evolution can be well traced with large numerical simulations using cold dark matter (CDM) as the main ingredient. (iv) The structure evolution in the non-linear regime and the increasing importance of complex non-gravitational physics (*'gas-a)strophysics'*) on small scales is only accessible with elaborate numerical experiments. This regime includes all relevant galaxy scales and hence turns the detailed understanding of galaxy formation and evolution into a very difficult and unsolved task. However, down to the galaxy cluster scale of ~ 10 Mpc analytic approximations and models can still provide the basic structure formation framework and valuable physical insights.

In preparation for the cosmological tests presented in the next section and to provide a basic understanding of the formation process of galaxy clusters, we will summarize four main aspects of structure formation theory with a focus on galaxy clusters: (i) the general growth of density perturbations, (ii) the top-hat collapse model, (iii) the Press-Schechter mass function, and (iv) the spatial distribution of clusters.

3.2.1 Growth and collapse of density perturbations

Perturbation Growth

We will first have a closer look at how the primordial density fluctuations seeded by the inflationary epoch grow in general. This growth is mainly driven by the cold dark matter density component ρ_{CDM} which only interacts gravitationally. In the early Universe, however, the strong coupling of photons and baryons (the *photon-baryon fluid*) has important consequences on the structure formation. The homogeneous *Dark Energy* density ρ_{DE} , as the fourth player of perturbation growth, has an additional indirect influence by governing the dynamics of the expanding background cosmology.

The hydrodynamic equations are the starting point for the description of the gravitational instability of density fluctuations. Besides *Euler's Equation* (momentum conservation), the continuity equation (mass conservation) and *Poissions's Equation* are needed to close the system. These equations are transformed to comoving coordinates and the matter density field $\rho(\mathbf{x}, t) = \bar{\rho}_m(t) \cdot [1 + \delta(\mathbf{x}, t)]$ is expressed through the dimensionless

density contrast $\delta(\mathbf{x}, t)$

$$\delta(\mathbf{x}, t) = \frac{\rho(\mathbf{x}, t) - \bar{\rho}_m(t)}{\bar{\rho}_m(t)} . \quad (3.29)$$

The system can then be linearized for small fluctuation amplitudes $|\delta| \ll 1$ on top of the mean matter density field $\bar{\rho}_m$ and separated into the homogeneous background solution for the Hubble expansion (Equ. 3.4) and the inhomogeneous solutions for the evolution of the density contrast δ . The result of the perturbation analysis is a second order differential equation that governs the gravitational amplification of the fractional density contrast δ , which can be expressed in its general form as a damped wave equation

$$\ddot{\delta} + 2\frac{\dot{a}}{a}\dot{\delta} = \delta \left[4\pi G\bar{\rho}_m - \frac{c_s^2 k^2}{a^2} \right] . \quad (3.30)$$

The left hand side contains the acceleration and the damping term, where the Hubble expansion $H = \dot{a}/a$ acts as a friction force or a *Hubble drag*. The right hand side of Equ. 3.30 shows the gravitational force due to density fluctuation and an additional term originating from *Euler's Equation* when considering fluids with pressure, as is the case for the *photon-baryon fluid* of the early Universe. The speed of sound for this relativistic fluid with equation-of-state according to Equ. 3.5 is then given by $c_s^2 = \partial p / \partial \rho \simeq c^2/3$. For sufficiently large perturbation wave numbers $k = 2\pi/L$, corresponding to small wavelength scales L , the right hand side is negative implying an oscillating solution.

At this point, we will focus on the growing solution, which is obtained for the large scale perturbations with $k \ll (a/c_s)\sqrt{4\pi G\bar{\rho}_m}$ in the early Universe or as the general perturbation growth mode after matter-radiation decoupling, when the baryonic pressure vanishes. For a negligible oscillation term on the right hand side, Equ. 3.30 does not contain any spatial derivatives implying that the time evolution for the perturbation growth is separable from the initial spatial perturbation field $\delta_{i+}(\mathbf{x}, t_i)$ according to

$$\delta(\mathbf{x}, t) = D_+(t) \cdot \delta_{i+}(\mathbf{x}, t_i) + D_-(t) \cdot \delta_{i-}(\mathbf{x}, t_i) . \quad (3.31)$$

The decaying solution $D_-(t)$ is of little physical interest and will not be considered. The general expression for the growing perturbation solution $D_+(t)$ (*e.g.* Borgani, 2006) in linear approximation as a function of redshift z is given by

$$D_+(z) = \frac{5}{2}\Omega_m E(z) \cdot \int_z^\infty \frac{1+z'}{E(z')^3} dz' . \quad (3.32)$$

In an Einstein-de Sitter Universe ($\Omega_m = 1$) the perturbation amplitudes grow proportional to the scale factor $D_+ \propto a \propto (1+z)^{-1} \propto (t/t_i)^{2/3}$. For an empty Universe ($\Omega_{\text{tot}} \equiv 0$), (virtual) perturbations are frozen and do not grow at all. In a low density Universe (*e.g.* $\Omega_m \sim 0.3$, $\Omega_{\text{DE}} = 0$) the driving gravitational force on the right hand side of Equ. 3.30 is decreased resulting in a slower growth rate at low redshifts. At early epochs, however, the matter density of such models is still close to critical, *i.e.* to the Einstein-de Sitter case, with an analogous fast early growth phase which slows once the matter density drops significantly

below the critical value. When looking backwards in time from the present perspective, the effect of this slowed structure evolution is an increased number of objects, *e.g.* clusters, at high redshift relative to a critical matter density Universe. For a concordance cosmological model ($\Omega_m \sim 0.3$, $\Omega_{DE} = 0.7$), the addition of a *Dark Energy* component results in an intermediate degree of evolution, since the Hubble expansion must have been slower in the past, relative to an open Universe, leading to a smaller friction term in Equ. 3.30. Note that the ‘*Hubble drag*’ term depends on the cosmological parameters, which implicitly influence the perturbation growth in addition to the explicit dependance on the mean matter density $\bar{\rho}_m$.

Top-hat collapse

An important approach to tackle the non-linear structure evolution regime is provided by *Birkhoff’s theorem*, which states that a closed sphere within a homogeneous Universe evolves independent of its surroundings, *i.e.* as if no external forces are exerted on the sphere¹⁰. This implies that any overdense region of the Universe can be conceived as a homogeneous mini-Universe with the evolution driven by the local density parameters of the region under consideration.

The spherical top-hat model is the only system for which the collapse of an overdense region of the Universe can be treated analytically. For this we consider a spherical region with radius R and a homogeneous overdensity δ_{TH} embedded in a background field with constant density $\bar{\rho}_m$. According to *Birkhoff’s theorem* the evolution of this region is independent of the background field and can be described by the Newtonian approximation of the first Friedmann equation 3.1, *i.e.* with vanishing pressure and zero cosmological constant term. In analogy to a closed Universe, this finite region will expand up to a maximum radius R_{max} at turn-around time t_{turn} and then re-collapse in a time-symmetric fashion at time $t_{col} = 2 \cdot t_{turn}$. In practice, the overdense region will not collapse to a point but stabilize in a bound dynamic equilibrium state at radius $R_{vir} \simeq R_{max}/2$ once the *Virial* condition $2 \cdot \bar{E}_{kin} + \bar{E}_{pot} = 0$ is fulfilled. The gravitationally bound, virialized object with total energy¹¹ $E_{tot} = \bar{E}_{pot}/2 = -3GM^2/(5 \cdot 2R_{vir})$ is now detached from the Hubble flow, *i.e.* it does not take part in the overall expansion of the background cosmology.

In the case of an Einstein-de Sitter cosmology with $\Omega_m = 1$ some universal characteristics of the collapse process can be specified, with only small variations for other cosmologies. The density contrast at turn-around time t_{turn} , *i.e.* at the time of decoupling from the Hubble flow, is about $\delta_{turn} \simeq 4.55$. At collapse time t_{col} the contrast has increased to its final (universal) equilibrium value¹² of $\delta_{vir} \simeq 177$, which gives rise to the widely used definition of R_{200} as the cluster radius with an average density of 200 times the critical density ρ_{cr} . In comparison, the linear extrapolation of the density contrast according to Equ. 3.32 at t_{col} yields $\delta_{vir}(linear) \simeq 1.69$, and at turn-around $\delta_{turn}(linear) \simeq 1.06$, emphasizing the onset

¹⁰In reality residual tidal forces are expected which can be neglected for this discussion.

¹¹A factor of $3/5$ arises for the potential energy of a sphere with uniform density.

¹²This density contrast is roughly obtained from the turn-around density by considering the compression factor during collapse and the evolution of the critical density during the formation process.

of the non-linear regime and the break-down of the linear approximation during object collapse. Note that a virialized cluster with final radius $R_{\text{vir}} \simeq 1.5 h_{70}^{-1}$ Mpc originates from a collapsed region of size $\sim 6 \cdot R_{\text{vir}} \simeq 10 h_{70}^{-1}$ Mpc.

These considerations imply that any spherical overdensities reaching the critical density contrast δ_{turn} detach from the Hubble flow and form a virialized object at $t_{\text{vir}} = t_{\text{col}} \simeq 2 \cdot t_{\text{turn}}$. For the cold dark matter standard model with a scale invariant initial perturbation spectrum, sub-galactic halos are the first to decouple from the Hubble flow, since perturbations on small length scales have greater amplitudes (see Equ. 3.36). Galaxy clusters on the other hand have formed relatively recently and hence appear late on the cosmic stage, marking the largest mass scales that have had sufficient time to virialize.

The top-hat collapse model enables important physical insights into the cluster formation process. However, it rests upon many simplifications (spherical symmetry, homogeneous mass distribution, no external tidal forces, only gravitational physics) which are at best only an approximate description of the cluster formation conditions. The *Millennium Run* simulation of Springel *et al.* (2005) provides the most detailed and realistic cluster formation scenarios currently available. Figure 3.4 shows simulation snap-shots of the formation of a rich galaxy cluster over the last 10 Giga years of cosmic time ($2 \geq z \geq 0$). Besides the detailed dark matter distribution in the left panels, these simulations also trace the intracluster medium gas density (center panels) and the ICM temperature (right panels), which are directly accessible through X-ray observations. Note that the ICM gas density is a very good tracer of the underlying dark matter distribution, and that the substructure and asymmetry increases drastically beyond $z \gtrsim 1$.

3.2.2 Galaxy cluster statistics

After discussing the principal formation process of individual objects of the large-scale structure, we will now turn to the statistical properties of the overall galaxy cluster population. This section will focus on two essential properties of clusters which provide a sensitive link to cosmological models: (i) the distribution of cluster masses (mass function), and (ii) the spatial clustering properties (power spectrum).

Cluster mass function

The basic framework to quantitatively approximate the comoving number density of (relaxed) dark matter halos as a function of mass and redshift $n(M, z)$ is provided by the *Press-Schechter* formalism (Press and Schechter, 1974). The main idea of this procedure is the statistical evaluation of the Gaussian fluctuation field $\delta(\mathbf{x}, t)$ and the identification of density peaks above the critical collapse value after applying a spatial filter function corresponding to a minimum object mass M_{min} .

¹³The simulation movie, from which the snap-shot images are taken, can be found at http://www.mpa-garching.mpg.de/galform/data_vis/index.shtml.

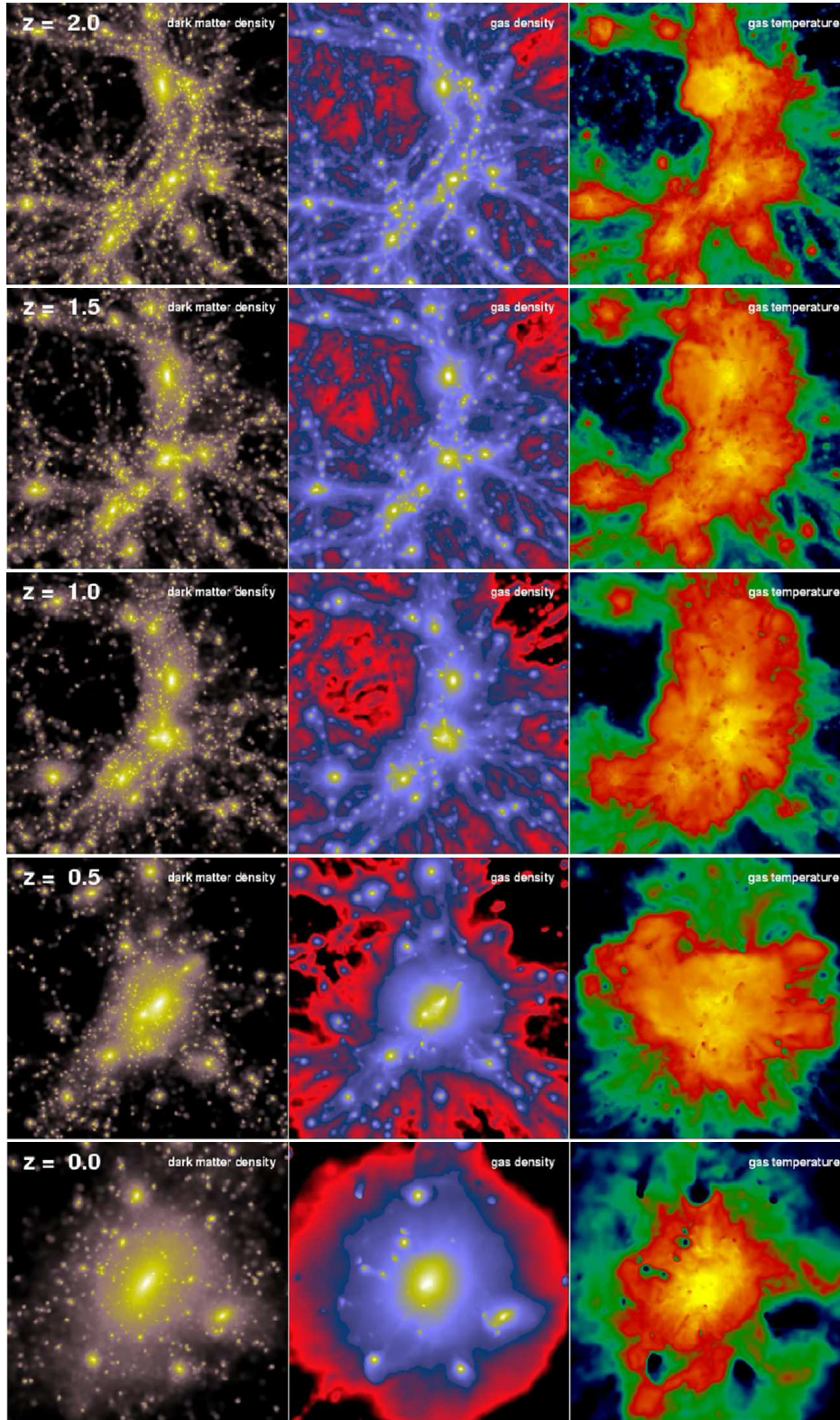


Figure 3.4: High resolution simulation of the formation of a rich cluster of galaxies from the *Millennium Run*. From *top to bottom* snapshots at redshifts of 2.0, 1.5, 1.0, 0.5, and $z=0$ are shown. The *left panels* illustrate the dark matter distribution, the *center panels* the gas density, and the *right panels* the temperature structure at the corresponding redshift. Note the significant increase of substructure and asymmetry with redshift. The gas density and temperature are in principle accessible cluster observables by means of X-ray observations. Credits: V. Springel.¹³

Since the filtering concept will be of central importance for this section, we will first have a closer look at the properties of smoothed density fields. Let us denote $W_R(\mathbf{x})$ as a (3-D) spatial window function with smoothing length scale R . In the simplest case of a top-hat filter this will just be a sphere with radius R , which has a zero value outside and a normalized constant value $W_R(|\mathbf{x}| \leq R) = (4\pi R^3/3)^{-1}$ inside the sphere. A filtered density field will hence contain the average value within this sphere surrounding any given point \mathbf{x} . Another widely used window function is a Gaussian filter, but more complicated functional forms are conceivable. Mathematically spatial filtering is equivalent to a convolution of the density field $\delta(\mathbf{x})$ with the window function W_R

$$\delta_R(\mathbf{x}) = \delta_M(\mathbf{x}) = \int \delta(\mathbf{y}) W_R(|\mathbf{x} - \mathbf{y}|) d\mathbf{y} , \quad (3.33)$$

where $\delta_R(\mathbf{x})$ denotes the filtered field. In the case of the spherical top-hat filter, the average mass M contained inside the window function is $\langle M \rangle \simeq 4\pi R^3 \bar{\rho}_m / 3$, providing a one-to-one correspondence between the comoving smoothing length scale R and the mass scale M . Since a spatial convolution translates into a simple multiplication in \mathbf{k} -space, working with the Fourier representation of the density contrast is often advantageous

$$\tilde{\delta}(\mathbf{k}) = \frac{1}{(2\pi)^{3/2}} \int d\mathbf{x} \delta(\mathbf{x}) e^{i\mathbf{k}\mathbf{x}} . \quad (3.34)$$

The filtered density contrast in Fourier space is then $\tilde{\delta}_R(\mathbf{k}) \propto \tilde{\delta}(\mathbf{k}) \cdot \tilde{W}_R(\mathbf{k})$, with $\tilde{W}_R(\mathbf{k})$ being the Fourier transform of the window function. The averaged squared density fluctuations in Fourier space define the important *power spectrum* $P(k)$, or more accurately, the power spectral density function

$$P(k) \equiv \langle |\tilde{\delta}(\mathbf{k})|^2 \rangle = \frac{1}{2\pi^2} \int dr r^2 \xi(r) \frac{\sin(kr)}{kr} . \quad (3.35)$$

The right hand side shows that the power spectrum $P(k)$ is in effect the Fourier transform of the 2-point correlation function $\xi(r)$, which states the probability to find two objects at separation r in excess to a random distribution. The power spectrum expresses the amount of cosmic structure as function of wavenumber k corresponding to the length scale $L \simeq 2\pi/k$. As a second order statistic, the power spectrum provides a complete statistical characterization of the underlying Gaussian¹⁴ fluctuation field, in analogy to the mean and standard deviation as parameters for the one dimensional Gaussian distribution.

Combining the discussions on spatial filters and Fourier representations, we can introduce the variance of the smoothed fluctuation field $\delta_R(\mathbf{x})$ as

$$\sigma_R^2 = \sigma_M^2 = \langle \delta_R^2 \rangle = \langle \tilde{\delta}_R^2 \rangle = \frac{1}{2\pi^2} \int dk k^2 P(k) \tilde{W}_R^2(k) . \quad (3.36)$$

Here *Parseval's theorem*¹⁵ was applied and in the last step, Equ. 3.35 and the isotropy assumption were used, implying that the final result can only depend on the norm of

¹⁴Gaussianity is one of the underlying assumptions for the *Press-Schechter* theory.

¹⁵The norm of a function is invariant under Fourier transformation, *i.e.* $\int |f(\mathbf{x})|^2 d\mathbf{x} = \int |\tilde{f}(\mathbf{k})|^2 d\mathbf{k}$.

the wave vector \mathbf{k} but not its direction. As discussed, the smoothing scale R is directly related to the mass scale M and thus to the mass variance $\sigma_M^2 \equiv \langle |\delta M/M|^2 \rangle$, with the exact functional form depending on the shape of the used filter.

We can now return to the *Press-Schechter* theory and outline the procedure to obtain an approximate dark matter halo mass function $n(M, z)$, which can be interpreted as galaxy cluster mass function. In addition to the spatial dependence of the fluctuation field, the time evolution, or equivalently the redshift dependence, has to be considered according to the linear theory evolution of Eqs. 3.31 & 3.32. As pointed out, the collapsed objects reach a virialized state once a critical linearly extrapolated density contrast $\delta_c = \delta_{\text{vir}}(\text{linear}) \simeq 1.69$ is reached, with a weak dependance of the exact numeric value on the cosmological model and the redshift. For a linear extrapolation to the present time t_0 or $z = 0$, density contrast peaks with amplitude δ_c can be identified with objects currently reaching the virial equilibrium state, *i.e.* presently formed systems. On the other hand, objects that have already collapsed and formed at higher redshift z_{form} will have a higher density contrast today $\delta_{0,c} = \delta_c / D_+(z_{\text{form}})$ (see Equ 3.31). The linear growth factor $D_+(z)$ with normalization $D_+(z=0) \equiv 1$ is hence the main factor for the redshift evolution of collapsed objects. For an Einstein-de Sitter Universe the last expression reduces to $\delta_{0,c}(\text{EdS}) = 1.69 \cdot (1 + z_{\text{form}})$, but generally both the critical overdensity δ_c and the linear growth factor $D_+(z)$ are cosmology dependent.

In order to obtain the number of collapsed objects at redshift z with mass M the following procedure is applied: (i) Determine the smoothing length scale R corresponding to the mass scale M . (ii) Filter the present fluctuation field with the window function W_R to arrive at $\delta_R(\mathbf{x}, t_0)$. (iii) Count the smoothed density peaks for amplitudes above δ_c at redshift z , *i.e.* for the minimum present amplitude $\delta_{\text{min}} > \delta_{0,c} = \delta_c / D_+(z)$. These peaks are interpreted as collapsed objects of mass $\geq M$ at redshift z . The probability $p(\delta_{0,c})$ to find amplitudes above the collapse threshold $\delta_{0,c}$ follows from Gaussian statistics and is given by

$$p(\delta_{0,c}, R) = \int_{\delta_{0,c}}^{\infty} p(\delta, R) d\delta = \frac{1}{2} \text{erfc} \left(\frac{\delta_{0,c}}{\sqrt{2} \cdot \sigma_R} \right), \quad (3.37)$$

where $\text{erfc}(x)$ is the error function¹⁶ and $\sigma_R = \sigma_M$ the smoothed fluctuation amplitude of Equ. 3.36. This probability can be interpreted as spatial filling factor or mass fraction of collapsed objects above the threshold mass.

The final *Press-Schechter* mass function $n(M, z)$ (*e.g.* Borgani, 2006), *i.e.* the redshift evolution of the dark matter halo number density, is derived from the above filling factor of collapsed objects at redshift z in the mass interval $[M, M+dM]$ as

$$\frac{dn_{\text{PS}}(M, z)}{dM} = -\frac{\partial p}{\partial M} \frac{2}{V_M} = \sqrt{\frac{2}{\pi}} \cdot \frac{\bar{\rho}_m}{M^2} \cdot \frac{\delta_c}{\sigma_M(z)} \cdot \left| \frac{d \log \sigma_M(z)}{d \log M} \right| \cdot \exp \left(-\frac{\delta_c^2}{2 \sigma_M^2(z)} \right). \quad (3.38)$$

¹⁶The error function is defined as $\text{erfc}(x) = \frac{2}{\sqrt{\pi}} \int_x^{\infty} e^{-t^2} dt$.

To go from a filling factor per unit volume to a cluster number, one has to divide by the occupied volume of the object $V_M \simeq M/\bar{\rho}_m$. The additional factor of two corrects for a shortcoming of the *Press-Schechter* theory namely that the integral of Equ. 3.37 over all mass scales only accounts for half the total mass (the ‘cloud-in-cloud’ problem). The mass dependence of the probability $p(\delta_{0,c})$ is implicitly contained in the mass-scale smoothed amplitude σ_M of the fluctuation field. This important factor also contains the dependence on cosmological parameters through the linear growth factor $D_+(z)$ governing the σ_M evolution with redshift. This implies that the high-mass end of the cluster mass function, where the last term dominates, is ‘exponentially sensitive’ to variations of cosmological parameters.

The *Press-Schechter* theory in the form presented here rests upon several strong assumptions, *e.g.* a spherically symmetric collapse without substructure, and some *ad hoc* procedures such as the correct filter form or the cloud-in-cloud problem. Meanwhile *extended Press-Schechter* formalisms provide more rigorous derivations of the mass function (*e.g.* Bond *et al.*, 2001; Bower, 1991). Sheth & Tormen (2001) have generalized the mass function for the more realistic assumption of an ellipsoidal collapse. A particularly well tested and widely used fitting formula for the mass range 10^{12} – $10^{15} M_\odot$ has been given by Jenkins *et al.* (2001) based on large numerical simulations. A comparison to the more precise *Jenkins* mass function

$$\frac{dn_J(M, z)}{dM} = 0.315 \cdot \frac{\bar{\rho}_m}{M^2} \cdot \frac{d \ln \sigma_M^{-1}}{d \ln M} \cdot \exp \left(-|\ln \sigma_M^{-1} + 0.61|^{3.8} \right) \quad (3.39)$$

reveals that the *Press-Schechter* mass function underestimates the number density of massive clusters and overestimates the abundance of low-mass objects.

Figure 3.5 illustrates the results of the *Millennium Run* simulation and the very good agreement with the predictions of the *Jenkins* mass function. Shown is dark matter halo multiplicity function $(M^2/\bar{\rho}_m) dn/dM = N \cdot (M/dM) \cdot (V_M/V)$, *i.e.* the mass fraction carried by objects in a unit mass bin. Note that the density from $z=0$ to $z=1.5$ drops by three orders of magnitude for halo masses of $\sim 10^{15} h^{-1} M_\odot$ and by one order of magnitude for masses of $\sim 10^{14} h^{-1} M_\odot$.

Cluster power spectrum

As a last application of the standard structure formation scenario, we will take a closer look at the spatial distribution of galaxy clusters, *i.e.* the clustering properties of clusters. Figure 3.6 shows the simulated cosmic web of the large-scale structure on a 500 Mpc scale (left) and zoomed in by a factor of four (right). The top panels show the simulated dark matter distribution at redshift $z = 1.4$ and the bottom panels the present day structure. The main aim of this section is to introduce the basic tools for a quantitative statistical description of the large-scale structure and how the observed spatial galaxy cluster distribution is connected to cosmological parameters. The tools and tests of this subsection will

¹⁶<http://www.mpa-garching.mpg.de/galform/virgo/millennium/index.shtml>

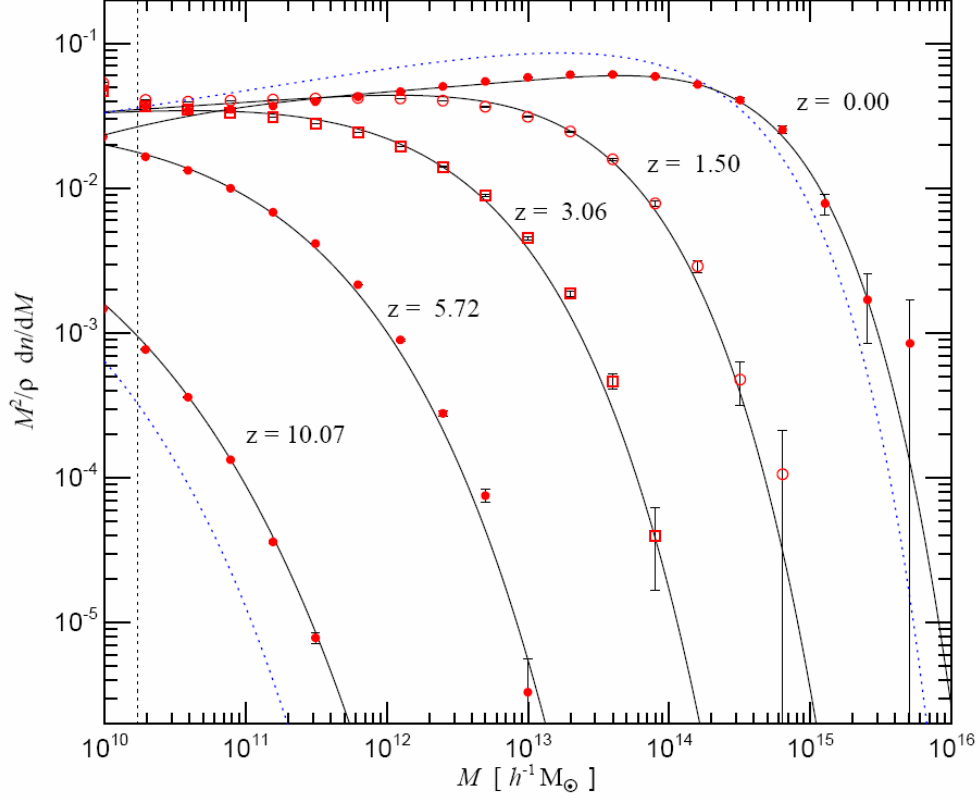


Figure 3.5: Differential dark matter halo number density as a function of mass and epoch as obtained with the *Millennium Run* simulation. Shown is the halo multiplicity function ($M^2/\bar{\rho}_m$) dn/dM against the halo mass for different redshifts. Of particular interest are the observationally accessible curves at redshift $z = 0$ and $z = 1.5$. Solid lines show predictions using the *Jenkins* fitting formula (Equ. 3.39), dotted lines show *Press-Schechter* model predictions of Equ. 3.38. Plot from Springel *et al.* (2005).

not have direct applications for the current XDCP survey but will be of prime importance for the next generation of galaxy cluster surveys (see Chap. 12), for which XDCP assumes a pathfinder role for high-redshift clusters.

The power spectrum $P(k)$ is the main tool for the statistical description of the large-scale structure and has been introduced in Equ. 3.35. Whereas the overall shape and features of $P(k)$ can be theoretically derived, the amplitude or normalization of the power spectrum has to be empirically determined. This can be achieved with the help of σ_8 , a very important but probably the least intuitive cosmological parameter.

For a given filtering length scale R , Equ. 3.36 provides the link between the mass variance σ_R^2 on this scale and the power spectrum $P(k)$, which fixes the *a priori* unknown absolute normalization of $P(k)$. The chosen filter scale R should on one hand be sufficiently large to ensure the validity of linear theory and on the other hand small enough

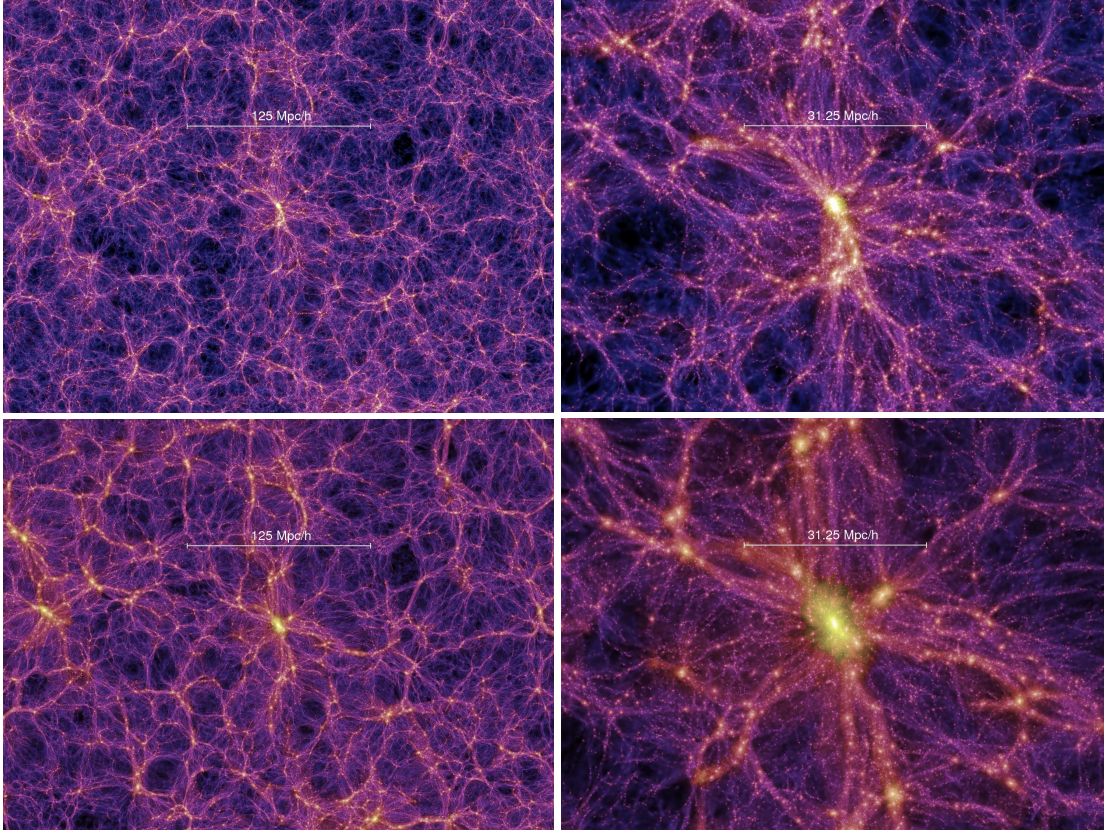


Figure 3.6: The cosmic large-scale structure as seen with the *Millennium Run* simulation. The *top panels* show the dark matter distribution at redshift $z=1.4$ for a comoving image scale of approximately 500 Mpc (*left*) and 125 Mpc (*right*) on a side. The same regions at redshift $z=0$ are illustrated in the *bottom panels*. Note that the cosmic web is basically in place at $z > 1$, but the nodes, *i.e.* the clusters, still actively accrete large amounts of matter until the present. Credits: V. Springel¹⁶.

to allow observations of a large amount of structure¹⁷. A sensible choice for fixing the filtering scale is $R \equiv 8 h^{-1} \text{Mpc}$, which was motivated by results of early galaxy surveys finding $\delta_{\text{gal}}(R = 8 h^{-1} \text{Mpc}) \simeq \delta N_{\text{gal}}/N_{\text{gal}} \simeq \delta M/M \simeq 1$, *i.e.* the variance of galaxy counts in spatial bins of radius $8 h^{-1} \text{Mpc}$ is similar to the mean value. The mass scale of this filtering length is $M \simeq 5 \times 10^{14} M_{\odot}$ and corresponds to the collapsed region of a massive galaxy cluster. The mass variance of order unity on the $8 h^{-1} \text{Mpc}$ scale also marks the transition region from the linear regime with $\delta \lesssim 1$, *i.e.* $L \gtrsim 8 h^{-1} \text{Mpc}$, to the non-linear regime at $L \ll 8 h^{-1} \text{Mpc}$.

In short, σ_8 is the average fluctuation amplitude¹⁸ of the linearly evolved (Eqs. 3.31 & 3.32), present day dark matter density contrast field $\delta_8^{\text{DM,lin}}(\mathbf{x}, t_0)$ smoothed with a top-hat filter of comoving radius $R = 8 h^{-1} \text{Mpc}$. The formal definition and its

¹⁷The homogeneity of the Universe on very large scales decreases the mass variance with increasing filtering length R . For large R and the use of a spherical top-hat filter one obtains $\sigma_M \simeq \delta M/M \propto M^{-2/3}$.

¹⁸Meaning the root-mean-square (rms) or standard deviation of the Gaussian field.

connection to the power spectrum is then given by

$$\sigma_8^2 = \langle \delta_{8h^{-1}\text{Mpc}}^2 \rangle_0 = 4\pi \int \frac{dk k^2}{(2\pi)^3} P_0^{\text{DM}}(k) \tilde{W}_{8h^{-1}\text{Mpc}}^2(k) . \quad (3.40)$$

The single dimensionless number σ_8 hence determines the height of density peaks and consequently the object abundance. The discussed galaxy cluster mass function (Eqs. 3.38 & 3.39) provides a direct measure of σ_8 . (Nevertheless, σ_8 is probably the least securely determined prime cosmological parameter.)

The second important parameter related to the large-scale structure in the Universe is the power law index n_s of the primordial (*i.e.* initial) power spectrum $P_i(k) \propto k^{n_s}$. This index is observationally confirmed (Spergel *et al.*, 2007) to be very close to the ‘scale-free’ *Harrison-Zeldovich spectrum* $P_i^{\text{HZ}}(k) \propto k^1$ (*i.e.* $n_s = 1$), which is also predicted by inflationary theories.

From the known evolution of the density fluctuation field $\delta(t) \propto D_+(t)$ (Equ. 3.31) and the definition of the power spectrum (Equ. 3.35), the time evolution of $P(k, t)$ starting with the initial fluctuation spectrum seeded after inflation is then given by

$$P(k, t) = D_+^2(t) \cdot A k^1 \cdot T^2(k, t) . \quad (3.41)$$

The *a priori* unknown amplitude A of the power spectrum (today) is directly linked to σ_8 as an alternative normalization method (cluster normalization). $T(k)$ is the so-called *transfer function* which is an extra term containing all evolutionary effects that alter the original linear form of the primordial seed power spectrum. In particular, the *transfer function* incorporates important scale-imprinting effects on the initially scale-invariant power spectrum.

The first imprinted physical scale with prime influence on the present day overall shape of $P(k)$ is the (particle) horizon at the epoch of matter-radiation equality $D_{\text{equ}}^{\text{H}}$ at redshift z_{equ} . This characteristic length scale represents the distance over which causal influence can propagate during the radiation dominated era of the Universe and is given by

$$D_{\text{equ}}^{\text{H}} = \frac{c}{\sqrt{2} H_0} \frac{1}{\sqrt{(1 + z_{\text{eq}}) \Omega_{\text{m}}}} \simeq 16 (\Omega_{\text{m}} h^2)^{-1} \text{Mpc} \sim 100 \text{Mpc} . \quad (3.42)$$

During the radiation dominated early epoch with a coupled *photon-baryon fluid*, the pressure term in Equ. 3.30 becomes important and causes an oscillatory behavior of the fluctuations *inside* the horizon $D_{\text{equ}}^{\text{H}}$. Fluctuation growth on scales $L \lesssim D_{\text{equ}}^{\text{H}}$ is therefore effectively suppressed, and the structure growth can only proceed on super-horizon scales $L > D_{\text{equ}}^{\text{H}}$ beyond the causal influence of the radiation pressure.

For the following arguments, we only consider the (cold) dark matter component as the dominant contribution to the matter density. The decisive criterion for the growth of perturbation modes with wavenumber $k = 2\pi/L$ during the rapid expansion phase of the radiation-dominated early epoch is determined by whether or not the length scale of the mode is contained within the expanding horizon $D^{\text{H}}(z)$ at redshift z . Modes that are outside this region of causal influence $k_{\text{grow}}(z) < 2\pi/D^{\text{H}}(z)$ do not ‘feel’ the radiation

pressure implying that the modes grow according to the linear expectations of Equ. 3.41 with $T(k) = 1$. Once the expanding causality horizon encompasses perturbation modes $k_{\text{suppr}}(z) > 2\pi/D^{\text{H}}(z)$, the growth suppression sets in and the perturbation amplitudes essentially remain constant.

For the growth evolution in the radiation dominated phase starting after inflation and ending with the epoch of matter radiation equality at $z_{\text{equ}} \sim 3500$, we obtain the following scenario: (i) Initially the primordial *Harrison-Zeldovich spectrum* evolves homogeneously as the modes on all length scales grow proportional to $D_+^2(t)$, *i.e.* only the amplitude of the linear power spectrum increases with time. (ii) Once the length scale of a perturbation mode enters the particle horizon at z_{enter} , *i.e.* $k_{\text{enter}}(z_{\text{enter}}) = 2\pi/D^{\text{H}}(z_{\text{enter}})$, further growth is suppressed and the amplitude of the mode halts at the value of horizon entering. (iii) This process proceeds from the smallest scales, *i.e.* large wavenumbers k , to larger scales as the horizon expands with time, which implies that the structure growth suppression first influences small regions and over time gradually halts the growth for modes of increasing scales. Upon horizon entering, the spectral power density of the corresponding perturbation mode $P(k_{\text{enter}})$ will be held constant, while the modes of smaller wavenumbers continue to grow. The overall shape of the power spectrum $P(k, t)$ will hence bend over towards lower amplitudes for modes with $k \gtrsim k_{\text{enter}}(z)$. (iv) After matter-radiation equality z_{eq} , the matter density dominates the dynamics of the Universe. The *photon-baryon fluid* decouples, resulting in a vanishing pressure for the baryons and an associated resumed structure growth on all scales. The largest length scale which experiences a growth suppression is thus the introduced horizon scale at equality D_{eq}^{H} , which defines the break point k_{eq} of the present power spectrum.

This horizon-crossing growth suppression mechanism in the early Universe completely fixes the overall shape of the present day cold dark matter power spectrum $P_{\text{CDM}}(k, t_0)$ imprinting the characteristic length scale D_{eq}^{H} as a break point. For small wavenumbers $k \ll 2\pi/D_{\text{eq}}^{\text{H}}$ the form of the primordial power spectrum is conserved with $P_{\text{CDM}}(k \ll k_{\text{eq}}, t_0) = A k$, *i.e.* $T(k) \approx 1$. Large wavenumbers with $k \gg k_{\text{eq}}$ have experienced an extended early period of growth suppression resulting in a transfer function $T(k) \approx (D_{\text{eq}}^{\text{H}} k)^{-2}$ and consequently a power spectrum of the form $P_{\text{CDM}}(k \gg k_{\text{eq}}, t_0) \propto k^{-3}$. The break point $k_{\text{eq}} = 2\pi/D_{\text{eq}}^{\text{H}} \propto (\Omega_{\text{m}} h^2) \text{Mpc}^{-1}$, *i.e.* the maximum of the power spectrum, is sensitive to the matter density Ω_{m} and moves towards higher wavenumbers with increasing matter content, reflecting the earlier epoch of matter-radiation equality.

In principle, this result compresses the statistical information present in the simulated large-scale dark matter distribution shown in Fig. 3.6. The locally observed galaxy cluster power spectrum is shown in the next Chapter in Fig. 4.2 (upper curve in right panel). The broad maximum of the power spectrum is visible but will only be well constrained with the extended sample of local X-ray cluster surveys currently in preparation. Note that the well-fit $P(k) \propto k^{-3}$ behavior at large wavenumbers confirms the cold dark matter paradigm. Hot (HDM) or warm (WDM) forms of dark matter would exhibit a different power spectrum shape, as small scale perturbations are additionally damped by diffusion processes of the fast particles ('free streaming').

The final ingredient to fully understand the observed cluster power spectrum of Fig. 4.2

and its vertical offset to the galaxy power spectrum is the concept of *biasing* (Kaiser, 1984). So far we have mostly related the discussion to the cold dark matter power spectrum $P_{\text{CDM}}(k)$, which is not directly accessible to observations. Different classes of observable objects could have systematic offsets of their density field with respect to the dark matter density contrast $\delta_{\text{object}} = b \cdot \delta_{\text{CDM}}$. The pre-factor b is the *bias* of the object class which can be determined from first principles. The origin of galaxy clusters from the highest peaks in the initial density contrast field results in a large bias factor of $b \simeq 2.6$, *i.e.* clusters have an amplified¹⁹ power spectrum $P_{\text{cluster}}(k) = b^2 \cdot P_{\text{CDM}}(k) \simeq 6.8 \cdot P_{\text{CDM}}(k) \sim 6.8 \cdot P_{\text{galaxy}}(k)$. This greatly enhanced clustering strength can be understood in terms of the underlying long-wavelength fluctuation modes of the dark matter density field. The probability for a cluster-scale density perturbation to reach the critical collapse threshold value δ_c is highly increased if this region is found on top of a larger perturbation mode with small wavenumber. On the other hand, the probability is suppressed if the cluster-scale perturbation coincides with a minimum of the underlying long-wavelength mode. The *biasing* of different object classes is hence expected to increase with object mass. Clusters in this respect are amplified probes and can thus yield valuable results with a lower number of objects compared to galaxies.

The second important imprinted physical scale in the transfer function $T(k)$ is the sound horizon at matter-radiation decoupling. We are now considering the baryon component of the matter density which implies that the expected second order baryonic effects are about an order of magnitude smaller than those due to the dark matter. Nevertheless, the theory is well understood (*e.g.* Hu & Sugiyama, 1996; Eisenstein & Hu, 1998), and observations of the so-called *baryonic acoustic oscillations* (BAOs) bear great promise to yield valuable results for the *Dark Energy* studies over the next two decades.

The inclusion of baryons during the strongly coupled baryon-photon fluid phase before recombination at redshift z_{rec} requires the consideration of the last oscillation term in Equ. 3.30. For small scales inside the sound horizon (SH) $D^{\text{SH}}(z)$ the relativistic photon-baryon system behaves like a damped, forced oscillator where the self-gravitation of matter overdensities acts as driving force and the photon induced pressure as counter action. In this relativistic fluid sound waves, *i.e.* pressure and density perturbations, can propagate at the sound speed of $c_s = \sqrt{\partial p / \partial \rho} \simeq c / \sqrt{3}$. At the epoch of hydrogen recombination at $z_{\text{rec}} \approx 1100$, photons and baryons decouple, which implies that pressure waves cease to expand and are frozen into the (baryonic) matter distribution. The longest *baryonic acoustic oscillation* wavelength, *i.e.* the first harmonic, is hence the comoving distance a sound wave could have propagated before recombination and is given by the sound horizon at z_{rec} (Hu, 2004)

$$D_{\text{rec}}^{\text{SH}} \simeq 147 \cdot (\Omega_{\text{m}} h^2 / 0.13)^{-0.25} (\Omega_{\text{b}} h^2 / 0.023)^{-0.08} \text{ Mpc} = 147.8 \pm 2.6 \text{ Mpc} . \quad (3.43)$$

The numeric value was measured with WMAP (Spergel *et al.*, 2007) with about 2% accuracy and is expected to be determined on the percent level within the next few years.

¹⁹The biasing factor depends on the typical cluster mass in a survey. The given numeric values are taken from the REFLEX survey (see Sect. 4.2).

The first harmonic acoustic wave hence imprints an overdensity in the matter distribution which will be detectable as a peak, implying enhanced structure, in the 2-point correlation function $\xi(r)$ at scale $D_{\text{rec}}^{\text{SH}}$ or as a modulation peak in the power spectrum at the corresponding wavenumber. Higher order harmonics give rise to additional acoustic peaks at shorter wavelengths resulting in a characteristic *baryonic acoustic oscillation* pattern in the power spectrum.

The imprinted sound horizon of $D_{\text{rec}}^{\text{SH}} \simeq 148 \text{ Mpc}$ acts as a high-precision comoving ‘standard ruler’. In principle, any object class can be used to probe the *baryonic acoustic oscillations* and to determine their locations in the power spectrum as a function of redshift. However, as second order effect, BAO measurements are extremely difficult and require high-precision measurements of $P(k)$. It is also expected that the oscillations are damped or washed out at low redshift due to the onset of non-linear effects.

The detection of the first acoustic peak in the correlation function of luminous red SDSS galaxies at $z \sim 0.35$ has been reported (Eisenstein *et al.*, 2005). The measurement of *baryonic acoustic oscillations* in power spectra of galaxy clusters provides a potentially powerful cosmological tool for the future (*e.g.* Angulo *et al.*, 2005) but requires cluster samples of the order of ten thousand.

3.3 Cosmological Tests with Galaxy Clusters

In the last two sections some important aspects of the close interplay between the observable properties of galaxy clusters and the underlying global geometry and structure formation process in the Universe were introduced. This section will shortly summarize a number of cosmological tests that use galaxy clusters as probes and have been successfully applied in the past or will become feasible within the next decade.

For the dawning era of precision cosmology it will be crucial to measure cosmological parameters with tests sensitive to the global geometry of the *homogeneous Universe* **and** methods probing the structure evolution of the *inhomogeneous Universe*. The very different physical nature of the methods and their underlying theoretical frameworks will allow important consistency cross-checks of the emerging cosmological concordance model. Galaxy clusters in this respect enable several independent cosmological tests for both fundamental aspects which qualifies the cluster population as one of the most versatile cosmological probes.

The majority of cosmological tests can be reduced to the measurement of effectively four cosmic evolution functions for which the dependence on the underlying cosmological parameters have been discussed: (i) the cosmic expansion history $H(z)$ (Equ. 3.16), (ii) cosmic distances $D(z)$ (Eqs. 3.19, 3.20, 3.21), (iii) cosmic age $t(z)$ (Equ. 3.28), and (iv) the linear growth factor $D_+(z)$ (Equ. 3.32). The first three methods are linked to the global geometry and probe the *homogeneous Universe*, the last one traces the structure growth of the *inhomogeneous Universe*.

- (1) **Cluster Mass Function:** The cluster abundance of the local Universe mainly depends on the matter density Ω_m and the amplitude of the density fluctuation field

σ_8 . The mass function is related to the statistics of rare high amplitude peaks in the primordial matter distribution. For a direct comparison to the observed cluster population, the predicted mass function $n(M)$ is converted to the measured X-ray luminosity function (XLF) via $\phi(L_X) = n[M(L_X)] \cdot dM/dL_X$. The X-ray luminosity function at $z \sim 0$ has been well established (Böhringer *et al.*, 2002a) and serves as local reference for evolution measurements. The local XLF is degenerate concerning the parameter combination $\sigma_8 \cdot \Omega_m^{0.5}$, *i.e.* the effect of a larger fluctuation amplitude can be compensated by a lower matter density. The degeneracy can be broken in combination with the power spectrum or by measuring the redshift evolution in the next test.

- (2) **Number Density Evolution:** The redshift evolution of the cluster abundance out to $z \sim 1.5$ will be the main cosmological test of the final XDCP sample. The evolution of the cluster mass function $n(M, z)$ combines two tests simultaneously: (i) the comoving volume elements $dV_{\text{com}} \propto D^2/H(z)$, governed by the expansion history, and (ii) the growth of the mass fluctuation spectrum driven by $D_+(z)$. The cosmological test also becomes increasingly sensitive to variations of the *Dark Energy* parameters Ω_{DE} and w at redshifts above $z \gtrsim 0.8$. Up to now, the changing demographics of the entire cluster population has been investigated out to intermediate redshifts of $z \sim 0.8$ by Mullis *et al.* (2004) and Borgani *et al.* (2000) (see Fig. 4.3), but only weak evolutionary effects have been found. The redshift at which the cluster number density decreases significantly is yet to be determined and will be one of the goals for XDCP.
- (3) **Amplitude and Shape of Power Spectrum:** The clustering properties and the general shape of the cluster power spectrum depend on the matter density Ω_m and the amplitude of the dark matter fluctuation spectrum σ_8 as discussed in Sect. 3.2.2. Reliable measurements require large area contiguous surveys such as the ROSAT All-Sky Survey. The currently best measured cluster power spectrum has been obtained with the REFLEX survey (see Fig. 4.2) which will soon be improved upon with the extended NORAS 2 and REFLEX 2 samples (see Sect. 4.2). Future X-ray surveys such as eROSITA (see Sect. 12.2) will be able to measure the power spectrum as a function of redshift and will thus directly probe the evolution of the growth function $D_+(z)$.
- (4) **Baryonic Acoustic Oscillations:** Measurements of the locations of the acoustic peaks in the cluster power spectrum as a function of redshift will be one of the main aims and challenges of the eROSITA mission (Sect. 12.2) and will require a total of 50 000–100 000 clusters with approximate redshifts. This cosmological test, however, is one of the cleanest methods to probe *Dark Energy* since it is least affected by systematic uncertainties. It is based on the well-understood ‘standard ruler’ imprinted by the sound horizon at the epoch of last scattering $D_{\text{rec}}^{\text{SH}}$. Measurements of the transverse ‘baryonic wiggles’ probe the angular size distance $d_{\text{ang}}(z)$ (Equ. 3.21)

while measurements in the radial direction trace the expansion history $H(z)$ through Equ. 3.19.

- (5) **Cluster Baryon Mass Fraction:** This conceptually simple and attractive test rests upon the assumption that clusters, as objects that have collapsed from a region of $10 h^{-1} \text{Mpc}$, represent a fair accounting of the relative matter content in the Universe, *i.e.* that their baryon mass fraction f_b is representative. The cluster gas mass fraction f_{gas} can be well measured with X-ray observations. With corrections for the galaxy mass in clusters, one obtains the universal total cluster baryon fraction which is asymptotically approaching values of $f_b \sim 0.12\text{--}0.14 h_{70}^{3/2}$ towards the cluster outskirts. If the baryon content Ω_b of the Universe is taken as prior from cosmic nucleosynthesis calculations, the total matter density can be determined by $\Omega_m = \Omega_b/f_b$ (*e.g.* Allen *et al.*, 2003).
- (6) **Evolving Gas Mass Fraction:** This method is a generalization of test (5) and uses the cluster gas mass fraction f_{gas} as ‘standard ruler’ to probe the global geometry of the Universe (Sasaki, 1996). The additional assumption is that the gas mass fraction is universal at all redshifts $f_{\text{gas}}(z) \approx \text{const}$. Since measurements of the gas mass ($M_{\text{gas}} \propto h^{-5/2} d_{\text{ang}}^{5/2}$) and total mass ($M_{\text{tot}} \propto h^{-1} d_{\text{ang}}$) obey different scaling relations with distance, the resulting observed gas mass fraction scales with $f_{\text{gas}}(z) \propto d_{\text{ang}}^{3/2}(z)$. The measured gas mass fraction hence depends on the assumed angular diameter distance to the cluster, and will deviate from the (assumed) universal value $\bar{f}_{\text{gas}}(z=0)$, if the reference cosmology is incorrect. This geometric test can constrain the parameters Ω_m , Ω_{DE} , and w and has been applied by Allen *et al.* (2004) based on detailed X-ray observations of 26 dynamically relaxed clusters at $z \lesssim 0.9$.
- (7) **Absolute Distance Measurements:** When X-ray and SZE observations are combined, the absolute distance to a cluster can be determined, allowing the measurement of the Hubble constant H_0 . The SZ effect (see Sect. 2.3.6) yields the observed temperature decrement $\Delta T \propto \int n_e T_e dl \propto n_0 T_0 R_{\text{cl}}$, and the observation of the thermal X-ray emission (see Sect. 2.3.1) results in the flux $S_X \propto \int n_e^2 \Lambda(T_e) dl \propto n_0^2 R_{\text{cl}}$, where R_{cl} is the clusters radius, n_0 the gas density, and T_0 the gas temperature. Elimination of n_0 results in an expression for the physical cluster radius R_{cl} , which can be related to the observed angular diameter θ_{cl} to yield the angular diameter distance via

$$d_{\text{ang}}(z) = \frac{R_{\text{cl}}}{\theta_{\text{cl}}} = \frac{\Delta T^2}{S_X} \frac{1}{T_0^2 \theta_{\text{cl}}} \cdot \text{const} \approx \frac{c z}{H_0}. \quad (3.44)$$

The last step is a low redshift approximation for H_0 , which can be generalized for more distant clusters to $H(z)$. Achievable accuracies for H_0 based on individual cluster measurements are about $\pm 20 \text{ km s}^{-1} \text{Mpc}^{-1}$.

- (8) **Cluster Number Counts:** Cumulative cluster number counts provide a model independent test since only X-ray flux measurements are needed. Generalizing Equ. 3.26

for the cluster population yields the number of clusters per steradian brighter than flux S (*e.g.* Borgani, 2006) as

$$N(>S) = \int_0^\infty dz \frac{cD^2(z)}{H(z)} \cdot \int_S^\infty dS \, n[M(S, z); z] \frac{dM}{dS} . \quad (3.45)$$

Here the first integral accounts for the comoving volume per steradian (Equ. 3.25) and the second term yields the observable clusters in this volume at flux S . Deviation of the Euclidean slope of Equ. 3.26 are hence related to (i) the flux limit, (ii) evolution effects of the cluster population, and (iii) cosmological distances. A compilation of different $\log N$ – $\log S$ functions is shown in Fig. 4.6. The observed slope on the bright end starts with the expected Euclidian value 1.5 and then flattens to a value of $\simeq 1$ towards faint fluxes (Rosati *et al.*, 2002). Cluster number counts are nowadays mainly used as a consistency check with other surveys and for an estimation of the survey flux limit.

- (9) **BCG Hubble Diagram:** The brightest cluster galaxies exhibit a remarkably low scatter of about ± 0.3 mag in their average absolute magnitude \bar{M}_{BCG} , which qualifies them as decent ‘standard candles’, similar to supernovae type Ia. With the observed apparent BCG magnitudes m_{BCG} of a given filter, we arrive at the m_{BCG} – $\log(z)$ Hubble diagram by combining Equ. 3.23 & 3.24

$$\begin{aligned} m_{\text{BCG}}(z) &= M_{\text{BCG}} + K_{\text{BCG}}(z) + 25 + 5 \log(d_{\text{lum}} [\text{Mpc}]) - 5 \log h_{70} \\ &= M_{\text{BCG}} + K_{\text{BCG}}(z) + 25 + 5 \log \left(\frac{c h_{70}^{-1}}{H_0} [\text{Mpc}] \right) + 5 \log \left((1+z) \int_0^z \frac{dz'}{E(z')} \right) \\ &= M_{\text{BCG}} + K_{\text{BCG}}(z) - 5 \log h_{70} + 43.16 + 5 \log(1+z) + 5 \log \left(\int_0^z \frac{dz'}{E(z')} \right) \end{aligned} \quad (3.46)$$

Here $K_{\text{BCG}}(z)$ is the redshift dependent K -correction and in the second line the luminosity distance²⁰ d_{lum} was substituted with Equ. 3.20. Assuming a concordance model cosmology and considering redshift dependent terms up to an order of $\mathcal{O}(z^2)$ in Equ. 3.46, we obtain the low-redshift approximation

$$m_{\text{BCG}}(z) \approx M_{\text{BCG}} + K_{\text{BCG}}(z) + 43.16 + 5 \log z + 1.68 \cdot z , \quad (3.47)$$

with the expected linear $m(z) \propto \log z$ behavior for the local approximation $z \ll 1$. Variations of the Hubble constant H_0 result in a constant vertical offset, whereas the sensitivity on the cosmological parameters Ω_{m} , Ω_{DE} , and w change the form of the Hubble relation at higher redshifts (last term in Equ. 3.46). Based on this effect, SNe Ia measurements have established the existence of a non-vanishing *Dark*

²⁰ Assuming a flat geometry, *i.e.* $k=0$.

	Cosmological Test	Effective Test	N ^o	Parameters
1	cluster mass function $n(M)$	D_+	tens	Ω_m, σ_8
2	number density evolution $n(M, z)$	$D_+(z), V_{\text{com}}(z)$	tens	$\Omega_m, \sigma_8, \Omega_\Lambda, w$
3	cluster power spectrum $P(k)$	D_+	hundreds	Ω_m, σ_8
4	baryonic acoustic oscillations	$d_{\text{ang}}(z), H(z)$	ten thousands	$\Omega_m, \Omega_\Lambda, w$
5	cluster baryon fraction f_b	Ω_b/Ω_m	few	Ω_m
6	evolving gas mass fraction $f_{\text{gas}}(z)$	$d_{\text{ang}}(z)$	tens	$\Omega_m, \Omega_\Lambda, w$
7	absolute distances	$d_{\text{ang}}(z)$	few	H_0
8	cluster number counts $N(> S)$	D_+	hundreds	Ω_m, σ_8
9	BCG Hubble diagram $m_{\text{BCG}}(z)$	$d_{\text{lum}}(z)$	tens	Ω_m, Ω_Λ

Table 3.2: Cosmological tests using X-ray galaxy clusters as probes. The table summarizes the discussed methods, the effectively measured cosmic property, lower limits on the number of objects required, and the cosmological parameters for which the method is most sensitive to. The first six tests have the potential to provide competitive parameter constraints, while the last three are to be seen as consistency checks without strong constraining power.

Energy component (Perlmutter *et al.*, 1999). The BCG Hubble diagram has been applied for cosmological studies by Collins & Mann (1998) and by Aragón-Salamanca, Baugh & Kauffmann (1998) using clusters at $z < 1$. With the concordance model in place, the BCG Hubble diagram is nowadays more suitable to probe evolutionary effects in the brightest cluster galaxy population as will be shown in Sect. 11.1.

The cosmological tests using X-ray luminous galaxy clusters as probes are summarized in Tab. 3.2. The methods can be loosely classified into two categories: (A) tests **1–6** having the potential to yield competitive constraints on cosmological parameters, and (B) tests **7–9** which are more to be considered as consistency checks, either for the underlying model (**7**), survey cross-comparisons (**8**), or to disentangle evolutionary effects (**9**).

For distant cluster cosmology, the uncertainties in the mass calibration derived from observed properties and the redshift evolution of the scaling relations pose the largest current limitations. Improving these uncertainties and characterizing $z > 1$ clusters as cosmological probes are important goals for the XDCP survey. The main cosmological application of the XDCP sample will be test **2**, which is expected to yield competitive parameter constraints 4–5 years from now. For tests **6** & **7**, XDCP can provide additional high- z clusters in order to increase the redshift leverage. Methods **8** & **9** are applicable even for an uncompleted survey and are presented in Sect. 9.1.2 & 11.1.

Chapter 4

X-ray Cluster Surveys

This last introductory chapter will shortly summarize some of the major achievements of galaxy cluster X-ray surveys. In addition, the state-of-the-art of distant X-ray luminous clusters at the start of this thesis will be discussed.

4.1 X-ray Selection

Cosmological evolution studies of the galaxy cluster population impose three essential requirements on any suitable survey sample (*e.g.* Rosati, Borgani & Norman, 2002):

1. An efficient method to **find clusters** over a wide redshift range;
2. An observable **estimator of cluster mass**;
3. A method to **evaluate the survey volume** within which clusters are found.

Finding distant clusters is the main aim of this thesis and will be discussed in detail in the next four chapters. A suitable observable proxy for the cluster mass has to be calibrated with local surveys and is shown in the next section. The survey volume V_{\max} or equivalently the selection function $S_{\text{sky}}[f(L, z)]$ ¹, *i.e.* the effective sky coverage as a function of limiting flux, are essential to determine the comoving density of clusters and hence to relate the observations to model predictions.

For a strictly flux-limited X-ray survey with limit f_{lim} and corresponding sky coverage $S[f_{\text{lim}}]$, the comoving maximum search volume $V_{\max}(L)$ for objects with luminosity L is straightforward to calculate using Equ. 3.25. The maximum redshift z_{\max} is obtained from the luminosity distance (Equ. 3.20) by solving $d_{\text{lum}}(z_{\max}) \equiv \sqrt{L/(4\pi f_{\text{lim}})}$ for z_{\max} . The search volume (see Fig. 3.2) is then given by

$$V_{\max}(L) = V_{\text{com}}[z_{\max}(f_{\text{lim}}, L)] = \int_0^{z_{\max}} S_{\text{sky}}[f_{\text{lim}}] \left(\frac{d_{\text{lum}}(z)}{1+z} \right)^2 \frac{c dz}{H(z)} . \quad (4.1)$$

¹Here the flux is denoted with f and the sky coverage in units of steradian with S_{sky} , not to be confused with the flux S often used as a notation for number counts.

For an inhomogeneous sensitivity distribution, as typical for serendipitous surveys, the sky coverage² rises gradually over an extended flux range from the most sensitive regions with limit f_{low} to the flux f_{high} covering the full survey area. In this case, the search volume is obtained by a second integration over the flux limit and proper accounting of the additional survey area dS/df at higher fluxes

$$V_{\text{max}}(L) = \int_{f_{\text{low}}}^{f_{\text{high}}} \frac{dV_{\text{com}}[z_{\text{max}}(f, L)]}{df} df = \int_{f_{\text{low}}}^{f_{\text{high}}} \int_0^{z_{\text{max}}(f)} \frac{dS_{\text{sky}}[f]}{df} \left(\frac{d_{\text{lum}}(z)}{1+z} \right)^2 \frac{c dz}{H(z)} df. \quad (4.2)$$

In principle, galaxy clusters can be systematically selected in several independent ways: (i) Optical/NIR selection based on the cluster signature of a spatial galaxy overdensity (and clustering in color or redshift space), (ii) X-ray detection of the extended ICM emission, and for future surveys (iii) selection based on the SZE, or (iv) the weak gravitational lensing signature of clusters. The main important advantages of X-ray galaxy cluster surveys can be summarized as follows:

- Bright thermal X-ray emission is only observed for **well evolved clusters** with a deep gravitational well (Sect. 2.3);
- The X-ray emission is highly peaked which **minimizes projection effects** (Sect. 2.3);
- The X-ray luminosity is tightly correlated with the gravitational mass and is providing a **reliable mass proxy** based on the survey data (Sect. 4.2);
- The **X-ray selection** can be accurately assessed allowing a simple evaluation of the survey volume (this section);
- Cosmological applications with X-ray clusters can build upon **several decades of survey experience** (Chaps. 1 & 4).

4.2 Local Cluster Surveys

The success story of X-ray surveys for clusters of galaxies is largely built upon the German-American ROSAT (ROentgenSATellit) mission from 1990–1999. The X-ray imaging capabilities of its main instrument, the Position Sensitive Proportional Counter (PSPC), allowed for the first time a cluster selection based on source extent, in particular for the mission phase of pointed observations after the completion of the ROSAT All-Sky Survey (RASS). The central 0.2 deg^2 of the PSPC field-of-view achieved a point spread function with a FWHM resolution of $30''\text{--}45''$ enabling the resolved detection of extended emission of clusters with fiducial core radii of $250 h^{-1} \text{ kpc}$ out to $z \sim 1$ (*e.g.* Rosati, Borgani & Norman, 2002). Considering that the extragalactic AGN point source population outnumbers clusters by approximately a factor of 10:1 at faint flux levels ($f_X \sim 10^{-14} \text{ erg s}^{-1} \text{ cm}^{-2}$), the selection based on the extent criterion greatly enhances the cluster survey efficiencies.

²Additional correction terms might be necessary, *e.g.* to take the detection efficiency as a function of cluster core radius or off-axis angle into account (see Sect. 9.1.3).

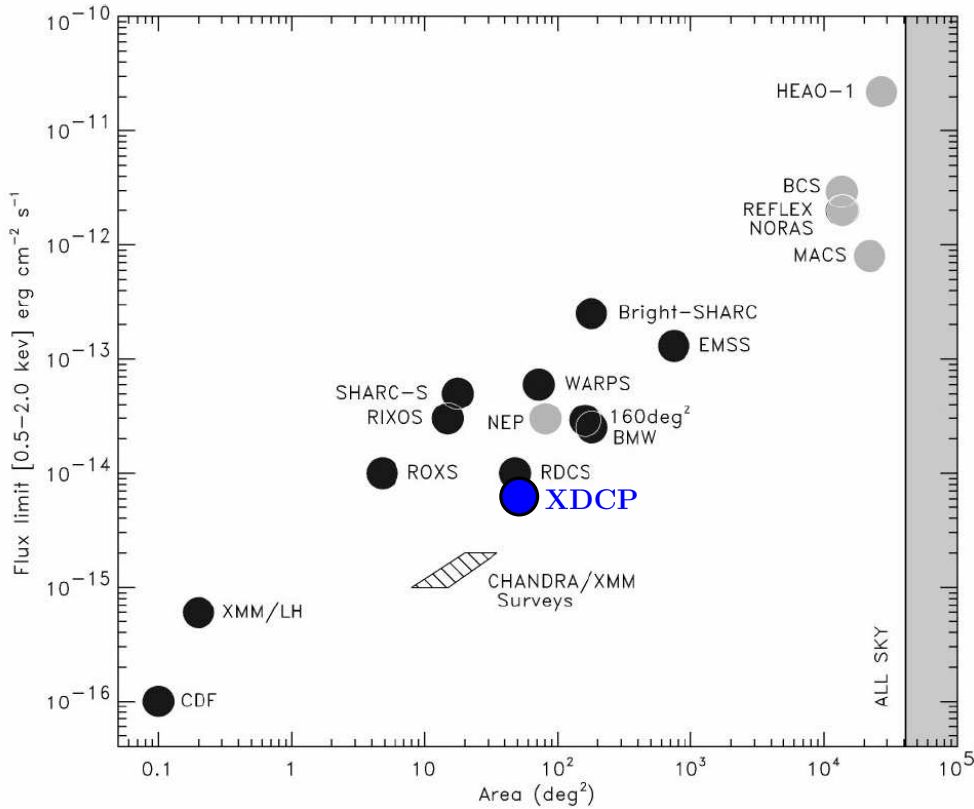


Figure 4.1: Comparison of X-ray cluster surveys over the past two decades. The approximate survey flux limits and solid angles are plotted for different contiguous area surveys (light shaded circles) and serendipitous surveys (dark circles). The position of the XDCP survey has been added. Plot adapted from Rosati, Borgani & Norman (2002).

Two basic types of X-ray surveys can be distinguished. (i) *Contiguous sky area surveys* covering a single connected region, and (ii) *serendipitous surveys* making use of the ensemble of sky patches of numerous individual pointed observations. Both survey types have their merits and strengths for different science applications. Contiguous surveys, in particular with all-sky coverage, span large solid angles with typically relatively bright flux limits. They are well-suited to detect the rarest, most luminous systems in the large survey volume and to investigate their clustering properties. Serendipitous surveys, on the other hand, are typically sensitive to significantly fainter flux limits, thus providing complementary information on more common systems with lower luminosities and more distant objects. Samples compiled from this survey type are particularly fit for cluster evolution studies.

Figure 4.1 provides an overview of the major X-ray cluster projects of the last two decades. Contiguous area surveys are indicated by the light shaded symbols, whereas serendipitous surveys are represented by dark circles. The approximate location of the XMM-Newton Distant Cluster Project in the solid angle versus flux limit plane has been added in blue. First, we will have a short look at the major all-sky survey samples providing a local cluster census and reference system.

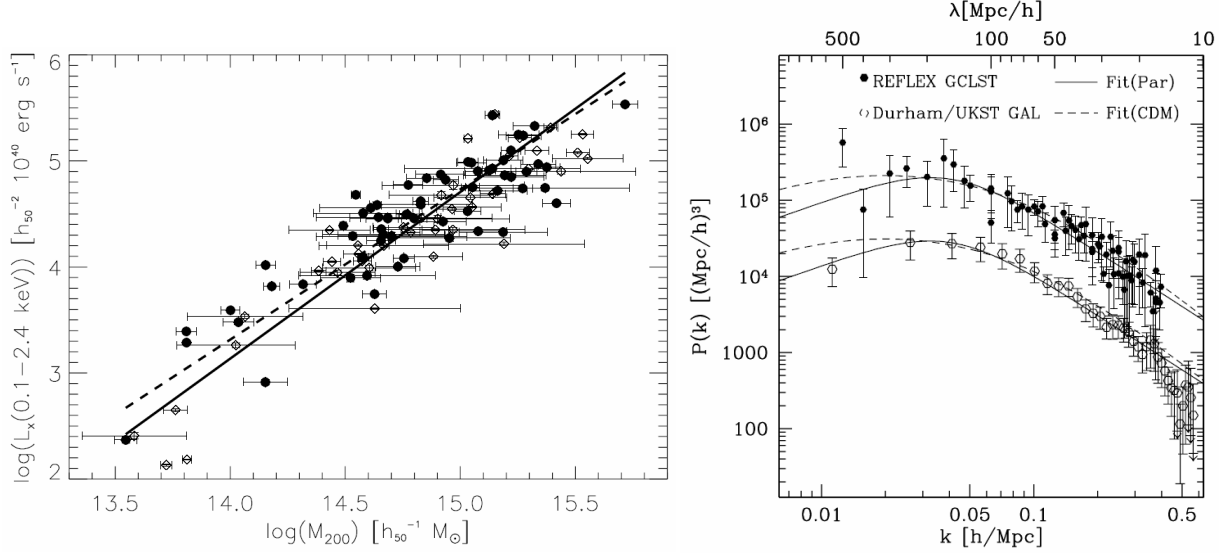


Figure 4.2: Important results of local cluster surveys. *Left:* The empirical L_X - M relation of Reiprich & Böhringer (2002) based on the HIFLUGCS sample of the 63 brightest galaxy clusters in the sky (*solid line*) and an extended sample of 106 objects (*dashed line*). *Right:* Galaxy cluster power spectrum from the REFLEX survey (*top filled symbols*) in comparison to a galaxy power spectrum (*bottom open symbols*). The power spectra amplitude of the two object classes differ by the *biasing factor* $b^2 \simeq 6.8$. Plot from Schuecker *et al.* (2001).

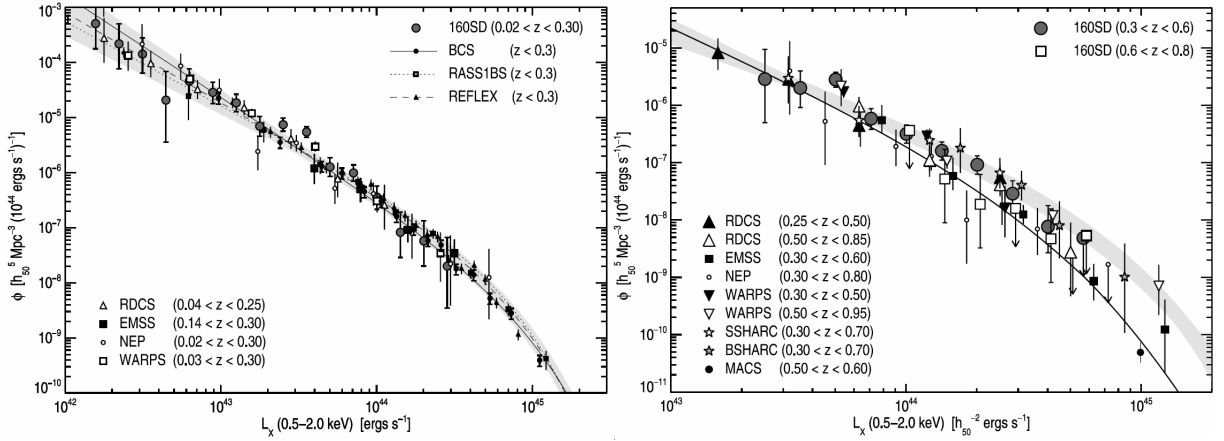


Figure 4.3: X-ray luminosity functions (XLF) as determined by different cluster surveys. *Left:* The local ($z < 0.3$) X-ray luminosity functions of eight flux-limited surveys show excellent agreement and serve as the no-evolution baseline for comparisons with distant cluster samples. *Right:* XLFs derived from cluster samples of intermediate redshifts ($0.25 < z < 0.95$). The shaded regions indicates the local XLF of the left panel. Significant evolution effects have only been observed for the highest luminosity clusters manifested in a lower observed space density at $z \sim 0.8$. Plots from Mullis *et al.* (2004).

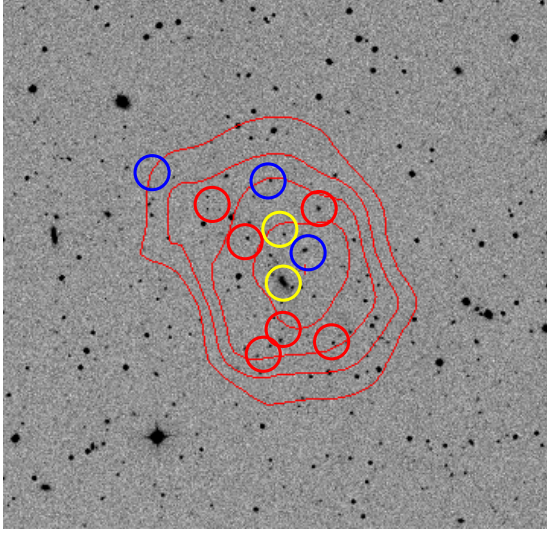


Figure 4.4: The NORAS 2 cluster of galaxies RXC J0834.9+5534 at $z=0.239$ as a typical example of a low-redshift object detected in the ROSAT All-Sky Survey. The red X-ray contours are shown on top of the $12' \times 12'$ optical DSS image. The circles indicate the locations of spectroscopically confirmed cluster galaxies of early type (red), late type (blue), and Seyfert type 1 (yellow).

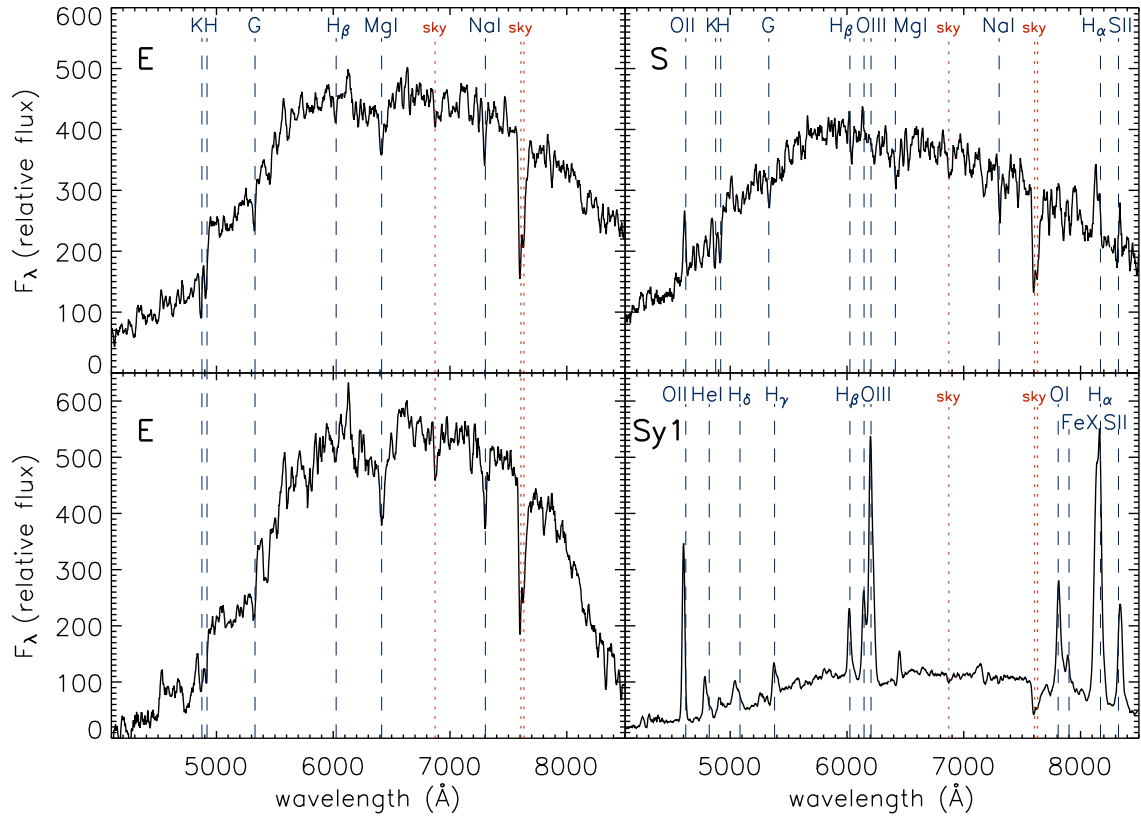


Figure 4.5: Typical spectra of galaxy members of the cluster RXC J0834.9+5534 at $z=0.239$ shown above. Important spectral features are indicated by dashed blue lines with corresponding labels, atmospheric features by red dotted lines. *Left:* Early type galaxy spectra with their characteristic D4000 break redshifted to about 5000 Å and other labelled absorption features. *Right:* Late-type galaxy spectrum (*top*) and a Seyfert type 1 spectrum (*bottom*) with indicated emission lines.

Highest X-ray FLUX Galaxy Cluster Sample (HIFLUGCS): This sample includes the 63 brightest X-ray clusters in the (extragalactic) sky and has a flux limit of $f_X = 2 \times 10^{-11} \text{ erg s}^{-1} \text{ cm}^{-2}$ in the ROSAT 0.1–2.4 keV band (Reiprich, 2001). The major achievement with this brightest cluster sample has been the empirical calibration of the (local) L_X – M relation as shown in the left panel of Fig. 4.2 (Reiprich and Böhringer, 2002). This relation establishes the crucial mass proxy and hence the link to cosmological applications for large X-ray survey samples.

ROSAT-ESO Flux-Limited X-ray cluster survey (REFLEX): The REFLEX sample (Böhringer *et al.*, 2004) is currently the largest statistically complete published compilation of X-ray clusters. It contains 447 objects in the Southern sky ($\delta < +2.5^\circ$) down to the flux limit of $f_X = 3 \times 10^{-12} \text{ erg s}^{-1} \text{ cm}^{-2}$ [0.1–2.4 keV]. REFLEX provides the local reference of the luminosity function (left panel of Fig. 4.3) (Böhringer *et al.*, 2002a) and has been used for a wide variety of cosmological studies (*e.g.* Schuecker *et al.*, 2003a, Schuecker *et al.*, 2003b). A major achievement has been the measurement of the galaxy cluster power spectrum on scales of 15–800 $h^{-1} \text{ Mpc}$ as shown in the right panel of Fig. 4.2 (Schuecker *et al.*, 2001). An extension of the survey, REFLEX 2, is in preparation and will roughly double the number of objects by lowering the flux limit to $f_X = 1.8 \times 10^{-12} \text{ erg s}^{-1} \text{ cm}^{-2}$.

Northern ROSAT All-Sky survey (NORAS): NORAS (Böhringer *et al.*, 2000) is the counterpart of REFLEX in the Northern hemisphere containing 378 clusters out to $z \lesssim 0.3$. The survey extension NORAS 2 is in preparation. The combined extended samples NORAS 2 and REFLEX 2 with a total of approximately 1 800 X-ray clusters will provide the next milestone for a local power spectrum analysis. This thesis work also included the spectroscopic analysis of 35 clusters for the extended NORAS 2 survey. Figures 4.4 & 4.5 show one example of a low-redshift cluster at $z = 0.239$ and some typical cluster galaxy spectra as local reference for the discussions on the spectral energy distribution (SED) in Chap. 7 and spectroscopic features (Chap. 8) of distant cluster galaxies.

4.3 Deep Surveys

Three of the major deep ROSAT surveys are introduced and the corresponding cluster samples used as the basis for discussing evolution effects of the X-ray luminosity function.

North Ecliptic Pole survey (NEP): The North ecliptic pole is the area with the deepest effective exposure time of the ROSAT All-Sky Survey owing to the survey scan pattern along great circles perpendicular to the ecliptic. 81 square degrees with the most sensitive coverage around the North pole have been used as the basis for a complete spectroscopic identification of all X-ray sources. The North Ecliptic Pole survey (Henry *et al.*, 2006) with a median sensitivity of $f_X \sim 7 \times 10^{-14} \text{ erg s}^{-1} \text{ cm}^{-2}$ includes 62 galaxy clusters out to a maximum redshift of $z = 0.81$ and is the only deep ROSAT survey with a contiguous area coverage.

160 deg² large area survey (160 deg²): The 160 deg² serendipitous survey (Vikhlinin *et al.*, 1998) with a median flux limit of $1.2 \times 10^{-13} \text{ erg s}^{-1} \text{ cm}^{-2}$ [0.5–2.0 keV] and deepest coverage of $4 \times 10^{-14} \text{ erg s}^{-1} \text{ cm}^{-2}$ contains 201 clusters. The 22 objects at $z > 0.5$ allow an assessment of evolution effects out to redshifts $z \sim 0.8$. This survey has recently been extended to a sky coverage of 400 deg² (Burenin *et al.*, 2007).

ROSAT Deep Cluster Survey (RDCS): The RDCS (Rosati *et al.*, 1998) is the deepest ROSAT survey available and has compiled a sample of 103 clusters out to $z = 1.27$, which marks the ‘ROSAT redshift horizon’. Based on deep PSPC pointed observations, the serendipitous survey covers a sky area of about 50 square degree down to a flux limit of $f_X = 3 \times 10^{-14} \text{ erg s}^{-1} \text{ cm}^{-2}$ [0.5–2.0 keV] yielding 26 systems at $0.5 < z < 0.85$. Only the high-redshift extension of RDCS with an effective survey area of about 5 square degrees and a sensitivity down to $f_X = 1 \times 10^{-14} \text{ erg s}^{-1} \text{ cm}^{-2}$ allowed the detection of the first four $z > 1$ X-ray clusters.

Figure 4.6 shows a compilation of the cumulative cluster number counts ($\log N - \log S$) derived for different local and deep surveys. From the deepest flux levels probed by ROSAT, a surface density estimate of about 10 galaxy clusters per square degree is expected at $f_X \sim 1 \times 10^{-14} \text{ erg s}^{-1} \text{ cm}^{-2}$ [0.5–2.0 keV]. On the opposite end, *i.e.* for the HIFLUGCS selection criterion, only one cluster per 400 square degree sky area exists.

We can now assess the evidence for an evolution of the galaxy cluster X-ray luminosity function (XLF) as established by ROSAT-based surveys. The compilation of Mullis *et al.* (2004) in Fig. 4.3 summarizes the measurements of the local cluster luminosity function (left panel) and the distant XLF out to $z \sim 0.8$ (right panel). The differential luminosity function $\phi(L_X, z)$ is commonly parameterized in the form

$$\phi(L_X, z) dL_X = \frac{d^2 N}{dV dL_X}(L_{X,z}) = \phi^* \left(\frac{L_X}{L_X^*} \right)^{-\alpha} \exp \left(-\frac{L_X}{L_X^*} \right) \frac{dL_X}{L_X^*}, \quad (4.3)$$

where N denotes the number of clusters of luminosity L_X in volume V at redshift z . The *Schechter* function on the right hand side is parameterized by the characteristic luminosity L_X^* , the faint-end slope α , and the normalization ϕ^* (in units $h^3 \text{ Mpc}^{-3}$), which is directly related to the space density of clusters brighter than a minimum luminosity L_{\min} via $n_0 = \int_{L_{\min}}^{\infty} \phi(L) dL$.

The local X-ray luminosity function shows a remarkable overall agreement between the surveys considering the independent selection techniques and data sets and is hence a robustly determined reference measure for evolution studies. The parameters for the local XLF can be summarized as follows (*e.g.* Böhringer *et al.*, 2001; Rosati, Borgani & Norman, 2002): $L_X^* \simeq 4 \times 10^{44} \text{ erg s}^{-1}$ [0.5–2.0 keV], $\alpha \simeq 1.8$ (15% variation), and $\phi^* \simeq 2.7 \times 10^{-7} h_{70}^3 \text{ Mpc}^{-3}$ (50% variation).

A meaningful parametrization of evolution effects of the XLF (Rosati *et al.*, 2000) is given by

$$\phi(L, z) = \phi_0 (1 + z)^A \cdot L^{-\alpha} \exp \left(-\frac{L}{L^*(z)} \right), \quad (4.4)$$

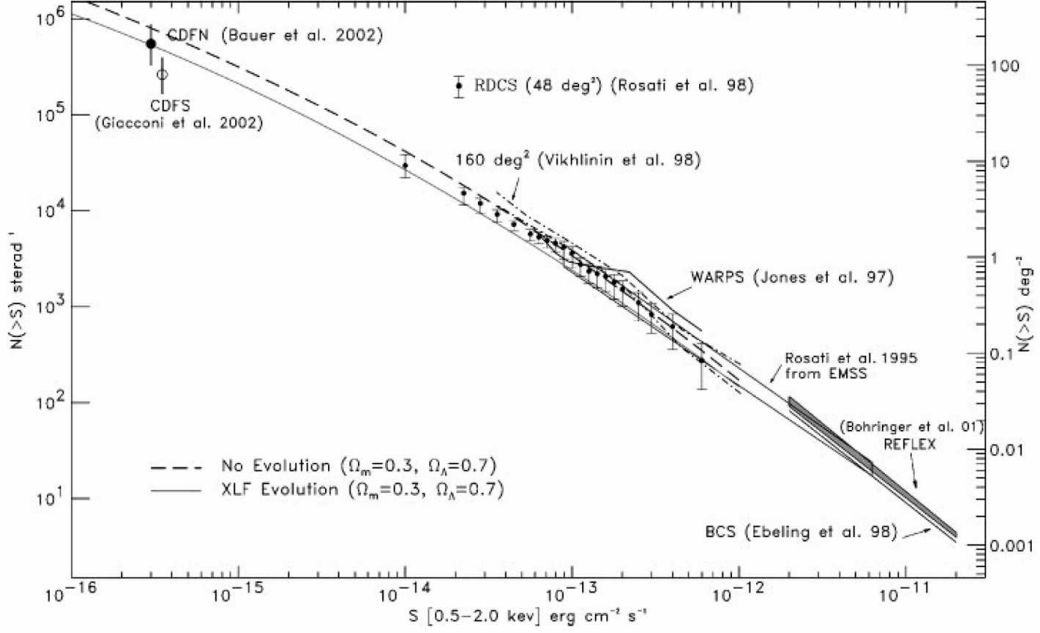


Figure 4.6: Compilation of cumulative cluster number counts as a function of X-ray flux for different ROSAT surveys. The $\log N$ – $\log S$ has been measured over four orders of magnitude in flux. The right-hand scale indicates the total cluster surface density per square degree at a given flux. Plot from Rosati, Borgani, & Norman (2002).

with the free parameters A for the evolution of the local space density normalization ϕ_0 , and B for an evolving characteristic luminosity $L^*(z) = L_0^*(1+z)^B$. The current data out to $z \sim 0.8$ show no detectable evolution effects for galaxy clusters with luminosities $L_X \lesssim 10^{44} \text{ erg s}^{-1}$, *i.e.* the measurements are consistent with $A = B = 0$ (right panel of Fig. 4.3). Only at the highest luminosities at $L_X > 10^{44} \text{ erg s}^{-1}$ a mild but significant deficit in the volume density compared to the local value is confirmed at a confidence level of $>3\sigma$ (Mullis *et al.*, 2004).

In summary, a moderate negative evolution, *i.e.* objects were rarer at high redshift, has been established for the most luminous, massive clusters out to $z \sim 0.8$, but the bulk of the cluster population is approximately constant for at least the second half of cosmic time. This means that the epoch of a significant number density change of the overall cluster population is yet to be determined.

4.4 Distant Galaxy Clusters in 2004

The ROSAT era has led to the discovery of five X-ray luminous galaxy clusters at $z > 1$ (see Tab. 9.1), four of them detected within the RDCS survey, and one in the deep Mega-second observation of the Lockman Hole (LH) field (Hashimoto *et al.*, 2005). The ongoing detailed multi-band follow-up observations of these rare systems have revealed rather advanced evolutionary states despite the large lookback time, showing a metal-rich, hot ICM and

a red and passively evolving galaxy population. Figure 4.7 displays a multi-wavelength overlay (left panel) and a high-resolution HST image (right panel) of RDCS J1252.9-2927 at $z=1.237$, the most massive and best studied $z > 1$ galaxy cluster in 2004.

The situation of distant cluster studies at the start of this thesis is summarized in the cone diagram of Fig. 4.8, illustrating the distribution of known X-ray clusters in redshift space. Out to redshifts of $z \sim 0.7$ (red circles), the cluster population is well-sampled by the local and deep ROSAT surveys. Orange circles represent the small sample of all known X-ray clusters at $z > 0.7$, about ten in the redshift range $0.7 < z \lesssim 1$, and the mere five test objects at $1 < z \leq 1.27$. The yellow star indicates the position of the cluster XMMU J2235.3-2557 in this diagram, which will be presented in detail in Sect. 5.4.

The highly active phase of galaxy cluster surveys has continued into the XMM-Newton era. Here we summarize some of the major projects, which will have a significant impact on the study of distant X-ray clusters.

Cosmic Evolution Survey (COSMOS): The 2 deg^2 field of the COSMOS survey (Scoville *et al.*, 2007) has obtained deep multi-wavelength coverage with basically all major astronomical facilities. The project is designed to probe the correlated evolution of galaxies, star formation, AGN, dark matter, and the large-scale structure. More than 2 Msec of XMM-Newton data have been obtained (Hasinger *et al.*, 2007) allowing the detection of extended sources down to flux levels of $f_X \sim 10^{-15} \text{ erg s}^{-1} \text{ cm}^{-2}$. An early set of the COSMOS X-ray data has been used to test the XDCP selection procedure and efficiency (Sect. 6.5). The COSMOS survey has the ability to detect and study dozens of high-redshift groups and clusters (Finoguenov *et al.*, 2007). However, the limited solid angle restricts the survey to the inclusion of a single structure of order $2 \times 10^{14} M_\odot$, implying that the high mass end of the XLF cannot be sufficiently probed.

XMM Large-Scale Structure survey (XMM-LSS): The XMM-LSS project (Pierre *et al.*, 2006) is designed as a designated multi-wavelength galaxy cluster survey over a fairly large contiguous sky area. However, the large demand of XMM resources has limited the currently available X-ray data to roughly 9 deg^2 with a typical depth of 10 ksec. The XDCP sample hence provides a wider and deeper coverage. It has an overlap with XMM-LSS of about 0.8 deg^2 , which can be used for a survey comparison study.

XMM Cluster Survey (XCS): The ambitious XCS (Romer *et al.*, 2001) serendipitous survey aims at the detection of *all* galaxy clusters in *all* XMM archive fields. In principle, XCS fully overlaps with the XDCP survey. However, the XCS project is centered on fairly bright cluster sources with a sufficient number of photons for an accurate temperature determination and is not focussed on very distant clusters with their typically low flux and count levels.

³The images can be found at http://chandra.harvard.edu/photo/2004/rdcs1252/rdcs1252_xray_opt.jpg and http://chandra.harvard.edu/photo/2004/rdcs1252/rdcs1252_hst_optical.jpg.

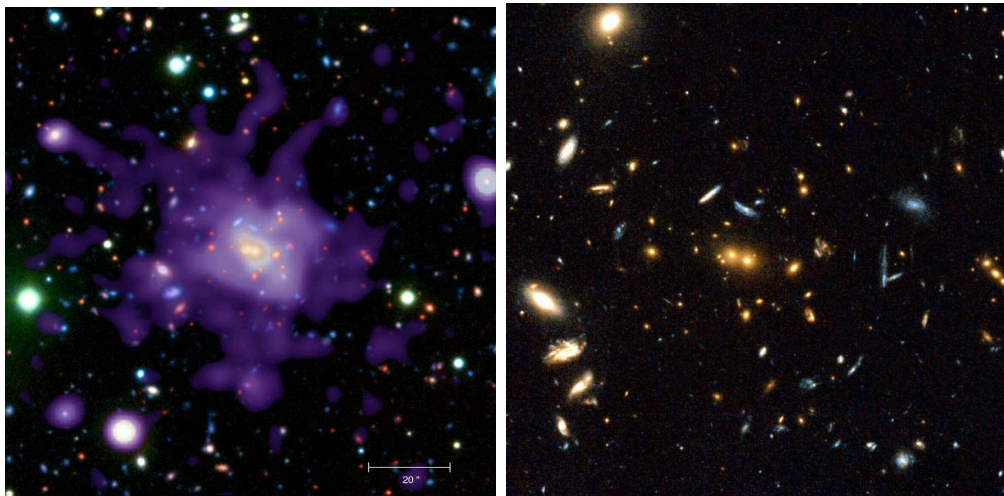


Figure 4.7: Multi-wavelength view of the distant cluster of galaxies RDCS J1252.9-2927 at redshift $z = 1.237$, the most massive and best studied $z > 1$ cluster discovered with ROSAT. *Left:* $2' \times 2'$ color composite image of the cluster X-ray emission (purple) overlaid on the optical/near-infrared data showing the red galaxy population. *Right:* $1' \times 1'$ high resolution Hubble Space Telescope image of the cluster core. Images from press release³.

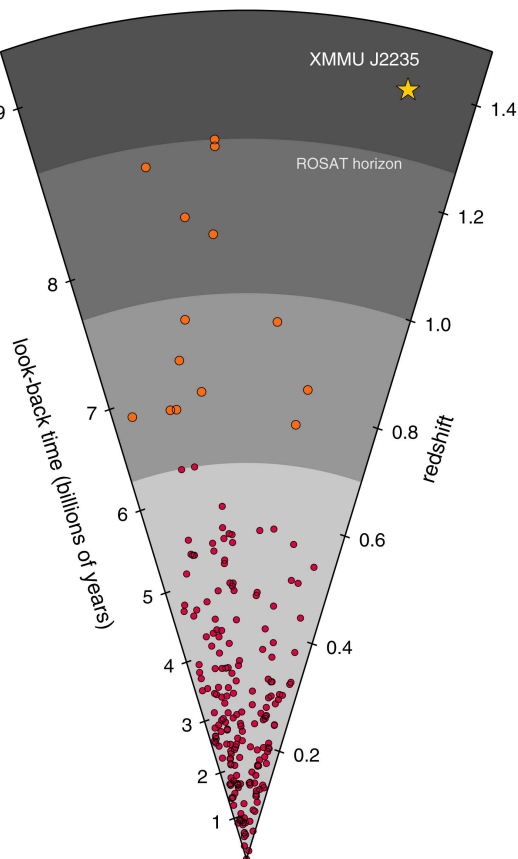


Figure 4.8: Schematic cone diagram of known X-ray luminous galaxy clusters in 2004. The redshift increases from bottom to top, left to right illustrates the right ascension distribution. The red symbols at $z < 0.7$ represent a small selection of known low-redshift clusters, orange circles at $0.7 \leq z \lesssim 1.3$ indicate all known ROSAT X-ray clusters in the high-redshift regime. The XDCP cluster XMMU J2235.3-2557 at $z \sim 1.4$ (see Sect. 5.4) was the first XMM selected system that could break the 'ROSAT redshift horizon'. Plot from C. Mullis.

Chapter 5

The XMM-Newton Distant Cluster Project

This chapter will provide an overview of the XMM-Newton Distant Cluster Project. The principal survey strategy is introduced followed by a discussion of early results and gained experiences of a pilot study.

5.1 Motivation

The main *scientific motivations* for starting an extensive new serendipitous distant cluster survey have been outlined in the introductory chapters 2–4. Among the vast number of astrophysical and cosmological applications of distant X-ray luminous galaxy clusters, the accurate determination of the cluster number density evolution out to $z \sim 1.5$ is the prime goal and science driver of the XDCP. The time window for a ‘new generation’ survey apt for this ambitious task has only opened in the year 2003 owing to the rapid *advance of technology* over the last few years. The European X-ray satellite XMM-Newton has been providing an ever increasing amount of archive data with unprecedented sensitivity to a depth that will be unrivalled for at least another decade (see Sect. 12.2). These advances in X-ray technology go hand-in-hand with the availability of ground-based 8–10 meter class telescopes, most notably the European Very Large Telescope (VLT), which now allow the spectroscopic confirmation and further detailed studies of cluster galaxies at $z > 1$.

As discussed in Chap. 1, the cluster samples associated with the scientific goals of the XDCP can be grouped into three different categories with increasing time line and scope: (1) provide $z > 1$ galaxy clusters as *individual astrophysical laboratories* for detailed studies, (2) compile *pathfinder samples* for the characterization of high-redshift clusters as cosmological probes for large upcoming surveys, and (3) establish a statistically complete *cosmological sample* for various cosmological tests. The fundamental pre-requisite for compiling these cluster samples is an efficient survey strategy for finding and confirming the rare distant X-ray luminous systems; the basic steps are introduced in the following section.

5.2 XDCP Survey Strategy

The XMM-Newton Distant Cluster Project (Böhringer *et al.*, 2005) is based on the following six-step strategy aiming at the efficient selection and confirmation of X-ray luminous $z \gtrsim 1$ clusters of galaxies. The intermediate results of the different survey steps are illustrated in Fig. 5.1 using the galaxy cluster XMMU J2235.3-2557 as an example case.

Step 1: Detection of serendipitous extended X-ray sources. Deep XMM-Newton archive fields ($\gtrsim 10$ ksec) at high galactic latitude ($|b| \geq 20^\circ$) are analyzed for serendipitous extended X-ray sources in the field-of-view.

Step 2: Source screening and selection of candidates. The detected extended X-ray sources are visually inspected and their sky positions cross-correlated with available optical data and extragalactic database information. X-ray sources without an identified optical counterpart are selected as *distant* cluster candidate sources.

Step 3: Two-band follow-up imaging: For the candidate targets, follow-up imaging data is obtained in (at least) two filter bands to sufficient depth, which allows a preliminary cluster identification based on a red overdense galaxy population coincident with the extended X-ray source.

Step 4: Photometric redshift estimate. The full photometric analysis yields a cluster redshift estimate based on the color of the red-sequence which allows a refined selection of photometrically confirmed $z \gtrsim 0.9$ candidates.

Step 5: Spectroscopic confirmation. Promising high-redshift cluster candidates are spectroscopically observed for the final cluster confirmation and redshift determination.

Step 6: Detailed follow-up studies. For the most interesting $z \gtrsim 1$ systems, additional detailed imaging and spectroscopic follow-up observations in X-ray, optical, NIR, IR, and the radio regime will be obtained to disclose the high-redshift cluster properties and physics.

It should be emphasized at this point that the vast majority of *extended* X-ray sources (steps 1 & 2) in high galactic latitude fields are expected to originate from galaxy clusters (see *e.g.* the NEP survey in Sect. 4.3). Due to the sequential dependency of the different survey steps and the increasing demands on observatory resources, the completion rates at an intermediate survey stage will drastically decrease from top to bottom. The first two steps are discussed in detail in Chap. 6 and are based on publicly available data only, hence providing a 100% coverage for the current survey phase. Steps 3 & 4 are presented in Chap. 7 achieving a survey coverage of about 40% for the thesis data. The observational bottleneck is the spectroscopy of step 5, which is introduced in Chap. 8, and which is currently available only for few systems. The final step 6 will not be discussed in this thesis beyond the overview provided in Sect. 5.4 since detailed follow-up data has only been obtained for the cluster XMMU J2235.3-2557.

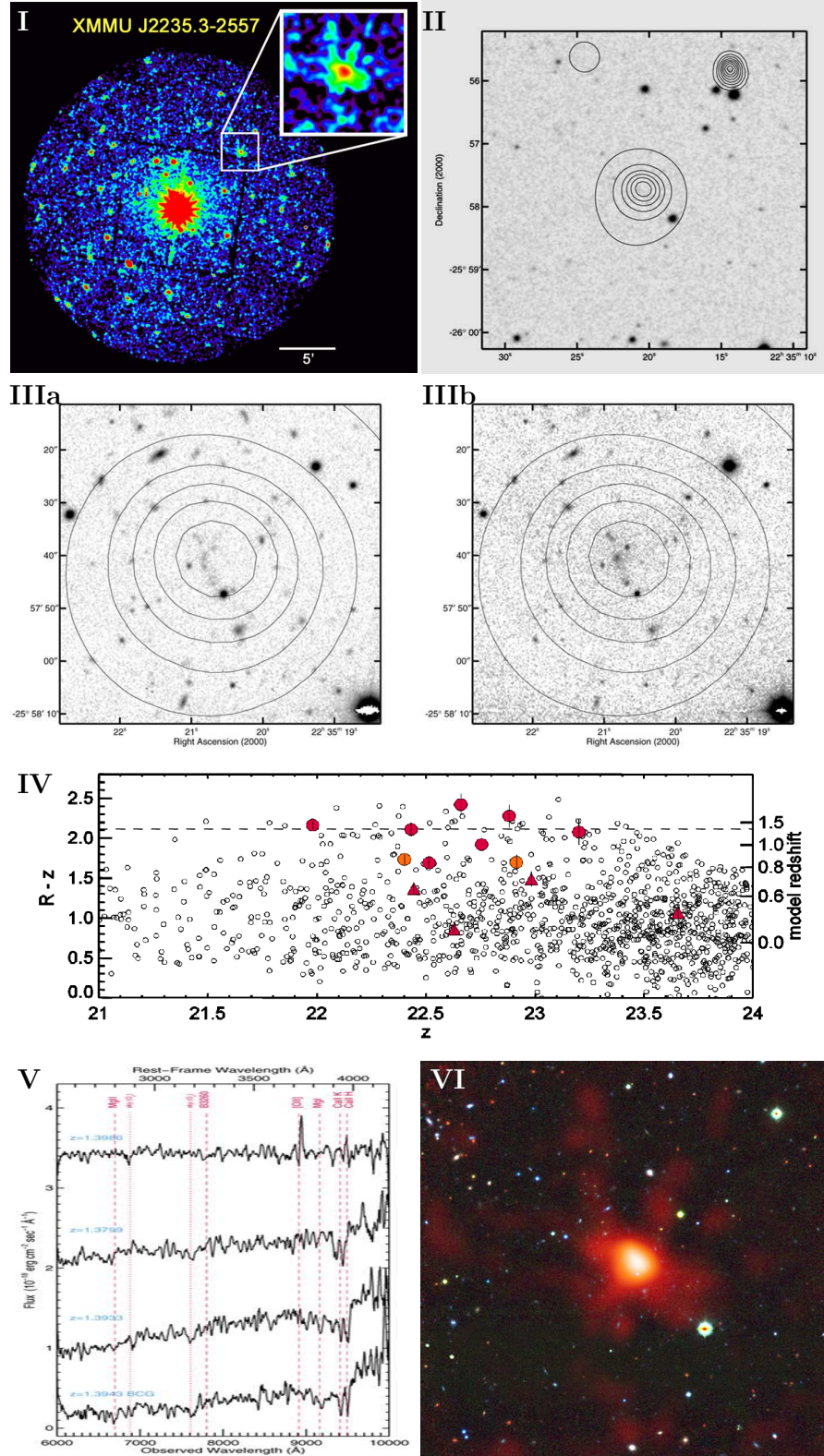


Figure 5.1: Schematic steps of the XDCP survey strategy. *I*: Detection of serendipitous extended X-ray sources in suitable archival XMM-Newton fields. *II*: X-ray source screening using available optical and NIR data (DSS). *III*: Two-band follow-up imaging to verify the presence of a cluster as overdensity of red galaxies (*IIIa* R-band, *IIIb* Z-band). *IV*: Photometric redshift estimation using the color of the red-sequence as distance indicator. *V*: Spectroscopic confirmation of the cluster redshift. *VI*: Detailed multi-wavelength follow-up of the most interesting objects. Plots provided by C. Mullis.

5.3 Pilot Study Results

The XMM-Newton Distant Cluster Project started in the year 2003 with a pilot study to test the feasibility and efficiency of the survey strategy. Since this feasibility study and most of the related work began prior to this thesis, the results and main lessons of this initial project phase are summarized without going into the details.

120 archival XMM-Newton pilot study fields were analyzed for serendipitous extended X-ray sources (**step 1**). From these about 60 distant cluster candidate sources were selected (**step 2**) and observed with VLT FORS2 R and Z-band snap-shot imaging (**step 3**). Based on the R–Z red-sequence analysis, a dozen promising high-redshift candidates with photometric redshift estimates $z \gtrsim 0.9$ could be identified (**step 4**) and have been proposed for spectroscopic confirmation (**step 5**). For the first discovered high- z cluster (see Sect. 5.4) detailed multi-wavelength follow-up observations have been proposed and obtained (**step 6**).

The most important XDCP pilot study conclusion was the confirmation that high-redshift galaxy clusters can indeed be efficiently selected based on their extended X-ray signature in conjunction with two-band imaging data. The strategy described in Sect. 5.2 could thus be established as the basis for a large systematic distant galaxy cluster archival survey. The early results have been very encouraging and have pointed to the great scientific potential achievable with such a project.

However, besides the positive overall observational feedback, the XDCP pilot study has also revealed optimization potentials for most of the survey chain, in particular for the first four process steps.

- **Step 1:** The pilot study X-ray selection of distant cluster candidates was in effect based on sources with at least 200 detected X-ray photons. For a 10 ksec net XMM exposure, this implies an approximate detection limit of $f_{\text{lim}} \simeq 2 \times 10^{-14} \text{ erg s}^{-1} \text{ cm}^{-2} (0.5\text{--}2.0 \text{ keV})$, *i.e.* comparable to the deepest ROSAT surveys (see Fig. 4.1). In order to achieve significant sensitivity improvements compared to existing surveys, the detection of extended sources with less than 100 X-ray photons is a desirable aim. Consequently, the first optimization goal is an improved sensitivity for detecting extended X-ray sources.
- **Step 2:** The pilot study returned a large fraction of intermediate-redshift systems at $z \simeq 0.3\text{--}0.6$, which contributed almost 40% to the identified cluster sample but are not of particular interest for the prime XDCP science objectives. An improved screening could significantly decrease the number of such intermediate-redshift objects and thus increase the $z > 1$ cluster fraction in the candidate sample. A more efficient low-redshift cluster identification and rejection is the second optimization goal.
- **Step 3:** For several confirmed high-redshift candidates and clusters between $z \simeq 1.1\text{--}1.45$ the VLT FORS2 ‘snap-shot imaging’ with net exposure times of 480 s in Z ($Z_{\text{lim}}(\text{AB}) \sim 23.0 \text{ mag}$) and 960 s in R ($R_{\text{lim}}(\text{AB}) \sim 24.5 \text{ mag}$) did not allow a secure

cluster identification, *i.e.* the data did not have sufficient depth. The third optimization goal is thus a more complete two-band imaging cluster confirmation at the high redshift end.

- **Step 4:** The R–Z color exhibits large intrinsic redshift uncertainties at $z > 1$. The final optimization goals are thus improved and more secure redshift estimates based on two-band imaging data.

The first two optimization items dealing with the X-ray selection process will be discussed and implemented in Chap. 6. The latter two concerning the two-band follow-up imaging will be treated in detail in Chap. 7. As the highlight result of the XDCP pilot study, the galaxy cluster XMMU J2235.3-2557 is now introduced.

5.4 XMMU J2235.3-2557

The XDCP discovery of XMMU J2235.3-2557 was announced¹ in March 2005 with the results published in the accompanying paper of Mullis *et al.* (2005). At the time of publication, XMMU J2235.3-2557, at a redshift of $z = 1.393$, was the most distant galaxy cluster known, and the first XMM-Newton selected system at $z > 1$. It was also the first XDCP object for which spectroscopic follow-up observations were obtained.

The selection procedure for XMMU J2235.3-2557 is shown in Fig. 5.1 as an illustration of the survey strategy steps. The cluster’s extended X-ray emission was detected in a 44 ksec XMM-Newton observation of the Seyfert galaxy NGC 7314 at an off-axis angle of 7.7′ (panel I). The corresponding sky position on the DSS plates is devoid of objects, which classified the source as a distant cluster candidate (panel II). The subsequent R (panel IIIa) and Z-band (panel IIIb) follow-up images reveal a galaxy cluster signature of red galaxies with a significant central overdensity. The color-magnitude diagram (panel IV) exhibits a cluster red-sequence with a color of $R-Z \sim 2.1$ indicating a high-redshift cluster candidate at $z > 1$. Deep VLT-FORS2 spectroscopy with an exposure time of 4 hours confirmed the cluster at a redshift of $z = 1.393$ based on 12 identified spectroscopic cluster member galaxies. The detailed multi-band follow-up program (panel VI) is discussed below.

The cluster properties, as they have been derived from the survey data set (*i.e.* steps 1–5), are summarized in Tab. 5.1 and a more detailed view of XMMU J2235.3-2557 is presented in Fig. 5.2. With 280 net source counts in the 0.3–4.5 keV energy range, XMMU J2235.3-2557 is a fairly bright X-ray source which had been serendipitously detected, without optical identification, in a ROSAT pointed observation. The source flux of $(2.6 \pm 0.2) \times 10^{-14} \text{ erg s}^{-1} \text{ cm}^{-2}$ in the 0.5–2.0 keV band with a corresponding total unabsorbed flux of $(3.6 \pm 0.3) \times 10^{-14} \text{ erg s}^{-1} \text{ cm}^{-2}$ yields a rest-frame luminosity estimate of $(3.0 \pm 0.2) \times 10^{44} h_{70}^{-2} \text{ erg s}^{-1}$ (0.5–2.0 keV). Assuming a thermal (MEKAL)

¹Press release articles can be found under <http://www.eso.org/public/outreach/press-rel/pr-2005/pr-04-05.html> or <http://www.mpg.de/bilderBerichteDokumente/dokumentation/pressemitteilungen/2005/pressemitteilung20050228/presselogin>.

emission model with a metallicity of $0.3 Z_{\odot}$ and a galactic hydrogen absorption column of $n_{\text{H}} = 1.47 \times 10^{20} \text{ cm}^{-2}$, a spectral temperature fit (lower right panel of Fig. 5.2) with $kT_{\text{X}} = 6.0^{+2.5}_{-1.8} \text{ keV}$ is obtained. With a mass estimate of $\sim 3 \times 10^{14} M_{\odot}$ based on the $L_{\text{X}}-M$ relation (see Fig. 4.2), XMMU J2235.3-2557 is likely the most massive galaxy cluster known at redshifts $z > 1$. The derived X-ray properties for the cluster are consistent, within errors, with the determined $L_{\text{X}}-T$ relations of other surveys as shown in the right central panel of Fig. 5.2.

The follow-up imaging observations (top panels and central left panel of Fig. 5.2) of XMMU J2235.3-2557 revealed an old and evolved galaxy population in the cluster center already in place at a lookback time of 9 Gyr. The brightest cluster galaxy exhibits an extended surface brightness profile typical for massive cluster cDs and has a spatial offset to the X-ray centroid of $3''.7$, corresponding to 31 kpc at $z = 1.393$, which might hint at a recent subcluster merger in the Northeast-Southwest direction. The spectroscopic redshift distribution in the bottom left panel of Fig. 5.2 shows the clear redshift peak at $z \sim 1.4$ with 12 confirmed cluster members (red) and two additional galaxies at slightly lower redshift (orange). The preliminary velocity dispersion estimate based on this data is $762 \pm 262 \text{ km s}^{-1}$.

Meanwhile, XMMU J2235.3-2557 has been the subject of an extensive multi-wavelength follow-up program (**step 6**). The above discussion has been purposely limited to the discovery data set² since this will be typical in data quality and quantity for routine detections within the XDCP core survey program (**step 1–5**). As an outlook of the follow-up science for the most interesting XDCP clusters, we will summarize the obtained follow-up observations and the principal science objectives for XMMU J2235.3-2557.

In X-rays, the cluster has been re-observed with XMM-Newton for a nominal total exposure time of 80 ksec complemented by a 200 ksec observation with Chandra. The main science objectives for the high spatial resolution Chandra data are (i) the reliable measurement of the structural parameters free from the potential impact of point sources for an accurate mass determination, (ii) probing small-scale features (*e.g.* substructure) to provide further insight into the global state of the system, and (iii) to test for the presence of a cool core. The enhanced spectroscopic performance of XMM-Newton in addition allows (iv) an ICM temperature determination to better than 10%, (v) precise measurements of the X-ray surface brightness, gas mass, and gravitational mass profiles, (vi) the first ICM metallicity evaluation and detection of the iron line at this redshift, and (vii) test the predicted evolving scaling relation (*e.g.* $L_{\text{X}}-T$, $M-T$) and self-similarity of the surface brightness and entropy structure. With all this at hand, XMMU J2235.3-2557 can be (viii) established as a ‘standard candle’ at $z \sim 1.4$ and used for the cosmological baryon fraction test of Sect. 3.3.

With the additional VLT FORS 2 spectroscopy (ix) more cluster member galaxies can be identified for an improved velocity dispersion measurement and reference data set for photometric studies. The imaging data baseline has been broadened to the R, I, Z, J, H, Ks,

²All preliminary cluster properties have been confirmed (within the stated errors) by the deeper follow-up observations.

X-ray Properties		Optical Properties	
f_X [erg s ⁻¹ cm ⁻²]	$(2.6 \pm 0.2) \times 10^{-14}$	spectroscopic members	12
L_X [h_{70}^{-2} erg s ⁻¹]	$(3.0 \pm 0.2) \times 10^{44}$	\bar{z}	1.393
kT_X	$6.0^{+2.5}_{-1.8}$ keV	velocity dispersion	762 ± 262 km s ⁻¹
M_X	$\sim 3 \times 10^{14} M_\odot$	color of red-sequence	R-Z ~ 2.1
X-ray photons	~ 280	BCG type	cD-like
core radius	~ 140 kpc	BCG X-ray centroid offset	31 kpc

Table 5.1: X-ray and optical properties of galaxy cluster XMMU J2235.3-2557 as derived from the initial data set. The unabsorbed flux f_X and the rest-frame X-ray luminosity L_X are given for the 0.5–2.0 keV band.

3.6 μ m, and 4.5 μ m-bands, *i.e.* from 0.6–4.5 μ m corresponding to a rest-frame photometric coverage from the UV to the NIR. Deep I, Z, and H-band coverage has been obtained with the Hubble Space Telescope ACS and NICMOS cameras (>30 hours in total), J (2 700 s) and Ks-band (3 600 s) data with VLT ISAAC, and the mid-infrared 3.6 μ m and 4.5 μ m-bands with the Spitzer observatory (4 hours in total). This eight-band data set allows (x) detailed SED fitting of the spectroscopic members to yield formation ages, crude star formation histories and stellar masses, (xi) an accurate morphology mix determination based on the high-resolution HST data to probe whether the galaxy Hubble sequence is already in place, and (xii) a comparison of the ages and stellar masses of early-type cluster galaxies with the field elliptical population at similar redshifts to probe the expected accelerated galaxy evolution in high-density environments. (xiii) The accurate measurement of the normalization, scatter, and slope of the Z–Ks red-sequence will accurately constrain the formation epoch and can probe evolutionary trends compared to lower redshift studies. (xiv) The construction of the rest-frame NIR luminosity function out to M^*+3 can shed light on the role of merging and stellar mass assembly of galaxies, since the faint-end slope is expected to steepen at high redshift as the cluster galaxies in hierarchical models break up into their progenitors. Additional science objectives mentioned here are (xv) fundamental plane (FP) studies of the cluster ellipticals and (xvi) an investigation of the cluster mass-to-light ratio in combination with the available X-ray data.

In summary, the XDCP discovery of the massive galaxy cluster XMMU J2235.3-2557 at $z = 1.393$ has triggered an extensive follow-up program to address a number of open questions within the cluster and galaxy evolution scenarios to be discussed in detail in forthcoming publications. At this point it should be emphasized again that the search for such rare massive high-redshift systems is best performed within the scope of large-area serendipitous surveys covering several dozen square degrees. For the discussions in the upcoming chapters one should keep in mind that less than one out of a hundred serendipitous extended X-ray sources will be of similar cluster quality and scientific impact. XMMU J2235.3-2557 has thus marked a very positive XDCP start and has encouraged the extended systematic survey for this thesis work.

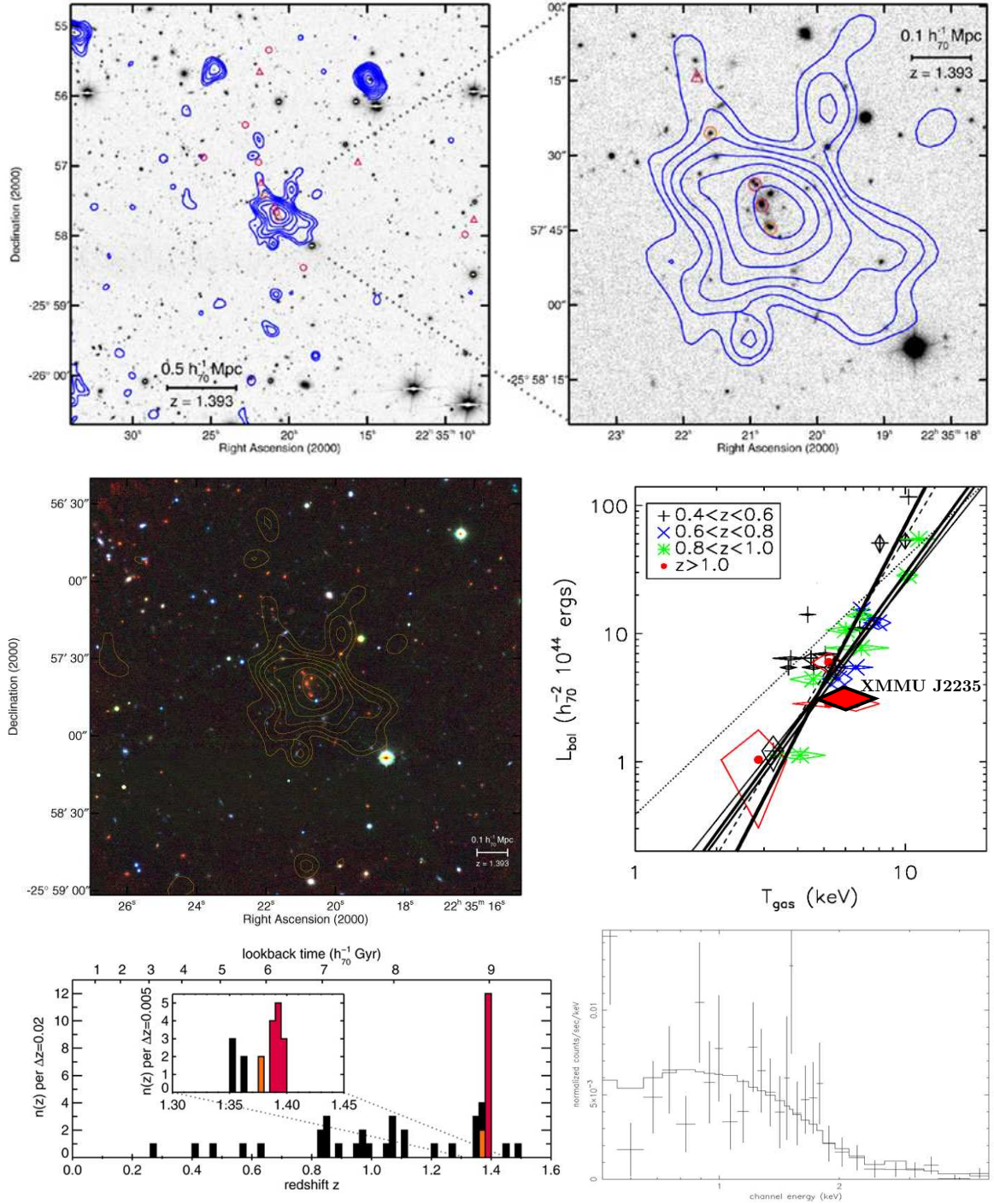


Figure 5.2: A detailed view of galaxy cluster XMMU J2235.3-2557 at $z = 1.393$. *Top left:* VLT-FORS2 R-band image (1140s) with X-ray contours overlaid in blue. *Top right:* 1.5' \times 1.5' zoom on a 3600s VLT-Isaac Ks-band image. The colored objects correspond to the red and orange peaks of the redshift histogram in the *bottom left panel*. *Center left:* R+Z+Ks pseudo-color composite with field size 2.5' \times 2.5'. *Center right:* XMMU J2235.3-2557 (red filled diamond) in comparison to L_X - T relations as derived for different surveys (Ettori *et al.*, 2004). *Bottom right:* Spectral X-ray energy distribution of XMMU J2235.3-2557 (vertical bars) in the 0.5–4.0 keV range and the thermal model fit (solid line) based on the 280 X-ray photons in the archival XMM-Newton field. Plots from Mullis *et al.* (2005) and H. Böhringer.

Data	N ^o Fields	Raw Data	Reduced Data	Survey Fraction
XMM X-ray archive	546	280 GB	600 GB	100%
NIR imaging	56	112 GB	480 GB	40%
optical spectroscopy	1 (+35)	3 GB	8 GB	2%

Table 5.2: Thesis data overview. The data type, number of different fields, and data amounts are indicated. The last column gives an estimate of the corresponding data fraction for the ongoing XDCP survey phase.

5.5 Thesis Data Overview

Before turning to the detailed discussion of the individual survey steps in the next three chapters, a data overview is provided in Tab. 5.2. One of the prime goals for the thesis is a systematic XMM-Newton archival survey for serendipitous distant cluster sources with subsequent follow-up observations following the survey steps 1–5 of Sect. 5.2. In total, the following chapters are based on more than 1 TB of processed data products.

The XDCP survey area for the thesis project phase is defined by the XMM archival status as of November 2004 and consists of approximately 550 X-ray fields. The sky coverage is thus more than quadrupled compared to the pilot study and requires the processing of about 280 GB of raw X-ray data, which will be presented in the next Chap. 6.

The second large amount of data included here has been acquired through several follow-up near-infrared imaging campaigns as discussed in Chap. 7. These imaging observations cover about 40% of all identified distant cluster candidates.

The spectroscopic confirmation of the distant cluster candidates is currently gaining momentum but is still at an early stage with only few XDCP designated observations available. Achieving a spectroscopic survey completion will be the most challenging part and will realistically require another five years. The thesis work included the spectroscopic analysis of 35 low-redshift clusters for the NORAS 2 survey (see Sect. 4.2) which is not further discussed here. In order to maintain the balance for the current project status, Chap. 8 covering the spectroscopy is kept short and is focussed on the main aspects.

Chapter 6

X-ray Analysis of XMM-Newton Archival Data

In this chapter, we will discuss in detail the X-ray selection of distant cluster candidates. The first three sections will introduce the X-ray data, survey fields, and source detection procedures (survey **step 1**). Section four will review the source classification and candidate selection (survey **step 2**), and the final two sections will present test results and general diagnostic plots.

The X-ray analysis constitutes the backbone of the XDCP survey and is crucial for the overall success of the project. The final goal of this X-ray part is the compilation of a well-selected sample of distant cluster candidates which should (i) exploit the maximum sensitivity achievable with XMM archive data, (ii) minimize the low-redshift cluster fraction, and (iii) include only an acceptable fraction of false positive sources while remaining highly complete for true high-redshift clusters.

The assessment of the extended nature of X-ray sources is of prime importance for the cluster selection process. Estimations of the source extent and the X-ray flux are the main accessible observables at this point of the survey chain. In combination with a qualitative evaluation of the X-ray morphology, first clues to the dynamical state of the cluster sources can be obtained. After completion of survey **steps 3–5**, the X-ray source properties can be transformed to physical object quantities such as luminosity, temperature (for brighter sources), and a mass estimate.

6.1 XMM-Newton in a Nutshell

The XMM-Newton data archive constitutes the basis and starting point of the XDCP survey. A detailed understanding of the data properties, capabilities, and limitations is hence the pre-requisite for a proper analysis and for the survey application. In this introductory section, the main XMM-Newton characteristics related to distant cluster searches are summarized and evaluated.

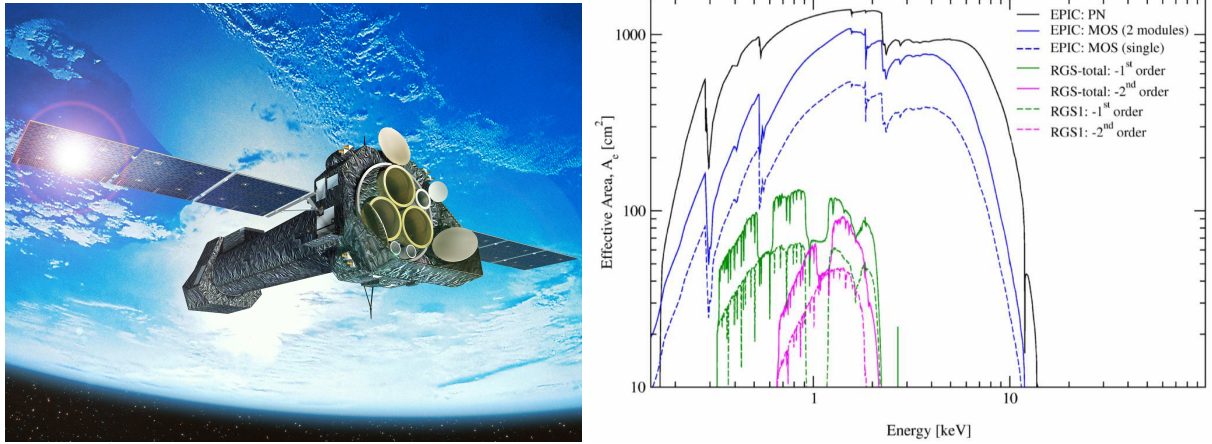


Figure 6.1: *Left:* The XMM-Newton observatory with its three X-ray telescopes. *Right:* Effective area as function of energy. The total XMM-Newton effective area for X-ray imaging consists of the sum of the two upper curves. Plots from Ehle *et al.* (2007).

XMM-Newton, the X-ray Multi-Mirror Mission, was launched on 10 December 1999 as the second of ESAs four cornerstone missions of the *Horizon 2000* program. With a length of more than 10 m and a weight of almost 4 tons, XMM-Newton is the largest scientific satellite ever built in Europe (see Fig. 6.1). The observatory was launched into a highly elliptical 48 hour orbit with a perigee of 6 000 km and an apogee¹ of 115 000 km allowing about 130 ksec of uninterrupted science observations per revolution outside Earth's radiation belts².

The main scientific payload consists of three co-aligned X-ray mirror systems made up of 58 nested mirror shells each. This large number of Wolter type X-ray mirrors provide an unprecedented effective geometric³ area of 1 550 cm² per module. The total gathering power is shared by five simultaneously operating focal plane X-ray instruments, two Reflection Grating Spectrometers (RGS) and three European Photon Imaging Cameras (EPIC).

The XMM-Newton EPIC imaging instruments use two different kinds of X-ray CCD technologies. The two identical MOS (Metal Oxide Semiconductors) cameras use seven front-illuminated 600×600 pixel CCDs with a frame store region as data buffer. Each MOS camera shares a mirror module with one of the RGS spectrometers resulting in a reduced effective area for imaging of 44%. The more sensitive PN camera,⁴ on the other hand, receives the full reflected light of one of the three X-ray telescopes. The twelve backside-illuminated CCD chips with a total of 376×384 pixels are fabricated from a single Silicon

¹An orbital manoeuvre in February 2003 has changed the orbital parameters to the current perigee and apogee values of 20 000 km and 101 000 km (Ehle, 2007).

²Science observations can typically be conducted at elevations above 46 000 km.

³The combined area, *i.e.* the sum of all thin shell-like regions from where (on-axis) photons are focussed onto the detector, is equivalent to the area of a circle with a diameter of 44.4 cm.

⁴PN is derived from the pn-junction of the silicon semiconductor technology used in the detectors. For easier readability, the capitalized form PN, instead of pn, is used throughout the thesis.

wafer. They have a higher quantum efficiency ($QE_{\text{PN}} > 90\%$) than the MOS detectors ($QE_{\text{MOS}} \sim 40\text{--}85\%$), and allow higher frame rates through the integration of readout nodes for each individual pixel column. The PN chips lack frame store buffers, which in practice has the consequence of so-called out-of-time events (OoT). Since the pixels still register incoming X-ray events during the column readout phase, which lasts a few percent of the full integration cycle,⁵ bright sources will imprint a smeared event streak over the full pixel column (Y direction) due to falsely identified photon positions during readout.

For survey applications, we are mainly interested in full-frame imaging mode observations of the instruments.⁶ In contrast to optical or NIR pixel arrays (see Chaps. 7 & 8), X-ray CCDs are operated in single photon counting mode enabling non-dispersive low resolution spectroscopy. Incident X-ray photons produce a number of recorded electrons inside the detector pixel via an internal photoelectric effect which scales with the X-ray energy. If the CCD readout is sufficiently fast to ensure at most a single X-ray photon interaction per pixel neighborhood⁷ and clocking cycle, the energy resolution is achieved by matching the measured pixel signal to a calibrated energy.⁸

Table 6.1 summarizes the most important XMM-Newton imaging mode characteristics. After the general overview, we will now discuss the main instrumental factors for distant galaxy cluster searches ordered with decreasing priority.

Effective Area: The effective area A_e is the prime instrument characteristic related to the achievable sensitivity per unit time. The effective *instrumental* photon gathering power is determined as the product of the geometric area of the mirror modules, their reflectivity, and the quantum efficiency of the detectors, shown in the right panel of Fig. 6.1 for all XMM-Newton camera systems. The solid black line illustrates A_e as a function of photon energy for the PN camera as the most sensitive imaging instrument. The two MOS⁹ detectors provide lower quantum efficiencies and are only exposed to 44% of the geometric mirror area resulting in the dotted blue line for the individual instrument and the solid blue line for the sum of both modules. The total effective area for all three XMM imaging instruments adds up to $A_e \simeq 2\,500\text{ cm}^2$ at 1 keV. XMM-Newton achieves a photon gathering power which outperforms the Chandra observatory sensitivity by about a factor of four, and roughly by a factor of ten in comparison to ROSAT (*e.g.* Romer *et al.*, 2001).

The grazing-incidence reflection efficiency of X-ray photons on the mirror shells is very sensitive to the incident angle with respect to the optical axis of the module. This

⁵The out-of-time fraction is 6.3% for full frame mode and 2.3% for the extended full frame mode.

⁶Various other timing, burst, or small window modes are available for different science applications.

⁷X-ray photons can deposit their energy over several connected pixels, a pixel cluster, which have to be isolated spatially and temporally for an accurate energy reconstruction. Typically, only single and double pixel events are considered for the science analysis.

⁸Pile-up events, *i.e.* several photons recorded in the same pixel, can be identified and discarded during the data processing.

⁹The PN camera is effectively a factor of 3.3 more sensitive than the individual MOS cameras at 1 keV. A factor of 2.3 is attributed to the different geometric mirror area, the remaining factor of 1.5 is due to the QE differences.

gives rise to the *vignetting* effect, *i.e.* the decreasing effective area with increasing off-axis angle from the optical axis, which is shown in the left panel of Fig. 6.2. At $\Theta \simeq 10.5$ arcmin the photon gathering power has dropped to 50% of the central value and continues to fall towards the outskirts of the FoV. An integration of the vignetting function over the detector area out to a given off-axis angle yields the average vignetting factor $\bar{V}_{\text{vig}}(\leq \Theta)$ as $\bar{V}_{\text{vig}}(\leq 10') \simeq 0.72$, $\bar{V}_{\text{vig}}(\leq 12') \simeq 0.65$, and $\bar{V}_{\text{vig}}(\leq 15') \simeq 0.55$.

Field-of-View: The total XMM-Newton field-of-view is about 30 arcmin in diameter, corresponding to $\sim 0.2 \text{ deg}^2$. The relevant instrument characteristic for survey applications is the product of the FoV solid angle and the effective area, the so-called *grasp* $g \equiv A_e \cdot \Omega$, which determines the required time to cover a unit sky area to a specified depth. Taking the average vignetting factors into account, we obtain (at 1.5 keV) $g_{15} \simeq 270 \text{ cm}^2 \text{ deg}^2$ for a maximum off-axis angle of 15 arcmin, and $g_{12} \simeq 204 \text{ cm}^2 \text{ deg}^2$ and $g_{10} \simeq 157 \text{ cm}^2 \text{ deg}^2$ when restricting to FoV to off-axis angles of 12 arcmin or 10 arcmin, respectively. The motivation to constrain the field-of-view for a cluster survey arises from the PSF properties discussed below.

Spatial Resolution: The first two items determine the number of photons per source and unit time and the total sky area per observation. The most crucial point for any serendipitous cluster survey is the assessment of the source extent properties, which serve as primary selection criteria. Simply speaking, a source can be spatially resolved if its extent is larger than the instrumental point-spread-function (PSF). This implies that an accurate knowledge of the PSF shape at the source position is the pre-requisite for determining a spatial extent of the source. As was the case for the vignetting factor, the PSF varies strongly as a function of off-axis angle. Figure 6.3 illustrates the changing shape of the XMM point-spread-function in 3 arcmin steps from the center. The increasing asymmetry and complexity towards the FoV outskirts is obvious, and is the main reason for prevailing uncertainties in the off-axis PSF calibration even after more than seven years of XMM operations.

The central PSF is well described by a King profile of the form

$$PSF(r) = \frac{A}{\left[1 + \left(\frac{r}{r_c}\right)^2\right]^\alpha}, \quad (6.1)$$

with core radius r_c , index α , and normalization A . All fitting parameters are functions of off-axis angle and energy. The on-axis PSF core radii at 1.5 keV have been determined¹⁰ as $r_c(\text{MOS1}) \simeq 4.7''$, $r_c(\text{MOS2}) \simeq 4.5''$, and $r_c(\text{PN}) \simeq 6.2''$. The instrumental XMM on-axis resolution limit is hence set at cluster core radii of $r_c \simeq 5''\text{--}6''$, corresponding to a physical resolved cluster core scale at $z > 1$ (see Fig. 3.1) of $r_c^{\text{lim}} \sim 50 \text{ kpc}$. However, the on-axis PSF sets a lower ideal resolution limit, which is not applicable outside the very center of the FoV. From the lower row of PSF images

¹⁰PSF calibration documentation EPIC-MCT-TN-012, 2002 by S. Ghizzardi. See http://xmm.vilspa.esa.es/external/xmm_sw_cal/calib/documentation/index.shtml.

Characteristic	XMM Performance
number of telescopes and imaging detectors	3
total effective area at 1keV	$\sim 2\,500\text{ cm}^2$
field-of-view	30' diameter $\simeq 0.2\text{ deg}^2$
spatial resolution (FWHM)	5''–15''
half-energy width (HEW)	14''–20''
pixel scale PN / MOS	4''1 / 1''1 per pixel
energy resolution at 1keV	$\sim 80\text{ eV}$
point source sensitivity in 10 ksec (all cameras)	$\sim 5 \times 10^{15}\text{ erg s}^{-1}\text{ cm}^{-2}$

Table 6.1: XMM-Newton imaging-mode characteristics.

in Fig. 6.3 it becomes obvious that the azimuthally symmetric King profile is not a good approximation to the increasing asymmetry of the core. Meaningful calibration data characterizing the off-axis PSF is sparse, and a formal application of the King profile fit even returns a decreasing core radius at increasing off-axis angles. A more practical illustration of the off-axis dependence on the resolution limit is given in the right panel of Fig. 6.2, which shows Gaussian full-width at half-maximum (FWHM) measurements of sources in three deep fields. The combined photon images of all three detectors were used, thus returning the properties of the average XMM PSF. The red line in Fig. 6.2 indicates the averaged results and is consistent with the expected off-axis trend of a FWHM broadening from about 8'' in the center to roughly 14''–15'' in the detector periphery. The uncertainty in the off-axis PSF calibration is one of the main reasons for the detection of spurious extended sources and has to be adequately taken into account for the source classification.

Background Characteristics: The X-ray background is the second critical issue for the detection of extended sources, as uncertainties in the model background can also result in spurious extended sources. For low surface brightness objects such as clusters, the X-ray background is the prime limitation of the achievable sensitivity. Concerning the background properties, XMM-Newton is not in an ideal orbit (see Sect. 6.6.1) as observations are contaminated from frequent background flaring events and exhibit rather high quiescent levels. This has the consequence that cluster studies require significant efforts for the suppression and proper treatment of the X-ray background (see Sect. 6.3.2).

Energy Resolution: The XMM-Newton energy resolution in imaging mode of $\sim 80\text{ eV}$ at 1 keV is the least critical among the discussed items for distant cluster searches. However, it enables (i) the *a posteriori* definition of band-passes, (ii) the assessment of hardness ratios for all sources, and (iii) more detailed spectroscopic studies of confirmed clusters, *e.g.* for a temperature determination of sufficiently bright sources.

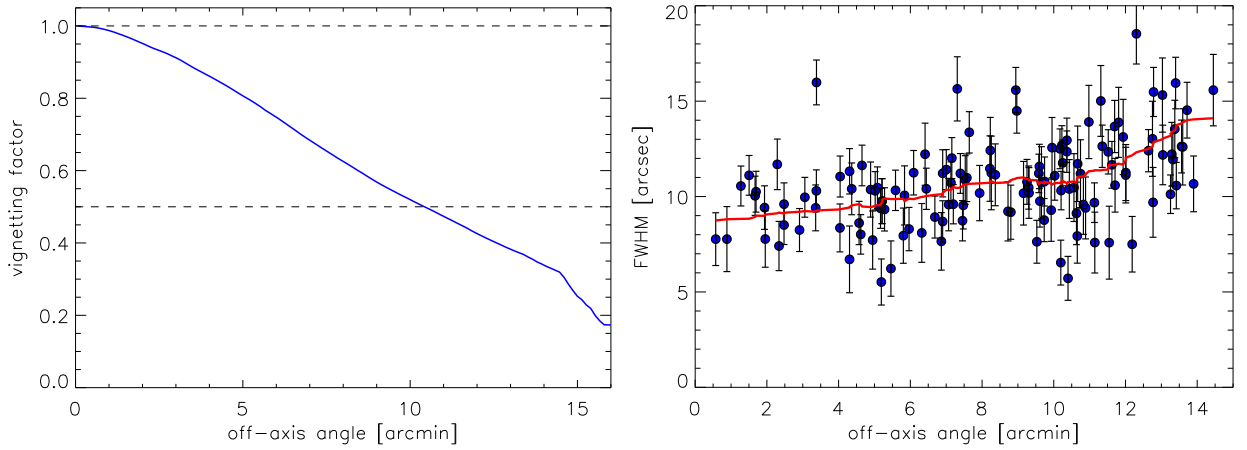


Figure 6.2: XMM vignetting and PSF properties as function of off-axis angle. *Left:* Average vignetting function of all three XMM X-ray telescope systems, with the PN optical axis used as central reference point. The horizontal dashed lines indicate the 100% and 50% effective area levels, the latter is reached at an off-axis angle of about 10.5 arcmin. The sharp drop starting at ~ 14.5 arcmin off-axis angle indicates the onset of the FoV edge of some detectors. *Right:* Gaussian FWHM of sources as determined in three deep fields. The measurements were performed in the combined image of all three detectors. The error bar length is proportional to the ratio of the FWHM in the X and Y direction, *i.e.* to the amount of PSF asymmetry. The red solid line illustrates the smoothed trend of the average FWHM between about $8''$ in the center and $15''$ at the FoV edge.

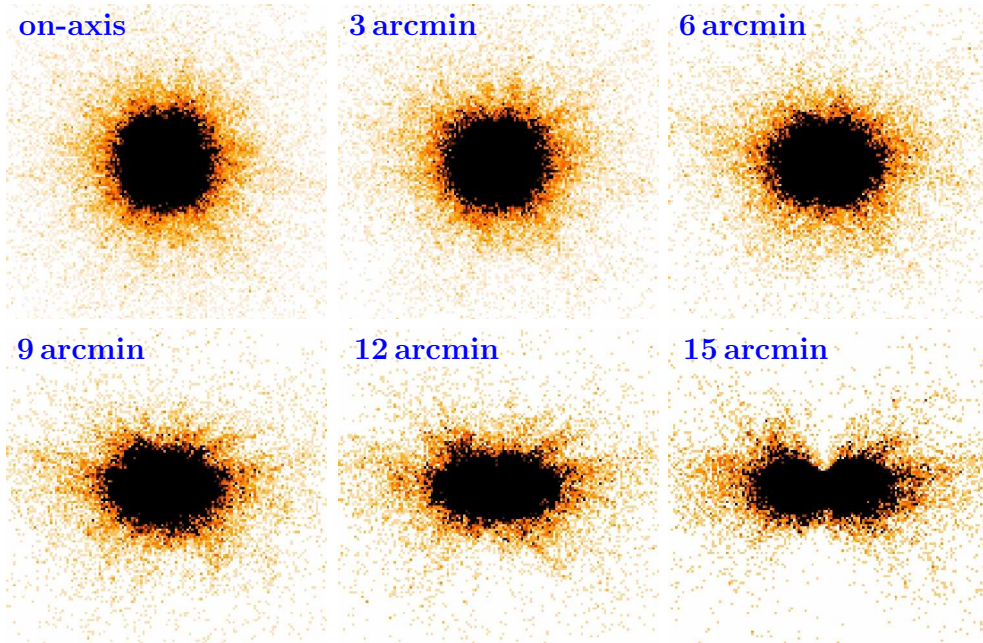


Figure 6.3: XMM PSF shape variations as a function of off-axis angle. Shown are the 2-D PSF images of the PN mirror module in off-axis angle steps of 3 arcmin as provided by the XMM calibration data base. The increasing asymmetry towards the FoV edge poses a bigger problem to the detection of extended sources than the moderate overall broadening of the PSF core.

6.2 X-ray Data Archive and Survey Definition

All five X-ray instruments of the XMM-Newton observatory are operating simultaneously during targeted observations. Even for science programs that are not focussed on XMM's imaging capabilities, any idle PN or MOS camera proceed with the data acquisition. All observations are collected in the online XMM data archive¹¹, where they become publicly available after a proprietary period of typically twelve months. The XMM archive is hence constantly growing with now more than seven years of successful operations.

In order to obtain a well controlled sample for the current project phase, the general XDCP survey field definition has been frozen at the archive status of **2 November 2004**. After almost five years of in-orbit operations, the XMM data archive exhibited the following statistical properties¹²:

- 2960 fields with expired proprietary period were available in total with a total nominal exposure time sum of $\Sigma \simeq 72.3$ Msec;
- 2016 of these observations had at least one camera operating in full frame imaging mode;
- 1910 remained after rejecting sky regions 'contaminated' by the Large and Small Magellanic Clouds and by the Andromeda galaxy M31;
- 1109 fields were located at sufficiently high galactic latitudes with $|b| \geq 20^\circ$ and had nominal exposure times of more than 10 ksec (see dotted black line in Fig. 6.4 for exposure time distribution);
- 1018 observations were not attributed to designated survey programs with separate source identification programs, *e.g.* XMM-LSS, COSMOS, Chandra Deep Fields (black solid line in Fig. 6.4);
- 575 fields were VLT accessible at declinations $\text{DEC} \leq +20^\circ$ (blue solid line) defining the *XDCP raw survey sample* with the sky distribution shown in Fig. 6.5;
- 546 data sets (see field list in Tab. A.1) passed a first quicklook check and were processed with the XDCP X-ray reduction pipeline ($\Sigma \simeq 17.5$ Msec);
- **469** fields were fully analyzed and are in principle suitable for distant cluster searches, defining the **XDCP core survey sample** ($\Sigma \simeq 15.2$ Msec);
- 106 analyzed observations are located within the South Pole Telescope SZE survey region at $\text{DEC} < -30^\circ$ and $21 \text{ h} < \text{RA} < 7 \text{ h}$ indicated by red symbols in Fig. 6.5 ($\Sigma \simeq 3.3$ Msec).

¹¹The XMM-Newton data archive can be accessed through http://xmm.vilspa.esa.es/external/xmm_data_acc/xsa/index.shtml.

¹²The software for processing XMM archive lists and for automated data download was originally written by Chris Mullis.

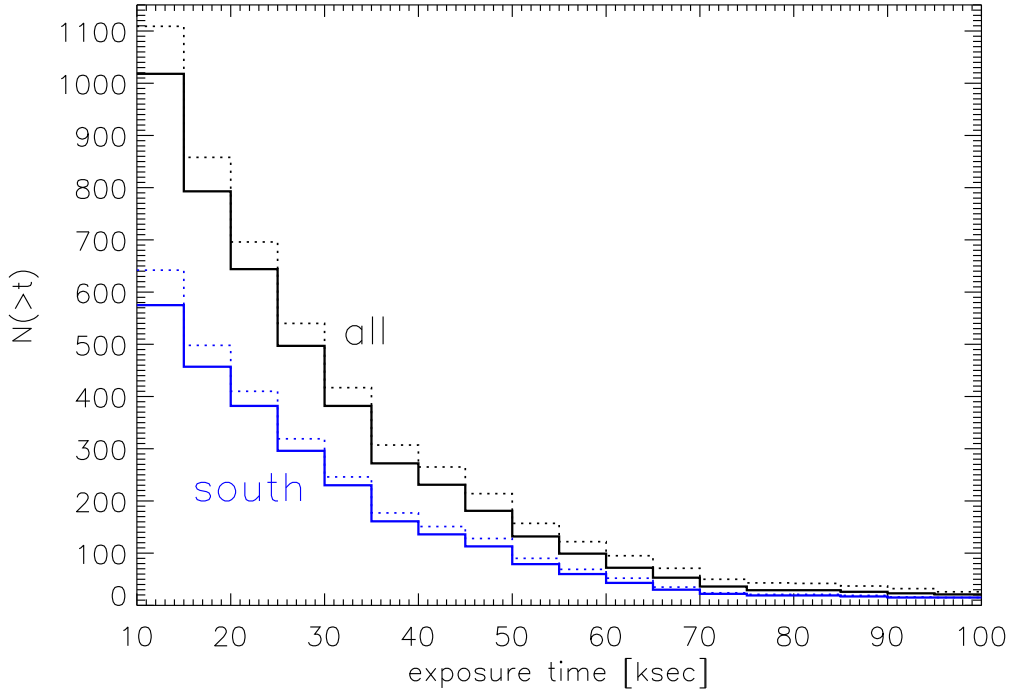


Figure 6.4: Cumulative distribution of XMM-Newton archival fields suitable for a serendipitous survey as of status November 2004. The blue solid line shows the Southern sample ($\text{DEC} < +20^\circ$) of 575 XMM-Newton observations used for the analysis in this thesis. The black solid line depicts the full sample including the Northern sky, dashed lines include in addition observations of designated deep surveys (e.g. XMM-LSS, COSMOS, see Sect. 4.4).

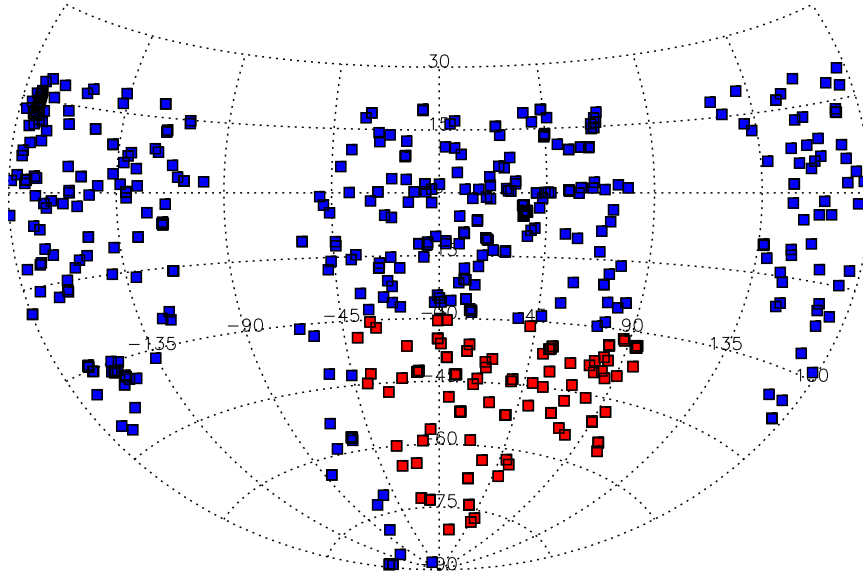


Figure 6.5: Sky distribution of the 575 Southern XMM-Newton fields suitable for a survey (*raw XDCP sample*). The red squares indicate fields which will be covered by SZE observations with the South Pole Telescope. Square symbols are not to scale.

6.3 Development of an X-ray Reduction and Analysis Pipeline

In this section, the basic concepts of the X-ray data reduction and source detection processes are introduced. The handling of hundreds of XDCP survey field data sets required the development of a designated, distant cluster-optimized X-ray reduction pipeline. The driver and final goal of the X-ray pipeline development is the maximally achievable sensitivity for faint extended cluster sources in the archival data. This development is based upon the available tools of the XMM Science Analysis Software¹³ (SAS), the mission software package to reduce and analyze XMM data.¹⁴ In particular for the critical source detection procedure, the performance of the SAS tasks impose a ‘boundary condition’ for the survey outcome.

The overall reduction and analysis approach aims at the compilation of a versatile *raw* survey masterlist, obtained by homogeneously applying the same procedure to all fields of the predefined XDCP sample. These *raw* results should comprise a super-set of the finalized survey sample in terms of number of analyzed fields, detector area, significance thresholds, and source characterization and should enable cross-checks and performance evaluations. The final XDCP *science survey sample* can then be defined *a posteriori* based on optimized and more restrictive cuts concerning (i) the flux limit, (ii) significance thresholds, (iii) usable detector area, and (iv) survey field selection. Since the XDCP is pushing the limits of what is achievable with XMM for distant cluster detection, this versatile approach promises the most flexibility for selection adjustments and the final survey characterizations once additional observational feedback is available.

6.3.1 Search strategy

For faint object detections in any waveband, the crucial characteristics is always the signal-to-noise ratio (SNR), *i.e.* the source signal in a given aperture divided by the total noise in the same area. A first possible distant cluster optimization is hence related to the energy range of the applied detection bands. As discussed in Sect. 2.3, the observed thermal bremsstrahlung spectra of plasmas at temperature T (Equ. 2.2) are characterized by an exponential cut-off beyond energies of $E_{\text{cut}} \simeq k_{\text{B}}T$ at the high-energy end and a galactic hydrogen absorption suppression at the low-energy end of $E_{\text{abs}} \lesssim 0.3 \text{ keV}$. While the latter spectral boundary is redshift-independent, the first one scales as $E_{\text{cut}}(z) \simeq k_{\text{B}}T/(1+z)$. A fiducial $T \sim 5 \text{ keV}$ cluster at $z \sim 1$ will hence exhibit the spectral break at about 2.5 keV, which will shift towards lower energies at even higher redshifts. These simple considerations imply that distant cluster searches should be focussed on the soft bands of the XMM sensitivity range.

Scharf (2002) has determined the optimal XMM detection bands for yielding the highest SNR for galaxy clusters and groups with different temperatures and redshifts. Figure 6.6 summarizes these results for the MOS detectors (left panel), the PN instrument (center

¹³The SAS homepage can be found at <http://xmm.vilspa.esa.es/sas>.

¹⁴SAS tasks such as `ebxdetect` are set in typewriter font for easy identification.

panel), and the SNR improvement for the PN (right panel). The XDCP prime target objects are $z \gtrsim 1$ clusters with temperatures $2 \text{ keV} \lesssim T \lesssim 8 \text{ keV}$, *i.e.* we are mainly interested in the extrapolation of the upper three black lines for 6 keV, 4 keV, and 2 keV model clusters in Fig. 6.6. Based on this study, a single optimized XDCP distant cluster detection band with an energy range of 0.35–2.4 keV (blue lines) was defined, which promises an enhanced performance for distant objects over a wide range of temperatures. The lower limit of this optimized band is essentially representing the average of the case study model clusters (dotted lines in Fig. 6.6), the upper limit is motivated by the high- z trends of hot systems (upper solid lines of left and central panel). Two main aspects determining the efficacy of an optimized single detection band are (i) the SNR of the sources as prime parameter for the *detection*, and (ii) the number of source photons for the source *characterization*, *i.e.* in particular the extent measurement (see Fig. 6.20). Whereas the achieved improvements of the SNR for hot systems are moderate compared to a standard 0.5–2.0 keV band-pass (see right panel of Fig. 6.6), the total number of photons for distant cluster sources can be significantly increased (~ 30 –50%) for the optimized, wider 0.35–2.4 keV band, which in turn yields more accurate source parameters. In the following, three different band-pass schemes are defined, which aim at a detection optimization in different ways:

- (1) **Single Band Scheme:** The conceptually simplest search strategy for distant clusters is the use of a single detection band. As discussed, the 0.35–2.4 keV band is expected to optimize the target signal-to-noise ratio *and* the total number of source photons over a wide range of the expected source characteristics. This band-pass is used as the primary XDCP detection scheme and almost coincides with the ROSAT band (0.1–2.4 keV). A single defined energy band will simplify the survey calibration and the determination of the selection function through extensive simulations (see Sect. 9.1.3).
- (2) **Spectral Matched Filter Scheme (SMF):** The first detection scheme does not allow the determination of spectral hardness ratio properties and additionally makes use of justified but fairly strong priors on the expected spectral source properties. It is conceivable that very hot systems at $T \gtrsim 10 \text{ keV}$ exist in the distant Universe, *e.g.* as the result of a recent major merger event. In order to broaden the energy baseline and hence increase the sensitivity for hotter objects, the second scheme covers the full 0.3–7.5 keV range, but assigns different weights to parts of the spectral range, as shown by the blue line in Fig. 6.7. By enhancing the softer energy regions, the shape of the weight function roughly follows the (expected) continuum form of hot distant clusters (see lower right panel of Fig. 5.2) and is consequently termed *spectral matched filter scheme* (SMF). The effective weight function is achieved in practice by using five (partially) overlapping¹⁵ bands (0.3–0.5, 0.35–2.4, 0.5–2.0, 2.0–4.5, 0.5–7.5 keV). The SMF scheme is to be considered as an *experimental* approach, which has yielded promising performance results in early comparison tests. The empirically

¹⁵For the source characterization and the associated likelihoods, this implementation is statistically equivalent to the use of a single broad band (0.3–7.5 keV) with different assigned weights over the spectral range.

determined likelihood offset factors for the significance evaluation and the comparison to the other schemes will be discussed in Sect. 6.6.2.

- (3) **Standard Scheme (STD):** The third applied scheme makes use of the combination of three XMM standard bands in the range 0.3–0.5 keV, 0.5–2.0 keV, and 2.0–4.5 keV, *i.e.* it provides continuous coverage from 0.3–4.5 keV. This approach is widely used and can hence be considered as the *standard* scheme.

Figure 6.7 summarizes all three detection schemes and their energy coverage. All methods offer some advantages and complementarity. The first detection scheme is attractive for its simplicity, the second for its additional sensitivity to ‘exotic systems’, and the third for its standardized source parameters. Three main reasons motivated the application of a complementary multi-scheme detection method:

- achieving the best possible survey completeness of detected extended sources;
- enabling a cross-comparison of methods to test for systematic selection effects;
- increasing the reliability of the source classification close to the detection threshold by evaluating the stability of important source parameter solutions.

6.3.2 X-ray data reduction

The general outline of the developed XDCP X-ray reduction pipeline is illustrated in Fig. 6.8. Raw XMM-Newton data for each observation are organized in a so-called Observation Data File (ODF), a directory with a collection of ~ 200 files containing the uncalibrated data of all instruments, satellite attitude files, and calibration information. ODFs have unique identifications numbers (OBSID) and can be considered as the basic starting data set from which all science products can be derived. An arbitrarily long list of ODFs serves as the input for the X-ray pipeline and is passed on to the top-level script, which organizes the ODF handling and the calls of the individual reduction modules. In practice, 1–3 modules are applied to typically 100 data sets at a time, followed by quality and completion checks of the intermediate data products. All data sets have been homogeneously¹⁶ reduced with the XMM Science Analysis Software version SAS 6.5.

The full XDCP pipeline can be subdivided into three main parts: (i) The actual *X-ray data reduction* modules, which create calibrated science images from the raw satellite data, (ii) the *source detection* and characterization procedures resulting in lists of extended sources, and (iii) the *interactive* individual detailed source analysis and classification using *X-ray-optical image overlays*. In this sub-section, we will have a closer look at the data reduction modules¹⁷ of the first part.

¹⁶An early reduction run of 120 XMM observations using SAS 6.1 has been repeated with SAS 6.5, released in August 2005.

¹⁷The individual X-ray reduction modules are adapted and extended versions of codes originally written by Hans Böhringer.

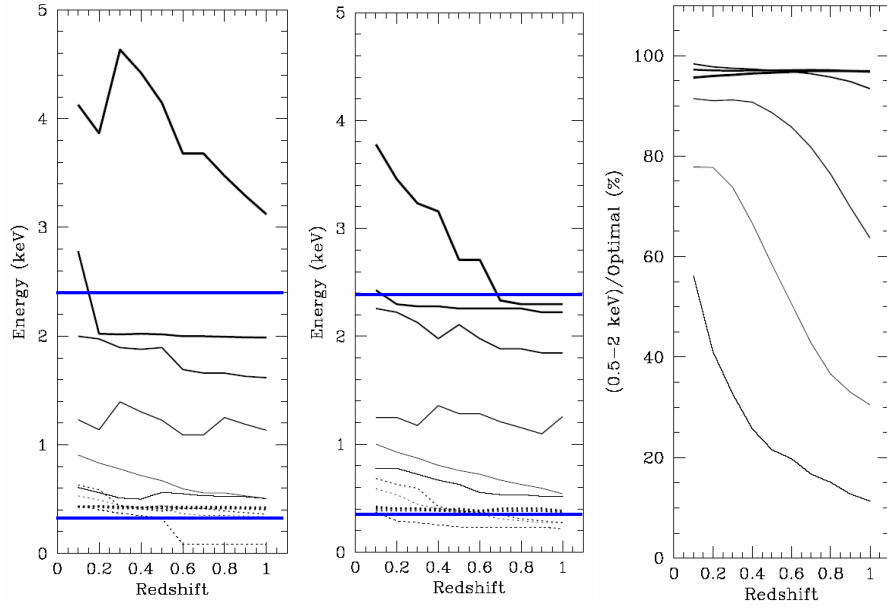


Figure 6.6: Optimized X-ray source detection bands for galaxy clusters and groups as derived by Scharf (2002). *Left:* Upper (black solid lines) and lower (black dotted lines) detection band-pass versus object redshift for the XMM MOS detectors for systems with different temperatures. From top to bottom the assumed cluster/group temperature is 6, 4, 2, 1, 0.5, 0.2 keV. The blue solid lines illustrate the XDCP detection band with an energy range of 0.35–2.4 keV, which was chosen to yield an optimized high-redshift detection performance over a wide range of temperatures. *Center:* Same plot for the XMM PN detector. *Right:* Expected PN signal-to-noise ratio of the standard 0.5–2.0 keV band divided by the SNR of the optimized bands (black lines) in the center panel. The SNR gain is most notable for lower temperature systems at $T \lesssim 2$ keV. Plots adapted from Scharf (2002).

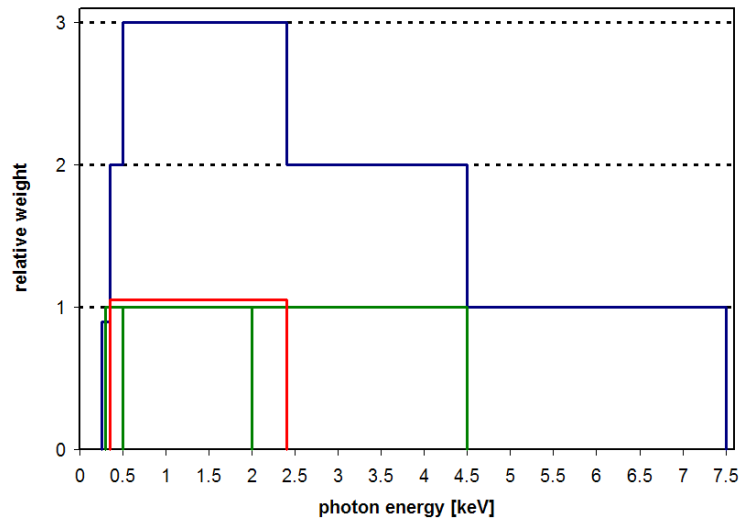


Figure 6.7: Detection schemes. The relative photon weight factor is plotted against the energy for the unweighted *single band scheme* (red line), the three-band *standard scheme* (green), and the *spectral matched filter scheme* (blue) featuring different photon weights across the spectral range. Small offsets are applied for easier distinction of band boundaries.

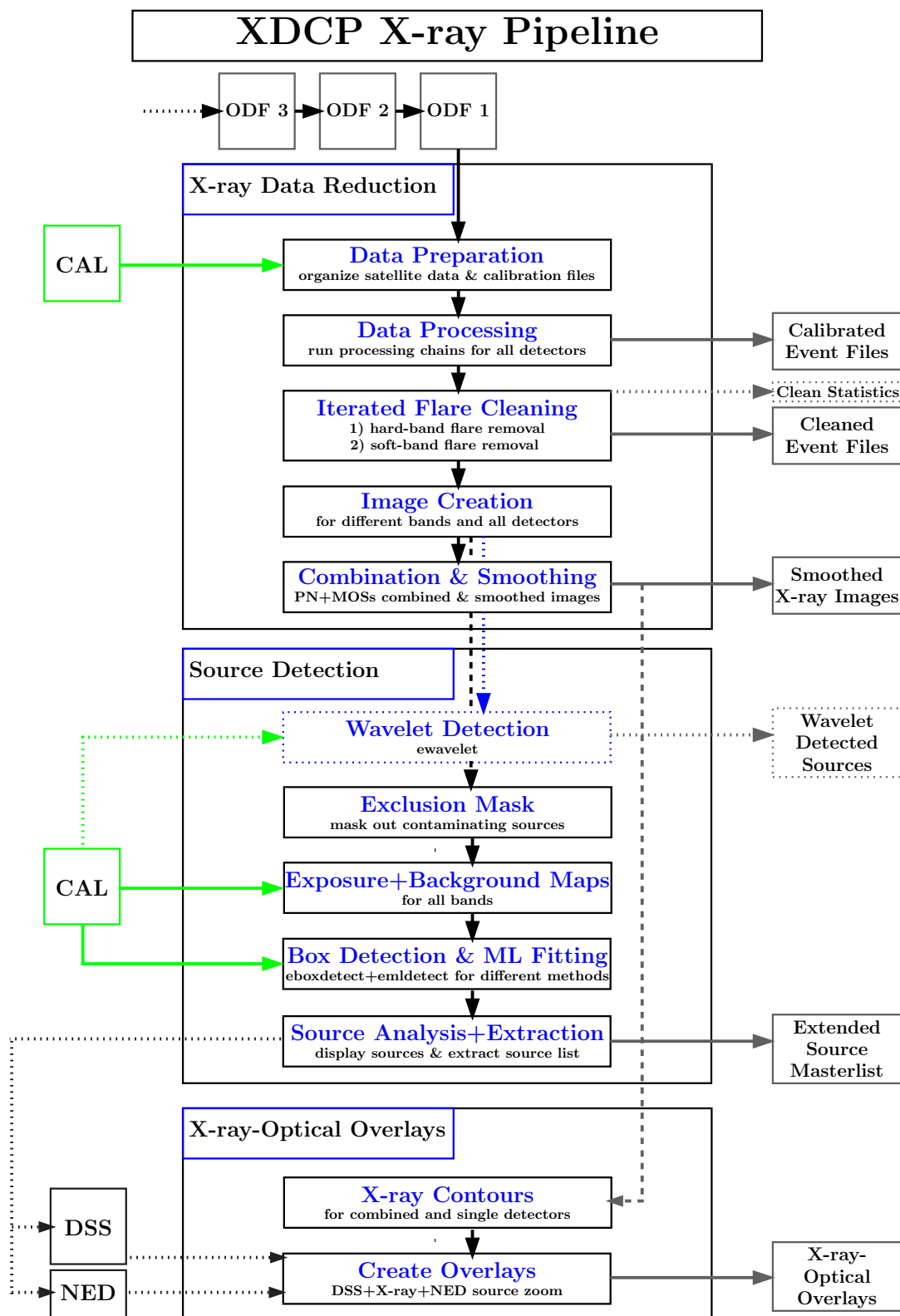


Figure 6.8: X-ray reduction and analysis pipeline flow chart.

XMM data setup

The first task is to transform the XMM sets of raw satellite data, each ODF containing typically ~ 500 MB of data, into a suitable format for further processing. This is achieved with few straightforward **SAS** procedures which keep the complexity of the underlying raw data hidden from the user. The task **cifbuild** matches the input data with the appropriate calibration files, which are accessible through the so-called Calibration Access Layer (CAL). **odfingest** extracts and organizes the satellite housekeeping data necessary to accurately reconstruct the observations. The instrument specific processing chains **epchain** for the PN and **emchain** for the MOS cameras generate calibrated photon event lists for the complete observation with reconstructed sky positions, energies, arrival times, and event characteristics for each individual X-ray photon.

In Sect. 6.2, one of the survey field selection criteria was a minimal *nominal* exposure time of 10 ksec, which is the period XMM was pointing at the target location. However, the *nominal* on-target times are not equivalent to the effective *science-usable clean* exposure times, which can be significantly lower for two main reasons. (i) Instrument calibration overheads at the beginning of an observation require about 0.5–1.5 h for the PN, and 10 min for the MOS instruments in order to compute the *optical loading* of the CCD chips, *i.e.* the signal fraction attributed to optical light rather than X-ray photons. The more sensitive PN camera hence achieves on average about 1 h less on-target time than the MOS instruments. (ii) In addition to the constant hardware overheads, the more or less unpredictable *space weather* can contaminate observations resulting in extended periods of lost time. The *space weather* effects and the different XMM background components are discussed in the following.

X-ray backgrounds and flare cleaning

The XMM background is the prime constraint for the achievable sensitivity limit of low surface brightness extended sources. For its importance, the main background components¹⁸ are shortly introduced followed by a discussion of the implemented flare cleaning procedure.

Cosmic X-ray Background (CXB): The cosmic X-ray background can be separated into two main contributions. (i) The *hard component* of the CXB dominates at energies $\gtrsim 1$ keV and is mostly attributed to the integrated light of faint, unresolved extragalactic X-ray sources, predominantly Active Galactic Nuclei (AGN). Extremely deep 1 Msec pencil-beam observations with Chandra have resolved the largest fraction of the hard CXB into individual point sources (*e.g.* Mushotzky *et al.*, 2000; Giacconi *et al.*, 2001). The total CXB flux in the 2–10 keV hard band reaches an approximate surface brightness of $5 \times 10^{-15} \text{ erg s}^{-1} \text{ cm}^{-2} \text{ arcmin}^{-2}$. (ii) The *soft component* of the CXB, dominating below 1 keV, can be attributed to thermal diffuse emission of galactic origin. It originates from plasma of the Local Hot Bubble, the Galactic Disk, and

¹⁸All XMM background components are summarized by A. Read at <http://www.star.le.ac.uk/%7Eamr30/BG/BGTable.html>.

the Galactic Halo and is consistent with thermal emission of about $T \sim 0.1\text{--}0.2\text{ keV}$. The CXB is constant in time, but the *soft component* varies spatially across the sky.

Flaring Particle Background: This background component was severely underestimated before the launch of XMM and is responsible for most of the lost science time. The flaring background has strong rapid variability and is attributed to soft protons of solar origin with energies of a few 100 keV. These protons, which seem to be organized in ‘clouds’ populating the Earth’s magnetosphere, are funnelled by the X-ray mirrors towards the detectors, where they typically deposit several keV of their energy in the CCD pixels. The occurrence of the soft proton flares is unpredictable but is related to the solar activity and the satellite position with respect to the magnetosphere. Flare intensities can reach 1 000 times the quiescent background level implying that contaminated time intervals have to be carefully cleaned and removed from the science data. Since the soft protons pass the mirror system, they imprint a (partially) vignetted background component onto the detectors.

Quiescent Particle Induced Background: This second particle induced component dominates the quiescent background level. It is attributed to high-energy cosmic ray events of some 100 MeV, where a charged particle interacts with the detector material and the surrounding structures to produce fluorescence emission. This more stable internal background component typically varies only on the $\pm 15\%$ level during observations, but can be an order of magnitude enhanced in high radiation periods. The cosmic rays induce a background component originating from the detector material itself, *i.e.* the quiescent particle background is not vignetted, but reflects the spatial structure of the surrounding detector material. The most prominent instrumental fluorescence lines are due to the Al-K α transition at 1.5 keV for all instruments and additional Si-K α emission at 1.7 keV for the MOS detectors. Another intense line complex of several elements (*e.g.* Cu, Ni, Zn) arises around 8 keV for the PN and is hence beyond the considered bands for the survey.

Instrumental Noise: The last considered background contribution is electronic detector noise. This component is negligible in the harder bands but becomes significant at low energies of $\lesssim 0.3\text{ keV}$. The low energy band limit for the survey of 0.3 keV is thus motivated by the onset of increased instrumental noise in conjunction with enhanced galactic hydrogen absorption.

The top left panel of Fig. 6.9 shows a typical 100 sec-binned light curve in the PN 12–14 keV hard band of a 47 ksec pointing. The soft proton flare during the central part of the observation is obvious and can be particularly well identified in the hardest band due to the flat nature of the flare spectrum. The pipeline flare removal procedure of the *first cleaning stage* automatically identifies the stable quiescent level based on a Gaussian peak-fit in the count-level histogram of the time series (center left panel of Fig. 6.9). All observation periods with background levels less than three standard deviations above the determined quiescent level are accepted as good time intervals (GTI) for the initial hard band cleaning.

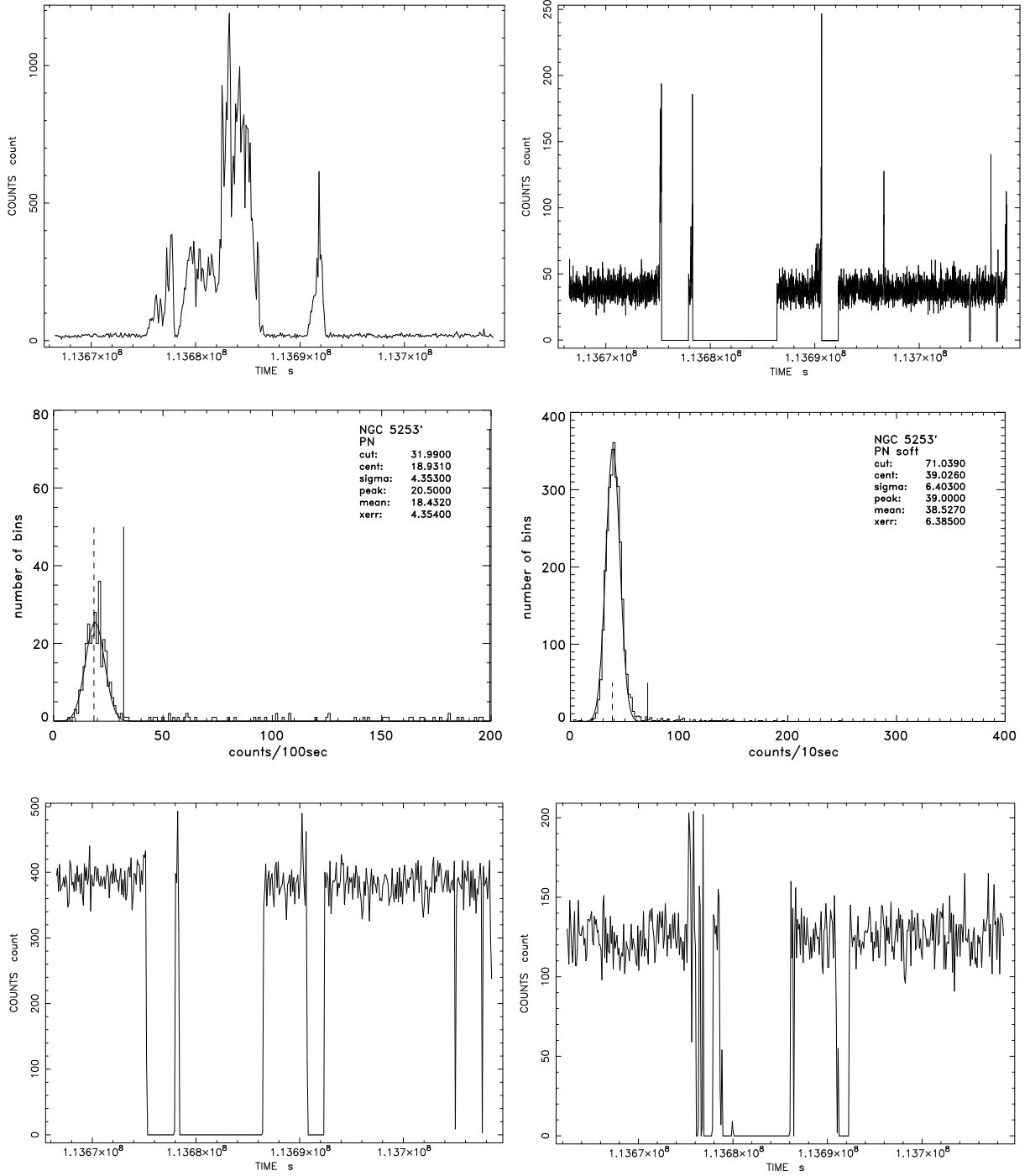


Figure 6.9: X-ray flare cleaning procedure. *Top row left:* 100sec-binned PN light curve of the complete field in the hard X-ray band at 12–14 keV. The flared periods are easily visible and are removed during the first cleaning stage. *Right:* 10sec-binned PN 'soft' band light curve at 0.3–10 keV. The missed rising flanks close to the onset of flare periods and short flares are identified during the second cleaning stage. *Center row:* Automatic good time interval analysis based on the identification of the quiescent level and specified $\kappa\sigma$ -clipping cut-levels for cleaning stage one (*left*) and stage two (*right*). *Bottom row:* Final light curve of the identified good time intervals for the PN (*left*) and MOS (*right*) detectors.

This *first cleaning stage* efficiently removes the largest fraction of flare-contaminated data. However, at lower energies the flares can exhibit a different time behavior than the main hard component, which is currently attributed to lower energy particles at the edges of the encountered proton ‘clouds’. The upper right panel of Fig. 6.9 displays the 10 sec-binned light curve in the full 0.3–10 keV soft X-ray band after the initial flare removal. The residual flare peaks are identified during the *second soft-band cleaning stage*¹⁹ and are removed from the remaining good time intervals via 5- σ clipping of the soft energy histogram (center right panel of Fig. 6.9).

The lower panels of Fig. 6.9 show the resulting light curves (100 sec-binned) after the iterated flare cleaning procedure for the PN instrument (left) and one of the MOS cameras (right). The contaminated time intervals are completely removed from the final cleaned photon event lists resulting in an effective science-usable exposure time of 29.6 ksec or 63% of the nominal time for this field.

The flare removal procedure is applied to all instruments independently since the higher low energy sensitivity of the PN camera results in a different temporal response of the system. For about 80% of all XMM fields, the *automatic* double flare cleaning procedures yields good and stable results in identifying the good time intervals. If more than half of the observation is contaminated, the automatic determination of the quiescent background level might fail and require a manual definition of the GTI cuts.

X-ray images

With the cleaned photon event lists at hand, we can now create X-ray images for all subsequent analysis tasks. The energy information of the X-ray photon events allows the arbitrary definition of customized band-passes at this point. As discussed in Sect. 6.3.1, five different energy bands are considered for the XDCP survey. Photons of the 0.35–2.4 keV energy range are selected for the optimized single detection band, the ranges 0.3–0.5 keV, 0.5–2.0 keV, and 2.0–4.5 keV for the standard band method, and an additional 0.5–7.5 keV broad band for the spectral matched filter scheme, which uses all five bands.

The X-ray images are reconstructed with 4 arcsec pixels from the cleaned photon event lists by applying the appropriate energy cuts and conservatively selecting only well calibrated events as characterized by event quality flags. The absolute astrometry, *i.e.* the sky coordinate information, is typically accurately determined to within approximately one arcsecond. Images are produced for each instrument individually resulting in a total of 15 band-detector combinations.

At this stage, the correction for out-of-time events of the PN detector is performed. Based on the observed count rate in each pixel, the smeared streaks of photons with mismatched Y position information can be statistically reconstructed in an OoT image²⁰. This OoT frame is created for each band and subtracted from the corresponding raw PN data to yield a first order correction of the out-of-time image artifacts. Although the fraction of smeared photons is only 2.3% or 6.3% (depending on the imaging mode), the trails of very bright central target objects can mimic apparently extended sources and should therefore be corrected.

¹⁹The double flare cleaning procedure was originally proposed and applied by Pratt and Arnaud (2003).

²⁰A reconstructed OoT event list can be obtained with the task `epchain`.

Observations that have been interrupted, *e.g.* due to technical problems or strong flares, are often split up into several shorter data blocks per instrument. The separate event lists are individually reduced, cleaned, and transformed into X-ray images. These shorter exposures are co-added for each band-pass and instrument at this point in order to restore the full on-target integration time of the observation.

As a last step of the data reduction part, images of the same band are combined for the three detectors to yield the full XMM imaging information in the specified energy range. In order to enhance the contrast of weak sources for visual inspection, the combined images are additionally smoothed with a 4 arcsec Gaussian filter²¹. Figure 6.10 displays the raw (center left panel) and smoothed (upper left panel) combined 0.35–2.4 keV images of one of the deep XMM survey fields. The first part of the XDCP pipeline is now finished and we can proceed with the source detection module.

6.3.3 Detection of extended X-ray sources

The source detection procedure²² as shown in Fig. 6.8 requires several additional preparatory steps and intermediate data products. Figure 6.10 illustrates the X-ray image of the current reduction status (top left panel), the display of the final X-ray detection results (upper right panel), and a selection of intermediate data products in the numbered center and bottom panels.

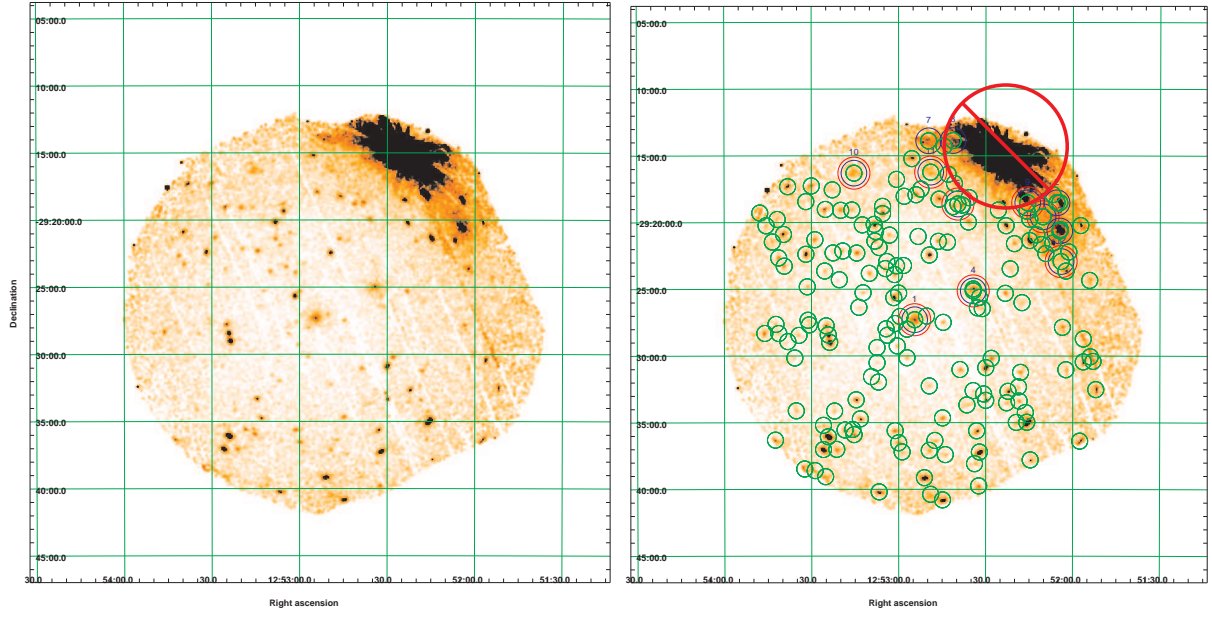
The first important calibration frames besides the raw photon count images (panel 1) are the *exposure maps* (panel 2), which correct for the varying sensitivity across the XMM field-of-view, similar to *flatfields* in optical and NIR imaging (see Sect. 7.3.2). Dividing a raw photon count image by its associated exposure map results in a sensitivity-corrected count rate image with units [counts·s⁻¹], normalized to the central, on-axis values. These calibrated count rates differ from the final physical flux units in each pixel only by a multiplicative energy-dependent constant, the (on-axis) count-rate-to-flux conversion factor.

In effect, the exposure maps contain the effective, local integration times associated with each detector pixel, scaled to the on-axis exposure. The radial shape of the exposure maps is mainly due to the vignetting function²³ (see Fig. 6.2), which accounts for the decreasing off-axis sensitivity. The task `eexpmap` also includes the calibration information on the energy dependent detector quantum efficiency, chip gaps, dead columns, the transmission of the optical blocking filters, and the detector field-of-view. Panel 2 shows the combined exposure map of all three instruments with dark regions indicating the most sensitive parts and lighter colors the areas with a reduced effective exposure time. The position of the optical axis, also named *boresight*, is indicated by the green cross. The circles illustrate the 12' (green) and 14.5' off-axis radius, with the latter one roughly coinciding with the FoV boundaries of the two MOS cameras.

²¹The filtering should average over several pixels to reduce the noise (pixel scale: 4''/pixel), but should not exceed the PSF FWHM to allow a distinction between point sources and extended objects.

²²The box detection procedure follows in part the scheme of Georg Lamer.

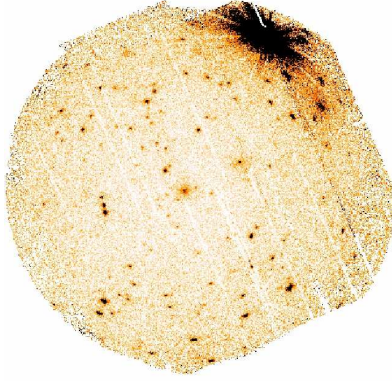
²³As an alternative method, vignetting effects can be accounted for by applying a weighting factor for each pixel.



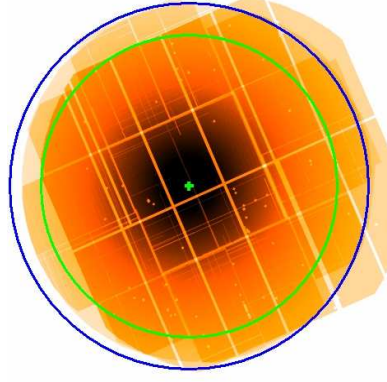
1. raw PN+MOS1+MOS2

2. combined exposure map

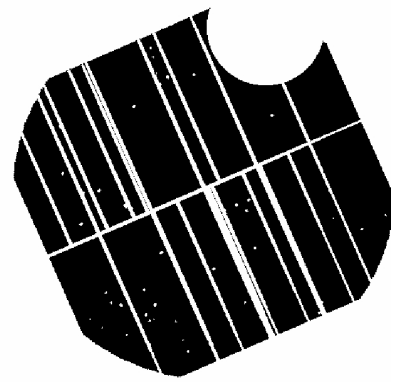
3. detection mask PN



4. background map PN



5. source map PN



6. sensitivity map PN

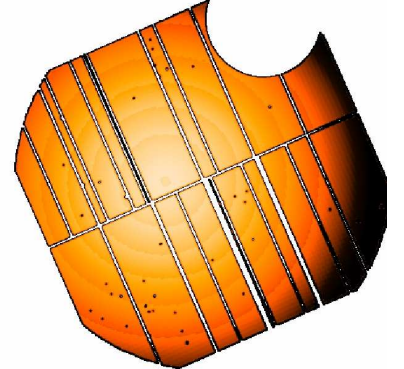
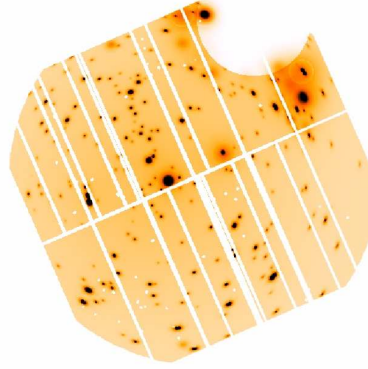
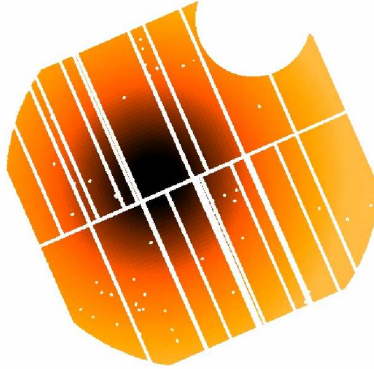


Figure 6.10: X-ray source detection products. *Top row left:* Smoothed X-ray image in the 0.35–2.4 keV detection band of the field with the distant cluster RDCS J1252-29 at $z = 1.24$ in the center. *Right:* Source detection results in the same field with point sources marked in green, extended sources indicated by larger circles, and the bright source in the upper right corner excluded from the detection area. *Center and bottom rows:* Labelled, intermediate image products of the source detection procedure. The green circle in the exposure map marks the 12 arcmin off-axis radius, blue indicates the 14.5 arcmin circle coinciding with the FoV edge of the MOS detectors.

The next step is the generation of detection masks with `emask`, as shown in panel 3 for the PN detector. The masks define the detector regions over which the source detection is performed (black areas), excluding chip gaps and dead columns (white). In addition, *manually defined* regions with bright contaminating sources are also cut out and excluded from the detection area. In the example case in Fig. 6.10, the bright off-axis source in the upper right corner has been removed (manually), but more typically the central target objects are cut out to ease serendipitous detections. Excluding bright and large area sources helps in two ways: (i) the occupied region does not contribute to the effective area of the survey and is this way automatically accounted for, and (ii) the background model is improved.

The crucial *background maps* for each detector and band are determined in the final preparatory step. The following procedure is applied. (i) A first sliding box detection run is performed with `eboxdetect` in *local mode*, *i.e.* the background is approximated locally around the detection cell. This yields a preliminary source list which is used to identify the positions of all sources and excise them from the field. (ii) The resulting ‘cheese image’ only contains X-ray background contributions and is used as input for the background modelling process with `esplinemap`.²⁴ The task performs a two-component model fit for the linear combination of a spatially constant background contribution (quiescent particle induced background and instrumental noise) and a vignettted component (CXB and residuals of the soft proton particle background). The final background model result is shown in panel 4 of Fig. 6.10. The applied reconstruction method is physically motivated by the different contributing background components and has the main advantage of a smooth radial profile, but the disadvantage that the global fit over the 30' FoV does not account for local variations. In any case, this model is preferable to the alternative spline fitting method, which accounts for local variations, but is also prone to producing numerous spurious extended sources as a consequence of local minima of the fitted splines.

Sliding box detection and maximum likelihood fitting

The actual source detection is performed in two steps. (i) A list of source candidates is obtained with the sliding box method, followed by (ii) the subsequent detailed analysis and source characterization via maximum likelihood (ML) fitting.

In order to achieve the best sensitivity for the candidate source list, the task `eboxdetect` is run in *map mode*, *i.e.* the improved reconstructed global background maps are used as input rather than the local approximation. In addition to the photon images and background maps, the exposure maps and the detection masks are supplied to the task. `eboxdetect` then takes a 5×5 pixel ($20'' \times 20''$) detection cell and slides it over the input images. At any image point, the PSF-weighted, integrated cell counts are compared to the expected background level and the likelihood for a random background fluctuation of this level is calculated. The sensitivity to extended sources is achieved, by iterating the procedure three times in conjunction with doubling the detection cell size to 10×10 , 20×20 ,

²⁴The task `esplinemap` can be used for spline fits or two-component model fits.

and 40×40 pixel boxes. All candidate sources above a specified combined likelihood are saved to an input file for the detailed source characterization.

The significance for the detection or the extent of an X-ray source is usually expressed in terms of the likelihood $L = -\ln p_{\text{Pois}}$ (Cruddace *et al.*, 1988), where p_{Pois} is the probability of a Poissonian random background fluctuation of counts in the detection cell, which would result in at least the number of observed counts. The L likelihood values are linear, *i.e.* the total likelihood of a source determined from the full band width is equivalent to the sum of the L_i values of the individual input bands. The probability of a source to be real p_{real} and *not* originate from a statistical fluctuation is hence given by $p_{\text{real}} = 1 - p_{\text{Pois}} = 1 - \exp(-L)$. For a selection of likelihood values L the following statistical probabilities for a real physical source are obtained: $p_{\text{real}}(L=1) \simeq 0.632$, $p_{\text{real}}(L=2) \simeq 0.865$, $p_{\text{real}}(L=3) \simeq 0.950$, $p_{\text{real}}(L=4) \simeq 0.982$, $p_{\text{real}}(L=5) \simeq 0.993$, $p_{\text{real}}(L=6) \simeq 0.998$, $p_{\text{real}}(L=8) \simeq 0.9997$, and $p_{\text{real}}(L=10) \simeq 0.99995$. The likelihoods are roughly related to positive outliers of Gaussian statistics with $n\sigma$ significance via $n \sim L/2$, *i.e.* $L=4$ corresponds approximately to 2σ significance and $L=6$ to a 3σ detection.

The task **emldetect** performs the final characterization of the candidate sources using the same input frames and the additional candidate source list of **eboxdetect**. A maximum likelihood PSF fit in the photon images is applied simultaneously for all input bands. Each candidate source is fit with free parameters for the source location (RA & DEC), the source extent, and the source count rate in each band. Before a source is classified as extended, **emldetect** attempts to fit two overlapping point sources to the photon distribution. Only if a single extended source fit yields a significant likelihood improvement in comparison to the 2-PSF fit of a double point source, the extended nature of the source is established.

emldetect characterizes extended sources based on a King profile fit (Equ. 2.6) with a fixed standard beta value of $\beta=2/3$ and the core radius Θ_c (or equivalently r_c) as free fit parameter. The observed photon distribution is to be compared to the King profile of the extended source convolved with the two-dimensional PSF shape at the specific detector location, which is a function of off-axis angle (Fig. 6.3), azimuthal angle (PSF rotation), and energy. If the maximum likelihood for the source extent, determined simultaneously for all input bands, exceeds a specified minimum threshold value the measured parameters for the *extended* source are saved to the final **emldetect** source list. In the case that the extent likelihood falls below the threshold, the corresponding *point source* parameters are determined and saved.

For the XDCP search strategy of Sect. 6.3.1, the **emldetect** maximum likelihood fitting procedure is performed once for each of the three different detection schemes. The minimum *detection* likelihood for a source is fixed at $L=6$ ($\sim 3\sigma$), whereas the *extent* likelihood is successively lowered for the different schemes. For the *single band scheme* with highest XDCP priority the minimum *extent* significance is set to $\sim 2.5\sigma$ ($L=5$), for the *spectral matched filter scheme*²⁵ to $\sim 2\sigma$ ($L \simeq 4$), and for the *standard scheme* to $\sim 1.5\sigma$ ($L=3$).

²⁵This is an effective value. The corresponding **emldetect** parameters is set to $L_{\text{min}} = 10$ but the enhanced weight of the central spectral region enters the total likelihood accordingly through the sum of overlapping bands.

The decreasing extent threshold is to ensure that the majority of sources are detected as a resolved objects for several detection schemes in order to allow a parameter cross-comparison. The aim for the raw extended source list as input for the screening procedure is a minimum extent significance of $2\text{--}2.5\sigma$ as will be discussed in Sect. 6.4.

Panel 5 of Fig. 6.10 displays the final reconstructed source image for the PN detector. Note the increasing tangential elongation of the PSF as a function of off-axis angle. Detected sources are also marked in the smoothed combined photon image in the upper right panel, where green circles symbolize point source detections and additional blue or red circles identify the extended sources.

The last panel 6 of Fig. 6.10 shows the PN sensitivity map of the observation, where light colors indicate the most sensitive central areas. The task `esensmap` approximates the local sensitivity limits for *point source* detections of a specified significance based on the exposure maps, the background maps, and the detection masks using Poissonian count statistics. Similar maps for the *extended source* sensitivity have to be calculated for the final XDCP survey assessment. The procedure for this more complex but crucial task is briefly discussed in Sect. 9.1.3.

Wavelet detection

Besides the traditional sliding box method, wavelet techniques have become a popular alternative approach for the detection of extended X-ray sources (*e.g.* Rosati *et al.*, 1995; Vikhlinin *et al.*, 1995; Herranz *et al.*, 2002). For the XDCP source detection procedure, the SAS task `ewavelet`²⁶ is used as a complementary source detection method to provide additional extent information, in particular for the evaluation of faint sources. The basic concepts of the wavelet technique are briefly summarized.

Wavelet functions allow a multi-scale analysis of images and enable a significant enhancement of the contrast of sources of different sizes against a non-uniform background. Wavelets can be considered as an extension of Fourier transformations with the difference that they are (i) localized in space, and have (ii) a zero normalization. Wavelets additionally satisfy (iii) translational invariance and (iv) scaling properties according to $W_{b,\sigma}(x) = (1/\sigma)W((x-b)/\sigma)$, where $W(x)$ is the wavelet function, b the translation, and σ the scaling parameter.

The most popular wavelet function for X-ray source detection is the so-called *Mexican hat* (MH) wavelet, which is related to the second derivative of a Gaussian function and can be written in its two dimensional form as

$$g_{\text{MH}}\left(\frac{r}{a}\right) = \left(2 - \frac{r^2}{a^2}\right) e^{-\frac{r^2}{2a^2}}, \quad (6.2)$$

with the wavelet scale a and $r^2 = x^2 + y^2$. The MH has a Gaussian core with positive values out to radius $r = \sqrt{2}a$ and negative values outside.

²⁶See the `ewavelet` manual at <http://xmm.vilspa.esa.es/sas/7.1.0/doc/ewavelet/index.html> for more information.

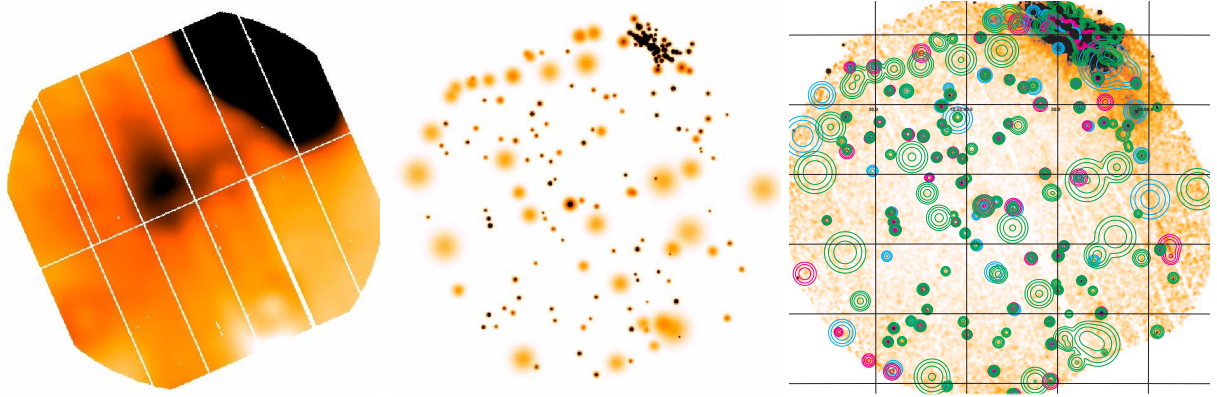


Figure 6.11: Wavelet source detection products of the same field as in Fig. 6.10. *Left:* Wavelet-reconstructed background map for the PN detector. *Center:* Reconstructed PN source map. *Right:* Wavelet detection results for the PN (green) and the MOS (blue and pink) detectors. This example illustrates for the PN camera how a poorly determined background leads to numerous spurious extended sources in the center and right panel. The SAS *ewavelet* detection results are hence only used as complementary information for the source evaluation.

The basic principle of the *ewavelet* detection method works as follows: (i) The X-ray image is convolved with the *Mexican hat* wavelet (analogous to Equ. 3.33). In effect, the MH acts like a sliding cell, where the positive part resembles the source cell of scale a , and the negative part the background area. The normalization ensures that the wavelet transform of a homogeneous background is zero. Local maxima in the convolved image correspond to source candidates of wavelet scale a . (ii) If the significance of the local maximum in the wavelet transform is above a specified threshold, the source location and peak height at scale a is saved. (iii) The convolution procedure is repeated for various wavelength scales a , starting with the PSF size, and successively increasing the scale by factors of $\sqrt{2}$ up to a given fraction of the image size. (iv) The final scale of the identified objects corresponds to the highest peak in all wavelet transforms at the source position.

The wavelet technique does not require a supplied external background, but rather reconstructs it from the data. The *ewavelet* determined PN background for the same XMM field as before is shown in the left panel of Fig. 6.11. In contrast to the box detection case, the wavelet reconstructed background traces local variations in addition to the off-axis dependence. The reconstructed PN source map in the central panel displays the effect of a poorly determined local background, in this case probably induced by the bright source, which cannot be excised for the *ewavelet* task. Numerous spurious extended sources are detected at the positions of local minima (lighter regions in left panel) in the background. The right panel illustrates the wavelet detection results for all detectors with sources and their scales overlaid on the smoothed photon image. Since the *ewavelet* source characterization is known to be less reliable than the maximum likelihood fitting method, the results of the wavelet detection, as visualized in the latter image, are used as an additional qualitative extent indicator for the cross-comparison with the sliding box detected extended sources.

X-ray source characterization

As the final step of the source detection procedure, the *extended* sources for each XMM field are extracted from the final `emldetect` source lists associated with the different detection schemes. These field lists are then merged for all XMM observations resulting in a *global extended source masterlist*, which is the starting point for the screening procedure of Sect. 6.4.

Listed in decreasing priority, the relevant `emldetect` parameters for the characterization of extended sources are (i) the maximum likelihood of the source extent (EXTML), (ii) the detection maximum likelihood (DETM), (iii) the source extent, *i.e.* the determined core radius (r_c), (iv) the total number of detected counts per band, (v) the derived flux (f_X), (vi) the off-axis angle of the source (Θ), (vii) the hardness ratios for the multi-band schemes (HR), and (viii) the total effective exposure at the source location.

`emldetect` measures the total count rate of a source in a given energy band. Physical X-ray fluxes are obtained from the count rate values by multiplying with the Energy Conversion Factors (ECF), which depend on the instrument response in the considered energy band, the optical blocking filter, the initial photon selection cuts, the galactic hydrogen column density, and the spectral source properties. For galaxy cluster sources, this implies that the true ECFs are a function of cluster temperature, ICM metallicity, and redshift, which are *a priori* not known and additionally differ from object to object. Final accurate flux measurements for individual clusters hence require the full source characterization, which is generally not available prior to the redshift confirmation (*i.e.* survey step 5). For the global flux characterization of the source population in early survey stages, *fiducial* source fluxes are obtained by using standard, fixed Energy Conversion Factors.²⁷ These ECFs are similar to the values for a fiducial distant cluster ($z \sim 1$, $T \sim 5$ keV) and have been confirmed for several sources to typically yield results with 10–20% accuracy in the standard 0.5–2.0 keV band.

As the final point of the X-ray data discussion, we consider the main reasons for *spurious* detections of extended sources using the sliding box detection and maximum likelihood fitting method. Two types of spurious extended sources are to be distinguished: (i) *spurious detections* (SD), *i.e.* the X-ray source is not real, and (ii) *spurious extents* (SE) implying that the actual source is point-like or a blend of several point sources. It should be emphasized, that the determined detection and extent likelihoods are purely of statistical nature and cannot account for systematic errors of the supplied calibration data. In decreasing order of occurrence, the dominant reasons for false positive detections beyond the statistical expectations are:

1. secondary detections in wings of large extended sources (SD);
2. PSF residuals due to uncertainties in the off-axis calibration (SE+SD);

²⁷Following the XMM-Newton calibration document SSC-LUX-TN-0059 (2003) at <http://isar.star.le.ac.uk/pubdocs/docindex.shtml>. A power law spectrum with a photon index of 1.7 and an absorbing column of $3 \times 10^{20} \text{ cm}^{-2}$ is assumed.

3. detections at detector or chip boundaries (SE+SD);
4. blends of three or more point sources (SE);
5. background residuals due to a poor local determination (SD+SE);
6. out-of-time trail residuals (SD);
7. optical loading residuals caused by bright optical sources (SD).

The brackets indicate, whether the artifacts result mostly in spurious extents (SE), spurious detections (SD), or both (SE+SD). The upper right panel of Fig. 6.10 illustrates as example several spurious sources in the wings of the excised bright object in the upper right corner.

Valtchanov, Pierre & Gastaud (2001) have benchmarked half a dozen techniques for the detection of extended X-ray sources in XMM-Newton data. The main conclusion is that there is no existing single detection technique without any drawbacks. Concerning the performance of `ebxdetect` in combination with `emldetect`, they confirm a very good detection rate and decent parameter reconstruction at the expense of numerous spurious sources, in particular related to the splitting of larger objects. `ewavelet` also shows a good sensitivity, but exhibits poor photometric parameter determinations.

In any case, the detection of faint extended X-ray sources is a very challenging task. The available techniques and methods are still evolving, in particular for their application to ongoing missions such as XMM-Newton. This section has provided an overview of the principal methods and has discussed some of the complexities and issues arising therefrom.

At this point, it should be emphasized again that one of the main objectives of the XDCEP approach is to *push the X-ray source detection to the very limit* and fully exploit the achievable XMM sensitivity. The inevitable price for maintaining a high completeness level of real cluster sources at very faint flux levels is an increased contamination fraction at early stages of the survey confirmation process (steps 1–4), *i.e.* before the observationally expensive spectroscopy (see Chap. 8). The largest fraction of detected spurious extended sources can be removed during the screening procedure described in Sect. 6.4 (step 2); the remaining non-cluster sources will be identified during the follow-up imaging stage (steps 3 & 4) discussed in Chap. 7. For the challenging aim of finding and confirming the most distant X-ray clusters at $z > 1$, using less than half of the (relatively inexpensive) imaging time for the identification of the remaining false positive sources seems to be an adequate and tolerable observational price to pay.

6.3.4 X-ray-optical overlays

As a preparatory step for the source screening procedure of Sect. 6.4, the final part of the XDCEP pipeline handles the generation of X-ray-optical overlays for the individual detected extended sources. These overlays provide essential information for the final assessment of (i) the X-ray quality of the source, and (ii) possible optical counterparts.

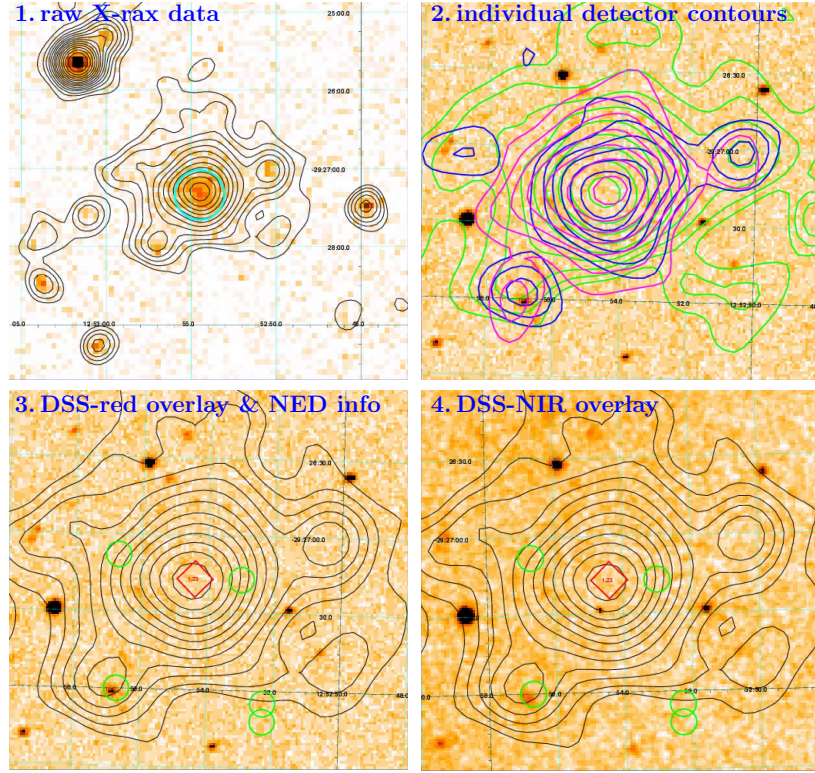


Figure 6.12: X-ray-optical overlays for the source classification procedure as complementary information to the `emldetect` source parameters. *Top left:* Unfiltered $5' \times 5'$ photon image in the 0.35–2.4 keV band with the smoothed contours overlaid and the core radius indicated by the blue circle. *Top right:* Individual detector contours for the PN (green) and the MOS instruments (blue and pink) as a means for cross-checking instrumental artifacts. *Bottom row left:* DSS-red image ($2.5' \times 2.5'$) with smoothed X-ray contours and NED object information overlaid. The source is identified as the known cluster RDCS J1252-29 at $z = 1.24$ (red diamond), green circles indicate NED sources without redshift information. *Right:* Same material overlaid on the DSS NIR image.

Combining data of several different wavebands into a single image can be achieved through the use of contours, which are overlaid onto a second image. The first step for the overlay production is hence the generation of X-ray contours, which are obtained from the smoothed single detection pre-band images at 0.35–2.4 keV. The contours are computed for logarithmically-spaced, pre-defined flux levels for the combined image and the three detector frames individually.

For the assessment of the X-ray quality of the source, the combined contours are overlaid onto the raw X-ray photon image with a FoV size of $5' \times 5'$ centered on the source. In addition the determined King profile core radius of the extended source is overplotted. Panel 1 of Fig. 6.12 illustrates this raw data zoom for the example source of the distant cluster RDCS J1252-29 at $z = 1.24$. Note the point source in the upper left corner for comparison. As a means for checking artifacts introduced by one of the detectors, the contours for the individual instruments are placed on top of each other in the $2.5' \times 2.5'$ image shown in panel 2.

The optical source classification is based on image data provided through the Second Digitized Sky Survey²⁸ (DSS-2). Of particular interest for distant cluster applications are the red band (DSS-red) and the NIR data (DSS-NIR), which reach almost all-sky coverage and are online accessible. The imaging data is complemented by a near-position query around the source location to the NASA Extragalactic Data Base²⁹ (NED), which contains information on all published extragalactic objects such as source type, spectral properties, and redshift, if available. The returned object list is filtered and transformed into region files, which can be overlaid onto the image data in addition to the X-ray contours.

Panels 3 & 4 of Fig. 6.12 display the resulting $2.5' \times 2.5'$ image zooms for the DSS-red data (left) and the DSS-NIR (right). Additional $5' \times 5'$ overlay images of the source environment allow an inspection on a larger scale. Green circles indicate NED objects without redshift information, whereas red diamonds display the location of objects with the NED specified redshift. In the example of Fig. 6.12, the indicated central redshift is associated with the distant ROSAT-discovered target cluster of the observation.

6.3.5 Distant cluster optimizations

The largely automated XDCP X-ray pipeline processing, as outlined in Fig. 6.8, is now completed. The two newly tested non-standard detection schemes (single band and spectral matched filter), for a complementary use to the standard source detection approach, can be considered as key characteristics. Numerous additional features of the XDCP pipeline aim at an optimization of the distant cluster detection and source classification efficiency. The efficacy of the newly implemented XDCP pipeline characteristics has been tested in initial performance comparisons to ‘standard method’ results and cross-checked with early observational feedback from follow-up imaging campaigns. In general, four categories can be distinguished for which improvement effects compared to a standard detection procedure are expected: (i) the survey usability of additional XMM fields (F), (ii) an improved extended source sensitivity (S), (iii) a higher extent reliability (R), and (iv) an optimized low-redshift screening efficiency (Z). The main high- z optimization features are summarized in the following, effect categories (F, S, R, Z) are indicated in brackets after the items:

- a strict double flare cleaning procedure (F+S);
- correction for out-of-time events (R);
- use of detection masks with excised bright sources (F+S+R);
- use of an optimized distant cluster band for the detection and visual inspection (S);
- use of a smooth background model fit instead of spline interpolations (R+S);
- four box detection iterations with increasing cell size for an improved extended source sensitivity (S);

²⁸The ESO DSS archive can be accessed at <http://archive.eso.org/dss>.

²⁹The NED homepage is found under <http://nedwww.ipac.caltech.edu>.

- a maximum extent radius of 20 pixels ($80''$) to constrain the possible extended source parameter space and prevent very extended spurious sources (R);
- maximum likelihood tests for a possible double point source blend (R);
- use of detection parameter information of three different schemes for cross-comparison (S+R);
- use of the wavelet detection method for complementary extent information (R);
- individual detector artefact assessment using separate X-ray source contours (R);
- additional use of DSS-NIR data for an object cross-correlation with DSS-red images (Z);
- automated NED object projections for source identifications (Z).

6.4 Source Screening and Candidate Selection

The XDCP X-ray pipeline has been applied to the 546 XMM-Newton archive fields that have passed the survey definition selection (see Sect. 6.2) and a first visual screening³⁰. These fields are listed in Tab. A.1 in the appendix with their positions, nominal and clean exposure times, galactic hydrogen column density, and the survey status. The total nominal exposure time of this data set of 17.5 Msec corresponds to 6.7 months of continuous observations, and the full X-ray reduction required about two months of CPU time.

77 of the data sets have been discarded from survey use for three possible reasons. (i) The observation was completely contaminated by soft proton flares, (ii) the central target covered most of the field-of-view, or (iii) data corruption preventing a proper processing. The remaining 469 XMM fields with a total nominal exposure time of 15.2 Msec define the **XDCP core survey sample**, *i.e.* the data sets that are in principle usable for serendipitous distant cluster searches.

More than **2 000 extended X-ray sources** have been detected in these survey fields. In this section, we will discuss the screening and classification procedure for these sources with the final goal of compiling a well-selected XDCP *distant cluster candidate list* as a starting point for further follow-up observations.

The challenges associated with the detection of extended sources at faint flux levels, in particular the various reasons for the expected significant fraction of *spurious* non-cluster sources, have been discussed in Sect. 6.3.3. The final classification of the detected sources is too complex (see *e.g.* Fig. 6.10) to be reliably implemented in an automated and objective fashion. The screening process of the individual extended X-ray sources hence requires human intervention for a due assessment of possible problems and for achieving the best results. A certain level of subjectivity is inevitable at this point. However, after an initial ‘training phase’ with observational feedback (see *e.g.* Sect. 6.5), a relatively homogeneous classification of the sources is possible.

³⁰Some (contaminated) XMM fields can be discarded from the survey sample based on the inspection of available quicklook data images.

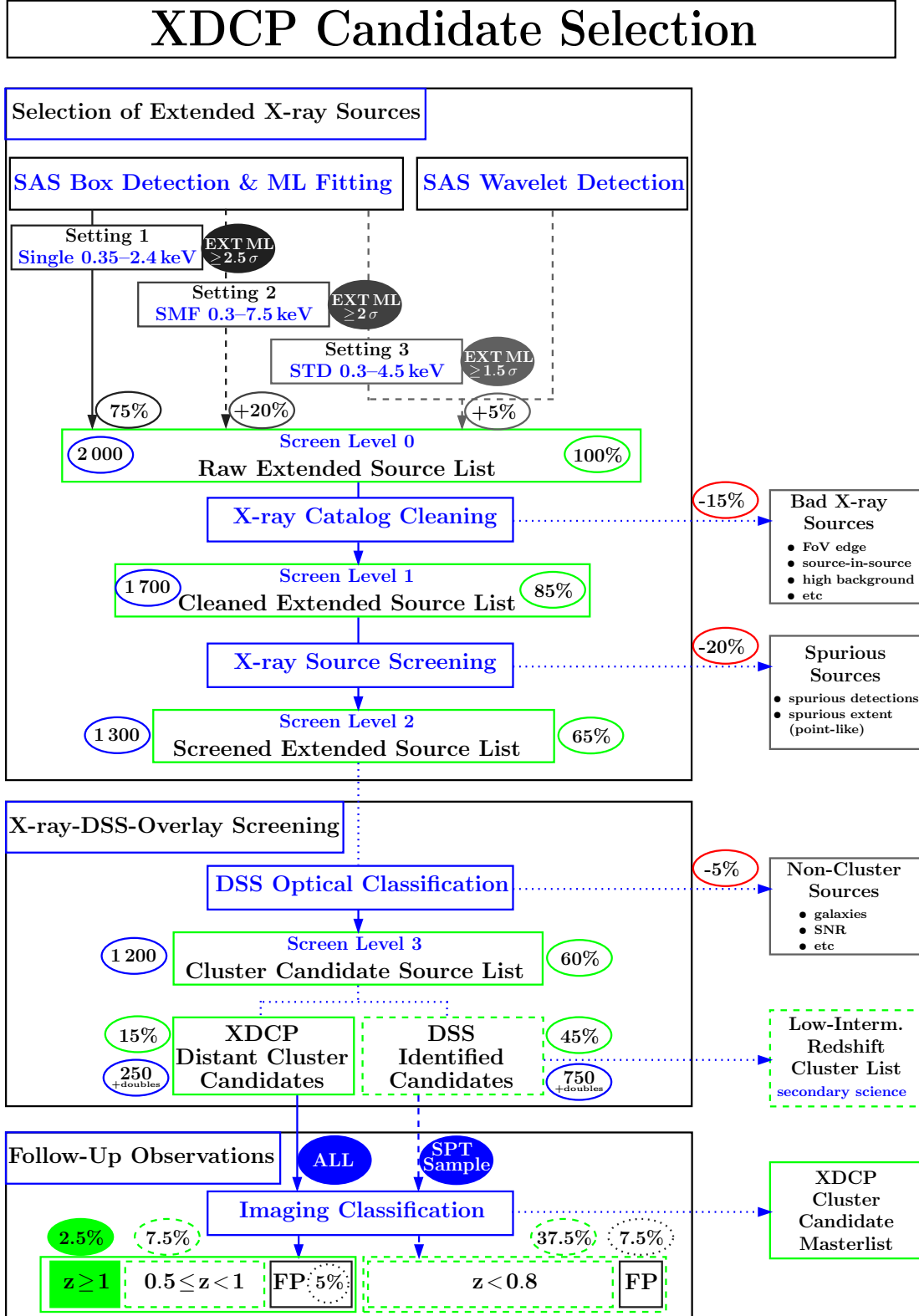


Figure 6.13: Source screening flow chart. Used abbreviations are EXT ML: Extent Maximum Likelihood, SMF: Spectral Matched Filter, STD: Standard Method, DSS: Digitized Sky Survey, SPT: South Pole Telescope, FP: False Positives. Stated percentages refer to the *Level 0* starting sample, absolute numbers are circled in blue.

6.4.1 Screening steps

The complete XDCP screening and classification procedure is illustrated in the flow chart of Fig. 6.13. The selection process can be structured into the two independent parts: (i) the X-ray quality assessment of the source and (ii) the optical counterpart identification. The third part in Fig. 6.13 displays some rounded preliminary success rates of follow-up observations, covered in Chap. 7, in order to complete the start-to-end source accounting. Numbers circled in blue refer to approximate absolute extended source counts at the given screening stage, the green circled percentages are relative to the starting sample at *screen level 0*.

The *sample completeness* is a prime factor for the XDCP science applications. Consequently care has to be taken not to lose any real clusters during the screening procedure. Ambiguous sources at a given screening stage are therefore passed to the next level for a re-evaluation before they are rejected. In the end, the survey completeness and the follow-up efficiency have to be balanced, *i.e.* the false positive fraction should be acceptable for a given completeness level. The source flagging and classification scheme should thus be flexible enough to allow re-adjustments of the selection cuts as a consequence of observational follow-up feedback.

X-ray selection

The starting point for the selection process is the *raw extended source list* or *screen level 0*, which is compiled in a automated and objective way. The first aim of this starting source sample is the complete coverage of the *single band scheme* detections on the 2.5σ extent significance level, which contribute about 75% (see Fig. 6.13). The second aim is to test for possible selection effects introduced by a given detection scheme. We thus include the extended sources detected with the *spectral matched filter scheme* on the 2.0σ significance level which are not on the list and comprise about 20% of the initial sample. Below an extent significance of 2.0σ most additional detected sources are very uncertain. For the *standard scheme* results at the 1.5σ extent level, only those new sources are added to the list, which are also confirmed as extended by the wavelet method. With these last 5% of sources detected at lower significance, the *raw extended source list* with a total of just over 2 000 extended sources is completed. From this point on, all subsequent classification steps (*screen levels 1–3*) rely on human intervention.

As a first screening level, the raw X-ray source catalog is cleaned of obvious spurious detections based on the summary plots as shown in the upper right panel of Fig. 6.10. At this time, the majority of the source-in-source detections, FoV boundary sources, wing detections of bright point sources, and pronounced out-of-time residual detections are removed. With about 15% of the X-ray sources flagged as ‘artifact detections’, the cleaned *screen level 1* sources are passed on two the next level.

The detailed X-ray source screening of the second level makes use of the zoomed X-ray data overlays as shown in panels 1 & 2 of Fig. 6.12 and (up to) three sets of returned source parameters of the maximum likelihood fitting procedure. At this stage, sources with more

subtle reasons for a spurious *extent* or a spurious *detection* are identified. The most common causes are misclassified point sources, point source blends, high noise environments, poorly determined backgrounds, and detections at high off-axis angle due to PSF residuals. Besides the visual confirmation of the *existence* and *extent* using the overlay panels 1 & 2, the source quality is evaluated based on (i) the wavelet detection result, (ii) the number of extent detections and their significance within the three schemes, (iii) the stability of the extent determination, and (iv) the hardness ratio of the source. Spurious *extents* of point sources can often be identified based on cross-checks with items (i), (ii), and (iv); spurious *detections* on the other hand typically do not exhibit stable extent solutions of item (iii) or are not re-detected at all for tests (i) and (ii).

An additional $\sim 20\%$ of the initial source sample are identified as spurious sources in this way and flagged accordingly. Extended sources that passed the X-ray quality screening but are close to the cut threshold are marked as sources with lower X-ray significance and retained in the object list. The *screen level 2* source list has been cleaned of about 35% of the initial sample. This large fraction of spurious sources is to be predominantly attributed to systematic effects inherent to the available SAS source detection and calibration tools and *not* to the expectation rate of false positives of the statistical likelihood. The main reason for the built-in redundancies in the XDCP source detection procedure is the improved identification and removal of this spurious source fraction while retaining the full sensitivity. The *screen level 2* extended source list completes the X-ray object selection and characterization and should now closely reflect the statistical expectations of a sample with a $2\text{--}2.5\sigma$ significance threshold.

Optical classification

The screened extended source list is the input for the optical classification, which constitutes the second part of the candidate selection process. The main tools for the optical counterpart search are the X-ray-DSS overlays for each source as shown in panels 3 & 4 of Fig. 6.12. As a first step of the optical classification, the non-cluster sources (*e.g.* single nearby galaxies) are visually identified using the DSS imaging data and removed from the sample. The remaining 60% percent of the input sample comprise the *screen level 3* cluster candidate source list of roughly 1 200 objects, still including multiple detections of the same source in different fields.

In the last step, these sources are visually classified either as *DSS-identified cluster candidates* or as *XDCP distant cluster candidates* based on their optical counterpart or the lack thereof. The classification scheme will be discussed in the following Sect. 6.4.2. About three quarters of the *screen level 3* cluster candidates (45% of the initial sample) can be identified with an optical cluster counterpart signature on the X-ray-DSS overlays. These approximately 750 distinct objects are flagged as low–intermediate redshift cluster candidates and are saved for secondary science projects beyond the XDCP scope.

The ~ 250 extended X-ray sources without an DSS-identified optical counterpart enter the *distant cluster candidate* master list, which constitutes the basis of the subsequent follow-up imaging program. In order to provide a full accounting of the extended X-ray source population at the XDCP sensitivity level, approximate cluster yields are stated in

Fig. 6.13 as derived from the follow-up imaging programs of Chap. 7. The numbers related to the DSS-identified candidates are based on a preliminary evaluation of the wide-field follow-up program in the South Pole Telescope (SPT) survey region (see Sect. 9.2 & 12.1). The first important finding from these data is the confirmation that the sources flagged as *spurious* are indeed *not* associated with optical clusters out the data limit of $z \sim 0.9$.

The final cluster accounting establishes the following approximate cluster yields for the distant cluster candidates: About one out of six candidates is a true $z \gtrsim 1$ system, half of the sources are associated with $z < 1$ clusters, and roughly a third are false positives (FP), *i.e.* spurious sources. For the DSS-identified candidate sources, about 5/6 are $z \lesssim 0.8$ clusters or groups with a false positive rate of 1/6.

The XDCP candidate selection task (including spurious sources) can hence be globally summarized as follows (see Fig. 6.13). (i) About 1/40 of all extended X-ray sources are associated with the targeted population of $z \gtrsim 1$ galaxy clusters. (ii) $\sim 1/10$ of all extended sources are clusters beyond the DSS identification limit. (iii) $\sim 1/2$ of all extended sources are galaxy clusters. (iv) $\sim 3/4$ of all cluster sources can be identified with an optical DSS counterpart.

Concerning the required cleaning of spurious sources, the following picture is obtained. (v) For each distant cluster candidate more than two spurious sources were removed from the initial sample in early cleaning stages. (vi) $\sim 3/4$ of all spurious sources can be identified as such within the screening procedure without follow-up observations. (vii) $\sim 1/10$ of all spurious sources pass the screening procedure and need to be identified as *false positive* sources in the follow-up data of the distant cluster candidate sample. (viii) After removing all spurious sources from the object catalog, $\gtrsim 90\%$ of the *non-spurious* extended sources in the high galactic latitude survey fields are associated with galaxy clusters. Additional source diagnostic plots will be presented in Sect. 6.6.

6.4.2 Classification scheme

After the general overview of the screening procedure, we will now have a closer look at the cluster candidate classification scheme. As discussed, the selection process is comprised of the two independent parts of the X-ray quality assessment of the source, followed by the subsequent evaluation of possible optical counterparts on DSS imaging data.

These two screening dimensions are reflected in the classification scheme illustrated in the left panel of Fig. 6.14. In a schematic way, the optical DSS visibility is plotted against the X-ray quality of the source. Beyond the X-ray significance and quality threshold (vertical dashed line), sources are flagged as spurious (red region). The DSS limit (horizontal dashed line) divides the plane into the distant cluster candidates in the upper half (green) and DSS-identified systems in the lower half (blue). In this scheme the ideal distant candidates, featuring excellent X-ray quality in combination with a blank DSS sky region, are located in the upper left corner. Approaching the DSS limit, *i.e.* moving downwards, results in traces of possible cluster galaxies at a level insufficient for a secure cluster identification and towards the right side of the plot, the X-ray significance of the extended sources is reduced.

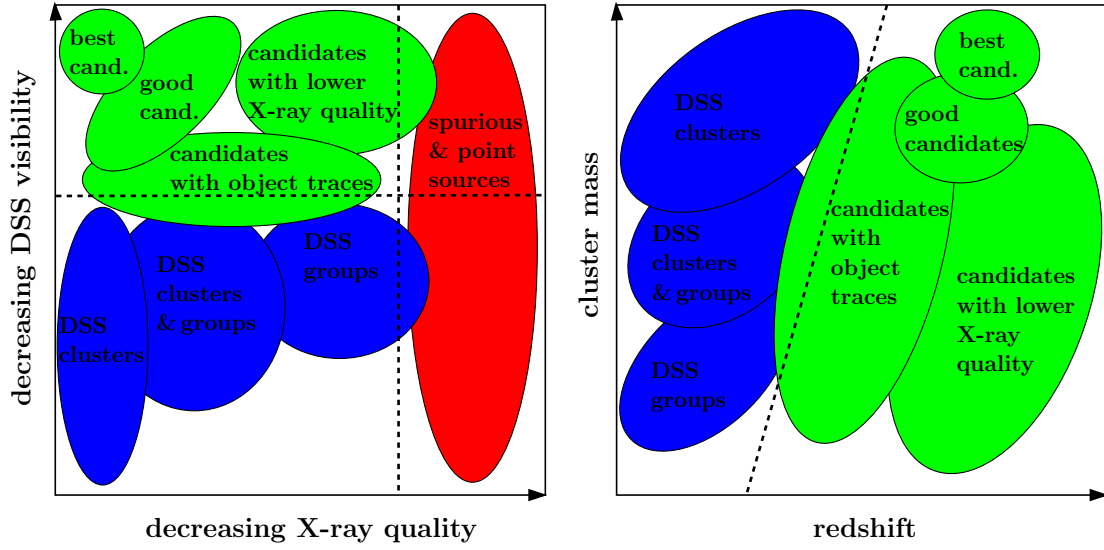


Figure 6.14: Qualitative X-ray source flagging scheme. *Left:* Practical implementation in the DSS-object-visibility versus X-ray-quality plane. The dashed lines indicate qualitatively the DSS limit (horizontal) and the X-ray quality limit (vertical) beyond which sources are classified as spurious or point-like. *Right:* Qualitative correspondence of the flagging scheme in the cluster mass versus redshift plane for ideal clusters. The dashed line represents the DSS identification limit.

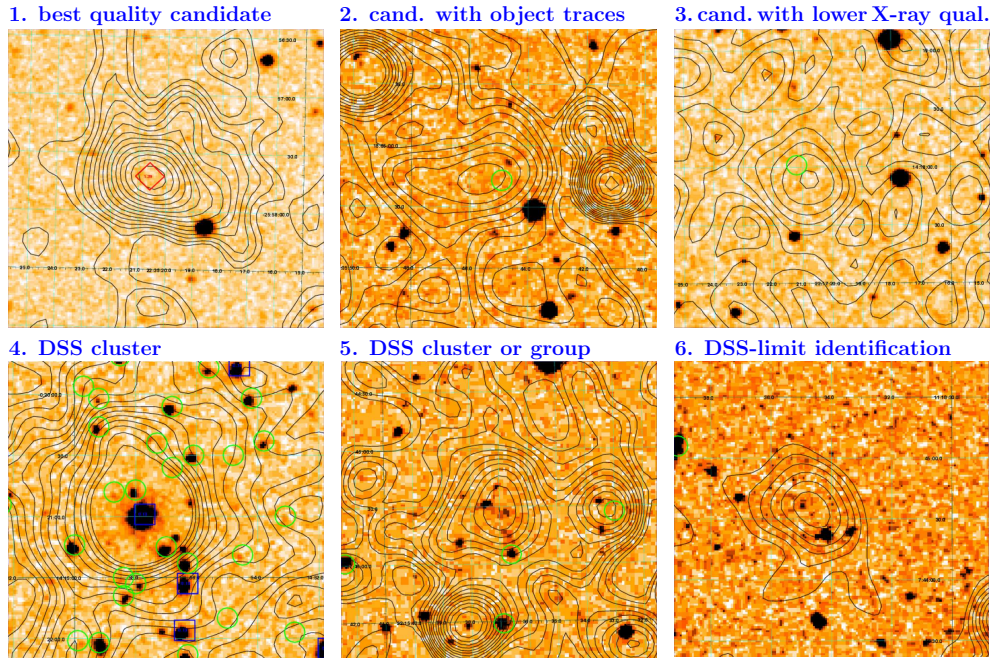


Figure 6.15: Candidate classification prototypes ($2.5' \times 2.5'$ FoV) following the scheme in the left panel of Fig. 6.14. *Top row:* Distant cluster candidates of best quality (*left*), with slight object traces (*center*) and with weaker X-ray significance (*right*). *Bottom row:* DSS-identified cluster and group sources with high confidence (*left*), medium-high confidence (*center*), and a DSS-limit case (*right*) requiring the cross-comparison of the optical and NIR DSS data for enhancing the object likelihood of weak traces. The NED label in the upper left panel identifies XMMU J2235.3-2557 at $z = 1.39$.

Relating DSS visibility qualitatively to redshift and X-ray quality to cluster mass, the classification scheme is transformed, in first order, to depend on the prime cluster characteristics (right panel of Fig. 6.14). The diagonal dashed line indicates the DSS limit which is pushed towards higher redshift for increased cluster masses. Increasing the redshift of a system or decreasing the mass results on both cases in a lower X-ray ‘quality’ of the cluster candidate (*i.e.* a lower signal).

In general, the qualitative classification dimensions DSS visibility and X-ray quality are related to the physical cluster characteristics redshift and mass in a more complex way. Besides the mass and redshift dependence, the observed X-ray significance and quality of the candidate is influenced by (i) the effective exposure time at the source location, (ii) the source extent, (iii) the level of the X-ray background, (iv) the galactic hydrogen column at the source location, (v) nearby contaminating sources in the field, (vi) AGN emission in the cluster, or (vii) ongoing merging activity in the system. The DSS counterpart identification, on the other hand, is additionally influenced by (i) the magnitude and location of the brightest cluster galaxies, (ii) the local DSS depth, (iii) an increasing foreground object density at lower galactic latitude, (iv) contamination from optically bright nearby objects, and (v) the lack of DSS-NIR data in some sky regions.

Figure 6.15 illustrates the classification prototypes following the discussed scheme. The classification is applied to all cluster candidates of the *screen level 3* list. The prototypes in the upper row show distant cluster candidates, whereas in the bottom part examples for DSS-identified systems are displayed. In the next section, we will address the question of the DSS identification limit in some more detail.

6.4.3 DSS identification limit

The image data of the second generation Digitized Sky Survey (Reid *et al.*, 1991) is based on photographic plate scans of several wide-field surveys using 1 m-class Schmidt telescopes. The typical exposure times for the DSS-red plates, corresponding roughly to the R filter band (see Tab. 7.1), are 60-70 min. The DSS-NIR plates have been exposed for 80-90 min and with a central wavelength of $\lambda_c \sim 8500 \text{ \AA}$ this band is similar to the (optical) I band. The average limiting point source sensitivities (Vega magnitudes) are $R_{\text{lim}} \simeq 20.8 \text{ mag}$ (DSS-red), and $I_{\text{lim}} \simeq 19.5 \text{ mag}$ (DSS-NIR) with local variations of about $\pm 0.4 \text{ mag}$ for sky regions with the deepest and shallowest coverage. The limit in the R-band for the DSS-red data corresponds to the expected apparent magnitude of an M^* elliptical galaxy at redshift $z \sim 0.5$, an M^*-1 elliptical at $z \sim 0.65$, or an M^*-2 object at $z \sim 0.8$ (see Fig. 7.1 and Tab. 7.2). For the I-band of the DSS-NIR images the corresponding redshifts are $z \sim 0.45$ for an M^* galaxy, $z \sim 0.65$ for M^*-1 , and $z \sim 0.85$ for an M^*-2 object.

The brightest cluster galaxies (BCGs) are typically 1-2 magnitude brighter than the characteristic luminosity L^* (see Sect. 11.1). This implies that BCG signatures should be generally visible in DSS-NIR images out to redshifts of $z \sim 0.5-0.8$. The significance of DSS sources close to the limiting magnitude can be additionally enhanced by cross-comparing the DSS-red and DSS-NIR images for spatially coincident object traces.

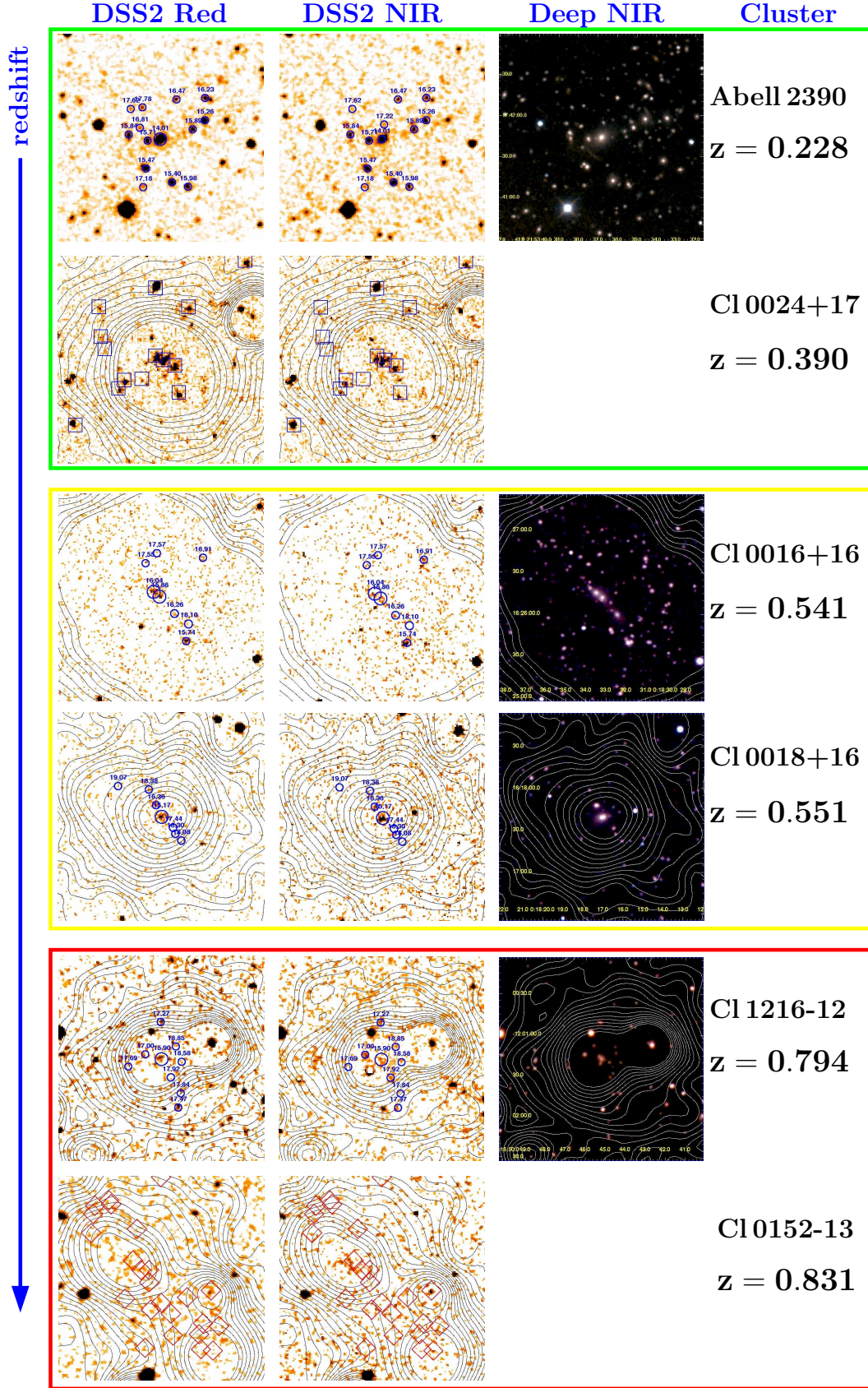


Figure 6.16: DSS identification limit for rich clusters. Marked object positions are either associated with color selected cluster members (circles) with shown H-band Vega magnitudes or spectroscopically confirmed cluster members (squares and diamonds). All images are $2.5' \times 2.5'$ in size.

Figure 6.16 shows a compilation of six spectroscopically confirmed galaxy clusters with redshifts $0.2 \lesssim z \lesssim 0.8$. The corresponding $2.5' \times 2.5'$ DSS-red (left) and DSS-NIR images (center) are displayed with high-contrast color cuts around the noise limit of the data. The right panels present NIR color composites taken, if available, from the follow-up imaging data of Chap. 7 to indicate the underlying deep optical cluster signature. The overlaid blue circles on the DSS data represent color selected cluster members with associated H-band magnitudes. For the two systems without additional follow-up data, the sky positions of spectroscopically confirmed cluster members are marked.

As can be seen from Fig. 6.16, the optical DSS-identification of clusters out to $z \sim 0.4$ (green box) is straightforward and is generally possible at high confidence levels. In the redshift range $0.4 \lesssim z \lesssim 0.6$ (yellow box), the majority of objects can still be identified based on the BCG and the next few brightest cluster galaxies. In the case of cluster Cl0016+16 5–6 objects are visible, but for Cl0018+16 only 2–3 cluster galaxies are above the DSS noise limit. At $z > 0.6$ the DSS-based cluster identification becomes increasingly difficult and is beyond the DSS capabilities in the general case. However, for favorable combinations of BCG properties, cluster richness, and local DSS depth, the optical counterpart can, in some cases, be identified out to $z \sim 0.8$. Cl1216–12 exhibits weak traces of about half a dozen probable cluster galaxies, whereas for Cl0152–13 only one probable AGN counterpart is securely detected and some weak indications of the BCG are visible in the DSS-NIR image.

We conclude that the average DSS cluster identification limit is in the redshift range $z \simeq 0.5$ – 0.6 , if the full depth of the DSS-red *and* DSS-NIR images is exploited. This limit is also confirmed by early XDCP selection performance tests in the COSMOS field as presented in the next section.

6.5 Performance Tests in the COSMOS Field

The XDCP X-ray pipeline of Sect. 6.3 and the candidate selection procedure of Sect. 6.4 has been tested in its early version in the COSMOS survey field (see Sect. 4.4). The COSMOS data set³¹ is particularly well suited for a performance benchmark since (i) the individual XMM pointings are of similar depth as the average XDCP survey fields, and (ii) the multi-wavelength coverage of the field enables a direct cross-comparison between detected extended X-ray sources and galaxy overdensities with corresponding accurate photometric redshifts.

The XDCP reduction and selection machinery has been (blindly) applied to 20 individual XMM fields of the first COSMOS X-ray data set, corresponding to about 85% of the observations required to cover the full 2.1 deg^2 field. The average cleaned exposure time of 24.9 ksec per field is about 30% deeper than the median coverage of the XDCP fields. The fields are overlapping to contiguously map the $1.4^\circ \times 1.4^\circ$ area. In contrast to the COSMOS X-ray analysis of Finoguenov *et al.* (2007), which made use of the reconstructed mosaic image with the full co-added effective exposure at each position, the XDCP test

³¹Only the first XMM data set has been used, meanwhile the available COSMOS X-ray coverage has more than doubled in exposure time.

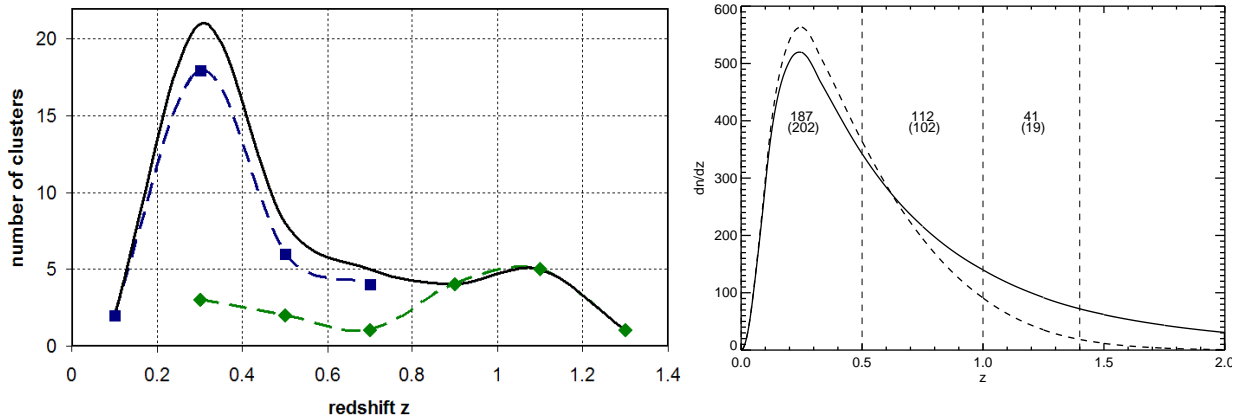


Figure 6.17: *Left:* Redshift distribution of identified clusters and candidates in the COSMOS field (black line). The blue dotted line shows the distribution of DSS-identified clusters in redshift bins of $\Delta z = 0.2$, the green dashed line represents the distant cluster candidates. The photometric redshift estimates are based on early internal versions of the COSMOS galaxy catalog. The bump at $z \sim 1$ is also present in the published cluster catalog (Finoguenov *et al.*, 2007) and is still under investigation. The five candidates at $z < 0.6$ were identified as low mass groups, which are harder to identify on DSS images. *Right:* The expected shape of the redshift distribution for an XDCP-like survey without cluster evolution (solid line) and with evolution (dashed line). Plot from C. Mullis.

procedure was applied to the *individual* XMM fields as for the real survey fields. Following the compilation of the final *screen level 3* source sample with distant cluster candidates and DSS-identified systems, the XDCP object list was cross-correlated with the proper COSMOS X-ray cluster list, which is based on the deeper mosaic data in conjunction with the photometric confirmation based on the optical data.

The left panel of Fig. 6.17 illustrates the results of this test in form of the binned photometric redshift distribution of all 46 XDCP identified clusters (black line). The blue dashed line represents the *DSS-identified clusters*, whereas the green line indicates the selected *distant cluster candidates*. Six distant $z \gtrsim 1$ clusters with X-ray fluxes down to $\sim 4 \times 10^{-15} \text{ erg s}^{-1} \text{ cm}^{-2}$ [0.5–2.0 keV] were successfully identified. The five candidates at the lower redshift end at $z \lesssim 0.6$ (green line) have been revealed as lower mass groups, mostly in the range $M \simeq 3\text{--}4 \times 10^{13} M_{\odot}$. Due to their lower optical richness, these systems are harder to distinguish from possible foreground objects. The blue line for the DSS-identified clusters, on the other hand, confirms the average DSS redshift limit of $z \simeq 0.5\text{--}0.6$. The fraction of false positive sources in the XDCP sample turned out to be 6/22 (27%) for the distant cluster candidates, and 2/32 (6%) for the DSS flagged objects. A slightly worse performance for the real XDCP survey data can be expected due to more contaminations in serendipitous fields, which have not been specifically selected for deep extragalactic survey applications.

The right panel of Fig. 6.17 shows the expected shape of the cluster redshift distribution for an XDCP-like survey, derived for early sensitivity estimates. The solid line represents a model without cluster evolution, whereas the dashed line includes evolution effects as expected from the X-ray luminosity function analysis of Fig. 4.3.

Finoguenov *et al.* (2007) find no substantial evolution in their analysis of the initial 72 cluster COSMOS sample out to $z \sim 1.3$, selected from the first 36 XMM pointings. The COSMOS cluster luminosities cover the range $8 \times 10^{42} - 2 \times 10^{44} \text{ erg s}^{-1}$ and hence do not include the high mass end for which mild evolution effects have been established (Sect. 4.3). The pronounced bump in the observed redshift distribution around $z \sim 1$ (left panel), also present in the published COSMOS data and still under investigation, is likely attributed to either physical large-scale structure or systematic effects in the derived photometric galaxy redshifts.

In summary, the XDCP X-ray pipeline performance test in the COSMOS field has confirmed (i) the high achievable detection sensitivity, (ii) the good identification efficiency of low–intermediate redshift DSS clusters, and (iii) a high fraction of probable $z \gtrsim 1$ systems in the distant cluster candidate sample, giving additional support to the selection procedure.

6.6 Field and Source Diagnostics

In the last section of this chapter on XMM archival X-ray data, we will have a closer look at some selected statistical properties of the survey fields and the detected extended sources.

6.6.1 XMM data yield and field statistics

The 540 reduced fields of the first 4.5 years of XMM operations give the possibility to trace the XMM science data yield over the course of a year and to assess the data losses due to flare periods (see Sect. 6.3.2). Figure 6.18 illustrates the seasonal changes of the science-usable data fraction. The upper panel shows the instrument-weighted clean imaging time fraction with respect to the nominal exposure time for *all* fields that passed the flare removal procedure. In effect, this represents the total archival *imaging data percentage*, and has an average value³² of 57%.

The lower panel displays the absolute clean and lost times for the fields with all instruments in imaging mode. The resulting mean clean time fraction of 67% is representative for the *overall XMM science data yield*. Hence one third of the nominal pointing time is on average lost, predominantly due to soft proton flares and a smaller fraction due to instrument overheads.

Both representations show an increased lost data fraction during the summer months and a higher data yield during winter with differences of about 20% of the total time. These pronounced seasonal *space weather effects* are thought³³ to be related to the solar cycle and the XMM orbit evolution caused by external perturbations. The latter effect can also introduce long term changes from year to year.

³²The 10% difference compared to the overall XMM science data yield is due to the fact that the full sample of 540 fields contains observations, in which some instruments were not operated in imaging mode, *i.e.* science modes not usable for the XDCP survey.

³³See longterm compilations at <http://xmm.vilspa.esa.es/docs/documents/USR-TN-0014-1-0.pdf>.

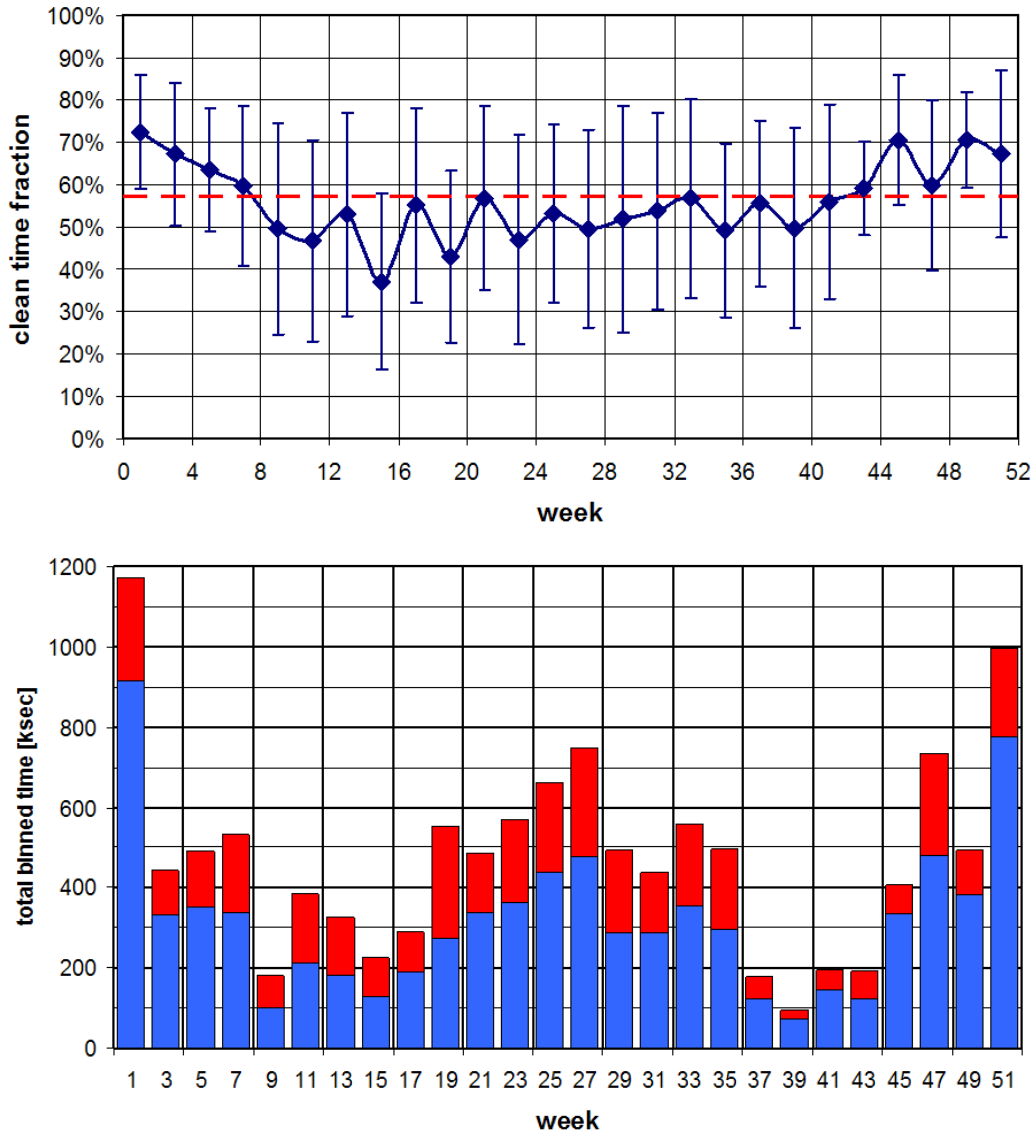


Figure 6.18: Seasonal changes of the clean time fraction. *Top:* Average clean time fraction versus the time of the calendar year in bins of two weeks. The data points are based on 540 processed XMM archive fields observed within a 4.5 year period between January 2000 and August 2004. The dashed horizontal line represents the sample average of the weighted effective clean imaging time fraction of 57%. In contrast to most optical telescope sites, the space weather is favorable in terms of data yield in the winter months between October and February. *Bottom:* Absolute clean exposure times (blue) and flared periods (red) in two week bins for the 439 fields for which all three detectors have been operating in imaging mode. The average clean time fraction is now 67% and is representative for the overall XMM science usable data fraction.

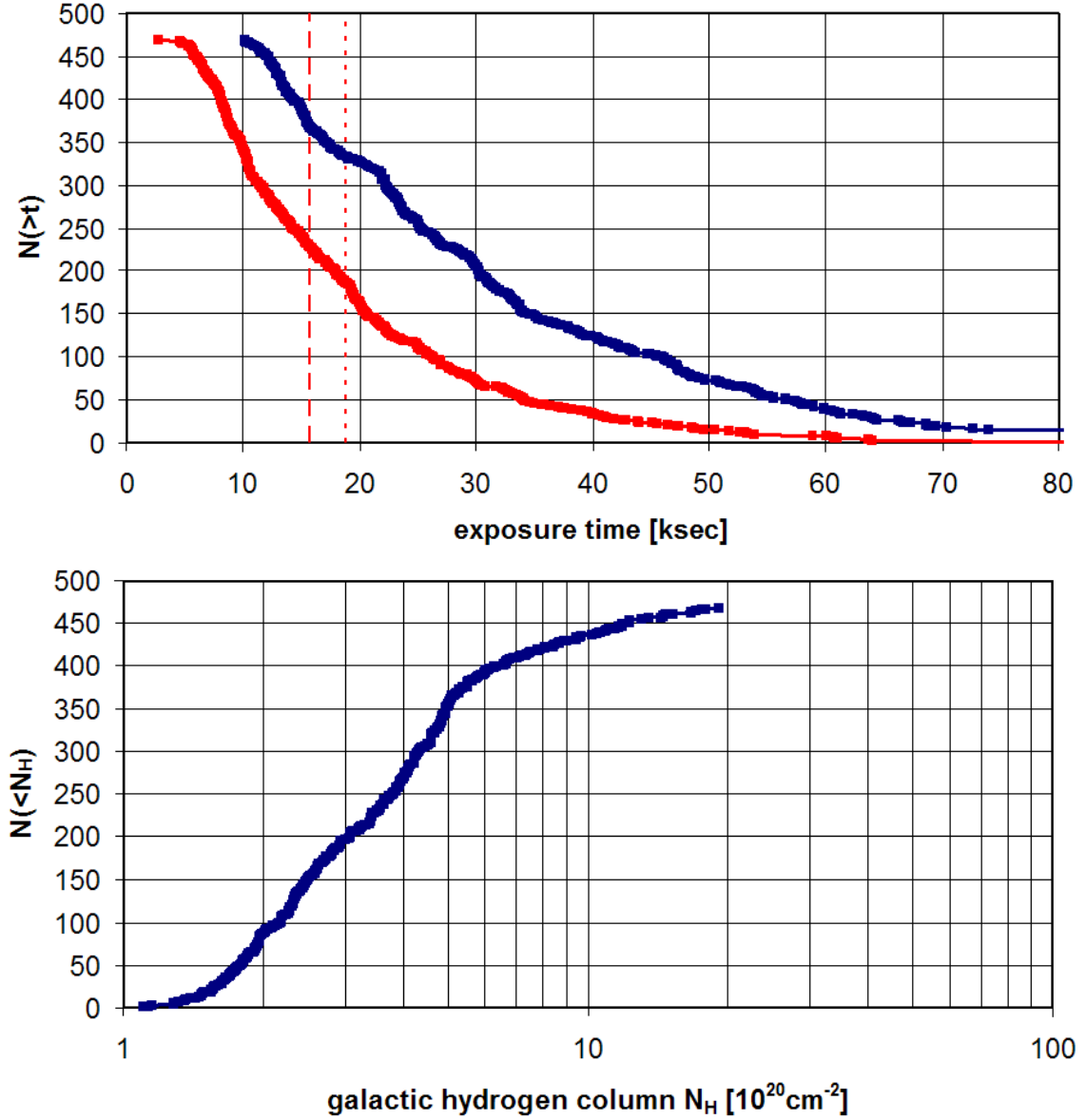


Figure 6.19: XDCP survey field statistics. *Top:* Cumulative distribution of nominal exposure times (blue line) and flare cleaned times (red line) for the 469 usable XDCP survey fields. The average clean exposure time of 18.78 ksec is indicated by the vertical dotted line, the median of 15.71 ksec is illustrated by the dashed line. *Bottom:* Cumulative distribution of the galactic hydrogen column for the survey fields.

The statistical properties of the 469 fields of the XDCP core survey sample are summarized in Fig. 6.19. The top panel illustrates the cumulative distribution of the resulting clean exposure times (red) in comparison to the nominal distribution (blue). The average clean XDCP field depth is 18.78 ksec (dotted vertical line), the median is 15.71 ksec (dashed line). The lower panel shows the cumulative field distribution as a function of the galactic hydrogen column N_{H} with a median value of $3.55 \times 10^{20} \text{ cm}^{-2}$.

6.6.2 Extended source diagnostics

We now turn to the properties of the extended X-ray sources and their detection efficiency. Figure 6.20 provides a global summary of all extended X-ray sources detected with the *single band detection scheme*. Plotted are the maximum likelihoods for the extent of the source (EXTML) versus the total source counts in the 0.35-2.4 keV band. The horizontal cut-off at EXTML=5 indicates the lower significance threshold for the detection run.

Distant cluster candidates are represented by dark blue circles. The median number of total source counts for this population is 193, the median EXTML is 11.7, corresponding to 5–6 σ significance, and the median detection likelihood amounts to 36.6. The lighter blue circles indicate the population of *DSS-identified cluster candidates*. Red symbols illustrate the distribution of sources classified as *spurious extent* (plus signs) or *spurious detections* (crosses). The extent maximum likelihood exhibits a decent correlation with the total photon number of the cluster candidates (blue symbols), with a scatter of about a factor of two. The extended sources classified as *spurious* show on average a lower EXTML for a given total number of source counts. Even though *spurious* sources show a systematic offset in their EXTML, they still occupy almost the full parameter space populated by cluster sources, in particular at the important fainter levels.

The first important conclusion from this global view on the detected extended source population is that *spurious* sources *cannot* be automatically separated from real clusters by means of appropriate parameter cuts. This is to be attributed to the discussed systematic (calibration) effects that dominate the *spurious* detections for the **eboxdetect** and **emldetect** methods. The second preliminary conclusion is that the sensitivity goal for extended sources down to a total number of 100 counts and less seems to be achievable. The typical significance at which objects with ~ 100 X-ray photons can be resolved into extended sources is about 4σ . The final survey sensitivity limit has to be quantified based on detailed simulations (see Sect. 9.1.3).

As a next step, we can compare the extent likelihoods of the sources for the three different detection schemes, which is shown in Fig. 6.21 for the distant cluster candidate sample. The EXTMLs of the *standard scheme* are plotted along the abscissa, whereas the corresponding source likelihoods for the *single band scheme* (dark squares) and *spectral matched filter scheme* (light blue circles) are represented by the ordinate.

The likelihoods for the *single band scheme* and *standard scheme* scatter along the lower red line which indicates matching values. The corresponding comparison between the schemes with a wider spectral coverage exhibits a slightly tighter correlation about the upper red line, which indicates the average offset factor of 2.8 and corresponds to the

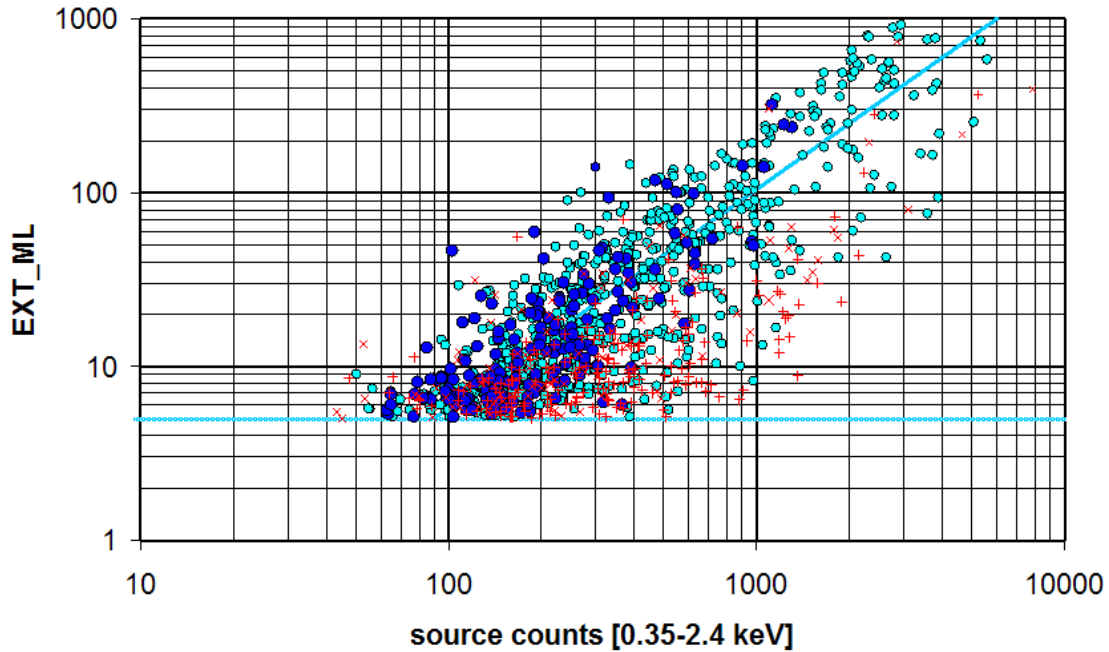


Figure 6.20: Extent likelihood versus X-ray source counts. Dark blue circles represent distant cluster candidates, light blue circles DSS-identified clusters, and red symbols sources that have been classified as spurious detections. The lower horizontal line indicates the minimum required extent likelihood, whereas the diagonal line shows the general correlation for the good sources. Sources that have been classified as spurious tend to have a lower extent likelihood compared to clusters candidates with the same number of counts. However, the populations are still largely overlapping which prevents an automated identification of false detection.

mean effective weight. The effective weighting factor of the *spectral matched filter scheme* is not fixed *a priori*, but depends on the spectral properties of the source. Below standard scheme EXT MLs of about 8, the distant cluster candidates appear to be systematically above the average correlation which points towards an achieved enhancement of the likelihoods at faint flux levels. The global statistics for the *spectral matched filter* detections confirm that the average likelihood offsets with respect to the *standard scheme* are increased by about 6% for distant cluster candidates compared to sources classified as spurious. However, no firm conclusion on the effectiveness of the *spectral matched filter* scheme can be drawn before a significant number of distant candidate clusters at lower EXT ML levels have been spectroscopically confirmed.

Last but not least important, the optimal detector area for serendipitous surveys is investigated. As discussed in Sect. 6.1, XMM-Newton’s *grasp* as survey instrument increases with the maximum off-axis angle Θ . On the other hand, the vignetting effect (Fig. 6.2) decreases the sensitivity towards the outskirts, and more importantly, the PSF shape (Fig. 6.3) broadens and becomes increasingly ill-behaved at large Θ , which hampers the detection of extended sources.

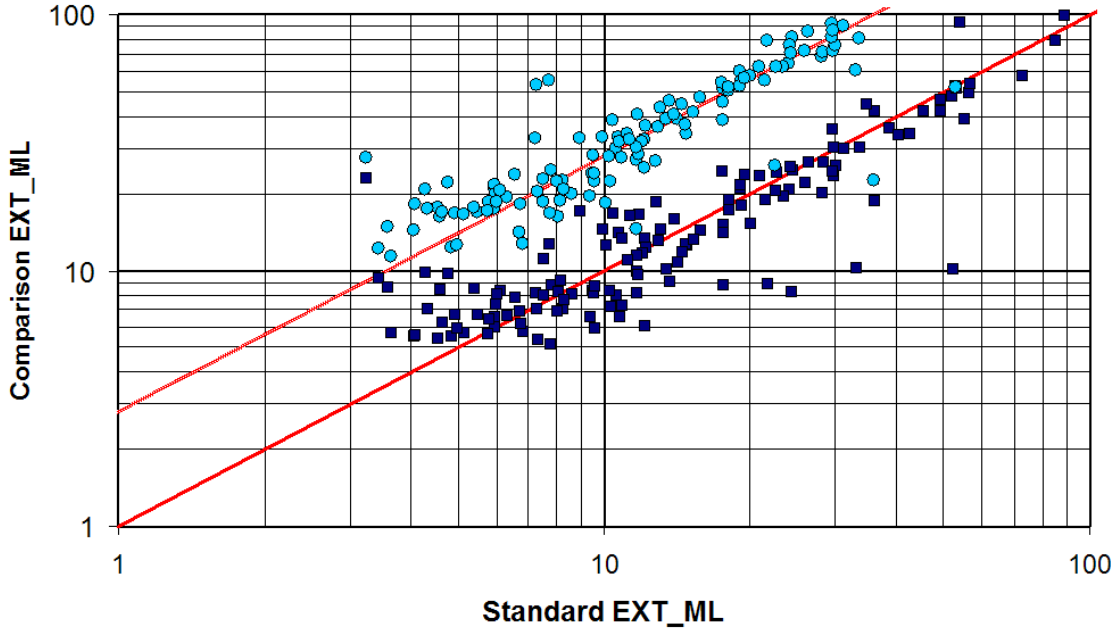


Figure 6.21: Extent likelihood comparison of the three detection schemes. The dark squares display the extent likelihoods of the *single* 0.35-2.4 keV detection band versus the EXT MLs of the *standard detection scheme* for distant cluster candidates with the lower red line indicating matching likelihoods. The top line and the lighter blue circles show the situation for the *spectral matched filter scheme* which exhibits an offset of roughly a factor of 2.8 corresponding to the average effective weight.

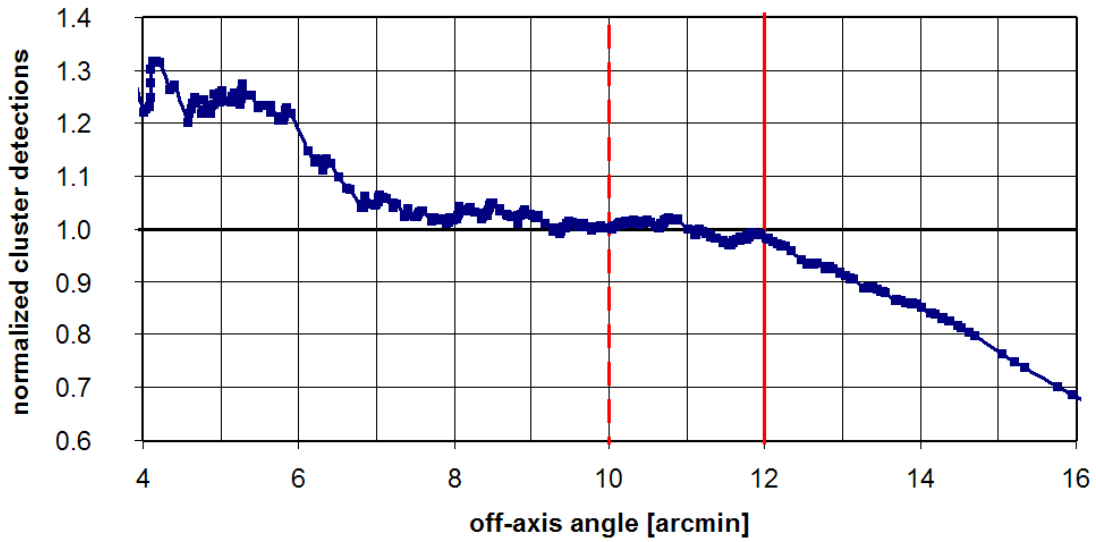


Figure 6.22: Cluster detections per unit sky area as a function of off-axis angle normalized to the detections at 10' off-axis angle (dashed red line). The detection rate is almost constant between 7' and 12' from the optical axis. In the central region the detection rate rises owing to the increased effective area. Beyond 12' the increasing vignetting and the broadened PSF decrease the cluster detections per unit area. The inner 12' (solid red line) are well-behaved and can be used for the core survey.

One way to address the issue of the maximum off-axis angle for a strictly selected survey sample is to ask at what point the cluster detections per unit sky area start dropping significantly. Figure 6.22 shows the results obtained from 120 fields without masked regions, *i.e.* no large foreground objects, and a total of 375 cluster sources (*screen level 3* objects). The plot traces the normalized cluster detections per unit sky area as a function of off-axis angle, which is derived from the cumulative distribution $N(< \Theta)$ divided by the enclosed sky area $\Omega(< \Theta)$ and normalized to the average value within $10'$ radius (dashed red line). From Fig. 6.22 it can be seen that the cluster detections per unit area are almost constant between off-axis angles of $7' \lesssim \Theta \lesssim 12'$. At larger radii the detection rate decreases significantly. Hence, a maximum off-axis angle of $\Theta_{\max} = 12'$ promises to be the best compromise between survey grasp and completeness. With this cut-off radius for the final XDCP core sample, the XMM survey grasp is $g_{12} \simeq 204 \text{ cm}^2 \text{ deg}^2$, a 30% improvement with respect to a $10'$ constraint.

6.7 Summary

At the end of the technical chapters 6–8, the main contributions and achievements of *this thesis work* towards the overall XDCP survey project are briefly listed. Concerning the X-ray analysis of XMM-Newton archival data this work can be summarized as follows:

- Definition of the current XDCP survey field sample based on a screening of the full XMM archive;
- Development of a distant-cluster-optimized X-ray pipeline for the data reduction, source detection, and creation of X-ray optical overlays;
- Conduction of performance tests for different detection schemes;
- Tests of the full XDCP selection procedure in the COSMOS field;
- Reduction of 546 XMM observations with a complete analysis of 469 XDCP suitable survey fields;
- Screening and classification of about 2 000 detected extended sources;
- Compilation of a final XDCP master source list with ~ 250 distant cluster candidates and about 750 additional DSS-identified cluster candidates at low or intermediate redshifts.

Chapter 7

Near-Infrared Follow-up Imaging

This chapter will deal with the follow-up imaging of the X-ray selected, distant cluster candidates, *i.e.* with **steps 3** and **4** of the survey strategy discussed in Sect. 5.2. Although the R–Z method used for the pilot study resulted in the discovery of XMMU J2235.3-2557, certain restrictions and limitations gave rise to the motivation to develop an alternative follow-up strategy. The following sections will discuss in detail the theoretical expectations of a NIR-based follow-up approach, its practical implementation, and the required software and analysis tools.

7.1 A New NIR Imaging Strategy

7.1.1 Motivation

A new two-band imaging approach should ideally cure both the practical restrictions related to the observatory site and telescope access and the intrinsic systematic limitations of the R–Z method. Wanted is thus an imaging strategy that:

1. is applicable to **4 m-class** telescopes and is thus not dependent on the VLT with its high over-subscription rate;
2. is extendable to the **Northern sky** for a future enlargement of the XDCP survey area;
3. yields **more accurate redshift estimates** in the main target range $1.0 \lesssim z \lesssim 1.5$;
4. has the potential to **reach beyond redshift 1.5** to allow detections of the most distant systems.

The first two items are telescope related practical issues for a survey project, the last two, however, are related to the performance of the R–Z method itself. At first sight, the goal of achieving a better performance (items 3+4) with smaller telescopes (item 1) seem mutually exclusive, but a closer look reveals that this does not have to be the case.

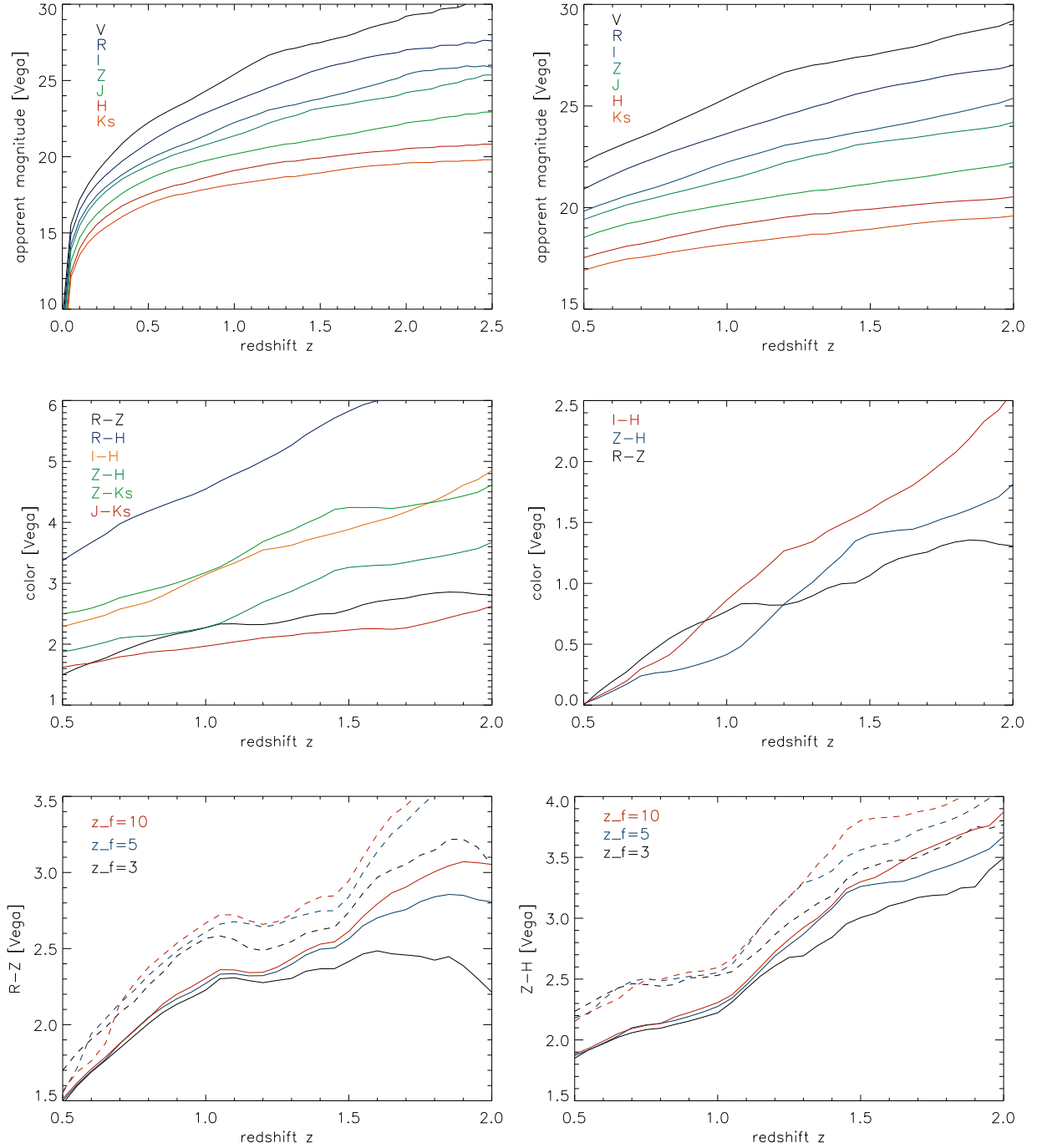


Figure 7.1: Simple stellar population (SSP) models for passively evolving galaxies. *Top panels:* Apparent magnitudes of L^* galaxies (Vega system) versus redshift diagrams for a formation redshift of $z_f = 5$ for the optical and NIR bands V, R, I, Z, J, H, and Ks. *Center left:* Color evolution diagram for a selection of colors ($z_f = 5$). *Center right:* R-Z, Z-H, and I-H color shifted to the same origin at $z = 0.5$. The slope of the relations determine the redshift sensitivity in the different redshift regimes. *Bottom panels:* Model grid of the R-Z (left) and Z-H (right) color evolution for formation redshifts of three, five, and ten (different colors) and solar (solid lines) and three times solar metallicity (dashed lines). Models computed by Daniele Pierini using PEGASE2 (Fioc and Rocca-Volmerange, 1997).

Filter	Center [μm]	Cut-on 5% [μm] (z_{start}^{D4000})	Cut-off 5% [μm] (z_{end}^{D4000})	m_{AB} (Vega)
R_{special}^1	0.655	0.53 (0.3)	0.75 (0.9)	0.195
I^2	0.798	0.70 (0.8)	0.89 (1.2)	0.440
Z^3	0.90	0.81 (1.0)	0.99 (1.5)	0.521
J	1.22	1.09 (1.7)	1.36 (2.4)	0.857
H	1.64	1.49 (2.7)	1.81 (3.5)	1.372
Ks	2.15	1.97 (3.9)	2.33 (4.8)	1.855

Table 7.1: XDCP filters of interest. For the three optical filters R, I, and Z and the standard NIR bands J, H, and Ks the central wavelength and the 5% transmission start and end points are listed. The values in brackets indicate the redshift when the D4000 break enters (z_{start}) and exits (z_{end}) the filter band. The last column shows the offsets between the standard photometric AB-system widely used in optical bands, and the classic Vega system which still prevails in NIR observations. The relation $m_{\text{AB}} = m_{\text{Vega}} + m_{\text{AB}}(\text{Vega})$ transforms the magnitudes.

7.1.2 Imaging strategy

The natural extension for distant cluster imaging beyond the reddest suitable optical combination of filters, R–Z, is to completely move into the near-infrared regime. Table 7.1 summarizes the characteristics of the reddest optical (standard) broad band filters (R, I, Z^4) and the three standard NIR bands J, H, and Ks⁵. Near-infrared imaging has only recently become a competitive alternative to optical observations and has been strongly boosted by great advances in the NIR imaging array technology. The latest generation of $2\text{k} \times 2\text{k}$ NIR arrays have been available for about 5 years now and have driven the development of a new generation of sensitive wide-field NIR instruments.

For a first approach to the problem, we can assume that suitable instrumentation exists for all six filter bands of interest and we can thus restrict ourselves to physical arguments related to the targets and the restrictions imposed by ground-based observations in general. A discussion of the practical implementation will follow in Sect. 7.2.

Secondly, the discussion will focus on the properties of the ubiquitous elliptical galaxy population in clusters, as introduced in Sect. 2.4. As ‘red and dead’ objects, the spectral energy distribution (SED) of elliptical galaxies can nowadays be accurately modelled and predicted with simple stellar population (SSP models) codes such as PEGASE2 (Fioc and Rocca-Volmerange, 1997) or GISSEL (Bruzual and Charlot, 2003). The SSP models under consideration assume an instantaneous star formation burst at a given formation redshift

¹For FORS2 R band see <http://www.eso.org/instruments/fors/inst/Filterers>.

²For EMMI I band see <http://www.ls.eso.org/lasilla/sciops/ntt/emmi/emmiFilters.html>.

³For Z, J, H, Ks filters see <http://www.mpa.de/IRCAM/02000/INFO/FILTERS/Filter-Status.html>.

⁴In order to avoid confusion with the redshift z , the SDSS broad-band filter termed z is capitalized and denoted as Z throughout this thesis.

⁵Ks is a modified ‘short’ K filter used by the 2MASS survey to reduce the thermal background at the long wavelength end.

Filter	Sky [mag asec ⁻²]	$m^*(z=0.5)$ [Vega (AB)]	$m^*(z=1.0)$ [Vega (AB)]	$m^*(z=1.5)$ [Vega (AB)]	$m^*(z=2.0)$ [Vega (AB)]	Δm_{1-2} [mag]
R _{special}	19.9–21.1	20.9 (21.1)	23.6 (23.8)	25.7 (25.9)	27.0 (27.2)	3.4
I	19.2–19.9	19.8 (20.2)	22.2 (22.6)	23.8 (24.2)	25.4 (25.8)	3.2
Z	18.1–18.8	19.4 (19.9)	21.4 (21.9)	23.3 (23.8)	24.2 (24.7)	2.8
J	15.8–16.7	18.5 (19.4)	20.2 (21.1)	21.2 (21.9)	22.2 (23.1)	2.0
H	13.8–15.0	17.5 (18.9)	19.1 (20.5)	19.9 (21.3)	20.5 (21.9)	1.4
K _s	12.7–13.0	16.9 (18.8)	18.2 (20.1)	18.9 (20.8)	19.6 (21.5)	1.4

Table 7.2: Benchmark of the apparent magnitude evolution of L* passive galaxies with formation redshift $z_f = 5$ and solar metallicity for various filter bands. The second column states the typical sky surface brightness as measured for the ESO La Silla site⁷. The given intervals span bright time (first value) and dark time (second value) in the Vega system. For faint galaxy observations with long exposure times, the assumption of background limited observing conditions is valid for all bands of interest. Columns 3–6 show the model expectations for the apparent galaxy magnitudes at various redshifts. The last column summarizes by how many magnitudes the galaxies drop between redshift 1 and 2, indicating that for the bluer bands even the largest telescopes will start losing the objects between $z \sim 1$ –1.5.

z_f and take a stellar initial mass function (IMF), the total stellar mass, and the rate of chemical enrichment as input. With this it is possible to compute the age-dependent distribution of stars in the Hertzsprung-Russell (HR) diagram and thus the properties of the stars contributing to the integrated light. Using this *evolutionary population synthesis* technique (Tinsley, 1978), the full SED of the passively evolving galaxies can be obtained at any time t after the burst by summing the contributions of the different stellar populations at this age using a stellar spectral flux library (Pickles, 1998).

The prediction of these simple stellar population models⁷ for a formation redshift $z_f = 5$ are summarized in the top panels of Fig. 7.1, where the apparent magnitudes in various bands are shown for passively evolving galaxies with characteristic absolute magnitude M^* . The derived color evolution for a variety of suitable colors are given in the left central panel. The illustrated (red) colors show mostly a well behaved monotonic functional form in the redshift range up to $z \sim 2$, which qualifies them in principle as redshift estimators. The redshift sensitivity, however, depends primarily on the slope of the color evolution $(d(X-Y)/dz)^{-1}$, where $(X-Y)$ denotes a given color. This sensitivity is emphasized in the right central panel for the color combinations I–H, Z–H, and R–Z, which are normalized to a common color origin at redshift $z = 0.5$, since this is the fiducial XDCP starting redshift beyond which follow-up imaging is needed. Note the flattening of the R–Z color at $z \sim 1$ and with a smaller effect at $z \sim 1.2$ for I–H and at $z \sim 1.5$ for Z–H. This feature occurs

⁶See <http://www.eso.org/gen-fac/pubs/astclim/lasilla/l-vanzi-poster>, <http://www.la.eso.org/lasilla/Telescopes/2p2T/D1p5M/misc/SkyBrightness.html>, and <http://www.eso.org/observing/etc/doc/ut2/uves/helpuves.html>.

⁷PEGASE2 models computed by Daniele Pierini.

when the 4000 Å break is completely redshifted beyond the cut-off (see Tab. 7.1) of the blue filter, in this case R, I, or Z. The small amount of flux in ellipticals below 4000 Å (see spectra in Fig. 4.5) is far less redshift dependent compared to the break passing through the filter.

The second important parameter influencing the slope of the color evolution is the formation redshift of the galaxy. The characteristic 4000 Å break of ellipticals only emerges when the young, hot, and blue stellar populations with their dominant UV flux have disappeared from the main sequence (main sequence turn-off), *i.e.* the flux break will evolve with the age of the stars. A younger stellar population at the epoch when the galaxy is observed, *i.e.* a lower formation redshift, will thus shift the observed color towards the blue. This bluing effect increases with decreasing galaxy age at the time of observation and is due to the rapid evolution of young stellar populations. The influence of the formation redshift z_f on the color evolution is depicted in the bottom panels of Fig. 7.1 for the R–Z and Z–H colors.

The model grid also illustrates the effect of increasing the metallicity, which makes up the final critical input parameter for the predictions. It can be seen that to first order an increasing metallicity results in a redder overall color, *i.e.* the color evolution curves are shifted upwards as a whole. Looking at epochs with a still relatively young stellar population, *i.e.* at $z \sim 1.5$, the age-metallicity degeneracy becomes obvious in this illustration as increasing age and metallicity have similar effects on the color. This degeneracy can be disentangled with a long redshift baseline as shown in Sect. 10.1.

The pre-requisites for measuring accurate galaxy colors are sufficiently deep exposures in each of the filter bands. Table 7.2 gives a benchmark summary of the predicted m^* apparent magnitudes for various redshifts as shown in Fig. 7.1. The second column of Tab. 7.2 lists typical levels of the sky surface brightness in the different bands as reference. Comparing these values in the J, H, and Ks-bands to the expected magnitudes of the targeted galaxies illustrates the main challenge of ground-based NIR observations, namely that the sources of interest are between a factor of 100 ($\Delta m = 5$) and 1000 ($\Delta m = 7.5$) fainter than the sky background.

For the optical R, I, and Z-bands, observations of distant galaxies are still background-limited ($b \gg s$). Under these observing conditions the signal-to-noise ratio (SNR) for a source with signal $s(t_{\text{exp}})$ and total background⁸ $b(t_{\text{exp}})$ enclosed in the source aperture will increase with exposure time t_{exp} as

$$\text{SNR} = \frac{s(t_{\text{exp}})}{\sqrt{b(t_{\text{exp}})}} \propto \sqrt{t_{\text{exp}}} . \quad (7.1)$$

For a fixed minimal SNR requirement the flux at the detection limit thus follows $f_{\text{lim}}(t) \propto$

⁸The Poisson statistics with standard deviation $\sigma_b = \sqrt{b}$ is applicable to the total number of detected electrons and not directly to the digital count units. For a proper statistical treatment the signal and background have to be transformed to these physical units first by multiplying with the *gain* g , *i.e.* the electrons-per-count conversion factor. Relation 7.1 further assumes that the dark current and read noise are small compared to the background noise, which is well-justified from Tab. 7.4 for the NIR.

$1/\sqrt{t_{\text{exp}}}$. Expressing this relationship in magnitudes yields $\Delta m_{\text{lim}} = 1 \rightarrow t_{\text{deep}} = 6.3 \cdot t_{\text{shallow}}$, *i.e.* going just one magnitude deeper requires more than six times the initial exposure time. For a doubling of the exposure time, the gain at the magnitude limit is $\Delta m_{\text{lim}} = 0.38$ mag. These simple considerations imply that the magnitude limit which can be reached within about $t_{\text{exp}} \sim 30$ min at a given telescope and filter is a solid constraint which cannot be pushed by more than $\Delta m_{\text{lim}} \sim 0.5$ mag with reasonable effort for large area survey projects. The last column of Tab. 7.2 states the galaxy dimming for the given filter from redshift 1 to 2. The rapid dimming in the optical R and I-bands of $\Delta m_{1-2} = 3.4$ compared to the moderate changes of $\Delta m_{1-2} = 1.4$ for H and Ks can be understood in terms of the *K*-correction introduced in Equ. 3.23. The long-wavelength filters H and Ks still probe the rest-frame peak emission of ellipticals even at very high redshifts, whereas the optical bands are restricted to the residual rest-frame UV-flux below the D4000 feature once the break is redshifted beyond the band. Consequently, reaching a depth to observe an m^* galaxy at $z \sim 1.5$ in the R-band is already challenging even with the Very Large Telescope, but the task becomes drastically easier when considering the longer wavelength-bands. The very same galaxy appears a factor of 100 brighter in flux in the Ks-band, roughly 60 times higher in the H-band, and the gain in the Z-band is still a factor of 7.

For a high-redshift two-band imaging strategy, the choice of the I or Z-filter (instead of R) as the blue band hence results in a significant gain in terms of depth requirements at the faint end. From the galaxy properties point-of-view, the red filter selection should be at the longest feasible wavelength. However, as pointed out in Tab. 7.2 Ks-band observations are very challenging and time consuming (long observational overheads) due to the dominating thermal background contribution. The red filter of choice for a new approach is consequently the H-band, which combines (i) good high- z galaxy observability, (ii) high-redshift sensitivity in conjunction with I or Z, and (iii) improved background conditions compared to Ks.

This discussion has shown that at the high-redshift end of the target regime around $z \sim 1.5$ a modified choice of observation bands can (over-)compensate for the geometrical telescope difference between the VLT and a 4 m-class telescope, which is of the order of 4–6 in collecting area. The next section will investigate the performance expectations concerning the redshift estimation of selected methods in more detail.

7.1.3 Performance expectations

The standard R–Z method is now compared to the two alternative methods I–H and Z–H. For a quantitative performance benchmark of the redshift sensitivity some simplifying assumptions are needed. For the total error budget of a red-sequence measurement one has to consider (i) intrinsic scatter about the sequence, (ii) photometric measurement errors of the galaxies, and (iii) calibration errors of the photometric zero points. The intrinsic red-sequence scatter for all known clusters out to $z \sim 1.3$ is typically $\sigma_{\text{scatter}} \lesssim 0.05$ mag. Of course, studying the evolution of the red-sequence properties at the highest redshifts will be an important science goal, but for now the assumption is that a well-defined and tight cluster red-sequence exists and that the average color can be measured

with good precision. Concerning the photometric measurement errors, the assumption of sufficiently deep observations in both filters has to be made. The discussion of the last section has shown (see Tab. 7.2) that this is not the case for the optical filters R, I, and Z. Depending on the telescope size, the limiting magnitude will unavoidably drop below m^* somewhere between redshift 1 and 2, and the bluer the band the earlier this will happen. The performance evaluation will thus assume idealized conditions, but in practice the achievable limiting magnitude of the blue filter will determine at what redshift the galaxy photometry will break down. Finally, calibration errors for the determination of the photometric zero points will add a constant color uncertainty. For well-calibrated data this offset should also be $\sigma_{\text{ZP}} \lesssim 0.05$ mag, which also neglects possible practical calibration issues. In any case, the total achievable color error will have a constant part, due to zero point offsets, and a redshift dependent part which is related to the increasing photometric error of fainter galaxies, fewer objects on the red-sequence due to the magnitude limit and a possibly intrinsically less populated locus of galaxies. For the following discussion a total red-sequence color error of $\sigma_{\text{color}} \approx 0.05 \cdot (1 + z)$ mag is assumed, which is a reasonable parametrization for good quality data ($\sigma_{\text{color}} \sim 0.1$ at $z=1$) out to $z \sim 1.5$.

The expected redshift uncertainties σ_z can then be estimated from the first derivative of the color evolution as presented in Fig. 7.1 as

$$\sigma_z \approx \frac{dz}{d(X-Y)} \cdot \sigma_{\text{color}} = \left(\frac{d(X-Y)}{dz} \right)^{-1} \cdot \sigma_{\text{color}}, \quad (7.2)$$

where $(X - Y)$ denotes the photometric method R-Z, I-H, or Z-H. The derivative of the color evolution was computed numerically using a boxcar-smoothed input curve in order to suppress the influence of small scale features of the coarsely sampled model on the local slope estimation. The obtained redshift uncertainty estimates are shown in Fig. 7.2 for solar metallicity models and formation redshifts three and five.

As expected, the best redshift performance is obtained in the redshift regime where the D4000 break is passing through the blue filter (see Tab. 7.1). The lowest achievable uncertainties of $\sigma_z \approx 0.04$ – 0.08 are assumed in the redshift interval $[0.3$ – $0.9]$ for the R-Z method, $[0.3$ – $1.2]$ for the I-H, and $[1.0$ – $1.4]$ for the Z-H approach.

The main performance characteristics of different red-sequence methods are summarized in Tab. 7.3. Based on the former discussions and the performance expectations, the final evaluation of the different suitable red-sequence imaging strategies is as follows:

- The **R-Z** approach has the advantage of being an optical method, *i.e.* observations and data reduction tools are standard. However, sensitive Z-band instruments are rare, which basically limits an efficient strategy to VLT FORS2. The method has two systematic drawbacks for high- z cluster searches: (i) The redshift uncertainties at $z > 1$ increase to at least $\Delta z \gtrsim \pm 0.2$ in the optimistic case ($z_f = 5$), and could be as much ± 0.4 , *i.e.* basically redshift-degenerate, for a lower formation redshift model. Since both bands have to be photometrically calibrated using standard star observations, there is little room to achieve a better performance by improving the calibration errors. (ii) The depth limitation in the R-band poses a serious risk to

not obtain sufficiently accurate color information on the galaxies or miss the highest redshift clusters completely. With a limiting magnitude of $R_{AB} \sim 24.5\text{--}25.0$ one can probe the cluster luminosity down to m^*+1 at $z=1$, but by $z=1.5$ this has dropped to m^*-1 . If the cluster does not contain several galaxies brighter than the characteristic magnitude m^* , the identification of a red-sequence could be an issue at redshifts as low as $z \sim 1.2$.

- **J–Ks** has been the standard NIR approach for high-redshift cluster investigations (Stanford *et al.*, 1997). The color evolution (Fig. 7.1, central left panel) has a constant but shallow slope, with modest uncertainties at all redshifts. The advantage of the method is that sufficient depth in the J and Ks-bands to probe galaxies out to $z \sim 2$ is fairly easy to achieve even with small telescopes. The disadvantage is the long overheads for NIR observations, in particular for Ks, which lowers the efficiency for routine follow-up. However, J–Ks can be very important to confirm very high-redshift cluster candidates that have been identified with any of the other approaches.
- The **I–H** method shows very promising performance characteristics at all redshifts. Sufficient I-band depth to at least m^* at $z = 1.5$ should be achievable with 4 m-class telescopes with reasonable exposure times, which allows this approach to be implemented at many observatories. The disadvantage, however, is the need to use different instruments for the optical and NIR observations. This results in less flexibility during the observations, more scheduling constraints, and adds extra steps to the data analysis. This method is currently in the test phase with first data obtained with the EMMI and SOFI instruments at the New Technology Telescope (NTT) at La Silla.
- The two-band imaging method of choice for this thesis is the **Z–H** strategy. This approach has the best performance expectations in the target redshift regime $1 \lesssim z \lesssim 1.5$ and modest uncertainties at lower and higher redshifts. The Z-filter as the blue band should allow sufficient depth with a 4 m-class telescope. The method has the advantage that both bands can be observed with a single modern NIR instrument, *i.e.* no additional optical instrument is required. The disadvantage is that Z-band observations with NIR instruments have never been tested. The practical implementation of the Z–H strategy will be discussed in the next section.

Color	Instrument	σ_z in $0.5 < z < 1$	σ_z in $1 \lesssim z \lesssim 1.5$	$z > 1.5$	Comment
R-Z	optical	0.05–0.15	0.15–0.4	no	sensitive to z_f
I-H	optical+NIR	0.06	0.06–0.15	possibly	instrument change
Z-H	NIR (+opt.)	0.08–0.12	0.06–0.1	yes	
J-Ks	NIR	0.08–0.14	0.14–0.18	yes	long overheads

Table 7.3: Performance summary of the different imaging methods. Columns 3 and 4 state the estimated redshift errors as discussed in Fig.7.2. Column 5 indicates whether the method has the potential to be used at redshifts $z > 1.5$.

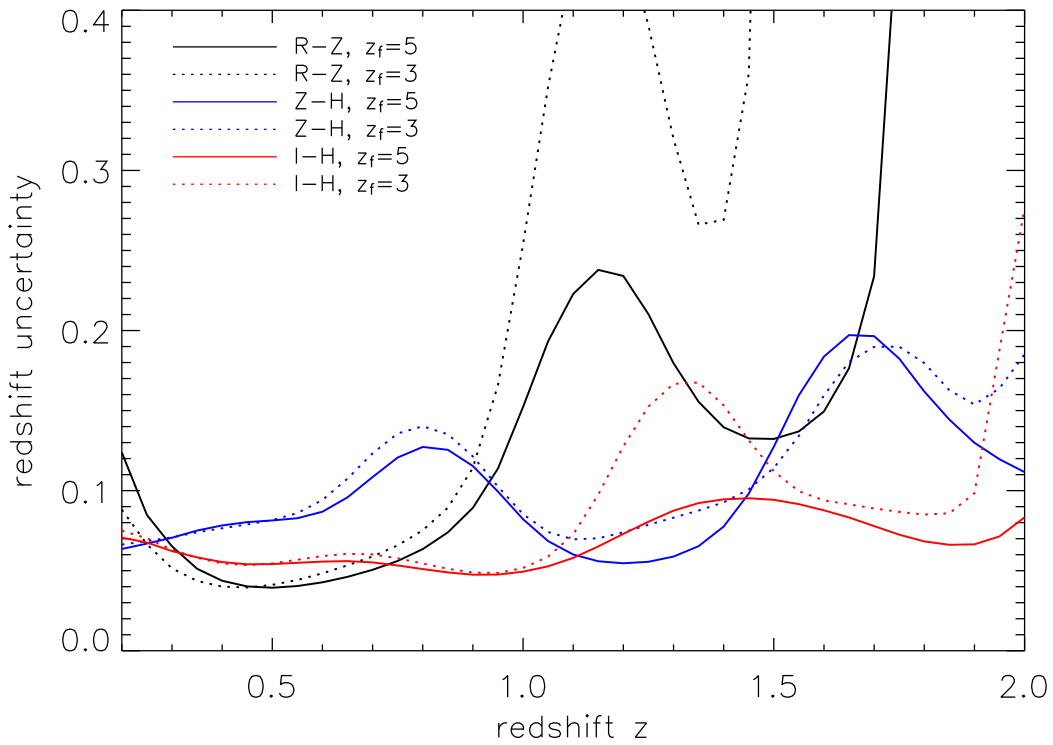


Figure 7.2: Absolute redshift uncertainties of different red-sequence methods for a realistic photometric color error assumption of $\sigma_{\text{color}} \approx 0.05 \cdot (1 + z)$ mag. Error estimates were obtained from the derivatives of the smoothed model colors in Fig. 7.1 using $\sigma_z \approx dz/d(X - Y) \cdot \sigma_{\text{color}}$, where $(X - Y)$ denotes the photometric method. The black solid line illustrates the estimated redshift error for the R-Z technique under the assumption of a formation redshift of $z_f = 5$, blue shows the Z-H method, and red I-H. The dotted lines use a model formation redshift of $z_f = 3$ for the same methods. The R-Z color is an accurate redshift estimator up to about $z \sim 0.9$, but at $z \gtrsim 1$ the uncertainties grow drastically and for low formation redshift models, the z -estimates even become degenerate (flat slope in lower left panel of Fig. 7.1). The Z-H strategy (blue) yields good redshift estimates all the way to $z \sim 1.5$, has the lowest uncertainties in the targeted regime $1 \lesssim z \lesssim 1.5$ and is rather insensitive to model variations. The I-H approach (red) is another promising alternative with good performance expectations at all redshifts. Note that the highest accuracy for any method is achieved in the redshift regime where the D4000 break passes through the blue filter (see Tab. 7.1).

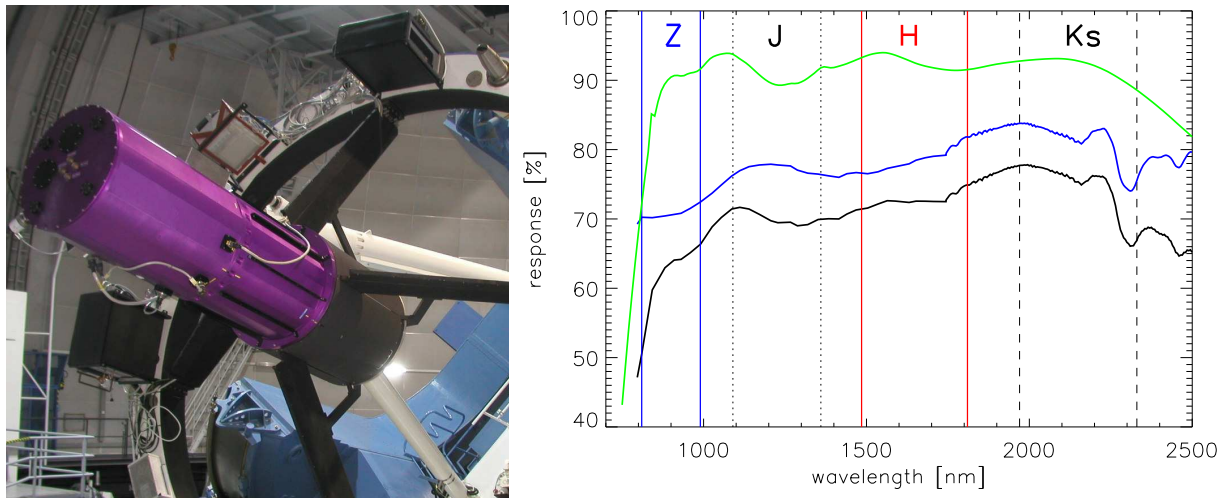


Figure 7.3: *Left:* The NIR wide-field camera OMEGA2000 at the Calar Alto 3.5m telescope. *Right:* OMEGA2000 instrument response. The green solid line indicates the transmission efficiency through the optical system as a function of wavelength, the blue line shows the HAWAII-2 detector quantum efficiency, and the black solid line gives the full response of the camera system. Filter band boundaries are overplotted as vertical lines. With a quantum efficiency of $\gtrsim 70\%$, the Z-band sensitivity of the OMEGA2000 NIR array is comparable to or better than the best optical instruments in this critical filter band. Data from H.-J. Röser (private communication).

7.2 Practical Implementation

The Z–H two-band imaging strategy can be ideally carried out with the NIR wide-field camera OMEGA2000 at the Calar Alto 3.5 m telescope. This section will briefly introduce the capabilities of the instrument, the observing strategy, and the obtained data.

7.2.1 OMEGA2000 in a nutshell

The left panel of Fig. 7.3 shows the prime focus instrument OMEGA2000 mounted at the 3.5 m telescope. Three main features establish this camera as the instrument of choice for testing the Z–H approach: (i) the high sensitivity from $0.8\text{--}2.5\ \mu\text{m}$, (ii) the large $15'.4 \times 15'.4$ field-of-view, and (iii) an online reduction system for an immediate data evaluation.

The instrument sensitivity is shown in the right panel of Fig. 7.3 as a function of wavelength. The blue solid line illustrates the quantum efficiency (QE) of the HAWAII-2 NIR array, the green line follows the transmission properties of the optical system of the camera, and the black line shows the total response of OMEGA2000 as the product of the two former functions. The QE efficiency in the classical NIR band J, H, K is about 80%, and at the short wavelength end in the Z-band one expects still a 70% sensitivity. For comparison, the red-optimized CCDs of the VLT FORS 2⁹ have an average Z-band QE

⁹See <http://www.eso.org/projects/odt/Fors2/qeu.html>.

Instrument		Detector	
field-of-view	$15'.4 \times 15'.4$ (237 arcmin^2)	array type	HAWAII-2
pixel scale	$0.45''/\text{pixel}$	array size	2048×2048 pixels
weight	300 kg	pixel size	$18 \mu\text{m}$
focal station	prime focus	wavelength range	$0.8\text{--}2.5 \mu\text{m}$
focal ratio	f/2.35	quantum efficiency	70–85%
telescope primary	3.5 m	dark current	$< 0.03 \text{ e}^- \text{ s}^{-1}$
broad band filters	Z, Y, J, H, Ks, K	read noise	$< 15 \text{ e}^-$
data rate	$\sim 10 \text{ GB} / \text{night}$	good pixels	$> 99\%$
online reduction	yes	fill factor	90%
commissioned	2003	full well capacity	$\simeq 100\,000 \text{ e}^-$

Table 7.4: OMEGA2000 instrument and detector characteristics. From Röser (2005) and Haas (2002).

of 65%, but most optical instruments provide quantum efficiencies $< 30\%$ in Z. Modern NIR arrays hence offer an attractive sensitive alternative at the long-wavelength end of the traditional optical regime. An additional advantage of NIR arrays with their individually isolated pixels is the absence of *fringing*, *i.e.* interference patterns caused by strong monochromatic atmospheric emission lines in CCDs; the disadvantage on the other hand are the numerous imperfections and flaws of NIR detectors that have to be accounted for during the reduction process (see Sect. 7.3).

The second prime feature of OMEGA2000 is the large field-of-view, which is still one of the largest available fields in the near-infrared. The 237 square arcminute FoV covers one quarter of the XMM-Newton field and is five times as large as the FORS 2 FoV. This has several important advantages: (i) often several cluster candidates can be simultaneously observed, (ii) lower redshift candidates and calibration sources can be placed in the FoV at no extra observational cost, and (iii) the photometric calibration in the J, H, and Ks bands is simplified by taking advantage of the numerous 2MASS sources in the field (see Sect. 7.4.2).

The available OMEGA2000 online reduction system is an additional important characteristic which helps to optimize the observational efficiency. Since the NIR background is so dominant (see Tab. 7.2), an evaluation of the data quality and the depth of the observation is usually difficult to obtain, in particular if the targets of interest are very faint. The online reduction pipeline can provide quicklook data products with sufficient quality while the data taking is active. This way, the reduced and co-added images of the ongoing observation are available with an approximate delay-time of 3 min to the running exposure and thus allows an instant evaluation of the target source and the observational status.

Further OMEGA2000 instrument and detector characteristics are summarized in Tab. 7.4.

7.2.2 Observational strategy

As a follow-up program of a large sample of X-ray selected cluster candidates, the observational survey mode strategy of the Z–H approach is driven by the two main goals (i) source identification and (ii) efficiency. The first goal implies that the observations have to be deep enough in order to identify even the most distant clusters as local galaxy overdensities. On the other hand, the bulk of clusters at lower redshifts require much shorter exposure times for a safe identification, which increases the survey efficiency if properly accounted for. For these considerations the following observing strategy has been pursued:

1. Start H-band observation of a distant cluster candidate field;
2. Check the online reduced co-added image products every 4–5 minutes and evaluate the appearance of the cluster candidate;
3. Stop the H-band observation once a galaxy cluster signature is clearly visible with at least 10–15 galaxies close to the candidate X-ray center;
4. If the target shows no cluster signature, stop after an exposure time of 50 min, which corresponds to a limiting 5σ H Vega magnitude of $H_{\text{lim}} \gtrsim 21$ (m^*+1 at $z \sim 1.5$). The candidate source is classified as ‘spurious’ and is not observed in any other band;
5. Observe sources with cluster signatures in the Z-band. Check again the pipeline products for sufficient depth and abort observations once reached;
6. Go to next candidate target field;
7. Obtain J and Ks-band observations for some of the most distant candidates to backup with a J–Ks color.

Starting with the redder H-band is important for the identification of the highest redshift clusters, which might be heavily dimmed in the Z-band (see Tab. 7.2), and correspondingly for the secure classification of a null-detection, *i.e.* spurious candidates. Galaxy clusters at redshift $z \lesssim 1$ can typically be well identified with exposure times of $t_{\text{exp}} \lesssim 15$ –20 minutes, *i.e.* the efficiency gain compared to the deepest observations is about a factor of three.

The photometric Z-band calibration requires additional observations of SDSS Z-band standard stars several times per night. Each targeted Z-band field also needs at least a few minutes of coverage under photometric conditions, which might have to be re-observed if the conditions during the initial exposure were not sufficient in quality.

The total exposure time t_{exp} for a deep observation is split up into many shorter observations t_{tel} , after which the telescope is offset, and these again consist of the sum of several single frames of integration time t_{single} . The elementary exposure time t_{single} is motivated by two boundary conditions. Firstly, the background in a given filter sets the maximum time before the detector saturates. Secondly, the difference between the saturation limit and the background level defines the effective dynamic range of the exposure, *i.e.* the interval in which the flux of astronomical targets can be accurately measured. In practice

this time is set in a way to include the brighter calibration objects well within the dynamic range and was fixed at $t_{\text{single}} = 5 \text{ s}$ (10 s) in the H-band (Z-band). These single exposures can be co-added in memory before they are saved to disk after a time t_{tel} during which the telescope points at the same position. The maximum time for t_{tel} is limited by the timescale of the temporal sky background variations which is a few minutes in the NIR and is less critical in bands with a lower background level. t_{tel} , as the exposure time of individual saved frames, is then directly linked to the data reduction strategy for the sky modelling (Sect. 7.3) and is set to $t_{\text{tel}} = 40 \text{ s}$ (60 s) in the H-band (Z-band). After the time t_{tel} the telescope is *dithered*, *i.e.* moved by a small pre-defined offset of $20''$ – $30''$ in order to place the objects at a slightly different position on the detector for the next exposure. This procedure is repeated until the total exposure time $t_{\text{exp}} = n \cdot t_{\text{tel}} = n \cdot m \cdot t_{\text{single}}$, with n the number of telescope positions and m the number of in-memory co-adds, is sufficient to reach the required depth. The total overheads¹⁰, *i.e.* the time the camera is not observing the target, can be 50–80% of the actual integration time and thus amount to a significant time fraction to be carefully considered and optimized within the requirements of the scientific program.

7.2.3 Imaging data overview

Following the above observing strategy, we have conducted two runs at the Calar Alto observatory, which were complemented by subsequent service observations. Table 7.5 summarizes the observation runs and the data yields. The total observing project was designed as a 10-day program to follow-up XDCP candidates in the Northern part of the survey region at $-20^\circ < \text{DEC} < +20^\circ$. The proposed program has reached a satisfactory completion of about 80%. This was made possible only through the enormous support of the Calar Alto staff and the use of buffer time outside the scheduled observing periods.

Table 7.5 lists an additional NIR observing run at the Cerro Tololo Inter-American Observatory (CTIO). This run followed-up Southern cluster candidates at $\text{DEC} < -30^\circ$ in H-band only, which complemented a multi-band optical observing program in this area. The data has been reduced and analyzed, but will not be further discussed here since the optical program is ongoing and the observing strategy followed a multi-band rather than a two-band imaging approach.

The listed data corresponds to a total of roughly 7 000 raw NIR images including calibration data. The data was partly taken in modest observing conditions with thin to moderate cloud coverage and seeing variations from $0.7''$ – $3''$. Additional non-ideal occurrences contained in the image data include (i) moon-light reflections from the dome, (ii) reflections and ghost images of nearby bright stars, (iii) scattered light from passing cars, (iv) airplane and satellite trails, and (v) time-varying wave patterns caused by the detector read-out electronics. All this has to be considered for the data reduction procedure which will now be discussed in detail.

¹⁰In order to minimize the read-out overheads, it is recommended to use a large number of in-memory co-adds m and short exposure times t_{single} , since an idle dummy read is performed at the beginning of each cycle.

Run	Date	Good Nights	Data Quality	Raw Data	Included
Calar Alto I	Jan 06	2.5 / 10	ok / non-phot.	29 GB	yes
CA Service A	May 06	0.2	fair / partly phot.	4 GB	yes
Calar Alto II	Nov 06	3.5 / 13	good / photometric	40 GB	yes
CA Service B	Jan 07	1.0	fair / partly phot.	12 GB	yes
CTIO I	Sep 06	2.0 / 3	ok / non-phot.	27 GB	no

Table 7.5: NIR data overview. The data for this thesis was obtained during two Calar Alto runs in 2006 complemented by two service observation blocks. Including data that was taken in challenging conditions, the proposed observing program achieved a satisfactory completion level of about 80%. The results of the CTIO run in the last row using the ISPI instrument are not included in this thesis, since the data is not self-contained (H-band only) and complements an ongoing optical imaging program.

7.3 Development of a NIR Science Reduction Pipeline

Near-infrared wide-field imaging instruments have only emerged over the last few years and OMEGA2000 in this respect is still a camera with one of the widest available field-of-views. Additionally, the NIR data reduction process is more challenging and complex than in the optical. Both aspects combined result in the fact that there is no generic ready-to-go data reduction software package available yet that would fulfill all demands. This gave rise to the motivation to develop a new science-grade NIR reduction pipeline optimized for the XDCP demands.

7.3.1 Requirements and specifications

From the expected science target characteristics discussed in Sect. 7.2.2 and the raw data properties of the last section, we can now define the requirements and demands on a science-grade reduction pipeline. The distant galaxy cluster detection and characterization result in the **scientific requirements** of:

- the best possible performance for faint extended objects;
- the maximum achievable depth for the detection of the faintest objects;
- accurate object photometry down to the limiting magnitude;
- quality control via intermediate data products.

Practical demands on the other hand motivate the following pipeline specifications of:

- handling of thousands of raw images from dozens of pointings and several filter bands;
- minimal requirements of manual interaction;

- handling of strongly varying observing conditions and data contamination;
- an OMEGA2000 optimization with the flexibility to easily adjust to other NIR instruments;
- a portable software package for easy public distribution and use for similar survey projects.

The science-grade NIR pipeline developments built upon the existing quicklook reduction pipeline which is discussed and characterized in detail in Fassbender (2003). The following discussion will mainly focus on the upgraded pipeline components and will only summarize the functionality of existing critical components. The reduction pipeline is implemented as a C-application program within the MIDAS environment. The MIDAS system provides the interface and tools for the image data handling, whereas all pixel-by-pixel image manipulations are based on C-coded algorithms.

7.3.2 NIR reduction steps

The implemented near-infrared data reduction scheme is illustrated in Fig. 7.4. Data products for the different reductions steps from the raw image to the final science frame are provided in Fig. 7.5. The full data reduction procedure can be broken up into the two independent processing blocks (i) *single image reduction* and (ii) *image summation*. The pipeline is designed in a way to yield final image products for one or both of the processing blocks without further manual interaction. The user provides an input catalog with an arbitrary number of raw images belonging to the same telescope pointing and taken with the same filter and upon pipeline start all further image handling procedures are automated.

Single image reduction

The first processing block handles the calibration steps of the individual raw frames (upper left panel of Fig. 7.5 and subpanel 1) and the subsequent sky modelling and subtraction as shown in Fig. 7.4.

As initial calibration step, the raw input image is *flatfielded* to correct the detector inhomogeneities. For NIR detector arrays this is particularly critical since (i) the quantum efficiency can vary by a factor of two over the FoV (global variations), and (ii) the electronically independent NIR pixels exhibit significant pixel-to-pixel changes (local variations). A *master flatfield* for each filter can be created from *dome flatfields* taken inside the telescope dome and *sky flatfields* taken during twilight in a region devoid of bright objects. Since the thermal dome emission imprints a significant amount of structure in the dome images, the *master flatfield* mainly relies on the detector variations determined from the sky calibration data with the *dome flatfields* acting only as initial correction of the former. The final *master flatfield* contains the information on the global and local detector variations. It is normalized to a median value of 1 and placed in a calibration frame directory, where the reduction pipeline can access it. By dividing the raw input frame by this *master flatfield* (subpanel 2) the intermediate image product contains variations due to the received signal and not the detector.

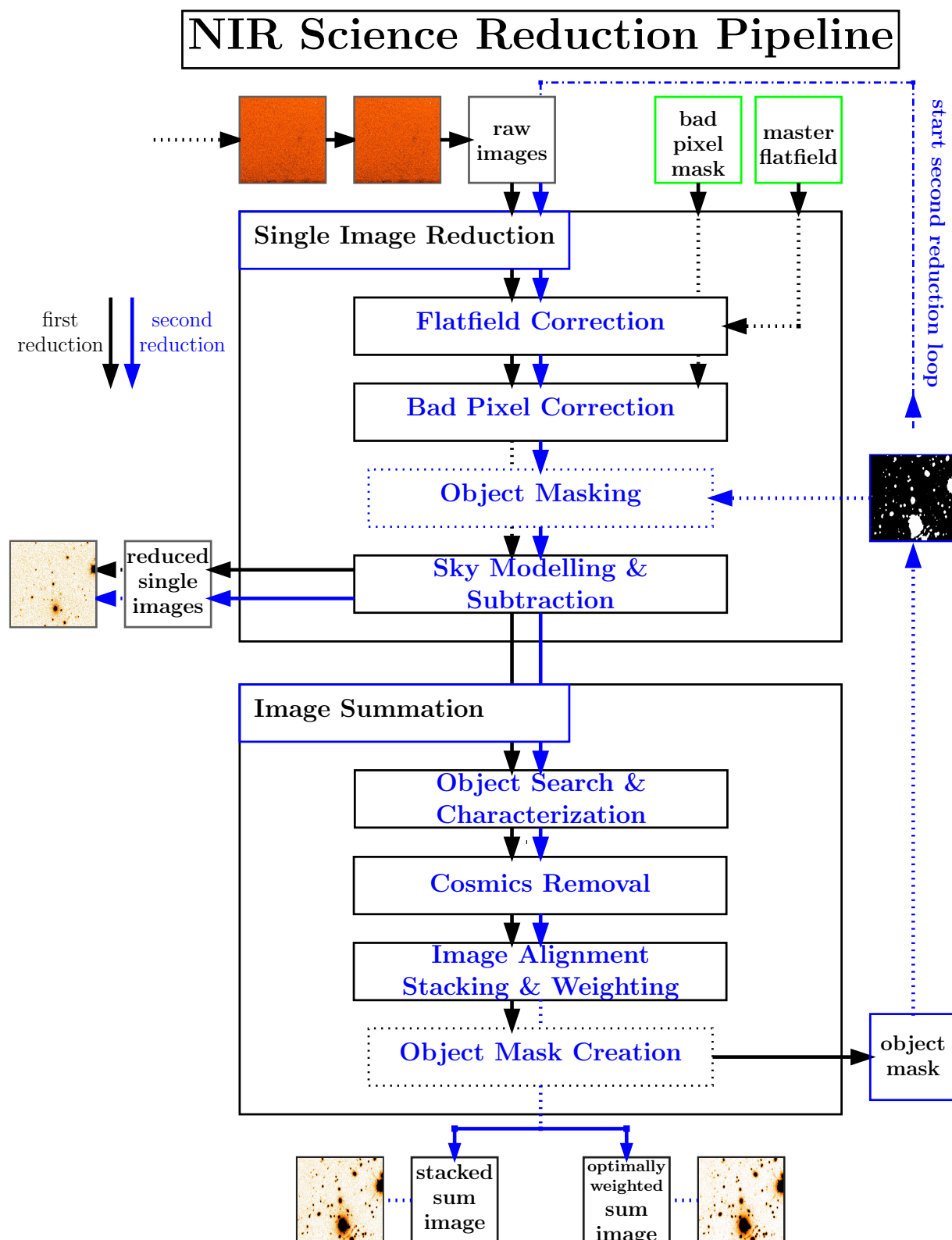


Figure 7.4: Near-infrared science reduction pipeline flow chart.

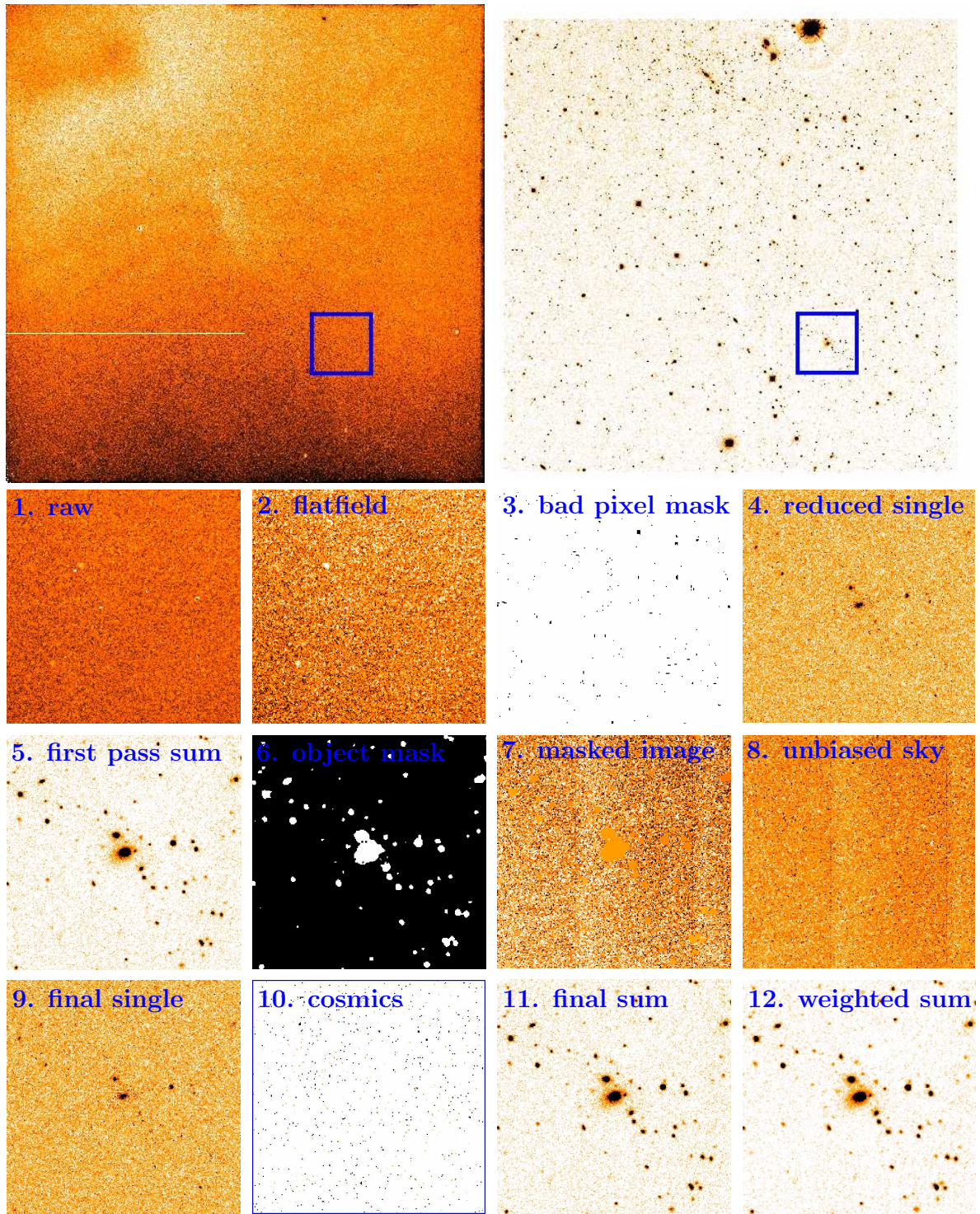


Figure 7.5: Near-infrared science reduction steps. The top panel shows the full $15.4' \times 15.4'$ FoV for a raw H-band image (*left*) and the final reduced sum image containing 75 input frames. Note that about $30''$ are lost at each field edge due to the dithering (*right*). The blue squares indicate the $2' \times 2'$ zoom field for the small panels centered on the galaxy cluster RX J0018.2+1617 at $z = 0.55$. The small cutouts with numbers 1-12 illustrate the reduction steps of Fig. 7.4 by showing intermediate data products.

As a second step, a *bad pixel correction* is applied. The OMEGA2000 detector array contains about 0.5% pixels which are either not functioning at all (dead pixels) or exhibit significant deviations from a time-linear signal response (hot or flickering pixels). These pixels can be identified through a linearity analysis and are flagged in the *bad pixel mask* (subpanel 3) of the calibration directory. The values of these flagged bad pixels in the flatfielded image are then replaced by the interpolated pixel value of the four closest good pixels.

Note that near-infrared measurements are usually obtained by reading out the detector array at the beginning and end of the integration time and subtracting the two to determine the signal. Hence this *double-correlated readout* scheme does not contain a *bias* offset as in CCD data. The detector *dark current*, *i.e.* the measured pixel values without an external signal, is in principle an additional (small) contribution to be corrected. However, tests have shown (H.-J. Röser, private communication) that the *dark current* is not stable enough to be accurately modelled and subtracted since it depends sensitively on the exact detector temperature and its thermal history. Instead of an explicit subtraction, the *dark current* is treated as part of the overall background and implicitly corrected with the *sky background subtraction*.

The most critical and important part in the near-infrared reduction process is the *sky background modelling*. The dominating background components are (i) atmospheric airglow (see Fig. 8.1) and (ii) thermal emission of the ambient structures at long wavelengths. Smaller contributions arise from (iii) scattered moonlight, (iv) Zodiacal scattered light (Cox, 2000), and (v) the uncorrected instrumental dark current. As discussed in Sect. 7.1, the science objects of interest can be easily a factor of 100–1 000 fainter than the background surface brightness. Consequently this implies that the local background around the astronomical objects has to be known with uncertainties of $< 10^{-3}$. The dominating airglow emission exhibits significant temporal changes on time scales of several minutes and spatial variations on scales of a few arcminutes. Hence the sky modelling requires a temporally and spatially local background estimation derived directly from science data. The pre-requisites to an accurate sky modelling have been implemented in the observing strategy through (i) a sufficiently short telescope pointing time t_{tel} that allows tracing the temporal variations and (ii) well-chosen dither offsets that enable a reconstruction of the local background without being biased by the flux of the astronomical objects of interest.

The following recipe yields an accurate but preliminary estimate of the sky background. (i) Take the image together with the three¹¹ preceding and following frames, *i.e.* the background is determined from a total of seven frames taken within a period of ± 3 –5 minutes. (ii) For every detector pixel (image coordinates) select the corresponding pixel values of all seven frames. Due to the dither strategy, which places the real objects at different detector positions for each image, most pixel values will only contain a background signal, whereas a minority will additionally have an object signal component¹². (iii) The median

¹¹Optimized pipeline parameters for the XDCP NIR data reduction are cited for this discussion. However, all critical parameters of the software can be specified and adjusted to the actual science needs. The background for the first (last) images of an observation series are estimated from the first (last) 7 frames.

¹²This assumption is in general well justified for extragalactic sparse fields. However, for (low redshift)

of these seven values is taken as a good initial guess of the actual background level for the specified pixel. However, any object flux in one or more of the seven values systematically biases the median to a slightly higher level, *i.e.* the background is overestimated due to the additional non-background component in some pixels. (iv) This background bias can be corrected in next order by applying a $\kappa\sigma$ -clipping algorithm to the data values. A Poisson estimate of the local background standard deviation σ is obtained from the initial background estimate, the gain¹³ of the detector array, and the local quantum efficiency of the detector pixel¹⁴. Any pixel values deviating more than three standard deviations from the initial background estimate are clipped, and the median is recomputed from the remaining object-cleaned values. (v) The $\kappa\sigma$ -clipped median value is taken as the background estimate for the specified pixel. The procedure is repeated for all detector pixels resulting in a full sky frame for the input science image. (vi) The modelled background sky is subtracted from the science image and replaced by a constant representing the average sky value in order to preserve the proper counting statistics.

The flatfielded, bad pixel corrected, and sky subtracted frame is written to disk as the final result of the first single image reduction loop (subpanel 4). However, the applied $\kappa\sigma$ -clipping for the first order correction of the local sky value could only eliminate object flux which has been detected at more than three standard deviations above the normal background level in the single frame, *i.e.* for fairly bright sources. The bulk of fainter sources and the wings of brighter objects below this clipping threshold will still bias the local background model to slightly higher values. The subtracted sky might thus still be overestimated resulting in a systematically lower flux for an object at the given position, which can reach significant levels for faint galaxies (see Sect. 7.3.3). This lost flux can be largely recovered with a second iterated background modelling loop as discussed below.

Image summation

The reduced single image contains the data of integration time t_{tel} , *i.e.* typically 60 seconds or less. In order to reach the required depth, the single images have to be stacked to build up a deep sum image with the full on-target exposure time t_{exp} . To achieve this, the dither offsets have to be reversed and the images aligned in world coordinates, *i.e.* the physically same objects in the individual frames have to end up on top of each other. During this stacking procedure cosmic ray events, or short *cosmics*, can be identified and removed.

The alignment and stacking procedure uses the following approach: (i) The first input image is declared as master frame onto which all others are positioned and co-added. (ii) The reduced single master image is searched for typically 50–100 reference stars, whose centers-of-mass, as derived from the stellar flux distribution, are recorded. (iii) From the

objects larger than the dither offsets of $20''$ – $30''$ the assumption is not fulfilled, but the introduced initial error is corrected during the second iteration.

¹³The gain of a detector is the conversion factor between digital count units and physically detected electrons via the photoelectric effect.

¹⁴In practice, an additional normalization factor has to be considered which is necessary to standardize the background levels in each frame.

image header of the next input frame, the expected offsets with respect to the reference master frame are computed. Using these approximate offsets, the catalogued reference stars are searched for in the vicinity of the expected detector positions. Once matched, the exact object centers are determined resulting in an improved offset determination. (iv) The final image offset is determined from the outlier-clipped average of all matched stars. Since the OMEGA2000 optics exhibits negligible image distortions over the whole FoV, the frames can be co-added at this stage by simple XY-coordinate shifting to the nearest integer pixel offsets.

The single images still contain the unwanted *cosmics* which are to be corrected for without modifying the flux of the real astronomical objects. Cosmic ray events, caused by charged particles going through the detector, can be identified from their characteristic signature of single or few isolated pixels with increased count levels without a corresponding counterpart in the next aligned image. In principle, the *cosmics* would be removed by a simple median process over a sufficient number of pixel-aligned images, similar to the procedure for the background determination. The complication arises that the median procedure efficiently removes everything that is not present in at least half of the images, including the outer wings of real astronomical objects in variable seeing conditions, and the central flux peak of objects. The peaks can exhibit large gradients towards the neighboring pixels and are thus likely damped when medianing over the different object flux distributions in each frame. This effect can decrease the total flux of stellar sources by about 20%, which is avoided by applying the following procedure: (v) The median image of eleven world-coordinate aligned input frames is determined and used as object reference image. This intermediate sum image is now devoid of *cosmics* and contains the real objects at the proper locations but with biased flux levels. (vi) Each individual frame is now checked pixel-by-pixel whether the value is more than five standard deviations above the corresponding median reference value, where the standard deviation is determined in analogy to the sky modelling procedure. (vii) If a *cosmics* candidate is detected, the reference median image is searched for an astronomical object within a radius of three pixels around the outlier position. In case a source is found, the initial pixel value is classified as object flux and co-added to the master image as is. If no source is matched, the outlier value is classified as *cosmic* and replaced by the median value of the reference image, which is in turn co-added to the master sum image. (viii) This procedure is repeated until all input images have been aligned, *cosmics* cleaned, and co-added to yield a final deep sum image (subpanel 5). The cosmic ray events, as shown in subpanel 10 of Fig. 7.5, have now been removed from the field without influencing the total flux of the astronomical sources.

The last two subsections have provided a summary of the full first data reduction loop, which is in principle equivalent to the quicklook reduction system available at the telescope. The next two subsections will discuss further improvements towards the goal of the best achievable science-grade data reduction quality.

Iterated background subtraction

The complete science-grade reduction process requires two additional main components. Firstly, the creation of an *object mask* with registered positions of all sources. Secondly, an additional iterated loop through the reduction procedure but now with removed source fluxes for an unbiased second order sky background correction.

The *object mask* is created from the final deep sum image of the first reduction pass (subpanel 5) which contains the best available information on the location and size of the astronomical objects at this processing stage. The objective of the *object mask* is to cover all sky areas in the FoV which contain a detectable source signal and use only the pixels with an unbiased background value for the reconstruction of the sky model. In practice the mask is created using an iterative $\kappa\sigma$ -clipping algorithm applied to the smoothed deep sum image. An initial smoothing is helpful for the identification of faint object halos, *i.e.* the PSF wings for point sources are extended halos for galaxies. Pixel values deviating more than about two standard deviations from the median background level are classified as object pixels and flagged in the mask frame. This procedure is iterated to push the depth of the mask to sufficiently faint levels. The final *object mask* is shown in subpanel 6, which now distinguishes the black regions with background pixel values and the masked white areas with object flux contributions.

With the *object mask* in hand, the second reduction loop can start from the very beginning (see Fig. 7.4). The initial calibration steps *flatfielding* and *bad pixel correction* are applied as before. The *sky modelling* procedure on the other hand is extended by two additional steps. (i) The *object mask* is projected onto each individual input frame. To do this projection properly, the exact image dithering offsets as determined during the first image summation loop are used to shift the *object mask* to the correct world-coordinate aligned location in each input image. (ii) The pixel values of the masked object regions are replaced¹⁵ by the unbiased median background level of the 100 nearest unmasked values. This replacement scheme is designed to yield robust results for arbitrary large objects and to take into account local background variations across the FoV. The masked input image (subpanel 7) with all object flux replaced is then passed on to the sky modelling procedure. The final unbiased sky model (subpanel 8) is now the result of a second order corrected flux-removed and $\kappa\sigma$ -clipped background determination. Subtraction from the original input image yields the final iterated reduced single image (subpanel 9), and after the subsequent summation and *cosmics* removal (subpanel 10) of all frames the final co-added deep sum image is available after the second processing loop (subpanel 11).

Advanced optimizations

The final sum image is a well-reduced and science-ready data product. However, with respect to the objective of reaching the maximum possible depth, two additional optimization schemes can be applied. Firstly, *fractional pixel offsets* instead of integer values can be implemented for the stacking procedure, and secondly, *optimal weighting* of the individual input frames can improve the final signal-to-noise ratio.

The discussed image summation procedure determined the accurate XY-offsets of the frames with respect to the master frame, but then rounded the exact values to the nearest integer pixel offsets in order to match the underlying pixel grid. This way, systematic

¹⁵Two additional replacement schemes with lower performance expectations are implemented. 1) The masked pixel is ignored for the sky determination, which leads to difficulties for very large objects. 2) The masked pixel is replaced by the global median, which does not take into account local variations.

truncation errors of up to half a pixel in each spatial direction are unavoidable. For the OMEGA2000 pixel scale of $0.45''/\text{pixel}$ this implies systematic XY-shifting errors of $0\text{--}0.225''$ per direction, which can add up in quadrature to a maximum systematic displacement error of $0.32''$ for a stacked frame. The integer pixel shifting has thus two consequences, both gaining importance in good seeing conditions. (i) The stacked object flux is not as compact as defined by the seeing limit and (ii) the 2-dimensional flux distribution of point sources does not follow its natural radially symmetric Gaussian shape. This latter tendency of the object cores to become boxy or square-like is easily visible for the fainter objects in the left panels of Fig. 7.6. The shape improvements after applying the *fractional pixel offset* scheme can be seen by eye in the right panels of the same figure.

In order to implement *fractional offsets* onto the underlying fixed detector grid of 2048×2048 pixels, the flux values in each pixel have to be distributed over four cells of the master grid in a flux conserved way. The flux distribution matrix is calculated once for each frame from the exact offsets according to the fractional geometrical overlap of a pixel with the underlying master grid. The pixel values of the frame to be co-added are then distributed using this pre-determined matrix. In turn, each pixel of the master grid, receives fractional flux contributions from four adjacent pixel values of the single image.

The question whether a faint object will be detected depends primarily on the signal-to-noise ratio of the source (see Equ. 7.1), *i.e.* on its contrast with respect to the noise properties of the background. So far, all input frames for the summation were treated as if they had the same SNR properties. However, this is in general not the case since the observing conditions for the seeing σ , the sky transparency T , and the background surface brightness levels B can change significantly during the observations. The source signal s will then vary as $s \propto T$ and the total background b confined in a seeing limited aperture will follow $b \propto B \cdot \sigma^2$. One can then ask the question for the best way to co-add two individual frames in order to achieve the best SNR for their sum. Following Gabasch (2004) for the case of faint sources ($b \gg s$), an optimal weight factor w_2 for the second frame can be derived by maximizing the resulting¹⁶ $\text{SNR}_{\text{tot}} = (s_1 + w_2 s_2) \cdot (b_1 + w_2^2 \cdot b_2)^{-1/2}$. Using dimensionless parameters for the source signal $\tilde{s} \equiv s_2/s_1$, the transparency change $\tilde{T} \equiv T_2/T_1$, the background variation $\tilde{B} \equiv B_2/B_1$ or $\tilde{b} \equiv b_2/b_1$, and the seeing ratio $\tilde{\sigma} \equiv \sigma_2/\sigma_1$ of the two observations, the optimal weight for the second frame is given by

$$w_2 = \frac{\tilde{s}}{\tilde{b}} = \frac{\tilde{T}}{\tilde{B} \cdot \tilde{\sigma}^2} = \frac{\tilde{f}}{\tilde{B} \cdot \tilde{\sigma}^2} . \quad (7.3)$$

In the last step, the change in the sky transparency \tilde{T} was replaced by the equivalent but directly observable source flux ratio of the two observations $\tilde{f} \equiv f_2/f_1 = \tilde{T}$. The optimal weighting factor w_2 for a new image to be co-added to the master frame is thus proportional to the received signal ratio \tilde{s} and inversely proportional to the total background ratio \tilde{b} in the object aperture, which is particularly sensitive to seeing variations. This is expressed in terms of the direct observables \tilde{f} , \tilde{B} , and $\tilde{\sigma}$ that allow an automatic monitoring for each

¹⁶For the second factor, the background noise is added in quadrature $\sigma_{\text{tot}}^2 = \sigma_1^2 + (w_2 \sigma_2)^2 = b_1 + w_2^2 b_2$. Note that in this relation σ denotes the standard deviation and not the seeing.

image. The background factor \tilde{B} is determined from the median sky level in each frame. The flux ratio \tilde{f} and the seeing ratio $\tilde{\sigma}$ can be obtained by averaging the stellar source properties as measured in the first step of the summation process, where all matched objects are characterized in terms of their $5''$ -aperture flux and the full-width-at-half-maximum (FWHM) of their radial source profiles.

In practice, the *fractional pixel offset* and *optimal weighting* schemes are combined and implemented as a separate optimized final sum image, as shown in the last subpanel 12 of Fig. 7.5. The effects of these additional optimization procedures as part of the science-grade data reduction will be investigated in the next section 7.3.3.

This last section has discussed the main steps and procedures to go from raw NIR data to science-ready optimized stacked images and how they are implemented as part of the newly developed NIR reduction pipeline. For the routine reduction of the data listed in Tab. 7.5 the following approach was pursued for each science field and filter band: (i) A full automatic pipeline reduction is run on the field with standard parameters. (ii) The data quality of the intermediate and final data products is inspected. This includes checks of the individual reduced images for possible data corruption, contamination from scattered light, cloud coverage, and satellite trails. Additionally, the object mask is investigated for proper depth, the masked input images for a correct mask projection, and the sky models and cosmics frame for unusual features. (iii) Identified contaminated data frames are then excluded from the reduction and the pipeline parameters are optimized if necessary. (iv) The reduction pipeline is then re-run on the optimized input data set to yield the final science-grade image products.

7.3.3 Faint object optimization

After introducing the basic functionality of the main science pipeline components in the last section, we will now turn to a discussion of the effects of the implemented reduction optimizations. Figure 7.6 illustrates the different optimization schemes for $1' \times 1'$ co-added image cutouts centered on the calibration cluster RX J0018.2+1617 at $z = 0.55$, displayed with high image contrast. The upper panels show the sum images after the first reduction loop, whereas the lower panels have the results after the *iterated background subtraction*. Going from left to right adds the *optimal weighting* scheme and the *fractional pixel offsets*. Hence the upper left panel displays the reduction quality achievable with a single loop (quicklook) reduction, and the lower right panel shows the same data with all optimizations incorporated requiring about the threefold CPU time.

We will first consider the effects of the *iterated background subtraction*, *i.e.* the difference between the upper and lower panels of Fig. 7.6. By masking out all objects and their halos during the second reduction loop, the sky background determination is unbiased compared to the systematically slightly higher median levels when source fluxes are included. This lower background value at the object positions results in additional object flux when the sky background is subtracted. The *iterated background subtraction* hence recovers object flux and consequently makes the sources brighter. This flux recovery is expected to be

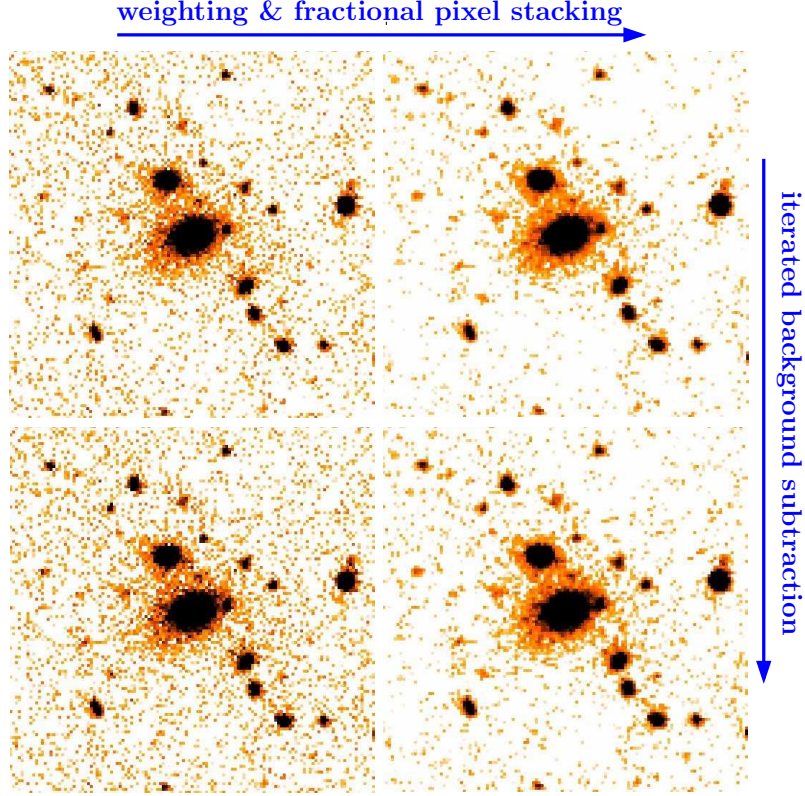


Figure 7.6: Faint object optimization. The *upper left panel* shows a high-contrast $1' \times 1'$ zoom on the calibration cluster RX J0018.2+1617 at $z=0.55$ as seen in the stacked sum image after the first reduction pass (see panel 5 in Fig. 7.5). Going to the right panels adds fractional pixel offsets and optimal weighting. The lower panels show the image results after the second iterated sky subtraction. The final best image including all optimizations is thus placed in the *lower right panel*. While the iterated sky subtraction recovers a significant amount of flux of faint and extended objects, the optimal weighting scheme increases the limiting magnitude by improving the signal-to-noise ratio of the faint sources (see Fig. 7.7 for quantitative results).

more significant for extended low surface brightness objects compared to stellar point sources. A useful approximation to convert measured magnitude offsets into flux differences $\Delta f = f_2 - f_1$ for small variations ($\Delta m \ll 1$) is given by the relationship

$$\Delta m = -2.5 \cdot \log \left(\frac{f_2}{f_1} \right) = -2.5 \cdot \log \left(1 + \frac{\Delta f}{f_1} \right) \approx -\frac{2.5}{\ln(10)} \cdot \frac{\Delta f}{f_1} \approx -1.1 \cdot \frac{\Delta f}{f_1}, \quad (7.4)$$

implying that small magnitude differences reflect approximately the fractional flux difference.

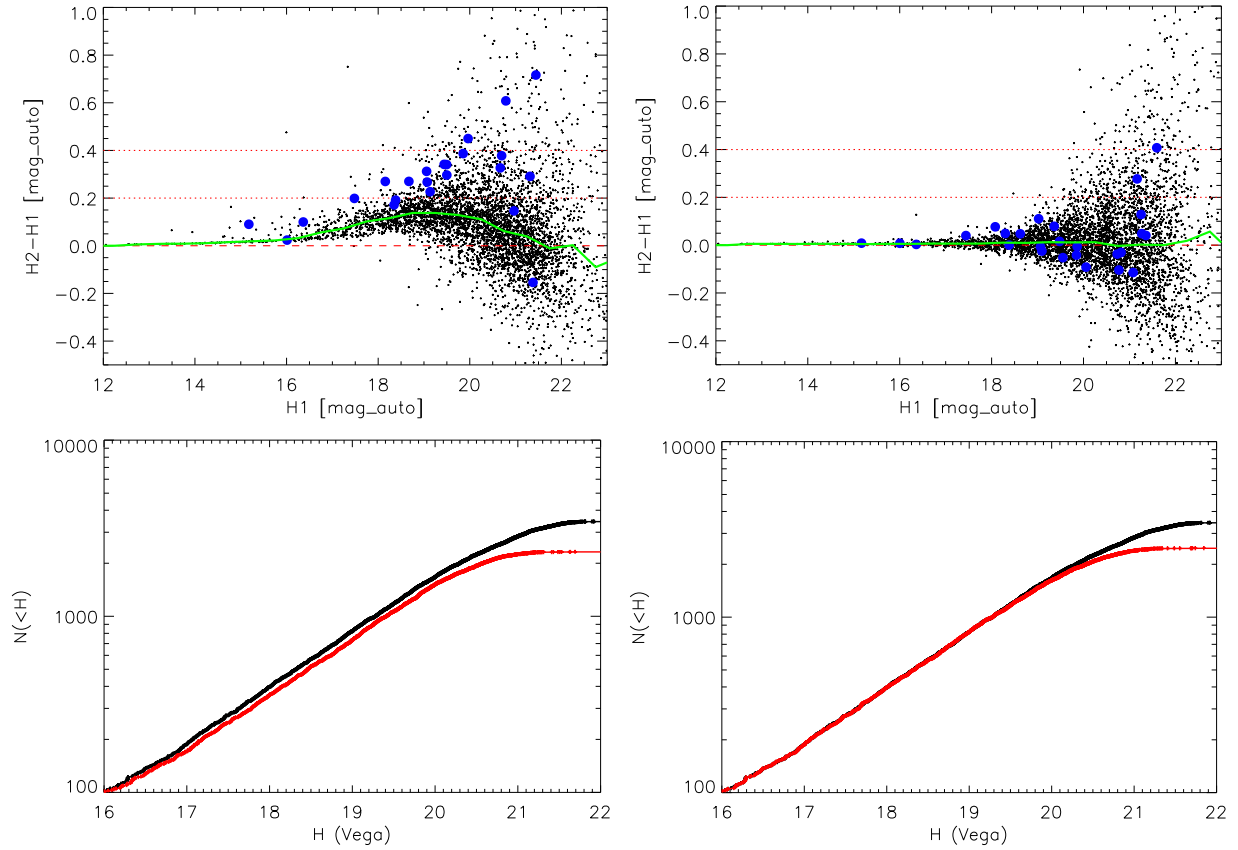


Figure 7.7: Effects of advanced reduction schemes. *Top panels:* Difference photometry in the H-band for various reduction stages as shown in Fig. 7.6 using the same deep detection image. *Left:* Total magnitude difference between the sum image with iterated background subtraction (here H1, lower left panel in Fig. 7.6) and the sum image after a single reduction loop (here H2, top left panel in Fig. 7.6). The dashed red line represents a zero offset (*i.e.* the same measured magnitudes), black crosses show all objects in the FoV, big blue circles represent the galaxies seen in Fig. 7.6 (*i.e.* cluster members of RX J0018.2+1617), and the green solid lines follows the median offset taken in 0.5 mag bins. At $H > 16$, the recovered flux from the iterated background subtraction becomes noticeable and increases to a median difference of 0.1–0.15 mag (about 10–15% in flux) between H magnitudes of 18–21. At $H > 21$ the difference drops back to zero which reflects the depth of the object mask. Note that the recovered flux is drastically increased for the faint extended cluster galaxies (blue circles) compared to the median difference. *Right:* Same plot for the difference between the final weighted image (H1, lower right panel in Fig. 7.6) and the iterated background subtracted image without weighting (H2). The total magnitudes are now consistent, since weighting cannot change the flux, but only the signal-to-noise ratio of the sources. *Left bottom panel:* $\log N - \log S$ of the final reduced image (black solid line) and the first sum image (red solid line) in a field with significant seeing and transparency variations during the observations. The systematic vertical offset is due to the iterated background subtraction. The difference in total number of detected sources on the other hand can be attributed to the optimal weighting scheme. The effect is separated in the *right panel*, which shows the results of the best final image (black) and the non-weighted image (red). The limiting magnitude is significantly improved by the weighting and the total number of detected sources can be boosted by as much as 30–40% in fields with strongly varying conditions.

The effect of the *iterated background subtraction* is quantified in the upper left panel of Fig. 7.7 where the difference photometry with and without the second reduction loop is shown against the total object magnitudes. For both images the measurements were performed in the exact same apertures by using a common deep multi-band detection image (see Sect. 7.4.1), *i.e.* any offsets are due to object flux differences. No measurable effects would thus imply zero offsets (dashed null line), and more object flux after the iterated loop will manifest itself in a positive magnitude offset (the brighter, *i.e.* smaller, magnitudes are subtracted). The measurements for all objects are plotted as black dots, for the cluster members in Fig. 7.6 as blue circles, and the median averaged differences in 0.5 mag bins are traced by the green solid line. Following this line shows practically matching magnitudes out to $H \sim 15$, which is expected due to the photometric calibration procedure using bright 2MASS stars as discussed in Sect. 7.4.2. At $H > 16$, the recovered flux from the iterated background subtraction becomes noticeable, *i.e.* the magnitudes are systematically brighter, which increases to a median difference of 0.1–0.15 mag (about 10–15% in flux) between H magnitudes of 18–21. At $H > 21$ the averaged difference drops back to zero reflecting the depth of the object mask which does not cover the faintest sources anymore. Note that the recovered flux is drastically increased for the cluster galaxies (blue circles) compared to the median difference. The difference for the bright cD galaxy with its extended halo is 0.1 mag and in the important regime between $18 < H < 21$ the effect grows to 0.2–0.4 magnitudes or equivalently to approximately 20–40% in flux. This pronounced effect for the cluster environment, *i.e.* for the main science applications, has two reasons. (i) Most cluster galaxies are faint extended low surface brightness objects and (ii) the large halo of the central cD galaxy biases the background modelling in its vicinity, which is the main contribution for this particular environment.

The effects of *fractional pixel offsets* and the *optimal weighting* are investigated in combination, since both optimizations only improve the signal-to-noise ratio of faint sources but do not change the flux of the objects. This can be seen in the right panel of Fig. 7.7 where now the difference photometry is applied to the fully optimized image (lower right panel of Fig. 7.6) and the non-weighted version (lower left panel of Fig. 7.6). The median net flux differences is now consistent with zero and the increased scatter at the faint end can primarily be attributed to photometric measurement errors dominated by the image with lower SNR.

The main contribution of the stacking procedure using *fractional pixel offsets* is the improved reconstruction of the natural seeing-limited point-spread function (PSF). In Fig. 7.6 this is best seen for the stellar source at the right edge center of the panels and the fainter galaxies which change from box-like object cores in the left panels to symmetrically round PSF shapes (for the star) on the right. The recovered natural PSF shape is also the most compact flux configuration with an expected improved FWHM of approximately the average displacement error of $\mathcal{O}(0.1'')$. On the other hand, the implemented *fractional pixel offset* scheme introduces correlated noise, since the flux from a single independent pixel is now distributed onto four pixels of the master grid. A main concern would be spurious detections introduced from correlated single pixel noise, *e.g.* an uncorrected cosmic or flickering pixel, that passed the object detection threshold of at least four adjacent pixels

more than one standard deviation above the background (see Sect. 7.4.1). However, for a stacked sum of only ten images (typically 20–80) this would already require a single image pixel-noise outlier of $\sigma_{\text{single}} \gtrsim 4\sqrt{10} \approx 12$ above the background, which implies that it would have been easily detected and removed by the *cosmics* removal procedure. Even a constantly hot pixel not included in the *bad pixel mask* would most likely not lead to a spurious source since (i) it would show up in the sky model and be subtracted with it, and (ii) these outliers would again be removed from the *cosmics* routine since they do not align in world coordinates. In conclusion, the *fractional pixel offsets* procedure is not expected to cause any significant number of spurious source detections through correlated noise.

The last step towards the maximally achievable image depth is the implemented *optimal weighting* scheme. The measurable effects of this optimization strongly depend on the variability of the observing conditions according to Equ. 7.3. However, since the execution time per field and filter is typically 30–80 min long, changes of the external conditions are likely, leading to significant improvements if weighting is applied. Variations that modulate the weighting factors include (i) pronounced background changes at the beginning or end of the night or due to the moon setting or rising, (ii) transparency drops induced by partial cloud coverage, and most sensitively (iii) seeing variations in the atmosphere or the telescope dome, *e.g.* if the primary mirror is warmer than the ambient air.

The optimization of the signal-to-noise ratio at the faint source end has two important effects. Firstly, objects can be characterized with higher photometric accuracy, *i.e.* the measurement errors decrease. Secondly, very faint formerly undetected sources are now pushed over the detection limit requiring a minimum fixed SNR. This latter effect is of particular importance since the total number of sources increases rapidly with the flux limit as $N_{\text{tot}} \propto f_{\text{lim}}^{-3/2}$ (Equ. 3.26) and allows to probe the galaxy luminosity function in clusters to fainter levels. The number counts for a field observed under strongly varying conditions in the lower right panel of Fig. 7.7 illustrates the achievable gain. The black curve shows the detection results for the image with the applied *optimal weighting* scheme, the red line gives the outcome on the non-weighted image. Up to $H \lesssim 20$ the number counts are basically identical but at $H \sim 20.5$ the red non-weighted curve turns over and reaches its plateau. The black weighted line on the other hand exhibits a significantly improved limiting magnitude, which in turn boosts the total number of detected sources for this field by almost 40% at no extra observational cost. The depth optimization via *fractional pixel offsets* and *optimal weighting* thus takes effect in the magnitude range $20 \lesssim H \lesssim 22$, which includes about half of all detectable sources.

For comparison, the lower left panel of Fig. 7.7 shows the number counts in the same field but with the first loop non-weighted (quicklook) image used for the red line. The number counts now exhibit a systematic vertical offset starting at $H > 16$ due to the discussed *iterated background subtraction*, which is the consequence of the objects being systematically brighter, hence more sources exist at a given fixed magnitude.

In summary, the implemented optimization schemes¹⁷ for the science-grade reduction

¹⁷The faint object optimization effects in this section have been discussed using H-band data, since this is the master filter for the Z–H imaging strategy. The achievable improvements scale with the background

pipeline have an important impact on the targeted science applications. The *iterated background subtraction* corrects the systematic biasing of the total object magnitudes, whereas the combined effects of the *fractional pixel offsets* and the *optimal weighting* scheme improve the limiting depth of the data. With respect to the intended distant galaxy cluster identifications the achieved improvements are of prime interest. (i) The measured object magnitudes need to be accurate in the full range $16 \lesssim H \lesssim 21$ in order to derive accurate colors and thus allow a red-sequence identification and model comparisons. (ii) The increased number of detected cluster galaxies enhances the cluster signature, eases the evaluation, and increases the redshift grasp.

7.3.4 Pipeline and instrument performance

In this section we will apply the NIR reduction pipeline to real multi-band data of the XDCP follow-up program, compare the achieved depth to the requirements of Sect. 7.1.2, and discuss the expected background object densities. The analysis is performed in the follow-up field North of the cluster of galaxies Abell 383 with deep and a fairly homogeneous data coverage for the bands Z, J, H, and Ks.

Figure 7.8 displays a Z+J+H pseudo-color composite of the study field. The two zoomed regions give an impression of the achievable image quality with OMEGA2000 under good observing conditions. The distortion-free camera optics in combination with the applied reduction schemes yield a homogeneously high image quality over the full FoV, which is demonstrated by the recovery of the subtle gravitational arc at the field edge in the lower right panel.

The observing strategy of Sect. 7.2.2 aimed for a maximum net exposure time of 50 min per filter and field, in particular for the Z–H approach. The A 383 field was covered in all four bands to approximately this exposure time limit and is thus well suited for a cross-comparison. The data includes observations under photometric conditions for 58 minutes in Z, 50 minutes in J, and 50 minutes in the Ks-band. The 60 minute coverage of the H-band has been obtained under non-photometric conditions with partial cloud coverage, hence it provides only lower limits on the achievable depth. We follow Harris’ (1990) definition of a limiting magnitude as the magnitude at which the completeness of detected sources drops to 50% (50%-completeness limit). This limit can be robustly estimated from the differential number counts and corresponds approximately to a 5σ detection significance of the sources.

The cumulative and differential number counts as derived for the central 192 square arcminutes ($13'8 \times 13'8$) of the FoV are shown for all four filter bands in Fig. 7.9. From the differential number counts in 0.1 magnitude bins in the left panels, the 50%-completeness limits are estimated as indicated by the dashed vertical lines. These limiting magnitudes are also shown for the cumulative number counts in the right panels. The normalization to square arcminute units directly provides the surface densities at a given magnitude limit

brightness and the number of individual images to be co-added. For both cases the expected optimization performance will increase with filter wavelength, *i.e.* in the order Z, J, H, Ks.

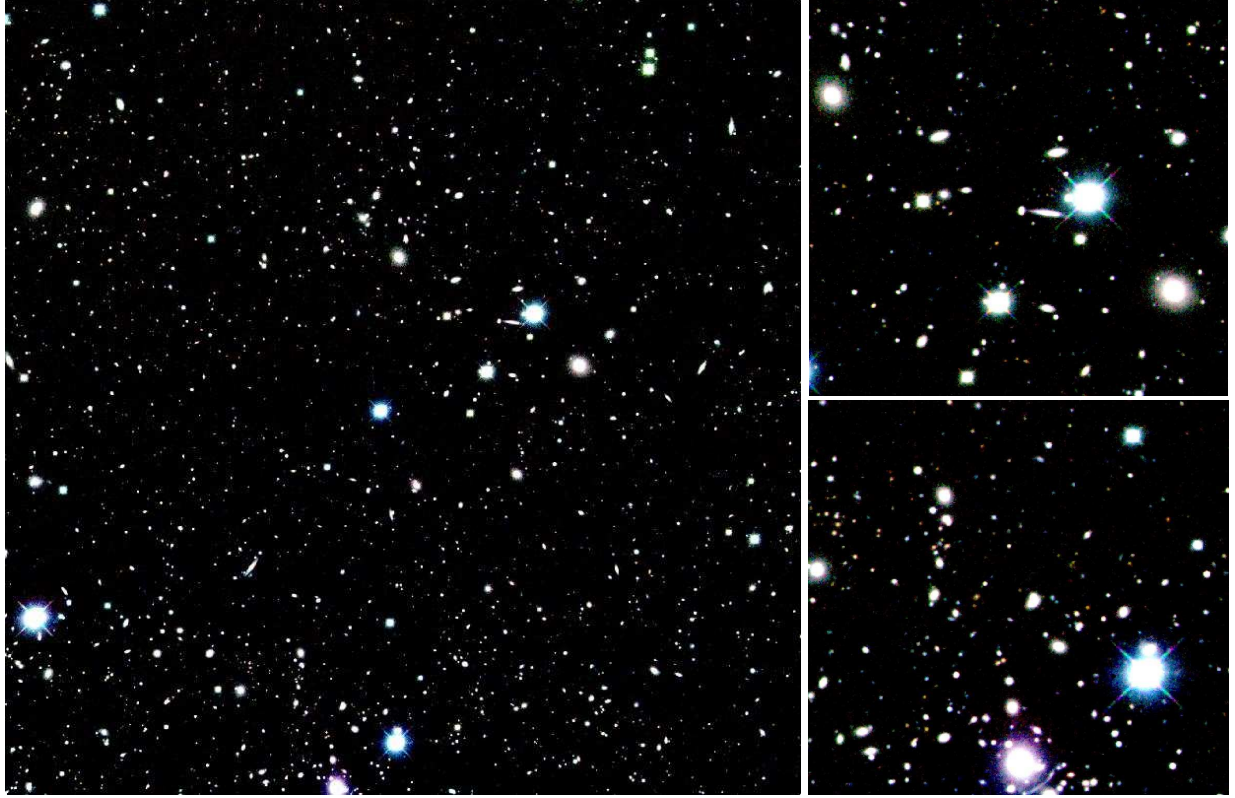


Figure 7.8: Z+J+H pseudo color image of the field North of Abell 383 used for the number counts in Fig. 7.9. *Left:* The full 192 square arcminute FoV considered for the analysis. The cD galaxy of Abell 383 is just visible at the bottom center. *Right:* 4x4 arcmin zoom on the central part of the field (*top*) and the Northern part of Abell 383 with its giant gravitational arc (*bottom*).

given by the dashed horizontal lines for the derived limiting magnitude in each band.

The 50%-completeness limit for the **Z-band** in the top panels of Fig. 7.9 is determined as $Z_{\text{lim}}(\text{AB}) \simeq 23.9$ corresponding to $Z_{\text{lim}}(\text{Vega}) \simeq 23.4$. This limit confirms the expected high sensitivity of the NIR detector array in this last optical band. Comparing to Tab. 7.2 yields expectation values to what extent the Z-band galaxy luminosity function of a cluster will be probed at this maximum depth with respect to the characteristic magnitude m^* . At $z=1$ this corresponds to m^*+2 , at $z=1.5$ to $m^*+0.1$, and at $z=2$ to $m^*-0.8$, revealing $z \sim 1.5$ as the redshift where the maximum Z-band depth falls below the characteristic magnitude. As a related consequence it can be expected that a possible red-sequence at $z \gtrsim 1.5$ will be observable only with large scatter due to the increased photometric uncertainties in the Z-band.

The average background surface source density at the limiting Z-magnitude is 22 arcmin^{-2} . At these densities even a *bona fide* cluster at intermediate redshifts as RX J0018.2+1617 in Fig. 7.6 reaches merely an overdensity of 40% above the background in the cluster center. For a $4' \times 4'$ region centered on the cluster, the overdensity drops to zero and the cluster galaxies completely dissolve in the background of roughly 350 objects

within this sky area. This example illustrates the importance of (i) accurate positional information ($5''$ – $10''$) as provided by the X-ray selection of candidates, and (ii) reliable color information in order to enhance the density contrast and allow a cluster identification.

The number counts in the **H-band** are shown in the third row of Fig. 7.9. The 50%-completeness limit of $H_{\text{lim}}(\text{Vega}) \simeq 21.4$ is routinely achieved in a good fraction of the XDCP fields even with shortened exposure times but better observing conditions concerning the transparency. This limiting magnitude is approximately 1 000 times fainter than the sky surface brightness. The H-band surface density of sources at this limit is 17 arcmin^{-2} and is thus about 20% lower than in the Z-band. At the same time the redshift grasp is greatly enhanced yielding a LF coverage to $m^*+2.3$ at $z=1$, $m^*+1.5$ at $z=1.5$, and $m^*+0.9$ at $z=2$. This implies that the fraction of high-redshift objects is significantly increased in the H-band due to the very moderate redshift dimming of elliptical galaxies and the efficient relative suppression of blue foreground sources at these NIR wavelength. The second important conclusion is that the cluster luminosity function can be sufficiently probed out to redshifts of $z \sim 2$. For the Z–H method this yields the performance expectations that a sufficient number of cluster galaxies will be detectable in the H-band even at $z \gtrsim 1.5$, but that the quality of the color information is decreased due to the photometric uncertainties of the Z-band magnitudes.

The situations in the **J-band** (second row) and **Ks-band** (bottom row) are similar to H and can both probe the cluster luminosity function to about m^*+1 at $z=2$. The deep J-band limit of $J_{\text{lim}}(\text{Vega}) \simeq 23.1$ exhibits a surface density of $\gtrsim 30 \text{ arcmin}^{-2}$. The Ks observations suffered from dome-scattered moonlight in a good fraction of the FoV which manifests itself in the suspicious upturn¹⁸ of the number counts at $Ks \gtrsim 20$. The counts are thus only trustworthy up to a number density of $\sim 20 \text{ arcmin}^{-2}$ at $Ks \sim 20$. A realistic corrected limiting Ks magnitude is approximately $Ks_{\text{lim}}(\text{Vega}) \simeq 20.5$. In any case, the J–Ks method is capable of providing accurate color information out to the highest redshifts and is thus very valuable in conjunction with the Z–H strategy for the identification of the most distant clusters to be found.

In summary, we have shown that the achievable data quality and reduction performance fulfills the depth requirements and expectations of Sects. 7.1.2 & 7.2.2. The applied imaging strategy with maximal net exposure times of ~ 50 min per filter and field is sufficiently deep to provide stand-alone Z–H colors out to $z \sim 1.5$ and has the potential to go significantly beyond this limit with complementary J and Ks observations. The expected surface density of background sources of typically $\sim 20 \text{ arcmin}^{-2}$ in deep XDCP fields emphasizes the need for accurate color information. The procedures for obtaining the final photometry, object catalogs, and pseudo color images from the reduced data will be introduced in the next section.

¹⁸The highest positive spatial fluctuations of the additional scattered light surpass the detection threshold and are falsely interpreted as faint objects.

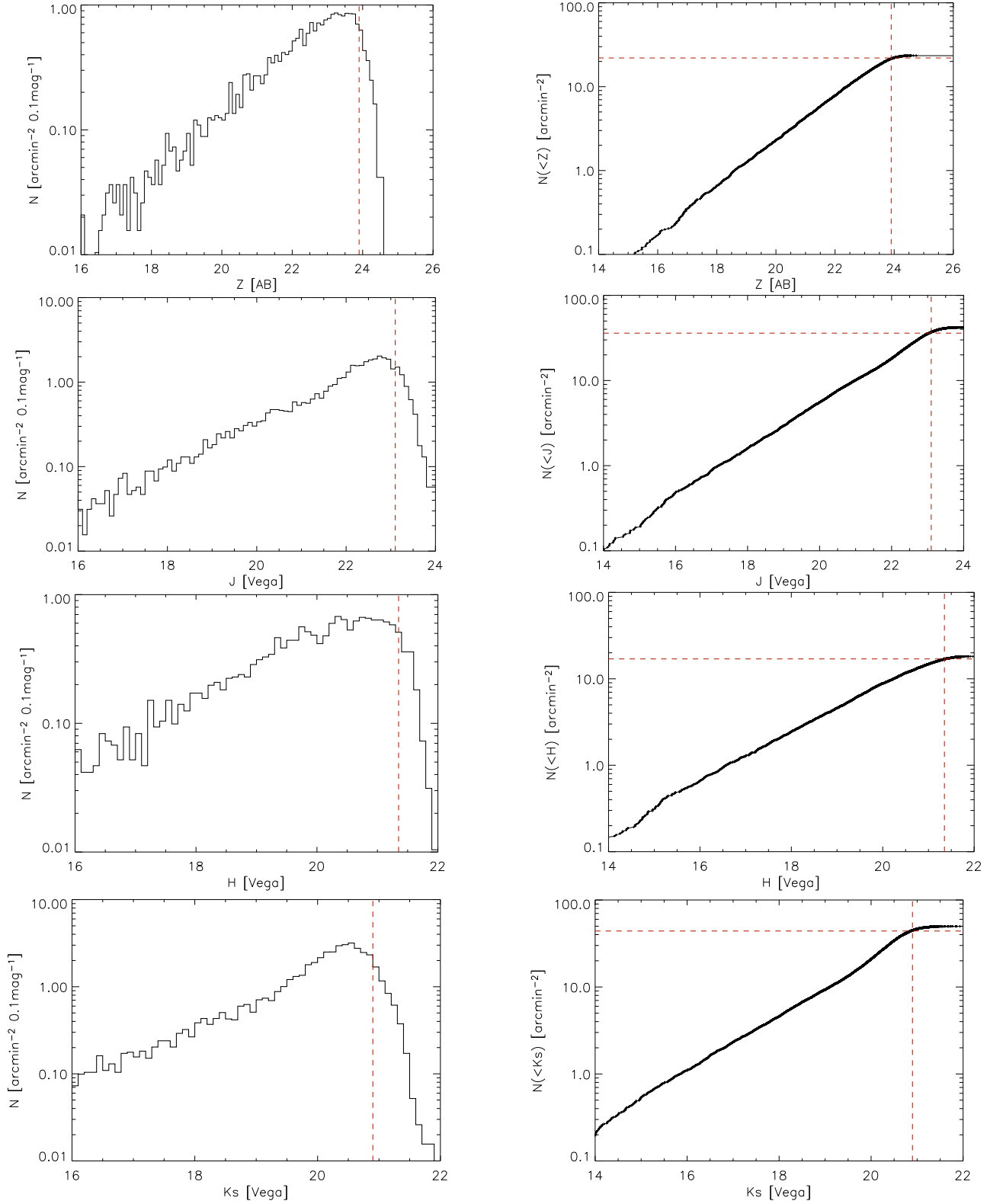


Figure 7.9: Z, J, H, and Ks number counts of the field displayed in Fig. 7.8. Z (58 min), J (50 min), and Ks (50 min) were observed in photometric 1''-seeing conditions, the H-band (60 min) observations were not photometric and suffered from partial cloud coverage, *i.e.* the limit is a lower bound. The *left panels* show the differential number counts in 0.1 magnitude bins. The 50%-completeness limit is given by the dashed vertical line. The log N -log S distributions are displayed in the *right panels*, with the horizontal dashed lines indicating the average total object density at the limiting magnitude.

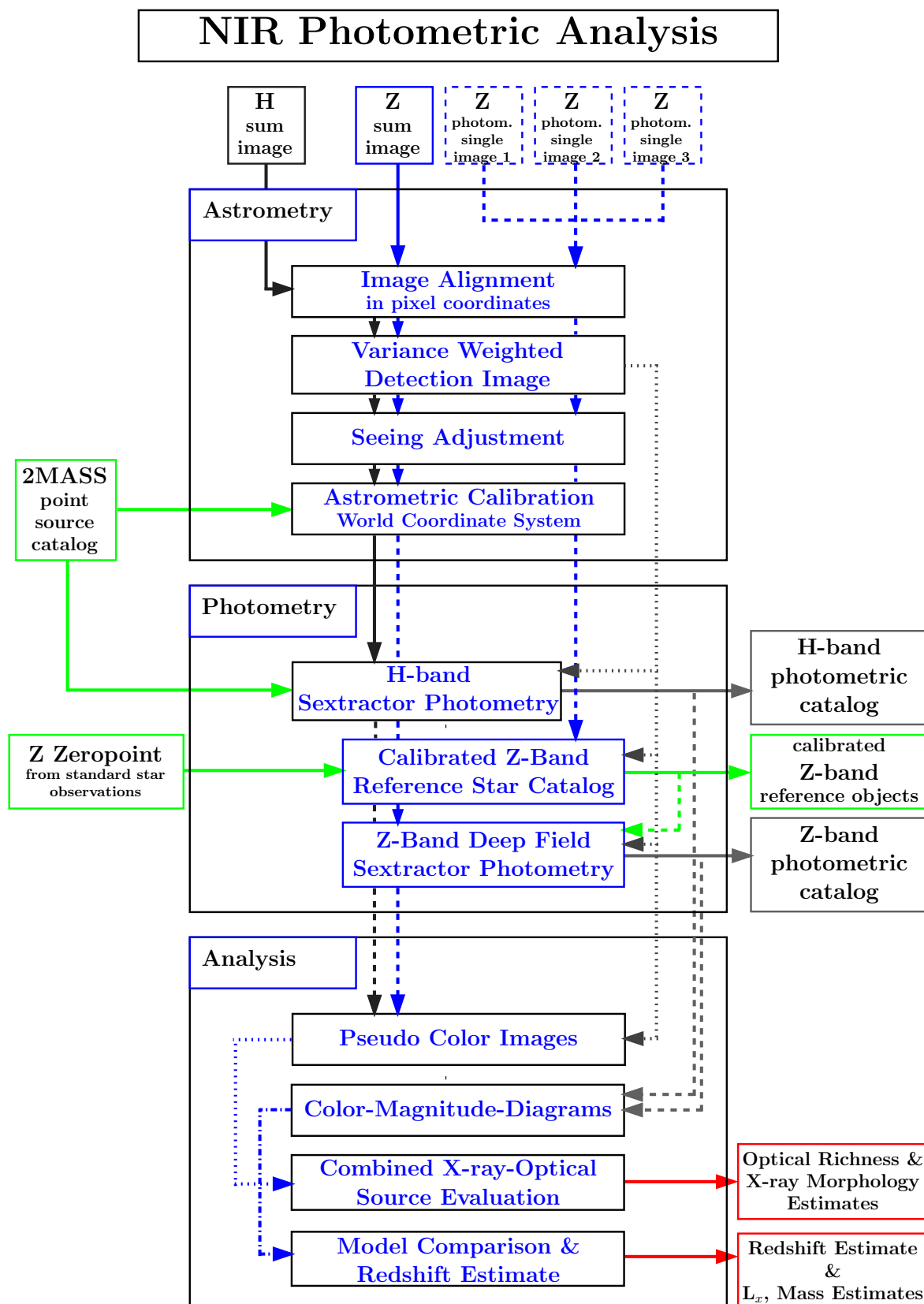


Figure 7.10: Near-infrared photometric analysis flow chart.

7.4 Photometric Analysis

With the final optimized data products from the NIR reduction process in hand, we can now turn to the photometric analysis. The general objective will be the measurement of the cluster red-sequence location with an absolute color accuracy of $\sigma_{\text{color}} \sim 0.1$ mag in order to achieve the redshift accuracies ($\sigma_z \sim 0.1$) as discussed in Fig. 7.2.

7.4.1 General procedure

The generic photometric analysis procedure as implemented for the XDGP follow-up program is illustrated in the flow chart of Fig. 7.10. The analysis process from the image level to final redshift estimates can be subdivided into three main modules: (i) The *astrometry part* during which images are aligned, combined, seeing adjusted, and finally transformed to sky coordinates, (ii) the *photometry module* dealing with object detection, characterization, and calibration for all filter bands, and finally (iii) the *analysis and evaluation section* based on composite color images, color-magnitude diagrams, and comparison to model predictions. The discussion will focus on the constituents of the Z–H method, however, the procedures for complementary J or Ks-band data are analogous to the H-band analysis.

Astrometry

Accurate image alignment in pixel coordinates is a pre-requisite for the source extraction software *SExtractor* (Bertin and Arnouts, 1996) and is performed as a first step. Input images for the alignment procedure are the final deep summed images in the H-band and Z-band, plus additionally three single Z-band images acquired under photometric conditions for the calibration process. In practice, the H image is used as master grid, and all Z-band images are integer-pixel¹⁹ aligned in sky coordinates via object matching and saved with the new coordinate grid. Since this procedure is similar to the summation process in Sect. 7.3.2, the NIR pipeline can be tuned to provide the accurate automatic object alignment in conjunction with a meta script organizing the proper image handling.

During the same process a combined deep detection image DET_{ZH} is created from the variance-weighted sum of the Z and H-band frames as $\text{DET}_{\text{ZH}} = \text{Z} \cdot \sigma_{\text{Z}}^{-2} + \text{H} \cdot \sigma_{\text{H}}^{-2}$, where σ_{Z} and σ_{H} are the measured *global* background standard deviations in the frames. This detection frame serves the three main objectives (i) to maximize the depth and the number of detectable objects, (ii) to provide averaged object profiles for an unbiased²⁰ magnitude and color determination, and (iii) to be used in the green (neutral) channel for color-composite images. This detection frame will be handed over to *SExtractor* for finding sources and determining their source apertures, while the actual measurement is performed in the individual H or Z image. The variance-weighted image combination makes direct

¹⁹Fractional pixel offsets cannot be applied in this case since the Z-band images are only aligned to the master grid, but not co-added.

²⁰Due to possible positional truncation errors during the alignment, detecting sources in H and measuring the magnitude in Z bears the risk of a systematic bias towards fainter Z magnitudes.

use of the deep frames as provided by the NIR pipeline in order to achieve a maximized detection depth, even though the frames might still exhibit different seeing levels. Since there will be no color information without an initial detection of a source, the source detection depth is given priority over the color accuracy.

A fixed measurement aperture applied to images observed under discrepant seeing conditions probes different physical scales of the same galaxy, *e.g.* a $1.5''$ aperture might contain most of the (distant) galaxy light under good conditions while under bad seeing the measured flux will be dominated by the galaxy center. Since elliptical galaxies often exhibit color gradients as a function of distance from the center, the same physical scales need to be considered for an unbiased and well-defined color measurement. The potentially discrepant seeing conditions are adjusted in the next step, where additional smoothing with a Gaussian kernel of radius r_{smooth} is applied to the image with better seeing σ_{good} . Since the standard deviation of the Gaussian kernels add in quadrature, the smoothed frame will have the same effective seeing σ_{bad} , measured as the full-width-at-half-maximum²¹, if the condition $\sigma_{\text{bad}}^2 = \sigma_{\text{good}}^2 + (2.36 \cdot r_{\text{smooth}})^2$ for the smoothing radius r_{smooth} is fulfilled. Measuring the color in these seeing adjusted images ensures a flux extraction from the same physical galaxy scale while maintaining the maximized depth of the detection image.

As a final preparatory step, the aligned and seeing-adjusted images are equipped with a proper equatorial world coordinate system (WCS). The transformation equations from XY image coordinates to the right ascension (α or RA) and declination (δ or DEC) system are obtained by finding the astrometric plate solution from sources in the FoV with accurately known absolute positions. In practice this task can be performed with the *WCS Tools*²² software package which automatically queries the 2MASS point source catalog for reference sources, finds and matches objects, solves for the plate solution via least-square fitting, and updates the image header with the appropriate WCS keywords. Details on the exact transformations and the representation of the world coordinate system in the FITS image header can be found in Calabretta & Greissen (2002).

Source detection and characterization

We can now turn to the actual objective of the imaging enterprise, the detection and photometry of astronomical sources with the focus on faint distant galaxies. This central task is performed with the help of the widely used source extraction and characterization software *SExtractor*. This versatile photometry code detects, de-blends, measures and classifies sources from astronomical images and saves the results in a photometric catalog for further processing.

For the science objectives of deep imaging and accurate colors we make use of *SExtractor's* *dual image mode*. In this configuration, the object search and structural characterization takes place in the depth-optimized variance-weighted detection image, from which the final source list and the individual object extraction regions are determined. The ac-

²¹The relationship between the standard deviation σ and the full-width-at-half-maximum of a Gaussian profile is $\text{FWHM} = 2.36 \cdot \sigma$.

²²The free software is available at <http://tdc-www.harvard.edu/software/wcstools>.

tual photometry measurements, *i.e.* the final source flux determinations, are subsequently performed in the aligned individual filter band images, Z or H, using the exact object position and extraction region information of the input source list. This technique ensures that all objects in all filters have the same photometry areas and apertures appropriate for measuring colors and eases the cross-identification of objects in different catalogs. The pre-requisites for this method, aligned images with the same size, have been fulfilled in the astrometry module. The last requirement of coincident sky areas of the different input images is met by providing external variance maps to *SExtractor* which exclude the non-overlapping dither and pointing offsets of the images from the photometric analysis. For the overlapping region of interest, the variance maps contain estimates of the local noise levels for the individual images. These noise maps are obtained from an empirical variance measurement in a central statistics window divided by the smoothed flatfield to account for variations due to large-scale changes of the detector quantum efficiency. The detection and measurement images, variance maps, the photometric zero point, seeing and saturation level estimates, and other data characteristics are then pipelined to *SExtractor* for the photometry.

In short, *SExtractor* performs the following steps: (i) estimate the background and its local noise properties, (ii) determine whether pixels belong to background or objects, (iii) split up object areas into separate objects, and (iv) determine the properties of each object. A critical component for the detection performance is again the quality of the background estimation, which should be determined from a fine enough grid to account for large-scale variations and at the same time robust enough to avoid local biasing from nearby bright objects. The second crucial set of parameters is related to the threshold for an object detection. As minimal object significance, the implemented threshold requires at least four connected pixels with values higher than one standard deviation above the background noise, which implies a $2\text{-}\sigma$ detection for the limiting case. Since the main scientific interest focusses on the spatial and color distribution of cluster galaxy populations rather than individual faint galaxies, the expected spurious source rate on the percent level is an acceptable trade-off for a deeper coverage. The second shortcoming of the implemented approach is a less accurate determination of the structural object parameters²³ from the combined, and thus averaged, detection image, which is again outweighed by the optimized depth and color information. Finally, the photometric precision and error estimates are compromised somewhat by performing the measurements in the deep sum images, instead of the individual single images, which would allow the object properties to be determined from an ensemble of measurements. The latter approach enables *e.g.* the elimination of cosmic ray events inside the object apertures, but the expected marginal gain does not justify the significant extra effort for red-sequence-based methods.

The last consideration concerning *SExtractor* photometry deals with relating the measurements to the galaxy model predictions. The models specify total apparent object magnitudes for the different filters, which are best matched by the **MAG AUTO** magnitude, for which *SExtractor* applies automatic flexible elliptical apertures to each object in order

²³The expected median image alignment offset of about $0.1''$ between the H and Z frames introduces a slight object ‘smearing’, which decreases the quality of the stellarity index measurement, *i.e.* the point source identification.

to estimate the total flux. For an accurate object color determination, however, the use of a smaller aperture containing only pixels with a sufficiently high signal-to-noise ratio is advantageous over measurements including the low SNR object periphery. This can be achieved in practice through **MAG ISO** magnitudes for the Z–H color determination. These isophotal magnitudes are measured from all connected object pixels above the detection threshold.

Analysis and redshift estimation

The analysis and candidate evaluation represents the last module of the NIR imaging procedure. For this all available information on the cluster candidate are combined into final data products.

For the visual cluster identification, a pseudo color composite image is created from all filter bands. In the common case with only Z and H-band data available, the detection image is used for the third color channel. Color images in general are obtained by overlaying a red, a green, and a blue data channel (RGB colors). Applied to our case, the Z-data is loaded into the blue channel, the detection image into the (neutral) green channel, and the H-band is represented in red. The combined imaging data can be complemented by overlaying the matching X-ray contours and the extracted photometric information for each object.

As the second important diagnostic tool, color-magnitude diagrams are created from the photometric Z and H-band catalogs for the quantitative analysis. The pre-matched object catalogs are read, the Z-magnitudes transformed to the Vega system, and the Z–H isophotal object colors determined. These are then plotted against the total H-magnitude for all objects, and sources within $30''$ and $1'$ -apertures around the centers of cluster candidates are highlighted. As an additional diagnostic the object overdensity with respect to the average background density is computed for the given apertures. No special efforts are taken to separate galaxies from stellar sources since (i) stars are typically easily recognizable in the color composites and can be appropriately taken into account if located close to a cluster, (ii) *SExtractor*'s stellarity classification is less reliable when applied to the variance-weighted detection image, and (iii) the automatic classification breaks down at faint magnitudes anyway.

If a red-sequence is identified for a cluster candidate, the best-fit color estimate can be directly transformed into a redshift estimate based on a formation redshift $z_f=5$ model with solar metallicity (see Sect. 10.1) as shown in the lower right panel of Fig. 7.1. Since the follow-up photometric accuracy is typically not sufficient to trace the red-sequence slope for high-redshift clusters, one has to aim at an average red-sequence color which will be naturally hinged at m^* galaxies as a result of the achievable depth limit.

Combining the cluster redshift estimate with the X-ray flux measurement, an approximate X-ray luminosity L_X and a preliminary mass proxy can be obtained based on the L_X – M scaling relation. The relative galaxy overdensity and red-sequence population additionally yield a first clue on the optical richness of the cluster, and the features in the X-ray morphology might hint at the dynamical state of the system. For an extended cluster

candidate evaluation, the following cluster features can be considered: (i) the presence of a central dominant galaxy (see Sect. 11.1), (ii) a systematic BCG offset from the X-ray center (see Fig. 11.1), (iii) a possible AGN contribution to the X-ray emission, or (iv) the potential coincidence of galaxy and X-ray features such as filamentary extensions (see Sect. 10.2).

We have finally arrived at the initial objective of the two-band follow-up imaging strategy. As survey **step 3**, the presence of a cluster can be confirmed based on the observed overdensity of red galaxies, and for **step 4** a redshift estimate is obtained from the color of the red-sequence. Promising high-redshift candidates are now ready for spectroscopic confirmation as discussed in Chap. 8.

7.4.2 Photometric calibration

We will now come back and discuss the photometric calibration procedure, which was left out in the last section. Due to the different nature of the optical Z-band and the NIR H-filter, the calibration methods differ in both band-passes and will be introduced separately.

2MASS NIR calibration

The 2-Micron All-Sky Survey (2MASS) (Cutri *et al.*, 2003) provides full sky coverage in the J, H, and Ks-band to a minimum depth²⁴ of $J_{\min}(\text{Vega})=15.9$, $H_{\min}(\text{Vega})=15.0$, and $Ks_{\min}(\text{Vega})=14.3$ for $10\text{-}\sigma$ point source detections. The availability of this high quality data set allows a direct and easy cross-calibration to the 2MASS photometric systems via serendipitous point sources of sufficient brightness in OMEGA2000's large FoV.

Since the 2MASS calibration stars with known calibrated magnitudes are in the science data and are only extracted after the observations, they have experienced the same atmospheric extinction as all sources in the field. This implies that airmass corrections as for the Z-band are not needed, and that a calibration is even possible under non-photometric observing conditions. Homogenous extinction across the $15'$ -FoV is the only assumption that is made for the case of low or varying transparency, *e.g.* due to moderate cloud coverage. This assumption is justified in most cases and can be cross-checked by testing for systematic photometric offsets across the FoV. Hence, the H-band calibration has low requirements on the conditions and allows continuing observations even under challenging circumstances.

In practice, the calibration process is achieved through the following steps. (i) The raw photometric H-band catalog²⁵ of the science field is matched to the 2MASS catalog of the bright ($H < 14.5$ mag) point sources in the FoV as was obtained during the astrometric calibration. (ii) The zero point offset of each source is determined by subtracting the instrumental $4''$ -aperture magnitudes from the calibrated H-band object magnitudes in the

²⁴See http://www.ipac.caltech.edu/2mass/releases/allsky/doc/sec2_2b.html. Minimum depth means that this value is achieved for the full survey area, while parts of the sky have a deeper coverage.

²⁵2MASS data products can be downloaded from <http://irsa.ipac.caltech.edu/applications/Gator/>.

reference catalog. (iii) The average effective zero point (ZP) for the observation and its standard deviation is computed via iterated outlier clipping of all calibration sources. (iv) This ZP is provided to *SExtractor* as an additive offset for the second processing which will yield calibrated magnitudes.

The calibration process for a sample field is illustrated in the upper right panel of Fig. 7.11 which shows the distribution of the individual calibration source zero points. The typically 20–80 serendipitous bright 2MASS stars per field provide a zero point accuracy of approximately $\sigma_{\text{ZP}} \simeq 0.02\text{--}0.04$ mag. The upper right panel of Fig. 7.11 demonstrates that the determined zero points do not exhibit a systematic trend with the object color, *i.e.* a color term correction is not necessary.

Z-band calibration

Unfortunately, a 2MASS-like all-sky survey in the Z-band does not exist yet resulting in a photometric calibration process for this filter which requires more effort. The Sloan Digital Sky Survey (SDSS), with 10 000 square degree multi-band imaging coverage in the Northern hemisphere, overlaps with about 15–20% of the XDCP survey fields and thus only allows calibration cross-checks but no substitute for designated standard star observations.

In order to achieve an accurate calibration to the SDSS photometric system, several Z-band standards from the Smith *et al.* catalog (2002) were observed at different airmasses over the course of each photometric night. Since a good fraction of the Z-band science observations were performed in non-photometric conditions, we obtained additional short image series for these fields during the photometric nights resulting in a minimum of five available frames per field for the calibration process. This photometric overlap subsequently allows ‘bootstrapping’ of the calibration for the deep science observation as will be discussed.

Since no experience with the OMEGA2000 Z-band calibration existed before the XDCP program, all necessary calibration information had to be derived from the data. The following photometric transformation equation is considered

$$Z_{\text{cal}} = Z_{\text{instr}} + A_0 - A_1 \cdot X + A_2 \cdot (R - Z) , \quad (7.5)$$

where A_0 is the nightly photometric zero point²⁶, A_1 is the Z-band atmospheric extinction coefficient per unit airmass, and A_2 is a potential color term that could be introduced by a different filter-detector response relative to the SDSS system. The extinction term $-A_1 \cdot X$ corrects the measured magnitudes to the original flux values above the atmosphere, *i.e.* the lost flux due to atmospheric extinction is added.

²⁶The instrumental magnitude is given by $m_{\text{instr}} \equiv -2.5 \log(\text{counts s}^{-1})$. Hence, the zero point is in effect the apparent magnitude of a source for which the instrument-telescope system detected one count per second.

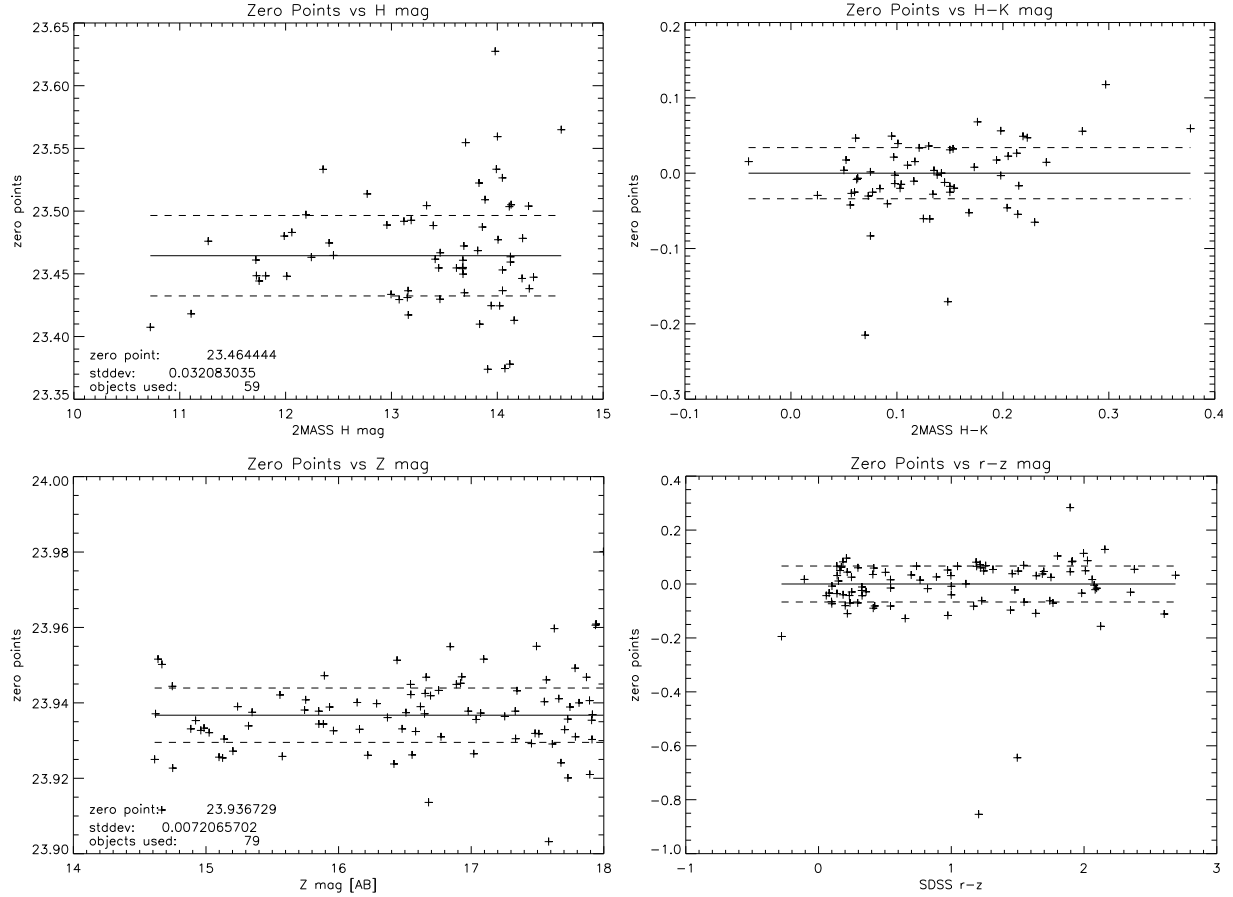


Figure 7.11: Photometric calibration. *Top row:* Photometric zero point calibration in the H-band using bright 2MASS reference point sources in the field-of-view (*left*). The large FoV usually contains several dozen suitable calibration stars for any pointing and allows a zero point calibration to typically $\sigma_H \sim 0.03$ mag. The increased scatter towards the faint end reflects the photometric uncertainties of the shallower 2MASS survey and is the reason for only selecting calibration reference sources with $H < 14.5$. The right panel shows the zero point offset from the mean as a function of the object H-Ks color and illustrates that a color term correction with respect to the reference 2MASS system is negligible. *Bottom row:* Z-band calibration to the SDSS photometric system. Since most XDCP fields do not have direct SDSS coverage, the nightly zero points have to be obtained from Z-band standard star observations, with which a calibrated reference star catalog can be obtained from short photometric exposures of the science field. The catalog is then used to calibrate the zero point in the deep Z-band field in the same manner as for the H-band (*left panel*). The color term check (*right panel*) also yields a correction term that is close to zero.

The available standard star observations were not sufficient in quality and quantity to solve the transformation equation simultaneously for the three unknown parameters A_0 , A_1 , and A_2 . We thus choose the following approach: (i) Determine the color term coefficient A_2 from the best suitable field with SDSS²⁷ coverage. (ii) Measure the extinction coefficient A_1 with fixed color term A_2 for the photometric night with best standard star coverage and use this value for all nights. (iii) Compute the photometric zero point A_0 for each photometric night using the pre-determined values for A_1 and A_2 .

The bottom right panel of Fig. 7.11 displays the zero point offsets as a function of (R–Z)-color for a SDSS calibration field with about 100 reference stars. The color coefficient A_2 is obtained from the slope of the linear regression analysis yielding $A_2 = 0.014 \pm 0.01$ and is thus consistent with zero within the errors. This formal result is good news confirming *a posteriori* that the Z-band NIR instrument response is very similar to the optical SDSS system. The small color term correction on the percent level thus eases the direct comparison of the OMEGA2000 Z-band magnitudes to SDSS reference values.

With the color term fixed at the above value, the extinction coefficient A_1 is determined from data of the highest quality night (10 November 2006). The instrumental magnitudes m_{instr} for the observed standard stars are plotted against the airmass under which the data was taken. The average slopes of these relations for each standard star then yield the Z-band atmospheric extinction coefficient $A_1 = 0.045 \pm 0.01$ per unit airmass. This result is consistent with the values obtained at other observatories and implies that the instrumental Z-band magnitudes are only dimmed by ~ 0.05 mag for observations at airmass two compared to zenith pointings. This moderate extinction, which continues to decrease in the NIR bands, is a manifestation of the atmospheric Rayleigh scattering with cross-section $\sigma_R \propto \lambda^{-4}$. The small extinction correction of $A_1 \cdot X \sim 0.05\text{--}0.1$ also justifies keeping the coefficient A_1 at a fixed value for all nights.

The last unknown parameter for the photometric transformation of Equ. 7.5 is the nightly zero point A_0 . The zero point is obtained by applying Equ. 7.5 to all standard star observations of a given night and using the above values for A_1 and A_2 . Out of the seven photometric nights used for the Z-band calibration, estimated zero point errors of $\sigma_{\text{ZP}} \sim 0.02\text{--}0.03$ mags were achieved for five nights; two nights of service observations turned out to be non-photometric with estimated zero point uncertainties of $\sigma_{\text{ZP}} \sim 0.2$ mags.

We now have all the tools at hand to perform the photometric ‘bootstrap’ calibration of the deep Z-band science fields as illustrated in Fig. 7.10. The approach uses the following steps: (i) The astrometric preparatory module is applied to three single photometric snapshot observations in the same way as the deep Z-band science image, *i.e.* the images are aligned and seeing adjusted. (ii) *SExtractor* source detection is performed on these calibration images in dual image mode with the deep detection image as reference. (iii) The magnitudes²⁸ of the three resulting object catalogs are photometrically calibrated using Equ. 7.5 with the appropriate nightly zero point. (iv) Bright but unsaturated stellar

²⁷SDSS data release5 (DR5) archive data products can be retrieved from <http://cas.sdss.or./astodr5/en/tools/search/IQS.asp>.

²⁸The SDSS *model magnitudes* for m_{cal} of the calibration stars are matched to the measured total MAG AUTO magnitudes for m_{instr} .

sources with $14.5 \lesssim Z \lesssim 18$ are selected. The stars with a maximum magnitude discrepancy of 0.02 mag in all three catalogs are chosen as reference objects and saved in a Z-calibration catalog. (v) This reference catalog with calibrated object Z-magnitudes in the science field is now equivalent to the 2MASS input catalog implying that the same calibration procedure can be applied.

In effect, we have used the standard star observations in combination with the photometric snap-shots to bootstrap a calibrated reference catalog for each field. The discussed NIR calibration procedure is then applied as illustrated in the left bottom panel of Fig. 7.11. The nightly zero point uncertainties of A_0 add in quadrature to the scatter of the reference objects resulting in typical achievable Z-band calibration uncertainties of $\sigma_{ZP} \simeq 0.03\text{--}0.05$ mag.

7.5 Summary

After this long and comprehensive chapter on near-infrared imaging, the main achievements within this thesis work are now summarized:

- Development of a new NIR-based Z–H follow-up imaging strategy;
- PI of a two-semester 10-night imaging proposal to Calar Alto and award of both observing runs with class A priority;
- Led observations at the Calar Alto 3.5 m telescope with 24 nights of on-site presence;
- Co-led a three-night NIR imaging run at the CTIO 4 m Blanco telescope which complemented an optical follow-up program with ten nights of on-site presence (results not included in thesis);
- Development of a versatile NIR science-grade reduction pipeline;
- Development of science analysis tools for red-sequence applications;
- Reduction and analysis of the data from all NIR imaging runs.

Chapter 8

Spectroscopic Follow-up

The spectroscopic confirmation of distant cluster candidates is **step 5** of the survey strategy discussed in Sect. 5.2 and constitutes the observational bottleneck for cluster studies at high redshift. At $z \gtrsim 1$, spectroscopy of cluster galaxies is currently only feasible with very few instruments at 8–10 m-class telescopes, and at $z \gtrsim 1.5$ any study is extremely challenging with the available technology.

The final objectives of the spectroscopic analysis in survey mode are: (i) the confirmation of the cluster as a three-dimensionally bound object, (ii) a precise determination of its redshift, (iii) identification of cluster member galaxies, and (iv) a first estimate of the cluster velocity dispersion. A combination with the available X-ray properties of the cluster enables the derivation of the X-ray luminosity and thus a mass proxy (see Sect. 2.3.4). These physical quantities are crucial for linking the observations to theoretical predictions and hence for the use of clusters as cosmological probes. Further in-depth investigations for individual selected systems (**step 6**) allow (v) the study of the cluster dynamics, (vi) a substructure and LSS analysis, and (vii) detailed investigations of the cluster galaxy population such as derivations of the star formation history, age, and metallicity of individual galaxies.

Since the spectroscopic work for this thesis has been less extensive than the observational data described in the previous sections, this chapter is intended to provide a compact overview¹ of the basic spectroscopic methods and applications.

8.1 Basics of Spectroscopy

Simply speaking, an optical spectrograph consists of (i) a slit aligned to the target in the focal plane, (ii) a collimator, (iii) a light dispersing element, (iv) a camera lens, and (v) a detector. Many modern spectrographs use gratings as dispersing elements, which consist of a combination of a transmission grating and a prism. The latter counteracts the redirection from the optical axis and thus allows compact and linear on-axis arrangements. The

¹A more detailed description of the reduction process can be found in Novak (2003).

principal diffraction maxima of order m at angle θ for light rays with an incident angle i obey the grating equation

$$m \cdot \lambda_{\max} = d \cdot [\sin(i) + \sin(\theta)] , \quad (8.1)$$

where d is the grating constant (slit distance). Taking the focal length ratio f_{cam} of the optical system into account, this translates into the linear dispersion Δl in the detector plane

$$\frac{\Delta l}{\Delta \lambda} = f_{\text{cam}} \cdot \frac{m}{d \cdot \cos(\theta)} . \quad (8.2)$$

The resulting spectral resolving power R of the grating is then given by the expression

$$R = \frac{\lambda}{\Delta \lambda} = m \cdot N, \quad (8.3)$$

with N being the total number of lines. Depending on the science application, the grisms can be optimized (*blazed*) to yield the maximum throughput at a given central wavelength λ_{cen} for the desired spectral resolution R .

The XDCP science goals aim at multi-object spectroscopy of very faint, high-redshift galaxies which requires the use of red-sensitive spectrographs at 8 m-class telescopes. The XDCP instrument-of-choice is the **FO**cal **R**educer and low dispersion **S**pectrograph for the Very Large Telescope, or short VLT FORS2 (Jehin, 2006), a first generation VLT multi-purpose instrument which has been refurbished with red-optimized CCDs providing an average quantum efficiency of about 65% in the critical Z-band. FORS2 offers multi-object spectroscopic capabilities with exchangeable laser-cut slit masks (MXU unit) for a simultaneous coverage of about 30 target spectra within the $6.8' \times 6.8'$ field-of-view. The GRIS.300I+21 grism with a central wavelength of $\lambda_{\text{cen}} = 8600 \text{ \AA}$ and a peak efficiency of 70% achieves a wavelength coverage of 6 000–11 000 \AA with a resolution of $R=660$ or 13 \AA (corresponding to four binned pixels). This setup optimizes the signal-to-noise ratio of the target continuum flux, while still resolving the major spectral object features and the sky emission lines.

The most prominent optical spectral features of galaxies are listed in the left panel of Tab. 8.1. For galaxies without active nuclei, the spectra reflect the underlying dominant stellar populations which depend on the star formation history. As discussed in Sect. 2.4, the centers of clusters are characterized by the highest density of early-type galaxies, with mostly ‘old, dead, and red’ stellar populations dominated by red giants. Owing to the absence of recent star-formation, elliptical and lenticular galaxies exhibit predominantly absorption features in their spectra. The most prominent spectral characteristic of early-type galaxies is the D4000 break around 4 000 \AA . This break is caused by a complex interplay of a large number of absorption lines (*e.g.* Fe I, Mg I, and Balmer lines) in conjunction with the declining continuum of cold stars towards shorter wavelengths. Most notable are the strong H & K resonance lines of single-ionized Calcium originating in the stellar atmospheres of G and K-giants. The D4000 break requires only a moderate signal-to-noise

Feature	Rest Wavel. [Å]	Type	E/S	Sky Feature	Wavel. [Å]	Type
Mg II	2 800	a	E, S	O ₂ B-band	6 867–6 919	a
[O II]	3 727.0	e	S	O ₂ A-band	7 607–7 633	a
Ca II K	3 933.6	a	E, S	H ₂ O	9 400–9 9700	a
Ca II H	3 968.5	a	E, S	[O I]	5 577.3	e
H δ	4 101.7	e or a	S	Na I D	5 892.5	e
CN G-band	4 300.4	a	E	[O I]	6 300.3	e
H γ	4 340.5	e or a	S	[O I]	6 363.8	e
H β	4 861.3	e or a	S	OH ⁻	6 820–7 000	e
[O III]	4 958.9, 5 006.8	e	S	OH ⁻	7 240–7 580	e
Mg I	5 175.4 (blend)	a	E	OH ⁻	7 720–8 100	e
Na I D	5 892.5 (blend)	a	E	OH ⁻	8 290–8 500	e
H α	6 562.8	e	S	OH ⁻	8 760–9 100	e
[S II]	6 717.0, 6 731.3	e	S	OH ⁻	9 300–10 200	e

Table 8.1: Optical spectral galaxy and night sky features. *Left:* Rest wavelength for the most prominent optical absorption and emission lines for early and late-type galaxies. The line type indicates emission lines (e) or absorption lines (a), E (S) means that the spectral feature is predominantly found in elliptical (spiral) galaxies. *Right:* Important telluric absorption lines (*top*) and sky emission lines (*bottom*) as shown in Fig. 8.1. Brackets around the element name mark forbidden transition lines. For more details see Cox (2000).

ratio for identification, shows little contamination from reddening, and does not require absolute fluxes, hence it is the most important redshift indicator for early-type galaxies.

Spiral galaxies have experienced a more recent star formation epoch and thus have hotter stars contributing to the spectra. Their D4000 breaks are less pronounced than in ellipticals and can exhibit emission lines (*e.g.* H α , H β , [O II], [O III]). Also common in clusters are galaxies with active nuclei, *e.g.* Seyfert-type galaxies, which show very strong emission lines. Sample spectra of typical low-redshift cluster galaxies with identified features have been shown in Fig. 4.5.

8.2 Challenges of Distant Galaxy Spectroscopy

The spectral galaxy features with rest-frame wavelength λ_0 are redshifted by the cosmological expansion to the observed wavelength λ_{obs} given by

$$\lambda_{\text{obs}} = (1 + z) \cdot \lambda_0 . \quad (8.4)$$

For $z \gtrsim 1$ objects this implies that the important D4000 break of early-type galaxies is shifted into the I and Z-band, limiting the number of spectral features usable for a secure redshift determination to a few lines with $\lambda_0 < 4\,500 \text{ Å}$ (see Tab. 8.1). At $z \gtrsim 1.5$ the D4000

break is completely lost for optical observations, which marks the onset of the so-called ‘redshift-desert’.

Besides the decreasing number of accessible spectral features, the second observational challenge is posed by the onset of atmospheric contamination in the I-band and in particular in the Z-band. Figure 8.1 illustrates the telluric² absorption (left panel) and the atmospheric emission (right panel) in the wavelength range from 6 000 to 10 000 Å. The visible telluric absorption features in the left panel are caused by O₂ and H₂O. The strong oxygen A-band around 7 620 Å and the B-band at 6 900 Å can easily mimic galaxy absorption features and have to be carefully excised, in particular if object lines are nearby. Towards the NIR, water vapor becomes the principal absorber with the first strong absorption band starting at around 9 400 Å.

The atmospheric emission in the right panel depicts the spectrally resolved reason for the background challenge in the near-infrared, the hydroxyl OH[−] emission. These radicals are produced during the day in an excitation reaction of ozone O₃ and hydrogen H at an altitude of 85–100 km and radiate away their excess energy during the night. The airglow emission becomes dominant beyond about 7 000 Å and is the limiting factor for ground based observation throughout the NIR regime. The so-called *Meinel bands* are easily discernable and correspond to different vibrational molecular transitions, whereas the lines within a band originate from rotational dipole transitions. For comparison, the strong emission lines beyond 8 000 Å have peak fluxes roughly 1 000 times brighter than the continuum of typical $z \sim 1$ galaxies. Sky line residuals will thus manifest a noise limit for the identification of galaxy spectral features.

In order to obtain a sufficiently high signal-to-noise ratio for passive cluster galaxies of candidates at redshifts $1 \lesssim z \lesssim 1.4$, typical exposure times of 2–4 hours are required even with VLT FORS2. XMMU J2235-2557 sample spectra at $z \sim 1.4$ were shown in Fig. 5.1; additional $z \sim 1$ galaxy spectra will be discussed (see Fig. 10.5).

Efficient strategies for the spectroscopic confirmation of the highest redshift cluster candidates at $z \gtrsim 1.5$ have yet to emerge and are currently at the limit of the technological capabilities. In principle, there are two approaches to tackle the problem of $z > 1.5$ redshifts, (i) the classical optical spectroscopy with extremely long exposure times to enable the identification of the weak rest-frame UV features, or (ii) moving to near-infrared spectroscopy in analogy to the imaging strategy.

The optical multi-object spectroscopy approach has been used to probe the general galaxy population in the ‘redshift-desert’ for the Gemini Deep Deep Survey (GDDS) (Abraham *et al.*, 2004) targeting galaxies with redshifts 1–2. Even with typical exposure times of 20–30 hours per field as for the GDDS, a secure redshift determination for passive galaxies is very hard once the D4000 is shifted beyond the probed wavelength range. Owing to the extreme exposure time requirements, the optical spectroscopy approach is not well-suited for routine cluster confirmations of the highest redshift candidates, but is invaluable up to $z \sim 1.5$.

² *Telluric* means in Earth’s atmosphere.

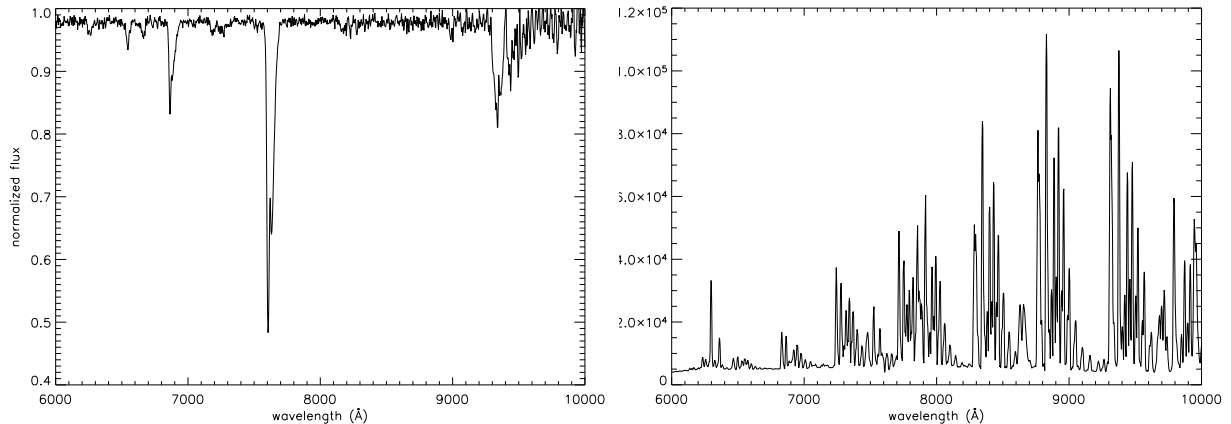


Figure 8.1: Spectral absorption and emission features introduced by the night sky. *Left:* Normalized telluric absorption lines as determined from the analysis of an intrinsic featureless spectrum of a white dwarf. The strong absorption bands around 6900 Å and 7620 Å are caused by atmospheric O₂. *Right:* Night sky emission spectrum dominated by the OH⁺ radical at wavelength above 6800 Å. The different molecular *Meinel-bands* are easily visible. The apparent weakening towards longer wavelength is caused by the decreasing response of the camera system; the intrinsic line brightness continues to grow drastically towards the NIR regime. The lines above 8000 Å exhibit peak flux levels which are approximately a factor of 1000 above the continuum level of typical distant cluster galaxies.

Near-infrared spectroscopy could in principle take over once the 4000 Å rest-frame features are redshifted into the NIR, *i.e.* at around $z \sim 1.4$ – 1.5 . However, several observational and technological issues turn this approach also into a challenging enterprise. (i) The wavelength regimes outside the J, H, and K-band are heavily absorbed by the atmosphere, *i.e.* spectra are not homogeneously probed in wavelength. (ii) The sky emission lines within the NIR bands are so strong and numerous that the identification of the galaxy continuum and its absorption features is very difficult. (iii) Current NIR spectroscopy instruments typically exhibit significant trade-offs between wavelength coverage, spectral resolution, and multi-object capabilities, *i.e.* for optimal instrument settings single object spectroscopy might be required. The technological aspect of the last item will improve significantly over the next few years with several powerful NIR multi-object spectrographs under development or in the commissioning phase. Their performance and application concerning high-redshift passive galaxies with spectral absorption features only is yet to be tested carefully. A possible modified strategy in the NIR regime would be the emphasis on bluer emission line cluster galaxies, resulting in an easier redshift determination at the expense of a less secure object pre-selection, *i.e.* a significant fraction of blue objects will be foreground sources.

In summary, the spectroscopic confirmation of galaxy clusters at $z > 1$ will always be the observational bottleneck for XDCP-like projects. The best currently available optical spectrographs allow routine identifications in survey mode, *i.e.* with reasonable exposure

times, out to $z \simeq 1.4$ – 1.5 . Moving beyond this limit into the ‘redshift desert’ is extremely challenging and will likely require the best new NIR multi-object spectrographs of the near future. In any case, the spectroscopic demands posed by the highest redshift clusters are at the technological limit of 8–10 m-class telescope and will remain challenging for at least another decade.

8.3 Spectroscopic Data Reduction

In contrast to the reduction software developments in Chaps. 6 & 7, the optical spectroscopic data reduction introduced in this section is standard and did not require an extensive customization beyond the available *IRAF*³ reduction routines. Therefore the discussion is kept short with the main aim of providing an overview of the different steps from raw data to the final spectroscopic redshifts.

Figure 8.2 illustrates the principal reduction steps of optical spectroscopy in a flow chart with *IRAF* packages and the main routines indicated. The reduction procedure can be subdivided into three main modules: (i) the general CCD image reduction, (ii) the extraction and calibration of the 1-D spectra, and (iii) the redshift analysis.

The CCD image reduction, as the first module, is similar to some of the basic steps discussed for the NIR pipeline in Sect. 7.3. As additional preparatory steps for CCD images, the frames have to be first trimmed to extract the actual data section, and then bias subtracted in order to remove the pedestal count level featured by CCDs. The additive applied bias voltage offset can be measured from the overscan CCD regions and designated bias frames taken with zero exposure time. The reconstructed master bias frame is then subtracted from the data to yield intermediate products which contain the measured signal values. As a second calibration step, the multiplicative flatfield correction is applied by dividing through the fixed-pattern-noise frame. In contrast to the NIR imaging flatfield, which included the global quantum efficiency variations, the spectroscopic flatfield only contains the local pixel-to-pixel variations since the full spectrum is now spectrally dispersed over the CCD length. In practice, the local pixel-to-pixel sensitivity variations are extracted by dividing the global spectroscopic dome flatfields, taken with the proper slit or mask configuration, by a smooth continuum fit along the dispersion axis to remove the global large-scale modulation⁴ and keep the local median levels to unity. In case a proper flux calibration is required (which is often not necessary for a redshift determination) a correction function along the dispersion axis can be constructed from observations of a spectroscopic flux standard star with accurately known spectral properties. The CCD image reduction is completed by applying the bad pixel correction and summing all individual frames per science target (typically three) to a *cosmics* cleaned final sum image, in analogy to the NIR imaging procedure.

³For software and documentation see <http://iraf.noao.edu>.

⁴The large-scale variations are caused by the detector QE function and the unknown spectral shape of the flatfield lamp.

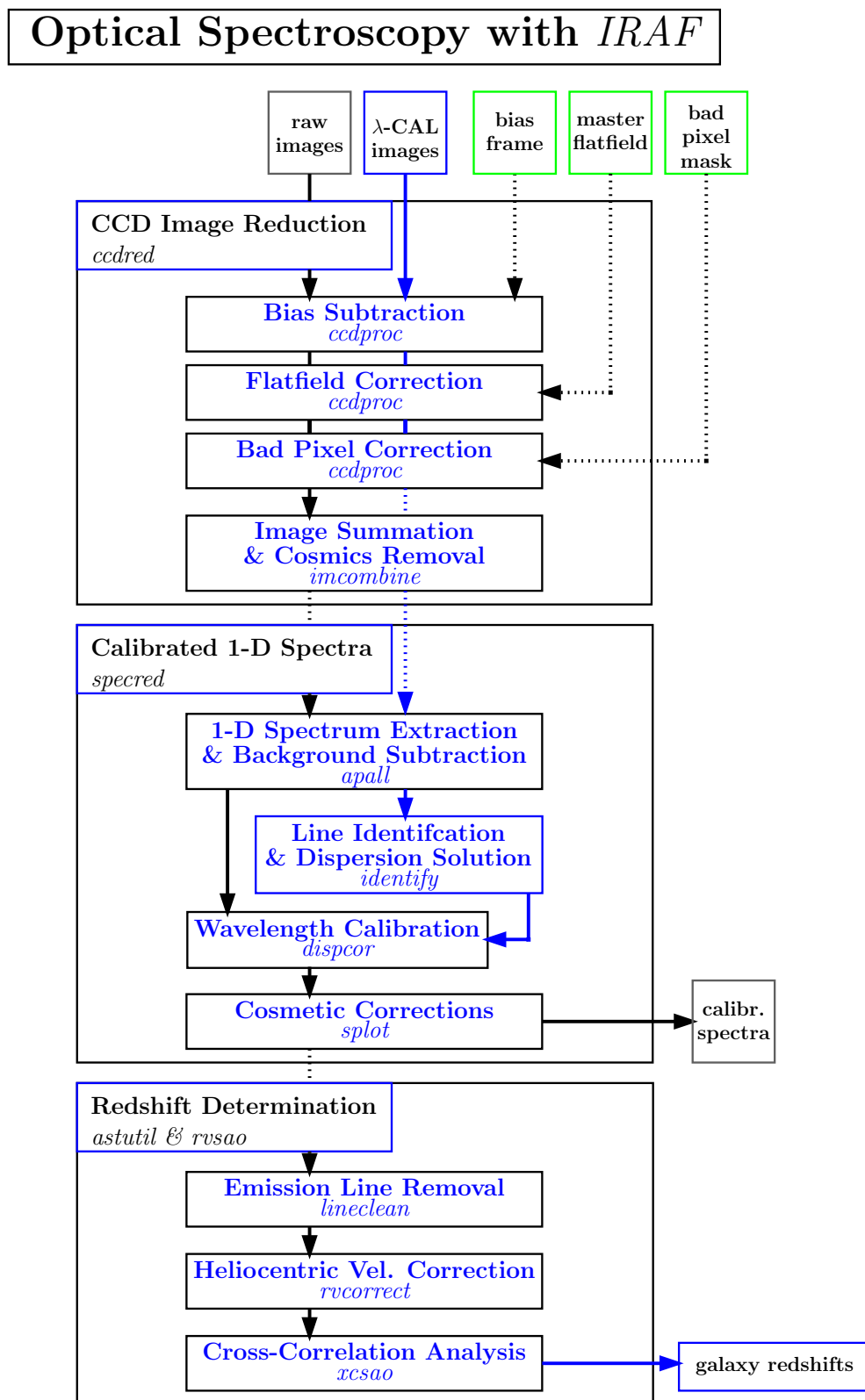


Figure 8.2: Principal data reduction steps for optical spectroscopy with *IRAF*. The employed *IRAF* packages and main tasks are indicated in the corresponding module boxes.

The second module of the reduction procedure in Fig. 8.2 has the main objective of obtaining wavelength-calibrated 1-D spectra from the reduced 2-D CCD images. As a first task, the object spectra with a corresponding accurate background estimation have to be extracted from the CCD image. For each object an extraction aperture with two adjacent background windows is defined by viewing a CDD cut along the spatial direction for every mask slit. These object apertures are traced along the dispersion axis by following the peak of the spatial source profile. The object flux in the defined apertures is then summed in the spatial direction to recover the full source signal. The same procedure is applied to the designated background pixels, where the sky contribution is scaled to the same area per pixel element as the object aperture, and then subtracted to yield raw 1-D spectra with source signal only. Due to the dominating sky emission lines in the red part of the spectrum (right panel of Fig. 8.1), this last sky subtraction step is critical for the resulting signal-to-noise ratio.

The extracted 1-D spectra for each object contain the relative source flux values as a function of image coordinate in the dispersion direction. The next task is to find the exact transformation of the image coordinates to physical wavelength units, *i.e.* to determine the dispersion solution. This is achieved with the help of wavelength calibration observations using an internal Helium-Argon lamp as a source with numerous sharp and well known emission lines spread over the whole spectral range. The calibration lamp data have been taken with the same slit configuration and ideally at the same telescope position as the science target and are reduced in the same way as the target spectra. For the last extraction step, the 1-D calibration spectra are obtained from exactly the same aperture traces along the detector as the science objects, which results in one raw image-coordinate-matched Helium-Argon calibration spectrum for each object. By identifying several dozen calibration lines with their physical wavelength over the full spectral range, the dispersion solution is derived for each spectrum by iteratively fitting a smooth polynomial function to the data points. The final converged functional form for transforming image coordinates to wavelength is now applied to the raw science spectra yielding the final wavelength calibration. After some manual cleaning of sky line residuals, the calibrated 1-D science spectra are ready for the redshift determination of the next section.

8.4 Redshift Determination

In principle, the identification and subsequent wavelength measurement of a single spectral feature determines uniquely the galaxy redshift according to Equ. 8.4. However, for routine survey applications it is favorable to use a more elaborate cross-correlation analysis for several reasons: (i) for passive galaxies the continuum shape and relative position of the spectral features is important; (ii) all spectral absorption features are taken into account and thus a higher accuracy is achieved; (iii) the quality and error of the redshift measurement can be quantified; (iv) the procedure can be fully automated.

The cross-correlation analysis (Tonry and Davis, 1979) uses template spectra with high signal-to-noise ratios as a reference. Since our main interest focuses on absorption line spectra of passive galaxies, good templates for a representative selection of different subclasses of elliptical and lenticular galaxies are of prime importance as a correlation input.

The object spectra for the redshift determination need to be prepared for the correlation analysis in three ways. First, emission lines are removed by replacing the spectral sections deviating more than a given threshold above a smooth continuum fit. This measure is performed since emission lines could originate from physically different locations in a galaxy (*e.g.* H II regions in spiral disks, and galactic winds) compared to the old stellar populations responsible for the absorption features, and could thus have a slightly different intrinsic redshift. Second, atmospheric spectral features need to be excised or removed to avoid an artificial correlation biasing, in particular with the strong telluric absorption lines (left panel of Fig. 8.1). Third, the *heliocentric velocity correction* is to be computed for each observation. With this correction, the stationary reference point for velocity comparisons is placed at the solar system barycenter, *i.e.* the center-of-mass, and takes out the seasonal and nightly velocity modulations of up to $\pm 30 \text{ km s}^{-1}$ due to Earth's motion relative to this reference point.

The input spectra are now ready for the *xcsao* correlation analysis which performs the following simplified steps (Kurtz and Mink, 1998): (i) Object and template spectra are rebinned to a logarithmic wavelength scale in order to achieve redshift independent separations between spectral features. From Equ. 8.4 we arrive at $\ln(\lambda_{\text{obs}}) = \ln(1+z) + \ln(\lambda_0)$ and thus at z -independent logarithmic intervals $d\ln(\lambda_{\text{obs}}) = d\ln(\lambda_0)$. (ii) The spectral continuum is fitted by a smooth function and subsequently subtracted to extract the absorption lines. (iii) The rebinned, continuum-subtracted template and object spectra are Fourier transformed into frequency space, where they are filtered for high and low frequencies beyond the instrumental resolution limits. (iv) The cross-correlation function in wavelength space $c_\lambda(z)$ between object spectrum o_λ and all template spectra t_λ is proportional to the convolution of the spectra $c_\lambda(z) \propto o_\lambda \otimes t_\lambda(z)$, *i.e.* the correlation signal obtained when shifting the template spectrum to redshift z (with logarithmic binning). In practice, the correlation function is computed in Fourier space, where the convolution simplifies to a multiplication of the object spectrum with the template spectra. (v) The location of the highest correlation peak in any of the template correlation functions is interpreted as the proper redshift of the observed spectrum. (vi) From the width of the peak a velocity error estimate is obtained, whereas the peak height relative to the average noise peaks yields a measure for the quality and reliability of the determined redshift.

After cross-correlation redshifts have been obtained for all available object spectra, the galaxy cluster redshift is determined as the outlier-clipped average of all cluster members. An object is classified as a cluster galaxy if its redshift deviates less than 3–4 times the expected velocity dispersion from the median redshift, *i.e.* within typical member selection cuts of about $\pm 3000 \text{ km s}^{-1}$ relative to the average cluster redshift.

As a last application of this chapter, the proper measurement of the cluster radial velocity dispersion is discussed. Following Danese, De Zotti, & Tullio (1980), the spectroscopic cluster galaxy redshifts can be decomposed in three components: (i) the peculiar velocity of the Milky Way z_0 , (ii) the proper cosmological redshift z_R due to the Hubble expansion, and (iii) the galaxy peculiar velocity in the cluster z_G . These components have to be multiplied⁵ (not summed) to yield the observed object redshift z_{obs} according to

⁵The multiplication is intuitive when considering that the cluster velocity dispersion interval is stretched by the cosmological redshift by a factor $(1+z_R)$ as all intervals of observables.

$$z_{\text{obs}} = (1 + z_0)(1 + z_R)(1 + z_G) . \quad (8.5)$$

Neglecting the first term z_0 as a $\mathcal{O}(10^{-3})$ effect and approximating the proper cosmological redshift by the average cluster redshift $z_R \approx \bar{z}$, we are left with the contribution of the galaxy motion within the cluster. This redshift component is to be interpreted as a special relativistic Doppler shift due to the line-of-sight velocity v_{\parallel} of a particular galaxy in the cluster potential

$$1 + z_G = 1 + \frac{\Delta\lambda}{\lambda_0} = \sqrt{\frac{c + v_{\parallel}}{c - v_{\parallel}}} \approx 1 + \frac{v_{\parallel}}{c} + \mathcal{O}\left(\frac{v_{\parallel}^2}{c^2}\right) . \quad (8.6)$$

Since $z_G \ll 1$ for the Doppler shifts of galaxies in clusters, only the first order term needs to be taken into account for the last approximation. Plugging this result into Equ. 8.4 and solving for the line-of-sight velocity v_{\parallel} of a given galaxy yields

$$v_{\parallel} = c \left(\frac{z_{\text{obs}} - \bar{z}}{1 + \bar{z}} \right) . \quad (8.7)$$

The final result for the velocity dispersion of a galaxy cluster with N spectroscopic member galaxies with measured redshifts $z_{\text{obs}}(i)$ is then

$$\sigma_{\parallel}^2 = \frac{c^2}{N-1} \left[\sum_{i=1}^N \left(\frac{z_{\text{obs}}(i) - \bar{z}}{1 + \bar{z}} \right)^2 \right] - \left(\frac{\delta}{1 + \bar{z}} \right)^2 , \quad (8.8)$$

where the last term corrects for the spurious contribution due to the intrinsic average redshift measurement error δ . For a meaningful estimate of the true velocity dispersion σ_{\parallel} a minimum of about ten cluster member redshifts is required.

We have now accomplished the main objectives of **step 5** for the spectroscopic confirmation by measuring an accurate cluster redshift, determining cluster galaxy memberships, and deriving a velocity dispersion estimate. This also completes the technical part of Chaps. 6–8 with discussions on the applied X-ray, near-infrared, and optical observational methods and strategies for the XDCP survey.

8.5 Summary

The main spectroscopy contributions within this thesis work include the following:

- Reduction and analysis of two NORAS 2 spectroscopy runs (see Fig. 4.5) with data of 35 low redshift clusters (results not included);
- Reduction and spectroscopic analysis of a $z \sim 1$ XDCP cluster candidate obtained through DDT time (see Sect. 10.2);
- Led a spectroscopy proposal for the GMOS instrument at the 8m Gemini South telescope with 16 hours of class C time awarded; observations not executed;
- PI of an experimental NIR spectroscopy DDT proposal with Gemini's GNIRS instrument for a high-redshift cluster confirmation; not accepted.

Chapter 9

XDCP Survey Status and Outlook

This chapter summarizes the current XDCP status and provides cluster candidate and survey characteristics. In addition, open survey tasks will be briefly discussed.

9.1 X-ray Analysis Status

The complete detection and identification procedure of serendipitous extended distant cluster candidate sources for the current XDCP survey phase has been discussed in detail in Chap. 6. In this section, a preliminary assessment of the global survey characteristics is provided.

9.1.1 Sky coverage

An essential ingredient for the evaluation of the survey search volume (Equ. 4.2) is the computation of the survey sky coverage as a function of limiting flux. The final determination of the XDCP selection function, *i.e.* the probability to find a cluster with properties $C = [z, L_X, T_X, r_c, M, \dots]$ in the given data set with local characteristics $D = [t_{\text{eff}}, B, \Theta, \dots]$, is a challenging task for XMM-Newton surveys and will require extensive simulations over the next two years (see Sect. 9.1.3). At this point, approximate global XDCP characteristics can be derived based on some simplifying assumptions.

The dashed lines in Fig. 9.1 show the cumulative sky coverage¹ $S_{\text{sky}}(< f_X)$ as a function of limiting 0.5–2.0 keV *point source sensitivity* for the full survey area (blue) and the restricted core survey (black) with a maximum off-axis angle of 12'. The *point source sensitivity* can be evaluated for every XMM field with the SAS task `esensmap` (see panel 6 of Fig. 6.10), which computes the local 3σ point source detection threshold² (DETM) for the combined detectors outside the masked regions from (i) the local background levels B , (ii)

¹ $S_{\text{sky}}(< f_X)$ denotes the total survey area with a detection sensitivity of at least the given flux f_X or better.

²Standard ECF values for a power law spectrum with a photon index of 1.7 and an absorbing column of $3 \times 10^{20} \text{ cm}^{-2}$ are assumed.

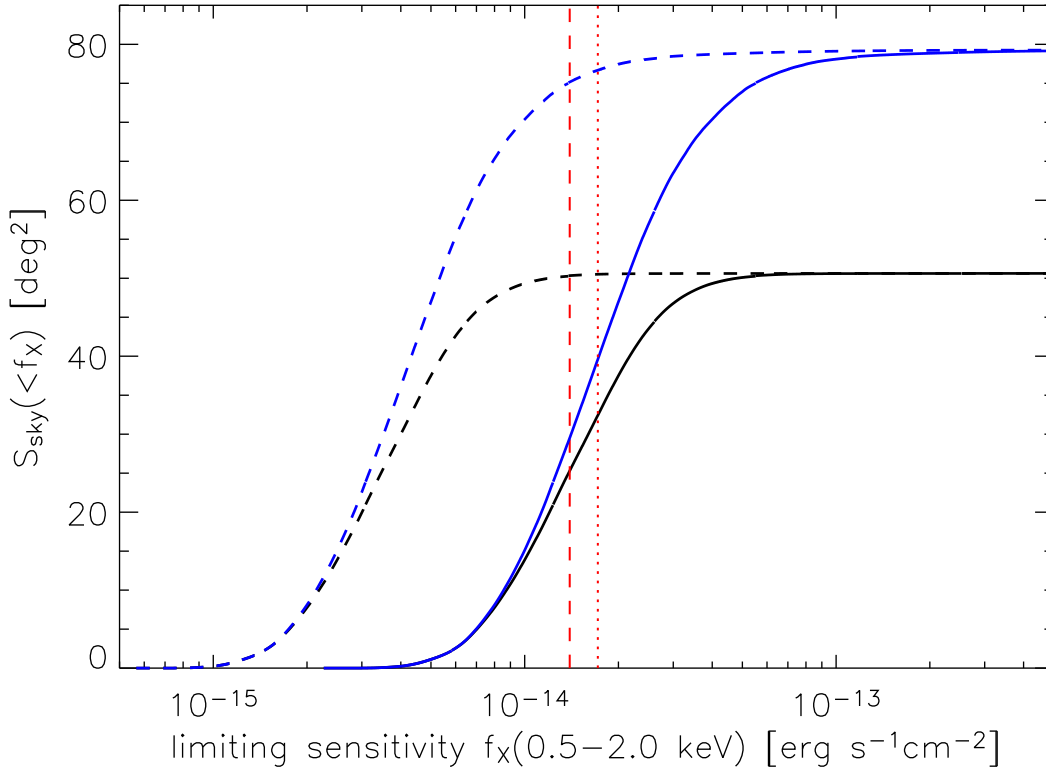


Figure 9.1: XDCP sky coverage. Dashed lines indicate the full survey area (*blue*), 79.3 square degrees in total, and the coverage with a $12'$ off-axis angle restriction (*black*), 50.6 square degrees in total, as a function of limiting *point source* sensitivity in the 0.5–2.0 keV band. Solid lines show conservatively estimated *extended source* sensitivities corresponding to approximately a 4σ extent significance and 100 source counts in the *single* 0.35–2.4 keV detection band. At these levels, to be interpreted as *upper limits*, the median sensitivity for the full area is $1.7 \times 10^{-14} \text{ erg s}^{-1} \text{ cm}^{-2}$ (*dotted red line*), and $1.4 \times 10^{-14} \text{ erg s}^{-1} \text{ cm}^{-2}$ for the restricted core survey region (*dashed red line*).

the effective exposure time t_{eff} at the pixel position, and (iii) the PSF dependent detection aperture at the given off-axis angle. The determined local *point source sensitivities* for each pixel element are then merged for the 469 XDCP survey fields. Sky areas with XMM coverage in multiple observations are corrected for by only retaining the most sensitive value of all overlapping pixels. The resulting *exact* total sky coverage for the XDCP survey is $\mathbf{S_{sky}(\text{tot})=79.3 \text{ square degrees}}$ for the full area and $\mathbf{S_{sky}(\Theta \leq 12')=50.6 \text{ square degrees}}$ for the restricted core survey region. The *point source sensitivity* varies (10–90% of S_{sky}) within the *full* survey (*blue*) by about a factor of five from $2\text{--}10 \times 10^{-15} \text{ erg s}^{-1} \text{ cm}^{-2}$, and by about a factor of 3.5 from $2\text{--}7 \times 10^{-15} \text{ erg s}^{-1} \text{ cm}^{-2}$ for the core survey region (*black*).

Conservative preliminary estimates of the effective XDCP sky coverage as a function of the *extended source sensitivity* can be obtained by applying an empirically determined offset factor to the *point source sensitivity*. At the detection limit, the average *point source* contains a total of about 25 counts in the 0.35–2.4 keV band. Comparing this value to

the identified *extended sources* in Fig. 6.20 and choosing a conservative extended source count number limit of ~ 100 photons, corresponding to about a 4σ extent significance, an average offset factor between the point source detection limit and a realistic reliable extended source threshold of a factor of four is obtained. Applying this empirical offset to the *point source sensitivity* yields a conservative XDCP sky coverage estimate for *extended sources* illustrated by the solid lines in Fig. 9.1.

The median *extended source sensitivity* for the full XDCP survey is then approximately $f_X^{\text{med}}(\text{tot}) \simeq 1.7 \times 10^{-14} \text{ erg s}^{-1} \text{ cm}^{-2}$ (dotted red line) and $f_X^{\text{med}}(\Theta \leq 12') \simeq 1.4 \times 10^{-14} \text{ erg s}^{-1} \text{ cm}^{-2}$ (dashed red line) for the core survey region. The median XDCP survey sensitivities determined in this way are to be considered as conservative upper limits since the empirical offset factor of four compared to the point source threshold is quite large. The question how far the *extended source sky coverage* curves (solid lines) can be shifted to the left, *i.e.* towards lower limiting flux levels, while retaining a high completeness will be answered with simulations in the near future.

9.1.2 Cluster number counts

The cumulative *raw* XDCP cluster number counts in the 0.5–2.0 keV band for *distant cluster candidates* (top blue line) and *all* identified cluster candidate sources (top green line) are shown in Fig. 9.2, where the lighter lines indicate the distribution for a core survey restriction with a maximum off-axis angle of $12'$. This $\log N$ – $\log S$ (see Equ. 3.45) is to be considered as *raw* in the following sense: (i) the number counts are not normalized to a unit solid angle, (ii) the candidate sample still contains *false positives*, (iii) the flux determination is based on fiducial values for the Energy Conversion Factor (see Sect. 6.3.3) and the β parameter (Equ. 2.6), and (iv) fluxes are consistently determined for the PN detector, which is not available for about 10% of the (missing) candidate sources due to a non-imaging operation mode of the PN for this fraction of all observations.

The overall shape of the cumulative number count distribution yields important diagnostic information for the survey sensitivity characteristics. The flux level where the $\log N$ – $\log S$ slope starts deviating from the observed number counts in deeper surveys (see Fig. 4.6) indicates the approximate flux limit of the survey below which the source counts become incomplete. In Fig. 9.2 this estimated XDCP completeness level is represented by the red dashed line at $f_X^{\text{com}} \simeq 1 \times 10^{-14} \text{ erg s}^{-1} \text{ cm}^{-2}$. The $\log N$ – $\log S$ approaches a constant value, *i.e.* no additional sources are found at lower flux levels, at the point where the effective sky coverage of the survey at the given limit drops rapidly towards zero. This approximate minimum survey sensitivity is indicated by the second dashed line at $f_X^{\text{min}} \simeq 5 \times 10^{-15} \text{ erg s}^{-1} \text{ cm}^{-2}$. At the bright end, the observed cumulative number count distribution appears to be (artificially) truncated for the most luminous clusters. This effect can be attributed to two features of the source detection algorithm which (i) has a fixed upper size limit of $80''$ for the core radius in the XDCP pipeline setup and (ii) the intrinsic tendency of the `eboxdetect` task to split very extended cluster sources into several sub-clumps.

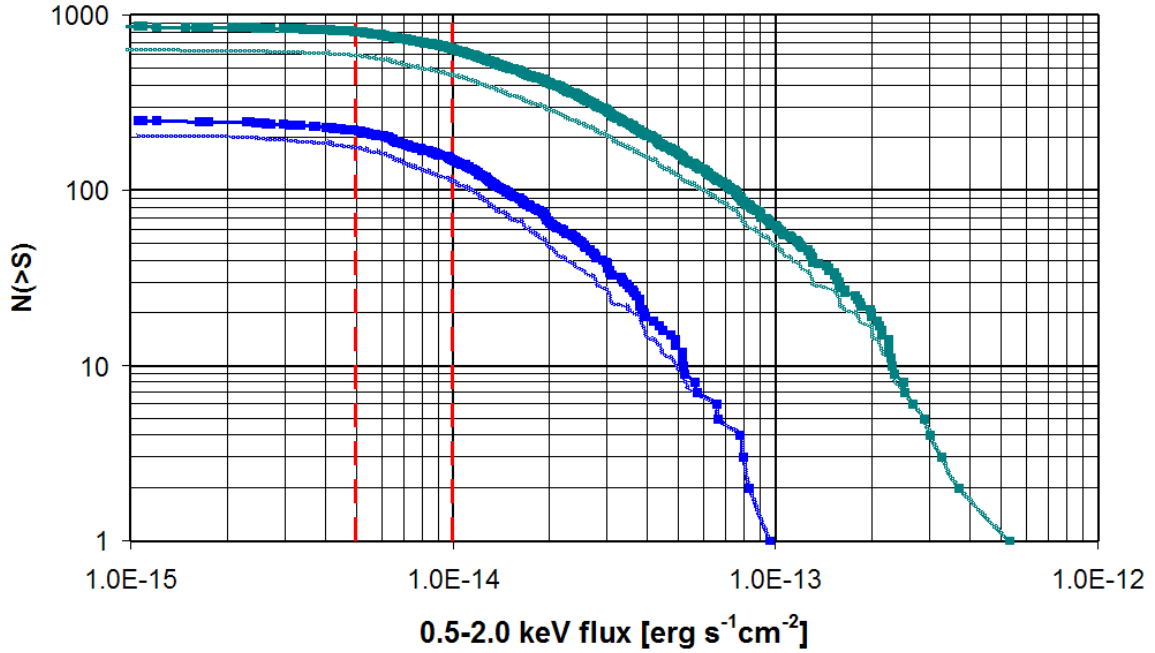


Figure 9.2: Raw $\log N$ – $\log S$ of XDCP candidates and identified clusters. The total number of objects is shown as a function of the 0.5–2.0 keV flux measured for the PN detector, which is available for about 90% of all sources. The green lines display all identified clusters *and* distant candidates for the full XMM detector area (*top green line*) and the FoV restricted to 12' off-axis angle (*lower green line*). The blue lines illustrate the cumulative distribution of the distant cluster candidates only. Vertical red lines indicate the position where the $\log N$ – $\log S$ curves start to turn over at approximately $1 \times 10^{-14} \text{ erg s}^{-1} \text{ cm}^{-2}$ and the flux level where the effective area becomes small around $5 \times 10^{-15} \text{ erg s}^{-1} \text{ cm}^{-2}$.

With the total number of cluster candidates and the survey area available, we can now estimate the observed XDCP galaxy cluster surface density. In total, the full XDCP sample contains 990 unique cluster candidates, 276 of which are *distant cluster candidates* and 714 are *DSS-identified cluster sources*. For the restricted core survey at off-axis angles of less than 12', the 226 distant and 526 DSS-identified candidates make up a combined core sample of 752 sources. Subtracting the approximate *false positive* fraction of 1/3 for distant and 1/6 for low redshift candidates, the expected sample size of *real* galaxy clusters is obtained as ~ 780 for the full region of 79.3 square degrees and ~ 590 objects for the core survey area of 50.6 square degrees. Note that this cluster sample size is comparable to the largest local all-sky surveys (see Sect. 4.2), with the difference that the XDCP survey is not aiming at a full identification of all clusters.

The approximate average XDCP surface density is thus ~ 9.8 clusters per square degree for the overall area and ~ 11.6 clusters per square degree for the more sensitive core survey area with $\Theta \leq 12'$. From the observed $\log N$ – $\log S$ of Fig. 4.6, a cluster surface density of 10 objects per square degree is obtained at a flux limit of $1 \times 10^{-14} \text{ erg s}^{-1} \text{ cm}^{-2}$. The identified combined XDCP cluster candidate sample is thus fully consistent with an average limiting

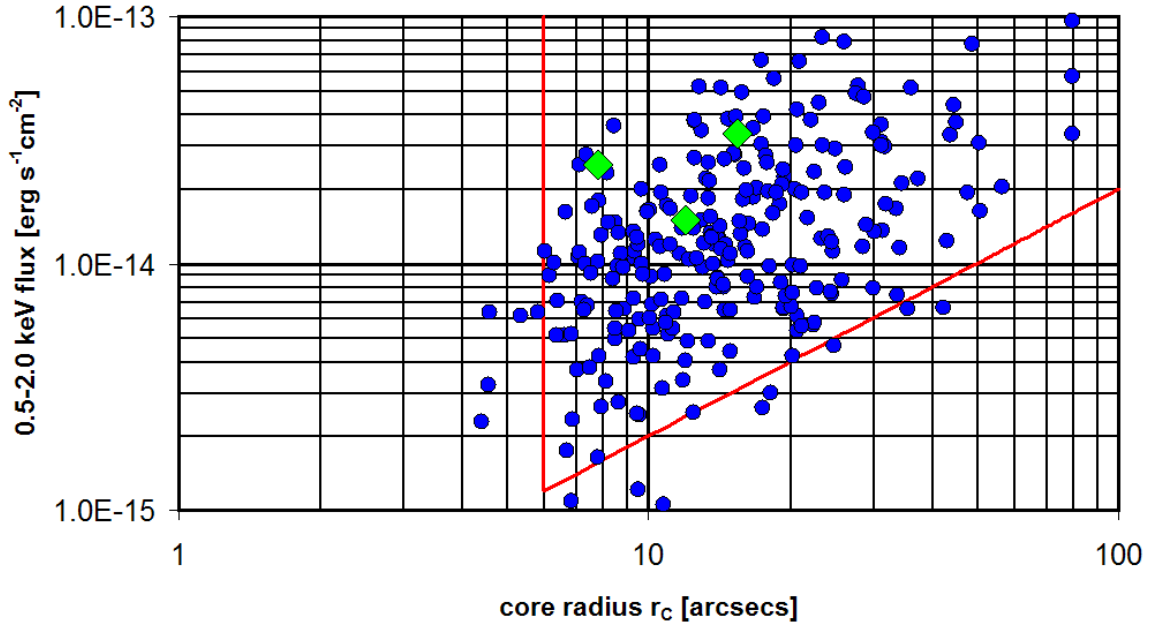


Figure 9.3: XDCP distant cluster candidates in the 0.5-2.0 keV flux versus core radius plane. The parameter space of detected candidates is confined by the XMM resolution limit (*vertical red line*) at core radii of about 6'' and the background limit (*lower red line*), where the cluster surface brightness drops below the detection threshold. Green diamonds indicate the positions of three most distant spectroscopically confirmed clusters in the Southern hemisphere (using the source parameters of the XDCP X-ray pipeline), from left to right: XMMU J2235-25 at $z = 1.39$, XCS J2215-17 at $z = 1.45$, and RDCS J1252-29 at $z = 1.24$, see Sect. 9.5 for references.

sensitivity of $\bar{f}_X^{\text{lim}} \simeq 1 \times 10^{-14} \text{ erg s}^{-1} \text{ cm}^{-2}$ for the full survey area and slightly below this value for the core sample.

The estimated XDCP sensitivity limits from the *raw* $\log N$ - $\log S$ and the total candidate numbers in this section are about 30% lower than the conservative median sensitivities derived in the previous section. This apparent discrepancy originates from the attempt to characterize an XMM serendipitous surveys with a single number, the flux limit f_X^{lim} . The difficulties arising from this concept of a global survey flux limit will be briefly discussed in the next sub-section.

9.1.3 Selection function

In this final section on X-ray properties of XDCP cluster candidates, some important aspects concerning the selection efficiency of serendipitous extended sources with XMM-Newton are summarized.

Figure 9.3 displays the extended X-ray sources of the XDCP *distant cluster candidate sample* in the 0.5-2.0 keV flux versus core radius³ plane (see Equ. 2.6), the two prime source

³Core radii r_c are determined with `emldetect` (see Sect. 6.3.3), *i.e.* using a fixed $\beta = 2/3$.

parameters governing the detection probability. This empirical plot illustrates nicely the two main XMM limitations that constrain the accessible parameter space of distant cluster candidate sources (see Sect. 6.1). The XMM *resolution limit* sets a lower core radius cut-off at about $6''$ (vertical red line), whereas the *background* imposes a limit on the maximum core radius for sources of given flux (lower red line). Note that the currently three most distant spectroscopically confirmed clusters in the Southern hemisphere (green diamonds) are well away from the sample limits, in particular concerning the accessible minimum flux threshold (vertical offset to the lower red line).

The *selection function* characterizes a galaxy cluster survey in terms of the extended source detection probability of clusters with given properties in the X-ray data. The most important *cluster characteristics* with prime influence on the detection rate are given in the following:

Source Flux: For an idealized, homogenous X-ray survey, the flux limit is the *single* characteristic that determines the detection probability of a source. The received X-ray flux f_X in a given energy band depends on the cluster luminosity L_X , the spectral shape governed by the gas temperature T_X , the redshift z , and the galactic hydrogen absorption column N_H . Note that high cluster redshifts lead to severe cosmological surface brightness dimming (Equ. 3.22) and can hence introduce selection biases at faint flux levels, where the surface brightness drops below the signal-to-noise threshold (for a real survey with background).

Core Radius: Once the background surface brightness reaches levels comparable to that of the source, the physical size of the cluster, characterized by the projected core radius r_c ⁴ (see Equ. 2.6), becomes the second prime property governing the detection rate. For further analytical considerations it is important to note that the source flux fraction encircled within the core radius $f_X(r < r_c)$ is constant for β -models, *i.e.* it does not vary with the size of the source⁵. For extended sources whose SB-profiles follow the applied $\beta = 2/3$ model, this fraction is $f_X(r < r_c)/f_X(\text{tot}) = 0.293$, *i.e.* about 30% of the flux originates from the core region.

Cooling Core Activity: Cooling core activity in clusters (see Sect. 2.3.5) is connected to very peaked inner SB profiles with smaller core radii than non-cooling core clusters (*e.g.* Chen *et al.*, 2007). For possible high-redshift CCC, the peaked inner profile can have positive *or* negative effects on the detection probability. Moderate cooling core activity, as found for XMMU J2235.3–2557 at $z = 1.393$ (Santos *et al.*, submitted), increases the SB contrast and hence improves the signal-to-noise ratio. However, if the core radius of a strong CCC drops below the XMM resolution limit, the extended source detection probability drops and the cluster might be missed.

⁴To avoid confusion with the off-axis angle Θ , the notation r_c is used for the projected core radius throughout the following discussion.

⁵This can be shown by integrating Equ. 2.6.

Cluster Morphology: For the detection process, cluster sources are usually idealized as spherically symmetric. This might not be a good approximation (*e.g.* Hashimoto *et al.*, 2005), in particular at high redshifts, where clusters are either dynamically very young objects or are still in the formation process with a high merger frequency (see Fig. 3.4). Deviations from spherical symmetry and in particular cluster substructure will lower the detection probability, since the cluster emission might be mistaken for several point sources.

AGN Activity: If a cluster hosts an X-ray bright AGN, the chance for a misidentification as a point source increases. While only 5% of local clusters have bright AGN close to their center (Böhringer *et al.*, 2004), the point source contamination for high-redshift systems can be significant (*e.g.* Stanford *et al.*, 2001).

The relevant *XMM instrumental and data characteristics* for the detection of faint extended sources have been discussed in Sect. 6.1. As a function of detector position, *i.e.* off-axis angle Θ and azimuth ϕ , the key features are (i) the effective, vignetting corrected clean exposure time $t_{\text{eff}}(\Theta)$, (ii) the PSF FWHM(Θ) defining the minimum resolvable cluster angular size $r_{\text{min}}(\Theta)$, (iii) the background surface brightness $B(\Theta, \phi)$, and (iv) detector defects (*e.g.* gaps, dead columns, hot pixels).

Close to the detection threshold for extended sources, XMM observations are, in very good approximation, always *background limited* (see Equ. 7.1). Assuming that the detection threshold is defined by a minimum signal-to-noise ratio SNR_{min} in a given detection aperture, *e.g.* the core radius of the source, then the limiting flux threshold scales as $f_{\text{lim}} \propto \sqrt{B(\Theta, \phi) / t_{\text{eff}}(\Theta)}$ with the exposure time t_{eff} and the background level B . Similarly, the increased detection aperture of larger extended sources at a given background level has the scaling effect $f_{\text{lim}} \propto \sqrt{\pi B r_c^2} \propto r_c$. This expected linear dependance of the core radius on the detection limit is reflected by the lower red line in Fig. 9.3. *A priori* unknown effects can be taken into account by introducing fudge factors for the cluster AGN and foreground flux contamination of nearby sources $A_{\text{contam}} \gtrsim 1$ and for possible morphological cluster distortions $B_{\text{morph}} \gtrsim 1$. By defining the *local* flux limit as the level where a cluster with resolvable core radius $r_c > r_{\text{min}}(\Theta)$ is detected with a specified probability, *e.g.* 50%, then the combination of all factors yields

$$f_{\text{lim}}(r_c > r_{\text{min}}) \propto r_c \frac{\sqrt{B(\Theta, \phi)}}{\sqrt{t_{\text{eff}}(\Theta)}} A_{\text{contam}} B_{\text{morph}} \neq \text{const} . \quad (9.1)$$

The effective *local* extended source flux limit is hence a function of the XMM field characteristics (t_{eff} , B), the location on the detector (Θ , ϕ), the sky position for contaminating nearby sources $A_{\text{contam}}(\text{RA}, \text{DEC})$, and the cluster properties (r_c , B_{morph}). A single *global* flux limit for background limited XMM serendipitous surveys is hence *not well defined*. The variation of the cluster core radius over typical values in the local Universe of 50-500 kpc already introduces a difference in the limiting sensitivity of one order of magnitude. A stated flux limit for XMM surveys is only meaningful for a specified cluster size, *e.g.* for

core radii of $r_c = 15''$, which can be resolved over the full FoV. All other factors combined cause sensitivity variations across the XDCP survey of approximately another factor of ten from the deepest to the shallowest fields.

The currently best modelled selection function of all XMM-Newton surveys has been provided by the XMM-LSS project (see Sect. 4.3). For the published five square degrees of data with 29 clusters, Pacaud *et al.* (2006, 2007) have determined the detection probability of sources as a function of core radius from simulated data assuming symmetric β -model cluster profiles. As a result, the XMM-LSS survey has abandoned the concept of a *single global flux limit*, for the discussed reasons, and replaced it by *local likelihood thresholds* for the source extent *and* detection significance.

In close collaboration with a team led by Joe Mohr at the University of Illinois, simulation efforts have started to determine the XDCP selection function for each of the 469 survey fields. The final goal is to go one step beyond the XMM-LSS modelling and use *realistic* artificial clusters from high-resolution simulations with different masses, redshifts, morphologies, and dynamical states. These simulated clusters will be placed in mock images that take the XMM-Newton instrumental characteristics into account. After adding background and a point source population that follows the observed AGN number counts, the XDCP detection pipeline will be applied to multiple mock realizations of the same field. From the comparison of the detected extended source list with the cluster input catalog, the completeness and contamination functions can be evaluated for each field as a function of input cluster mass M , size r_c , morphology, and redshift z .

9.2 Imaging Status

The results of the two Calar Alto Z–H follow-up imaging campaigns (Chap. 7) are summarized in Fig. 9.4. In total, data was obtained for 63 *distant cluster candidates*. The redshift distribution for 43 systems with detected optical counterparts is shown in the top panel, based on Z–H red-sequence redshift estimates for most of the sources and some additional available redshifts from the literature (see Sects. 10.1 & 10.2). The red hashed region displays secure cluster detections, the top dashed line also includes systems with lower confirmation confidence, usually attributed to sparse, less obvious red-sequences (if real). Two sources with central galaxy overdensities exhibit an ambiguous color distribution and are not included in the plot. Three objects with counterparts in the H-band still lack Z-band data for a redshift estimate, and 15 X-ray sources were classified as spurious. In combination with a few additional expected non-cluster sources from the lower confirmation confidence sample, an approximate *false positive fraction* of 1/3 is obtained, as was already discussed in Sect. 6.4. A total of **21 cluster candidates** with photometric redshift estimates of $z > 0.9$ were discovered, the 15 secure systems being high-priority candidates for spectroscopic follow-up.

The center panel of Fig. 9.4 displays the redshift histogram of *DSS-identified low redshift cluster candidates* (see Sect. 6.4) that could be imaged together with distant targets at no extra observational cost. As discussed in Sect. 6.4.3, the blue histogram confirms

that a good fraction of clusters out to $z \sim 0.6$ can be successfully identified during the classification procedure, with the positive consequence that the resulting *distant cluster candidate* distribution (red histogram) is skewed towards a peak at $z \sim 0.9$. The large fraction of uncertain identifications at low redshifts (top blue line) is to be attributed to low mass groups with only few probed member galaxies and expected Z–H colors in the CMD regions associated with high background object densities. The lower black panel illustrates the combined Calar Alto cluster sample obtained from the sum of the upper red and blue distributions and five additional XMM target clusters that are not part of the XDCP *serendipitous* cluster catalog.

The observed *distant cluster candidates* at Calar Alto constitute about 1/4 of the complete XDCP sample. XDCP imaging data for about 2/3 of all candidates have been obtained and will likely be extended to 80% by the end of 2007. In total, the XMM-Newton Distant Cluster Project has been awarded with ten follow-up imaging runs at four different observatories making use of four different cluster identification techniques (see Sect. 7.1):

- The pilot study (Sect. 5.5) started with a two semester VLT FORS 2 R–Z imaging program in the years 2003/2004;
- Additional FORS 2 R–Z imaging data of cluster candidates was obtained during two recent runs in 2006/2007;
- The two Calar Alto Z–H campaigns in 2006 have been discussed in Chap. 7, results will be shown in Chap. 10;
- The I–H method has been tested during two runs in 2007 using the SOFI and EMMI instruments at ESO’s New Technology Telescope (NTT);
- A different *multi-band photometric redshift method* using *g r i z* imaging complemented by H-band observations for very distant cluster candidates has been pursued at the CTIO observatory in 2006 and will be continued in fall 2007.

The latter *multi-band* imaging program is being conducted in close collaboration with the group of Joe Mohr at the University of Illinois. The scientific aim of this special XDCP sub-project is the optical identification and characterization of *all* X-ray selected clusters in the SZE survey region of the South Pole Telescope (SPT) (see Sects. 2.3.6 & 12.1). The future SZE coverage of the 106 fully analyzed XDCP fields in the SPT region (red symbols in Fig. 6.5) with a total effective clean XMM exposure time of almost 2 Msec will open new possibilities for joint X-ray-optical-SZE cluster studies. The X-ray selected sample of approximately 200 clusters with multi-band photometric redshifts over a large baseline will allow a detailed survey cross-calibration between the X-ray-based XDCP and the SZE survey of the South Pole Telescope, a critical pre-requisite for the use of distant clusters as sensitive cosmological probes.

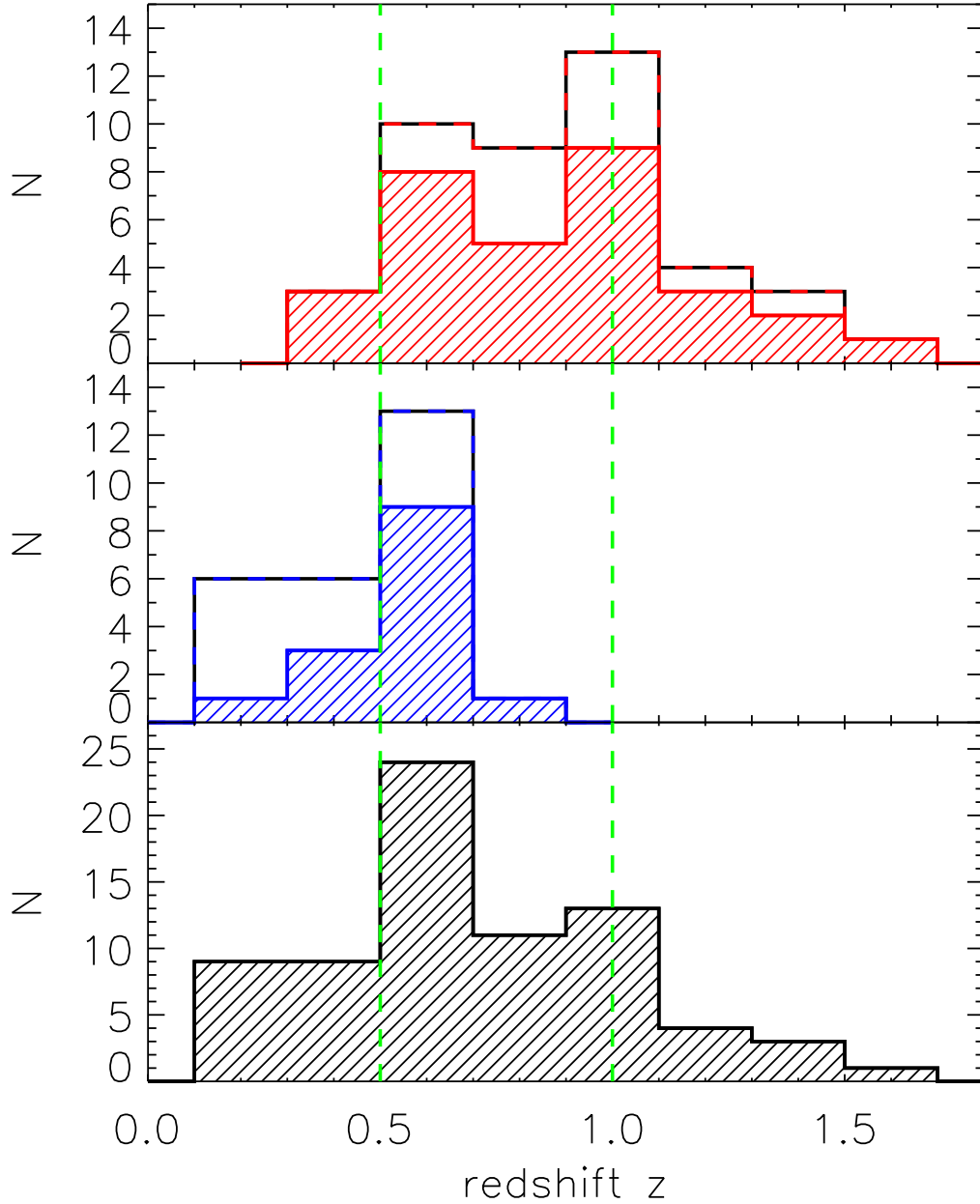


Figure 9.4: Histogram of the final Calar Alto imaging cluster sample based on estimated Z–H red-sequence redshifts. *Top:* Redshift distribution of the targeted *distant cluster candidates* in $\Delta z = 0.2$ bins with a secure photometric confirmation (*red hashed*) and including sources with lower photometric confirmation confidence (*top line*). Vertical dashed lines indicate redshifts of 0.5 and 1.0. *Center:* Distribution of *DSS-identified* cluster candidates that were included in the OMEGA 2000 field-of-view of distant candidates. *Bottom:* Redshift histogram of the combined Calar Alto X-ray cluster sample as the sum of the two upper red and blue curves and five additional XMM target clusters, which are not part of the serendipitous object class. The total Calar Alto sample includes 21 X-ray cluster candidates with photometric red-sequence redshift estimates of $z > 0.9$, 15 of them with a high confidence level.

9.3 Spectroscopy Status

The spectroscopic confirmation of $z > 1$ galaxy cluster candidates is the observational bottleneck of the XDCP survey since it requires the highly competitive use of red-sensitive multi-object spectrographs on 8 m-class telescopes (see Chap. 8). The XDCP status of spectroscopically confirmed high-redshift clusters can be summarized as follows:

- XMMU J2235.3-2557 at $z = 1.393$ was the first spectroscopically targeted XDCP distant cluster in 2004 (Sect. 5.4);
- XMMU J0104.4-0630 was the second followed-up pilot study candidate in 2005 and was confirmed at $z = 0.947$ (see Sect. 10.2);
- Three cluster candidates with estimated redshifts of $z \sim 0.9$ have been spectroscopically observed at one of the 6 m-class Magellan telescopes;
- Four other XDCP distant cluster candidates have been spectroscopically confirmed through other channels and surveys (see Sect. 9.5) at redshifts of 1.45, 0.976, and two at $z = 1.05$;
- Two spectroscopic VLT FORS 2 XDCP programs are currently being executed targeting a dozen high-redshift objects, completing the pilot study program on one hand and starting the confirmation of Z-H selected Calar Alto candidates on the other;
- Spectroscopy time for eight additional FORS 2 observations has been granted for the upcoming semester.

9.4 XDCP Outlook

With the X-ray candidate selection for the current survey phase completed (Chap. 6) and more than half of all XDCP distant cluster candidates followed-up with imaging observations (Chap. 7), the XDCP project focus will shift towards the spectroscopic confirmation of high-redshift clusters (Chap. 8) over the next few years.

The XDCP **X-ray analysis** will change its scope from the search and identification of distant cluster candidates to the detailed characterization of the survey sample. The initiated collaborative project of realistic simulated cluster data (Sect. 9.1.3) will be used to evaluate the *XDCP selection function* in detail. By applying the XDCP X-ray pipeline to simulated cluster fields, the probability for the detection of extended sources as a function of various input parameters (*e.g.* off-axis angle, exposure time, core radius, background) will be quantified in conjunction with the fraction of missed cluster sources (*e.g.* due to AGN dominated X-ray flux, distorted morphologies, compact cores). With this information at hand, the final strict X-ray selection cuts for the XDCP core survey cluster sample will be defined, which will provide the assessment of the associated cluster search volumes for the upcoming cosmological studies.

After a full evaluation of all available **follow-up imaging** data of distant cluster candidates and the different identification techniques, the completion of the final quarter of the two-band photometric identification program of XDCP can be prepared in 2008. The available (and scheduled) optical coverage of the full XMM field-of-view for approximately 20% of the survey overlapping with the SPT region will additionally allow the quantitative assessment of the applied screening procedure of Sect. 6.4, in particular the fraction of *false negatives*, *i.e.* detected real distant cluster sources that were not added to the *distant cluster candidate list*.

The completion of the **spectroscopic follow-up** has the longest time line and will likely require 3–4 more years. The compilation of an X-ray selected, well characterized and spectroscopically confirmed $z \gtrsim 1$ cluster sample over ~ 50 square degrees within this time span will be highly competitive as a prime cosmological tool and as pathfinder sample for several of the upcoming larger cluster surveys (*e.g.* SPT, eROSITA, see Chap. 12).

In principle, the XMM-Newton Distant Cluster Project could be extended in the future on several different scales, provided sufficient man power is available. First, the planned enlargement of the XDCP sky coverage in the SPT region will add approximately 100 additional XMM archive fields to the survey that have accumulated over the past three years. Second, new archival data could be included for the full Southern hemisphere XDCP sample based on the selection criteria discussed in Sect. 6.2, which would increase the number of XMM fields by about 400. The largest sky coverage increase with more than 600 new XMM fields would result from a Northern sky ($\text{DEC} > +20^\circ$) extension of the survey. Suitable efficient follow-up imaging methods applicable for Northern sky observatories have been developed and tested (Chap. 7) and new large facilities, such as the Large Binocular Telescope (LBT), could be involved in the spectroscopic distant cluster work. In total, XMM archival data for a tripling of the current XDCP survey sky coverage up to ~ 150 square degrees has accumulated, but the related work to *fully* exploit this unique data set would fill several more PhD theses in the future.

The highest priority of the XMM-Newton Distant Cluster Project is therefore the completion of the ongoing survey phase and the scientific exploitation of the **first X-ray selected distant cluster sample with $\gtrsim 30$ systems at redshifts of $z \gtrsim 1$** . The top three XDCP science drivers to be addressed over the coming years are (i) the determination of the cluster number density evolution out to $z \sim 1.5$ for constraints of prime cosmological parameters (see Sect. 3.3), (ii) the characterization of evolving cluster properties at $z \gtrsim 1$ as a function of redshift and cluster mass (see Sects. 2.3.3 & 2.3.4), and (iii) the exploration of the cluster galaxy population evolution at large lookback times (see Sect. 2.4). First XDCP results on galaxy evolution in clusters will be presented in Chap. 10.

ID	Object Name	Survey	z	$f_{X,0.5-2.0\text{ keV}}$ erg s ⁻¹ cm ⁻²	$L_{X,\text{bol}}$ 10 ⁴⁴ erg s ⁻¹	T_X keV
1*	XMMXCS J2215.9–1738	XCS	1.45	1.2×10^{-14}	4.4	7.4
2*	XMMU J2235.3–2557	XDCP	1.393	2.6×10^{-14}	11.1	6.0
3	CIG J0848.6+4453	RDCS	1.273	1.0×10^{-14}	1.0	2.9
4	RX J0848.9+4453	RDCS	1.261	1.8×10^{-14}	2.8	5.2
5*	RX J1252.9–2927	RDCS	1.237	2.5×10^{-14}	6.6	6.0
6	XLSS J0223.1–0436	XMMLSS	1.22	6.2×10^{-15}	1.1	3.8
7	RX J1053.7+5735	LH	1.134	2.0×10^{-14}	2.0	4.9
8	RX J0910.8+5422	RDCS	1.106	1.1×10^{-14}	2.5	7.2
9*	XLSS J0224.1–0413	XMMLSS	1.05	3.1×10^{-14}	4.8	4.1
10*	XLSS J0227.1–0418	XMMLSS	1.05	1.1×10^{-14}	1.5	3.7
11	Cl J1415.1+3612	WARPS	1.03	1.1×10^{-13}	10.4	5.7

Table 9.1: Spectroscopically confirmed $z > 1$ X-ray luminous galaxy clusters in August 2007. Specified values for the X-ray flux f_X , bolometric luminosity L_X , and temperature T_X are rounded, see references in text for details. Marked objects (*) in the first column are part of the XDCP distant cluster sample.

9.5 Spectroscopically Confirmed $z > 1$ Clusters in 2007

This chapter on the XDCP survey status is closed with a compilation of all spectroscopically confirmed X-ray luminous galaxy clusters at $z > 1$ published by August 2007. Since the beginning of this thesis work the total number of $z > 1$ X-ray clusters has increased from five to eleven, indicating the advances in the XMM-Newton era on one side but also emphasizing that these systems are still ‘*rare beasts*’.

Table 9.1 lists the cluster names, surveys within they were confirmed, the redshift, and basic cluster properties of the eleven known systems. Five out of six confirmed $z > 1$ clusters in the Southern hemisphere are part of the XDCP distant cluster survey sample indicated by the star in the first column⁶.

Note that several optically selected clusters at high redshift have recently been spectroscopically confirmed, most notable two infrared selected clusters with Spitzer at redshift $z = 1.41$ (Stanford *et al.*, 2005) and at $z = 1.51$ (McCarthy *et al.*, 2007). These clusters are not yet confirmed in X-rays and are therefore not listed in Tab. 9.1.

The references for clusters with identification number [ID] are: [1] Stanford *et al.* (2006), [2] Mullis *et al.* (2005), [3] Stanford *et al.* (1997), Ettori *et al.* (2004), [4] Rosati *et al.* (1999), [5] Rosati *et al.* (2004), [6] Bremer *et al.* (2006), [7] Hashimoto *et al.* (2005), Hashimoto *et al.* (2002), [8] Stanford *et al.* (2002), [9,10] Andreon *et al.* (2005), Pierre *et al.* (2006), and [11] Maughan *et al.* (2006), Perlman *et al.* (2002).

⁶RX J1252.9–2927 was also detected as a *serendipitous* source in addition to the targeted observations.

Chapter 10

High-Redshift Cluster Studies: First Results

The results of the follow-up observations are now used to address some of the scientific questions discussed in the introductory Chaps. 2 & 3. The cluster studies in Chaps. 10 & 11 rely on photometric data obtained during two imaging campaigns at the Calar Alto Observatory (see Tab. 7.5 and Chap. 7). This chapter will focus on early results based on the available sub-sample of *spectroscopically confirmed* clusters.

In Sect. 10.1, the new Z–H method is calibrated with the spectroscopic sample in order to establish a reference model for the red-sequence color evolution and to provide first constraints on the formation epoch of the bulk of the stellar populations in early-type galaxies. This model is the basis for the photometric redshift estimates of the full distant cluster candidate sample.

Section 10.2 presents the spectroscopic, photometric, and X-ray analysis of a newly confirmed galaxy cluster at $z=0.95$. This example provides a first *a posteriori* test for the photometric Z–H red-sequence technique and strengthens its applicability to the cluster identification and redshift estimation.

10.1 The Formation Epoch of Red-Sequence Galaxies

Formation models for ellipticals and implications of the observed red-sequence properties of cluster galaxies have been discussed in Sect. 2.4.2. In this section, we compare observed red-sequence Z–H colors of ten calibration clusters with known spectroscopic redshifts to the SSP model expectations (see Sect. 7.1).

10.1.1 Calibration of the Z–H method

Figure 10.1 displays the observed evolution of the average Z–H red-sequence color as a function of redshift (*blue dots*) together with different model expectations (*solid and dashed lines*). In order of increasing redshift, the following clusters have been used to calibrate

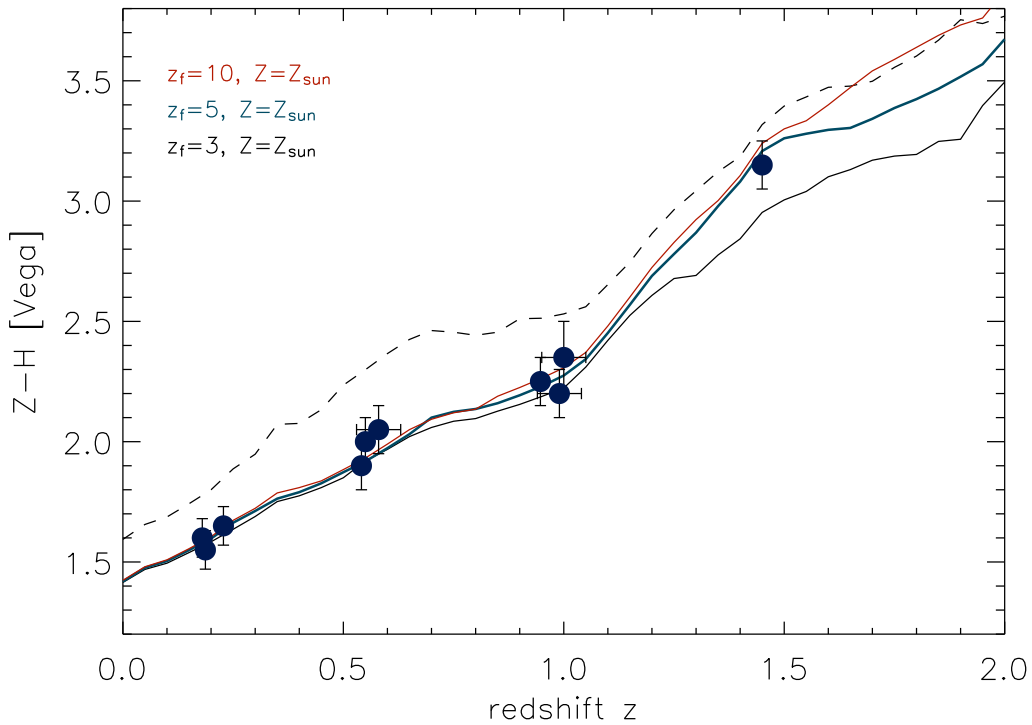


Figure 10.1: Redshift evolution of the Z–H color of red-sequence galaxies. Measured (average) red-sequence colors with 1σ uncertainties for ten galaxy clusters with known redshifts in the range $0.18 \leq z \leq 1.45$ (blue dots) are shown together with different synthetic evolutionary tracks set by different models of passively evolving galaxies (*i.e.* single burst models). Solid lines represent solar metallicity models with formation redshifts $z_f = 3$ (black), $z_f = 5$ (blue), and $z_f = 10$ (red). The dashed black line indicates the color offset for a $z_f = 3$ model with three times higher metallicity. The blue model ($z_f = 5$, $Z = Z_\odot$) has been used to derive red-sequence redshift estimates for all observed cluster candidates.

the model for the Z–H color evolution: WARPS J0943+1644 at $z = 0.180$ (Vikhlinin *et al.*, 1998), A 383 at $z = 0.187$ and A 2390 at $z = 0.228$ (Struble and Rood, 1999), CL 0016+1609 at $z = 0.541$ and RX J0018+1617 at $z = 0.55$ (Connolly *et al.*, 1996), XLSS J0227-0411 at $z = 0.58^1$ (Pierre *et al.*, 2006), XMMU J0104-0630 at $z = 0.947$ (see Sect. 10.2), XMMU J2215-1740 at $z = 0.99 \pm 0.05^2$ (Lamer *et al.*, in preparation), XLSS J0227-0418 at $z = 1.0^3$ (Valtchanov *et al.*, 2004), and XMMXCS J2215-1738 at $z = 1.45$ (Stanford *et al.*, 2006).

As can be seen in Fig. 10.1, the solar metallicity $z_f = 5$ simple stellar population model (blue line) is fully consistent with all measurements. For this reason, the ($z_f = 5$, $Z = Z_\odot$)-

¹An additional redshift error of ± 0.05 has been added, since the spectroscopic redshift appears uncertain.

²Photometric redshift estimate based on deep multi-color CFHT photometry.

³Spectroscopic redshift, but the presence of a second overlapping foreground structure at $z \sim 0.9$ decreases the reliability (see also Pierre *et al.*, 2006).

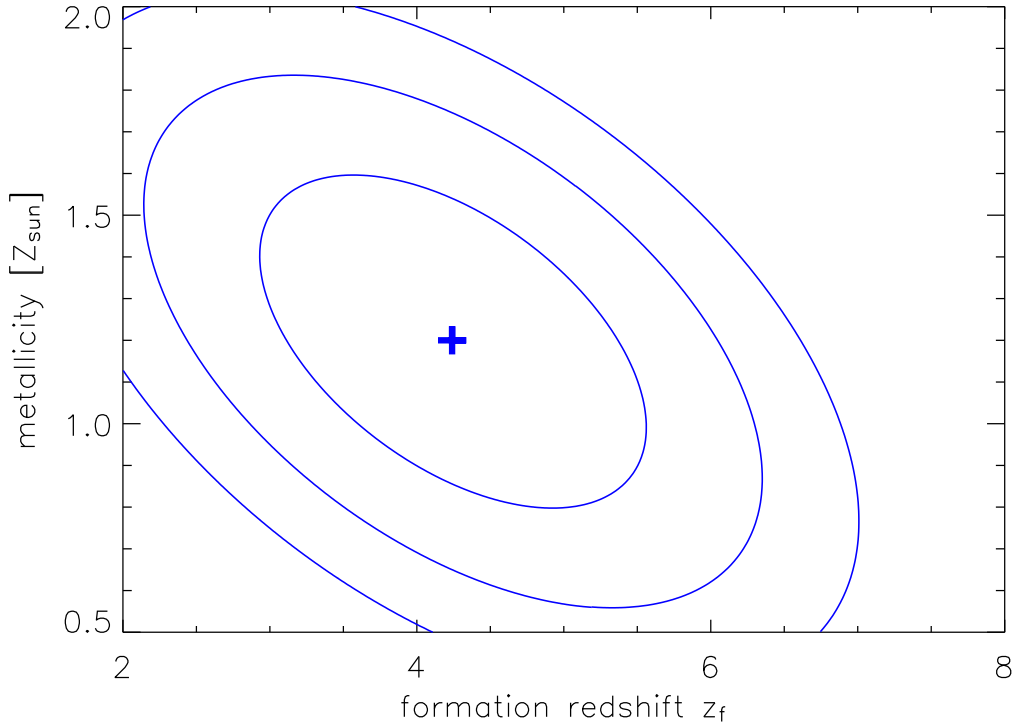


Figure 10.2: Maximum likelihood fit of the formation redshift z_f of passively evolving red-sequence galaxies and their metallicity Z . The long redshift baseline allows simultaneous constraints of both parameters yielding a best fit model (1σ errors) of $z_f = 4.24 \pm 1.1$ and $Z = (1.20 \pm 0.35) Z_\odot$.

model was selected as *master calibration reference* for the photometric red-sequence redshift estimates of all observed XDCP cluster candidates (see Fig. 9.4). The visual inspection of Fig. 10.1 reveals that the discrimination power between the model formation epochs rests upon the highest redshift cluster at $z = 1.45$. This single data point currently excludes a $z_f = 3$ model on the 1.5 – 2σ level, whereas the high-redshift $z_f = 10$ model is still within the 1σ uncertainties.

Nevertheless, the unprecedented redshift baseline for X-ray cluster red-sequence studies in conjunction with the monotonic color-redshift relation of the new Z–H method allow first reasonable simultaneous constraints of the two main formation model parameters z_f and Z . Formation epoch (*i.e.* age) and metallicity are highly degenerate in terms of resulting colors, although they are *independent* model parameters (see lower right panel of Fig. 7.1). Whereas the formation redshift impacts the galaxy colors at high redshifts of $z > 1$, an increasing metallicity results in an almost constant overall reddening of the color. We can hence parameterize the age and metallicity effects as a linear combination of the form

$$M_{\text{SSP}}[z_f = (5+A), Z = (1+B) Z_\odot] \approx M[5, Z_\odot] + A \frac{M[5] - M[3]}{2} + B \frac{M[3 Z_\odot] - M[Z_\odot]}{2}, \quad (10.1)$$

where $M_{\text{SSP}}[z_f, Z]$ denotes the simple stellar population model of formation redshift z_f and metallicity Z used for predicting the Z–H colors as a function of redshift. The ($z_f = 5$, $Z = Z_\odot$)-model is used as reference, and the formation redshift parameter $A \equiv z_f - 5$ and the metallicity offset $B \equiv (Z/Z_\odot) - 1$ allow continuous model variations based on the linear interpolation of the initially coarse parameter grid.

10.1.2 Discussion

The maximum likelihood fit result of the parameterized model to the data is displayed in Fig. 10.2, where the contours define the 1σ , 2σ , and 3σ confidence regions. The best fit values with 1σ errors are $\mathbf{z_f} = 4.24 \pm 1.1$ for the formation epoch of the bulk of the stellar populations of red-sequence galaxies and $\mathbf{Z} = 1.20 \pm 0.35 Z_\odot$ for their average metallicity. The determined direct observational constraint on the formation epoch based on the *Z–H color evolution* is fully consistent with the lower limits obtained from individual red-sequence studies at high redshift (*e.g.* Mei *et al.*, 2006a), the age of high- z massive ellipticals (*e.g.* Dunlop *et al.*, 1996), age measurements of local early type galaxies (*e.g.* Thomas *et al.*, 2005), and the latest high resolution simulation results (De Lucia *et al.*, 2006).

The current constraints are based on only ten clusters with known redshifts. By populating the redshift regime $0.9 \lesssim z \lesssim 1.5$ with the XDCP targets currently scheduled for spectroscopic confirmation, we will soon be able to significantly lower the uncertainties on the cosmic formation epoch of early type red-sequence galaxies in clusters using the Z–H red-sequence method.

Eight⁴ of the calibration clusters over the full redshift baseline together with their color-magnitude diagrams are shown in Figs. 10.3 & 10.4; XMMU J0104-0630 will be presented in Sect. 10.2. The dashed red horizontal lines in the right column indicate the determined red-sequence colors based on the data, dotted red lines illustrate the estimated color uncertainties. Spectroscopically confirmed BCGs are marked by green arrows in images, their corresponding locations in the CMDs are indicated by green circles. Additional confirmed cluster members are circled in blue in Fig. 10.4 for the three calibration clusters with highest redshifts.

In preparation of the preliminary BCG study of Sect. 11.1, a closer look at the spectroscopic sample can provide some observational guidelines for the selection and interpretation of BCGs. The BCG identification for all calibration clusters at $z \lesssim 0.6$ is unambiguous based on the central position in the cluster and the total apparent H-band magnitude. At these low and intermediate redshifts, all case study BCGs are located on the red-sequence within the uncertainties of the color determination, which justifies the assumption that stellar populations of BCGs are passively evolving. The reduced redshift sensitivity of the Z–H method at $z < 0.9$ is partially compensated by the lower color uncertainties of well populated red-sequences.

At $z \gtrsim 0.9$, the observational task of locating the cluster red-sequence for the redshift

⁴The low-mass cluster XLSS J0227-0411 at $z = 0.58$ has the largest uncertainties, *i.e.* the lowest weight, among the calibration objects at $z \lesssim 0.6$ and is therefore not explicitly discussed.

estimate is more challenging. The red-sequences are often sparsely populated, as shown in the lower three rows of Fig. 10.4. However, the redshift leverage of the Z–H color increases (see Fig. 10.1) and the background (black small dots) in the CMD decreases for redder colors. In absence of an obvious sequence, the Z–H color of the red envelope (formed by the filled symbols) promises to be a reliable redshift proxy, as shown for the cases of XLSS J0227-0418 and XMMXCS J2215-1738 in Fig. 10.4. These two case study examples also suggest that BCGs at high redshifts might not sit at the X-ray center and that their color can be slightly bluer than the upper envelope. For the identification of BCGs of high- z clusters based on photometric data only, the spectroscopic sample points at an outer radius of $\sim 30''$ and maximum color tolerances of ~ 0.5 mag as reasonable search constraints.

10.2 Indications for Large-Scale Structure at $z \sim 1$

In this section, the full XDCP survey analysis (**steps 1–5**) is applied to the environment of the X-ray cluster XMMU J0104.4-0630, the second pilot study selected object with available XDCP spectroscopic follow-up data. The relevant background information concerning cluster red-sequences (Sect. 2.4.2) and environmental effects of galaxy evolution (Sect. 2.4.3) have been discussed in the introductory chapter. At the cluster redshift of $z \simeq 0.95$, the lookback time is 7.5 Gyr and one arcsecond corresponds to a physical comoving scale of 7.9 kpc (see Fig. 3.3 & 3.1). The results presented here follow closely the journal letter of Fassbender *et al.* which has been submitted for publication in *Astronomy & Astrophysics*.

10.2.1 Observations

X-ray Data

The galaxy cluster XMMU J0104.4-0630 was selected as a serendipitous extended X-ray source in a high-galactic latitude archival field ($b = +69^\circ$; nominal exposure time: 26.7 ksec; OBSID: 0112650401; here field 1). A second, partially overlapping XMM-Newton observation (nominal exposure time: 24.9 ksec; OBSID: 0112650501; here field 2) extends the X-ray coverage to the South, providing moderately deep X-ray data over a field of about $25' \times 45'$.

The data were reduced following the procedure discussed in Sect. 6.3. High background periods were excluded by applying a two-step flare cleaning procedure first in the hard (10–14 keV) and subsequently in the 0.3–10 keV band following Pratt & Arnaud (2003). The remaining clean exposure times for field 1 (field 2) are 15.1 ksec (13.7) for the EPIC PN camera, 23.2 ksec (19.7) for MOS1, and 23.5 ksec (21.2) for MOS2, resulting in an effective (sensitivity weighted) clean exposure time of about 18 ksec throughout most of the covered field. Images in different bands for the PN and MOS detectors were created from the cleaned event lists and later combined for the overlapping sky region of fields 1 and 2.

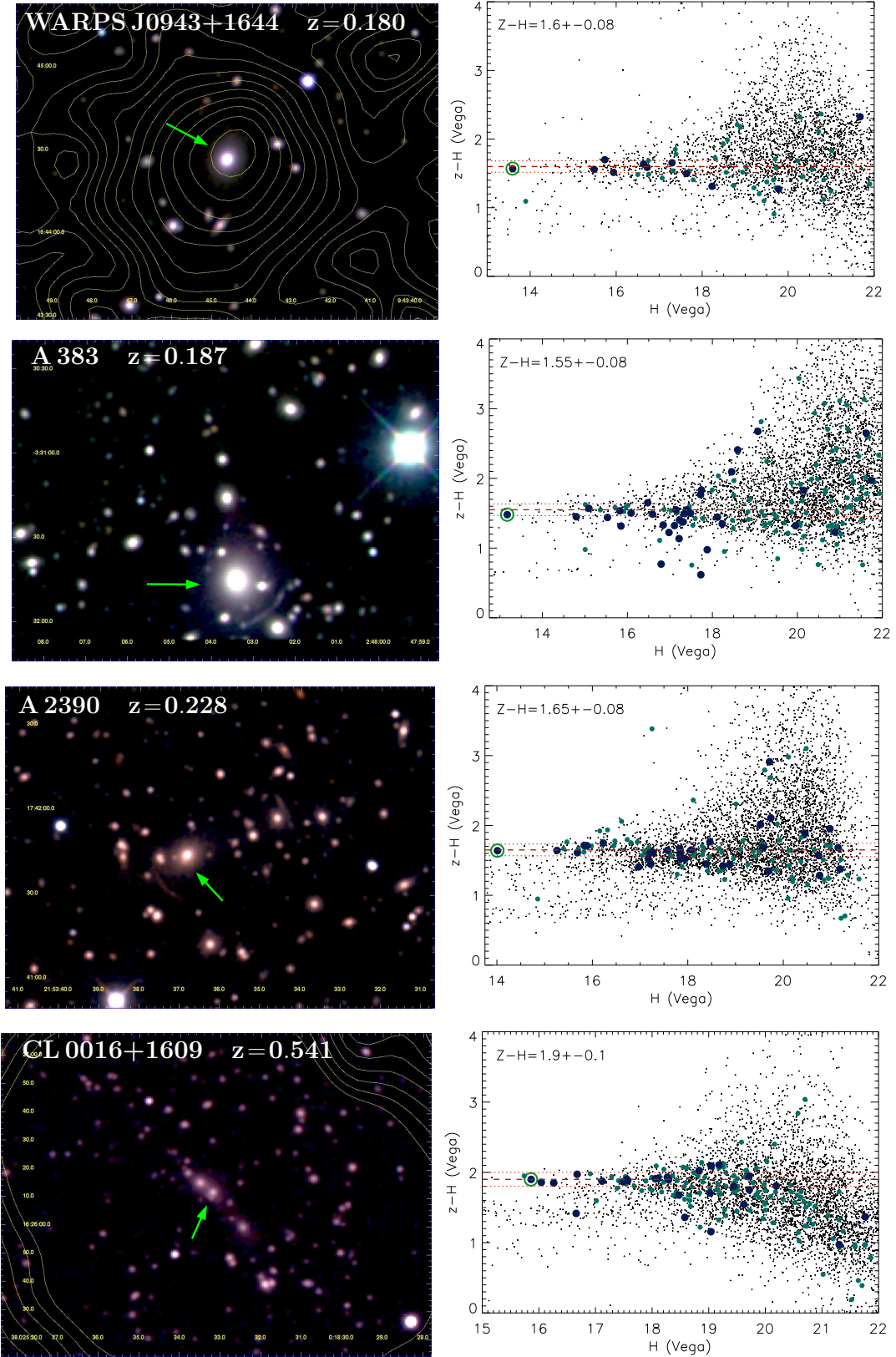


Figure 10.3: $2' \times 2.5'$ image cutouts and Z-H CMDs for the low- z calibration clusters. X-ray contours are shown in yellow and BCGs are indicated by green arrows (left column) or a green circle (right column). The red-sequence color (red dashed line) and the estimated color uncertainties (red dotted lines) are marked. Dark blue symbols represent objects located within a region of $30''$ from the center, smaller green circles objects within $30-60''$, black dots mark all other objects in the field.

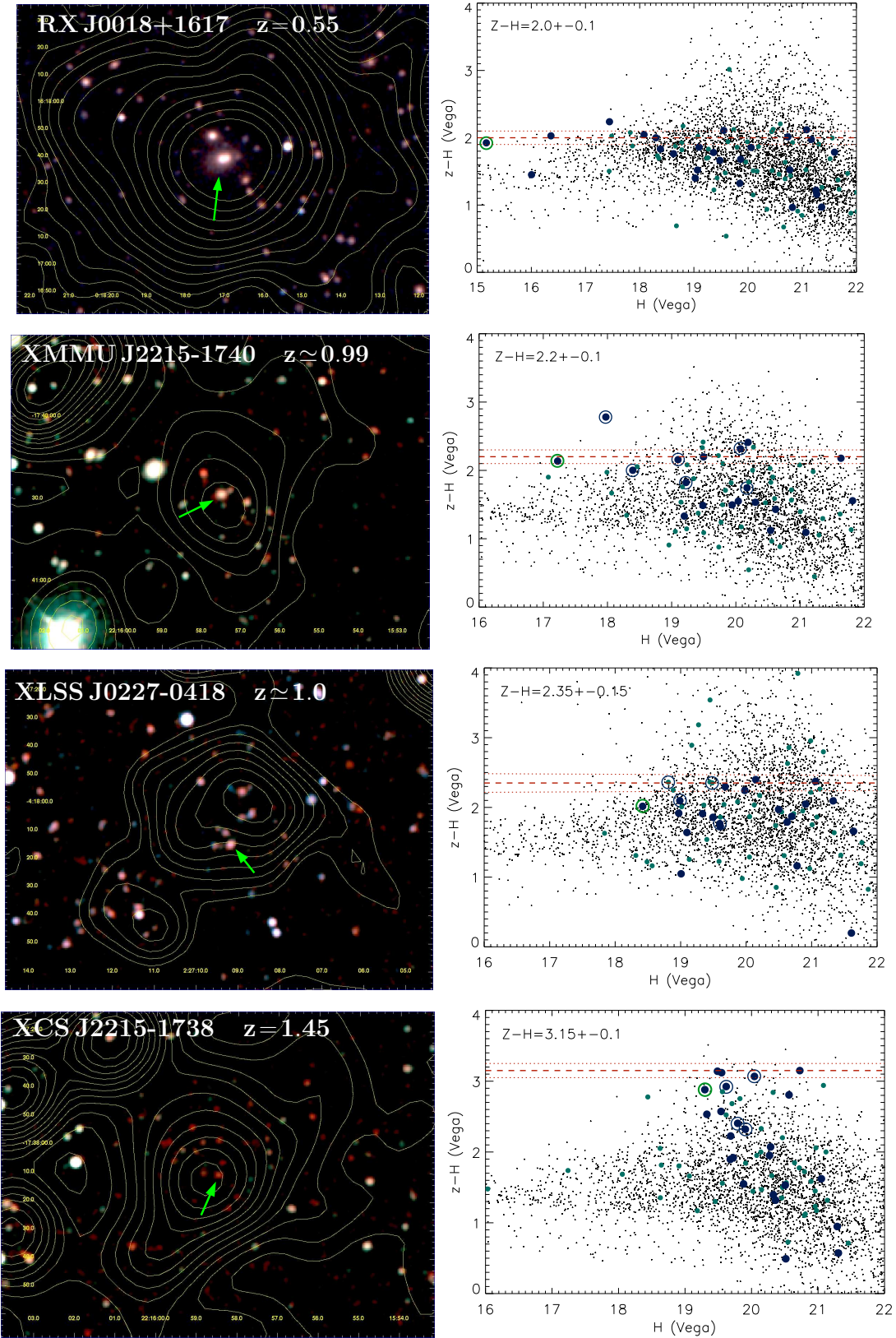


Figure 10.4: 2' \times 2.5' image cutouts and Z-H CMDs for the high- z calibration clusters with known redshifts. Spectroscopically confirmed cluster galaxies in addition to the BCG are indicated by blue circles for the three most distant systems. In the case of XMMU J2215-1740, galaxies with multi-band photometric redshifts in the range $0.93 \leq z \leq 1.05$ are marked.

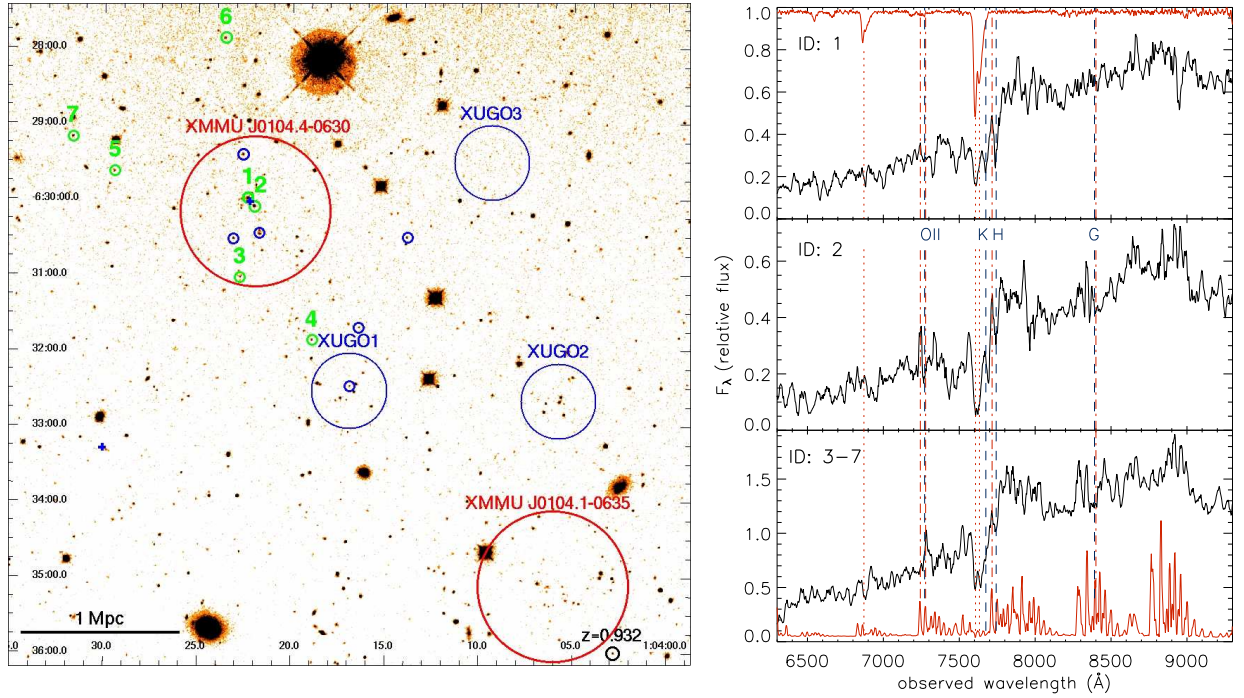


Figure 10.5: Spectroscopic confirmation of XMMU J0104.4-0630. *Left:* $9' \times 9'$ H-band image of the environment of XMMU J0104.4-0630. Spectroscopically confirmed cluster members are indicated by green circles with identification numbers; tentative cluster members are marked by blue circles, radio sources by crosses, and the consistent literature redshift is shown in black. The cluster radio source is located in between the BCG (ID 1) and the galaxy coincident with the X-ray center (ID 2). *Right:* VLT FORS2 spectra of the galaxies with secure and concordant redshifts giving the cluster redshift of $z = 0.947 \pm 0.005$ as labelled in the left panel (smoothed with a 7 pixel boxcar filter). Flux units are arbitrary; sky emission lines and telluric absorption lines are shown in red at the bottom and top, respectively. The two spectra from the top belong to the two brightest cluster galaxies in the center, the bottom panel displays the stacked spectrum of the galaxies with IDs 3–7.

A total of six extended X-ray sources were detected in the individual fields using the SAS tasks `eboxdetect` and `emldetect`. This work focusses on two of the sources, the main galaxy cluster XMMU J0104.4-0630 (here cluster A) and a second system XMMU J0104.1-0635 at a projected distance of $6.4'$ to the South-West (here cluster B). Cluster A was detected at an off-axis angle of $5.5'$ in field 1 with an aperture corrected, unabsorbed flux of $(1.7 \pm 0.3) \times 10^{-14} \text{ erg s}^{-1} \text{ cm}^{-2}$ in the 0.5–2.0 keV energy band, using $N_{\text{H}} = 5.08 \times 10^{20} \text{ cm}^{-2}$ from the 21 cm survey of Dickey & Lockman (1990). The estimated core radius for a $\beta = 2/3$ model is $(18.8 \pm 0.8)''$ corresponding to 150 kpc at $z = 0.95$. The flux of cluster B at $7.2'$ off-axis angle in field 2 is $(1.2 \pm 0.4) \times 10^{-14} \text{ erg s}^{-1} \text{ cm}^{-2}$, its estimated core radius of $(45 \pm 4)''$, corresponding to 340 kpc, is significantly larger. The main properties of the systems are summarized in Tab. 10.1.

Optical and Near-IR follow-up

The sky region around XMMU J0104.4-0630 was followed-up with R (1140s) and Z-band (480s) imaging on 18 October 2003 with VLT-FORS 2 ($6'.8 \times 6'.8$ FoV). The target was reobserved in H (1000s) and Z (1800s) on 30 October 2006 in photometric conditions ($1''$ seeing) using the NIR wide-field camera OMEGA2000 (Bailer-Jones *et al.*, 2000) at the Calar Alto 3.5m telescope with a larger $15.4' \times 15.4'$ field-of-view, which also covered the second cluster XMMU J0104.1-0635 to the South-West. The *SExtractor* photometry in this larger field is calibrated to the Vega system using 2MASS point sources (Cutri *et al.*, 2003) in H, and designated SDSS standard star observations (Smith *et al.*, 2002) in Z (see Chap. 7). In both bands the limiting magnitudes (50% completeness) of $H_{\text{lim}} \sim 20.7$ and $Z_{\text{lim}} \sim 22.8$ correspond to $m^* + 1.6$ for passively evolving galaxies at the cluster redshift (see Tab. 7.2). Figure 10.5 (left) provides an overview of the field, Fig. 10.6 (top panels) displays the R+Z+H false-color composite image of XMMU J0104.4-0630 (left), the Z+H images of XMMU J0104.1-0635 (center), and the region halfway between the clusters (right). The corresponding Z–H color magnitude diagrams are shown in the bottom panels of Fig. 10.6.

Spectroscopic observations were obtained on 2 November 2005 using a VLT-FORS 2 MXU slit-mask centered on XMMU J0104.4-0630 for a total exposure time of 60 minutes (see Chap. 8). The incomplete execution of the program, originally scheduled for 3 hours, and the rather poor seeing conditions (about $2''$) resulted in a data quality that allowed a redshift determination for only about half the targeted sources. However, seven galaxies were found at the same redshift and could thus be identified as secure cluster members (see Fig. 10.5, right panel), yielding a cluster redshift for XMMU J0104.4-0630 of $z = 0.947 \pm 0.005$. Eight additional galaxies (blue circles in the left panel) are classified as tentative members, with indications of the D4000 break at the expected position but significant contamination from telluric absorption and sky emission lines.

10.2.2 Discussion

Cluster XMMU J0104.4-0630

XMMU J0104.4-0630 (Fig. 10.6, top left) with a 0.5–2.0 keV luminosity of $L_x = (6.4 \pm 1.3) \times 10^{43} \text{ erg s}^{-1}$ is an intermediate mass cluster of $M_{500} \sim 1.1 \times 10^{14} M_\odot$ and $T_X \sim 3 \text{ keV}$, based on scaling relations following Finoguenov *et al.* (2007). The system has a compact and fairly regular X-ray appearance with slight extensions to the North-East and South-West.

The cluster core is dominated by early-type red galaxies as in low redshift clusters. The X-ray center coincides with the second brightest galaxy (ID 2 in left panel of Fig. 10.5). The brightest cluster galaxy and the densest part of the cluster core exhibit an offset of about $10''$ ($\sim 80 \text{ kpc}$) to the North-East. The color of the cluster red-sequence of Z–H $\simeq 2.2$ (Vega) is fully consistent with model predictions (Fioc and Rocca-Volmerange, 1997) of solar metallicity passively evolving galaxies with formation redshift $z_f \sim 5$ (see left panel of Fig. 10.6 and Fig. 7.1). The spectroscopic confirmation of XMMU J0104.4-0630 at a redshift very close to the photometric Z–H red-sequence estimate is hence a successful test for the new method. The BCG of this cluster is within 0.1 mag of the expected color for the passive evolution model as indicated by the green square in the CMD of Fig. 10.6.

ID	Name	z	$f_X(0.5-2.0 \text{ keV})$ $10^{-14} \text{ erg s}^{-1} \text{ cm}^{-2}$	r_c "	$L_X(0.5-2.0 \text{ keV})$ $10^{43} \text{ erg s}^{-1}$
A	XMMU J0104.4-0630	0.947 ± 0.005	1.7 ± 0.3	18.8 ± 0.8	6.4 ± 1.3
B	XMMU J0104.1-0635	0.95 ± 0.05	1.2 ± 0.4	45 ± 4	4.4 ± 1.4

Table 10.1: Properties of the two newly discovered X-ray clusters.

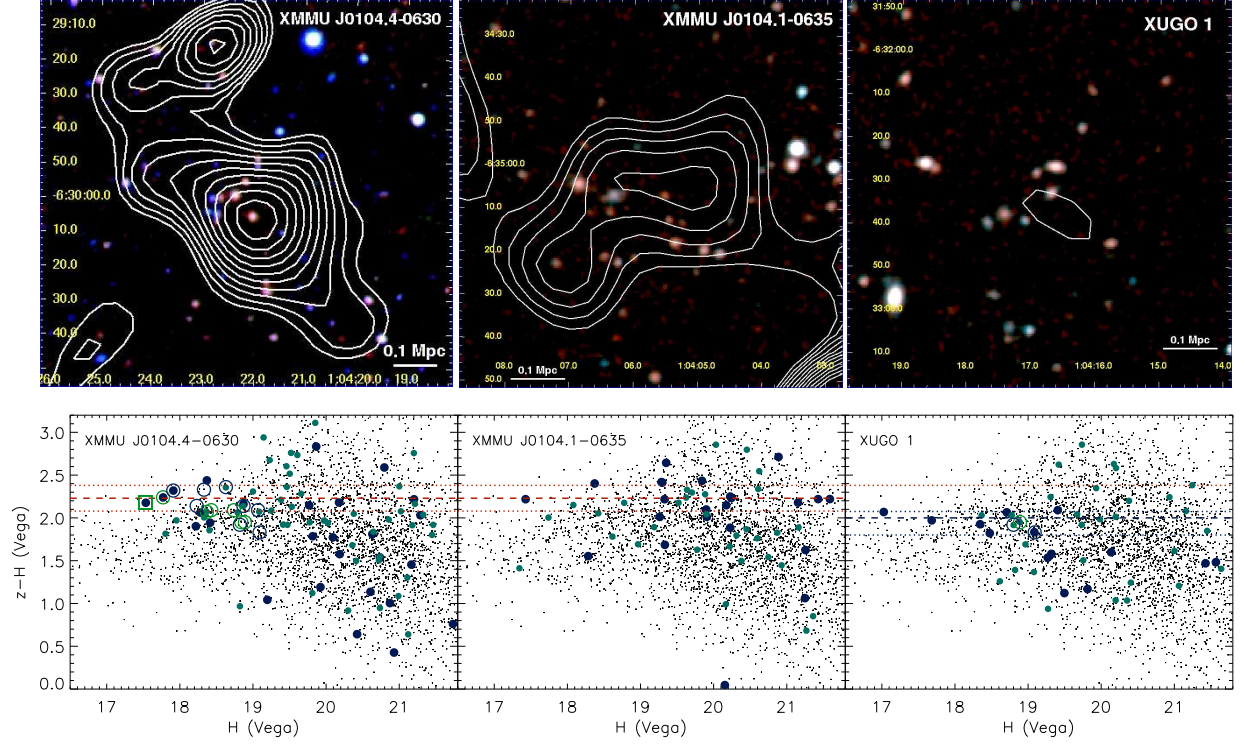


Figure 10.6: Color composites and color magnitude diagrams for different target regions of the field. *Top left:* $2' \times 2'$ R+Z+H color image of XMMU J0104.4-0630 at $z = 0.947$ with white X-ray contours overlaid. *Top center:* $1.5' \times 1.5'$ Z+H color composite of the second X-ray selected cluster XMMU J0104.1-0635 with the same redshift estimate from its Z–H red-sequence. *Top right:* $1.5' \times 1.5'$ zoom on one of the X-ray undetected overdensities of bluer galaxies in the center of the field. *Bottom row:* Z–H CMDs of the three objects shown in the top panels. Filled dark symbols indicate objects within a $30''$ radius from the center, filled green symbols are from $0.5' - 1'$, black dots are all objects in the field. *Left and center:* CMDs of the two X-ray selected galaxy clusters with concordant red-sequence colors. The dashed horizontal lines indicate the predicted model color for passively evolving galaxies at $z = 0.95$, the dotted red lines define an interval of ± 0.15 magnitudes around the red-sequence model color represented as the red-galaxy population in Fig. 10.7. Spectroscopically confirmed cluster members of XMMU J0104.4-0630 are indicated in the left panel by open symbols. The BCG is marked by the green square, the six additional secure members by green circles, and the eight tentative cluster members by blue open circles. *Right:* CMD of the galaxy overdensity between the two X-ray clusters with a bluer red-sequence color. The three galaxies there with available spectroscopy are indicated by open circles. The dashed blue line is shown at the color of the apparent locus, the blue dotted lines define the color cuts for the bluer galaxy population in Fig. 10.7.

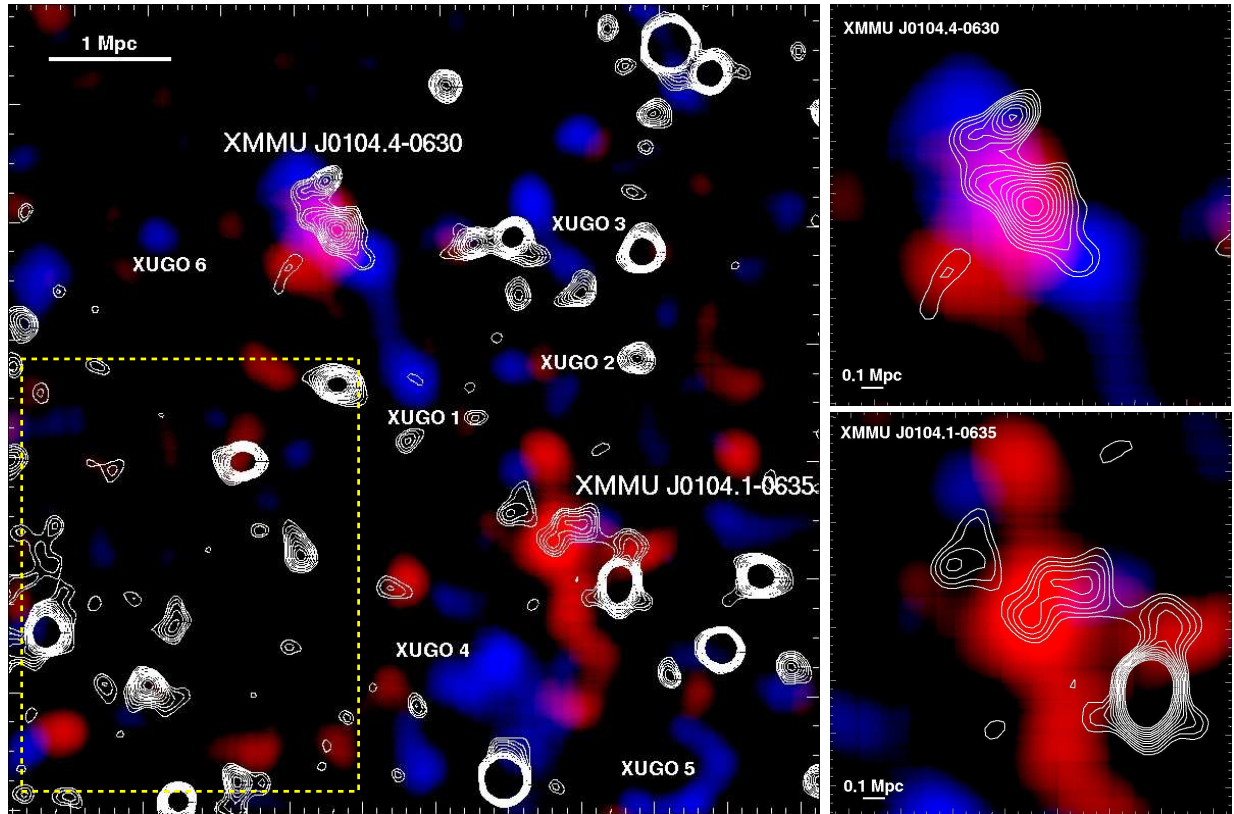


Figure 10.7: Red and blue galaxy overdensities in the field of XMMU J0104.4-0630. *Left:* $14' \times 14'$ field-of-view of galaxy overdensities smoothed with a 150 kpc-kernel of the *red* and *blue* galaxy populations (as defined in Fig. 10.6) encoded with the corresponding color; X-ray contours are overlaid in white. The color cuts for both populations span a range of $1.5\text{--}5\sigma$ relative to the control field in the lower left quadrant (yellow dashed region), which served as the control field. Labels are showing the locations of the two X-ray selected galaxy clusters corresponding to $7\text{-}\sigma$ peaks in the red population, and optically selected 3-6 sigma peaks (XUGO 1–6) in the blue population. *Right:* $3.5' \times 3.5'$ zoom on the two X-ray clusters.

The cluster center has been identified as the position of a 1.4 GHz radio source with a flux of 11.9 ± 1.0 mJy in the NVSS survey (Condon *et al.*, 1998), which is likely to be attributed to a radio galaxy with a radio power $P_{1.4\text{GHz}} \sim 5 \times 10^{25} \text{ W Hz}^{-1}$. The positional error circle of a few arcseconds radius includes the two brightest cluster galaxies. The fairly strong radio emission could be an indication of cooling core activity in the cluster center. In any case, radio emission of this order in high- z clusters is a prime concern for the cluster selection of upcoming SZE-surveys (Lin and Mohr, 2007) and requires further detailed studies (see Sect. 2.3.6 & Sect. 12.1).

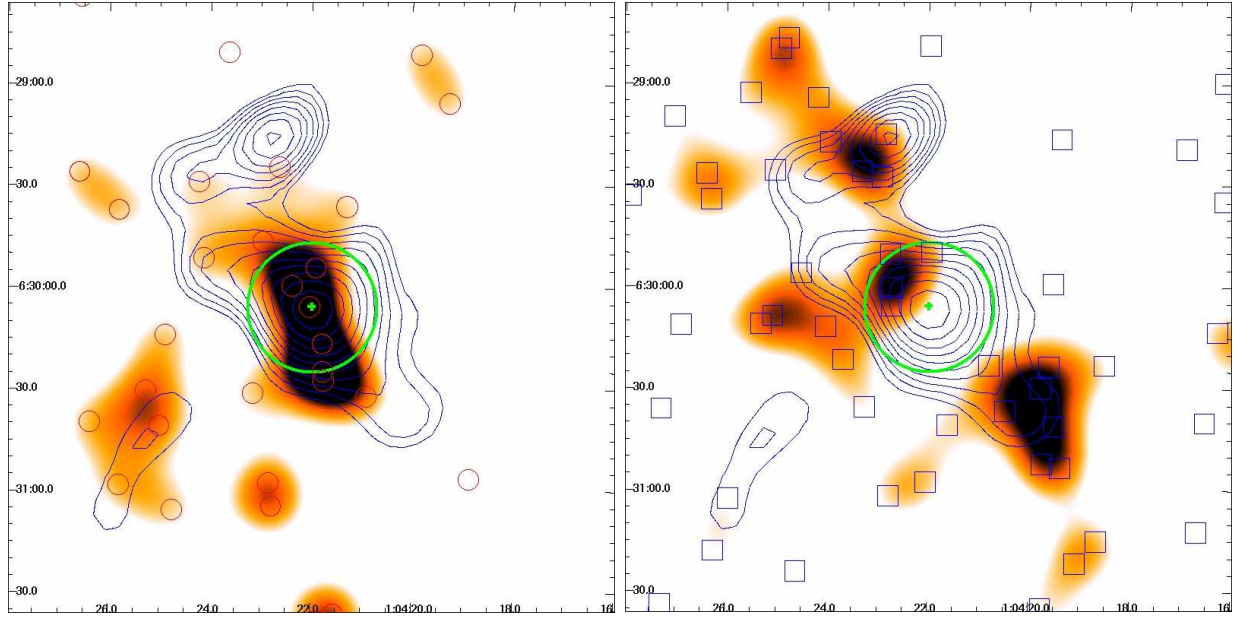


Figure 10.8: Galaxy populations of XMMU J0104.4-0630 at $z=0.947$. *Left:* $3' \times 3'$ view on the *red* galaxy population smoothed with a 75 kpc kernel and displayed in color cuts spanning overdensities of 2–5 σ . Red circles indicate the positions of individual galaxies, the green cross marks the X-ray determined cluster center of the blue contours, and the circle represents the cluster core radius of $r_c \simeq 19''$, corresponding to 150 kpc. *Right:* Same FoV and representation for the *blue* galaxy population.

Detection of the second X-ray cluster XMMU J0104.1-0635

The CMD of the second X-ray selected cluster XMMU J0104.1-0635 reveals a red-sequence color fully consistent with the same redshift as the main cluster A, but with a fainter galaxy population. The overdensity of red galaxies (see Fig. 10.7) selected with a (red) color-cut of 2.23 ± 0.15 (corresponding to the photometric color uncertainty at $H \sim 20.2$) shows a 7σ peak (6.5σ for cluster A) relative to the mean density and standard deviation in the 45 square arcminute control field in the lower left quadrant. We thus assign a photometric red-sequence redshift of $z = 0.95 \pm 0.05$ to cluster B. We propose that cluster A and B are physically associated with each other, forming a double cluster with a projected separation in the plane of the sky of 3 Mpc. A literature redshift of $z = 0.932$ from the XMM-Newton Serendipitous Survey (Barcons *et al.*, 2002) for a BL Lac object $75''$ to the South-West of cluster B supports the idea of a large-scale structure filament along the axis of the two systems (see lower right corner of Fig. 10.5). Currently only two X-ray luminous double clusters at higher redshifts are reported in the literature (*e.g.* Hashimoto *et al.*, 2005; Nakata *et al.*, 2005). The photometric identification of XMMU J0104.1-0635 confirms the efficacy of the X-ray detection and selection procedure (Chap. 6) even for faint extended sources with large core radii (see Sect. 9.1.3).

Associated large-scale structure environment

The center of the proposed 3 Mpc-scale cluster-cluster-bridge is marked by an additional significant overdensity of slightly bluer galaxies, with very weak X-ray emission well below the detection threshold for extended sources. The color composite and CMD of this X-ray Undetected Galaxy Overdensity (XUGO) are shown in the right panels of Fig. 10.6 revealing a tight red-sequence at a ~ 0.25 mag bluer color. Without additional spectroscopy, there are two plausible scenarios for this object: (i) XUGO 1 is a foreground group or low-mass cluster at $z \sim 0.7$ based on the observed $Z-H$ color, or (ii) this galaxy overdensity is part of the LSS at $z \sim 0.95$ with a systematically bluer galaxy population. This speculative interpretation is supported by three tentative cluster redshifts within $30''$ (see right lower panel of Fig. 10.6) and the suggestive geometric alignment with the two X-ray clusters.

In order to investigate the nature of this system, we set a second (blue) adjoint color-cut at $1.8 \leq Z - H < 2.08$, corresponding to the blue dotted lines in Fig. 10.6. The spatial distribution of color selected objects was smoothed with a Gaussian kernel of 150 kpc physical scale ($19''$), the approximate core radius of cluster A. The resulting overdensity plot of the $14' \times 14'$ field-of-view is shown in Fig. 10.7, displayed with color cuts ranging from 1.5 to 5σ overdensity relative to a control field in the lower left quadrant. The two brightest peaks in the red galaxy population mark the X-ray selected clusters and are well-centered on the diffuse X-ray emission. On the other hand, the optically selected system (XUGO 1) corresponds to a $4.5\text{-}\sigma$ peak of the bluer population. Figure 10.7 (left panel) shows that this population can be traced to the outskirts of the main cluster A, where blue $5\text{-}\sigma$ peaks to the NE and SW enclose the cluster center along the axis laid out by the X-ray morphology. The drop to 3.5σ in the very center of cluster A in conjunction with the rising red overdensity to 6.5σ (see Fig. 10.7, top right) suggests that this is a direct consequence of the proposed scenario of delayed star formation quenching in lower density environments (*e.g.* Thomas *et al.*, 2005; Cucciati *et al.*, 2006). Under the burst model assumption, the observed 0.15–0.3 mag $Z-H$ color shift towards the blue is consistent with an age difference of the stellar populations of 1.2–2.2 Gyr. In Figure 10.8, the two different galaxy populations of XMMU J0104.4-0630 are displayed in separate panels showing the red cluster core galaxies in the left panel and the proposed filament population on the right.

Systematic blue shifts of the S0 population have been observed in several clusters at lower redshift (*e.g.* van Dokkum *et al.*, 1998; Abraham *et al.*, 1996) and at $z \sim 1.1$ (Mei *et al.*, 2006a). The observed *blue* population in Fig. 10.7, which includes the spectroscopic cluster members with IDs 3, 4, 6 and two additional tentative members, could hence be interpreted as an evolving S0 population. However, firm conclusions on physically associated filaments and member galaxies of XMMU J0104.4-0630 will only be possible with additional spectroscopic observations of the field.

10.3 Summary and Conclusions

- In Sect. 10.1, the Z–H red-sequence method was calibrated using ten spectroscopically confirmed clusters. It was shown that the ($z_f = 5$, $Z = Z_\odot$)-passive evolution model is fully consistent with all observations and was therefore applied as reference model for the photometric redshift estimation of the full cluster candidate sample.
- The observed Z–H red-sequence color evolution over the redshift baseline $0.2 \lesssim z \lesssim 1.5$ was used to simultaneously constrain the average metallicity and the formation epoch of red-sequence galaxies yielding $z_f = 4.2 \pm 1.1$ and $Z = (1.2 \pm 0.4) Z_\odot$. These early results, based on only ten reference objects, confirm the well-established old age of the stellar populations of red-sequence galaxies. Using additional spectroscopically confirmed high-redshift clusters of the ongoing XDCP follow-up program, the Z–H red-sequence method has the potential to put stringent constraints on the early-type galaxy formation epoch in the near future.
- In Sect. 10.2, details of the newly discovered X-ray luminous cluster of galaxies XMMU J0104.4-0630 at redshift $z = 0.947 \pm 0.005$ were presented. The compact, intermediate mass cluster is found to be in an evolved state and hosts a strong central radio source. It was shown that the cluster shows a pronounced stratification of galaxy populations. Whereas the spatial distribution of the red-sequence population of early type galaxies coincides well with the X-ray emission, a significantly bluer population dominates beyond 1–2 core radii from the center, suggesting a cluster environment-driven effect of differential galaxy evolution, *e.g.* delayed star formation quenching in the outskirts.
- The Z–H color of the cluster red-sequence was shown to be in good agreement with the predictions of the reference model and confirmed the applicability of the method for reliable photometric redshift estimates.
- A second X-ray selected cluster, XMMU J0104.1-0635, 6.4' to the South-West could be photometrically identified at $z \simeq 0.95$. It was speculated that this object is part of the large-scale structure environment of the main cluster, which could include additional optically selected galaxy overdensities.

Chapter 11

Preliminary Studies and Science Outlook

The available Z–H follow-up observations aimed primarily at the cluster *identification* and *confirmation* of the principal strategy in terms of limiting depth, photometric precision, and the choice of filter bands. However, the application of the calibrated Z–H-redshift relation to the full distant cluster candidate sample allows a preliminary study of the luminosity evolution of the *brightest* cluster galaxies in the redshift range $0.2 \lesssim z \lesssim 1.5$, presented in Sect. 11.1. Section 11.2 provides a brief outlook on upcoming investigations of the *faint* end of the cluster red-sequence. The chapter ends with a gallery of selected, newly discovered high-redshift systems awaiting spectroscopic confirmation.

11.1 The Assembly History of Brightest Cluster Galaxies

In this section, the cosmic evolution of the brightest cluster galaxies is investigated. Background information and the latest simulation results on BCGs have been provided in Sect. 2.4.4. The Hubble diagram (see Equ. 3.46 and Sect. 3.3) will be applied as a diagnostic tool for BCG evolution in a *fixed* concordance model cosmology. Absolute BCG H-band magnitudes out to $z \sim 1.5$ are derived and compared to predictions of passive evolution models, which have been shown to be very successful for the description of the Z–H color evolution in Sect. 10.1.

11.1.1 BCG sample and selection

The preliminary study presented here uses the full Calar Alto sample (see Fig. 9.4) of X-ray selected clusters, which fulfilled these selection criteria: (i) a significant detection of an optical cluster counterpart *and* (ii) a reliable red-sequence redshift estimate with a maximum accepted uncertainty of $\Delta z = 0.2$. The remaining BCG cluster sample contains a total of 63 systems between $z = 0.18$ and $z \simeq 1.5$.

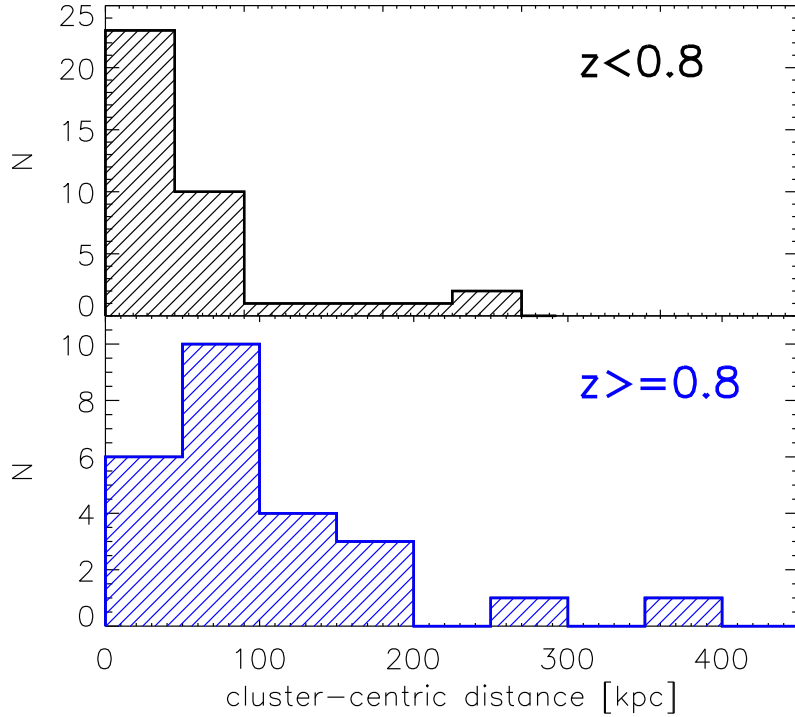


Figure 11.1: Binned projected cluster-centric distance histogram of the 63 selected BCGs with respect to the X-ray center position. *Top:* The BCG locations of the low and intermediate redshift bin with $z < 0.8$ (38 objects) are predominantly coincident with the X-ray marked cluster center. *Bottom:* At high redshifts of $z \geq 0.8$ (25 clusters) the distribution is skewed towards slightly larger offsets from the X-ray center. Extreme outliers in both histograms can be mostly attributed to X-ray center biases due to point source flux contaminations.

The brightest cluster galaxies are selected based on their H-band magnitude, in combination with selection cuts concerning the cluster-centric distance, defined with respect to the X-ray center, and the Z–H color offset from the red-sequence. The increasing foreground contamination of galaxies with magnitudes similar to the BCGs of *distant* clusters requires tightening identification constraints with increasing cluster-centric distance to ensure a *robust* BCG selection. In the absence of a spectroscopic identification and photometric redshifts derived from deep multi-band data, the BCG selection based on cluster-centric distance *and* reasonable Z–H cuts is currently the best applicable method for the available data. The following selection criteria were applied for the BCG identification in the 63 X-ray clusters:

1. 21 central dominant galaxies within $5''$ of the X-ray marked center are accepted as BCGs without color cuts;
2. 37 identifications are based on galaxies with cluster-centric distances of $5''$ – $30''$ *and* a color cut of ± 0.5 mag around the red-sequence Z–H color;
3. 5 selected BCGs are located $30''$ – $60''$ off-center but are within ± 0.3 mag of the red-sequence color.

These selection criteria are motivated by the first experiences with the spectroscopically confirmed sub-sample discussed in Sect. 10.1.2. However, the robustness of these preliminary selection criteria needs to be investigated and quantified with upcoming follow-up observations of high-redshift candidates.

The maximum search radius of $60''$ corresponds to about 500 kpc at $z \gtrsim 0.8$. For the majority of *X-ray selected* clusters, the identification of BCGs close to the X-ray center is straightforward and fairly unambiguous. The sample contamination level for non-BCG selections is currently expected to be no more than of order 10%, *i.e.* sub-sample averages should be statistically robust. Figure 11.1 displays the histogram of binned cluster-centric distances of the identified BCGs for low and intermediate redshift clusters at $z < 0.8$ (*top panel*) and for high-redshifts systems at $z \geq 0.8$ (*bottom panel*). A slight shift towards higher off-center distances can be observed at high redshift as a first tentative indication that BCGs at large lookback times are not yet in their final configuration with respect to the cluster center.

11.1.2 The BCG H-band Hubble diagram

Using the observed apparent *total* BCG magnitudes and the estimated red-sequence redshifts, we can construct the H-band BCG Hubble diagram out to $z \simeq 1.5$. H-band galactic extinction corrections A_H have been applied to all BCG magnitudes using the galactic reddening maps¹ of Schlegel, Finkbeiner & Davis (1998). The final BCG H-band Hubble diagram, *i.e.* the $(m_H(\text{BCG}) - A_H)$ versus $\log z$ relation, is shown in the top panel of Fig. 11.2. Black dashed lines indicate the model expectations for solar metallicity, passive evolution burst models with formation epoch $z_f = 5$ for m^* , $m^* - 1$, $m^* - 2$, and $m^* - 3$ galaxies (top to bottom). Red arrows mark objects with strong signs of object blending of the *SExtractor* photometry, *i.e.* the determined magnitudes are lower limits (implying upper limits of the luminosity). Photometric errors are typically small, except for blended sources, since all BCGs are at least two magnitudes brighter than the limiting H-band image depth. Errors are hence dominated by the redshift uncertainties of the Z–H red-sequence method. The lower panel of Fig. 11.2 shows the same plot with a *linear* redshift axis, which provides a better illustration of the effects of redshift errors, in particular at low- z where the apparent magnitudes faint rapidly with increasing distance.

Instead of assuming standard candle properties of the BCGs and applying the Hubble diagram as a cosmological test for parameter constraints (*e.g.* Collins & Mann, 1998; Aragón-Salamanca *et al.*, 1998), we assume a *fixed concordance cosmology* and use the Hubble diagram as a tool for BCG evolution studies. Equation 3.46 reveals that variations of the Hubble constant H_0 introduce a normalization offset, whereas different values for Ω_m , Ω_Λ , and w change the shape of the Hubble relation at high redshifts. However, parameter changes within the concordance model uncertainties introduce variations in the luminosity distance d_{lum} at the high-redshift end $z \sim 1.5$ of less than 10%.

¹A galactic extinction calculator is available at <http://nedwww.ipac.caltech.edu/forms/calculator.html>.

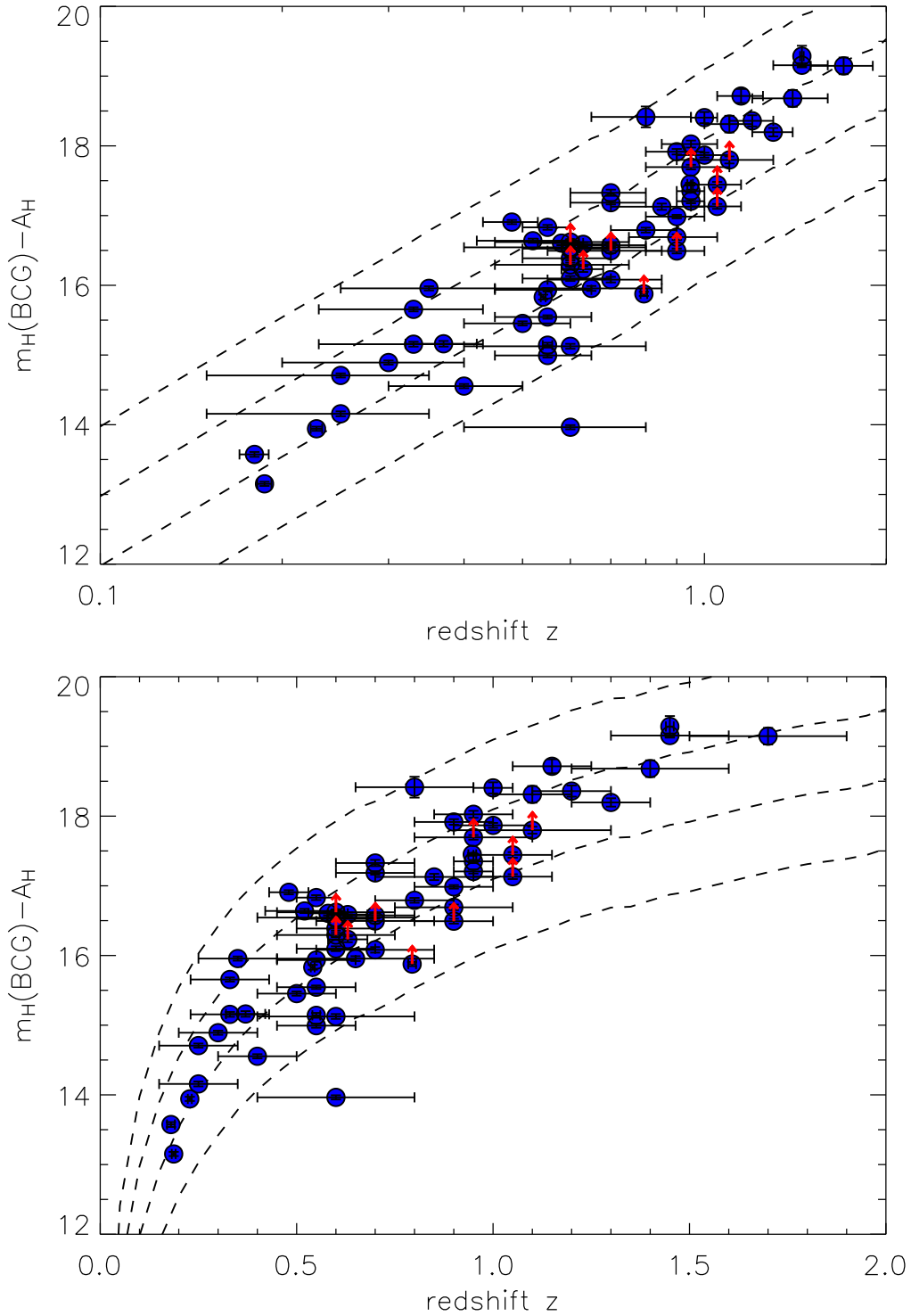


Figure 11.2: *Top:* H-band Hubble diagram for the BCGs of 63 X-ray selected clusters between redshifts of $z=0.18$ and $z \simeq 1.5$. Dashed lines indicate solar metallicity, passive evolution burst model expectations for a formation epoch of $z_f=5$ and galaxy luminosities of m^* , m^*-1 , m^*-2 , and m^*-3 (top to bottom). BCGs with photometry affected by blending are marked by red arrows. *Bottom:* Same plot with a linear redshift axis.

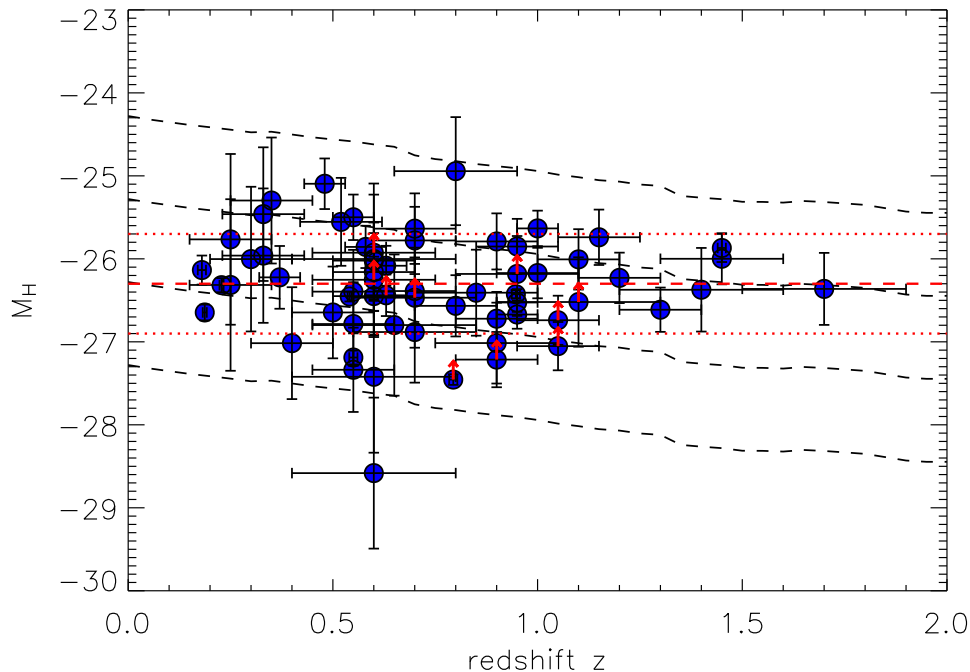


Figure 11.3: Redshift evolution diagram of the absolute H-band BCG magnitudes with estimated 1σ errors. The observations are fully consistent with a non-evolving absolute magnitude of $M_H = -26.3$ mag (red dashed line), with an rms scatter of 0.6 mag (red dotted lines), which is mostly introduced by the photometric redshift uncertainties. Black dashed lines indicate the expected evolution of passive galaxies, which are expected to dim by about one magnitude from redshift $z \simeq 1.5$ to the present epoch. Purely passive BCG luminosity evolution can be excluded at the 2.6σ level.

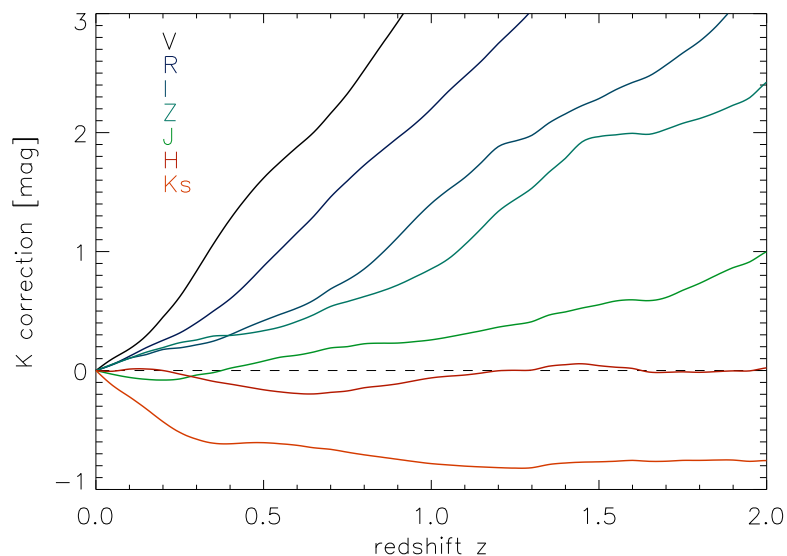


Figure 11.4: K -correction terms as a function of redshift for a $z_f = 5$ passive evolution BCG model for different bands. The applied H-band correction term (red line) is very small at all relevant redshifts.

BCGs as standard candles

As a first application, the absolute H-band magnitudes for the BCGs are computed following Equ. 3.46

$$M_{\text{H}}(\text{BCG}) = m_{\text{H}}(\text{BCG}) - A_{\text{H}} - K_{\text{H}}(z) - 25 - 5 \log \left(d_{\text{lum}} [h_{70}^{-1} \text{Mpc}] \right) . \quad (11.1)$$

The K -correction terms² K_{H} to transform observed m_{H} magnitudes at redshift z into *rest-frame* H-magnitudes have been calculated for the standard $z_{\text{f}} = 5$, solar metallicity passive evolution model and are displayed by the red line in Fig. 11.4. Note that the H-band observations exhibit the smallest absolute K -correction terms of all bands, implying that the observed apparent H-band magnitudes are very close to the associated *rest-frame* values.

The BCG redshift uncertainties, as the dominant error source for all non-spectroscopically confirmed clusters, enter the error budget of the absolute magnitudes via $dM_{\text{H}} = dm_{\text{H}} + 5 [(d \log d_{\text{lum}})/dz] dz$. In particular at $z \lesssim 0.4$, where the luminosity distance is a steep function of z (see lower panel of Fig. 11.2), the photometric redshift errors influence dM_{H} in a magnified way.

The absolute BCG H-band magnitude diagram of Fig. 11.3, with a full accounting of the error budget included, reveals an astonishing result: the brightest cluster galaxies of X-ray selected clusters are fully consistent with being true standard candles with constant absolute rest-frame H-band luminosity of $M_{\text{H}} \simeq -26.3$ mag out to $z \simeq 1.5$.

This result is statistically very robust. The median *and* mean values of (i) the *full* sample of 63 BCGs, (ii) the *three lowest redshift* clusters (spectroscopically confirmed), and (iii) the *five highest redshift* objects all agree within ± 0.06 mag. The scatter of the full sample around the mean value $M_{\text{H}} \simeq -26.3$ mag is $\sigma_M \simeq 0.6$ mag, which is for the largest part to be attributed to the redshift uncertainties. A linear fit to the full BCG sample yields the formal functional form $M_{\text{H}} = (-26.23 \pm 0.20) + (-0.10 \pm 0.22) \cdot z$, also fully consistent with a *non-evolving* absolute H magnitude.

The full BCG sample contains four outliers, all of which have associated literature redshifts, *i.e.* their estimated M_{H} errors are small. The BCGs of the two clusters A383 with $M_{\text{H}} = -26.65 \pm 0.1$, and RX J0018+1617 with $M_{\text{H}} = -27.2 \pm 0.1$ (see Sect. 10.1 for references) are likely truly super-luminous systems compared to the sample average. The remaining two outliers are clusters LCDS 0504 with spectroscopic redshift $z = 0.794$ and LDCS 0505 with a photometric literature redshift of $z \simeq 0.48$ from the Las Campanas Distant Cluster Survey (Gonzalez *et al.*, 2001). The BCG of LCDS 0504 with $M_{\text{H}} = -27.45$ is flagged as a photometric blend (see panel 11 of Fig. 11.7). In the case of LDCS 0505, with an apparently underluminous BCG of $M_{\text{H}} = -25.1$, the Z–H red-sequence color suggests that the published photometric redshift of $z \simeq 0.48$ is underestimated. The latter two outlier objects can thus be attributed to systematic effects rather than significant intrinsic deviations from the mean absolute BCG magnitude.

²Models computed by Daniele Pierini.

The fact that BCGs are good standard candles has long been established for redshifts of $z < 1$ (see Sect. 2.4.4). The new preliminary result from the sample of this work with the increased redshift baseline out to $z \simeq 1.5$ is the conclusion that the observations are **not consistent with pure passive evolution**. The dashed black lines in Fig. 11.3 indicate the expected fading of the absolute H-band luminosity for passively evolving galaxies by one magnitude from $z \simeq 1.5$ to $z = 0$, corresponding to an average slope of $dM_{\text{model}}/dz \simeq -0.67$. Comparing this result to the constraints obtained from the linear fit to the observed data of $dM_{\text{H}}/dz \simeq -0.10 \pm 0.22$, excludes a purely passive BCG luminosity evolution at the 2.6σ level.

BCG luminosity evolution

As the next step, the BCG luminosity evolution *relative to the passively evolving model* is investigated. The apparent magnitudes of the standard $z_{\text{f}} = 5$, solar metallicity model for an L_{mod}^* galaxy, m_{model} , are subtracted from the extinction corrected observed magnitudes $m_{\text{H}}(\text{BCG}) - A_{\text{H}}$. The results³ are shown in Fig. 11.5, with the same meaning of the symbols as before. In this representation, passively evolving L_{mod}^* galaxies would be located along the null line (top horizontal dashed line). The bulk of the BCG population is observed in the diagram region in between galaxies one magnitude (center dashed line) and two magnitudes (lower dashed line) *brighter* than L_{mod}^* . The errors in the model-subtracted magnitudes originate from the redshift uncertainties of the BCGs, $m_{\text{model}}(z \pm \Delta z)$, in analogy with Fig. 11.3.

Since Fig. 11.5 displays the magnitude *residuals* after accounting for passive evolution, more negative data points at low redshifts can be interpreted in terms of an *increased* luminosity, in excess of passive evolution, compared to the high-redshift BCGs. As a first approach for modelling the residual BCG luminosity evolution, we can assume a linear relationship with redshift of the form $m_{\text{H}}(\text{BCG}) - m_{\text{model}} = A_0 + B \cdot z$, with fit parameters A_0 for the local magnitude difference, and B for the slope. A linear fit to the *full* BCG sample over all redshifts yields the parameter constraints $A_0 = -2.0 \pm 0.2$ and $B = 0.60 \pm 0.22$, shown by the green line in the top panel of Fig. 11.6. Black symbols with error bars represent the observed BCG data, with one outlier to either side not displayed in the zoomed representation of the central residual magnitude interval of interest. Blue dots symbolize the magnitude and redshift medians of 13 *independent* bins of five BCGs in order of decreasing redshift (three objects for the lowest z bin). The medians are less affected by outliers compared to averaging, *e.g.* due to blends in the photometry, and should represent a robust smoothed trend of the observed data as visual guide. A linear fit to the median smoothed data results in consistent parameters but with decreased uncertainties, ruling out a flat model with passive evolution at the 3.7σ level, whereas the raw data fit yields a 2.7σ confidence level.

³The galactic extinction correction term A_{H} is omitted in the axis label for better clarity, $m_{\text{H}}(\text{BCG})$ implicitly denotes extinction corrected magnitudes.

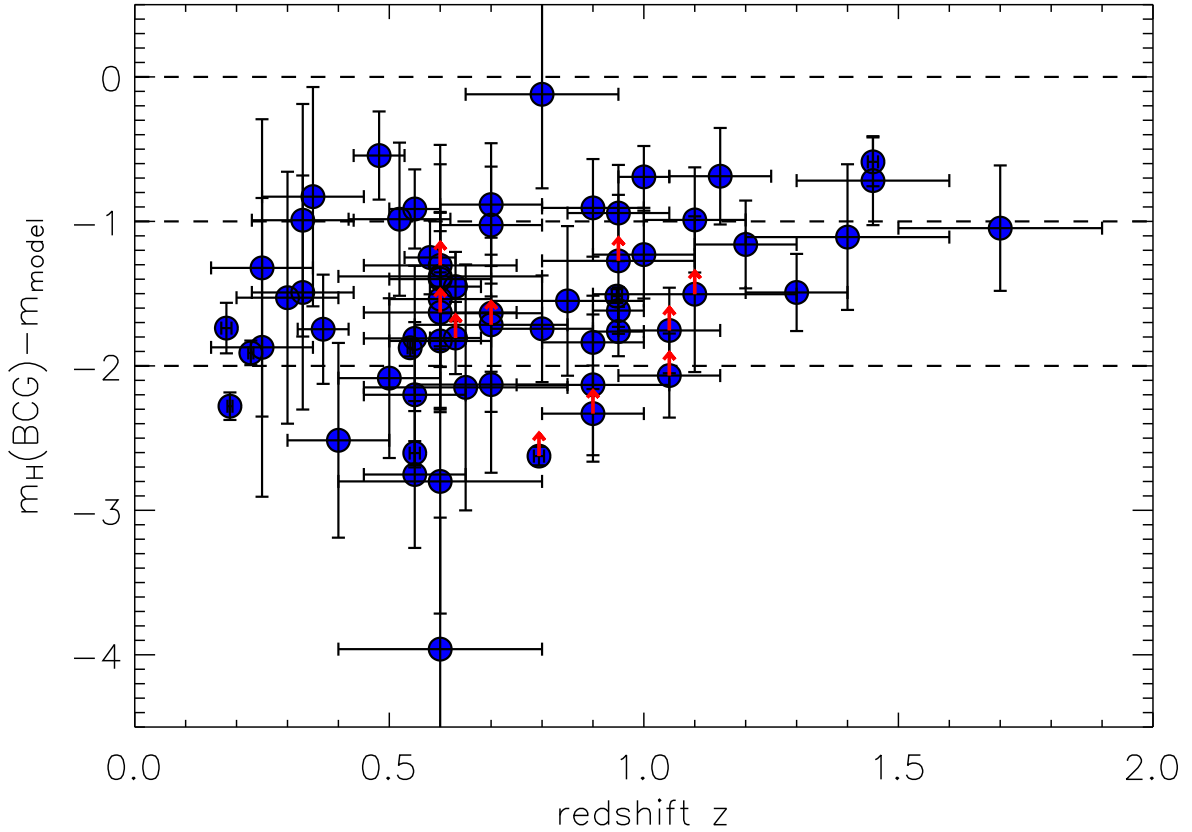


Figure 11.5: Observed apparent magnitude evolution relative to expectations of passive evolution models. The expected apparent model magnitudes $m_{\text{mod}}^*(z)$ for an L_{mod}^* galaxy have been subtracted, implying that the two dashed lower lines represent galaxies one (center line) and two (bottom line) magnitudes *brighter* than M^* .

A linear relationship would imply that 2/3 of the luminosity evolution happened at redshifts below unity, at variance with observations (*e.g.* Burke *et al.*, 2000). The apparent discrepancy can be resolved by splitting the BCG sample into a low-intermediate redshift bin at $z \leq 0.9$, approximately corresponding to the range accessible by former BCG analyses, and a high-redshift bin with 18 objects with $z > 0.9$. The linear fits to the two sub-samples yield the parameter constraints $A_0 = -1.7 \pm 0.4$, $B = 0.0 \pm 0.5$ for the low redshift bin, and $A_0 = -2.2 \pm 0.5$, $B = -0.8 \pm 0.4$ for the independent high- z sub-sample, displayed by the red lines in the top panel of Fig. 11.6. The observed low-intermediate redshift BCGs at $z \leq 0.9$ are hence consistent with a passive evolution model, although with increased errors, in agreement with previous findings. At $z > 0.9$, a significant jump in the residual BCG magnitudes is apparent. Note that the non-passive evolution signal is present for the three rightmost blue points, representing the median values of the 15 highest redshift BCGs. The observed effect is hence robust against the removal of individual high- z objects from the sample.

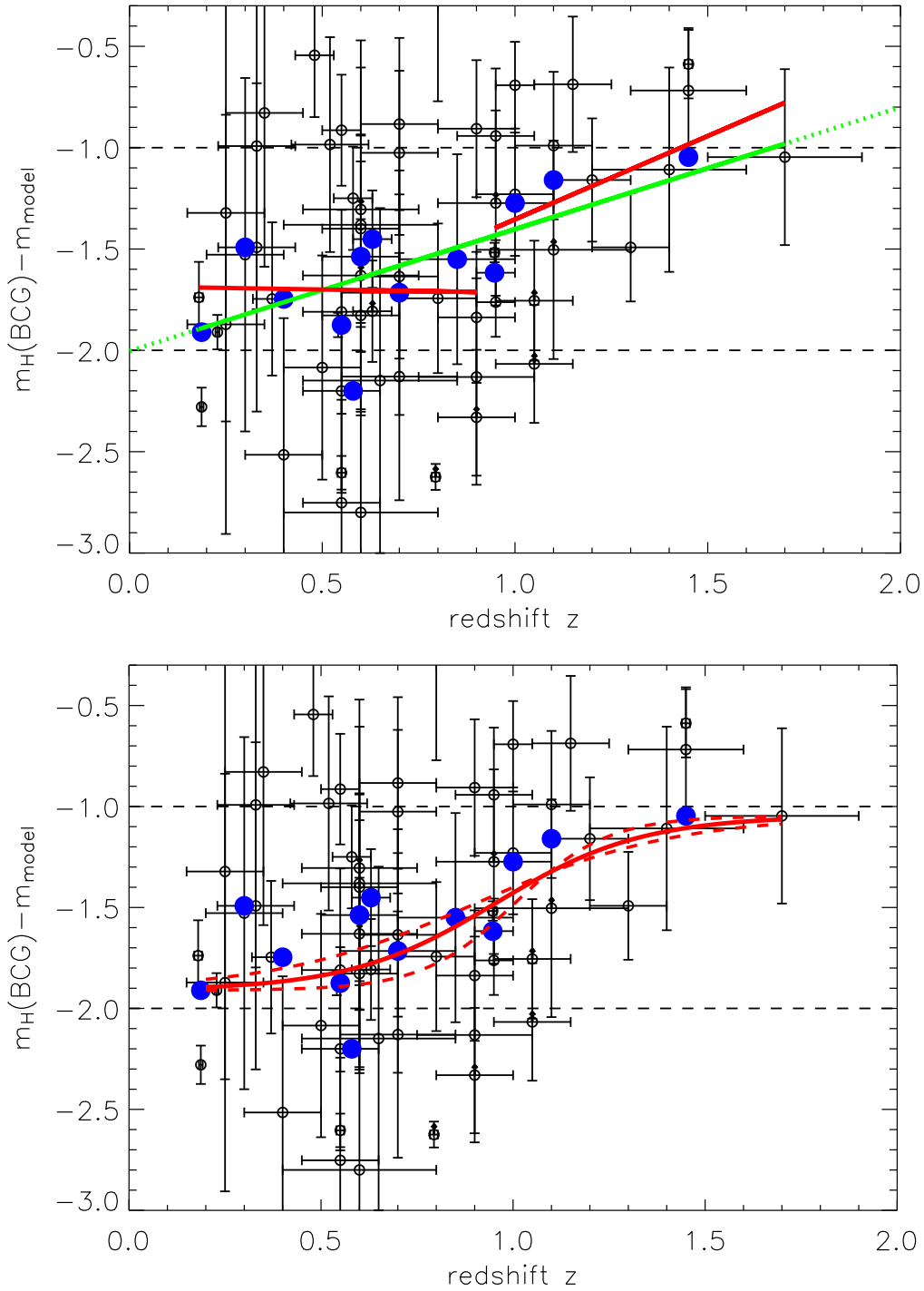


Figure 11.6: BCG luminosity evolution models compared to observations. *Top:* Linear fits to the data over the full sample (green line), and separate linear models for $z \leq 0.9$ and $z > 0.9$ sub-samples (red lines). Black background symbols show the observed data, blue circles represent the medians of independent bins of five objects. *Bottom:* Maximum likelihood model fit for a step function with a softened transition zone given by the red solid line, dashed lines display 1σ variations of the fit parameters. The observations are consistent with a mass assembly phase of the BCGs centered at $z \sim 0.95$. Since their colors evolve as for passively evolving stellar populations, the increase in luminosity is driven by an increase in stellar mass.

The observed discontinuity for the split sample suggests the application of a step function model with a gradual transition zone, in analogy to a Fermi function. The functional form can then be parameterized as

$$m_{\text{H}}(\text{BCG}) - m_{\text{model}} = (A_0 + \Delta m) - \frac{\Delta m}{1 + \exp(\frac{z - z_a}{b})}, \quad (11.2)$$

where A_0 is the local magnitude residual, Δm the step height, z_a the central BCG ‘assembly’ redshift, and b a softening parameter that determines the width of the transition zone. Since the data is not sufficient to provide meaningful constraints for a functional fit with *four* free parameters, the end points are fixed at $A_0 = -1.91$ (at $z \simeq 0.2$) and $\Delta m = 0.86$, consistent with the results of a constant absolute luminosity in Fig. 11.3 and the linear fit in Fig. 11.6 (green line in top panel).

A maximum likelihood fit to the data⁴ with two remaining free parameters yields the constraints $z_a = 0.96 \pm 0.05$ for the central ‘assembly’ redshift and $b = 0.19 \pm 0.07$ for the transition zone width. The solid red line in the bottom panel of Fig. 11.6 displays the best fit model, with the effects of 1σ parameter variations shown by the dashed red lines. The reduced χ^2 value of 1.78 for this softened step function model is improved compared to the linear fit (green fit) with a χ^2 of 1.89. The luminosity evolution fit shown in the lower panel of Fig. 11.5 is currently the best preliminary model for the available BCG data, consistent with only small deviation from passive evolution at low redshifts as reported by former studies.

Biases and systematics

We will now address the question whether the observed deviations from passive BCG luminosity evolution models could be an artefact introduced by systematic effects and selection biases. The main areas of concern are briefly discussed in the following:

Non-Representative Cluster Sample: Using a heterogeneous cluster sample with varying object properties as a function of redshift can introduce biases that mimic cosmic evolution. In fact, Burke, Collins & Mann (2000) showed that the initial claim of a non-passive BCG luminosity evolution of Aragon-Salamanca, Baugh & Kauffmann (1998) could be attributed to the bias of mixing an optically selected high- z sample and an X-ray selected low-redshift sample. Owing to the observed weak correlation of cluster mass and BCG luminosity $L_{\text{BCG}} \propto M_{200}^{1/4}$ (see Sect. 2.4.4), the target selection from high-redshift clusters with systematically lower mass, and hence lower X-ray luminosity, introduces the *selection artefact* of intrinsically fainter distant BCGs.

The cluster sample presented here is X-ray selected at all redshifts, introducing a general selection bias with the opposite sign, *i.e.* an effective ‘*anti-bias*’. At a given approximate flux limit, the minimum cluster luminosity is increasing with redshift

⁴The magnitude errors of the four outliers identified in the absolute magnitude diagram of Fig. 11.3 have been ‘softened’ to 1σ deviations to prevent the likelihood fit being dominated by individual objects (with systematics).

according to $L_X \gtrsim 4\pi f_{X,\text{lim}} d_{\text{lum}}^2$, implying an increasing minimum cluster mass for the 58 serendipitously detected objects. The five additional XMM target clusters (see Sect. 9.2) at low and intermediate redshifts are high X-ray luminosity, massive clusters, of which three were identified as BCG outliers on the bright end. The X-ray selection bias of finding predominantly low mass clusters and groups at lower redshifts (*e.g.* Pacaud *et al.*, 2007) contributes to the observed increased scatter at low- z in Fig. 11.3. The detected non-passive BCG luminosity evolution of $\Delta m \simeq 0.9$ mag is hence to be interpreted as a *lower limit*, with a *larger* effect to be expected using a representative cluster sample. In other words, we find distant BCGs to be *fainter* than expected from passive evolution, despite the fact that the high-redshift objects have an X-ray selection bias towards *intrinsically brighter* absolute magnitudes, *i.e.* we observe a *positive* slope in Fig. 11.6 but would expect a *negative* correlation. The X-ray selection bias effectively increases the confidence in the detection of non-passive BCG evolution, but has to be taken into account for the comparison with unbiased predictions from simulations.

BCG Selection: The BCG selection has been discussed in Sect. 11.1.1. While individual misclassifications based on the two-band data are possible, the sample statistics should be robust. A significant bias is only expected if a large fraction of distant BCGs is either located at cluster-centric distances of >500 kpc, or the BCG color is more than 0.5 mag bluer than the red-sequence; both scenarios seem unlikely based on known cluster populations. Since the BCG identification is more difficult at high redshift, the current approach needs to be justified once additional data is available leading to possibly refined selection criteria.

Cluster Redshift Estimates: To be consistent with passive evolution models, the redshifts of the high- z clusters would have to be significantly *underestimated* (see lower panel of Fig. 11.2). This would be nice from the distant X-ray cluster discovery point-of-view, but is very unlikely given the high redshift-sensitivity of the Z-H technique at $z \gtrsim 0.9$ (see Sect. 7.1.3). Using the ‘red-envelope’ in the color-magnitude diagram as distance indicator for high- z clusters (see Sect. 10.1.2) could possibly lead to a slight overestimation of the redshift for some distant clusters, which would again lead to an *anti-bias* in the sense that the distant BCGs are intrinsically even fainter than measured. Note that the spectroscopically confirmed cluster XMMXCS J2215.9–1738 at $z=1.45$ exhibits the faintest BCG of the whole sample.

Cosmological Model: As discussed, a modified Hubble parameter H_0 only changes the normalization of the Hubble diagram, but not its shape (see Equ. 3.46). Varying Ω_m within reasonable limits of $0.2 \lesssim \Omega_m \lesssim 0.4$ changes the luminosity distance of a flat cosmology d_{lum} by less than 10% at $z \sim 1.5$, which would result in apparent magnitude differences at the highest redshifts of $\Delta m \lesssim 0.2$ mag (see Equ. 7.4), *i.e.* less than 1/4 of the observed magnitude offset.

Cosmological Surface Brightness Dimming: The severe cosmological surface brightness dimming (Equ. 3.22) can introduce significant selection biases for very distant ($z \gtrsim 2$) galaxy studies close to the detection limit (Lanzetta *et al.*, 2002). However, all galaxies of the BCG sample are at least two magnitudes above the H-band completeness limit, implying that surface dimming should not play a significant role.

Biased Photometry: The H-band BCG data is taken from a homogeneous data set, observed with the same instrument and reduced in a standardized way. Great care has been taken to optimize the NIR sky subtraction to avoid background biases, in particular for faint, low surface brightness objects (see Sect. 7.3). The *SExtractor* photometry software is well tested and robust at the BCG magnitudes well above the detection threshold. *SExtractor* systematics due to source blending effects have been discussed and are marked in diagrams by arrows to indicate lower limits. *Without* source blending, the affected BCGs in the range $0.5 \gtrsim z \gtrsim 1.1$ could be intrinsically slighter fainter, with minor effects on the overall form of the luminosity evolution.

Passive Evolution Models: BCGs typically exhibit red, old stellar populations, and are in most cases the top ranked galaxies on the red-sequence (see Sect. 10.3). The assumption that the stellar populations of BCGs evolve passively seems therefore to be well justified. In Sect. 10.1, we could show that the red-sequence Z–H color evolution out to the highest accessible redshifts is fully consistent with passive evolution models with an early formation epoch. In addition, the X-ray selection process *disfavors* clusters with central (strongly non-passive) AGN activity with their associated point-like X-ray flux contribution. For the BCGs in our *X-ray selected, red-sequence confirmed cluster sample* passive evolution is a good description for the colors of their stellar populations. This means that recent star formation episodes or moderately strong active nuclei are expected to play a minor role.

For the comparison to passive evolution expectations, the *standard* $z_f = 5$, solar metallicity model is applied, which was shown to be close to the best fit parameters of Fig. 10.2. Variations of the formation age result in a slightly different m_H evolution over the observed redshift range from $z \sim 1.5$ to $z \sim 0.2$. At a fixed local apparent H-band magnitude, a $z_f = 3$ passive galaxy is expected to be about 0.2 mag brighter at $z \sim 1.5$ compared to the standard model, whereas formation redshift $z_f = 10$ objects are 0.2 mag fainter. This implies that subtracting passive evolution models with $z_f < 5$, as derived in Sect. 10.1, results in an increased magnitude offset at high redshifts, since the BCG magnitudes are compared to brighter model galaxies. The observed non-passive BCG luminosity evolution will hence be *enhanced*, if the formation redshift is lowered.

Although a number of possible biases and selection effects could be identified, all *individual* sources of error can at most, under reasonable assumptions, account for 1/4 of the observed non-passive component shown in Fig. 11.6. The main aim of this preliminary study at this point is to provide conclusive direct observational indications, rather than final exact

values, that BCGs are indeed increasing their mass as expected from hierarchical galaxy formation models, whereas their stellar populations evolve passively. For an accurate quantitative measurement of the BCGs evolution, all of the discussed possible biases and systematic effects need to be carefully taken into account for detailed follow-up studies. The preliminary total observed non-passive luminosity evolution component of $\Delta m \simeq 0.9$ is likely a *lower limit*, due to the discussed *anti-bias* of the X-ray cluster selection and the use of a $z_f = 5$ model for comparison.

11.1.3 Observing the BCG assembly epoch

Under the assumption that BCGs are assembled from progenitors with passively evolving stellar populations, *i.e.* associating the luminosity gain to additional mass, the detected evolution should be accompanied by an increased merging activity at $z \sim 1$. The following sub-section will take a closer look at this scenario.

Merging activity

Before addressing the question of BCG merging events at high redshifts, we need to approximate the occurrence rate of chance projected alignments of galaxies in clusters. Assuming that the BCG is located close to the center and that the galaxy density in the inner core region is approximately constant, then the probability that a second detected *cluster* galaxy is within the projected radius r_{proj} of the BCG can be estimated as

$$p_{\text{proj}} \simeq N_{\text{gal}} \cdot \frac{V_{\text{proj}}}{V_{\text{tot}}} \simeq 1.5 N_{\text{gal}} \left(\frac{r_{\text{proj}}}{r_{\text{tot}}} \right)^2 \lesssim 0.1, \quad (11.3)$$

where $V_{\text{proj}} \simeq 2\pi r_{\text{proj}}^2 r_{\text{tot}}$ is the projected cluster volume within r_{proj} along the cluster diameter $2r_{\text{tot}}$, V_{tot} is the approximate total volume of the inner cluster region, and N_{gal} is the number of detected cluster galaxies. For distant objects, observed at seeing limited $\sim 1''$ resolution, we can set the radius for apparent projected encounters to $r_{\text{proj}} \simeq 3''$, *i.e.* 2–3 times the seeing, the cluster radius for the denser core to $r_{\text{tot}} \simeq 0.5 \text{ Mpc} \simeq 60''$, and the number of detected galaxies at the given image depth to $N_{\text{gal}} \simeq 20$, yielding a *projected encounter chance* of about 8%. This value is a first crude estimate of the occurrence rate of close galaxy pairs due to chance alignments in cluster cores at the observed image depth, but does not include additional foreground and background objects yet.

For analytic approximations of chance alignments, values for the considered outer cluster radius r_{tot} and the total number of detected objects N_{gal} have to be assumed, which are not accurately known. As an alternative method without strong assumptions, the *observed* occurrence rate of close pairs for non-BCGs galaxies in the cluster core can be determined and compared to the BCG values. In $1' \times 1'$ environments surrounding the BCGs at $0.9 \lesssim z \lesssim 1.2$, about 15% of the non-BCG galaxies are found as close pairs with separations of $\lesssim 3''$. Since this method also accounts for real mergers, the value can be considered as a conservative reference point. In summary, an occurrence rate for close

galaxy pairs of 10–15% can be accounted for by chance alignments at the image depth and resolution limit of the available data.

Figures 11.7 & 11.8 display a gallery of 24 selected BCGs (marked by green arrows). The ordering of panels 1–24 is a *speculative attempt* to place the observed BCG appearance along an evolutionary sequence, *i.e.* to provide ‘typical BCG snap-shots’ over the last 9 Gyr of cosmic time. At the earliest observationally accessible epochs (*e.g.* panels 1–3), the BCGs appear to be ordinary galaxies very similar to their neighbors. At redshifts of $z \lesssim 1.3$, almost 40% of all BCGs exhibit indications for possible ongoing merging events (*e.g.* panels 4–15), *i.e.* 2–3 times the value that can be accounted for by projection effects. While a few of these observed close galaxy encounters are expected to be chance alignments (*e.g.* panel 9), the majority is likely to be attributed to real BCGs merging events, in particular for the cases with more than two distinguishable objects (*e.g.* panels, 5, 6, 10–15). The apparent merger fraction remains high down to redshifts of $z \sim 0.5$, but the physical mechanism responsible for the close encounters appears to change, as radially infalling subgroups reach the center (*e.g.* panels 16–19). In the final phase of the apparent BCG evolution, the central dominant giant cD galaxies appear on the cosmic stage at redshifts $z \lesssim 0.6$ (*e.g.* panels 20–24 in Fig. 11.8).

The four phases of BCG assembly

Since the BCGs constitute *the* most homogeneous class of galaxies in the local Universe (see Sect. 2.4.4), it can be expected that their formation history is very similar. Based on the findings discussed in this section, the following **speculative, observationally motivated formation scenario for BCGs** is proposed, complemented by results of numerical simulations (see Sect. 2.4).

Phase A – Normal Galaxies at High Redshift: At the presently observationally highest accessible redshifts of $z \gtrsim 1.3$, BCGs (5 in the current sample, *e.g.* panels 1–3 in Fig. 11.7) seem to be ordinary galaxies with H-band magnitudes of approximately $m^* - 1$, consistent with a top ranked galaxy in the cluster luminosity function. Together with other massive cluster galaxies, BCGs migrate towards the bottom of the cluster potential well via the *dynamic friction* mechanism (see Sect. 2.4.1).

Phase B – Main Merging and Mass Assembly Epoch: During the cosmic epoch $1.3 \gtrsim z \gtrsim 0.6 - 0.7$, corresponding to lookback times between about 9 and 6 Gyr, the main BCG luminosity and mass assembly takes place through dynamic friction driven dry major merging events close to the cluster center. During this phase, the BCG roughly doubles in mass and luminosity (*e.g.* panels 4–12) and becomes the dominant cluster galaxy.

Phase C – Radial Infall of Groups and High Speed Encounters:

The central BCG is further fed by radially infalling groups of galaxies with small impact parameters (*e.g.* panels 13–19) in the redshift range $0.8 \gtrsim z \gtrsim 0.3 - 0.4$. In contrast to the friction induced, slow encounters of phase B, the high impact velocities

of the order of the cluster velocity dispersion prohibit direct merging (see Sect. 2.4.1). It seems likely that radially impacting galaxies are (partially) disrupted and the debris dispersed throughout the cluster core, from where it can settle back onto the BCG to eventually form the extended cD envelope (*e.g.* panels 17–22). The mass growth rate during this phase is slowed down, but the characteristic appearance of local cD galaxies is likely shaped in this evolutionary phase.

Phase D – Settlement and Equilibrium Configuration: Once the stellar debris has settled back onto the central BCG and groups have coalesced with the main cluster, the BCG can assume its final equilibrium configuration as a giant dominant cD galaxy at redshifts $z \lesssim 0.6$ (*e.g.* panels 23–24).

This speculative BCG formation picture provides a testable starting point for further, more detailed studies. In particular, the physical mechanism for the formation of the characteristic cD halo requires additional in-depth investigations. The current BCG sample is based on follow-up observations of about one quarter of the XDCP distant cluster sample, implying that significant progress is possible over the next few years using extended BCG samples in conjunction with spectroscopic and high-resolution studies.

Discussion and comparison with simulations

The NIR rest-frame H-band luminosity of galaxies is dominated by old stars and is therefore a good proxy for the total stellar mass. Under the assumption of passively evolving BCG stellar populations, we can obtain a first order photometric stellar mass estimate by relating the observed averaged apparent H-band magnitude to the model predictions for an L_{mod}^* galaxy with a total stellar mass of $M_{\text{tot}}(L^*) = 2.84 \times 10^{11} M_{\odot}$. For the best fit model of Fig. 11.6 (bottom panel), the averaged BCG magnitudes are $m^* - 1.05$ at $z \sim 1.5$, $m^* - 1.4$ at $z \sim 1.0$, $m^* - 1.7$ at $z \sim 0.5$, and $m^* - 1.9$ at $z \sim 0.2$. These magnitudes yield the estimated stellar mass evolution for BCGs of $M_{\text{tot}}^{\text{BCG}} \simeq 7.5 \times 10^{11} M_{\odot}$ at $z \sim 1.5$, increasing to $M_{\text{tot}}^{\text{BCG}} \simeq 1.0 \times 10^{12} M_{\odot}$ by $z \sim 1.0$ and $M_{\text{tot}}^{\text{BCG}} \simeq 1.4 \times 10^{12} M_{\odot}$ at $z \sim 0.5$, with a final mass of $M_{\text{tot}}^{\text{BCG}} \simeq 1.7 \times 10^{12} M_{\odot}$ at $z \sim 0.2$. The observed luminosity evolution from redshift $z \simeq 1.5$ to $z \simeq 0.2$ can therefore be translated into a **stellar mass increase by a factor 2.2** over this cosmic epoch. As discussed, this is to be interpreted as a lower limit for the stellar mass evolution due the *anti-bias* of the X-ray selection.

We can now compare our preliminary observational results to the BCG evolution predicted by semi-analytic hierarchical formations models summarized in Sect. 2.4.4. The left panel of Fig. 2.7 shows that the studied model BCG experiences a major mass assembly epoch around $z \sim 1$, roughly coincident with the observationally identified epoch of high BCG merging activity (phase B). For the averaged BCG population in the right panel of Fig. 2.7, the simulations predict a more gradual stellar mass increase by a factor of three from $z \simeq 1$ to the present epoch, or a factor of four for the observationally probed redshift interval $1.5 \gtrsim z \gtrsim 0.2$. The estimated lower limits for the BCG *mass evolution* are thus within a factor of two in agreement with the predictions. A similar offset is found when the crudely determined *total stellar* mass estimates are compared to the median BCG mass predictions of Fig. 2.9.

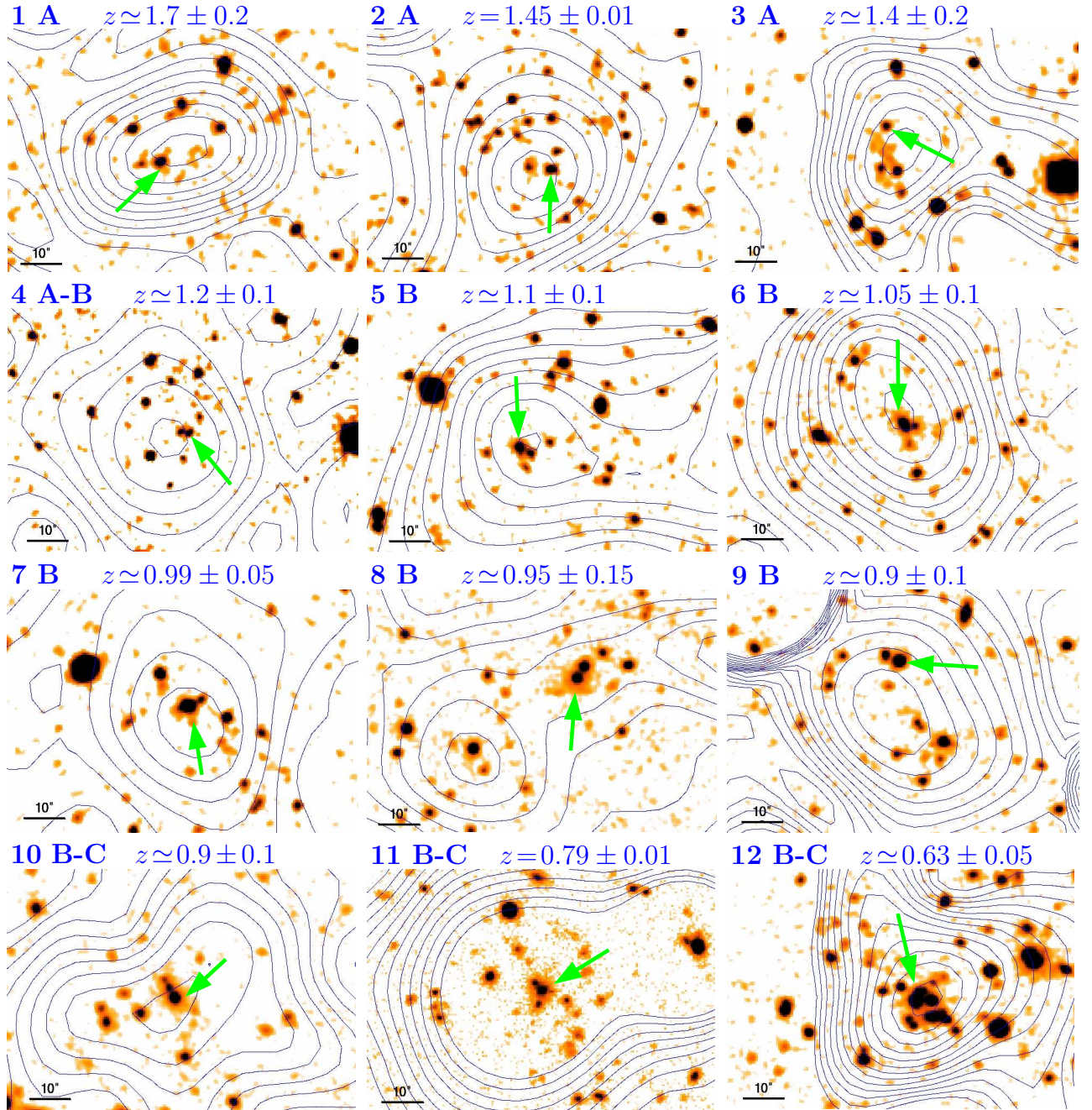


Figure 11.7: High-redshift BCG gallery. The panel number, the apparent BCG evolutionary phase indicated by the capital letter (or an intermediate stage), and estimated redshifts are given in the upper left. BCGs are marked by green arrows, X-ray contours are given in blue. All images show H-band or combined Z+H data with identical angular scales.

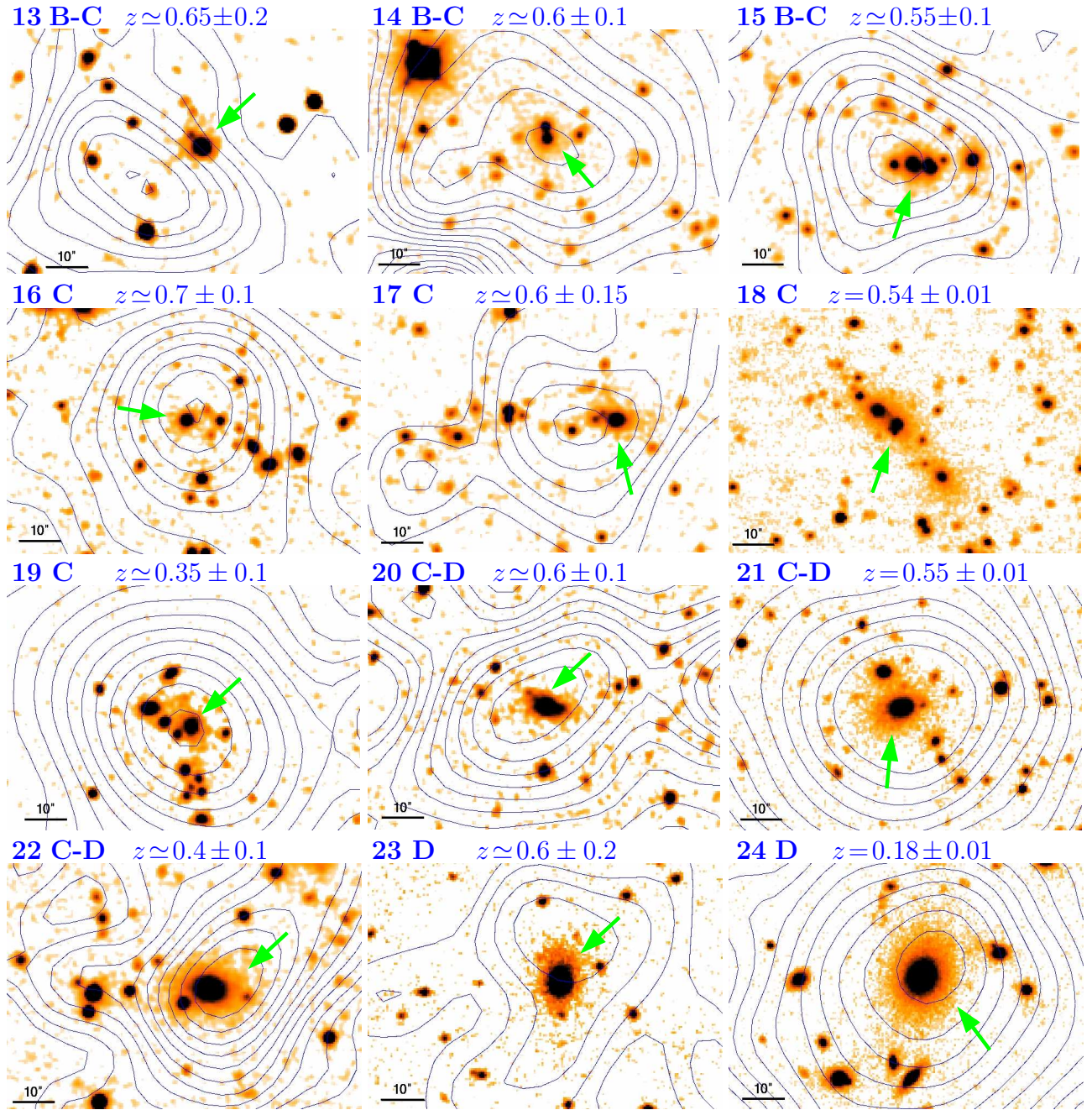


Figure 11.8: Low-redshift BCG gallery. Labels and data are the same as in Fig. 11.7.

The predicted BCG K-band evolution in Fig. 2.8 can be directly compared to the observed absolute H-band magnitudes in Fig. 11.3 and the model subtracted magnitude evolution in Fig. 11.6. If the X-ray cluster selection *anti-bias* is taken into account by restricting the simulated high-redshift sample to the brightest BCGs, *i.e.* the lower part of the sample bins in Fig. 2.8, the agreement with the simulations is remarkable and well within the uncertainties. The preliminary BCG sample study presented here hence manifests a significant step forward in the convergence process between observed properties of the most massive galaxies and the advancing predictions of the standard hierarchical galaxy formation paradigm.

11.2 Cluster Red-Sequences Studies

As discussed in Sect. 2.4.3, the effects of the ‘downsizing’ scenario have direct consequences on the red-sequence galaxy population and would result in a ‘truncation’ of the CMR beyond a redshift dependent observed magnitude. The most distant cluster for which a deficit in the faint red galaxy population has been reported is RDCS J1252.9-2927 and its surrounding LSS at $z = 1.24$, recently investigated in detail by Tanaka *et al.* (2007). While the main cluster exhibits a clear CMR down to magnitudes of $K_s(\text{AB}) \sim 23$ mag, the red-sequence of the identified associated clumps in the LSS seem to be truncated at $K_s(\text{AB}) \lesssim 22$ mag, consistent with the first reports of this effect at similar redshifts (Kajisawa *et al.*, 2000; Nakata *et al.*, 2001). The observations support the picture of an *environment dependent downsizing evolution*, where the star formation activity ceases first for the most massive galaxies in clusters and a *delayed* CMR build-up in lower density environments.

At redshift $z \lesssim 0.8$, De Lucia *et al.* (2007) find a deficit of faint red cluster galaxies in the luminosity range $0.4 \gtrsim L_{\text{faint}}/L^* \gtrsim 0.1$ relative to the fraction of $L_{\text{lum}} > 0.4 L^*$ objects. This luminous-to-faint galaxy number ratio, $N_{\text{lum}}/N_{\text{faint}}$, exhibits a decreasing trend towards lower redshift, implying that the faint end of the CMR becomes increasingly populated with increasing cosmic time. A similar evolution in the build-up of the faint red-sequence galaxy population is observed by Stott *et al.* (2007) at $z \lesssim 0.5$.

The current limited depth of the available Z and H-band follow-up data does not yet allow a quantitative assessment of the galaxy population at the *faint end* of the red-sequence. The detailed analysis of the red-sequence properties at $z \gtrsim 1$ requires deep, high-quality multi-band data for precision photometry and the selection of cluster members using photometric redshift techniques, currently available for only about half a dozen clusters listed in Tab. 9.1.

The detailed investigation of the ‘downsizing’ scenario and the related red-sequence truncation in galaxy clusters at high redshift will be a main XDCP science focus in the near future. Using guaranteed observing time at the 2.2 m telescope at the La Silla Observatory, we will use the multi-channel GROND⁵ camera to obtain deep optical and NIR photometric coverage for a sample of $z \gtrsim 0.9$ cluster candidates currently scheduled for

⁵More details can be found at <http://www.mpe.mpg.de/~jcg/GROND>.

spectroscopic confirmation. GROND provides the unique possibility of performing simultaneous observations in four optical filters and the J, H, and Ks NIR bands. This data will be used to determine accurate photometric redshifts and construct CMDs to completeness limits that are 1–2 magnitudes fainter than the currently available data.

In order to fully understand the build-up of the red-sequence and its evolution, the CMRs of distant clusters have to be studied as a function of redshift *and* cluster mass. Two of the important questions that can be addressed with the upcoming XDCP study are (i) whether the truncation of cluster red-sequences at high redshift is a universal phenomenon and (ii) how the cluster mass influences ‘downsizing’.

11.3 Gallery of High-Redshift Clusters

Before concluding, color composite images of a selection of newly discovered high-redshift clusters are shown in Fig. 11.9 for the redshift range $0.8 \lesssim z \lesssim 1.05$ and in Fig. 11.10 for candidate systems at $z \gtrsim 1.1$. All $2'.5 \times 2'$ color images have X-ray contours overlaid in yellow and are based on Z+H data obtained during the two Calar Alto follow-up campaigns. The displayed systems are not yet spectroscopically confirmed, but several of the cluster candidates are already scheduled for FORS2 spectroscopy. The redshift confirmation is of particular importance (and a challenge, see Chap. 8) for candidates at the highest accessible redshifts of $z \gtrsim 1.4$. Three Calar Alto selected candidate systems belong to the latter category, based on typically 4–6 very red objects close to the X-ray center, two of them are displayed in panels 11 & 12 in Fig. 11.10.

11.4 Summary and Conclusions

- In Sect. 11.1, the photometric Z–H red-sequence redshift estimates were used for a preliminary study of the brightest cluster galaxy evolution by constructing the H-band Hubble diagram for BCGs out to $z \simeq 1.5$.
- It was shown, that the observed X-ray selected cluster BCGs are consistent with being ‘standard candles’ of absolute H-band magnitude $M_H \simeq -26.3$ mag out to $z \simeq 1.5$.
- The increased redshift baseline allowed to exclude that the luminosity of BCGs evolves passively at the 3σ confidence level. Although a number of possible selection biases were identified, which need to be carefully quantified in future studies, none of these effects could fully account for the observed non-passive evolution component.
- The comparison to the expected apparent magnitude evolution of a single model galaxy with passively evolving stellar populations revealed the tentative result that BCGs have at least doubled their mass between redshifts of $z \simeq 1.5$ and $z \simeq 0.2$, whereas their stellar populations evolve passively.

- It was speculated that the tentatively identified active BCG assembly phase around $z \sim 1$ is accompanied by an increased observed merger rate at the cluster center, followed by an epoch where radially infalling groups of galaxies seem to be important for the final stages of the BCG evolution.
- The preliminary results suggest that the well-established old age of the stellar populations of BCGs and the expected late mass assembly can be observationally reconciled. Predictions for the BCG evolution from the latest simulations and semi-analytic models are in qualitative agreement with our tentative findings.
- Upcoming deep multi-band photometric studies of XDCP clusters at high redshift will allow a systematic investigation of the phenomenon of a red-sequence truncation and the related ‘downsizing’ scenario.
- A gallery of newly discovered X-ray luminous high-redshift galaxy cluster candidates was presented. These and other systems are currently awaiting their spectroscopic redshift confirmation.
- The refinement of the early results of Chap. 10 and the preliminary BCG evolution study presented in Sect. 11.1 will provide observational contributions towards an emerging consistent picture of galaxy evolution in clusters.

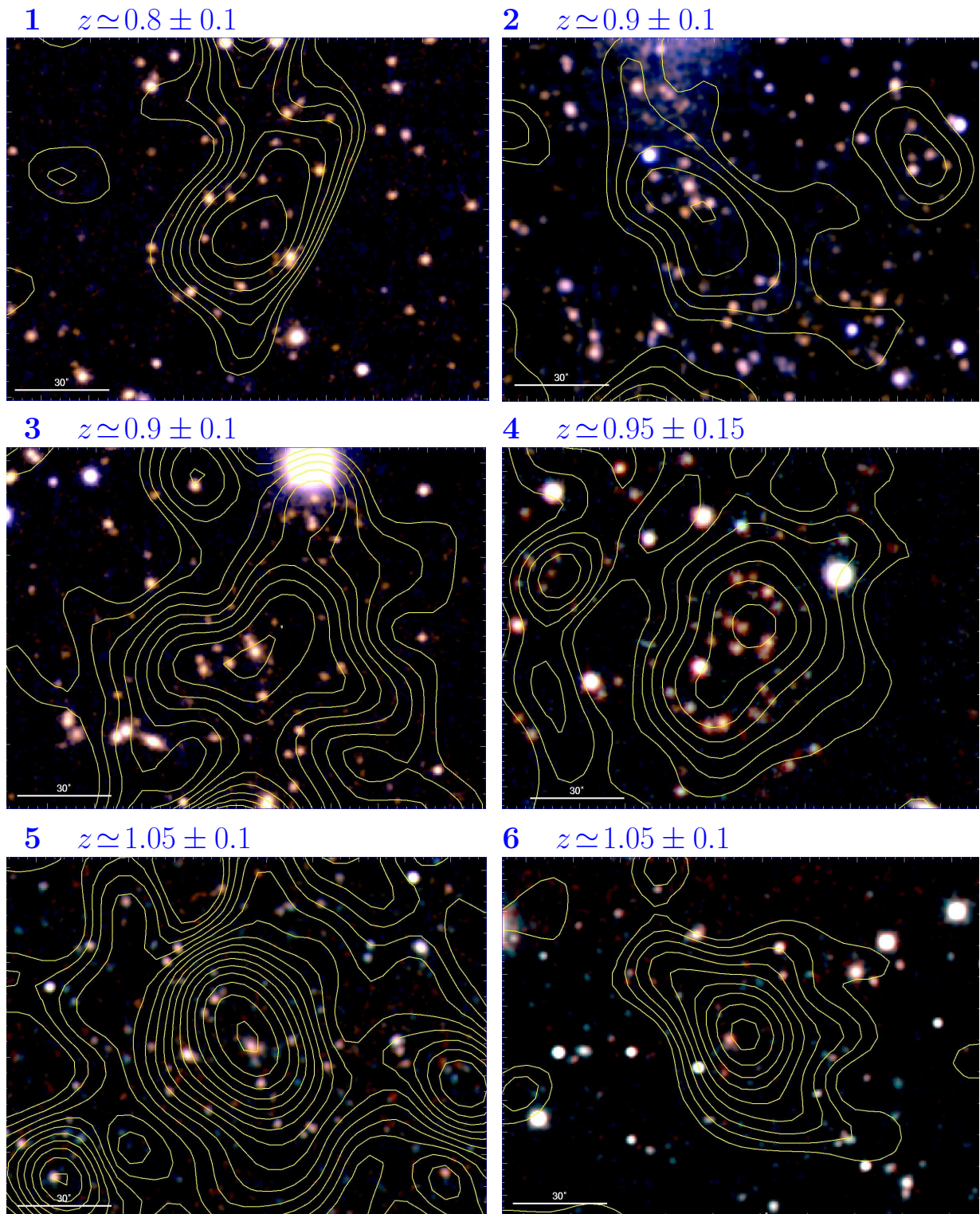


Figure 11.9: High-redshift galaxy cluster gallery A. $2.5 \times 2'$ Z+H color composites of a selection of newly discovered high-redshift clusters with photometric redshift estimates of $0.8 \lesssim z \lesssim 1.05$ are shown; X-ray contours are overlaid in yellow.

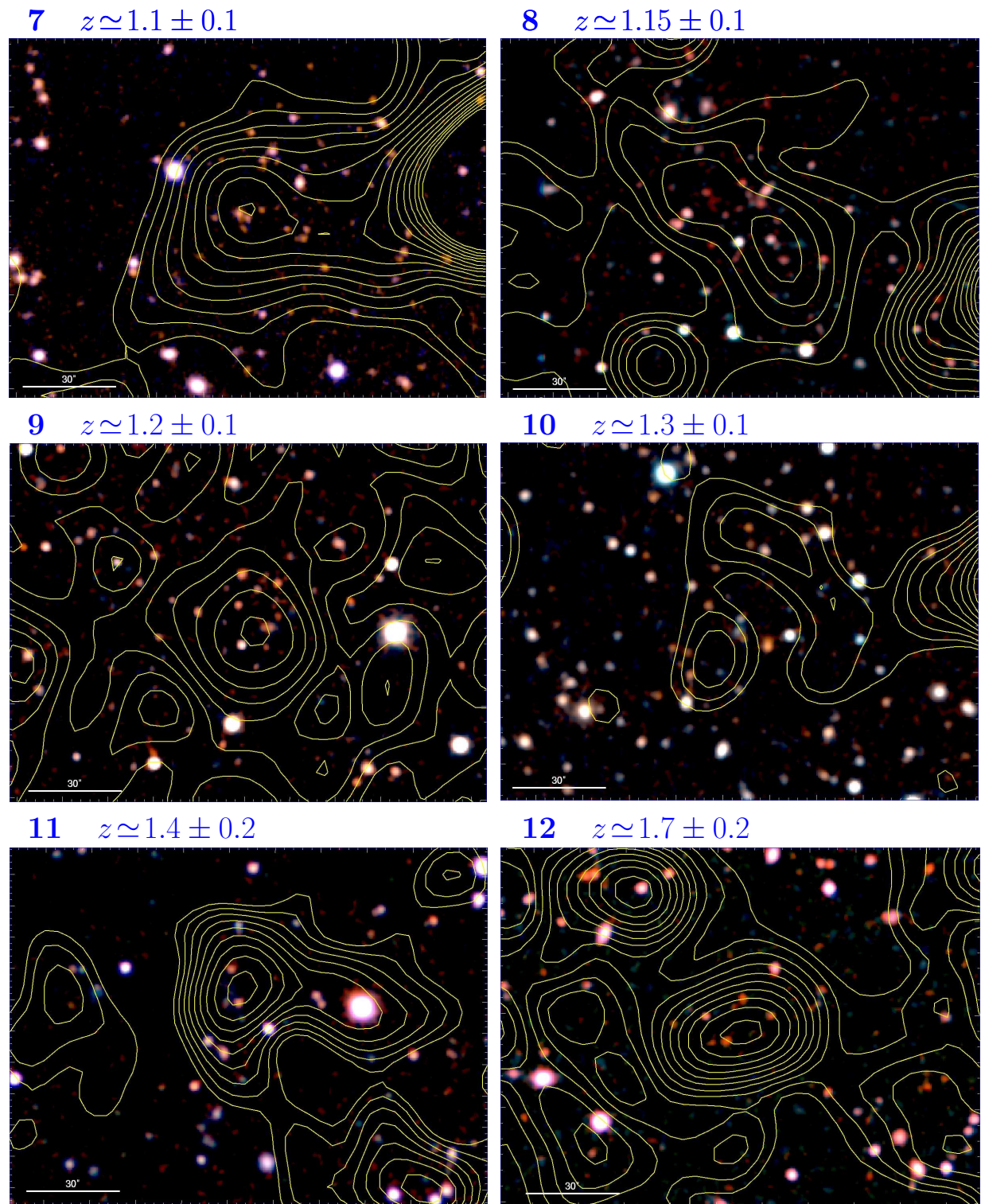


Figure 11.10: High-redshift galaxy cluster gallery B, displaying a selection of the new sample of candidate clusters with photometric redshift estimates of $z \gtrsim 1.1$.

Chapter 12

The Future of Galaxy Cluster Surveys

Before closing this work, a brief outlook of some of the expected major developments in distant galaxy cluster studies over the next decade(s) is presented.

12.1 SZE Surveys

A new generation of galaxy cluster survey instruments based on the *Sunyaev-Zeldovich effect* (SZE) is currently resuming routine operations. 35 years after the theoretical prediction (Sunyaev and Zeldovich, 1972), the SZE (see Sect. 2.3.6) is opening up a new observational survey window to cluster studies. The nearly redshift independent sensitivity to massive clusters and the complementarity with respect to X-ray measurements have raised high hopes for its impact on cosmological studies. The scientific focus of the large SZE surveys is the determination of the cluster number density evolution out to high redshifts as a means to constrain the properties of *Dark Energy* (Sect. 3.3). The cosmological applications are hence similar to the XDCP goals with the main differences that the SZE selected cluster samples (i) follow a shallower, less peaked redshift distribution compared to the X-ray selection (see right panel of Fig. 6.17), and (ii) have a contiguous, wider sky coverage allowing a clustering analysis.

The South Pole Telescope (SPT) survey¹ (Ruhl *et al.*, 2004) will cover approximately 4000 deg² in the mm-bands centered at 150 GHz, 219 GHz, and 274 GHz. The 10 m off-axis Gregorian telescope, shown in the left panel of Fig. 12.1, has seen first light in February 2007 and is currently preparing for routine survey observations. The SPT survey is of special importance for the XMM-Newton Distant Cluster Project because of the substantial overlap of more than 100 XDCP core sample fields with a total nominal exposure time of 3.3 Msec. The ongoing efforts to take full advantage of the joint SZE-X-ray-optical data synergies have been introduced in Sect. 9.2. The future cross-comparison of the X-ray and

¹The SPT homepage can be found at <http://spt.uchicago.edu/>.

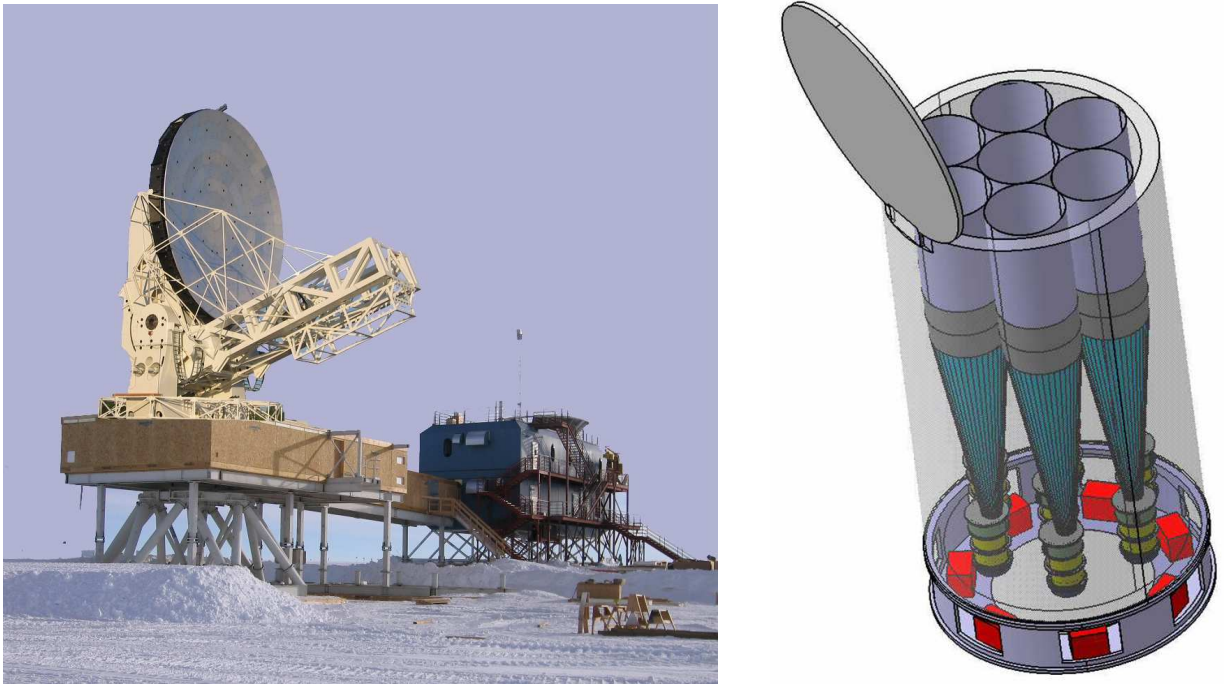


Figure 12.1: Instruments for upcoming major cluster surveys: *Left:* The 10 m South Pole Telescope has started SZE observations. Image from press release.²*Right:* eROSITA with its seven mirror and detector systems will conduct the next generation all-sky X-ray survey starting in 2011. Technical drawing from the mission definition document.³

SZE cluster selection functions will be of particular significance to understand the different survey systematics, which is crucial for the cosmological interpretation of the results.

This last important point for the use of galaxy clusters for precision cosmology gave rise to the motivation to conduct a designated X-ray cluster survey (PI: H. Böhringer) in the joint sky regions of the three major SZE instruments SPT, the Atacama Pathfinder EXperiment (APEX-SZ), and the Atacama Cosmology Telescope (ACT). The initial 1 Msec XMM proposal for a 12.5 deg^2 X-ray coverage with typical exposure times of 12 ksec has been 50% granted at present. XMM observations of the first 42 pointings are currently being conducted. The upcoming X-ray analysis of this cluster survey will largely benefit from the gained experience and developed tools of the XDCP survey.

²The image can be found at <http://www.nsf.gov/news/mmg/media/images/SPT%20complete%20s3.JPG>.

³The eROSITA mission definition document can be accessed at <http://www.mpe.mpg.de/erosita/MDD-6.pdf>.

12.2 eROSITA

The next generation all-sky X-ray surveys will be conducted with eROSITA (extended ROentgen Survey with an Imaging Telescope Array) starting in 2011. The eROSITA instrument (Predehl *et al.*, 2006) is fully funded and is currently in an active preparation phase as one of the three main experiments of the Russian Spectrum-RG mission.

As shown in the right panel of Fig. 12.1, eROSITA will combine seven Wolter-I X-ray mirror modules, each equipped with an improved PN-like detector array with a field-of-view⁴ of about 0.5 deg^2 . The satellite will be placed in an equatorial Low Earth Orbit with expected good X-ray background properties. The total effective area of $\sim 2500 \text{ cm}^2$ is comparable to the imaging mode capabilities of XMM-Newton, but the wider FoV leads to a total grasp of $g \simeq 700 \text{ cm}^2 \text{ deg}^2$, *i.e.* a survey efficiency improvement of a factor of 2.5 with respect to the full XMM field or a factor of 3.5 when restricting the XMM FoV to the inner 12 arcminutes. The design specifications concerning the PSF quality aim at a FWHM resolution of $15''$ on-axis and a $20''$ field-of-view average. The current eROSITA survey plans foresee an all-sky survey with a typical extended source sensitivity of $3 \times 10^{-14} \text{ erg s}^{-1} \text{ cm}^{-2}$ and a deeper survey region covering a few hundred square degrees to a flux limit of about $1 \times 10^{-14} \text{ erg s}^{-1} \text{ cm}^{-2}$.

The challenging main goal of eROSITA will be the identification of 50 000–100 000 galaxy clusters out to $z \sim 1.5$. This unprecedented sample size is required to achieve the prime science objective of tracing the cosmic evolution of the *Dark Energy* equation-of-state parameter w using the *baryonic acoustic oscillation* method discussed in Chap. 3.

XDCP will serve as an important pathfinder sample for eROSITA and its distant cluster cosmology applications. As probably the deepest XMM-Newton cluster survey with a sky coverage of $\gg 10 \text{ deg}^2$ and an average sensitivity 3–5 times better than the eROSITA all-sky survey, the XDCP sample will be valuable for quantifying the eROSITA performance and for calibrating the cluster selection function. In particular, the lower eROSITA resolution will constrain the accessible parameter region for a distant cluster selection based on extent and is hence to be closely investigated (see Fig. 9.3). In any case, eROSITA will increase the known X-ray cluster population by at least one order of magnitude and will open unprecedented possibilities for precision cosmology with galaxy clusters.

⁴The eROSITA detector design has recently been modified and now foresees a FoV diameter of about 60 arcminutes, which will also increase the stated total grasp.

ID	Method	Test Objects	σ_w	z_{\max}	X	O/IR	Hi Res
1	BAOs in galaxy cluster PS	1.75×10^5 GC	$<5\%$	2	×	×	
2	cosmic shear	10^9 G	$<5\%$	2		×	×
3	BAOs in galaxy PS	10^9 G	$<5\%$	3		×	
4	cluster number counts	1.75×10^5 GC	$<10\%$	2	×	×	
5	BAOs in AGN PS	5×10^6 AGN	$<10\%$	4	×	×	
	all methods combined		$\lesssim 1\%$		×	×	×

Table 12.1: Expected results and measurement precision on w of a five year VADER survey covering 3500 deg^2 and probing a comoving volume of 50 Gpc^3 for *all Dark Energy* tests ($z \leq 2$). From left to right the table lists the scientific priority (ID), the method, the object class with the expected sample size, and the covered redshift range. The last three columns specify the instrumental requirements for the given methods distinguishing X-ray coverage (X), multi-band optical/IR data (O/IR), and diffraction limited high spatial resolution (Hi Res). By combining all independent VADER measurements of w with their different degeneracies, a sub-percent level precision is achievable.

12.3 VADER – A Concept Study

The first two sections covered new galaxy cluster experiments already existing or in preparation. In this final section, a concept study is presented, which is closing in on an *ultimate cluster survey*, *i.e.* a mission that is able to identify essentially all observable galaxy clusters over a wide sky area. The result of this study is the Very Ambitious Dark Energy Research mission (VADER), a project that originated at the 2005 ESA summer school in Alpbach, Austria. The objective was a design study for a designated *Dark Energy* satellite mission within ESA’s *Horizons 2015–2025* program. The VADER project was continued after the school and led to a publication in the high energy mission section of the SPIE proceedings (Fassbender *et al.*, 2006).

12.3.1 Science case

The nature of *Dark Energy*, as the driving force of the observed acceleration of the Universe, is currently one of the deepest mysteries in astrophysics. A precise knowledge of the equation-of-state parameter w (see Equ.3.6) and in particular its redshift dependance is required to allow at least a phenomenological understanding of the dominant energy contribution in the Universe. The answer to the fundamental question whether DE is equivalent to Einstein’s cosmological constant ($w = -1$), phantom energy (Caldwell *et al.*, 2003) ($w < -1$), or time varying as in quintessence models (Wetterich, 1988) ($-1 < w < -1/3$) will not only shed light on the fate of the Universe but will also lead the way to a unified physical theory.

The main science objective of the proposed VADER mission concept is the measurement of the *Dark Energy* w parameter with percent-level precision and to accurately constrain its redshift evolution. This goal is to be achieved with a single experiment yielding a self-contained, space-quality data set. eROSITA, for example, will likely detect $\mathcal{O}(100\,000)$ ex-

tended X-ray sources, but the science applications depend critically on the time-consuming follow-up observation programs (see Chaps. 7 & 8).

VADER is designed as a multi-wavelength survey mission joining X-ray, optical, and IR instruments for a simultaneous spectral coverage from $4\ \mu\text{m}$ (0.3 eV) to 10 keV over a field-of-view of 1 square degree. This combination enables several independent *Dark Energy* tests with low systematics. Table 12.1 lists the five DE tests that were identified with highest priority. The associated expected object sample sizes for galaxy clusters (GC), galaxies (G), and Active Galactic Nuclei (AGN) are specified together with conservative estimates of the measurement accuracy, the covered redshift range, and the instrumental requirements. As the presumably cleanest *Dark Energy* test (see Sect. 3.2.2), a strong focus is placed on the accurate measurement of the *baryonic acoustic oscillations* in the power spectrum (PS). This cosmological test (see Tab. 3.2) effectively determines the Hubble expansion history $H(z)$ and angular size distance $d_{\text{ang}}(z)$ and can be performed independently for the different object classes of galaxy clusters (highest priority), galaxies (medium priority), and AGN (lower priority). Large area measurements of the *cosmic shear*, *i.e.* the weak lensing effect of the large-scale structure, is a promising alternative DE technique through its sensitivity to cosmic distances (see *e.g.* Schneider, 2006b). The determination of the number density evolution of galaxy clusters (Sect. 3.2) completes the main VADER portfolio of *Dark Energy* tests. Note that the BAO test, *cosmic shear*, and the cluster number density evolution have later been identified as three of the four most promising routes to *Dark Energy* research by the NASA Dark Energy Task Force⁵. Supernovae Ia studies, as the fourth recommended pillar, apply the Hubble diagram method (see Sect. 3.3) but require alternative observational techniques.

12.3.2 Satellite design concept

In short, the VADER design foresees the combination of two high-throughput XMM-Newton type X-ray imaging telescopes (0.1–10 keV) complemented by a 1.5 m wide-field corrected optical/IR telescope as sketched in the left panel of Fig. 12.2.

The optical/IR beam is dichroic-separated⁶ into eight bands (U G R Z J H K L) allowing the simultaneous coverage from 0.3–4 μm . The two X-ray and eight optical/IR imaging cameras all have a field-of-view of 1 square degree and survey the same patch of sky. As indicated in Tab. 12.1, the weak lensing technique requires high spatial resolution and good optical quality for galaxy shape measurements. Diffraction-limited images are achieved in the Z-band using a 3.7 Giga pixel optical camera with a scale of 0.064'' per pixel. Most of the other seven camera systems will yield undersampled images with roughly a doubled pixel scale and provide the photometric data for accurate photometric redshifts, the critical prerequisite of all DE methods. With the proposed eight photometric bands, the achievable expected redshift uncertainties are about $\Delta z \simeq 0.02(1+z)$ per galaxy and $\Delta z \lesssim 0.01(1+z)$ for the averaged cluster redshifts. The near-infrared bands J, H, K, and the additional

⁵<http://www.science.doe.gov/hep/DETF-FinalRptJune30,2006.pdf>

⁶The principal design is similar to the GROND camera. More detailed information can be found at <http://www.mpe.mpg.de/~jcgr/GROND>.

mid-infrared L-band at $3.6\ \mu\text{m}$ provide sensitivities which are inaccessible from the ground and can trace the bulk of the galaxy population out to redshifts of $z \sim 3$ and for AGN even further.

Additional X-ray imaging data is crucial for the three DE tests using galaxy clusters and AGN as cosmological probes (Tab. 12.1). The two VADER X-ray mirror modules are based on the XMM-Newton design in order to combine the total effective area of $2\,800\text{ cm}^2$ at 1.5 keV with an average spatial resolution of about $15''$ across the 1 square degree FoV. This largely *extended* field-of-view, compared to XMM as discussed in Sect. 6.1, can be achieved with a detector configuration that follows the curved focal plane of the grazing incident mirrors leading to a significant improvement of the off-axis PSF. Including vignetting effects, VADER's total effective X-ray grasp at 1.5 keV is about $1120\text{ cm}^2\text{deg}^2$, *i.e.* a factor of four better than XMM.

12.3.3 Survey and results

VADER is designed to perform a very deep extragalactic multi-wavelength survey over a contiguous sky area of $3\,500$ square degrees during the first five years of the mission. The selected survey region between the South Galactic Pole (SGP) and the South Ecliptic Pole (SEP) is illustrated in the right panel of Fig. 12.2, the possible survey extension and the location of an ultra-deep field are also indicated.

The satellite will operate in a highly elliptical 72 hour orbit allowing 60 hours of consecutive science data acquisition outside the radiation belts. The orbit was selected to optimize the observational and technical requirements of (i) a low X-ray, optical, and IR background, (ii) a high science data fraction per orbit, (iii) long, pointed observations, (iv) observations of a single, contiguous survey field, (v) a stable thermal environment, and (vi) a high downlink rate for data transmission.

The survey strategy is aiming for a gross exposure time of 10 h per field, achieved through an observation pattern of overlapping single 2 h exposures sampled over a period of a few weeks in order to additionally allow time domain astrophysics. Taking overheads and data losses into account, the average achievable X-ray flux limit will be about $1 \times 10^{-15}\text{ ergs}^{-1}\text{cm}^{-2}$ for point sources and $2 \times 10^{-15}\text{ ergs}^{-1}\text{cm}^{-2}$ for extended objects. With these sensitivities, the expected X-ray selected samples will include approximately 5×10^6 AGN out to redshifts of at least $z \sim 4$ and $175\,000$ galaxy clusters out to $z \sim 2$. These X-ray capabilities, complemented by the deep optical and infrared galaxy photometry, provide accessibility to essentially *all existing* clusters of galaxies within the survey region with masses of $M \gtrsim 1.5 \times 10^{14}\ M_{\odot}$. The typical achievable limiting AB magnitudes of $26\text{--}27\text{ mag}$ in the optical bands and $23\text{--}25\text{ mag}$ in the infrared bands will allow the detection, SED characterization, and photometric redshift determination of about one billion galaxies.

The special strength of the proposed VADER mission is its ability to provide the most *complete and versatile* survey data set for *Dark Energy* and general astrophysical studies. The independent *Dark Energy* tests using BAOs, *cosmic shear*, and the cluster number density evolution enable critical cross-checks between the methods. The final combination of all DE techniques with their different degeneracies brings *w* constraints with percent-level precision within reach.

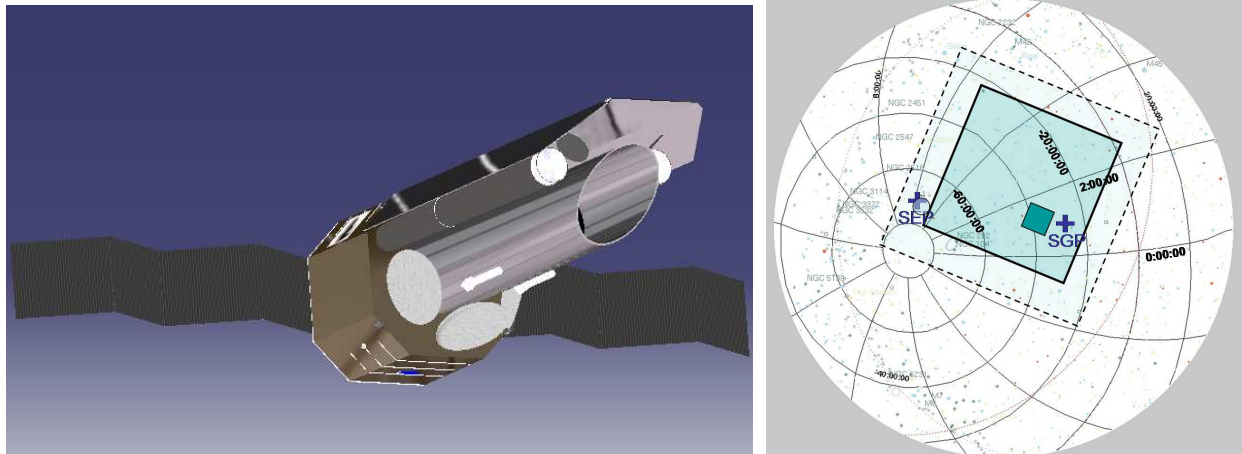


Figure 12.2: VADER spacecraft and survey region. *Left:* Scheme of the VADER spacecraft with its optical/IR telescope and the two X-ray mirror modules. *Right:* The solid square indicates the 3500 deg^2 sky area between the South Galactic Pole (SGP) and the South Ecliptic Pole (SEP) covered by a 5 year survey. The dashed box shows the prospects for an extended 10 year survey and the small square the location of the proposed 100 deg^2 deep survey field.

Concerning the technical feasibility of the mission, the X-ray part is mainly based on available technology and bears low risk. The wide-field optical/IR telescope with its multiplexed imaging capability will require a challenging optical design with substantial additional research and development activities. With the rapidly advancing detector technology, the first Giga pixel camera systems will soon be available and similar sizes in the near-infrared regime will become feasible within the next few years. The project scope for a realization of VADER would be an ESA cornerstone mission with a possible launch around 2020.

The aim of unveiling the very nature of the dominant *Dark Energy* component in the Universe has given rise to a hyper-active phase of proposals and developments of a full armada of DE experiments with the result that *Dark Energy* has become *the buzzword* in current astrophysics. However, the theoretical and observational developments in *Dark Energy* research over the next two decades are difficult to foresee and critical opinions on the merit of designated DE missions have appeared (*e.g.* White, 2007). In any case, the solution to the *Dark Energy* riddle is of fundamental importance and the route to its understanding might bear many surprises and dead ends.

12.4 Concluding Remarks

When speaking of the *Golden Age for Astronomy* and the dawning *Era of Precision Cosmology*, one can, without exaggeration, also conceive the next 10–15 years as the *New Age of Galaxy Cluster Surveys*. Here we have only touched on the upcoming developments in X-rays and for the SZ effect. Major survey projects with a strong focus on galaxy clusters are additionally ongoing or in preparation in the optical, near-infrared, and mid-infrared wavebands. Just to name a few, the Dark Energy Survey (DES), the Kilo Degree Survey (KIDS), the Panoramic Survey Telescope and Rapid Response System (PanSTARRS) are optical experiments with expected cluster sample sizes of at least a few thousand systems. At longer wavelength the Visible & Infrared Survey Telescope for Astronomy⁷ (VISTA) or the Spitzer mid-infrared fields⁸ aim at the compilation of hundreds of objects out to high redshift.

The common aim of all projects is the identification of systems out to redshifts of $z \gtrsim 1$, owing to the recognition of galaxy clusters as prime tracers of cosmic evolution. As a survey in an advanced state, the XMM-Newton Distant Cluster Project is in a good position to take on a pathfinder role to largely unexplored redshift regimes over the next few years. In conclusion, the future for distant galaxy cluster studies looks bright. Only the tip of the distant cluster iceberg has been found, the main body is yet to be unveiled.

⁷A list of VISTA surveys can be found at <http://www.eso.org/sci/observing/policies/PublicSurveys/sciencePublicSurveys.html#VISTA>.

⁸A list of Spitzer surveys is available at <http://ssc.spitzer.caltech.edu/legacy/all.html>.

Appendix A

XDCP Survey Field List

Table A.1: XDCP survey field summary. For each of the 546 processed XMM-Newton observations the central equatorial (RA, DEC) and galactic coordinates (GL, GB) are given followed by the corresponding galactic hydrogen column density N_{H} in units of 10^{21} cm^{-2} . The last five columns contain the XMM field identifier (OBSID), the nominal exposure time (EXT), the effective clean exposure time (CLT), the processing status (STAT), and the target name of the observation (TARGET). 469 fields have been successfully processed and analyzed (STAT=ok), 48 were highly flared (STAT=flared), and 29 were discarded for other reasons (STAT=discard).

RA h m s	DEC d m s	GL d.d	GB d.d	N_{H} $\times 10^{21}$	OBSID	EXT sec	CLT sec	STAT	TARGET
00 00 29.2	-25 07 20	40.0	-78.3	0.157	0125310101	46065	16360	ok	Abell 2690
00 02 51.2	-29 59 11	15.0	-78.9	0.131	0041750101	52270	46458	ok	BLANCO1
00 03 09.1	-35 57 00	349.2	-76.4	0.113	0145020201	54258	47354	ok	A 2717
00 03 26.1	-26 02 28	36.0	-79.2	0.163	0103060301	50537	32902	ok	Q0000-263
00 00 23.6	+02 04 39	98.0	-58.3	0.300	0201900101	29907	22485	ok	RXCJ0003.8+0203
00 10 30.5	+10 58 43	106.9	-50.6	0.576	0127110201	16311	2625	ok	IIIZW2
00 11 03.5	-12 07 18	88.7	-72.2	0.257	0150480501	22199	10960	ok	NGC34
00 11 25.1	-11 28 42	90.0	-71.7	0.268	0111970901	12857	9673	ok	WW Cet
00 14 19.0	-30 22 22	9.0	-81.2	0.165	0042340101	18463	12311	ok	RXCJ0014.3-3022
00 14 34.0	-39 10 56	333.1	-75.7	0.176	0028740101	31669	25236	ok	NGC 55 (West)
00 15 47.2	-39 15 34	332.1	-75.7	0.176	0028740201	33767	29338	ok	NGC 55 (East)
00 18 33.6	+16 26 07	111.6	-45.7	0.407	0111000101	37949	26769	ok	CL 0016+16
00 20 45.6	-25 41 43	42.9	-82.9	0.226	0201900301	31007	12852	ok	RXCJ0020.7-2542
00 21 18.5	-48 39 13	316.1	-67.6	0.262	0152330101	47961	21255	ok	SCG 0018-4854
00 26 07.5	+10 41 11	112.8	-51.6	0.498	0001930101	26609	14168	ok	IRAS F00235+10
00 26 36.6	+17 09 36	114.4	-45.3	0.431	0050140201	55009	41795	ok	C10024+17
00 30 26.7	+04 51 49	113.1	-57.6	0.292	0112320101	31229	8492	ok	PSR J0030+0451
00 33 53.0	-43 18 00	314.2	-73.4	0.293	0148961201	19863	15344	ok	ELAIS-S1-C

00 33 52.9	-43 18 00	314.2	-73.4	0.293	0148961301	48419	32683	ok	ELAIS-S1-C
00 33 53.6	-12 07 48	106.7	-74.4	0.242	0125920201	50809	7920	ok	G158-100
00 33 52.8	-43 18 00	314.2	-73.4	0.293	0148961401	25039	3379	flared	ELAIS-S1-C
00 34 16.1	-21 25 19	87.5	-83.0	0.156	0044350101	22870	11870	ok	IRAS00317-2142
00 34 24.6	-05 33 40	111.5	-68.0	0.432	0031740101	35738	7057	ok	PSR J0034-0534
00 35 51.3	-43 17 55	312.9	-73.5	0.263	0148960101	104416	47233	ok	ELAIS-S1-A
00 37 07.0	+09 09 07	116.9	-53.5	0.478	0084230201	30207	22255	ok	Abell 68
00 41 42.2	-09 22 26	115.0	-72.0	0.308	0065140101	13253	9026	discard	Abell 85
00 42 30.8	-09 41 25	115.6	-72.4	0.308	0065140201	13248	10324	ok	Abell 85
00 43 20.1	+00 51 05	118.6	-61.9	0.245	0090070201	21249	17844	ok	UM 269
00 43 24.8	-20 37 31	106.7	-83.2	0.154	0042340201	15006	8511	ok	RXCJ0043.4-2037
00 43 35.7	-17 59 25	111.3	-80.6	0.170	0112880601	13250	9422	ok	HR 188
00 46 51.5	-20 43 15	113.4	-83.5	0.157	0110990301	16889	2953	flared	NGC247
00 47 23.9	-25 15 25	96.8	-87.9	0.149	0110900101	33732	21384	ok	NGC 253 NW
00 47 36.0	-25 17 52	97.5	-87.9	0.128	0125960201	17537	5496	ok	NGC253
00 47 36.2	-25 17 52	97.5	-87.9	0.128	0125960101	60809	31583	ok	NGC253
00 47 39.3	-25 17 08	98.0	-87.9	0.128	0152020101	140799	63718	ok	NGC 253
00 49 59.2	-52 08 58	303.4	-64.9	0.340	0133120301	12022	8107	ok	BPM 16274
00 50 01.3	-52 08 11	303.4	-64.9	0.340	0123920101	57464	8833	ok	BPM 16274
00 50 03.0	-52 08 19	303.4	-64.9	0.340	0125320401	33728	17775	ok	BPM16274
00 50 03.3	-52 08 17	303.4	-64.9	0.340	0125320701	45951	10346	ok	BPM16274
00 50 07.1	-52 09 41	303.4	-64.9	0.340	0133120401	13707	8611	ok	BPM 16274
00 54 55.5	-37 41 09	299.1	-79.4	0.361	0112800101	46711	38155	ok	NGC 300
00 54 55.5	-37 41 08	299.1	-79.4	0.361	0112800201	36909	27667	ok	NGC 300
00 56 15.0	-01 18 39	125.6	-64.1	0.310	0012440101	34992	25332	discard	LBQS0053-0134
00 58 37.0	-36 06 02	293.7	-80.8	0.194	0102040701	21536	7855	ok	Q 0056-363
00 58 48.8	-28 25 00	251.6	-87.9	0.195	0111282301	14075	650	flared	SGP-9
00 58 53.8	-27 59 00	240.7	-88.1	0.195	0111280601	10944	7947	ok	SGP-6
01 02 41.4	-21 52 51	149.5	-84.1	0.160	0144310101	33917	17992	ok	Abell 133
01 03 59.4	-06 41 53	131.8	-69.3	0.506	0112650501	25035	16432	ok	G133-69 Pos.2
01 04 24.6	-06 24 10	131.9	-69.0	0.508	0112650401	27145	18405	ok	G133-69 Pos.1
01 06 22.2	+00 49 11	130.8	-61.8	0.316	0150870201	28815	715	flared	BRI0103+0032
01 06 55.9	-80 17 22	302.1	-36.8	0.664	0145540101	31315	22348	ok	IRASF01063-8034
01 07 45.8	-17 30 14	145.1	-79.6	0.140	0025540101	12572	3361	flared	IC1623
01 12 53.4	-45 32 04	291.2	-71.1	0.210	0067170101	47870	39004	ok	Phoenix field
01 13 49.9	-14 50 40	147.0	-76.6	0.163	0147920101	26915	20479	ok	MRK 1152
01 18 56.5	-00 59 16	138.2	-63.0	0.371	0153170101	22204	8626	ok	MS 0116.3-0115
01 20 20.8	-44 07 51	285.9	-72.0	0.241	0103860901	22608	18679	ok	ESO 244- G 017
01 20 39.0	-10 56 27	147.3	-72.4	0.353	0113040801	10768	3539	flared	C2001
01 22 43.0	-11 14 24	149.2	-72.4	0.353	0113040701	10045	2455	flared	C2001
01 23 46.1	-58 48 19	295.0	-57.8	0.282	0101040201	33006	26928	ok	Fairall 9
01 24 35.7	+03 47 20	138.7	-58.0	0.337	0025541601	13203	10287	ok	NGC520
01 25 33.4	+01 45 35	140.1	-59.9	0.308	0109860101	41694	33368	ok	A 189

01 25 47.3	-01 23 55	142.1	-62.9	0.356	0136340101	22515	16496	ok	Abell 194
01 31 54.3	-13 36 58	159.9	-73.5	0.156	0084230301	24709	14485	ok	Abell 209
01 33 01.1	-40 06 27	272.0	-74.4	0.201	0112630201	37870	21297	ok	QSO 0130-403
01 36 20.8	+15 44 24	138.5	-45.7	0.483	0154350201	24914	22087	ok	SN2002ap
01 36 24.3	+15 45 02	138.5	-45.7	0.483	0154350101	37259	26902	ok	SN2002ap
01 39 52.9	+06 18 31	144.0	-54.5	0.371	0110890901	27412	14774	ok	PHL 1092
01 40 10.5	-67 48 45	296.0	-48.6	0.235	0032140401	12561	5279	ok	1saxj0140.2-6748
01 40 55.2	-67 54 28	295.9	-48.5	0.235	0148440101	29559	26028	ok	BL Hyi
01 43 01.9	+13 38 22	141.6	-47.3	0.476	0093641001	12209	8034	ok	NGC 660
01 46 14.8	-39 22 05	263.4	-73.2	0.186	0090070101	33020	29584	ok	Q 0144-3938
01 48 59.9	+05 55 10	147.8	-54.1	0.445	0112551501	21446	14748	ok	ngc676
01 52 42.1	+01 00 30	153.0	-58.2	0.284	0084230401	30199	13453	ok	Abell 267
01 52 40.0	-13 58 52	173.3	-70.5	0.147	0109540101	53917	42618	ok	WARP J0152.7-13
01 53 03.9	-13 43 25	173.0	-70.3	0.169	0112300101	47478	18978	ok	ngc 720
01 53 37.2	-49 36 53	279.1	-64.5	0.241	0092970201	14368	10001	ok	ESO 197-G010
01 55 46.2	+00 28 58	154.7	-58.3	0.284	0145450201	12618	2216	flared	SDSS015543+00
01 59 49.6	+00 23 52	156.5	-57.9	0.251	0101640201	14778	4169	flared	Mrk 1014
02 07 39.4	+02 08 10	158.0	-55.4	0.311	0052140301	35006	26292	ok	HCG 15
02 07 52.8	+02 43 46	157.6	-54.9	0.350	0048740101	47340	9723	ok	NAB 0205+024
02 09 51.5	-63 18 38	288.8	-51.6	0.294	0111970401	15197	6033	ok	WX Hyi
02 15 13.1	-73 59 08	295.3	-41.8	0.339	0049150101	29614	5694	ok	Magellanic Bridge
02 15 19.6	-73 59 50	295.3	-41.8	0.339	0099840101	14256	9602	ok	Magellanic Bridge
02 15 27.2	-74 01 09	295.3	-41.8	0.339	0049150201	28609	4147	flared	Magellanic Bridge
02 15 35.6	-73 59 57	295.2	-41.8	0.339	0049150301	31426	15332	ok	Magellanic Bridge
02 19 23.7	-02 57 50	167.7	-57.9	0.244	0148500201	12218	10172	ok	Mira
02 22 00.2	-04 50 12	171.0	-58.9	0.255	0112680801	15617	10372	ok	MLS-4
02 24 03.2	-04 29 12	171.3	-58.3	0.251	0112680501	23645	17817	ok	MLS-8
02 24 36.9	-04 10 51	171.1	-58.0	0.232	0112680301	23411	19205	ok	MLS-3
02 25 08.0	+18 47 37	151.7	-38.7	1.042	0150180101	22208	19599	ok	RBS 315
02 25 13.3	-29 27 30	224.9	-69.2	0.170	0201900701	29481	0	flared	RXCJ0225.1-2928
02 25 20.5	-04 30 10	171.7	-58.1	0.232	0112681001	41946	19995	ok	MLS-7
02 26 02.8	-04 09 10	171.5	-57.7	0.232	0112680201	21648	8058	ok	MLS-2
02 26 43.0	-04 29 13	172.2	-57.9	0.232	0112681301	40381	13322	ok	MLS-6
02 27 20.6	-04 10 11	172.0	-57.5	0.273	0112680101	30351	22689	ok	MLS-1
02 28 00.4	-04 30 10	172.7	-57.7	0.273	0112680401	25050	20187	ok	MLS-5
02 28 56.1	-10 10 25	181.1	-61.4	0.260	0112860101	10035	4697	ok	Q0226-1024
02 32 21.0	-44 19 45	259.9	-63.4	0.261	0042340301	13645	9640	ok	RXCJ0232.2-4420
02 34 22.6	-43 47 43	258.4	-63.4	0.261	0148790101	48479	19176	ok	CC Eri
02 34 41.4	-08 46 35	180.8	-59.4	0.283	0150470601	57917	12453	ok	NGC 985
02 36 11.5	-52 19 16	272.2	-58.1	0.308	0098810101	24995	20509	ok	WW Hor
02 38 19.4	-52 11 38	271.6	-57.9	0.307	0067190101	34146	18519	ok	ESO 198-G24
02 38 38.5	+16 36 49	156.7	-39.1	0.885	0110990101	19851	16422	ok	AO0235+164
02 41 04.4	-08 15 12	182.0	-57.9	0.308	0093630101	16463	12911	ok	NGC 1052

02 42 40.9	-00 00 47	172.1	-51.9	0.355	0111200101	42258	33615	ok	NGC 1068
02 42 41.0	-00 00 46	172.1	-51.9	0.355	0111200201	46429	28657	ok	NGC 1068
02 48 06.6	-03 30 57	177.7	-53.4	0.412	0084230501	33645	25182	ok	Abell 383
02 49 33.7	-31 11 24	229.0	-63.9	0.227	0146510401	38914	29923	ok	IC1860 Group
02 52 54.5	-01 15 39	176.4	-51.0	0.525	0151490101	47204	19428	ok	NGC 1132
02 56 05.6	+19 22 48	159.2	-34.5	1.065	0112510301	30242	20763	ok	MBM 12 Pos_2
02 56 04.5	+19 28 50	159.2	-34.4	1.096	0110660101	24196	10395	ok	MBM 12
02 56 33.4	+00 06 00	175.9	-49.4	0.665	0056020301	25094	8676	ok	RX J0256.5+0006
02 57 52.5	+13 02 08	164.3	-39.4	1.058	0112260101	15409	9110	ok	A399
02 58 58.4	+13 33 47	164.2	-38.8	1.019	0112260301	13806	9988	ok	A399
02 59 51.4	+13 46 47	164.2	-38.5	1.019	0112260401	12755	8971	ok	A399
03 02 39.1	+00 07 31	177.5	-48.3	0.733	0041170101	51724	40890	ok	CFRS3h
03 05 22.2	+17 29 11	162.7	-34.8	1.106	0112190101	13647	9886	ok	MS0302.5+1717
03 06 37.6	+00 00 28	178.6	-47.6	0.668	0142610101	73918	32406	ok	S2F1a
03 07 04.4	-28 40 29	223.9	-60.0	0.136	0042340501	14767	10108	ok	RXCJ0307.0-2840
03 11 55.8	-76 51 52	293.4	-37.5	0.748	0122520201	46099	23563	ok	PKS0312-770
03 17 56.7	-44 14 10	252.9	-56.0	0.253	0105660101	24470	19260	ok	A3112
03 18 14.9	-66 29 48	283.3	-44.6	0.440	0106860101	42416	15312	ok	NGC 1313
03 19 59.4	+11 14 10	171.1	-37.3	1.671	0110661101	12796	8587	ok	MBM 16
03 20 07.6	-62 26 33	278.6	-47.0	0.422	0084960101	27842	6428	ok	Galactic Halo
03 23 21.1	-49 30 26	260.9	-53.3	0.172	0140190101	29614	25722	ok	RX J0323-4931
03 23 50.5	-37 17 11	240.2	-56.4	0.167	0091770101	60362	27252	ok	NGC 1316
03 32 53.2	-09 28 23	195.8	-48.0	0.413	0112880501	13420	11301	ok	HR 1084
03 32 52.8	-63 27 53	278.6	-45.3	0.504	0084960201	12846	10014	ok	Galactic Halo
03 33 30.3	-36 10 22	238.0	-54.6	0.135	0151370101	19417	15229	ok	NGC 1365-X1
03 33 38.8	-36 08 55	237.9	-54.5	0.135	0151370701	11417	6839	ok	NGC 1365-X1
03 36 41.1	+00 36 23	184.8	-41.5	0.805	0116150601	64197	22191	ok	HR1099
03 36 41.3	+00 36 24	184.8	-41.5	0.805	0116340601	28610	17959	discard	HR1099
03 36 43.7	-36 01 03	237.6	-53.9	0.139	0140950201	17417	14528	ok	NGC1386
03 36 47.2	+00 35 21	184.9	-41.5	0.805	0134540601	35740	28264	ok	HR1099
03 36 46.9	+00 35 27	184.9	-41.5	0.805	0129350201	31310	8460	flared	HR1099
03 36 47.0	+00 35 20	184.9	-41.5	0.805	0134540101	46325	13660	discard	HR1099
03 36 47.2	+00 35 19	184.9	-41.5	0.805	0134540801	51927	27	discard	HR1099
03 37 44.3	-25 22 17	219.8	-52.8	0.155	0107860401	63138	26483	ok	SHARC4
03 38 28.3	-35 26 52	236.7	-53.6	0.145	0012830101	29364	6170	ok	NGC 1399
03 38 29.8	+00 21 44	185.5	-41.3	0.735	0036540101	23004	17982	ok	SDSS033829+00
03 38 36.3	+09 57 50	176.2	-35.0	1.864	0109870101	30612	9118	discard	2A 0335+096
03 38 40.7	+09 58 17	176.2	-35.0	1.864	0147800201	140323	99140	discard	2A 0335+096
03 39 35.7	-35 25 55	236.6	-53.4	0.148	0055140101	51410	39957	ok	LP 944-20
03 41 30.2	-44 52 34	252.0	-51.8	0.166	0045940301	31893	22907	ok	AXJ0341.4-4453
03 45 46.0	-41 12 39	246.0	-51.7	0.188	0201900801	26912	12926	ok	RXCJ0345.7-4112
03 53 43.6	-00 04 33	188.9	-38.5	1.183	0134920901	20467	9150	ok	SA95-42
03 53 50.5	-10 24 35	200.6	-44.0	0.428	0093160201	28014	13589	ok	BR 0351-1034

03 54 35.6	-20 30 52	214.1	-47.8	0.394	0150910101	18920	7796	ok	NGC 1482
03 57 25.3	+01 11 41	188.3	-37.0	1.301	0094790201	21892	19221	ok	Hawaii 167
03 58 50.8	+10 25 21	179.8	-31.0	1.452	0064600301	11914	6857	ok	3C 98
03 58 57.9	+10 26 37	179.8	-31.0	1.452	0064600101	28904	9336	ok	3C 98
04 12 35.5	+10 15 34	182.4	-28.5	1.432	0112231601	38757	17000	ok	A478 off-set
04 13 30.2	+10 28 05	182.4	-28.2	1.527	0109880101	126748	53202	ok	A 478
04 19 34.3	+02 23 54	190.9	-31.8	1.159	0152150101	30912	19525	ok	NGC1550
04 19 33.2	+14 32 50	179.9	-24.5	1.470	0141400301	25218	8165	ok	LH0416+14
04 19 47.6	+15 37 33	179.0	-23.8	1.764	0024140101	63578	45054	ok	GammaTau
04 20 01.1	-50 23 54	258.1	-44.3	0.196	0141750101	22201	19269	ok	RXJ0420.0-5022
04 20 01.0	-50 23 55	258.1	-44.3	0.196	0141751001	21914	16225	ok	RXJ0420.0-5022
04 20 00.7	-50 23 56	258.1	-44.3	0.196	0141751101	22420	19204	ok	RXJ0420.0-5022
04 20 05.5	-50 21 47	258.1	-44.3	0.196	0141751201	21919	19404	ok	RXJ0420.0-5022
04 22 12.6	-38 45 55	241.7	-44.9	0.190	0104860101	22865	8417	ok	[HB89] 0420-388
04 24 12.7	+14 45 35	180.5	-23.5	1.670	0101440601	48757	33085	ok	VB50
04 24 12.9	+14 45 28	180.5	-23.5	1.670	0101441501	57513	32175	ok	VB50
04 26 11.2	+16 55 48	179.0	-21.8	1.915	0056020401	23659	8990	ok	RX J0426.1+1655
04 28 35.0	+15 57 45	180.2	-21.9	1.711	0101440501	47811	37399	ok	VB71
04 31 38.8	+18 10 15	178.9	-20.0	1.792	0109060301	57818	48640	ok	L1551 cloud
04 33 39.3	-13 15 45	209.5	-36.4	0.568	0135120201	30867	17308	discard	A 496
04 33 56.5	-08 35 24	204.4	-34.3	0.579	0150480201	23929	17124	ok	NGC1614
04 37 14.1	+00 44 13	195.3	-29.0	0.819	0042341601	18238	2955	flared	RXCJ0437.1+0043
04 37 22.0	-47 15 30	253.4	-41.9	0.169	0112320201	69412	24942	ok	PSR J0437-4715
04 40 16.9	-43 33 25	248.4	-41.5	0.147	0104860201	12868	10136	ok	[HB89] 0438-436
04 47 52.1	-06 27 17	204.0	-30.3	0.547	0014740601	28887	6505	ok	a0447-0627
04 48 12.6	-20 29 08	219.5	-35.9	0.321	0142240101	15208	7895	ok	Abell 514
04 48 30.8	-20 35 42	219.6	-35.8	0.321	0142240201	15203	7860	ok	Abell 514
04 52 34.4	-29 53 01	231.1	-37.5	0.180	0153100101	15925	9924	ok	IRAS 04505-2958
04 54 10.2	-53 22 40	261.1	-38.7	0.350	0148650101	58916	39557	ok	NGC 1705
04 54 44.8	-18 08 30	217.4	-33.6	0.425	0140210101	38947	29209	ok	RXCJ0454-1808
04 59 34.8	+01 47 17	197.6	-23.7	0.747	0112880401	20600	16321	ok	Gl 182
05 00 55.6	-38 40 12	242.4	-37.3	0.307	0083151201	13516	8438	ok	A3301
05 01 05.9	-24 25 18	225.2	-34.3	0.237	0110870101	25867	21755	ok	CL0500-24
05 05 19.4	-28 48 53	230.6	-34.6	0.154	0111160201	49616	26291	ok	SHARC-2
05 07 42.0	-37 31 00	241.2	-35.9	0.278	0110980801	43606	33560	ok	NGC 1808
05 12 55.9	-16 12 25	217.2	-28.9	0.600	0143370101	47265	37618	ok	Mu Lep
05 14 06.2	-40 02 43	244.5	-35.0	0.361	0151750101	23914	8177	ok	4U 0513-40
05 15 41.5	+01 04 28	200.4	-20.6	1.091	0010620101	31641	20228	ok	V1309 Ori
05 16 43.8	-54 30 26	262.2	-35.3	0.625	0042340701	15114	6620	ok	RXCJ0516.7-5430
05 19 49.8	-45 46 59	251.6	-34.6	0.449	0090050701	20521	8647	ok	PICTOR A
05 21 01.6	-25 21 58	227.8	-30.2	0.193	0085640101	12423	7693	ok	IRAS05189-2524
05 23 03.3	-36 27 22	240.6	-32.6	0.329	0065760201	31919	28588	ok	PKS0521-365
05 25 01.7	-33 43 47	237.5	-31.7	0.218	0149500801	13706	6745	ok	PMN-525-3343

05 25 01.7	-33 43 46	237.5	-31.7	0.218	0149500901	12205	5727	ok	PMN-525-3343
05 25 01.5	-33 43 46	237.5	-31.7	0.218	0149500601	12206	8994	ok	PMN-525-3343
05 25 01.7	-33 43 45	237.5	-31.7	0.218	0149500701	12206	8534	ok	PMN-525-3343
05 25 06.2	-33 42 51	237.5	-31.6	0.218	0050150301	28528	17343	ok	PMN 0525-3343
05 25 06.7	-33 43 12	237.5	-31.6	0.218	0050150101	21870	8102	ok	PMN 0525-3343
05 25 08.9	-33 42 09	237.5	-31.6	0.218	0149501201	12419	5663	ok	PMN-525-3343
05 28 56.0	-39 27 36	244.3	-32.1	0.210	0042340801	14112	5543	ok	RXCJ0528.9-3927
05 33 01.9	-37 01 21	241.7	-30.8	0.293	0042341801	12740	8292	ok	RXCJ0532.9-3701
05 33 44.0	-24 10 49	227.6	-27.1	0.233	0068940101	129506	21632	ok	CL1
05 33 43.7	-24 10 49	227.6	-27.1	0.233	0068940601	35178	11860	ok	CL1
05 40 12.0	-40 54 59	246.5	-30.2	0.353	0149420101	18217	14790	ok	ESO03060170
05 47 38.6	-31 52 42	236.9	-26.6	0.195	0201900901	25320	20193	ok	RXCJ0547.6-3152
05 50 40.8	-32 16 09	237.5	-26.1	0.220	0111830201	54576	15715	ok	PKS 0548-32
05 59 46.1	-50 26 59	257.9	-28.5	0.484	0125110101	57265	8000	ok	PKS0558-504
05 59 47.2	-50 26 52	257.9	-28.5	0.484	0129360201	26409	9031	ok	PKS0558-504
05 59 46.6	-50 27 07	257.9	-28.5	0.484	0119100201	45437	4340	flared	PKS0558
05 59 48.9	-50 26 37	257.9	-28.5	0.484	0137550201	14968	11568	ok	PKS0558-504
05 59 48.4	-50 27 10	257.9	-28.5	0.484	0137550601	14785	4640	ok	PKS0558-504
06 02 02.8	-39 57 37	246.4	-26.0	0.501	0151900101	47206	19753	ok	A3376
06 15 24.3	-33 24 56	240.5	-21.5	0.325	0092360301	15513	6363	ok	3EG 0616-3310
06 15 24.1	-32 55 00	240.0	-21.3	0.410	0092360401	15514	8972	ok	3EG 0616-3310
06 16 47.1	-47 48 12	255.6	-25.3	0.481	0201901101	44676	2156	flared	RXCJ0616.8-4748
06 17 47.1	-32 54 57	240.1	-20.9	0.410	0092360101	12512	8503	ok	3EG 0616-3310
06 17 47.1	-33 24 55	240.6	-21.0	0.384	0092360201	15068	10551	ok	3EG 0616-3310
06 45 21.9	-54 12 57	263.6	-22.5	0.657	0201901201	26397	10965	ok	RXCJ0645.4-5413
06 45 25.6	-54 12 11	263.6	-22.5	0.657	0201903401	23236	11474	ok	RXCJ0645.4-5413
06 58 16.8	-55 57 23	266.0	-21.2	0.634	0112980201	46756	21497	ok	RXJ0658-55
07 51 08.8	+18 07 50	202.7	21.0	0.502	0111100301	38499	9271	ok	PSR J0751+18
08 06 27.5	+15 27 49	206.9	23.4	0.248	0150800101	28719	17091	ok	RXJ0806.3+1527
08 39 57.5	+19 32 39	206.0	32.3	0.309	0101440401	48305	39011	ok	Praesepe
08 40 52.2	+13 12 39	212.9	30.1	0.422	0147670301	30914	8263	ok	3C 207
08 51 26.7	+11 47 08	215.7	31.9	0.377	0109461001	10160	7267	ok	EU Cnc
09 08 13.8	-09 36 35	239.1	24.6	0.421	0136740201	18366	5363	ok	A754_f2
09 08 45.6	-09 46 03	239.3	24.6	0.421	0112950401	16810	9772	ok	A754_f4
09 08 55.4	-09 32 04	239.1	24.8	0.421	0112950301	14771	9836	ok	A754_f3
09 09 26.7	-09 40 22	239.3	24.8	0.459	0136740101	18370	11654	ok	A754_f1
09 11 27.6	+05 51 05	224.6	33.6	0.391	0083240201	20814	11284	discard	RX J0911.4+0551
09 18 00.9	-12 05 11	242.9	25.0	0.486	0109980301	32995	14662	ok	Hydra A cluster
09 43 44.0	+16 44 34	216.3	45.5	0.282	0046940401	15560	11234	ok	WARPJ0943.7+16
09 43 43.8	+16 44 05	216.3	45.5	0.282	0046940201	33116	3149	flared	WARPJ0943.7+16
09 45 41.8	-14 19 40	249.7	28.7	0.517	0147920301	28917	19551	ok	NGC 2992
09 52 08.6	-01 48 07	239.4	38.0	0.384	0065790101	10111	5800	ok	RXJ 095208.7-014
09 53 04.9	+07 55 24	228.8	43.6	0.301	0103260801	84291	15600	ok	PSR B0950+08

09 53 14.3	-15 58 43	252.5	28.9	0.527	0140210201	38915	33996	ok	RXCJ0953-1558
09 53 36.5	+01 34 33	236.1	40.3	0.359	0070940401	26760	7633	ok	NGC 3044
09 53 41.0	+01 35 03	236.1	40.3	0.359	0070940101	11428	3713	flared	NGC 3044
09 54 48.8	-20 23 03	256.2	26.0	0.389	0141170101	61227	30122	ok	EIS0954-2023
09 54 56.7	+17 43 19	216.4	48.3	0.339	0112850101	33376	14111	ok	0952+179
09 56 11.7	-10 03 09	248.0	33.5	0.507	0148170101	102815	64021	ok	Abell 901
09 58 17.6	-11 03 29	249.3	33.2	0.506	0201903501	18285	6509	ok	RXCJ0958.3-1103
10 00 11.9	-19 38 08	256.7	27.4	0.449	0041180301	22358	18131	ok	NGC 3091 group
10 04 15.7	+05 12 53	234.1	44.6	0.233	0150610101	23624	8447	ok	PG 1001+054
10 07 21.7	+12 48 35	225.1	49.1	0.369	0140550601	22205	19384	ok	PG 1004+130
10 11 05.7	-04 41 20	246.1	39.8	0.391	0026340201	21618	6073	ok	Sextans A
10 19 59.8	+08 13 28	233.5	49.5	0.329	0093640301	24263	3845	flared	IRAS 10173+0828
10 21 37.4	+13 06 40	227.2	52.3	0.379	0146990101	21917	16357	ok	IRAS 10190+1322
10 23 30.8	+19 51 56	216.9	55.4	0.222	0101040301	40495	32296	ok	NGC 3227
10 23 40.0	+04 11 27	239.3	47.9	0.287	0108670101	56459	48492	ok	ZW 3146
10 28 34.2	-08 44 41	253.9	40.1	0.459	0153290101	43368	15915	ok	RXJ1028.6-0844
10 30 22.4	+05 24 45	239.4	50.0	0.339	0148560501	103876	60819	ok	SDSS 1030+05
10 36 28.2	-03 43 17	251.1	45.1	0.471	0150870401	31418	27773	ok	BRI1033-0327
10 41 12.8	+06 10 10	241.0	52.6	0.270	0151390101	59915	40999	ok	4C 06.41
10 44 32.9	-01 25 13	250.8	48.2	0.432	0125300101	62310	29778	ok	J104433.04-0125
10 50 26.2	-12 50 39	262.7	40.4	0.501	0146510301	40921	20572	ok	NGC3411 Group
10 56 59.8	-03 37 38	256.5	48.6	0.379	0094800101	41021	22223	ok	MS1054.4-0321
11 01 52.6	-34 42 37	278.6	22.9	0.473	0112880201	29776	25669	ok	TW Hya
11 06 34.2	-18 21 44	270.8	37.8	0.461	0112630101	36428	10464	ok	HE 1104-1805
11 13 17.2	-26 45 06	277.2	31.1	0.561	0071340201	22234	10958	ok	NGC 3585
11 15 18.1	-21 56 38	275.2	35.7	0.408	0094380101	33673	26861	ok	GRB011211
11 17 15.8	+17 57 42	230.8	66.4	0.143	0099030101	23795	13319	ok	DP Leo
11 18 17.3	+07 46 11	249.8	60.6	0.336	0082340101	63358	49529	ok	PG1115+080
11 18 55.1	+13 05 19	241.3	64.2	0.227	0082140301	33519	28398	ok	NGC3623
11 20 14.9	+12 59 24	241.9	64.4	0.264	0093641101	11363	6979	ok	NGC 3627
11 20 17.1	+13 35 31	240.8	64.7	0.196	0110980101	86739	41222	ok	NGC 3628
11 23 09.2	+05 30 29	254.7	59.8	0.433	0083000301	33361	24867	ok	3C 257
11 23 16.1	+01 37 42	259.5	56.8	0.423	0145750101	42208	21840	ok	Q1120+0195
11 30 02.3	-14 49 25	275.2	43.6	0.406	0112850201	30089	13489	ok	1127-145
11 31 56.5	-19 55 42	278.5	39.1	0.451	0042341001	15025	10122	ok	RXCJ1131.9-1955
11 32 00.5	-34 36 30	284.8	25.4	0.504	0112880101	29921	26857	ok	CoD-33_7795
11 38 22.5	+03 22 05	263.4	60.5	0.235	0111970701	12866	10213	ok	T Leo
11 39 01.7	-37 44 08	287.4	22.9	0.941	0112210201	137818	16000	ok	NGC3783
11 39 01.7	-37 44 08	287.4	22.9	0.941	0112210501	137815	20000	ok	NGC3783
11 39 02.3	-37 44 13	287.4	22.9	0.941	0112210101	40412	13509	ok	NGC3783
11 39 06.9	+17 07 15	240.1	70.5	0.203	0066950201	13383	4620	ok	UGC 6614
11 41 07.0	-01 43 09	269.7	56.5	0.245	0151230101	10919	6607	ok	UN J1141-0143
11 41 19.7	-12 16 20	277.3	47.0	0.330	0201901601	37932	24496	ok	RXCJ1141.4-1216

11 44 39.9	+19 47 00	235.0	73.0	0.255	0061740101	33366	26714	discard	A1367
11 50 41.5	+01 45 50	270.5	60.7	0.215	0044740201	49072	43910	ok	Beta Vir
11 51 02.4	-28 48 06	287.2	32.2	0.627	0027340101	45533	29905	ok	NGC 3923
12 00 48.0	-03 27 39	279.2	57.0	0.243	0056020701	30114	24816	ok	RX J1200.8-0328
12 01 53.1	-18 51 42	286.9	42.4	0.400	0085220101	24913	15885	ok	The Antennae
12 01 52.6	-18 51 41	286.9	42.4	0.400	0085220201	52777	34943	ok	The Antennae
12 04 27.4	+01 54 30	276.9	62.3	0.186	0093060101	16004	11301	ok	MKW4
12 12 15.8	+13 12 33	267.6	73.3	0.249	0112550501	23614	17974	ok	ngc4168
12 13 46.0	+02 48 53	280.9	64.0	0.174	0081340801	23206	19206	ok	IRAS12112+03
12 16 40.5	-12 01 17	289.6	49.9	0.385	0143210801	33916	22276	ok	cl1216-12
12 18 45.0	+14 24 53	270.3	75.1	0.271	0147610101	50920	15073	ok	NGC 4254
12 19 23.2	+05 49 47	281.8	67.3	0.163	0056340101	33360	23324	ok	NGC 4261
12 20 13.5	+06 41 15	281.5	68.2	0.158	0105070101	11482	5419	ok	1WGA J1220.3+06
12 22 54.9	+15 49 19	271.1	76.8	0.232	0106860201	36633	18017	ok	NGC 4321
12 23 06.8	+10 37 22	279.5	72.1	0.217	0108860101	22271	17203	ok	NGC 4325
12 25 42.4	+12 39 33	279.0	74.3	0.263	0110930301	18760	433	flared	NGC 4388
12 25 51.5	+12 39 43	279.1	74.3	0.263	0110930701	11915	8140	ok	NGC 4388
12 26 07.3	+12 56 38	279.0	74.6	0.264	0108260201	85636	55860	discard	M86
12 27 18.9	+01 29 11	289.2	63.7	0.181	0110990201	29679	9818	ok	HI1225+01
12 28 13.7	-15 46 59	294.7	46.7	0.378	0002740301	12234	6450	ok	Denis-J1228
12 28 44.2	+02 07 20	289.7	64.4	0.179	0126700401	27251	2696	flared	3C 273off+7min
12 29 03.3	+02 01 42	289.9	64.3	0.179	0126700201	26140	8678	ok	3C 273off-1.5min
12 29 30.2	+01 59 32	290.2	64.3	0.179	0126700101	27248	135	flared	3C 273off-7min
12 29 41.4	+07 59 45	286.8	70.1	0.159	0112550601	24622	11715	discard	ngc4472
12 29 57.5	+13 38 11	281.4	75.6	0.280	0112552101	14126	10301	ok	ngc4477
12 30 06.3	+13 38 53	281.5	75.6	0.258	0112550701	13488	4252	flared	ngc4477
12 30 45.5	+13 43 32	282.0	75.7	0.258	0106060401	13275	8099	ok	Virgo 4
12 30 45.4	+14 43 22	280.6	76.6	0.247	0106060701	14375	10637	ok	Virgo 7
12 30 45.3	+15 23 29	279.6	77.3	0.247	0106060901	15622	8970	ok	Virgo 9
12 30 45.3	+15 43 30	279.0	77.6	0.230	0106061001	15720	6231	ok	Virgo 10
12 30 45.2	+16 03 33	278.4	77.9	0.230	0106061101	16624	7389	ok	Virgo 11
12 30 45.2	+14 03 18	281.6	76.0	0.258	0106060501	17738	12421	ok	Virgo 5
12 30 45.4	+14 23 22	281.1	76.3	0.258	0106060601	14876	8756	ok	Virgo 6
12 30 45.2	+16 23 31	277.8	78.2	0.230	0106061201	18441	11858	ok	Virgo 12
12 30 45.4	+17 53 28	274.5	79.6	0.251	0106061301	16624	12174	ok	Virgo 13
12 30 45.3	+15 03 29	280.1	77.0	0.247	0106060801	13057	1660	flared	Virgo 8
12 30 49.1	+12 23 22	283.7	74.4	0.250	0114120101	60109	30143	discard	M87
12 30 49.9	+12 43 17	283.4	74.8	0.259	0106060101	10020	4160	flared	Virgo 1
12 30 53.9	+11 00 03	285.2	73.1	0.209	0145800101	107002	50080	discard	LBQS 1228+1116
12 31 58.3	+14 25 19	282.3	76.5	0.247	0112550801	14163	6669	ok	ngc4501
12 35 34.9	-39 54 50	299.6	22.8	0.719	0006220201	46207	35856	ok	NGC 4507
12 35 39.7	+12 33 17	287.9	74.9	0.259	0141570101	44838	20074	ok	NGC 4552
12 36 39.4	-33 54 03	299.4	28.8	0.561	0201901701	26147	5973	ok	RXCJ1236.7-3354

12 37 38.8	+11 49 03	290.3	74.3	0.261	0112840101	23669	15453	ok	NGC4579
12 39 38.9	-05 20 43	297.4	57.4	0.228	0109970101	28062	0	flared	NGC 4593
12 39 59.3	-11 37 11	298.4	51.1	0.385	0084030101	43456	23727	ok	M104
12 40 20.4	-83 14 57	302.5	-20.3	0.963	0092360801	16835	11397	ok	3EG 1249-8330
12 40 21.2	-83 44 57	302.6	-20.8	0.860	0092360701	13236	2275	flared	3EG 1249-8330
12 41 13.5	+18 34 32	287.0	81.1	0.170	0149900301	17412	14070	ok	Abell 1589
12 42 38.3	-11 19 31	299.4	51.4	0.374	0136950201	30265	26157	ok	RXJ1242
12 42 48.2	+02 41 21	297.7	65.4	0.175	0111190701	64406	53805	ok	NGC4636
12 42 51.8	+13 15 40	294.2	75.9	0.236	0112551001	15112	10990	ok	ngc4639
12 43 39.8	+11 33 15	295.8	74.3	0.194	0021540201	54210	43902	ok	NGC 4649
12 45 04.5	-00 27 41	299.5	62.3	0.174	0110980201	58237	50432	ok	NGC 4666
12 48 22.0	+08 29 24	300.5	71.3	0.192	0112551101	16912	10529	ok	ngc4698
12 48 48.9	-41 18 42	302.4	21.5	0.825	0046340101	47807	30632	discard	Centaurus cluster
12 49 13.8	-05 59 34	301.9	56.8	0.212	0060370201	41273	30143	ok	Q1246-057
12 52 24.2	-29 15 02	303.1	33.6	0.610	0111020201	36207	6496	ok	EX Hydrae
12 52 24.2	-29 15 02	303.1	33.6	0.610	0111020101	57802	0	flared	EX Hydrae
12 52 59.3	-29 27 13	303.3	33.4	0.600	0057740301	68621	60049	ok	c1252.9-2927
12 52 59.3	-29 27 03	303.3	33.4	0.600	0057740401	68626	60993	ok	c1252.9-2927
12 53 10.5	-09 11 56	303.6	53.6	0.293	0112270701	12866	9766	ok	HCG62
12 53 37.6	+15 42 24	305.5	78.5	0.191	0082990101	50900	29195	ok	3C 277.2
12 54 00.0	+10 11 25	305.0	73.0	0.162	0001930301	25335	18403	ok	IRAS F12514+10
12 54 33.6	-29 08 17	303.7	33.7	0.610	0030140101	17248	13787	discard	A3528
12 57 16.8	-30 22 11	304.4	32.4	0.596	0030140301	16895	11650	ok	A3532
12 57 28.2	-17 20 29	304.9	45.5	0.465	0010420201	22806	12570	discard	Abell 1644
12 58 00.5	-83 14 57	303.1	-20.3	0.710	0092360501	15383	7728	ok	3EG 1249-8330
12 57 59.9	-83 44 59	303.1	-20.8	0.689	0092360601	15380	8747	ok	3EG 1249-8330
12 58 48.0	-01 44 44	306.7	61.0	0.154	0093200101	43240	33950	ok	A1650
13 02 46.1	-02 30 29	308.6	60.2	0.171	0201901801	29149	20164	ok	RXCJ1302.8-0230
13 05 13.1	-10 20 50	308.4	52.3	0.322	0032141201	16003	12223	ok	1saxj1305.2-1020
13 05 43.9	+18 01 06	323.5	80.3	0.198	0017940101	56505	40187	ok	GP Com
13 11 29.3	-01 20 18	313.3	61.1	0.180	0093030101	39806	32201	ok	Abell 1689
13 15 23.8	-16 22 55	311.2	46.1	0.491	0037950101	24109	18674	ok	NGC 5044
13 15 28.6	-16 45 29	311.1	45.7	0.491	0152360101	39116	34508	ok	NGC 5044
13 19 16.5	-14 50 42	312.9	47.4	0.491	0110980601	53647	27626	ok	NGC 5073
13 24 05.1	+13 58 28	334.6	74.8	0.175	0108860701	26193	14219	ok	NGC 5129
13 25 19.9	-38 24 43	310.1	23.9	0.481	0110890101	64019	52553	ok	IRAS 13224-3809
13 27 57.2	-31 30 19	311.9	30.7	0.363	0107260101	44615	37883	discard	A3558
13 29 21.7	+11 46 24	334.8	72.2	0.195	0041180801	24948	16594	ok	NGC 5171 Group
13 30 53.8	-01 50 15	322.6	59.5	0.232	0112240301	34779	26166	ok	A1750
13 31 45.6	-31 48 02	312.8	30.2	0.398	0105261401	23338	10413	ok	A3562_f2
13 32 24.9	-31 37 27	313.0	30.4	0.391	0105261601	23847	17065	ok	A3562_f4
13 32 55.3	-31 52 05	313.1	30.1	0.398	0105261701	20911	17323	ok	A3562_f5
13 33 05.4	-31 41 25	313.1	30.3	0.391	0105261301	47167	36328	ok	A3562_f1

13 33 54.7	-31 30 26	313.4	30.4	0.391	0105261501	22648	18919	ok	A3562_f3
13 34 25.2	-31 44 20	313.5	30.2	0.391	0105261801	21847	8385	ok	A3562_f6
13 35 53.9	-34 17 49	313.2	27.6	0.409	0111570101	46453	8000	ok	MCG-6-30-15
13 35 53.9	-34 17 47	313.2	27.6	0.409	0111570201	66197	8000	ok	MCG-6-30-15
13 37 05.1	-29 51 46	314.6	31.9	0.397	0110910201	30638	20121	ok	M 83
13 37 44.4	-12 57 20	320.0	48.3	0.481	0147670201	13917	11814	ok	PKS B1334-127
13 38 11.5	+04 32 24	331.2	64.8	0.197	0152940101	67313	30686	ok	NGC 5252
13 39 56.2	-31 38 39	314.8	30.1	0.390	0035940301	47216	29616	ok	NGC 5253
13 41 19.7	+00 23 53	329.1	60.7	0.186	0111281001	10377	7333	ok	F864-1
13 41 19.6	-00 00 07	328.8	60.3	0.191	0111281301	14541	2342	flared	F864-4
13 47 15.5	+17 27 21	358.9	73.8	0.181	0144570101	66431	39983	ok	Tau Boo
13 47 22.7	-33 09 54	316.2	28.2	0.430	0147040101	31428	11078	discard	Abell 3571
13 47 30.7	-11 45 11	324.0	48.8	0.492	0112960101	38392	30423	ok	RXJ1347-1145
13 47 30.1	-32 51 52	316.3	28.5	0.393	0086950201	33642	23354	discard	A3571
13 49 19.0	-30 18 30	317.4	30.9	0.443	0101040401	13925	9262	discard	IC 4329a
13 50 43.9	-33 43 05	316.8	27.5	0.480	0201901901	26515	15442	ok	RXCJ1350.7-3343
13 54 12.6	-02 21 52	332.5	56.8	0.353	0112250101	33646	22728	ok	RXJ1354.3-0222
13 56 03.0	+18 22 33	5.8	72.7	0.208	0094401201	26850	22981	ok	Mrk 463
14 01 01.8	+02 52 40	340.3	60.5	0.224	0098010101	61353	27531	ok	A 1835
14 01 02.0	+02 52 33	340.3	60.5	0.224	0147330201	106844	38487	discard	Abell 1835
14 01 34.6	-11 07 35	329.2	48.1	0.472	0109910101	100219	42837	ok	A 1837
14 04 16.6	-34 02 05	319.7	26.4	0.549	0058940301	20049	15753	ok	1401-33
14 08 51.9	-07 52 38	333.8	50.2	0.273	0151590101	32318	10405	ok	pks1406-076
14 08 51.9	-07 52 43	333.8	50.2	0.273	0151590201	14299	4257	flared	pks1406-076
14 14 52.4	-00 23 45	342.4	55.9	0.322	0145480101	23567	12539	ok	Abell 1882
14 15 41.3	+11 29 27	358.6	64.7	0.180	0112251301	29642	25672	ok	H1413+117
14 15 45.9	+11 29 28	358.7	64.7	0.180	0112250301	26643	21461	ok	H1413+117
14 29 06.5	+01 17 01	349.2	55.1	0.285	0102040501	17951	2069	flared	MARK 1383
14 37 33.7	-15 00 31	337.5	40.6	0.778	0081341401	21892	14225	ok	IRAS14348-14
14 49 23.7	-10 10 23	344.4	42.9	0.788	0149620201	72555	17408	ok	SN 1995N
14 49 23.4	+08 59 53	5.4	56.7	0.202	0148520101	32854	20727	ok	Daddi field
14 49 23.4	+08 59 52	5.4	56.7	0.202	0148520301	32664	26914	ok	Daddi field
14 49 28.7	+08 59 47	5.4	56.7	0.202	0057560301	43147	34519	ok	ERO field
14 52 43.7	+16 45 00	18.9	60.1	0.184	0091140201	32749	26980	ok	A1983
14 53 53.2	+03 32 34	359.4	52.4	0.362	0150350101	47159	19737	ok	NGC5775
14 54 36.3	+18 38 53	22.8	60.4	0.239	0145020101	42037	27935	ok	A 1991
14 58 21.8	-31 40 17	332.2	23.8	0.958	0067750101	53559	20664	ok	Cen X-4
15 06 29.5	+01 36 24	0.4	48.7	0.425	0021540101	30178	13115	ok	NGC 5846
15 10 51.6	+05 44 22	6.4	50.5	0.307	0111270201	22222	10337	discard	A2029
15 16 14.6	+00 05 46	1.1	45.9	0.459	0201902001	28413	23397	ok	RXCJ1516.3+0005
15 16 29.4	-00 57 06	0.0	45.2	0.548	0201902101	30416	25126	ok	RXCJ1516.5-0056
15 16 35.5	+00 14 41	1.3	45.9	0.459	0103860601	13646	10581	ok	CGCG 21-63
15 16 43.9	+07 01 12	9.4	50.1	0.290	0109920101	31597	24994	ok	A 2052

15 17 00.9	-16 08 25	346.1	34.1	0.840	0164570401	53218	33847	ok	GRB040827
15 21 49.6	+07 41 18	11.3	49.4	0.315	0109930101	55413	32636	ok	MKW 3s
15 32 22.7	-08 32 07	356.2	37.1	0.868	0100240701	29906	14965	ok	UZ LIB
15 32 23.0	-08 31 56	356.2	37.1	0.868	0100240801	30204	22437	ok	UZ LIB
15 32 29.2	+04 40 42	9.8	45.5	0.400	0091140401	45414	24947	ok	MKW9
15 35 02.0	+01 20 39	6.6	43.0	0.466	0112190401	15111	3593	flared	MS1532.5+0130
15 40 48.3	-24 43 07	344.9	24.0	1.347	0152630301	13911	5242	ok	SXRB_3
15 50 37.0	-03 53 27	4.3	36.8	0.974	0138951501	12412	2336	flared	IRAS15480-0344
15 54 34.7	-25 14 54	347.1	21.5	1.224	0142630301	22210	15005	ok	3 Sco
15 56 25.2	-23 38 00	348.6	22.4	1.159	0112380101	48309	33833	ok	SCO-CEN PT1
16 01 14.2	+08 44 22	19.8	41.6	0.376	0147580201	13305	3462	flared	1AXGJ160118+08
16 05 02.3	+17 44 50	31.5	44.5	0.336	0147210301	19008	6312	ok	Abell 2151
16 05 02.4	+17 44 49	31.5	44.5	0.336	0147210101	29850	4682	flared	Abell 2151
16 05 06.4	+17 45 08	31.5	44.5	0.336	0147210201	29598	1204	flared	Abell 2151
16 07 13.2	+08 04 58	20.0	40.0	0.395	0067340601	15391	10580	ok	Field VI
16 13 06.9	-83 42 17	308.2	-23.0	0.898	0008820401	54463	35628	ok	GRB 020321
16 14 34.2	-06 09 14	6.5	30.7	1.184	0112230901	30809	7591	ok	A2163 of3
16 15 46.1	-06 09 09	6.7	30.4	1.227	0112230601	16364	8421	ok	A2163
16 15 45.9	-06 09 11	6.7	30.4	1.227	0112231501	13263	5502	ok	A2163
16 15 46.1	-05 51 16	7.0	30.6	1.184	0112230801	29400	15264	ok	A2163 of2
16 15 46.0	-06 27 13	6.4	30.2	1.227	0112231001	29695	21671	ok	A2163 of4
16 16 28.6	+12 12 24	26.1	39.8	0.457	0103460801	14448	10925	ok	McNaught-Hartley
16 16 47.8	-06 09 12	6.9	30.2	1.227	0112230701	30909	11901	ok	A2163 of1
16 17 02.2	+12 24 23	26.4	39.8	0.457	0103460901	15700	11978	ok	McNaught-Hartley
16 17 37.0	+12 37 00	26.7	39.7	0.427	0103461001	13100	9580	ok	McNaught-Hartley
16 21 34.3	-15 42 30	359.3	23.4	1.499	0153950201	25040	20409	discard	Sco X-1 large
16 21 44.6	-02 16 31	11.4	31.4	0.847	0164560801	26462	6683	ok	SN 2004dk
16 32 46.2	+05 34 35	21.0	33.2	0.594	0112230301	22964	16543	ok	A2204
16 42 16.7	+03 11 04	20.0	30.0	0.535	0067340501	15278	10211	ok	Field V
16 52 58.4	+02 24 18	20.7	27.2	0.549	0101640601	19003	7532	ok	NGC 6240
16 52 58.9	+02 24 00	20.7	27.2	0.549	0147420401	14115	7003	ok	NGC 6240
16 52 58.8	+02 23 53	20.7	27.2	0.549	0101640101	30111	10396	ok	NGC 6240
16 52 58.8	+02 24 07	20.7	27.2	0.549	0147420201	31638	4342	flared	NGC 6240
16 52 58.8	+02 24 05	20.7	27.2	0.549	0147420301	28077	1663	flared	NGC 6240
16 52 58.7	+02 23 56	20.7	27.2	0.549	0147420501	31219	1542	flared	NGC 6240
16 54 00.2	+14 17 47	33.1	32.3	0.551	0113070101	24532	15159	ok	nps_pos1
17 26 05.4	+02 19 41	25.0	20.0	0.842	0067340401	15280	10474	ok	Field IV
18 19 44.6	-63 45 31	330.8	-20.7	0.775	0146340601	18216	5958	ok	PKS 1814-637
18 19 43.7	-63 45 14	330.8	-20.7	0.775	0146340501	33855	2365	flared	PKS 1814-637
18 47 02.3	-78 31 54	315.7	-26.3	1.008	0147920401	10851	261	flared	H1846-786
19 21 13.9	-58 40 17	338.1	-26.7	0.495	0101040501	55489	14130	ok	ESO 141-G55
19 31 19.4	-72 39 09	322.5	-28.7	0.597	0081341001	23322	13874	ok	IRAS19254-72
19 35 13.0	-52 51 43	344.9	-27.7	0.371	0051610101	22624	14980	ok	grb980425

19 39 59.3	-30 57 50	8.7	-23.2	0.858	0111300101	26709	20646	ok	M 55
20 03 23.7	-32 51 32	8.4	-28.5	0.749	0104860601	30089	14036	ok	[HB89] 2000-330
20 07 47.8	-11 09 16	31.3	-21.9	0.675	0044350501	14921	10438	ok	IRAS20051-1117
20 07 50.9	-11 08 20	31.3	-21.9	0.675	0044350201	21638	4395	flared	IRAS20051-1117
20 10 57.8	-56 48 12	340.8	-33.1	0.459	0105260501	19503	11975	discard	A3667_f5
20 11 09.7	-56 38 40	341.0	-33.2	0.459	0105260201	20146	16130	ok	A3667_f2
20 11 21.8	-57 25 34	340.1	-33.2	0.333	0042341101	13916	3615	flared	RXCJ2011.3-5725
20 11 54.3	-56 54 54	340.7	-33.3	0.459	0105260601	26467	18472	discard	A3667_f6
20 12 13.7	-56 37 25	341.1	-33.3	0.459	0105260401	17469	13205	ok	A3667_f4
20 13 04.4	-56 53 11	340.7	-33.4	0.459	0105260101	21303	7504	discard	A3667_f1
20 13 08.2	-56 43 17	340.9	-33.4	0.459	0105260301	17871	13421	ok	A3667_f3
20 13 29.0	-41 47 22	358.7	-32.4	0.498	0081340501	21913	10696	ok	IRAS20100-41
20 13 59.7	-87 57 32	305.0	-27.8	1.141	0083210701	10779	5646	ok	1SAXJ2011.9-8758
20 18 18.1	-70 51 15	324.1	-32.5	0.497	0022340101	32858	18375	ok	Pavo group
20 40 10.0	-00 52 23	45.2	-24.4	0.703	0111180201	17270	10630	ok	AE Aqr
20 46 20.5	-02 48 54	44.2	-26.7	0.586	0112600501	11360	8305	ok	Mrk 896
20 48 14.0	-17 49 51	28.7	-33.5	0.478	0201902401	28257	21534	ok	RXCJ2048.1-1750
20 54 18.0	-15 55 36	31.5	-34.2	0.436	0083210101	11462	7154	ok	1SAXJ2054.3-1556
20 56 22.3	-04 37 59	43.8	-29.7	0.502	0112190601	17511	12272	ok	MS2053.7-0449
20 58 26.1	-42 38 54	358.6	-40.7	0.382	0081340401	21863	12027	discard	IRAS20551-42
21 04 10.3	-11 21 39	37.7	-34.5	0.466	0041150101	40565	30058	ok	NGC 7009
21 04 39.5	-12 20 03	36.7	-35.0	0.465	0038540301	17217	12791	ok	NGC7010
21 14 55.7	+06 08 31	57.0	-28.0	0.663	0150610201	16914	7408	ok	PG 2112+059
21 24 43.5	-33 58 34	10.9	-45.4	0.572	0112320601	70315	20215	ok	PSR J2124-3358
21 27 37.2	-44 48 41	355.3	-45.9	0.345	0088020201	32370	10164	ok	IRAS F21243-4501
21 29 11.5	-15 38 33	35.9	-41.8	0.493	0103060101	23564	15955	ok	PKS 2126-158
21 29 34.7	+00 04 53	53.6	-34.4	0.422	0093030201	58916	34048	ok	RX J2129.6+0005
21 32 29.9	+10 09 18	63.6	-29.0	0.465	0150470701	37917	12325	ok	UGC 11763
21 37 45.1	-14 32 51	38.4	-43.3	0.477	0092850201	59850	28012	ok	PKS 2135-147
21 40 14.7	-23 39 31	26.4	-46.9	0.356	0008830101	22769	9500	ok	ms2137-23
21 51 55.1	-30 27 42	17.0	-50.7	0.191	0103060401	25028	19943	ok	PKS 2149-306
21 52 01.3	-27 31 59	21.6	-50.3	0.236	0062940401	39421	17220	ok	HE2149-2745
21 53 36.5	+17 41 56	73.9	-27.8	0.669	0111270101	23263	9766	ok	A2390
22 01 49.7	-59 57 41	332.2	-46.3	0.284	0149670101	25437	19965	ok	Abell 3827
22 02 01.8	-31 52 13	15.1	-53.0	0.165	0147920601	16858	11831	ok	NGC 7172
22 03 10.6	+18 53 03	76.7	-28.5	0.572	0130920101	20217	13922	ok	HD 209458
22 04 30.7	-64 44 31	326.2	-44.0	0.291	0143250101	22216	17825	ok	HD 209295
22 05 09.3	-01 55 11	58.0	-42.9	0.607	0012440301	35366	24897	ok	PB5062
22 09 15.9	-47 10 00	349.5	-52.5	0.194	0111810101	49610	18189	ok	NGC7213
22 15 31.8	-17 44 09	39.2	-52.9	0.228	0106660501	11568	6085	ok	LBQS 2212-1759
22 15 32.0	-17 44 06	39.2	-52.9	0.228	0106660101	60508	51704	ok	LBQS 2212-1759
22 15 31.9	-17 44 09	39.2	-52.9	0.228	0106660201	53769	37107	ok	LBQS 2212-1759
22 15 31.3	-17 44 08	39.2	-52.9	0.228	0106660601	110168	82222	ok	LBQS 2212-1759

22 15 31.9	-17 44 08	39.2	-52.9	0.228	0106660401	35114	12805	ok	LBQS 2212-1759
22 17 04.5	-16 38 35	41.1	-52.8	0.261	0148060201	12800	2657	flared	BPS CS 22892-05
22 17 15.4	+14 15 03	76.0	-34.2	0.493	0103660301	47294	10301	ok	Mark 304
22 17 31.1	+00 14 15	63.0	-44.0	0.459	0094310101	68821	58820	ok	SSA22
22 17 31.1	+00 14 12	63.0	-44.0	0.459	0094310201	81270	60699	ok	SSA22
22 19 18.4	+12 08 05	74.7	-36.1	0.536	0103861201	13014	8526	ok	IIZw 177
22 20 45.8	-24 40 57	28.4	-56.1	0.199	0049340201	28359	22176	ok	NGC 7252
22 28 29.7	-05 18 46	59.1	-49.6	0.514	0100440101	46681	40544	ok	PHL 5200
22 29 44.9	-20 50 16	36.1	-57.1	0.268	0125911001	16692	12301	ok	NGC 7293
22 35 45.7	-26 02 55	27.1	-59.7	0.147	0111790101	44663	13638	ok	NGC7314
22 36 10.8	+13 44 45	79.9	-37.5	0.474	0153220601	12915	5617	ok	PG 2233+134
22 36 55.4	-22 13 04	34.6	-59.1	0.216	0103860201	11864	5675	ok	ESO 602- G 031
22 37 00.5	-15 16 18	46.8	-56.6	0.400	0056021601	25111	15633	ok	RX J2237.0-1516
22 39 56.5	-05 51 30	61.1	-52.1	0.402	0149410401	34475	19256	ok	BR 2237-0607
22 40 32.9	+03 22 16	71.8	-46.1	0.524	0110960101	42870	12551	ok	Q2237+0305
22 41 59.1	-44 04 00	351.9	-59.0	0.182	0153220101	10919	3344	flared	RX J2241.8-4405
22 44 19.2	-72 42 47	314.8	-41.3	0.409	0150050101	59915	20302	ok	Galactic Halo
22 49 39.9	-27 06 51	25.8	-62.9	0.178	0111970101	13358	10382	ok	TY PsA
22 49 50.0	-64 23 08	322.0	-47.9	0.280	0112240101	35013	25781	ok	A3921
22 51 48.7	-17 52 16	45.1	-60.9	0.269	0081340901	23365	19561	ok	IRAS22491-18
22 57 09.8	-36 27 33	4.6	-64.1	0.115	0135980201	32903	25360	ok	IC1459
23 02 28.9	+08 36 41	82.6	-45.5	0.487	0032140201	13275	6836	ok	1saxJ2302.5+0836
23 03 15.9	+08 52 22	83.0	-45.4	0.529	0112170301	24590	8989	ok	NGC7469
23 04 45.6	+03 11 34	78.4	-50.2	0.527	0033541001	13307	10070	ok	pg 2302+029
23 04 56.1	+12 19 30	86.2	-42.8	0.519	0025541001	13263	6410	ok	NGC7479
23 08 22.4	-02 11 19	73.8	-54.9	0.435	0042341201	12596	1651	flared	RXCJ2308.3-0211
23 13 58.5	-42 43 26	348.3	-64.8	0.185	0123900101	66664	29998	ok	A S 1101
23 13 59.1	-42 43 43	348.3	-64.8	0.185	0147800101	126314	83040	ok	Sersic 159-03
23 15 42.4	-59 04 11	323.7	-54.0	0.243	0081340301	23413	8782	ok	IRAS23128-59
23 16 10.7	-42 34 57	348.1	-65.2	0.185	0093640701	20760	7748	ok	NGC 7552
23 18 15.2	+00 16 14	79.8	-54.6	0.411	0066950301	12208	2387	flared	NGC 7589
23 18 16.4	+00 15 50	79.8	-54.6	0.411	0066950401	13324	4524	ok	NGC 7589
23 18 22.2	-42 22 05	348.0	-65.6	0.196	0112310201	23362	18843	ok	NGC 7582
23 19 43.4	-73 12 43	311.6	-42.3	0.191	0201903201	31029	0	flared	RXCJ2319.6-7313
23 19 50.1	-73 12 55	311.6	-42.3	0.191	0201903301	12616	7975	ok	RXCJ2319.6-7313
23 25 17.9	-12 06 23	65.3	-64.8	0.250	0147330101	120513	52958	ok	Abell 2597
23 25 21.4	-12 07 20	65.3	-64.8	0.250	0108460201	21073	12680	ok	Abell 2597
23 31 49.2	+19 56 29	98.5	-39.1	0.422	0112880301	15772	11809	ok	EQ Peg
23 31 52.8	+19 38 10	98.4	-39.4	0.422	0032140701	12311	7348	ok	1saxj2331.9+19
23 31 57.8	+19 44 16	98.5	-39.3	0.422	0147580301	15371	9780	ok	1AXGJ233200+19
23 33 40.6	-15 17 12	62.2	-68.4	0.196	0093550401	25209	19527	ok	LEDA 913766
23 36 12.1	+02 08 25	88.1	-55.5	0.493	0112522601	17140	13884	ok	NGC 7714
23 36 18.1	+02 10 07	88.2	-55.5	0.493	0112521301	22232	13123	ok	NGC 7714

23 37 41.6	+00 16 24	87.0	-57.3	0.385	0042341301	14115	9841	ok	RXCJ2337.6+0016
23 37 50.0	-56 24 43	322.1	-57.8	0.204	0083210201	10458	7655	ok	1SAXJ2337.8-56
23 39 54.9	-12 17 38	70.9	-67.6	0.306	0055990301	14965	10380	ok	Arp222
23 40 25.9	-11 43 12	72.2	-67.3	0.281	0152200101	53961	45458	ok	Abell 2638
23 47 20.2	-02 18 52	88.4	-60.8	0.362	0152860101	33656	24541	ok	HCG 97
23 47 22.3	+00 53 03	91.5	-58.0	0.362	0147580401	15369	13043	ok	1AXGJ234725+00
23 51 42.3	-26 04 13	34.0	-76.6	0.166	0148990101	31161	20013	ok	Abell 2667
23 54 08.5	-10 23 50	81.3	-68.5	0.292	0108460301	33298	13607	ok	Abell 2670
23 56 55.8	-24 24 39	42.3	-77.4	0.173	0125910301	11216	8211	ok	HD 224317
23 57 02.9	-34 45 39	356.3	-76.0	0.110	0109950101	30767	18525	ok	A 4059
23 57 02.9	-34 45 39	356.3	-76.0	0.110	0109950201	25967	19251	discard	A 4059
23 57 27.0	-30 27 29	14.0	-77.7	0.137	0103861501	16336	9388	flared	AM2354-304S

Appendix B

List of Technical Terms and Acronyms

2MASS: Two Micron All-Sky Survey

AB Magnitudes: Magnitude system which uses a fiducial source of constant flux $S_{\nu}^{\text{AB}} = 2.89 \times 10^{-21} \text{ erg cm}^{-2} \text{ Hz}^{-1}$ as reference standard (Schneider, 2006a). This value is chosen in a way that the V-band magnitudes are equivalent to the Vega system $m_V^{\text{AB}} = m_V^{\text{Vega}}$. Redder filter bands have a positive offset to the Vega system (fainter magnitudes), bluer bands have negative offsets (brighter magnitudes).

ACS: Advanced Camera for Surveys on board the Hubble Space Telescope

ACT: Atacama Cosmology Telescope

AGB: Asymptotic Giant Branch

AGN: Active Galactic Nuclei

APEX: Atacama Pathfinder EXperiment

Baffle: Light shield placed in the optical path to block stray light and reduce the thermal background radiation.

BAOs: Baryon Acoustic Oscillations

BCG: Brightest Cluster Galaxy

Bias: An offset voltage applied to all pixels in an array detector.

CA: Calar Alto Observatory in Southern Spain

CAL: Calibration Access Layer

CCD: Charge-Coupled Device

CDM: Cold Dark Matter

CFHT: Canada-France-Hawaii Telescope

Chandra: American-led X-ray observatory launched in 1999 with an on-axis spatial resolution of $0.5''$.

CMB: Cosmic Microwave Background

COSMOS: Cosmic Evolution Survey

Cosmic: Cosmic ray event in an image. Signal in isolated pixels caused by a charged cosmic particle hit.

CTIO: Cerro Tololo Inter-American Observatory

CXB: Cosmic X-ray Background

DDT: Director's Discretionary Time

DEC: Declination

DES: Dark Energy Survey

Descriptor: Data buffer with a name that contains information about an associated image.

DETF: Dark Energy Task Force

DET ML: Detection Maximum Likelihood

Dithering: Common observation technique in infrared astronomy. Multiple images of an object are taken with slight telescope offsets in between the images. By overlaying several images and using a median process, the local sky for the data reduction can be extracted from the science images.

ECF: Energy Conversion Factor

EMSS: Einstein Medium Sensitivity Survey

EMMI: The ESO Multi Mode Instrument at the NTT telescope in La Silla.

EoS: Equation-of-State relating density and pressure

EPIC: European Photon Imaging Cameras on XMM-Newton

eROSITA: extended Röntgen Survey with an Imaging Telescope Array

ESA: European Space Agency

ESO: European Southern Observatory, with its headquarters in Garching, Germany.

EXT ML: Extent Maximum Likelihood

FITS: Flexible Image Transport System. Standard format for astronomical images.

Flatfield: Image of a uniformly-illuminated area used for the correction of sensitivity variations across the detector.

FORS 2: The FOcal Reducer and low dispersion Spectrograph for the Very Large Telescope.

FoV: Field-of-View. Sky area that can be covered with one image of a particular instrument.

FP: False Positive

FPN: Fixed Pattern Noise. Pixel-to-pixel sensitivity variations that are corrected by dividing through a normalized flatfield.

Fringing: Interference patterns produced in CCD layers by strong monochromatic atmospheric emission lines at long optical wavelengths.

FWHM: Full-Width Half-Maximum, a measure of the width of an object in an image. The FWHM is a well-defined number obtained by fitting a Gaussian curve of the form $f(x) = 1/(\sigma\sqrt{2\pi}) \times \exp(-\frac{x^2}{2\sigma^2})$ to the intensity profile of an object. The standard deviation σ and the full width at half the peak intensity of the profile only differ by a constant factor of $\sigma = 0.424 \cdot \text{FWHM}$ (Stöcker, 1998).

Gain: Conversion factor from detected electrons to digital counts.

GDDS: Gemini Deep Deep Survey

GISSEL: Galaxy Isochrone Synthesis Spectral Evolution Library

GMOS: Gemini Multi-Object Spectrograph at the Gemini South 8 m telescope.

GNIRS: Gemini NIR Spectrograph at the Gemini South 8 m telescope.

GR: General Relativity

GROND: Gamma-Ray Burst Optical Near-IR Detector

GTI: Good Time Intervals

HEW: Half Energy Width

HgCdTe: Mercury-cadmium-telluride

HIFLUGCS: HIghest X-ray FLUx Galaxy Cluster Sample

HIROCS: Heidelberg InfraRed / Optical Cluster Survey

HR: Hardness Ratio

HR: Hertzsprung-Russell diagram

HST: Hubble Space Telescope

ICM: Intracluster Medium

Image Catalog: List of image names that can be used within the MIDAS environment to apply a set of commands to all images in the list.

IMF: Stellar Initial Mass Function

IRAC: InfraRed Array Camera on the Spitzer observatory

IRAF: Image Reduction and Analysis Facility. Multi-purpose astronomical software for image reduction and analysis.

I/O: Input/Output

IR: InfraRed

ISAAC: Infrared Spectrometer And Array Camera at the VLT

Keyword: Variable of a specified data type within the MIDAS environment.

LF: Luminosity Function

LH: Lockman Hole

LM: Limiting Magnitude. Apparent magnitude of objects with a signal-to-noise ratio of 5.

LSS: Large-Scale Structure

M67: Open star cluster in the constellation Cancer at $\alpha = 8^h 51^m$ and $\delta = 11.^\circ 82$.

Median: Central value in an ordered sequence of numbers.

MEKAL: Plasma emission code from MEwe, KAastra, and Liedahl

MH: Mexican Hat wavelet

MIDAS: Munich Image Data Analysis System. Astronomical software package developed and maintained by the European Southern Observatory.

ML: Maximum Likelihood

MOS: Metal Oxid Semi-conductor instrument on XMM-Newton

NED: NASA Extragalactic Data Base

NEP: North Ecliptic Pole survey

NICMOS: Near Infrared Camera and Multi-Object Spectrometer on the Hubble Space Telescope

NIR: Near-InfraRed. In this thesis, usually used for the spectral region $1\text{--}2.5\,\mu\text{m}$, unless otherwise noted.

NORAS: NORthern ROSAT All-Sky survey

NTT: The 3.5 m New Technology Telescope at La Silla Observatory in Chile.

OBSID: Unique identification number for each XMM observation.

ODF: Observation Data File

OMEGA2000: The NIR wide-field imager at the 3.5 m Calar Alto telescope.

OoT: Out-of-Time events

PanSTARRS: Panoramic Survey Telescope & Rapid Response System

PI: Principal Investigator

Pipeline: Automated data reduction software requiring only minimal user interaction.

Pixel Coordinates: Coordinate system based on the pixel row and column numbers on the detector.

PN: Imaging camera on XMM-Newton

Pointing: One principal telescope position. The sum of all images with a specific target in the field of view.

PSF: Point-Spread Function. Intensity distribution of a point-like light source in an astronomical image.

PSPC: Position Sensitive Proportional Counter, main instrument of ROSAT.

QE: Quantum Efficiency.

QSO: Quasi-Stellar Object

Seeing: “Blurring” of point-like astronomical objects caused by atmospheric turbulence. Without adaptive optics, the seeing limits the highest possible resolution in ground based observations. Typical seeing values for the Calar Alto observatory are somewhat better than 1 arcsec.

RA: Right Ascension

RASS: ROSAT All-Sky Survey

RCS: Red-Sequence Cluster Survey

RDCS: ROSAT Deep Cluster Survey

REFLEX: ROSAT-ESO Flux-Limited X-ray cluster survey

RGS: Reflecting Grating Spectrometer on XMM-Newton

ROSAT: ROentgen SATellite, German X-ray survey mission from 1990 to 1999.

RWM: Robertson-Walker-Metric

SAM: Semi-Analytic Model

SAS: XMM-Newton Science Analysis Software

SDSS: Sloan Digital Sky Survey

SED: Spectral Energy Distribution

SEP: South Ecliptic Pole

SFH: Star Formation History

SFR: Star Formation Rate

SGP: South Galactic Pole

SMF: Spectral Matched Filter Scheme

SNR: Signal-to-Noise-Ratio.

SPIE: Society of Photo-Optical Instrumentation Engineers

Spitzer: Mid-infrared space telescope launched in 2003.

SPT: South Pole Telescope

SRT: Special Relativity Theory

SSP: Simple Stellar Population models. Galaxy evolution models assuming a single formation redshift of the stellar population and only passive evolution afterwards.

STD: Standard Scheme

SZE: Sunyaev-Zeldovich Effect

UT: Universal time.

VADER: Very Ambitious Dark Energy Research mission

Vega Magnitudes: Magnitude system calibrated to the A0 star Vega for which all filter bands have by definition a magnitude of 0. Since Vega's spectrum has decreasing flux towards the red optical and NIR filters, these bands have magnitude values which are smaller (*i.e.* brighter) than the corresponding AB magnitudes. The Vega system is still the standard photometric system for NIR observations.

Vignetting: Obscuration of parts of the primary mirror as seen by a detector pixel.

VISTA: Visible and Infrared Survey Telescope for Astronomy in Chile

VLT: Very Large Telescope in Chile

VST: VLT Survey Telescope

WARPS: Wide Angle ROSAT Pointed Survey

WMAP: Wilkinson Microwave Anisotropy Probe

World Coordinates: Coordinate system that is based on absolute positions on the celestial sphere.

XCS: XMM Cluster Survey

XDCP: XMM-Newton Distant Cluster Project

XLf: X-ray Luminosity Function

XMM-LSS: XMM Large-Scale Structure survey

XMM-Newton: X-ray Spectroscopy Multi-Mirror Mission

XSA: XMM-Newton Science Archive

Bibliography

- Abell, G. O.: 1958, *Astrophys. J., Suppl. Ser.* **3**, 211
- Abraham, R. G., Glazebrook, K., McCarthy, P. J., Crampton, D., Murowinski, R., Jørgensen, I., Roth, K., Hook, I. M., Savaglio, S., Chen, H.-W., Marzke, R. O., and Carlberg, R. G.: 2004, *Astron. J.* **127**, 2455
- Abraham, R. G., Smecker-Hane, T. A., Hutchings, J. B., Carlberg, R. G., Yee, H. K. C., Ellingson, E., Morris, S., Oke, J. B., and Rigler, M.: 1996, *Astrophys. J.* **471**, 694
- Allen, S. W., Schmidt, R. W., Ebeling, H., Fabian, A. C., and van Speybroeck, L.: 2004, *MNRAS* **353**, 457
- Allen, S. W., Schmidt, R. W., Fabian, A. C., and Ebeling, H.: 2003, *MNRAS* **342**, 287
- Andreon, S.: 1998, *Astronomy & Astrophysics* **336**, 98
- Andreon, S., Valtchanov, I., Jones, L. R., Altieri, B., Bremer, M., Willis, J., Pierre, M., and Quintana, H.: 2005, *MNRAS* **359**, 1250
- Angulo, R., Baugh, C. M., Frenk, C. S., Bower, R. G., Jenkins, A., and Morris, S. L.: 2005, *MNRAS* **362**, L25
- Aragon-Salamanca, A., Baugh, C. M., and Kauffmann, G.: 1998, *MNRAS* **297**, 427
- Arnaud, M. and Evrard, A. E.: 1999, *MNRAS* **305**, 631
- Arnaud, M., Pointecouteau, E., and Pratt, G. W.: 2005, *Astronomy & Astrophysics* **441**, 893
- Arnaud, M., Pointecouteau, E., and Pratt, G. W.: 2007, *ArXiv Astrophysics e-prints*, arXiv:astro-ph/0709.1561
- Böhringer, H., Mullis, C. R., Rosati, P., Lamer, G., Fassbender, R., Schwobe, A., and Schuecker, P.: 2005, *ESO Messenger* **120**, 33
- Böhringer, H., Schuecker, P., Guzzo, L., Collins, C. A., Voges, W., Cruddace, R. G., Ortiz-Gil, A., Chincarini, G., De Grandi, S., Edge, A. C., MacGillivray, H. T., Neumann, D. M., Schindler, S., and Shaver, P.: 2004, *Astronomy & Astrophysics* **425**, 367
- Bailer-Jones, C., Bizenberger, P., and Storz, C.: 2000, in M. Iye and A. F. Moorwood (eds.), *Optical and IR Telescope Instrumentation and Detectors*, Vol. 4008, SPIE - The International Society for Optical Engineering, Bellingham, Washington (USA)
- Barcons, X., Carrera, F. J., Watson, M. G., McMahon, R. G., Aschenbach, B., Freyberg, M. J., Page, K., Page, M. J., Roberts, T. P., Turner, M. J. L., Barret, D., Brunner, H., Ceballos, M. T., Della Ceca, R., Guillout, P., Hasinger, G., Maccacaro, T., Mateos, S., Motch, C., Negueruela, I., Osborne, J. P., Pérez-Fournon, I., Schwobe, A., Severgnini, P., Szokoly, G. P., Webb, N. A., Wheatley, P. J., and Worrall, D. M.: 2002,

- Astronomy & Astrophysics* **382**, 522
- Baum, W. A.: 1959, *Publ. Astron. Soc. Pac.* **71**, 106
- Bertin, E. and Arnouts, S.: 1996, *Astronomy & Astrophysics, Suppl. Ser.* **117**, 393
- Bhavsar, S. P. and Barrow, J. D.: 1985, *MNRAS* **213**, 857
- Biviano, A.: 2000, in *Constructing the Universe with Clusters of Galaxies*
- Böhringer, H.: 2003, in R. E. Schielicke (ed.), *Reviews in Modern Astronomy*, Vol. 16 of *Reviews in Modern Astronomy*, p. 275
- Böhringer, H., Collins, C. A., Guzzo, L., Schuecker, P., Voges, W., Neumann, D. M., Schindler, S., Chincarini, G., De Grandi, S., Cruddace, R. G., Edge, A. C., Reiprich, T. H., and Shaver, P.: 2002a, *Astrophys. J.* **566**, 93
- Böhringer, H., Matsushita, K., Churazov, E., Ikebe, Y., and Chen, Y.: 2002b, *Astronomy & Astrophysics* **382**, 804
- Böhringer, H., Pratt, G. W., Finoguenov, A., and Schuecker, P. (eds.): 2007a, *Heating versus Cooling in Galaxies and Clusters of Galaxies*, Proceedings of the Joint Astronomy Conference Held in Garching, Germany, 6-11 August 2006
- Böhringer, H., Schuecker, P., Guzzo, L., Collins, C. A., Voges, W., Schindler, S., Neumann, D. M., Cruddace, R. G., De Grandi, S., Chincarini, G., Edge, A. C., MacGillivray, H. T., and Shaver, P.: 2001, *Astronomy & Astrophysics* **369**, 826
- Böhringer, H., Schuecker, P., Pratt, G. W., Arnaud, M., Ponman, T. J., Croston, J. H., Borgani, S., Bower, R. G., Briel, U. G., Collins, C. A., Donahue, M., Forman, W. R., Finoguenov, A., Geller, M. J., Guzzo, L., Henry, J. P., Kneissl, R., Mohr, J. J., Matsushita, K., Mullis, C. R., Ohashi, T., Pedersen, K., Pierini, D., Quintana, H., Raychaudhury, S., Reiprich, T. H., Romer, A. K., Rosati, P., Sabirli, K., Temple, R. F., Viana, P. T. P., Vikhlinin, A., Voit, G. M., and Zhang, Y.-Y.: 2007b, *Astronomy & Astrophysics* **469**, 363
- Böhringer, H., Voges, W., Huchra, J. P., McLean, B., Giacconi, R., Rosati, P., Burg, R., Mader, J., Schuecker, P., Simić, D., Komossa, S., Reiprich, T. H., Retzlaff, J., and Trümper, J.: 2000, *Astrophys. J., Suppl. Ser.* **129**, 435
- Bond, J. R., Cole, S., Efstathiou, G., and Kaiser, N.: 1991, *Astrophys. J.* **379**, 440
- Borgani, S.: 2006, *ArXiv Astrophysics e-prints*, astro-ph/0605575
- Borgani, S., Rosati, P., della Ceca, R., Tozzi, P., and Norman, C.: 2000, in M. Plionis and I. Georgantopoulos (eds.), *Large Scale Structure in the X-ray Universe, Proceedings of the 20-22 September 1999 Workshop, Santorini, Greece, eds. Plionis, M. & Georgantopoulos, I., Atlantisciences, Paris, France*, p. 167
- Bower, R. G.: 1991, *MNRAS* **248**, 332
- Bower, R. G. and Balogh, M. L.: 2004, in J. S. Mulchaey, A. Dressler, and A. Oemler (eds.), *Clusters of Galaxies: Probes of Cosmological Structure and Galaxy Evolution*, p. 325
- Bower, R. G., Lucey, J. R., and Ellis, R. S.: 1992a, *MNRAS* **254**, 601
- Bower, R. G., Lucey, J. R., and Ellis, R. S.: 1992b, *MNRAS* **254**, 589
- Bremer, M. N., Valtchanov, I., Willis, J., Altieri, B., Andreon, S., Duc, P. A., Fang, F., Jean, C., Lonsdale, C., Pacaud, F., Pierre, M., Shupe, D. L., Surace, J. A., and Waddington, I.: 2006, *MNRAS* **371**, 1427

- Bruzual, G. and Charlot, S.: 2003, *MNRAS* **344**, 1000
- Burenin, R. A., Vikhlinin, A., Hornstrup, A., Ebeling, H., Quintana, H., and Mescheryakov, A.: 2007, *Astrophys. J., Suppl. Ser.* **172**, 561
- Burke, D. J., Collins, C. A., and Mann, R. G.: 2000, *Astrophys. J., Lett.* **532**, L105
- Butcher, H. and Oemler, Jr., A.: 1978, *Astrophys. J.* **219**, 18
- Calabretta, M. R. and Greisen, E. W.: 2002, *Astronomy & Astrophysics* **395**, 1077
- Caldwell, R. R., Kamionkowski, M., and Weinberg, N. N.: 2003, *Physical Review Letters* **91**, 7
- Cassata, P., Guzzo, L., Franceschini, A., Scoville, N., Capak, P., Ellis, R. S., Koekoemoer, A., McCracken, H. J., Mobasher, B., Renzini, A., Ricciardelli, E., Scodeggio, M., Taniguchi, Y., and Thompson, D.: 2007, *Astrophys. J., Suppl. Ser.* **172**, 270
- Cavaliere, A. and Fusco-Femiano, R.: 1976, *Astronomy & Astrophysics* **49**, 137
- Chandrasekhar, S.: 1943, *Astrophys. J.* **97**, 255
- Chen, Y., Reiprich, T. H., Böhringer, H., Ikebe, Y., and Zhang, Y.-Y.: 2007, *Astronomy & Astrophysics* **466**, 805
- Churazov, E., Brüggen, M., Kaiser, C. R., Böhringer, H., and Forman, W.: 2001, *Astrophys. J.* **554**, 261
- Cimatti, A., Daddi, E., Renzini, A., Cassata, P., Vanzella, E., Pozzetti, L., Cristiani, S., Fontana, A., Rodighiero, G., Mignoli, M., and Zamorani, G.: 2004, *Nature* **430**, 184
- Clowe, D., Bradač, M., Gonzalez, A. H., Markevitch, M., Randall, S. W., Jones, C., and Zaritsky, D.: 2006, *Astrophys. J., Lett.* **648**, L109
- Coles, P. and Lucchin, F.: 2002, *Cosmology: The Origin and Evolution of Cosmic Structure, Second Edition*, Cosmology: The Origin and Evolution of Cosmic Structure, Second Edition, by Peter Coles, Francesco Lucchin, pp. 512. ISBN 0-471-48909-3. Wiley-VCH, July 2002.
- Collins, C. A. and Mann, R. G.: 1998, *MNRAS* **297**, 128
- Condon, J. J., Cotton, W. D., Greisen, E. W., Yin, Q. F., Perley, R. A., Taylor, G. B., and Broderick, J. J.: 1998, *Astron. J.* **115**, 1693
- Connolly, A. J., Szalay, A. S., Koo, D., Romer, A. K., Holden, B., Nichol, R. C., and Miyaji, T.: 1996, *Astrophys. J., Lett.* **473**, L67
- Cooper, M. C., Newman, J. A., Coil, A. L., Croton, D. J., Gerke, B. F., Yan, R., Davis, M., Faber, S. M., Guhathakurta, P., Koo, D. C., Weiner, B. J., and Willmer, C. N. A.: 2007, *MNRAS* **376**, 1445
- Cowie, L. L., Songaila, A., Hu, E. M., and Cohen, J. G.: 1996, *Astron. J.* **112**, 839
- Cox, A. N. (ed.): 2000, *Allen's Astrophysical Quantities*, New York: AIP Press; Springer
- Craddace, R. G., Hasinger, G. R., and Schmitt, J. H.: 1988, in F. Murtagh and A. Heck (eds.), *Astronomy from Large Databases*, pp 177–182
- Cucciati, O., Iovino, A., Marinoni, C., Ilbert, O., Bardelli, S., Franzetti, P., Le Fevre, O., Pollo, A., Zamorani, G., Cappi, A., Guzzo, L., McCracken, H. J., Meneux, B., Scaramella, R., Scodeggio, M., Tresse, L., Zucca, E., Bottini, D., Garilli, B., Le Brun, V., Maccagni, D., Picat, J. P., Vettolani, G., Zanichelli, A., Adami, C., Arnaboldi, M., Arnouts, S., Bolzonella, M., Charlot, S., Ciliegi, P., Contini, T., Foucaud, S., Gavignaud, I., Marano, B., Mazure, A., Merighi, R., Paltani, S., Pello', R., Pozzetti,

- L., Radovich, M., Bondi, M., Bongiorno, A., Busarello, G., de la Torre, S., Gregorini, L., Lamareille, F., Mathez, G., Mellier, Y., Merluzzi, P., Ripepi, V., Rizzo, D., Temporin, G., and Vergani, D.: 2006, *ArXiv Astrophysics e-prints*, astro-ph/0612120
- Cutri, R. M., Skrutskie, M. F., van Dyk, S., Beichman, C. A., Carpenter, J. M., Chester, T., Cambresy, L., Evans, T., Fowler, J., Gizis, J., Howard, E., Huchra, J., Jarrett, T., Kopan, E. L., Kirkpatrick, J. D., Light, R. M., Marsh, K. A., McCallon, H., Schneider, S., Stiening, R., Sykes, M., Weinberg, M., Wheaton, W. A., Wheelock, S., and Zacarias, N.: 2003, *2MASS All Sky Catalog of point sources.*, The IRSA 2MASS All-Sky Point Source Catalog, NASA/IPAC Infrared Science Archive
- Danese, L., de Zotti, G., and di Tullio, G.: 1980, *Astronomy & Astrophysics* **82**, 322
- Davis, T. M. and Lineweaver, C. H.: 2004, *Publications of the Astronomical Society of Australia* **21**, 97
- De Lucia, G. and Blaizot, J.: 2007, *MNRAS* **375**, 2
- De Lucia, G., Poggianti, B. M., Aragón-Salamanca, A., Clowe, D., Halliday, C., Jablonka, P., Milvang-Jensen, B., Pelló, R., Poirier, S., Rudnick, G., Saglia, R., Simard, L., and White, S. D. M.: 2004, *Astrophys. J., Lett.* **610**, L77
- De Lucia, G., Poggianti, B. M., Aragón-Salamanca, A., White, S. D. M., Zaritsky, D., Clowe, D., Halliday, C., Jablonka, P., von der Linden, A., Milvang-Jensen, B., Pelló, R., Rudnick, G., Saglia, R. P., and Simard, L.: 2007, *MNRAS* **374**, 809
- De Lucia, G., Springel, V., White, S. D. M., Croton, D., and Kauffmann, G.: 2006, *MNRAS* **366**, 499
- Dickey, J. M. and Lockman, F. J.: 1990, *Annual Rev. of Astronomy and Astrophysics* **28**, 215
- Dressler, A.: 1980, *Astrophys. J.* **236**, 351
- Dressler, A., Oemler, A. J., Couch, W. J., Smail, I., Ellis, R. S., Barger, A., Butcher, H., Poggianti, B. M., and Sharples, R. M.: 1997, *Astrophys. J.* **490**, 577
- Dunlop, J., Peacock, J., Spinrad, H., Dey, A., Jimenez, R., Stern, D., and Windhorst, R.: 1996, *Nature* **381**, 581
- Eggen, O. J., Lynden-Bell, D., and Sandage, A. R.: 1962, *Astrophys. J.* **136**, 748
- Ehle, M., e. a.: 2007, *XMM-Newton User's Handbook*, European Space Agency
- Eisenstein, D. J. and Hu, W.: 1998, *Astrophys. J.* **496**, 605
- Eisenstein, D. J., Zehavi, I., Hogg, D. W., Scoccimarro, R., Blanton, M. R., Nichol, R. C., Scranton, R., Seo, H.-J., Tegmark, M., Zheng, Z., Anderson, S. F., Annis, J., Bahcall, N., Brinkmann, J., Burles, S., Castander, F. J., Connolly, A., Csabai, I., Doi, M., Fukugita, M., Frieman, J. A., Glazebrook, K., Gunn, J. E., Hendry, J. S., Hennessy, G., Ivezić, Z., Kent, S., Knapp, G. R., Lin, H., Loh, Y.-S., Lupton, R. H., Margon, B., McKay, T. A., Meiksin, A., Munn, J. A., Pope, A., Richmond, M. W., Schlegel, D., Schneider, D. P., Shimasaku, K., Stoughton, C., Strauss, M. A., SubbaRao, M., Szalay, A. S., Szapudi, I., Tucker, D. L., Yanny, B., and York, D. G.: 2005, *Astrophys. J.* **633**, 560
- Ettori, S., Tozzi, P., Borgani, S., and Rosati, P.: 2004, *Astronomy & Astrophysics* **417**, 13
- Faber, S. M., Trager, S. C., Gonzalez, J. J., and Worthey, G.: 1995, in P. C. van der Kruit and G. Gilmore (eds.), *Stellar Populations*, Vol. 164 of *IAU Symposium*, p. 249

- Fabian, A. C. and Nulsen, P. E. J.: 1977, *MNRAS* **180**, 479
- Fabian, A. C., Sanders, J. S., Allen, S. W., Crawford, C. S., Iwasawa, K., Johnstone, R. M., Schmidt, R. W., and Taylor, G. B.: 2003, *MNRAS* **344**, L43
- Fassbender, R.: 2003, *Master's thesis*, University of Heidelberg
- Fassbender, R., Böhringer, H., Lamer, G., Mullis, C. R., Rosati, P., Schope, A., Kohnert, J., and Santos, J. S.: submitted, *Astronomy & Astrophysics*
- Fassbender, R., Stegmaier, J., Weijmans, A.-M., Köstner, S., Kruselburger, A., Diethart, C., Fertl, P., Valiante, E., Hayes, M., Schuecker, P., and Hasinger, G.: 2006, in M. J. L. Turner and G. Hasinger (eds.), *Space Telescopes and Instrumentation II: Ultraviolet to Gamma Ray. Edited by Turner, Martin J. L.; Hasinger, Günther. Proceedings of the SPIE, Volume 6266, pp. 626632 (2006).*, Vol. 6266 of *Presented at the Society of Photo-Optical Instrumentation Engineers (SPIE) Conference*
- Felten, J. E., Gould, R. J., Stein, W. A., and Woolf, N. J.: 1966, *Astrophys. J.* **146**, 955
- Finoguenov, A., Guzzo, L., Hasinger, G., Scoville, N. Z., Aussel, H., Böhringer, H., Brusa, M., Capak, P., Cappelluti, N., Comastri, A., Giodini, S., Griffiths, R. E., Impey, C., Koekemoer, A. M., Kneib, J.-P., Leauthaud, A., Le Fèvre, O., Lilly, S., Mainieri, V., Massey, R., McCracken, H. J., Mobasher, B., Murayama, T., Peacock, J. A., Sakelliou, I., Schinnerer, E., Silverman, J. D., Smolčić, V., Taniguchi, Y., Tasca, L., Taylor, J. E., Trump, J. R., and Zamorani, G.: 2007, *Astrophys. J., Suppl. Ser.* **172**, 182
- Fioc, M. and Rocca-Volmerange, B.: 1997, in *ASSL Vol. 210: The Impact of Large Scale Near-IR Sky Surveys*, p. 257
- Freedman, W. L., Madore, B. F., Gibson, B. K., Ferrarese, L., Kelson, D. D., Sakai, S., Mould, J. R., Kennicutt, Jr., R. C., Ford, H. C., Graham, J. A., Huchra, J. P., Hughes, S. M. G., Illingworth, G. D., Macri, L. M., and Stetson, P. B.: 2001, *Astrophys. J.* **553**, 47
- Gabasch, A.: 2004, *Ph.D. thesis*, Ludwig-Maximilian University Munich
- Giacconi, R., Rosati, P., Tozzi, P., Nonino, M., Hasinger, G., Norman, C., Bergeron, J., Borgani, S., Gilli, R., Gilmozzi, R., and Zheng, W.: 2001, *Astrophys. J.* **551**, 624
- Gioia, I. M., Henry, J. P., Maccacaro, T., Morris, S. L., Stocke, J. T., and Wolter, A.: 1990, *Astrophys. J., Lett.* **356**, L35
- Gladders, M. D. and Yee, H. K. C.: 2005, *Astrophys. J., Suppl. Ser.* **157**, 1
- Gómez, P. L., Nichol, R. C., Miller, C. J., Balogh, M. L., Goto, T., Zabludoff, A. I., Romer, A. K., Bernardi, M., Sheth, R., Hopkins, A. M., Castander, F. J., Connolly, A. J., Schneider, D. P., Brinkmann, J., Lamb, D. Q., SubbaRao, M., and York, D. G.: 2003, *Astrophys. J.* **584**, 210
- Gonzalez, A. H., Zaritsky, D., Dalcanton, J. J., and Nelson, A.: 2001, *Astrophys. J., Suppl. Ser.* **137**, 117
- Gott, J. R. I. and Gunn, J. E.: 1971, *Astrophys. J., Lett.* **169**, L13
- Gunn, J. E. and Gott, J. R. I.: 1972, *Astrophys. J.* **176**, 1
- Haas, A.: 2002, *HAWAII-2: 2048x2048 Pixel Focal Plane Array*, Rockwell Scientific
- Harris, W. E.: 1990, *Publ. Astron. Soc. Pac.* **102**, 949
- Hashimoto, Y., Hasinger, G., Arnaud, M., Rosati, P., and Miyaji, T.: 2002, *Astronomy & Astrophysics* **381**, 841

- Hashimoto, Y., Henry, J. P., Hasinger, G., Szokoly, G., and Schmidt, M.: 2005, *Astronomy & Astrophysics* **439**, 29
- Hasinger, G., Cappelluti, N., Brunner, H., Brusa, M., Comastri, A., Elvis, M., Finoguenov, A., Fiore, F., Franceschini, A., Gilli, R., Griffiths, R. E., Lehmann, I., Mainieri, V., Matt, G., Matute, I., Miyaji, T., Molendi, S., Paltani, S., Sanders, D. B., Scoville, N., Tresse, L., Urry, C. M., Vettolani, P., and Zamorani, G.: 2007, *Astrophys. J., Suppl. Ser.* **172**, 29
- Hausman, M. A. and Ostriker, J. P.: 1978, *Astrophys. J.* **224**, 320
- Henry, J. P., Gioia, I. M., Maccacaro, T., Morris, S. L., Stocke, J. T., and Wolter, A.: 1992, *Astrophys. J.* **386**, 408
- Henry, J. P., Mullis, C. R., Voges, W., Böhringer, H., Briel, U. G., Gioia, I. M., and Huchra, J. P.: 2006, *Astrophys. J., Suppl. Ser.* **162**, 304
- Herranz, D., Sanz, J. L., Barreiro, R. B., and Martínez-González, E.: 2002, *Astrophys. J.* **580**, 610
- Hu, W.: 2004, *ArXiv Astrophysics e-prints*, astro-ph/0402060
- Hu, W. and Sugiyama, N.: 1996, *Astrophys. J.* **471**, 542
- Jehin, E.: 2006, *Fors1+2 User Manual*, European Southern Observatory
- Jenkins, A., Frenk, C. S., White, S. D. M., Colberg, J. M., Cole, S., Evrard, A. E., Couchman, H. M. P., and Yoshida, N.: 2001, *MNRAS* **321**, 372
- Jones, C. and Forman, W.: 1984, *Astrophys. J.* **276**, 38
- Kaiser, N.: 1984, *Astrophys. J., Lett.* **284**, L9
- Kaiser, N.: 1986, *MNRAS* **222**, 323
- Kajisawa, M., Yamada, T., Tanaka, I., Maihara, T., Iwamuro, F., Terada, H., Goto, M., Motohara, K., Tanabe, H., Taguchi, T., Hata, R., Iye, M., Imanishi, M., Chikada, Y., Yoshida, M., Simpson, C., Sasaki, T., Kosugi, G., Usuda, T., and Sekiguchi, K.: 2000, *Publ. Astron. Soc. Jpn.* **52**, 61
- Kauffmann, G.: 1996, *MNRAS* **281**, 487
- Kauffmann, G. and Charlot, S.: 1998, *ArXiv Astrophysics e-prints*, astro-ph/9810031
- King, I. R.: 1966, *Astron. J.* **71**, 276
- Kitayama, T. and Suto, Y.: 1996, *Astrophys. J.* **469**, 480
- Kodama, T. and Arimoto, N.: 1997, *Astronomy & Astrophysics* **320**, 41
- Kodama, T., Arimoto, N., Barger, A. J., and Arag'ón-Salamanca, A.: 1998, *Astronomy & Astrophysics* **334**, 99
- Kodama, T., Smail, I., Nakata, F., Okamura, S., and Bower, R. G.: 2001, *Astrophys. J., Lett.* **562**, L9
- Kurtz, M. J. and Mink, D. J.: 1998, *Publ. Astron. Soc. Pac.* **110**, 934
- Lamer, G., Soucail, G., Fassbender, R., and et al.: in preparation, *Astronomy & Astrophysics*
- Lanzetta, K. M., Yahata, N., Pascarella, S., Chen, H.-W., and Fernández-Soto, A.: 2002, *Astrophys. J.* **570**, 492
- Lewis, I., Balogh, M., De Propriis, R., Couch, W., Bower, R., Offer, A., Bland-Hawthorn, J., Baldry, I. K., Baugh, C., Bridges, T., Cannon, R., Cole, S., Colless, M., Collins, C., Cross, N., Dalton, G., Driver, S. P., Efsthathiou, G., Ellis, R. S., Frenk, C. S., Glazebrook,

- K., Hawkins, E., Jackson, C., Lahav, O., Lumsden, S., Maddox, S., Madgwick, D., Norberg, P., Peacock, J. A., Percival, W., Peterson, B. A., Sutherland, W., and Taylor, K.: 2002, *MNRAS* **334**, 673
- Lin, Y.-T. and Mohr, J. J.: 2004, *Astrophys. J.* **617**, 879
- Lin, Y.-T. and Mohr, J. J.: 2007, *Astrophys. J., Suppl. Ser.* **170**, 71
- Lynden-Bell, D.: 1967, *MNRAS* **136**, 101
- Margoniner, V. E., de Carvalho, R. R., Gal, R. R., and Djorgovski, S. G.: 2001, *Astrophys. J., Lett.* **548**, L143
- Matthews, T. A., Morgan, W. W., and Schmidt, M.: 1964, *Astrophys. J.* **140**, 35
- Maughan, B. J., Jones, L. R., Ebeling, H., and Scharf, C.: 2006, *MNRAS* **365**, 509
- McCarthy, P. J., Yan, H., Abraham, R. G., Mentuch, E., Glazebrook, K., Yan, L., Chen, H.-W., Persson, S. E., Nair, P., Savaglio, S., Crampton, D., Juneau, S., Le Borgne, D., Carlberg, R. G., Marzke, R. O., Jørgensen, I., Roth, K., and Murowinski, R.: 2007, *Astrophys. J., Lett.* **664**, L17
- McNamara, B. R., Birzan, L., Rafferty, D. A., Nulsen, P. E. J., Carilli, C., and Wise, M. W.: 2007, *ArXiv e-prints*, astro-ph/0708.0579
- McNamara, B. R., Nulsen, P. E. J., Wise, M. W., Rafferty, D. A., Carilli, C., Sarazin, C. L., and Blanton, E. L.: 2005, *Nature* **433**, 45
- Mei, S., Blakeslee, J. P., Stanford, S. A., Holden, B. P., Rosati, P., Strazzullo, V., Homeier, N., Postman, M., Franx, M., Rettura, A., Ford, H., Illingworth, G. D., Ettori, S., Bouwens, R. J., Demarco, R., Martel, A. R., Clampin, M., Hartig, G. F., Eisenhardt, P., Ardila, D. R., Bartko, F., Benítez, N., Bradley, L. D., Broadhurst, T. J., Brown, R. A., Burrows, C. J., Cheng, E. S., Cross, N. J. G., Feldman, P. D., Golimowski, D. A., Goto, T., Gronwall, C., Infante, L., Kimble, R. A., Krist, J. E., Lesser, M. P., Menanteau, F., Meurer, G. R., Miley, G. K., Motta, V., Sirianni, M., Sparks, W. B., Tran, H. D., Tsvetanov, Z. I., White, R. L., and Zheng, W.: 2006a, *Astrophys. J.* **639**, 81
- Mei, S., Holden, B. P., Blakeslee, J. P., Rosati, P., Postman, M., Jee, M. J., Rettura, A., Sirianni, M., Demarco, R., Ford, H. C., Franx, M., Homeier, N., and Illingworth, G. D.: 2006b, *Astrophys. J.* **644**, 759
- Miley, G. K., Overzier, R. A., Zirm, A. W., Ford, H. C., Kurk, J., Pentericci, L., Blakeslee, J. P., Franx, M., Illingworth, G. D., Postman, M., Rosati, P., Röttgering, H. J. A., Venemans, B. P., and Helder, E.: 2006, *Astrophys. J., Lett.* **650**, L29
- Mitchell, R. J. and Culhane, J. L.: 1977, *MNRAS* **178**, 75P
- Mullis, C. R., Rosati, P., Lamer, G., Böhringer, H., Schwobe, A., Schuecker, P., and Fassbender, R.: 2005, *Astrophys. J., Lett.* **623**, L85
- Mullis, C. R., Vikhlinin, A., Henry, J. P., Forman, W., Gioia, I. M., Hornstrup, A., Jones, C., McNamara, B. R., and Quintana, H.: 2004, *Astrophys. J.* **607**, 175
- Mushotzky, R. F., Cowie, L. L., Barger, A. J., and Arnaud, K. A.: 2000, *Nature* **404**, 459
- Nakata, F., Kajisawa, M., Yamada, T., Kodama, T., Shimasaku, K., Tanaka, I., Doi, M., Furusawa, H., Hamabe, M., Iye, M., Kimura, M., Komiyama, Y., Miyazaki, S., Okamura, S., Ouchi, M., Sasaki, T., Sekiguchi, M., Yagi, M., and Yasuda, N.: 2001, *Publ. Astron. Soc. Jpn.* **53**, 1139

- Nakata, F., Kodama, T., Shimasaku, K., Doi, M., Furusawa, H., Hamabe, M., Kimura, M., Komiyama, Y., Miyazaki, S., Okamura, S., Ouchi, M., Sekiguchi, M., Ueda, Y., Yagi, M., and Yasuda, N.: 2005, *MNRAS* **357**, 1357
- Navarro, J. F., Frenk, C. S., and White, S. D. M.: 1997, *Astrophys. J.* **490**, 493
- Nipoti, C., Stiavelli, M., Ciotti, L., Treu, T., and Rosati, P.: 2003, *MNRAS* **344**, 748
- Novak, N.: 2003, *Master's thesis*, Technical University Munich
- Ostriker, J. P. and Tremaine, S. D.: 1975, *Astrophys. J., Lett.* **202**, L113
- Pacaud, F., Pierre, M., Adami, C., Altieri, B., Andreon, S., Chiappetti, L., Detal, A., Duc, P. ., Galaz, G., Gueguen, A., Le Fèvre, J. ., Hertling, G., Libbrecht, C., Melin, J. ., Ponman, T. J., Quintana, H., Refregier, A., Sprimont, P. ., Surdej, J., Valtchanov, I., Willis, J. P., Alloin, D., Birkinshaw, M., Bremer, M. N., Garcet, O., Jean, C., Jones, L. R., Le Fèvre, O., Maccagni, D., Mazure, A., Proust, D., Röttgering, H. J. A., and Trinchieri, G.: 2007, *ArXiv e-prints*, astro-ph/0709.1950
- Pacaud, F., Pierre, M., Refregier, A., Gueguen, A., Starck, J.-L., Valtchanov, I., Read, A. M., Altieri, B., Chiappetti, L., Gandhi, P., Garcet, O., Gosset, E., Ponman, T. J., and Surdej, J.: 2006, *MNRAS* **372**, 578
- Peacock, J. A.: 1999, *Cosmological Physics*, Cosmological Physics, by John A. Peacock, pp. 704. ISBN 052141072X. Cambridge, UK: Cambridge University Press, January 1999.
- Perlman, E. S., Horner, D. J., Jones, L. R., Scharf, C. A., Ebeling, H., Wegner, G., and Malkan, M.: 2002, *Astrophys. J., Suppl. Ser.* **140**, 265
- Perlmutter, S., Aldering, G., Goldhaber, G., Knop, R. A., Nugent, P., Castro, P. G., Deustua, S., Fabbro, S., Goobar, A., Groom, D. E., Hook, I. M., Kim, A. G., Kim, M. Y., Lee, J. C., Nunes, N. J., Pain, R., Pennypacker, C. R., Quimby, R., Lidman, C., Ellis, R. S., Irwin, M., McMahon, R. G., Ruiz-Lapuente, P., Walton, N., Schaefer, B., Boyle, B. J., Filippenko, A. V., Matheson, T., Fruchter, A. S., Panagia, N., Newberg, H. J. M., Couch, W. J., and The Supernova Cosmology Project: 1999, *Astrophys. J.* **517**, 565
- Peterson, J. R., Paerels, F. B. S., Kaastra, J. S., Arnaud, M., Reiprich, T. H., Fabian, A. C., Mushotzky, R. F., Jernigan, J. G., and Sakelliou, I.: 2001, *Astronomy & Astrophysics* **365**, L104
- Pickles, A. J.: 1998, *Publ. Astron. Soc. Pac.* **110**, 863
- Pierre, M., Pacaud, F., Duc, P.-A., Willis, J. P., Andreon, S., Valtchanov, I., Altieri, B., Galaz, G., Gueguen, A., Fèvre, J.-P. L., Fèvre, O. L., Ponman, T., Sprimont, P.-G., Surdej, J., Adami, C., Alshino, A., Bremer, M., Chiappetti, L., Detal, A., Garcet, O., Gosset, E., Jean, C., Maccagni, D., Marinoni, C., Mazure, A., Quintana, H., and Read, A.: 2006, *MNRAS* **372**, 591
- Pointecouteau, E., Arnaud, M., and Pratt, G. W.: 2005, *Astronomy & Astrophysics* **435**, 1
- Popesso, P., Böhringer, H., Romaniello, M., and Voges, W.: 2005, *Astronomy & Astrophysics* **433**, 415
- Postman, M., Franx, M., Cross, N. J. G., Holden, B., Ford, H. C., Illingworth, G. D., Goto, T., Demarco, R., Rosati, P., Blakeslee, J. P., Tran, K.-V., Benítez, N., Clampin, M., Hartig, G. F., Homeier, N., Ardila, D. R., Bartko, F., Bouwens, R. J., Bradley, L. D., Broadhurst, T. J., Brown, R. A., Burrows, C. J., Cheng, E. S., Feldman, P. D.,

- Golimowski, D. A., Gronwall, C., Infante, L., Kimble, R. A., Krist, J. E., Lesser, M. P., Martel, A. R., Mei, S., Menanteau, F., Meurer, G. R., Miley, G. K., Motta, V., Sirianni, M., Sparks, W. B., Tran, H. D., Tsvetanov, Z. I., White, R. L., and Zheng, W.: 2005, *Astrophys. J.* **623**, 721
- Postman, M. and Lauer, T. R.: 1995, *Astrophys. J.* **440**, 28
- Pratt, G. W. and Arnaud, M.: 2002, *Astronomy & Astrophysics* **394**, 375
- Pratt, G. W. and Arnaud, M.: 2003, *Astronomy & Astrophysics* **408**, 1
- Pratt, G. W., Böhringer, H., Croston, J. H., Arnaud, M., Borgani, S., Finoguenov, A., and Temple, R. F.: 2007, *Astronomy & Astrophysics* **461**, 71
- Predehl, P., Hasinger, G., Böhringer, H., Briel, U., Brunner, H., Churazov, E., Freyberg, M., Friedrich, P., Kendziorra, E., Lutz, D., Meidinger, N., Pavlinsky, M., Pfeffermann, E., Santangelo, A., Schmitt, J., Schuecker, P., Schwöpe, A., Steinmetz, M., Strüder, L., Sunyaev, R., and Wilms, J.: 2006, in *Space Telescopes and Instrumentation II: Ultra-violet to Gamma Ray. Edited by Turner, Martin J. L.; Hasinger, Günther. Proceedings of the SPIE, Volume 6266, pp. 62660P (2006).*
- Press, W. H. and Schechter, P.: 1974, *Astrophys. J.* **187**, 425
- Reid, I. N., Brewer, C., Brucato, R. J., McKinley, W. R., Maury, A., Mendenhall, D., Mould, J. R., Mueller, J., Neugebauer, G., Phinney, J., Sargent, W. L. W., Schombert, J., and Thicksten, R.: 1991, *Publ. Astron. Soc. Pac.* **103**, 661
- Reiprich, T. H.: 2001, *Ph.D. thesis*, Ludwig-Maximilian University Munich
- Reiprich, T. H. and Böhringer, H.: 2002, *Astrophys. J.* **567**, 716
- Renzini, A.: 2006, *Annual Rev. of Astronomy and Astrophysics* **44**, 141
- Richstone, D. O.: 1976, *Astrophys. J.* **204**, 642
- Romer, A. K., Viana, P. T. P., Liddle, A. R., and Mann, R. G.: 2001, *Astrophys. J.* **547**, 594
- Rosati, P.: 2001, in *ASP Conf. Ser. 234: X-ray Astronomy 2000*, p. 363
- Rosati, P., Borgani, S., della Ceca, R., Stanford, A., Eisenhardt, P., and Lidman, C.: 2000, in M. Plionis and I. Georgantopoulos (eds.), *Large Scale Structure in the X-ray Universe, Proceedings of the 20-22 September 1999 Workshop, Santorini, Greece, eds. Plionis, M. & Georgantopoulos, I., Atlantisciences, Paris, France*, p. 13
- Rosati, P., Borgani, S., and Norman, C.: 2002, *Annual Rev. of Astronomy and Astrophysics* **40**, 539
- Rosati, P., della Ceca, R., Burg, R., Norman, C., and Giacconi, R.: 1995, *Astrophys. J., Lett.* **445**, L11
- Rosati, P., della Ceca, R., Norman, C., and Giacconi, R.: 1998, *Astrophys. J., Lett.* **492**, L21
- Rosati, P., Stanford, S. A., Eisenhardt, P. R., Elston, R., Spinrad, H., Stern, D., and Dey, A.: 1999, *Astron. J.* **118**, 76
- Rosati, P., Tozzi, P., Ettori, S., Mainieri, V., Demarco, R., Stanford, S. A., Lidman, C., Nonino, M., Borgani, S., Della Ceca, R., Eisenhardt, P., Holden, B. P., and Norman, C.: 2004, *Astron. J.* **127**, 230
- Röser, H.-J.: 2005, *OMEGA2000 User's Manual*, MPI für Astronomie
- Ruhl, J., Ade, P. A. R., Carlstrom, J. E., Cho, H.-M., Crawford, T., Dobbs, M., Greer,

- C. H., Halverson, N. w., Holzapfel, W. L., Lanting, T. M., Lee, A. T., Leitch, E. M., Leong, J., Lu, W., Lueker, M., Mehl, J., Meyer, S. S., Mohr, J. J., Padin, S., Plagge, T., Pryke, C., Runyan, M. C., Schwan, D., Sharp, M. K., Spieler, H., Staniszewski, Z., and Stark, A. A.: 2004, in C. M. Bradford, P. A. R. Ade, J. E. Aguirre, J. J. Bock, M. Dragovan, L. Duband, L. Earle, J. Glenn, H. Matsuhara, B. J. Naylor, H. T. Nguyen, M. Yun, and J. Zmuidzinas (eds.), *Millimeter and Submillimeter Detectors for Astronomy II. Edited by Jonas Zmuidzinas, Wayne S. Holland and Stafford Withington Proceedings of the SPIE, Volume 5498*, pp. 11-29 (2004)., Vol. 5498 of *Presented at the Society of Photo-Optical Instrumentation Engineers (SPIE) Conference*, pp 11-29
- Sandage, A. and Visvanathan, N.: 1978, *Astrophys. J.* **223**, 707
- Santos, J. S., Rosati, P., Tozzi, P., Böhringer, H., and Ettori, S.: submitted, *Astronomy & Astrophysics*
- Sarazin, C. L.: 1986, *Reviews of Modern Physics* **58**, 1
- Sasaki, S.: 1996, *Publ. Astron. Soc. Jpn.* **48**, L119
- Scharf, C.: 2002, *Astrophys. J.* **572**, 157
- Schlegel, D. J., Finkbeiner, D. P., and Davis, M.: 1998, *Astrophys. J.* **500**, 525
- Schneider, P.: 2006a, *Einführung in die extragalaktische Astronomie und Kosmologie*, Peter Schneider. Berlin: Springer
- Schneider, P.: 2006b, in G. Meylan, P. Jetzer, P. North, P. Schneider, C. S. Kochanek, and J. Wambsganss (eds.), *Saas-Fee Advanced Course 33: Gravitational Lensing: Strong, Weak and Micro*, pp 269-451
- Schombert, J. M.: 1986, *Astrophys. J., Suppl. Ser.* **60**, 603
- Schombert, J. M.: 1988, *Astrophys. J.* **328**, 475
- Schuecker, P. and Böhringer, H.: 2003, in S. Bowyer and C.-Y. Hwang (eds.), *Astronomical Society of the Pacific Conference Series*, Vol. 301 of *Astronomical Society of the Pacific Conference Series*, p. 97
- Schuecker, P., Böhringer, H., Guzzo, L., Collins, C. A., Neumann, D. M., Schindler, S., Voges, W., De Grandi, S., Chincarini, G., Cruddace, R., Müller, V., Reiprich, T. H., Retzlaff, J., and Shaver, P.: 2001, *Astronomy & Astrophysics* **368**, 86
- Schuecker, P., Caldwell, R. R., Böhringer, H., Collins, C. A., Guzzo, L., and Weinberg, N. N.: 2003, *Astronomy & Astrophysics* **402**, 53
- Scoville, N., Aussel, H., Brusa, M., Capak, P., Carollo, C. M., Elvis, M., Giavalisco, M., Guzzo, L., Hasinger, G., Impey, C., Kneib, J.-P., LeFevre, O., Lilly, S. J., Mobasher, B., Renzini, A., Rich, R. M., Sanders, D. B., Schinnerer, E., Schminovich, D., Shopbell, P., Taniguchi, Y., and Tyson, N. D.: 2007, *Astrophys. J., Suppl. Ser.* **172**, 1
- Sheth, R. K., Mo, H. J., and Tormen, G.: 2001, *MNRAS* **323**, 1
- Silk, J.: 1976, *Astrophys. J.* **208**, 646
- Smith, J. A., Tucker, D. L., Kent, S., Richmond, M. W., Fukugita, M., Ichikawa, T., Ichikawa, S.-i., Jorgensen, A. M., Uomoto, A., Gunn, J. E., Hamabe, M., Watanabe, M., Tolea, A., Henden, A., Annis, J., Pier, J. R., McKay, T. A., Brinkmann, J., Chen, B., Holtzman, J., Shimasaku, K., and York, D. G.: 2002, *Astron. J.* **123**, 2121
- Spergel, D. N., Bean, R., Doré, O., Nolta, M. R., Bennett, C. L., Dunkley, J., Hinshaw, G., Jarosik, N., Komatsu, E., Page, L., Peiris, H. V., Verde, L., Halpern, M., Hill,

- R. S., Kogut, A., Limon, M., Meyer, S. S., Odegard, N., Tucker, G. S., Weiland, J. L., Wollack, E., and Wright, E. L.: 2007, *Astrophys. J., Suppl. Ser.* **170**, 377
- Springel, V., White, S. D. M., Jenkins, A., Frenk, C. S., Yoshida, N., Gao, L., Navarro, J., Thacker, R., Croton, D., Helly, J., Peacock, J. A., Cole, S., Thomas, P., Couchman, H., Evrard, A., Colberg, J., and Pearce, F.: 2005, *Nature* **435**, 629
- Stanford, S. A., Eisenhardt, P. R., Brodwin, M., Gonzalez, A. H., Stern, D., Jannuzi, B. T., Dey, A., Brown, M. J. I., McKenzie, E., and Elston, R.: 2005, *Astrophys. J., Lett.* **634**, L129
- Stanford, S. A., Elston, R., Eisenhardt, P. R., Spinrad, H., Stern, D., and Dey, A.: 1997, *Astron. J.* **114**, 2232
- Stanford, S. A., Holden, B., Rosati, P., Eisenhardt, P. R., Stern, D., Squires, G., and Spinrad, H.: 2002, *Astron. J.* **123**, 619
- Stanford, S. A., Holden, B., Rosati, P., Tozzi, P., Borgani, S., Eisenhardt, P. R., and Spinrad, H.: 2001, *Astrophys. J.* **552**, 504
- Stanford, S. A., Romer, A. K., Sabirli, K., Davidson, M., Hilton, M., Viana, P. T. P., Collins, C. A., Kay, S. T., Liddle, A. R., Mann, R. G., Miller, C. J., Nichol, R. C., West, M. J., Conselice, C. J., Spinrad, H., Stern, D., and Bundy, K.: 2006, *Astrophys. J., Lett.* **646**, L13
- Stöcker, H.: 1998, *Taschenbuch der Physik*, Frankfurt am Main: Verlag Harri Deutsch
- Stott, J. P., Smail, I., Edge, A. C., Ebeling, H., Smith, G. P., Kneib, J.-P., and Pimbblet, K. A.: 2007, *Astrophys. J.* **661**, 95
- Strazzullo, V., Rosati, P., Stanford, S. A., Lidman, C., Nonino, M., Demarco, R., Eisenhardt, P. E., Etti, S., Mainieri, V., and Toft, S.: 2006, *Astronomy & Astrophysics* **450**, 909
- Struble, M. F. and Rood, H. J.: 1999, *Astrophys. J., Suppl. Ser.* **125**, 35
- Sunyaev, R. A. and Zeldovich, Y. B.: 1972, *Comments on Astrophysics and Space Physics* **4**, 173
- Tanaka, M., Kodama, T., Kajisawa, M., Bower, R., Demarco, R., Finoguenov, A., Lidman, C., and Rosati, P.: 2007, *ArXiv Astrophysics e-prints*, astro-ph/0703135
- Thomas, D., Maraston, C., Bender, R., and Mendes de Oliveira, C.: 2005, *Astrophys. J.* **621**, 673
- Tinsley, B. M.: 1978, *Astrophys. J.* **222**, 14
- Tonry, J. and Davis, M.: 1979, *Astron. J.* **84**, 1511
- Valtchanov, I., Pierre, M., and Gastaud, R.: 2001, *Astronomy & Astrophysics* **370**, 689
- Valtchanov, I., Pierre, M., Willis, J., Dos Santos, S., Jones, L., Andreon, S., Adami, C., Altieri, B., Bolzonella, M., Bremer, M., Duc, P.-A., Gosset, E., Jean, C., and Surdej, J.: 2004, *Astronomy & Astrophysics* **423**, 75
- van Dokkum, P. G. and Franx, M.: 1996, *MNRAS* **281**, 985
- van Dokkum, P. G., Franx, M., Kelson, D. D., Illingworth, G. D., Fisher, D., and Fabricant, D.: 1998, *Astrophys. J.* **500**, 714
- Vikhlinin, A., Burenin, R., Forman, W. R., Jones, C., Hornstrup, A., Murray, S., and Quintana, H.: 2007, in H. Böhringer, G. W. Pratt, A. Finoguenov, and P. Schuecker (eds.), *Heating versus Cooling in Galaxies and Clusters of Galaxies*, p. 48

- Vikhlinin, A., Forman, W., Jones, C., and Murray, S.: 1995, *Astrophys. J.* **451**, 542
- Vikhlinin, A., McNamara, B. R., Forman, W., Jones, C., Quintana, H., and Hornstrup, A.: 1998, *Astrophys. J.* **502**, 558
- Voit, G. M.: 2005, *Reviews of Modern Physics* **77**, 207
- von der Linden, A., Best, P. N., Kauffmann, G., and White, S. D. M.: 2007, *MNRAS* **379**, 867
- Wetterich, C.: 1988, *Nuclear Physics B* **302**, 668
- White, S. D. M.: 1976, *MNRAS* **174**, 19
- White, S. D. M.: 2007, *ArXiv Astrophysics e-prints*, astro-ph/07042291
- White, S. D. M. and Rees, M. J.: 1978, *MNRAS* **183**, 341
- Worthey, G.: 1994, *Astrophys. J., Suppl. Ser.* **95**, 107
- Zhang, Y.-Y.: 2005, *Ph.D. thesis*, Ludwig-Maximilian University Munich
- Zibetti, S., White, S. D. M., Schneider, D. P., and Brinkmann, J.: 2005, *MNRAS* **358**, 949
- Zwicky, F.: 1937, *Astrophys. J.* **86**, 217

List of Figures

2.1	Bullet Cluster	5
2.2	Thermal X-ray Spectra	6
2.3	Cluster Mass Profiles	12
2.4	Cluster Temperature Profiles	13
2.5	Color-Magnitude Diagram for the Lynx Supercluster	22
2.6	Simulated Cluster Ellipticals	24
2.7	Mass Assembly History of BCGs	27
2.8	BCG Model Evolution	28
2.9	BCG Stellar Mass Distribution	28
3.1	Cosmological Distances	36
3.2	Fluxes and Comoving Volumes	36
3.3	Cosmic Time	37
3.4	Cluster Formation Simulations	42
3.5	Halo Number Density	46
3.6	LSS Simulations	47
4.1	X-ray Cluster Survey Comparison	59
4.2	Important Local Survey Results	60
4.3	X-ray Cluster Luminosity Function	60
4.4	NORAS 2 Galaxy Cluster	61
4.5	NORAS 2 Galaxy Cluster Spectra	61
4.6	ROSAT Cluster Number Counts	64
4.7	Distant Cluster RDCS 1252.9-2927	66
4.8	Cone Diagram of Known Galaxy Clusters	66
5.1	XDCP Survey Strategy	69
5.2	XMMU J2235 Properties	74
6.1	XMM-Newton	78
6.2	XMM Vignetting and PSF Functions	82
6.3	XMM PSF Shape	82
6.4	XMM-Newton Archival Fields	84
6.5	XMM-Newton Sky Coverage	84

6.6	Optimized Detection Bands	88
6.7	Detection Band Schemes	88
6.8	X-ray Pipeline Flow Chart	89
6.9	X-ray Flare Cleaning	92
6.10	X-ray Source Detection Products	95
6.11	Wavelet Source Detection	99
6.12	X-ray-Optical Overlays	102
6.13	Source Screening Flow Chart	105
6.14	Flagging Scheme	109
6.15	Classification Prototypes	109
6.16	DSS Identification Limit	111
6.17	Redshift Distribution of Identified COSMOS Clusters	113
6.18	Space Weather Seasons	115
6.19	XDCP Survey Field Statistics	116
6.20	Extent Likelihood versus X-ray Source Counts	118
6.21	Comparison of Detection Schemes	119
6.22	Cluster Detections versus Off-axis Angle	119
7.1	CMD Models	122
7.2	Redshift Uncertainties of Red Sequence Methods	129
7.3	OMEGA2000 Instrument Response	130
7.4	NIR Science Reduction Pipeline Flow Chart	136
7.5	NIR Science Reduction Steps	137
7.6	Faint Object Optimization	144
7.7	Advanced Reduction Schemes	145
7.8	Abell 383 Field	149
7.9	NIR Number Counts	151
7.10	NIR Photometric Analysis	152
7.11	Photometric Calibration	159
8.1	Spectral Sky Features	167
8.2	Spectroscopy Reduction Flow Chart	169
9.1	XDCP Sky Coverage	174
9.2	Raw $\log N$ - $\log S$ of XDCP Clusters	176
9.3	Extent Properties of XDCP Candidates	177
9.4	Calar Alto Imaging Cluster Sample	182
10.1	Z-H Evolution of the Red-Sequence	188
10.2	Formation Redshift of Ellipticals	189
10.3	Calibration Clusters A	192
10.4	Calibration Clusters B	193
10.5	Spectroscopic Confirmation of XMMU J0104.4-0630	194
10.6	CMD of XMMU J0104.4-0630	196

10.7 Galaxy Overdensities in the Field of XMMU J0104.4-0630	197
10.8 Galaxy Populations of XMMU J0104.4-0630	198
11.1 BCG Selection	202
11.2 BCG Hubble diagram	204
11.3 BCG Absolute Magnitudes	205
11.4 BCG K -correction	205
11.5 BCG Luminosity Evolution	208
11.6 BCG Assembly Models	209
11.7 High-redshift BCG gallery.	216
11.8 Low-redshift BCG gallery.	217
11.9 High-Redshift Cluster Gallery A.	221
11.10 High-Redshift Cluster Gallery B.	222
12.1 South Pole Telescope and eROSITA	224
12.2 VADER Spacecraft and Survey Region	229

List of Tables

2.1	Cluster Scaling Relation	15
3.1	Cosmological Concordance Parameters	37
3.2	Cosmological Tests with Galaxy Clusters	55
5.1	Properties of XMMU J2235.3-2557	73
5.2	Thesis Data Overview	75
6.1	XMM-Newton in a Nutshell	81
7.1	XDCP Filters	123
7.2	Apparent Magnitude Evolution	124
7.3	Summary of Imaging Methods	129
7.4	OMEGA2000 Characteristics	131
7.5	NIR Data Overview	134
8.1	Spectral Galaxy Features	165
9.1	Spectroscopically Confirmed $z > 1$ X-ray Clusters	185
10.1	X-ray Properties of XMMU J0104.4-0630	196
12.1	Expected VADER Results	226
A.1	XDCP Survey Fields	231

Acknowledgements

It is my pleasure to thank Hans Böhringer for being a superb supervisor, for giving me valuable advice when needed, for encouraging new projects and initiatives, for supporting new ideas and approaches, for sponsoring frequent travel, and for always spreading a positive, open attitude.

This thesis is dedicated to the late Peter Schuecker, my mentor and advisor, whose enthusiasm and love for the beauty of the Universe has been truly inspiring and will continue to live on.

I am indebted to many other people who contributed to this thesis either scientifically, financially, with moral support, or just by making MPE a great place to work. I would like to thank Prof. Gregor Morfill for his support over the years, his bottles of wine for late work sessions, and for being a humorous office neighbor. I thank Wolfgang Voges for being a great thesis committee member and for his encouragement.

Furthermore, I am grateful to the whole XDCCP team. Special thanks go to Chris Mullis for getting me started, Georg Lamer for his X-ray help, and Joana Santos for helping with the observations. I am also indebted to the Calar Alto staff for their support, with additional thanks to Aurora Simionescu and Filiberto Braglia for their participation. I have also enjoyed the CTIO observing run and the ongoing work with Joe Mohr. Special thanks go to Hermann-Josef Röser for the support of OMEGA2000, the active exchange of ideas and codes, and his advice. Thanks also to Harald Baumgartner and Joachim Paul for their essential technical support over the years.

My office mate Gabriel Pratt deserves special thanks for putting up with me, for the convivial work atmosphere, his X-ray support, and all the proofreading. I would also like to thank Alexis Finoguenov for sharing his expertise, data, and money with me. Very warm final thanks go to Daniele Pierini for providing all the models, galaxy expertise, guidance, and proofs, and to Martin Mühlegger for his careful reading and cheerful personality.

